



Isotope-Labeling Studies in Electrocatalysis for Renewable Energy Conversion

Scott, Søren Bertelsen

Publication date:
2019

Document Version
Publisher's PDF, also known as Version of record

[Link back to DTU Orbit](#)

Citation (APA):
Scott, S. B. (2019). *Isotope-Labeling Studies in Electrocatalysis for Renewable Energy Conversion*. Technical University of Denmark.

General rights

Copyright and moral rights for the publications made accessible in the public portal are retained by the authors and/or other copyright owners and it is a condition of accessing publications that users recognise and abide by the legal requirements associated with these rights.

- Users may download and print one copy of any publication from the public portal for the purpose of private study or research.
- You may not further distribute the material or use it for any profit-making activity or commercial gain
- You may freely distribute the URL identifying the publication in the public portal

If you believe that this document breaches copyright please contact us providing details, and we will remove access to the work immediately and investigate your claim.

Ph.D. Thesis

Isotope-Labeling Studies in Electrocatalysis for Renewable Energy Conversion

And the net CO₂ impact of this PhD Project

Søren Bertelsen Scott

Supervisor: Professor Ib Chorkendorff

Technical University of Denmark

Department of Physics
Surface Physics and Catalysis (SurfCat)
Villum Center for the Science of Sustainable Fuels and Chemicals

July 2019

Abstract

This thesis presents methods and results for isotope-labeling studies in oxygen evolution reaction (OER) electrocatalysis. The OER is an essential reaction for a transition to a fossil-fuel-free society. The OER is the main source of efficiency loss in the production of hydrogen by water electrolysis. Hydrogen from water electrolysis, in turn, is key for storing wind and solar energy and for using wind and solar electricity to decarbonize other sectors such as industry and transport. The first chapter of this Thesis puts this technological motivation in the context of the urgent need to mitigate climate change.

The second chapter describes and demonstrates the tools used in the isotope-labeling electrocatalysis studies. The primary tool is electrochemistry-mass spectrometry (EC-MS). The version of EC-MS used in this Thesis involves a silicon microchip to make the interface between the high vacuum of the mass spectrometer and the wet ambient environment of the electrochemistry experiment. The advantages of this technique, chip EC-MS, are high sensitivity, well-characterized mass transport, and the ability to dose reactant gases.

Isotope labeling studies are introduced with two examples. The first is an attempt to directly measure the hydrogen evolution exchange current density on platinum by electrochemical H-D exchange, which is however demonstrated to be mass-transport limited. The second is a set of CO stripping and CO oxidation experiments in labeled electrolyte (H_2^{18}O), which lead to a new way to probe the kinetics of the reaction of CO_2 and H_2O to form carbonic acid.

The third chapter is devoted to oxygen evolution electrocatalysis. The two main water electrolyzers, alkaline electrolyzer cells (AEC) and polymer electrolyte membrane electrolyzer cells (PEMEC), are briefly discussed in the context of the OER catalysts required. Then, the importance of measuring O_2 is demonstrated with two examples in which the electrochemical current would overestimate the OER activity. This motivates the study with EC-MS of oxygen evolution on RuO_2 , one of the only materials (together with IrO_2) that can catalyze the OER in the acidic environment of a PEMEC. Using isotope-labeled electrolyte to increase sensitivity, I measured the O_2 produced by a series of RuO_2 films and Ru foams down to a record low 1.29 V vs RHE. All of these samples follow approximately the same trend of turn-over-frequency (TOF) vs potential with a very strong potential dependence at low overpotentials.

The involvement of lattice oxygen in the oxygen evolution mechanism has received a lot of research attention in recent years. This is investigated by preparing an OER catalyst with one isotope of oxygen (^{16}O or ^{18}O) and measuring the isotopic composition of the O_2 evolved in an electrolyte with a different isotopic composition than the catalyst. I present a comprehensive comparison of these studies, with views on the advantages and disadvantages of the methods employed. Using RuO_2 and IrO_2 samples as examples, and coupling the high sensitivity of chip EC-MS with dissolution measurements by inductively coupled plasma - mass spectrometry (ICP-MS) and surface isotopic characterization by ion scattering spectroscopy (ISS), I show that lattice oxygen evolution does not necessarily mean lattice oxygen exchange. In other words, an isotope signal in the oxygen evolved from a labeled OER catalyst does not necessarily imply that lattice oxygen plays an important

catalytic role. Non-catalytic evolution of lattice oxygen is demonstrated to be the case for sputter-deposited Ru¹⁸O₂.

In the last experiments presented in this thesis, CO oxidation is used as a probe for lattice oxygen reactivity. Under the right conditions, isotope-labeled oxygen from the catalyst is incorporated in the CO₂ produced. These experiments can also be used as an *in-situ* proof that there is labeled oxygen at the surface of the electrocatalyst, for example after a negative result for lattice oxygen evolution in OER.

The final chapter ties the studies presented in this Thesis back to the motivation by estimating the amount of CO₂ emissions avoided by a marginal improvement in electrolyzer efficiency. Using a simple model and literature-based assumptions about the future European energy system, I find that to achieve a one-year payback time on the CO₂ costs of my PhD project by 2030 only requires that the results present here lead to an 0.03 mV improvement in the OER overpotential of electrolysis cells.

The Chapters of this thesis present a mix of published and as-of-yet unpublished results, and only a subset of the work done during my PhD project. The articles to which work from my PhD project have contributed are attached.

Resumé

Denne afhandling præsenterer metoder for og resultater fra isotopmærkningsstudier i iltudviklingsreaktion (OER) elektrokatalyse. OER er en essentiel reaktion for overgangen til en samfund uden fossile brændstoffer. OER er til grund for den primære kilde til effektivitets-tab i hydrogenproduktionen ved elektrolyse af vand. Hydrogen fra elektrolyse er blandt de bedste løsninger oplagring af energi fra vind og sol, og også for anvendelse af elektricitet fra vind og solenergi for at sænke CO₂ aftrykket i sektorer som industri og transport. Afhandlingens første kapitel sætter denne teknologisk motivation i klimakrisens kontekst.

Andet kapitel beskriver og demonstrerer de videnskabelige værktøjer som bruges til disse isotopmærkningsforsøg. Den primære værktøj udgøres af en version af enkeltkemimassespektrometri (EC-MS) som anvender en silicium mikrochip som interfase mellem massespektrometrets højvakuum og det våde miljø ved atmosfærisk tryk som det elektrokemiske forsøg udgør. Fordelene for denne teknik, som kaldes chip EC-MS, er høj følsomhed, velforstået massetransport, og muligheden for at dosere reaktantgasser.

Isotopmærkningsstudier bliver heri introduceret med to eksempler. Det første er et forsøg på direkte at måle udvekslingsstrømmen på platin ved brug af elektrokemisk H-D udveksling. Dette forsøg vises dog til at være begrænset af massetransport. Det andet eksempel er en serie CO stripping og CO oxidationsforsøg i isotop-mærket elektrolyt (H₂¹⁸O), som giver en måde at måle kinetikken for dannelse af kulsyre fra CO₂ og vand.

Afhandlingens tredje kapitel omhandler den elektrokatalytiske oxygenudviklingsreaktion. To primære elektrokatalyse teknologier, AEC og PEMEC, diskuteres kort i kontekst af de respektive påkrævede OER katalysatorer. Efterfølgende demonstreres vigtigheden af at måle O₂ i to eksempler, hvor den elektrokemisk målte strøm ville overvurdere OER aktiviteten. Dette motiverer undersøgelsen af ilt-udviklingen på RuO₂ med chip EC-MS. RuO₂ er der et af de eneste materialer (samt IrO₂) som kan katalysere OER i det syre miljø i en PEMEC. Ved brug af isotopmærket elektrolyt for at hæve følsomheden, måles ilt produceret af en og RuO₂ film og Ru skum ved rekordlave potentialer ned til 1.29 V vs RHE. Alle disse prøverne tilnærmelsesvis samme opførsel for omsætningsfrekvens (TOF) som funktion af potentialer, med meget stærk potentialafhængighed ved lave overpotentialer.

Hvorvidt oxygen fra et metaloxids krystalgitter medvirker til OER mekanismen har været stærkt omdiskuteret i de seneste år. Det undersøges ved brug af en OER katalysator med én isotop af oxygen (¹⁶O eller ¹⁸O), der anvendes til at udvikle ilt i en elektrolyt med end anden isotopisk sammensætning en katalysatoren. I denne afhandling sammenlignes disse studier fra litteraturen med henblik på de anvendte metoders fordele og ulemper. Ved anvendelse af en kombination af den høje følsomhed for chip EC-MS, måling af opløste metaller ved brug af ICP-MS og isotop karakterisering af prøverens overflade ved brug af ISS på RuO₂ og IrO₂, konkluderes der at iltudvikling fra oxygen i gitteret ikke nødvendigvis betyder udveksling af ilt i gitter. Sagt med andre ord, et isotop signal i den ilt udviklede fra en isotopmærket OER katalysatorer betyder ikke nødvendigvis at gitter ilt spiller en vigtig katalytisk rolle. Ikke-katalytisk udvikling af ilt med oxygen fra gitteret er påvist at være tilfældet for sputterdeponerede Ru¹⁸O₂.

I de sidste forsøg præsenteret her bruges CO oxidation som sonde for reaktiviteten af

oxygen i gitter. Under visse betingelser inkorporeres isotop-mærket oxygen i den resulterende CO_2 . Disse forsøg kan også anvendes som *in-situ* bevis for at der er isotopmærket oxygen ved elektrodens overflade, for eksempel efter et negativ resultat for udvikling af oxygen fra gitteret under OER.

I afhandlingens sidste kapitel kobles arbejdet tilbage til motivationen ved at estimere mængden af CO_2 udledning, der bliver reduceret ved en marginal forbedring i effektiviteten af elektrolyse af vand. Ved brug af en simpel model og literaturbaseret antagelse om Europas fremtidige energisystem, vurderes det at CO_2 forbruget i forbindelse med mit PhD project kan opvejes inden for et år hvis blot de opnåede resultater fra projektet sænker overpotentialen for OER i elektrolyseceller med 0.03 mV.

Afhandlingens kapitler præsenterer en blanding af publicerede og ikke-publicerede resultater i kun ét af de emner der blev udforsket i dette PhD projekt. Samtlige artikler, hvor jeg har været medvirkende, er vedhæftet.

Foreword

This Thesis

I had a goal of writing a short Thesis. I must apologize to the reader that I have failed at that. I ran out of time, and so it is long.

The tone is informal, and I've tried to make it read like a story, with each Section setting the stage for the next. I haven't held back in writing my thoughts, describing the uncertainties and mistakes in the experiments presented here and even in the Papers, as well as things that I found especially exciting. I hope that this informal tone helps make it easy to read, so that it doesn't feel quite as long as the number of pages reveals it to be.

I have tried at the same time to organize the Thesis in such a way that it can be jumped around in:

Some readers may not be especially interested in electrocatalysis or mass spectrometry or isotope labeling, but are instead drawn by the subtitle of this Thesis and by the first Section title, "How much needs to change and how fast." Such readers only need Chapters 1 and 4, which are admittedly much briefer than they have any right to be given the richness of the subject matter. I saved Chapters 1 and 4 to write last, and that was a good idea, because otherwise I could have spent the whole time available learning about the climate crisis, emissions reduction policy, and energy systems modeling.

A reader who wants the full story but is pressed for time can skip Section 2.2 (which I think is valuable, but a side story) and all of the Subsections of 3.3 (which chronicle learning-by-doing) without missing too much. A reader who only wants a representative sample both of the fun and the finished isotope studies could just read Subsections 2.3.1 and 2.3.2, and then jump to Section 3.4.

I've tried also to make this Thesis useful to potential readers. Some might only be interested in 2.2, which presents strategies for using electrochemistry-mass spectrometry as a platform for absolute quantification. There is an appendix describing some of the experimental procedures. I hoped to make a tutorial describing the use of EC_MS data analysis python package which I developed and used for almost all of the results and plots presented in this Thesis, but did not get to it by the hand-in date, and so instead provide a link to where it will be.

If I had stuck to the original outline for this Thesis, it might have become even longer. I had planned consecutive chapters called "Hydrogen" and "Oxygen", but realized that I had run out of time to do the additional experiments necessary to justify writing the Hydrogen chapter.

I had the opportunity to work with a lot of great people and become in a lot of projects during this PhD. This, and my poor control for length, made it essential to choose one topic to focus on. Isotope studies are the part of my PhD Project that I have felt the most personal ownership for, and thus which seemed most appropriate to express the medium of a PhD Thesis.

Acknowledgements

I really appreciate all the fantastic people I've gotten to work together during this PhD project, including many who have graduated or gone on to other exciting things. During the first year of the PhD I was treated routinely to exciting and enlightening lunchtime conversations with Robert Jensen and Kenneth Nielsen. I also really enjoyed all the time I got to spend with Anders Bodin, Bela Sebok,

Claudie Roy, and Daniel Trimarco, among others, and I'm glad our PhD periods overlapped. Daniel especially deserves credit for being a constant team-mate my first year, and for the visionary design and implementation of our electrochemistry-mass spectrometry system. I also want to shout out to Erlend Bertheussen, Thomas Hogg, and Thomas Maagaard, with whom I had a lot of fun going to beam times. It would take a while to mention all the PhD students and postdocs in our group and beyond that I've enjoyed working with, and so instead I've often mentioned these fantastic people in the text of this Thesis when describing what we've worked on together or are still working on.

The co-author lists on the attached Papers also give a sense of how many great scientists I've gotten to work with. I appreciate the valuable conversations with Brian Seger, Peter Vesborg, Jakob Kibsgaard, Ifan Stephens, and Jan Rossmeisl, among others. One especially deserves thanks: my principle supervisor, Ib Chorkendorff. Ib has fostered a fantastic environment in our research group. He is open and honest, quick to give feedback, demanding but kind, always motivating, and full of scientific wisdom and experience. It has been an honor to work with and learn from him, and I'll be proud if I can ever lead a scientific group (or anything) nearly as well as he does.

In the wider world, I'm grateful for conversations with my neighbors Anjila Wegge and Søren Storgaard, who have taught me a lot from outside my physics/chemistry bubble about climate and energy. I also want to express my appreciation for Rachel Woods-Robinson, who has been an important source of inspiration and encouragement during this PhD project.

Finishing a PhD project is hard. Not just because of the thesis writing process, but also because of the life transition that it represents. I can't thank enough all of the people who have helped me get through the past several months with their support. Thanks to my friends and colleagues including but not limited to Anders Bjerrum, Cille Kvium, Thomas Hogg, Grith Martinsen, Anjila Wegge, Lars Hemmingsen, Stefan Laage, Alexander Krabbe, Valeria Magri, George Kozlov, Peter Huggler, Melih Erdem, Maike Schäffer, Chioma Nri, the rest of Konvencio and Admi, my band Los Kaminantes, Mille, Mathias, Anders, Marianne, and many more important and wonderful people. Thanks especially to my family who have cheered me on from across the pond. Mom, dad, brotherman Stoff, sistergirl Sofie: I don't think I could have made it through this without you.

Dedication

Finally, I would like to dedicate this thesis to all of the climate activists who are pushing our reluctant societies into action.

The work of scientists, engineers, entrepreneurs, and politicians in understanding the crisis and turning it around is courageous and essential. But people working in these professions, including myself, are also investing in a prestigious career which they know will likely open the door to other options if the funding or markets or votes moved to other priorities. Not all of us would necessarily take such a plan B, but we should still remember that activists in contrast in general have no such security when they sacrifice their sweat and more to push us in the right direction. The volunteers and organizers of Greenpeace, Extinction Rebellion, Ende Gelände, Fridays for Future, Den Grønne Studenterbevægelse, 350, and so many other organizations, as well as everyone who gets out on the streets for climate marches: You have my intense respect and gratitude. You are forcing the health of our planet to the top of our attention and calling our societies to action.

Question 1.1 of this Thesis is *How can we cut our emissions to half or less by 2030?.* It is largely because of activists that so many of us today are focused on this and similar questions. We need even more people on board finding and implementing the answers, so, activists, please keep up your work.

List of Papers

The Chapters of this Thesis do not seek to repeat or summarize any of the papers I have been involved in, but instead to tell an independent story which sometimes comments and expands on the papers. Furthermore, while the Thesis does not cover all of what I've done during my PhD, it would not make complete sense to choose some of the papers to call within the scope of the thesis and leave the others out. All of the papers contributed to my thinking during this PhD project, and all are mentioned in the Chapters of the Thesis, if only in passing. They are therefore all included here indiscriminately, in order of publication or expected publication. Nonetheless, some are of course more central than others. Chapter 2 comments and expands on Paper I, and takes inspiration from work done behind the scenes of Paper III. Chapter 3 includes and comments on some of the most important results of Paper II and includes most of the content of what we expect to publish as Paper VII.

Paper V is notable among them for being a review and perspective article. My most important contribution to this work was writing the introduction, which includes an outline of the anthropogenic contribution to the global carbon cycle and strategies to close it. While in Paper V, this outline is used to motivate the direct electrocatalytic reduction of CO₂, it also motivates improving the efficiency and cost-effectiveness of hydrogen production via water splitting. Because Paper V is very long, I have only included the introduction in this thesis.

Here is the full list:

Paper I page 129
Enabling Real-Time Detection of Electrochemical Desorption Phenomena with Sub-Monolayer Sensitivity

Soren B. Scott*, Daniel B. Trimarco*, Anil H. Thilsted, Jesper Y. Pan, Thomas Pedersen, Ole Hansen, Ib Chorkendorff, and Peter C.K. Vesborg.

*These authors contributed equally to this work

Electrochimica Acta, 2018, 268, 520-530

DOI: 10.1016/j.electacta.2018.02.060

Paper II page 141

Impact of nanoparticle size and lattice oxygen on water oxidation on NiFeO_xH_y

Soren B. Scott*, Claudie Roy*, Bela Sebok*, Elisabetta M. Fiordaliso, Jakob E. Srensen, Anders Bodin, Daniel B. Trimarco, Christian D. Damsgaard, Peter C. K. Vesborg, Ole Hansen, Ifan E. L. Stephens, Jakob Kibsgaard and Ib Chorkendorff.

*These authors contributed equally to this work

Nature Catalysis, 2018, 1(11), 820-829

DOI: 10.1038/s41929-018-0162-x

Paper III page 152
Towards an Atomistic Understanding of Electrocatalytic Partial Hydrocarbon Oxidation: Propene on Palladium

Anna Winiwarter*, Luca Silva*, Soren B. Scott, Kasper Enemark-Rasmussen, Manuel Saric, Daniel B. Trimarco, Peter C. K. Vesborg, Poul G. Moses, Ifan E. L. Stephens, Brian Seger, Jan Rossmeisl, and Ib Chorkendorff.

*These authors contributed equally to this work

Energy and Environmental Science, 12, 1055-1067, 2019.

DOI: 10.1039/C8EE03426E

Paper IV

page 166

Absence of Oxidized Phases in Cu under CO Reduction Conditions

Soren B. Scott, Thomas V. Hogg, Alan T. Landers, Thomas Maagaard, Erlend Bertheussen, John C. Lin, Ryan C. Davis, Jefferey W. Beeman, Drew Higgins, Walter S. Drisdell, Apurva Mehta, Brian J. Seger, Thomas F. Jaramillo, and Ib Chorkendorff.

ACS Energy Letters. 4, 803804, 2019

DOI: 10.1021/acsenergylett.9b00172

Paper V

page 169

Progress and Perspectives of Electrochemical CO₂ Reduction on Copper in Aqueous Electrolyte

Stephanie A. Nitopi*, Erlend Bertheussen*, Soren B. Scott, Xinyan Liu, Albert K. Engstfeld, Sebastian Horch, Brian Seger, Ifan Stephens, Karen Chan, Christopher Hahn, Jens K. Nrskov, Thomas Jaramillo, and Ib Chorkendorff.

*These authors contributed equally to this work

Chemical Reviews. 12, 7610-7672, 2019

DOI: 10.1021/acs.chemrev.8b00705

Paper VI

page 183

Desorbing uphill: Anodic Hydrogen Evolution on Cu and Ru Electrodes

Sren B. Scott*, Albert K. Engstfeld*, Zenonas Jusys, Degenhart Hochfilzer, Nikolaj Knsgaard, Daniel B. Trimarco, Peter C.K. Vesborg, R. Jrgen Behm, and Ib Chorkendorff

*These authors contributed equally to this work

In Preparation

Paper VII

page 195

Mechanistic study of oxygen evolution on RuO₂ down to 60 mV overpotential

Soren B. Scott*, Reshma R. Rao*, Choongman M. Moon, Jakob E. Sørensen, Jakob Kibsgaard, Yang Shao-Horn, and Ib Chorkendorff

*These authors contributed equally to this work

In Preparation

Contents

Abstract	ii
Resumé	v
Foreword	vii
List of Papers	ix
1 Introduction: The Climate Crisis	1
1.1 How much needs to change, and how fast?	4
1.2 Electrocatalysis: An important piece of the answer	9
2 The Right Tools to Answer the Right Questions	17
2.1 Eelectrochemistry - mass spectrometry	19
2.1.1 Chip EC-MS: working principle	21
2.1.2 Example experiments: RHE potential measurement and CO stripping	24
2.1.3 Disadvantages	26
2.2 Quantitative mass spectrometry: counting molecules	30
2.2.1 Internal calibration by electrochemistry	30
2.2.2 External calibration based on the capillary flux	36
2.2.3 Sensitivity factors from theory, and non-ideal effects	38
2.2.4 Quantitative mass spectrometry in practice - methanol synthesis and CO reduction	40
2.3 Isotope labeling: tracking atoms	45
2.3.1 Example experiment: RHE potential measurement in D ₂ O	46
2.3.2 Example experiment: CO stripping in H ₂ ¹⁸ O electrolyte	49
2.3.3 Labeling the vacuum chamber	54
2.3.4 Other tools: Sputter deposition, ISS, and ICP-MS	56
3 Isotope-Labeling Studies in Oxygen Evolution Catalysis	61
3.1 You have to see the O ₂ !	63
3.1.1 Ru on graphene oxide	63
3.1.2 Nickel-iron: electrodeposited film vs annealed nanoparticles	64
3.2 How low can we go?	67
3.2.1 Sputtered RuO ₂ films	67
3.2.2 Hydrogen-bubble-template Ru foam	69
3.2.3 Turn-over-frequencies	71
3.2.4 The effect of O ₂ in the electrolyte	74
3.3 To leave or to remain in the lattice	77
3.3.1 Determining the TOF in NiFe nanoparticles	80
3.3.2 A contradiction	87
3.3.3 Electrochemically labeled RuO ₂ films	87
3.3.4 Using CO to get out the lattice oxygen	92

3.4	Evolving vs dissolving	99
3.4.1	Sputtered Ru ¹⁸ O ₂ and Ir ¹⁸ O ₂ films	99
3.4.2	Electrochemically labeled films	102
3.4.3	Exchange and extraction	103
3.4.4	Conclusion and perspective on oxygen evolution experiments	106
4	The Net Carbon Impact of this PhD	109
4.1	Burning	110
4.2	How much difference a millivolt makes	112
5	Conclusion	115
A	Setup and technique details and instructions	117
A.1	Sniffer setup at DTU	118
A.2	ECMS-200A at CAS in Fuzhou	121
A.3	Spectro Inlets	123
A.4	Sputtering Ru ¹⁸ O ₂ and Ir ¹⁸ O ₂	124
A.5	ICP-MS	126
B	Papers from this PhD Project	129
I	Enabling real-time detection of electrochemical desorption phenomena with sub-monolayer sensitivity	129
II	Impact of nanoparticle size and lattice oxygen on water oxidation on NiFeO _x H _y	141
III	Towards an Atomistic Understanding of Electrocatalytic Partial Hydrocarbon Oxidation: Propene on Palladium	152
IV	Absence of Oxidized Phases in Cu under CO Reduction Conditions	166
V	Progress and Perspectives of Electrochemical CO ₂ Reduction on Copper in Aqueous Electrolyte	169
VI	In Preparation - Desorbing uphill: Anodic Hydrogen Evolution on Cu and Ru Electrodes	183
VII	In Preparation - Mechanistic study of oxygen evolution on RuO ₂ down to 60 mV overpotential	195
C	Python Packages Developed During this PhD Project	197
C.1	EC_MS	197
C.2	EC_Xray	198
	Bibliography	199

Chapter 1

Introduction: The Climate Crisis

It was right around the year in which I was born that the American political economist Francis Fukuyama captured the mood of much of the world by claiming that history was ending [1]. This feeling was based on the fall of the Berlin wall and with it what seemed like the inevitable spread to the entire world of societal structures and lifestyles based on inclusive liberal democracy, technological progress, and market capitalism tempered to varying extent by regulatory welfare states. Now, a widely accepted view that history was ending seems itself to be part of a rather brief moment in history, shattered by several waves of headline-dominating setbacks to the advancement of these supposedly victorious ideals. But nothing poses a more devastating blow to the supposed inevitability of our lifestyles and societies than does the fact that they are simply unsustainable. History is not over, because if we try to keep on living the way we do today, we won't be able to keep living on this planet.

The un-sustainability of humanity in its present state encompasses the crossing of or encroaching on multiple interconnected planetary boundaries [4], but none pose a more existentially urgent challenge to human civilization than does climate change. The root of our problem, as we summarize it in the

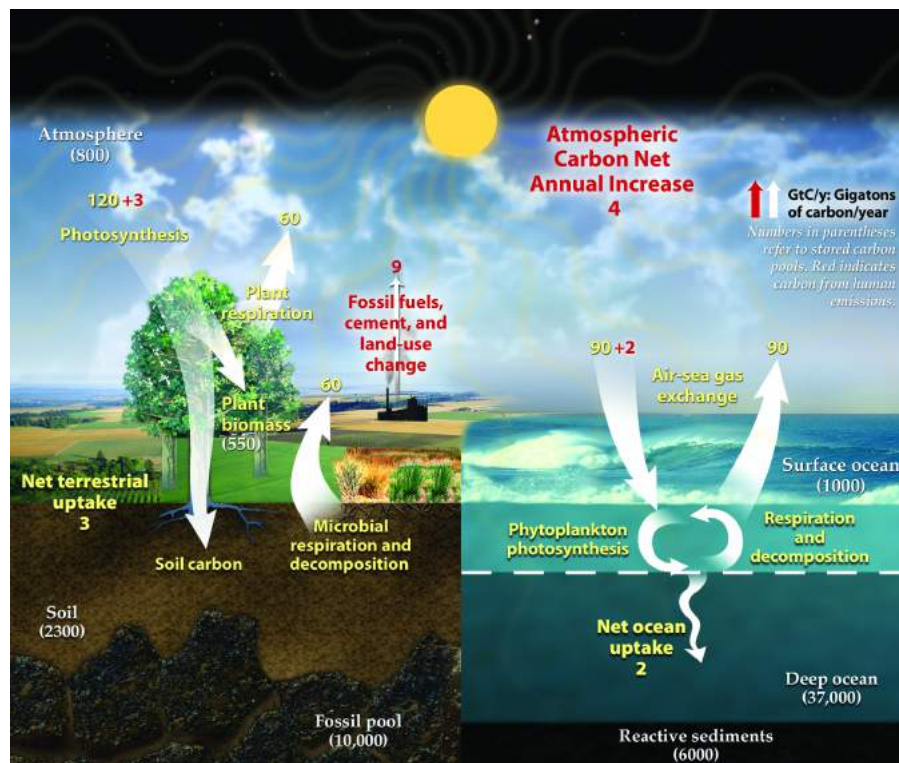


Figure 1.1: Diagram of Earth's carbon cycle. Red numbers indicate the fluxes and accumulations associated with the anthropogenic perturbation. From ref. 2, based on data from ref. 3

introduction to Paper V, is that:

“ At the core of biological metabolism is the ability to convert carbon between different oxidation states in order to store and release energy, as well as to synthesize functional molecules. Likewise, the oxidation of carbon is at the center of human civilization’s collective industrial metabolism consisting of our energy infrastructure and chemical industry. Whereas in biological metabolism, reduction of CO_2 in photosynthesis balances the oxidation of carbon in cellular respiration, carbon reduction is as of yet a missing piece of humanity’s industrial metabolism. This imbalance has become a significant perturbation to Earth’s natural carbon cycle... The resulting accumulation of the greenhouse gas CO_2 in the atmosphere is the primary driver of today’s climate change [5]. ”

This imbalance is illustrated in Figure 1.1 (from ref. 2) and in Table 1 of Paper V. So far, since humans began burning fossil fuels at scale in the 1800’s, we have moved approximately 400 gigatons of carbon (GtC) from the ground to the air as carbon dioxide (CO_2), about half of which has stayed in the atmosphere, increasing the atmospheric CO_2 concentration from less than 300 ppm to more than 400 ppm [5, 6]. At the writing of this Thesis, the atmospheric CO_2 concentration was 412 ppm and increasing at an annualized rate of about 3 ppm per year [7].

Climate science is beyond the scope of this Thesis, but, in brief: CO_2 and other greenhouse gases absorb infrared radiation, unlike the primary components of the atmosphere N_2 and O_2 . Infrared radiation is the main way earth sheds heat to space to balance all the energy coming in as sunlight, so CO_2 in the atmosphere acts like a blanket, heating up the earth. This has so far resulted in an increase in the average temperature of the earth’s surface of about 1°C , as shown in Figure 1.2. An increase in the average temperature of the earth is worse than it might sound, because the extra energy that this represents effects the entire climate system in profound ways. Climate change is increasing the intensity and frequency of all kinds of extreme weather events including heat waves, forest fires, floods, storms, and droughts [5, 10]. Weather is naturally variable, but the science of *climate attribution* has progressed in recent years. Now, the increase in the likelihood due to climate change of a given extreme weather event can be readily calculated, giving a clear picture of the worsening adverse effects of our

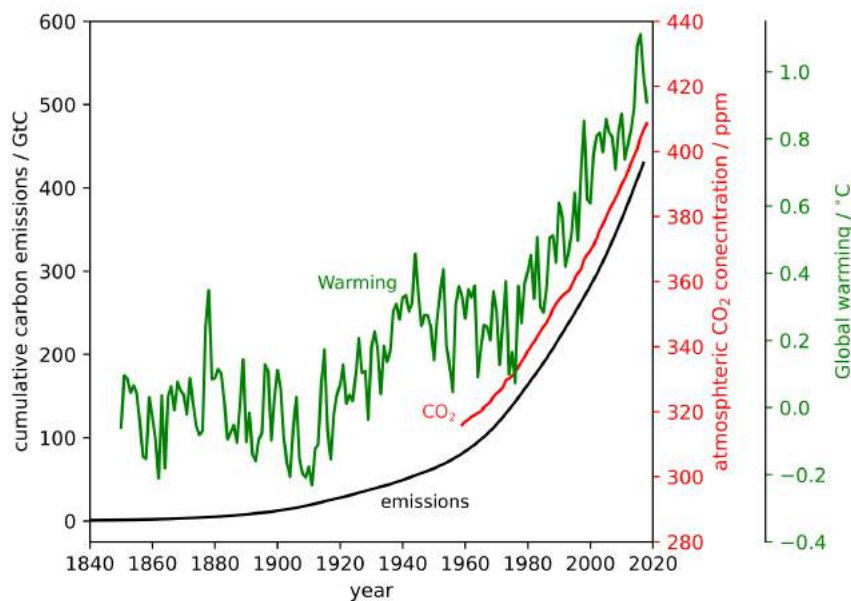


Figure 1.2: Cumulative carbon emissions (black), atmospheric CO_2 concentration (red), and global mean surface temperature relative to the 1850-1900 average (green). Made with data from refs. 6, 8, and 9.



Figure 1.3: Map of extreme weather events from 2011 to 2018. Red indicates that the risk of the extreme weather event was increased by climate change. From ref 10.

emissions [11]. Figure 1.3, from ref. 10, shows a map of recent extreme weather events, many of which are attributed to climate change. Extreme weather events and natural disasters are deadly even in developed countries with strong states. In developing countries they can destabilize societies and displace millions [12]. The frequency and severity of climate-change-related extreme weather events will worsen significantly if the present warming trend is not stopped [13].

Fortunately for those of us who broadly like living under or aspire to live under enlightenment ideals (and for Fukuyama's assertion), there is still reason to hope that the worst possible outcomes of climate change can be averted within the frameworks of liberal democracy and regulated market capitalism. However, this will not be easy. It will require far-sightedness on the part both of leaders and of everyone who chooses them. It will require almost unprecedented willpower from many corners of society. We will almost certainly need to change our lifestyles significantly, and we will with complete certainty have to change the way we power our lives entirely.

The scale and scope of these required changes, both societal and technological, is outlined (very briefly) in the first Section of this Chapter. The second Section describes a central component to the required technological changes: a growing role for electrochemistry in decarbonizing energy, transport, and industry. This will motivate Chapters 2 and 3 and all of the Papers, which describe methods and results in fundamental electrocatalysis studies which will hopefully contribute to breakthroughs accelerating electrochemistry's growing role. Finally, in Chapter 4, the Thesis ties these results back to the climate crisis by estimating the net CO₂ impact (emitted minus saved) resulting from this PhD project.

1.1 How much needs to change, and how fast?

The Paris Climate Accord commits its signatories to limiting global warming to “well below” 2.0°C and preferably to within 1.5°C [14]. 2.0°C has long been considered an essential goal to avoid severe damage to earth systems and possible run-away effects [5,15,16]. The inclusion of the more audacious 1.5°C ambition was an unexpected but welcome and important development in the 2015 negotiations leading up to the Paris Climate Accord. A 2018 report from the Intergovernmental Panel of Climate Change (IPCC), called the SR15 in their jargon, emphasized what is at stake in the difference between these two targets [13]. Some of the differences in the risks posed by 2.0 vs 1.5°C are shown in Figure 1.4, taken from that report. Risks posed to ecosystems and human quality of life are much higher at 2.0°C than 1.5°C.

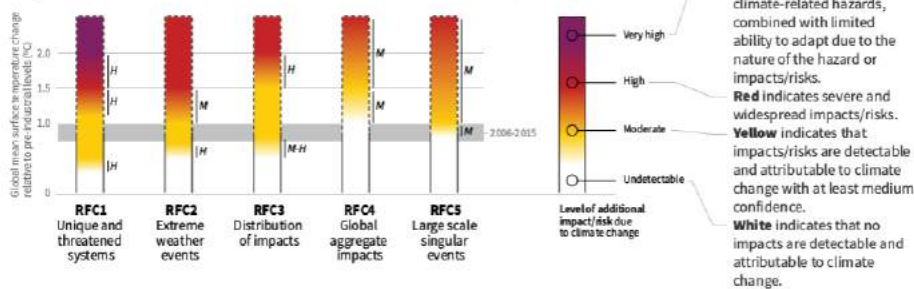
Carbon budgets are a powerful, if also a bit simplistic [17], way to think about the societal changes necessary to stay within a global warming target. The carbon budget remaining to have a 67% chance of confining global warming to 1.5°C is about 160 GtC (570 Gt CO₂) [18]. In other words, with 160 additional gigatons of carbon added to the air as CO₂, 67% of simulations using various climate models predict that the average temperature will remain within 1.5°C of the pre-industrial baseline. Temperature increase is approximately linear with cumulative CO₂ emissions to a point [18], so the carbon budget to limit global warming to 2°C is about 300 GtC.

The 1.5°C carbon budget of 160 GtC is more than 1/3 of the cumulative global emissions up to today, but only approximately 15 years of emissions at the present rate, which is just over 10 GtC/yr [6]. This means that emissions will have to fall very rapidly to keep climate change within relatively safe levels. The question of how rapidly emissions need to fall depends, more than anything else, on whether and to what extent we will, in the future, be willing to pay the bill of removing CO₂ from the atmosphere that we emit today. Figure 1.5, from the same IPCC report, summarizes this

How the level of global warming affects impacts and/or risks associated with the Reasons for Concern (RFCs) and selected natural, managed and human systems

Five Reasons For Concern (RFCs) illustrate the impacts and risks of different levels of global warming for people, economies and ecosystems across sectors and regions.

Impacts and risks associated with the Reasons for Concern (RFCs)



Impacts and risks for selected natural, managed and human systems

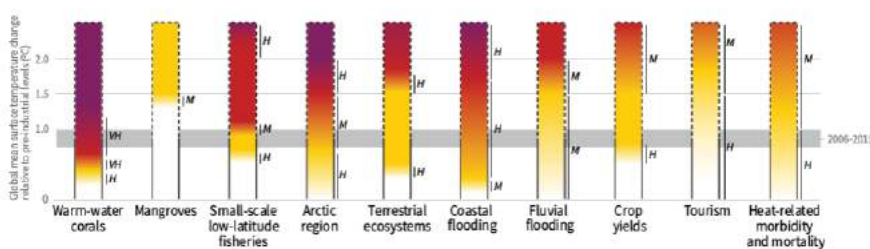


Figure 1.4: Severity of climate change risks increases from present warming (1°C) to 1.5°C and further to 2.0°C of warming. From the IPCC SR15’s Summary for Policy Makers (2018), ref. [13]



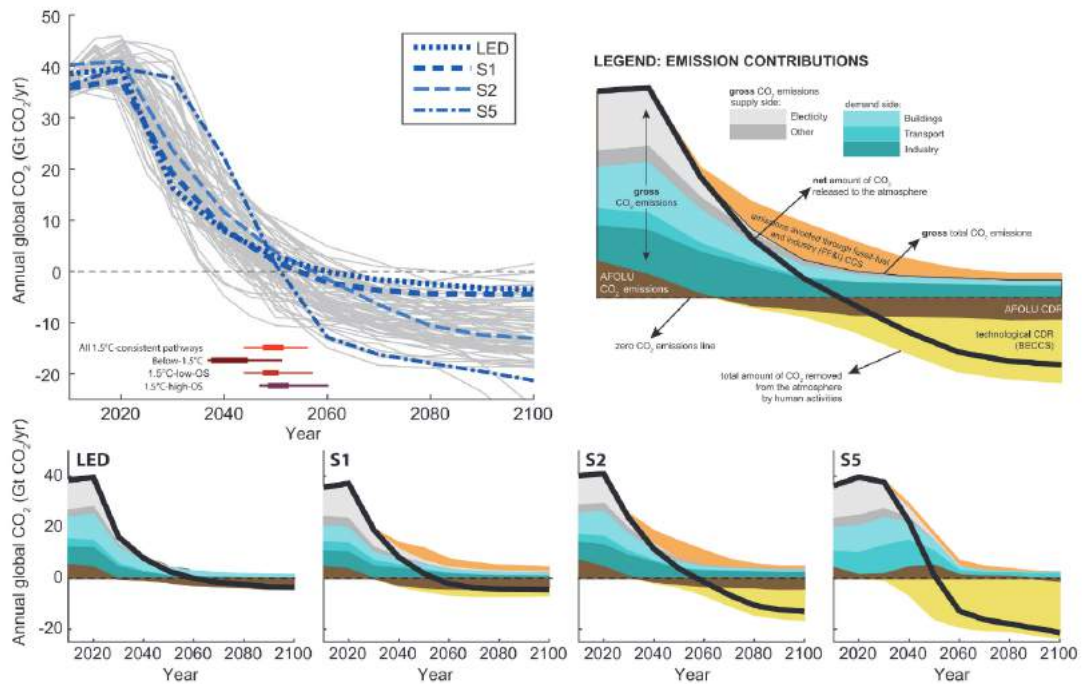


Figure 1.5: CO₂ emissions pathways consistent with max 1.5°C global warming involve emissions reductions of $\approx 50\%$ by 2030 and to net zero by around 2050. IPCC SR15 (2018) Chapter 2, ref. [18]

point.

Here, a number of scenarios for future emissions rates (referred to as pathways) are fed to various climate model which predict among other things the evolution of the global mean surface temperature between now and the year 2100. Figure 1.5 illustrates pathways for which global warming in the year 2100 predicted by most of the models is less than or equal to 1.5°C. It is important to note that in all of the pathways that involve significant CO₂ removal from the atmosphere, the temperature overshoots and then comes down again to 1.5°C of warming by the end of the century. All pathways that avoid such an overshoot of 1.5°C involve steep reductions in emissions starting more or less immediately. They tend to involve an approximately 50% reduction in CO₂ emissions from 2010 levels by 2030, and net zero emissions by around 2050 [18]. This can be used as a working, easy-to-remember policy guideline:

Definition 1.1. A policy is consistent with the Paris Agreement if it leads to 50% reduction (relative to 2010) in CO₂ emissions by 2030, and net zero emissions by 2050.

It is important to note that, while climate change is a global problem, policies are set more locally. Of course, if every country makes its policies in line with Definition 1.1, then it will be fulfilled globally. However, in reality, some countries will fall behind, and it should be considered the responsibility of developed countries with the capacity to do so to meet and exceed the criterion in Definition 1.1. All capable countries should enact policies in line with Definition 1.1 in order to minimize their contribution to any eventual overshoot of 1.5°C warming, to set an example, and to develop expertise that can then accelerate the required changes in slower countries.

In this context, the European Union’s present target of “At least 40% cut in greenhouse gas emissions compared with 1990” [19], which is only a 30% cut compared to 2010 [9], falls short, but will hopefully be tightened soon. Proudly, Denmark’s new government has put in place a target of 70% reduction by 2030 with respect to 1990 (60% reduction with respect to 2010) [20]. Denmark’s target is in line with the Paris Agreement by Definition 1.1.

The question, then, that should be on all of our minds, is:

Question 1.1. *How can we cut emissions to half or less by 2030?*

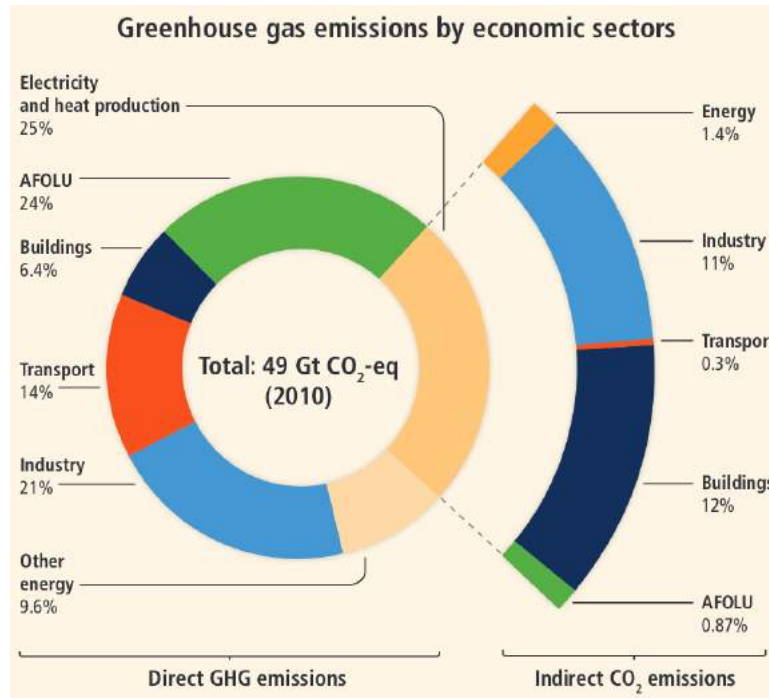


Figure 1.6: Global 2010 greenhouse gas emissions by sector, from the IPCC's AR5, 2014, ref. [5]

This is not an especially easy question to answer, since the combustion of fossil fuels has become a stubbornly fundamental cornerstone of the Western material lifestyle, which for better or worse is well on its way to spreading to the rest of the world. Almost everything we do, whether it's turning on a light, eating a burger, buying a new shirt, heating our home in the winter, commuting to work, charging a computer, or visiting an exciting new place is coupled to the release of greenhouse gases. Of course not all these activities do equal damage, but modern economies are so complexly interconnected that it is not reasonable to expect individuals to make these judgments, and so the answers to Question 1.1 are best found and implemented on levels starting from cities and up through regions, nations, and international organizations.

Figure 1.6, from the IPCC's previous report (AR5, from 2014) [5] divides global greenhouse gas emissions in 2010 up into sectors. The largest single source of greenhouse-gas emissions is due to electricity generation (25%), followed by the grouping of agriculture, forestry, and other land use (AFOLU, 24%), and then industry (21%).

The fact that electricity generation is the largest single source of greenhouse-gas emissions is in fact incredibly good news, since there are a number of technologies that can generate electricity with little to no greenhouse-gas emissions. Wind turbines and photovoltaics (solar panels) are becoming the most important CO₂-free electricity sources due to unlimited scalability (in contrast to hydro and geothermal power), broad societal acceptance (in contrast to nuclear fission), and technological maturity (in contrast to a number of emerging technologies) [21, 22]. Figure 1.7 illustrates the rapid growth in wind and solar energy. The combined installed capacity of wind and solar passed 1 TW [21] in 2018, corresponding to approximately one sixth of total electricity generation capacity [23]. The actual share of global electricity generated by wind and solar in 2018, though, is only 7.5% (2000 out of 27000 TWh) [24], slightly less than half as large a portion as installed capacity. This discrepancy is no quirk in the data - it is a fundamental drawback of wind turbines and solar panels: they only generate electricity when the wind is blowing or the sun is shining, respectively. (More on that in a moment.)

Wind and solar are expected to keep growing as a share of renewable energy generation for some time. The levelized cost per energy is already less than fossil fuels in most places and continues to fall as the total installed capacity increases [22, 25]. Wind and solar electricity generation is an incredible

ongoing success story. This is not least because reducing the carbon intensity of electricity works without requiring anything of the consumer, and thus represents a strategy to mitigate the risks of climate change with minimal disruption of society. Indeed, the most promising way to decarbonize many of the other sectors in Figure 1.6 is to *electrify* them.

Wind and sunlight may come for free, and building wind and solar capacity is now even cheaper than fossil fuel generation, but in the end the changes required by Definition 1.1 still don't come for free. And this is because of the *intermittency problem*, namely the fact that the wind and the sun are not kind enough to blow and shine exactly when we might need the electricity. It turns out that there are no cheap solutions to this problem, which will be described in more detail in the next Section.

One possible rough answer to Question 1.1 is then:

1. Install wind and solar as much and as fast as possible to decarbonize electricity production!
2. Electrify everything that can possibly be electrified! The main opportunities are in Buildings (6.4% of direct CO₂ emissions), Transport (14%), and Industry (21%).
3. Solve the problem of intermittency.
4. Do less of the things that are hard to electrify, and **stop doing the greenhouse-gas-emitting things that can't be electrified!**

These four steps can and must be advanced simultaneously.¹ The challenges are both technological and social. The technological challenges, today, are primarily in Items 2 and 3. The solutions to the intermittency problem and for electrifying other sectors are overwhelmingly based on *electrochemistry*, the subject of the next Section and the motivation for this PhD Project.

The societal challenges lie in getting people to accept the costs of implementing these technologies, through taxes and/or increased prices in electricity and other products; and in making lifestyle changes where electricity can't help, or can't help fast enough (Item 4). Notable carbon-intensive activities that cannot be electrified in the foreseeable future, if at all, include meat consumption (8.5% of global emissions [28]) and air travel (2-5% of global emissions and growing [29, 30]), and probably a much larger portion of the emissions for which the reader of this Thesis is responsible). A powerful and

¹Note that bio-energy is not included in this suggested answer at all. This is in part because bio-energy is out of the scope of this Thesis, but mainly because the climate impact of substituting fossil fuels with biofuels is highly scrutinized. Use of land for bio-energy, especially forest bio-energy may actually *increase* CO₂ concentrations in the atmosphere to 2050 and beyond compared to burning fossil fuels and leaving the biomass to grow. [26, 27]. As such, it is a terrible mistake that the EU counts forest biomass as carbon-free renewable energy!

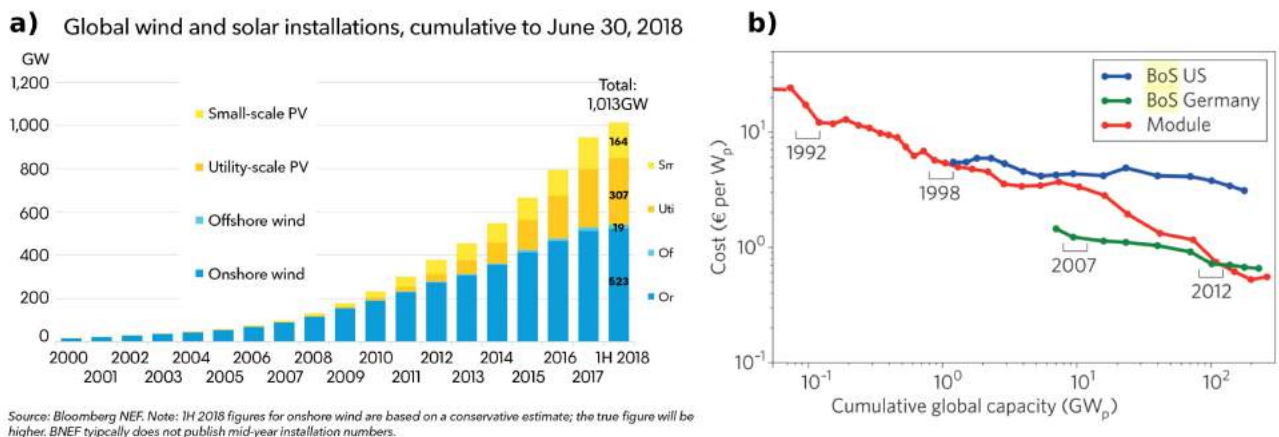


Figure 1.7: Rapid progress of renewables. (a), Growing installed capacity of wind and solar, from Bloomberg New Energy Finance (BNEF), 2019, ref. 21. (b), Solar learning curve including module and balance of system (BOS) prices, adapted from Creutzig et al, 2017, ref. 22.

indiscriminate way to promote all of the steps above within the framework of a free-market economy and to get individuals to make the necessary sacrifices with minimal intrusion is a universally applied CO₂ tax. This is the favored method by economists [31], but has to be high enough to influence both corporate and individual behavior.

The need for everyone to accept such sacrifices is where the climate crisis poses a challenge for capitalistic liberal democracies.² On the one hand, such societies feature political and economic systems which all too easily fall to the temptation of serving short-term interests. On the other hand, at the core of their values lie the free inquiry of science and the engagement of the public which which have succeeded in driving climate change mitigation to the top of the agenda in Europe. There is no guarantee we will be able to make the necessary changes fast enough to keep climate change from delivering the fatal blow to Fukuyama's dream. But there is reason to be optimistic.

²For a fascinating philosophical discussion of these challenges, Danish readers should read "Klimakrisens Rødder" by Anders Bodin, ref. [32].

1.2 Electrocatalysis: An important piece of the answer

In the last Section, I claimed that the most important remaining technological challenges that need to be solved to decarbonize society are (1) the intermittency problem, which is to say the need to keep the lights on when the sun isn't shining and the wind isn't blowing, and (2) the electrification of other sectors.

The intermittency problem becomes more important as the amount of intermittent renewable energy in a market increases. Figure 1.8 shows the electricity demand and intermittent renewable electricity generation in Denmark for a two-week period in the summer of 2017. Such datasets are available from energinet.dk. Overall, wind and solar met 45% of electricity demand during that period, and wind and solar generation even exceeded demand for short periods of time. However, there were also periods of time, such as day 222-223, with little to no wind and solar, where all of Denmark's electricity generation came from bio and fossil fuels or from neighboring countries.

The following are some of the solutions most often proposed for the intermittency problem [34–36]:

- Overcapacity of renewable generation, geographic diversification
- Flexible grid elements including battery vehicles
- **Hydrogen energy storage**

The first point is well under way, with cables linking Denmark's electricity network to the Swedish, Norwegian, and German grids, and cables planned to the Netherlands and Great Britain. Usually, the wind will be blowing or the sun shining in at least one of those places and, with enough wind generation overcapacity, that can help power neighboring regions. However, overcapacity is expensive, and there will still be times where demand is not met.

The second point involves utilizing market forces to get people to use electricity when it is most abundant. This could mean waiting until the wind is blowing and electricity is cheap to run a washing machine, or to charge a battery-powered vehicle. (Batteries are electrochemical devices, but out of the scope of this Thesis.) By extension, the varying price of electricity could even get people with battery

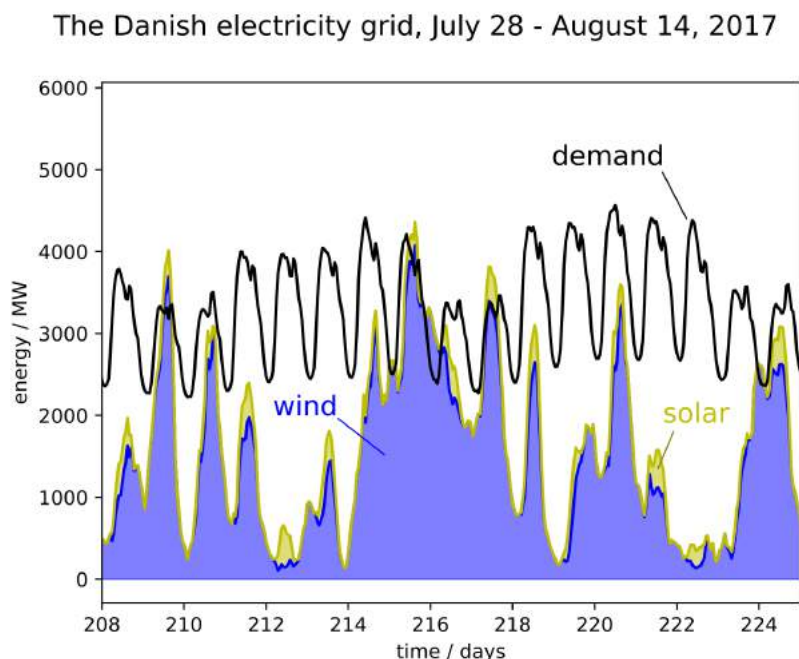


Figure 1.8: The intermittency problem. Electricity demand (black) compared to wind (blue) and solar (yellow) supply for Denmark over a two-week period in summer 2017. Data from energinet.dk, ref. 33

vehicles to discharge their batteries when the wind isn't blowing, and so with sufficient electrification of transportation, the vehicle fleet could become a source of *energy storage*. There are limitations in how far this can go: if every single car in Europe (300 million) was switched for an electric car with a typical car battery (30 kWh) and made fully accessible to the grid, this could power Europe (average 350 GW electricity in 2018) for

$$\frac{3 \cdot 10^8 \cdot 30[\text{kWh}]}{350[\text{GW}]} \approx 25[\text{h}],$$

or just about a day's electricity storage. Firstly, this is not enough energy storage to keep the lights on through a longer cloudy wind-still period. Secondly, most people will want to use their cars. Thirdly, full electrification of the personal vehicle fleet in Europe by 2030 is beyond any present ambition [36], and it is hard to imagine total battery capacity growing faster in any other sector. So, while batteries will help, they are not the full answer.

The last point, in bold, depends on electrochemical technologies - water *electrolyzers* which use electrochemical energy to split water into hydrogen and oxygen; and hydrogen *fuel cells* which generate electrical energy by the reaction of hydrogen and oxygen. Electrolyzers are described in more detail below.

The following have been proposed as means to electrify other sectors [36]:

- Buildings [37]: replace fuel heating with electric heat pumps
- Transport [38, 39]:
 - more reliance on electric-powered mass transit
 - battery-electric vehicles, mainly for personal vehicles
 - **hydrogen fuel cell vehicles**, mainly for buses & trucks, etc
 - Eventually **Use electrical energy to make fuels** for heavy transport
- Industry [40]:
 - Replace fuel heating with electrical heating.
 - When possible, replace fossil fuel reactants with **electrochemically produced hydrogen**.
 - When possible, **replace thermal processes with electrochemical processes**.

The points in bold depend on a number of electrochemical technologies, some mature and some emerging. One clear aspect is the central role of electrochemically generated hydrogen, not only for energy storage in the electrical grid, but also as a renewable energy input in other sectors. I will briefly describe the water electrolyzers used for electrochemical hydrogen production, and then mention some of its uses and some of the other electrochemical processes of interest for decarbonizing transport and industry.

Hydrogen (H_2) can be produced electrochemically by electrolysis of water (H_2O) into oxygen (O_2) and H_2 . The overall reaction is:



It is actually extremely simple to drive this reaction (inefficiently) with electrical energy. One need only tape wires to the two ends of a four-volt battery, and then put the wires in a cup of salt water. Bubbles will develop on both wires. The bubbles on the wire connected to the positive end of the battery (the anode) are O_2 , and the bubbles on the wire connected to the negative end of the battery (the cathode) are H_2 . The reaction is separated into *anodic* and *cathodic* reactions, the first of which involves *oxidizing* water to O_2 , and the second of which involves *reducing* water to H_2 . These two

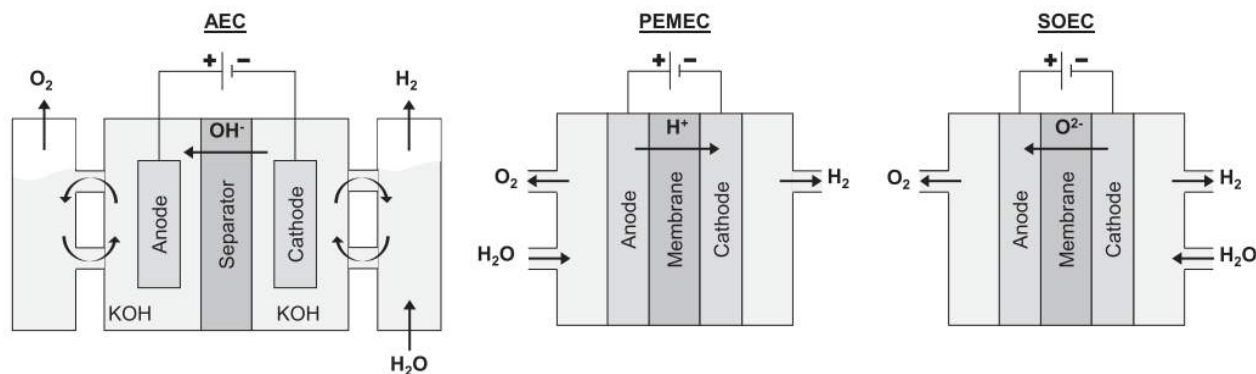


Figure 1.9: Schematic diagrams of the three types of water electrolyzer cells: Alkaline electrolysis cell (AEC), polymer electrolyte membrane electrolysis cell (PEMEC), and solid oxide electrolysis cell (SOEC). From ref. 41.

reactions, referred to, respectively as the oxygen evolution reaction (OER) and hydrogen evolution reaction (HER) are written as follows:



They are connected by *electrons* (e^-) flowing through the wires and the power source, and by *protons* (H^+) or other charge carriers moving through the liquid, which is therefore called an *electrolyte*. The voltage between the anode and cathode, called the *cell potential*, is what drives the reaction. It makes the electron energy lower on the anode and higher on the cathode, pushing both reactions, as written here, in the forward direction.

How much do we need to push the electrons? There is a minimum, 1.23 V, which is set by the thermodynamics of Reaction 1.1, but in practice it will always require more. It costs some potential - the electrical current times the *solution resistance* - to push the ions between the anode to the cathode. It also costs some potential to drive reactions 1.2 and 1.3 themselves. This potential, called the *catalytic overpotential* and depends on the electrode material. A material that minimizes the overpotential is a good *electrocatalyst*.

Three designs for *water electrolyzers* producing hydrogen from water by Reactions 1.2 and 1.3 are shown in Figure 1.9, from ref. 41. For detailed discussion and comparison of these technologies, I refer the reader to a number of excellent reviews, assessments, and perspectives including refs. 41–48. Briefly, the three technologies differ fundamentally in the type of electrolyte (indicated in **bold**) and electrocatalyst (in *italics*) used:

- Alkaline electrolysis cells (AEC's) are the electrolyzers most in use today, and the type that most resemble the wires-in-a-glass setup described above. In an AEC, the anode and cathode are immersed in an electrolyte of **concentrated alkaline solution**. The charge is carried by hydroxide ions through a porous ceramic called the separator. The separator's purpose is to keep the H₂ from the cathode and O₂ from the anode separate, but a small amount of H₂ will diffuse over to the anode side. This is the main drawback of AEC's: they must be run at high current density to avoid making an explosive mix of O₂ and H₂. This makes them less than ideal for solving the intermittency problem. Another drawback is a high solution resistance. The main advantage, as will be described in more detail at the start of Chapter 3, is that there are cheap electrode materials that can catalyze Reactions 1.2 and 1.3 in alkaline electrolyte. *Nickel* works reasonably well for both electrodes.
- Polymer electrolyte membrane electrolysis cells (PEMEC's) utilize a proton-conducting **polymer electrolyte membrane** such as the commercial Nafion from DuPont. The main advantages are that the resistance to proton transport across the membrane is very low while the

membrane is very effective at blocking gas crossover. The disadvantage, as will be described in more detail at the start of Chapter 3, is that the membrane is in effect a very acidic electrolyte, and that there are at present no cheap and stable electrocatalysts that can facilitate Reactions 1.2 in acid. Present PEMEC's use *platinum at the cathode and iridium and/or ruthenium oxides at the anode*. These are all very rare metals.

- Solid oxide electrolysis cells (SOEC's) are an up-and-coming technology. Here the electrolyte is a solid ***oxide-conducting ceramic*** such as yttrium-stabilized zirconia (YSZ), which transports oxide anions (O^{2-}) at high temperature. The disadvantage is that they have to run at very high temperature, on the order of 800°C , at which the materials degrade. The advantage is that there is little to no catalytic overpotential on the oxide itself at these temperatures, and so water splitting is done with very high energy conversion efficiency.

PEMEC's are expected by many experts to be the predominant water electrolysis technology by 2030, as hydrogen begins to play an important role in decarbonization [41]. Their dominance increases if more efficient and scalable electrocatalysts are developed. This is the main motivation for the materials of study in the Chapters of this Thesis. Most of the experiments presented in Chapter 2, though used primarily to characterize the experimental techniques, are done on platinum, which is used on the cathode of PEMEC's. Most of the experiments presented in Chapter 3 are done on ruthenium dioxide (RuO_2), which is a catalyst material for the anode of PEMEC's.

Electrochemically generated hydrogen can be stored in tanks, and used in any of the following ways:

- Electricity generation for the grid via a fuel cell. The dominant fuel cell technology today is a polymer electrolyte membrane fuel cell (PEMFC), which is the PEMEC of Figure 1.9 in reverse, with a platinum catalyst on the oxygen side [49]. Solid oxide fuel cells are an emerging technology.
- Transport in PEMFC electric vehicles.
- Reduction of iron ore for steel production. At present, steel is produced by the approximate reaction:



The stoichiometric carbon from this reaction accounts for more than 3% of global CO_2 emissions (Paper V).

An emerging steel-making process [50] uses direct reduction by H_2 instead:



In some models of the future energy+industrial landscape, this will be the primary use of renewable hydrogen in 2030 and beyond [35].

- The Habor-Bosch process which makes ammonia for fertilizer:



At present, the hydrogen used in this process comes from steam reforming of natural gas:



The stoichiometric amount of carbon used in steam reforming for ammonia production today is about 0.5% of global CO_2 emissions (Paper V).

- Production of liquid fuels by the reaction of H_2 and CO_2 captured from point sources or the air. This involves first producing syngas, a combination of CO and H_2 , by reacting an excess of H_2 with CO_2 by the water-gas shift reaction, and removing the water:



Syngas can be used to synthesize methanol or long-chain hydrocarbons (Fischer-Tropsch reaction) depending on the catalyst and reaction conditions [51].

With respect to the last point above, it is interesting to ask:

Question 1.2. *What products would be smart to make by using renewable energy to convert CO_2 ?*

Figure 1.10 is a generalized and simplified approach to answering that question. It shows the market price vs the energy content for a number of carbon products, with the size of the marker representing the market size. The lines represent the minimum cost to make a product given prices for the CO_2 starting material and the renewable electricity. Products above the line might be economically viable, while products below the line can not be. In Paper V, we use this analysis to motivate the production of ethylene (Reaction 1.9) and ethanol (Reaction 1.10) by direct electrochemical CO_2 reduction on copper electrodes:



This reaction has also been a focus of my PhD (Papers IV, V, and VI), though not the Chapters of this Thesis.

Because it is only based on thermodynamics, the economic argument in Figure 1.10 is equally valid with thermal reaction of CO_2 with H_2 produced by electrolysis with renewable electricity. I have added a possible Fischer-Tropsch reaction product, decane ($\text{C}_{10}\text{H}_{22}$), which is representative of

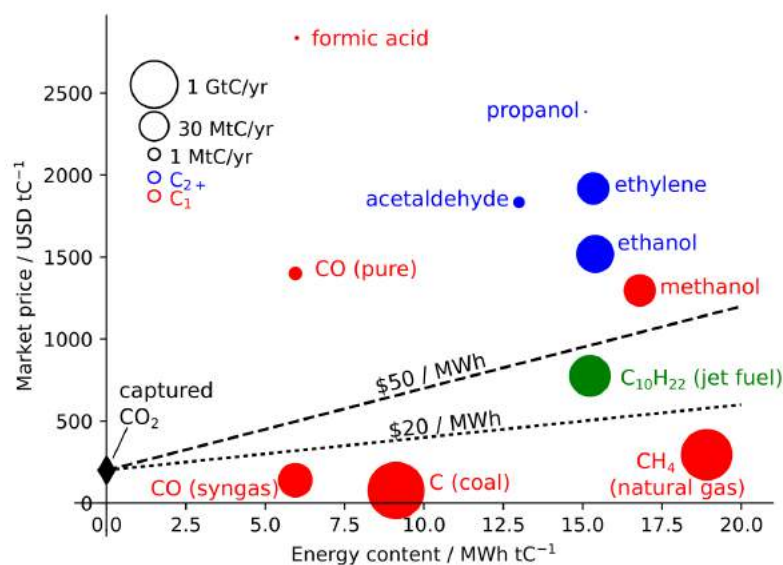


Figure 1.10: Mapping of fuels and chemicals comparing market price with minimum cost of electricity and CO_2 for two different electricity prices. The size of each dot indicates the market size, on a log scale. All quantities are normalized to mass of carbon. Adapted from Paper V. Jet fuel has been added assuming the carbon density and energy content of decane ($\text{C}_{10}\text{H}_{22}$).

heavy transport fuel (aviation fuel is primarily hydrocarbons of length 5-15). This product is not thermodynamically impossible to make at the present market price with electricity at 20 USD per MWh (near the record lows for solar installations), but is impossible at 50 USD per MWh (more typical of present solar installations). It is very important to realize, though, that the actual cost of making a product will be significantly higher than the lines in Figure 1.10 because of overpotentials, capital costs, and other operating costs.

The price of captured CO₂ in Figure 1.10, USD 200 per ton of carbon, is representative of carbon captured from a power plant [52]. Carbon captured from the air would be much more expensive, pushing the lines up. A carbon tax, however, would push the lines down, since captured and utilized CO₂ avoids the tax. This is clearly essential if renewable fuels are ever going to compete with the likes of coal and natural gas.

To conclude this Chapter, before diving into the heavy electrocatalysis of this Thesis, I should introduce one essential aspect in the study of electrochemistry, the *three-electrode setup*. A more complete introduction to electrochemistry [53,54] is beyond the scope of this Thesis, but with this one concept, a new reader might be able to follow the experiments in the next Chapters, which attempt to introduce other new concepts as they come up.

When running an electrochemical process in industry, there is typically only one potential difference that matters: the cell potential between the anode and the cathode. This potential difference, times the current, is the power being consumed. However, in electrocatalysis research, it is almost always preferable to study the anode or cathode reaction in isolation.

This means, most often, controlling the potential of the sample, referred to as the *working electrode* (WE), on an absolute scale while measuring the current passing through it. The absolute potential scale is accomplished by using a *reference electrode* (RE), which contains each of the reactants and products in a facile redox reaction at steady, well-defined activities. The reference electrode used for the experiments in this Thesis is a mercury/mercury sulfate reference electrode, based on the redox reaction



Since Hg and HgSO₄ are solids, only the activity of SO₄²⁻ can potentially vary. It is kept constant by using a saturated K₂SO₄ solution. The *equilibrium potential* of such a reaction is a constant value determined by thermodynamics, so as long as there is no current flowing through the reference electrode (above the tiny current that a voltmeter uses to measure a potential difference).

The absolute potential of the WE is determined on the scale of the RE just by measuring the potential difference between them with a voltmeter. Controlling the potential is a bit trickier. The way to change the potential of the WE is actually to run a current through it. This charges the

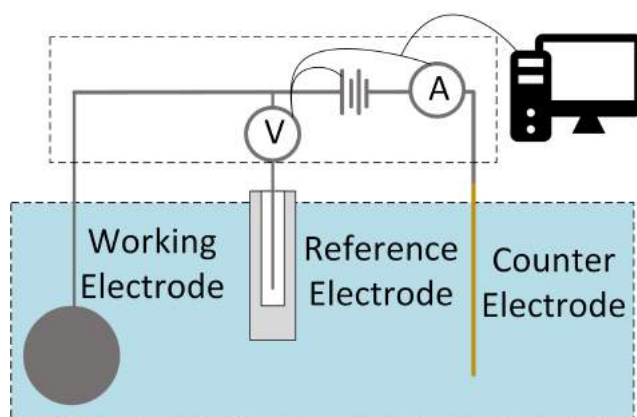


Figure 1.11: Diagram of the three-electrode setup. The dotted-line box at the top represents a potentiostat. From my master's thesis, ref. 54.

electrode-electrolyte interface, which is what determines the electrochemical potential. But running a current through the RE isn't an option, because then the redox reaction would no longer be at equilibrium and the potential would no longer be well defined. So we need a third electrode, called the *counter electrode* (CE) who's only purpose is to conduct the current needed to get the working electrode to the desired potential. The current through the CE is equal and opposite to the current through the WE.

So, to get the WE to a desired potential vs the RE, what actually happens is that a voltage is set between the WE and the CE, and the resulting current changes the absolute potential of the WE, which is measured against the RE, and this is iterated until the WE is at the requested potential against the RE. Then, the current is measured. This is often done while scanning the WE potential back and forth smoothly to measure the current as a function of the linearly changing potential, a technique called *cyclic voltammetry*. Doing this smoothly requires some fancy electronics, and the machine containing these electronics is called a *potentiostat*. This setup is shown in Figure 1.11.

So that's how we study one electrode material at a time. But you may notice that the only information we get from the potentiostat is the electrochemical current and potential. You may be wondering,

Question 1.3. *How do we know which reaction(s) the current is going to?*

That is the right question to bring us to the next Chapter.

Chapter 2

The Right Tools to Answer the Right Questions

As described at the end of the previous Chapter, electrochemistry will play a central role in a steady-state civilization where all of the inputs to our energy infrastructure and chemical industries are renewable or closed-cycle. This will require the development of a wide range of new electrochemical processes and technologies, and the transition will be accelerated by increasing the efficiency and lowering the cost of existing electrochemical technologies, first and foremost water electrolysis. Central to these technologies are the electrode materials, or electrocatalysts, on which the anode and cathode half-reactions take place. Research efforts around the globe have therefore flourished in recent years to develop new electrocatalyst materials and to improve the understanding of existing electrocatalyst materials [55–57]. While (it can not be repeated enough) no realistic pace of progress in these efforts could remove the necessity of high and rising taxes on CO₂ emissions, every bit of progress helps.

It is essential in electrocatalysis development to be sure that the reaction taking place is actually the desired reaction. This sounds obvious, but in electrochemistry it can be tempting to just measure the electrode current (the rate at which e⁻ are released or consumed) and not analyze the chemical products. Examples of when the electrode current can be misleading in oxygen evolution catalysis are given in the next Chapter (Section 3.1). The need for product detection is even more important in electrochemical reactions which intrinsically have many possible products, such as the CO₂ reduction reaction [58]. In general, we need product detection to determine the *Faradaic efficiency*, or the portion of the electrons transferred, for a specific reaction or product.

There are a number of product quantification methods including, for example, high pressure liquid chromatography (HPLC), gas chromatography coupled to temperature conductivity detection (GC-TCD) or flame ionization detection (GC-FID), nuclear magnetic resonance (NMR), or colorimetric methods which are all suitable for detecting various products of electrochemical reactions. These all have in common, though, that they typically require an electrochemical reaction to be run for some time to build up a concentration of a product. They are, in other words, ex-situ or batch product detection methods. Detecting electrochemical products after a batch reaction, while useful, is tedious and often leaves out the information of how Faradaic efficiencies can change over time, which can help in understanding stability and electrocatalyst fundamentals. For these reasons, we wish for an *in situ*, i.e. continuous or equivalently “real-time”, product detection. Mass spectrometry (MS), a readily available technology which is described in the start of Section 2.1, is a very useful tool in this regard because of its speed, ability to distinguish between molecules (*chemical resolution*), and sensitivity. A technique that I have helped develop to interface mass spectrometry with electrochemistry via a silicon microchip, *chip EC-MS*, is the subject of Section 2.1 and the subject of Paper I.

A pervasive idea in catalysis research is that an improved fundamental understanding of how and why the atoms move around on the surface of catalysts during the electrochemical reaction will enable the *rational design* of more efficient, more stable, and less expensive catalysts [59]. Electrocatalysis is no exception [57, 60–62]. In this effort, virtually no computational or experimental tool known

to materials science has gone unturned in the quest to understand specific electrocatalysts and the fundamentals of electrocatalysis.

Chip EC-MS has certain advantages, including sub-monolayer sensitivity, fast time response, and the ability to quickly dose reactive gases, that make it ideal for fundamental electrocatalytic studies. (It also happens to have some disadvantages, briefly described in 2.1.3.) These advantages make it ideal for *stripping experiments*, which probe the adsorbates on a surface by reactive desorption. This is a powerful type of experiment, in a word because the involvement of surface-adsorbed species is effectively the definition of catalysis. Papers I, III, and VI feature stripping experiments, and an example is included in 2.1.2.

The extremely high sensitivity of chip EC-MS is based on the fact that every molecule of a gas produced at the electrode being studied (such as H_2 or O_2 produced by water splitting) goes through the chip and to the vacuum chamber. This also makes it a fantastic platform for absolute *quantification* in mass spectrometry, in which a mass spectrometer signal is related not just to the concentration of an analyte, but to an absolute number of molecules of an analyte. This is the subject of Section 2.2, which includes recommended procedures for using EC-MS as a generalized platform for quantitative mass spectrometry.

The final Section of this Chapter brings us to the juicy heart of this Thesis.

Atoms are in general too small and too quick (when it's not extremely cold) to see them moving around. And there's the annoying problem that, in general, you can't tell two atoms of the same element apart, so it's impossible to keep track of them! If we wish, experimentally, to understand how atoms move around on an electrocatalytic surface, it is therefore very useful to *label* them. This can be done using *isotopes*, which are versions of an element that have different number of neutrons, and thus different masses. Since chemistry is dominated by protons and electrons (the number of which defines the element), different isotopes of the same element behave (to a reasonable approximation) identically in electrocatalytic reactions. A mass spectrometer, though, can tell the difference! There are a number of exciting things to look at in electrocatalysis with isotope labeling and a sensitive enough setup. Two examples are given in Section 2.3, and isotope labeling experiments in oxygen evolution electrocatalysis are the primary focus of the following Chapter.

2.1 Electorchemistry - mass spectrometry

Mass spectrometry is one of the most versatile and widely used analysis tools in science [63, 64]. It also has rich and fascinating history [65], some notable points in which are summarized in Figure 2.1. In essence, mass spectrometry is the study and use of methods to separate charged particles in high vacuum by their mass-to-charge (m/z) ratio. The mass-to-charge ratio of all molecular and atomic ions (at non-relativistic energies) is very close to an integer multiple of one atomic mass unit per fundamental charge, and so the m/z ratio is usually stated simply as an integer with the implied units of [atomic mass unit per fundamental charge]. Some mass spectrometers have such high resolution that they can separate ions with the same nominal (integer) m/z ratio [63], but for the quadrupole mass spectrometers used in this PhD thesis, m/z is in effect an integer.

The early development of mass spectrometry was inseparable from the fundamental study of how charged matter behaves under electric and magnetic fields in vacuum, and thus closely tied to many fundamental discoveries in early physics. This includes the discovery of the electron, the discovery of relativistic effects, and the discovery of isotopes. Mass spectrometry has been put to use in an astounding number of applications, including a prominent unsavory one: a modified mass spectrometer was used in one of the purification steps of ^{235}U for the first atomic bombs (diffusion-based methods and centrifugation have since become much more practical methods of separating this isotope) [72]. Other applications include, for example, trace element analysis (ICP-MS) and protein sequencing (MALDI-TOF).

A mass spectrometer consists of at least three components in a vacuum chamber [63]:

1. **Ion source.** The ion source for the electrochemistry-mass spectrometry (EC-MS) setups described in this Thesis is electron impact ionization (EI, Figure 2.2a). An electron beam is generated by heating up a filament until the high-energy tail of the Fermi distribution of the electrons in the material exceeds the work function of the material. This expels electrons into the vacuum. These electrons are accelerated through a voltage V and pick up an *ionization energy* of $q_e V$. The ionization energy in this diagram, and throughout this Thesis, is 70 eV. The electrons encounter the molecules to be analyzed (we'll get back to how these molecules got there) in an *ion volume* and impact some of them, imparting a large energy. Many of these impact events result in the expulsion of another electron (or multiple electrons), generating a positively charged ion. Many also result in *fragmentation*, or breaking of the molecules' bonds. It is these *fragments* which are separated and detected by m/z ratio. First they are accelerated from the ion volume to the mass separator.
2. **Mass separation.** For the EC-MS setups, this is accomplished by a quadrupole (Figure 2.2b). A quadrupole consists of four parallel rods separated by a distance on the order of a centimeter. The rods are connected in two pairs, which are biased by a constant DC bias superimposed on a radio-frequency AC bias. The result is that ions of a specific m/z ratio, which is a function of these two biases, are driven in a stable circular trajectory between the rods and in the plane perpendicular to the rods, whereas ions of other m/z ratios are thrown out by either the AC bias (small ions) or the DC bias (large ions). Ionized fragments enter the four rods with a velocity parallel to the rods, and those with the right m/z ratio fly in neat spirals long enough to make it through. The biases can be changed quickly to scan through a range of m/z ratios (for a *mass spectrum*) or jump between specific m/z ratios of interest to monitor their signals as a function of time (for a *mass-time* measurement). The separation power increases with the length of the quadrupole, and 10 cm is a typical length.
3. **Detection.** The ion fragments that make it through the quadrupole hit a detector. In the simplest case, called a *Faraday cup* the detector is just a grounded piece of metal, and the current from the ground, which is equal to the current due to the ions hitting the detector, is measured. However, for higher sensitivity, with a *secondary electron multiplier* (SEM), the ions hit the first of a series of charged plates, starting an electron cascade. The current coming out

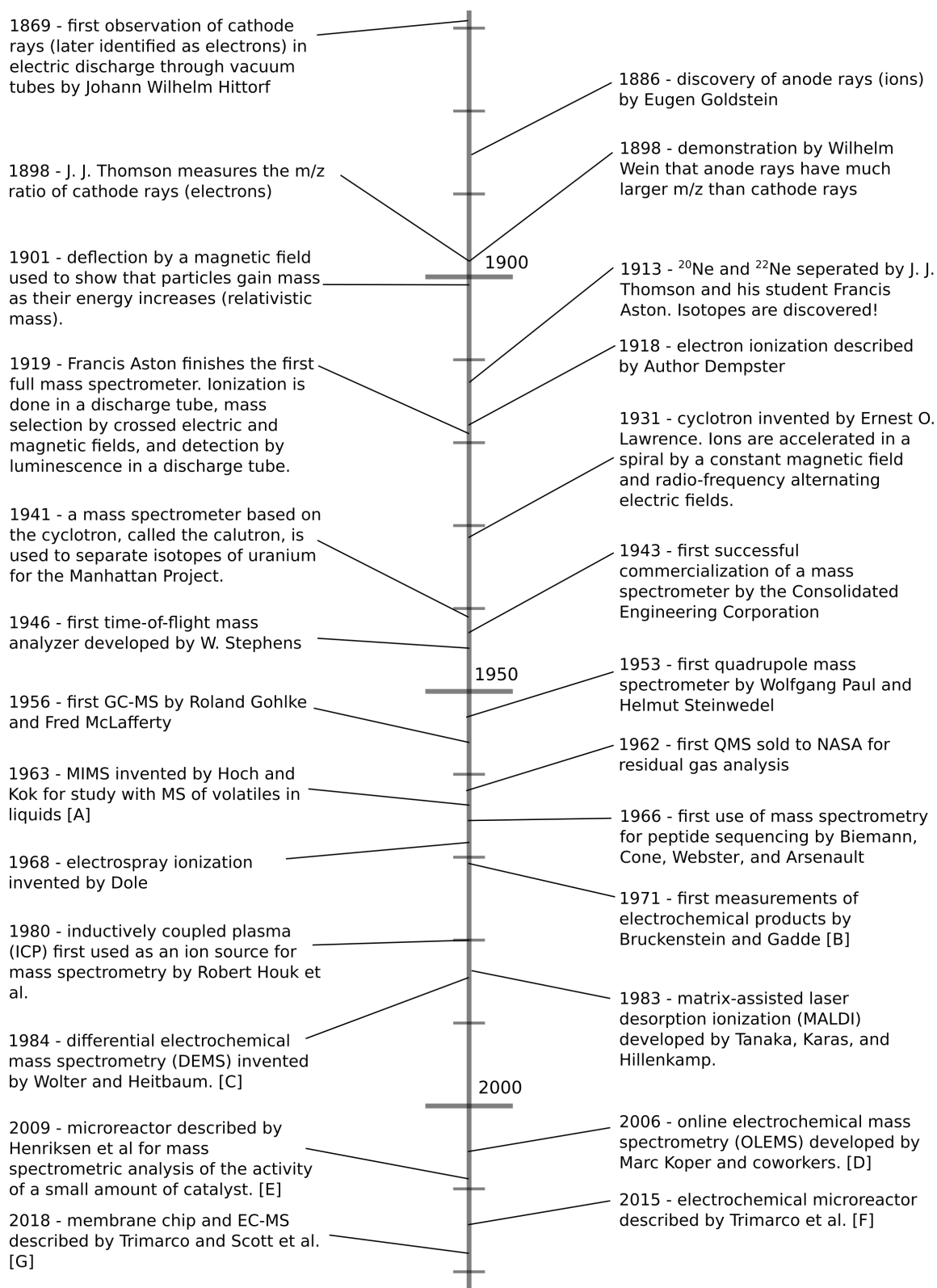


Figure 2.1: Brief history of mass spectrometry. Most events are described in ref. 65 and at https://en.wikipedia.org/wiki/History_of_mass_spectrometry. Several later events focus on the coupling of electrochemistry and mass spectrometry: [A], ref. 66; [B], ref. 67; [C], ref. 68; [D], ref. 69; [E], ref. 70; [F], ref. 71; [G], Paper I.

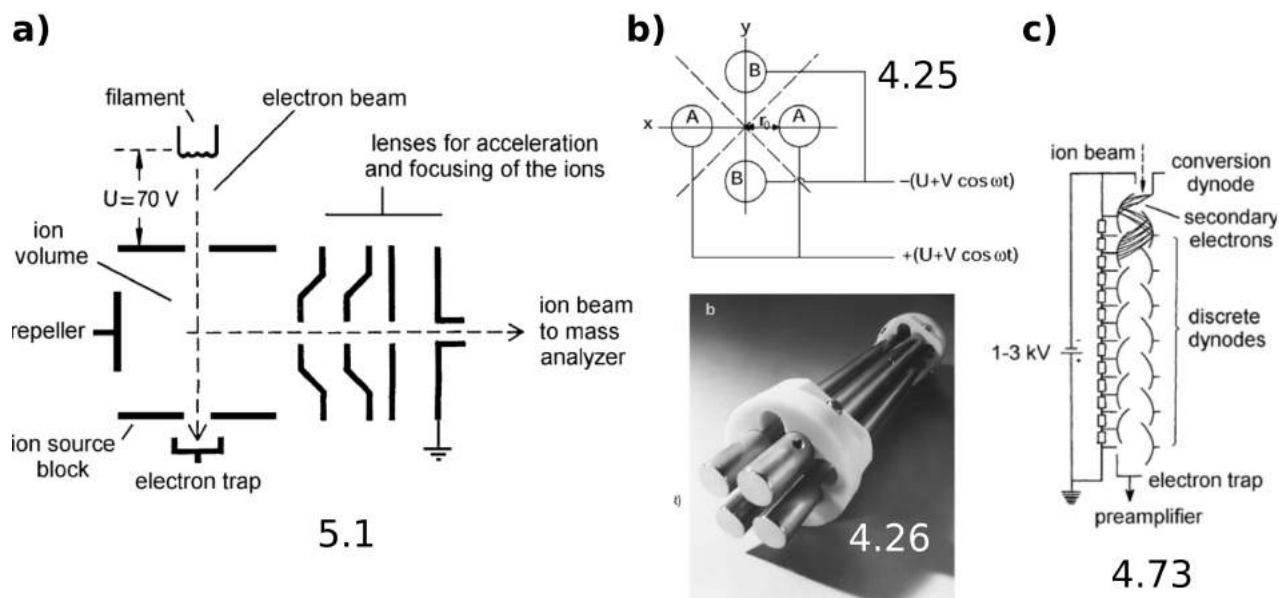


Figure 2.2: Diagram of the components of a quadrupole mass spectrometer (QMS): (a), electron impact ionization; (b) quadrupole mass separation; and (c), secondary electron multiplier detection. Adapted from J. Gross, “Mass Spectrometry”, ref. 63. Figure numbers in the image refer to that textbook.

of the last plate, which is orders of magnitude larger than than the ion current hitting the first plate, is recorded as the *mass spectrometer signal*. For the EC-MS setups in this Thesis, we use a SEM.

Each of the three components above necessarily operate in high vacuum [63, 73]. The coupling of mass spectrometry and electrochemistry, motivated at the start of this Chapter, therefore requires an interface allowing electrochemical products from a wet, ambient-pressure environment to enter a vacuum chamber while maintaining a pressure less than $\sim 10^{-6}$ mbar.

2.1.1 Chip EC-MS: working principle

Our version of electrochemistry - mass spectrometry involves making the interface between the liquid electrolyte and the vacuum chamber with a specially fabricated silicon microchip called the membrane chip. The motivation, design principles, and original implementation of Chip EC-MS are described extensively in a fantastic PhD Thesis by Daniel Trimarco (ref. [74]) and in the article which we wrote together, included in this Thesis as Paper I.

This strategy gives a number of unique advantages, and also some disadvantages, which make it ideal for fundamental studies but (in its present implementation) less ideal for high-current *in-operando* studies. For the latter type of study, conventional flow-cell differential electrochemistry - mass spectrometry (DEMS) [75] retains some advantages. Ours should therefore be thought of as a distinct technique, which we refer to as *chip EC-MS* or just *EC-MS*.

Figure 2.3 includes schematic diagrams of the key components of chip EC-MS. Membrane chips are fabricated at wafer-scale from semiconductor-on-oxide (SOI) wafers with standard clean-room techniques. Photographs of the front and the back of the chip, are shown in the bottom right corner. The photograph of the front of the chip is colorful due to the diffraction of visible light by the chip’s membrane. The membrane consists of thousands of holes with a diameter of $2.5 \mu\text{m}$ patterned over a circle 7 mm in diameter by UV lithography. Below the membrane is an empty volume, called the *sampling volume* formed by etching of the SOI’s oxide layer. The sampling volume is connected to the back of the chip by four holes formed by deep reactive ion etching (DRIE) from the back. A series of gas channels are formed on the back by UV lithography: a wide carrier gas reservoir channel connecting the carrier gas inlet to the carrier gas outlet (indicated in blue in the chip schematic at the

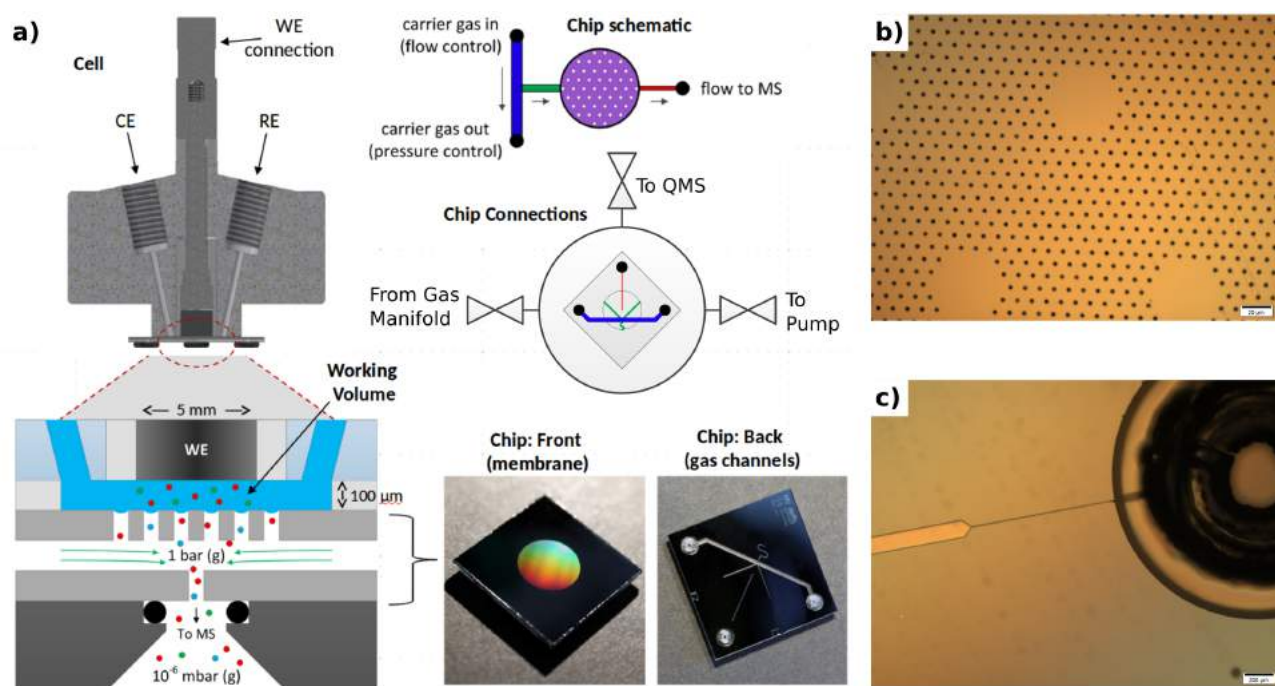


Figure 2.3: (a) Schematic diagrams of chip-based EC-MS and photographs of the membrane chip, adapted from Paper I (b-c) Visual microscopy images of the (a) front of the chip showing the membrane, scale bar = 20 μm and (b) back of the chip showing the capillary through the transparent Pyrex, scale bar = 200 μm.

top right of Figure 2.3a, three carrier gas delivery channels (intended to achieve symmetric gas flow - indicated by one green channel in the schematic), and a capillary connecting to the mass spectrometer inlet (red in the schematic). These gas channels are sealed by anodic bonding to a Pyrex glass wafer, such that the finished chip is silicon on the top and glass on the bottom. The holes for the carrier gas inlet, carrier gas outlet, and mass spectrometer inlet are formed in the Pyrex with a CO₂ laser prior to bonding. This membrane chip design is protected by a patent [76] and commercialized by Spectro Inlets ApS.

The membrane chip is intended as a *window* into what is happening on (or more specifically, what is desorbing from) the surface of an electrochemical sample. This requires setting up a three-electrode setup with the working electrode parallel to and close to the membrane. We accomplish this with an *EC-MS cell*, diagrammed on the top-left of Figure 2.3a and in Figure 2.4a. The cell is most simply described as a piece of polychlorotrifluoroethylene (PCTFE or Kel-F) with holes machined in it. The holes include a cavity through the center for the working electrode assembly. We use the Change-Disk RDE equipment commercially available from Pine Research Instruments for quick and versatile sample exchange. This system uses a PTFE U-cup, which is squeezed slightly between the sample and the cell, to hold the sample in place. The sample can be any 5 mm disk. The distance between the sample and the membrane of the chip, the *working distance*, is defined by a Teflon spacer, and is 100 μm throughout this Thesis. The volume between the surface of the working electrode and the membrane chip is called the *working volume*. The concentric 7 mm membrane and 5 mm membrane give rise to a 1 mm x 100 μm *edge volume* which is bound by the membrane but not the working electrode. The high aspect ratio of this edge volume ensures that little to no analyte produced at the electrode is lost by lateral diffusion.

The working volume is connected via channels in the EC-MS cell going from just past the edge volume to threaded openings at the top, which are generally fitted with Luer adapters for interfacing with liquid pathway components. In two of these, we place a piece of custom-made glassware with a Luer tip, a ceramic frit to prevent convection, and a large cylindrical volume above. These glassware house the reference and counter electrodes. The other two openings are then used as electrolyte inlet

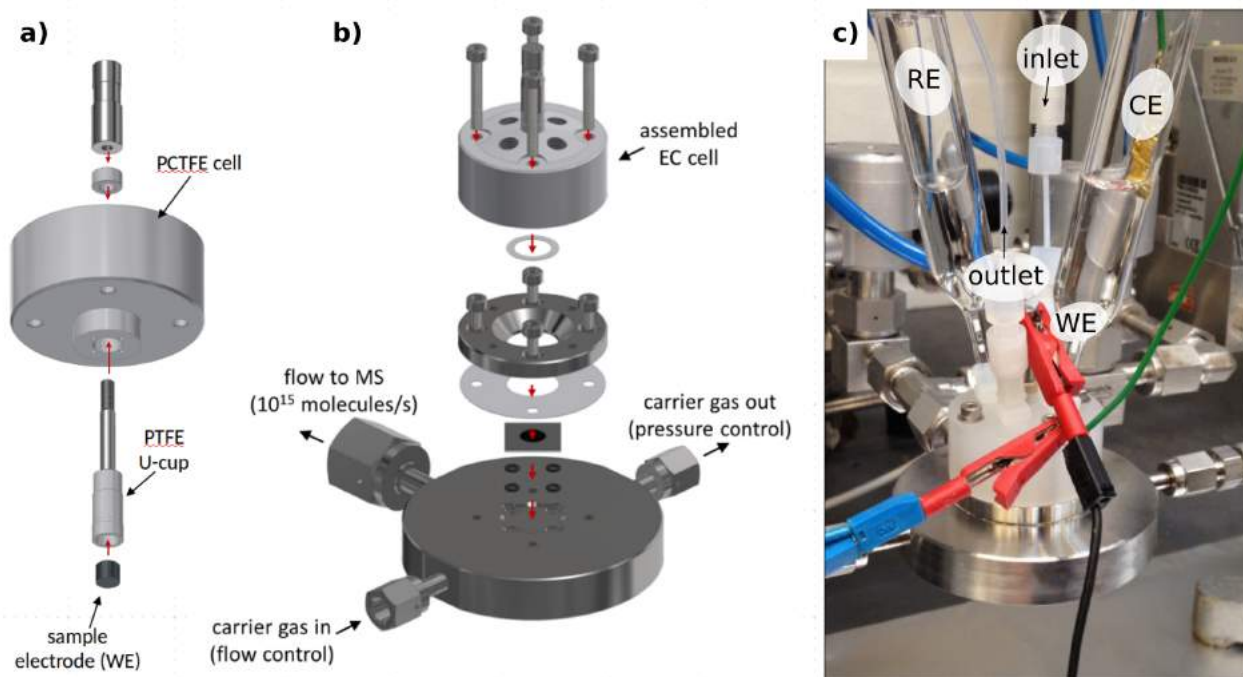


Figure 2.4: Diagrams of (a) the cell + working electrode assembly and (b) The cell + chip + interface block assembly. (c) Photo of the setup in use. From Paper I

and outlet. The full assembly is shown in the photograph in Figure 2.4c. To avoid bubbles, the cell must be filled with electrolyte through the inlet before the reference and counter glassware are inserted.

As mentioned at the start of this chapter, chip EC-MS has two advantages over conventional systems for fundamental studies in electrocatalysis:

1. Extremely high sensitivity. This is possible because the chip membrane serves as an equilibration step, letting volatile gases evaporate without sucking in solvent. The very low solvent flux means that no differential pumping stage is necessary, unlike DEMS. Furthermore, the low solvent flux is the reason it is possible to run long experiments without flowing electrolyte. Together, this means that *every molecule of volatile product produced on the electrode will make it to the mass spectrometer*
2. The ability to quickly dose and purge reactant gases. This is possible because the equilibrium of the gas-liquid interface at the chip's membrane works both ways: dissolved gases are released, and the gas fed into the chip saturates the electrolyte in the working volume.

Since electrolyte is not flowed during experiments, the cell is a *stagnant thin-layer* cell. The working volume functions as a perfect diffusion layer, making it relatively easy to model mass-transport in the system. This mass-transport model was first presented in my Master's Thesis [54], and later refined and verified experimentally in Paper I. I will not redevelop the model here, but I will use its results from time to time throughout this Thesis.

In practice, an external system for vacuum and gas handling is needed to realize the advantages of high sensitivity and quick reactant gas dosing and purging made possible by chip EC-MS. This Appendix describes two such vacuum systems that I worked on during this PhD project. The vast majority of my work was done on the so-called "Sniffer setup" at DTU. During my external stay in professor Zhenhai Wen's group at the Chinese Academy of Sciences (CAS) in Fuzhou, I designed a more compact version, which became the EC-MS 200A. Valve diagrams and descriptions of these setups are shown in Appendix A.

In the spirit of making this Thesis useful to my colleagues, Appendix A also describes procedures for changing chip and changing carrier gas for each of these setups with reference to the valve diagrams.

2.1.2 Example experiments: RHE potential measurement and CO stripping

Here I show two examples of common electrochemistry experiments as seen through the window of chip EC-MS. These two experiments also demonstrate the utility of the gas-exchange functionality, and happen to be quite interesting when instead done in isotope-labeled electrolyte. Isotope-labeled versions of these two experiments are shown later in this Chapter, in Subsections 2.3.1 and 2.3.2.

The first experiment is a measurement of the reference electrode potential on the reversible hydrogen electrode (RHE) scale. The reversible hydrogen electrode potential is defined as the potential at which the hydrogen evolution and hydrogen oxidation reactions (HER and HOR, respectively) are at equilibrium in electrolyte saturated by 1 bar hydrogen:



This situation can be easily created in a chip EC-MS setup using hydrogen as the carrier gas and a platinum electrode as the sample, since platinum is an excellent catalyst for the HER/HOR [77–79].

The experiment is shown in Figure 2.5a as an *EC-MS plot*, in which the electrochemical potential (left y-axis) and current (right y-axis) are plotted against time in the bottom panel and the concurrent mass spectrometry data is shown in the top panel on the same time axis.¹

Starting from the left: the platinum electrode is cycled between -0.7 and $+0.7$ V vs the reference electrode (Hg/HgSO_4) in helium-saturated electrolyte. Three full cycles are shown. Hydrogen is produced near the cathodic potential limit, giving rise to an increase in the mass spectrometer signal at $m/z=2$. The electrode is set to open-circuit potential (i.e., the current is set to zero) at the cathodic potential limit of the fourth cycle. This results in less H_2 than the first cycles, since in the first cycles HER continues at the start of the anodic scan. The open-circuit potential then drifts in the anodic direction until just before the onset of $*\text{OH}$ adsorption, which would draw current. At 300 s, H_2 is flowed through the chip, replacing He in the carrier gas reservoir channel. The H_2 very quickly enters the sampling volume of the chip, giving rise to a $m/z=2$ signal in the mass spectrometer.

¹Customized EC-MS plots, including all of the ones presented in this Thesis, can be produced in one line of code with the highly versatile `plot_experiment` function of the `EC_MS` python package, described in Appendix C.1.

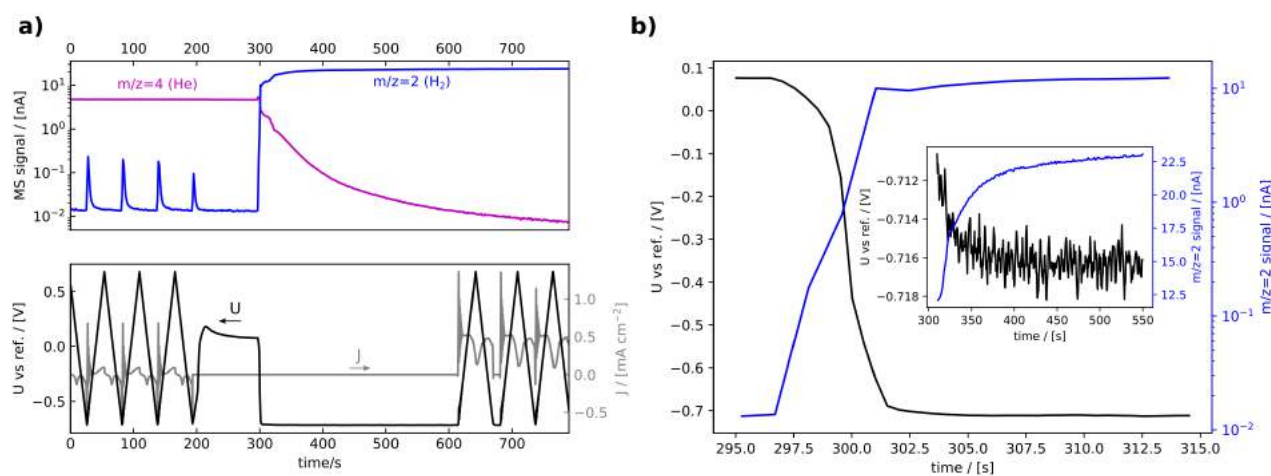


Figure 2.5: RHE calibration experiment using a polycrystalline platinum electrode in 0.1 M HClO_4 . (a) EC-MS plot with mass spectrometer signals in the top panel and the concurrent electrochemical data in the lower panel. (b) A zoom-in on the time at which the carrier gas is switched from helium to hydrogen while the electrode is at OCP, showing the electrode potential (black, left y-axis) co-plotted with the $m/z=2$ signal (blue, right y-axis)

Simultaneously, the H_2 saturates the electrolyte in the working volume. The first H_2 molecules to encounter the electrode are immediately oxidized to H_2O because there is a substantial overpotential to drive the HOR (Reaction 2.1 in the leftwards direction). However, since the electrode is at OCP, there is nowhere for the resulting electrons to go, and so they change the charge density of the electrochemical double layer, which functions as a capacitor [80]. This causes the potential to drop very quickly. The electrode soon reaches a potential at which Reaction 2.1 is in equilibrium. This equilibrium potential depends on the partial pressure of H_2 , and so the potential continues to change slowly as H_2 fully replaces He.

The example in Figure 2.5 is unfortunately not the most elegant gas exchange, as indicated by the inflection points in the MS signals as H_2 replaces He in Figure 2.5a. (This results from an overpressure in the gas manifold before opening Valve 8 in Figure A.1, which causes turbulence and gas mixing in the carrier gas inlet volume.) Figure 2.5b shows the simultaneous change in the H_2 signal and electrode potential during the gas switch. The electrode potential becomes stable to within a few millivolts just 10 seconds after the switch, but the last ≈ 2 mV to the RHE potential of -0.717 V vs the reference electrode take about 100 s (inset). This is, nonetheless, a much faster RHE measurement than can be accomplished when a macroscopic amount of electrolyte, for example in an H cell, needs to be fully purged with hydrogen. Such RHE measurements are used routinely to calibrate the reference electrode potential on the RHE scale in a new electrolyte.

Figure 2.6, from Paper I, demonstrates platinum electrochemistry involving carbon monoxide (CO).

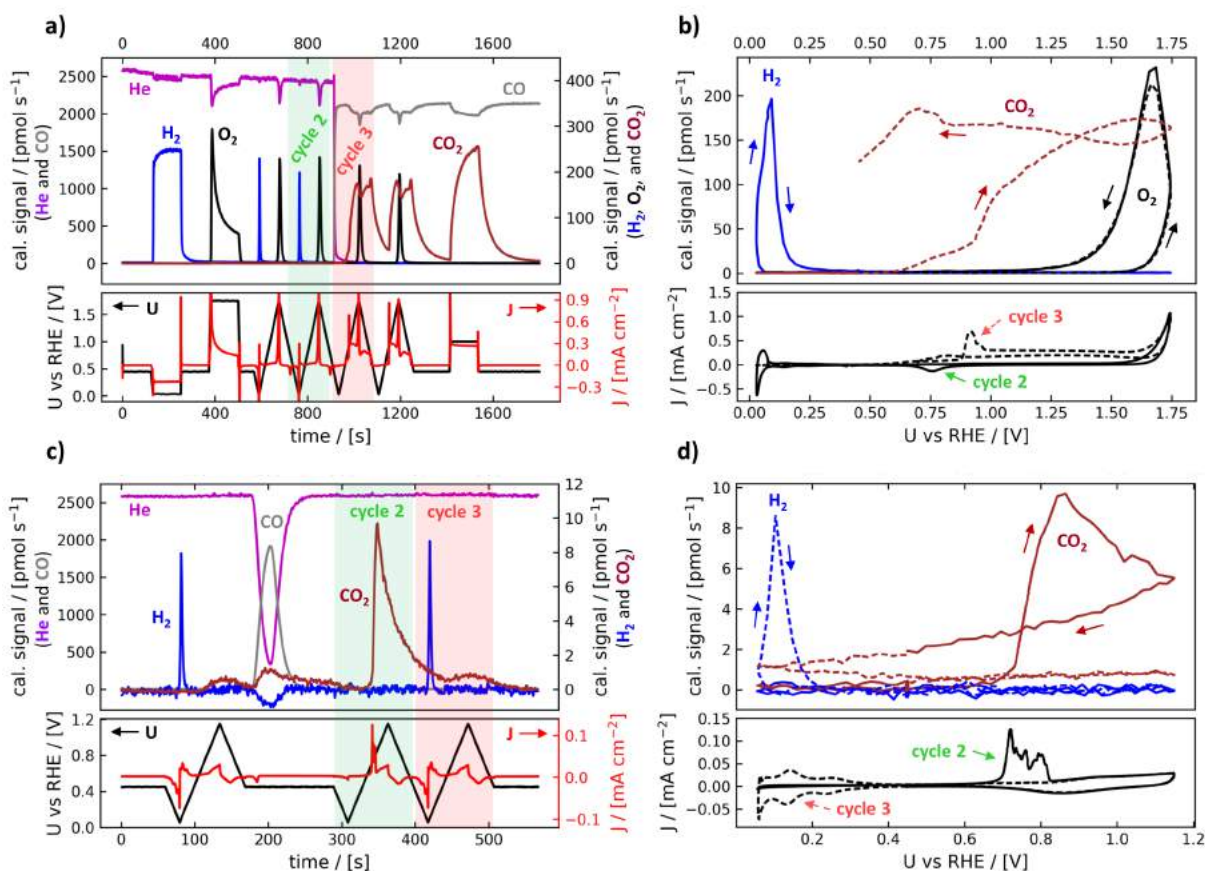
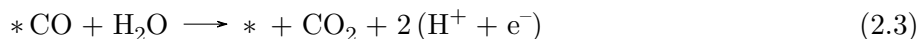


Figure 2.6: Experiments showing HER, OER, CO oxidation, and CO stripping on Pt in 1.0 M HClO_4 . (a) and (c) show EC-MS plots and (b) and (d) each show two parts of the respective data set co-plotted against potential. He, CO, H_2 , O_2 , and CO_2 fluxes were obtained by calibrating the $m/z=4$, 28, 2, 32, and 44 signals, respectively, according to the procedures described in Section 2.2. For a detailed discussion, see Paper I.

Here, the potential has been calibrated to the RHE scale as described above, and the mass spectrometer signals have been calibrated as described in Section 2.2. Figure 2.6a shows a long electrochemistry program including constant-potential steps and cyclic voltammetry, and a switch from He to CO in the middle. It is described in detail in the paper. Two cycles from this program (one in He and one in CO) are selected and plotted vs potential in Figure 2.6b, as is popular among users of DEMS and OLEMS.

Figure 2.6c and d show a CO stripping experiment, a common method of characterizing noble metal surfaces in electrocatalysis [81–84]. It consists of two steps: adsorption of CO, and oxidation of adsorbed CO, given in Reactions 2.2 and 2.3, respectively:



To study the oxidation of surface-adsorbed *CO in isolation, the *CO dosed in the first step has to be purged from the electrolyte before the second step.

In Figure 2.6c, after an initial cyclic voltammogram, a short pulse of CO is dosed using the 6-way valve in Figure A.1 and adsorbs on the surface, as indicated by the CO displacement current at ≈ 190 s. After the CO dose, the first cycle shows no H_2 signal or hydrogen adsorption current (Figure 2.6d), indicating the surface is fully poisoned by adsorbed CO. The anodic scan shows a CO stripping current starting at ≈ 0.7 V vs RHE. The final cycle is identical to the cycle before the CO dose. We like to brag that this is the fastest complete CO stripping experiment ever reported in the literature.

This experiment also demonstrates the sensitivity of the system: the integrated CO_2 signal corresponds to approximately 0.75 ML, i.e. 3 CO molecules adsorbed for every 4 Pt surface atoms; and the integrated H_2 signal at 410 s corresponds to approximately 0.05 ML.

2.1.3 Disadvantages

The attentive reader might be wondering why the shapes of the CO_2 and H_2 signals in Figure 2.6c are so different. Whereas the H_2 signal peaks at 10 pmol/s within a second or two of the cathodic potential limit and has completely passed a few seconds after that, the CO_2 signal, which corresponds to ≈ 15 times as many molecules, also peaks at ≈ 10 pmol/s but then falls very slowly. This is especially annoying when data are plotted against potential (Figure 2.6d), because the tail of the CO_2 signal lasts well into the cathodic scan, even though all of the CO_2 is produced by the electrode surface during the anodic scan. Since the ability to detect a signal is described by its height as well as its area, chip EC-MS is in effect less sensitive to CO_2 than H_2 .

It turns out that this is an inevitable part of chip EC-MS, inseparable from its major advantage of low solvent evaporation [54]. Both are cases of a general fact: the characteristic time for an analyte to leave the working volume and enter the mass spectrometer is strongly dependent on its Henry’s-Law constant of volatility. This is defined as the equilibrium ratio of its partial pressure in the gas phase to its concentration in the aqueous phase:

$$K_H^i = \frac{p^i}{c^i} \quad (2.4)$$

Because there is equilibrium across the chip membrane, the partial pressure of a uniformly dissolved analyte in the chip’s sampling volume, and thus the rate at which it is removed through the chip capillary, is proportional to its Henry’s-Law constant. The characteristic time, taking both diffusion through the working volume and evaporation across the chip’s membrane, for removal of analyte i from the working volume is [54]:

$$\tau^i = \frac{L^2}{2D^i} + \frac{Lp_{\text{chip}}^0 A_{\text{el}}}{\dot{n}_{\text{cap}}^0 K_H^i} \quad (2.5)$$

where L is the working distance, D^i is i ’s diffusion constant in water, $p_{\text{chip}}^0 = 1$ bar is the total pressure in the chip, and \dot{n}_{cap}^0 is the combined flux through the capillary. For all but the least soluble

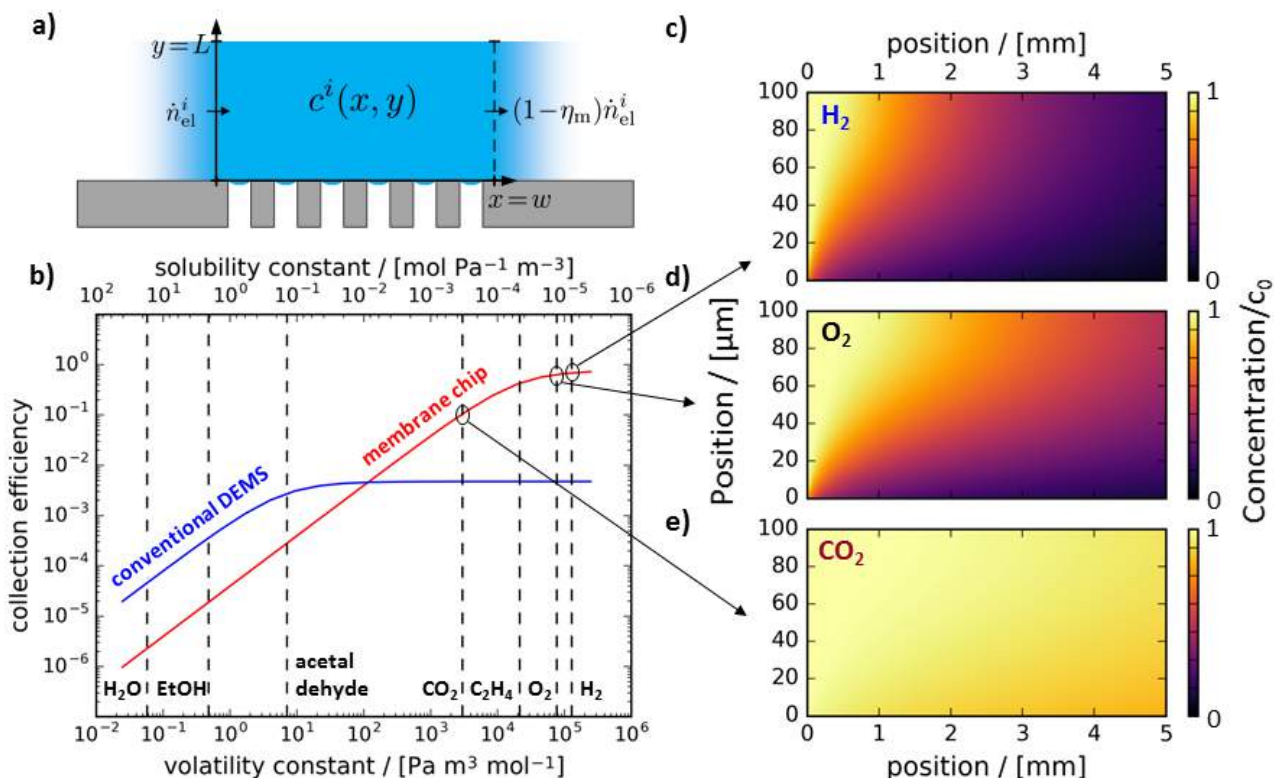


Figure 2.7: Model comparing the sensitivity of chip EC-MS to conventional DEMS via the collection efficiency in a hypothetical flow setup. Adapted from Paper I.

gases (including H_2 and O_2), this is dominated by the second term, which can vary many orders of magnitude. Thus, while any analyte with any vapor pressure will in principle reach the mass spectrometer eventually, detection of liquid products is highly impractical. The characteristic time is (ref. [54] and Paper I) 2 s for H_2 , 3 s for O_2 , 27 s for CO_2 , and $2.5 \cdot 10^5$ s for ethanol.

The question then comes up:

Question 2.1. *With respect to the sensitivity of product detection, when is it advantageous to use chip EC-MS and when is it advantageous to use conventional DEMS?*

Figure 2.7 rephrases this question in terms of *collection efficiency* in a hypothetical flow setup: if an analyte dissolved in an electrolyte is flowing past the vacuum inlet (essentially the collection chamber in a dual thin-layer flow cell [85,86]), will more molecules of the analyte reach the mass spectrometer if the inlet is chip EC-MS or DEMS? To answer this question, I modified the stagnant thin-layer mass transport model to give the concentration profile in such a flowing collection volume [54]. The model is diagrammed in Figure 2.7a and three cases are shown in Figure 2.7c-d. The resulting collection efficiencies are plotted as a function of Henry's-law constant in Figure 2.7b. For light gases like H_2 , chip EC-MS wins due to the lack of a differential pumping stage. For volatile liquids like ethanol, DEMS wins because the much faster non-equilibrium mass transport of products into the first stage of the vacuum chamber outweighs the loss due to differential pumping.

Thus, chip EC-MS is not ideal for, e.g., *in-operando* studies of CO_2 reduction, in which production rates can be high but the interesting products are liquid at room temperature.

Furthermore, while the sensitivity and ability to quickly dose reactant gases are major advantages for chip EC-MS in fundamental studies, it should not be considered a full substitute for a rotating disk electrode (RDE) setup or other setup optimized for cyclic voltammetry. It can sometimes be challenging to get good cyclic voltammograms in the setup. Figure 2.8a shows electrochemistry data from Figure 2.5a plotted against potential. The magenta cycle is with He as the carrier gas, and the

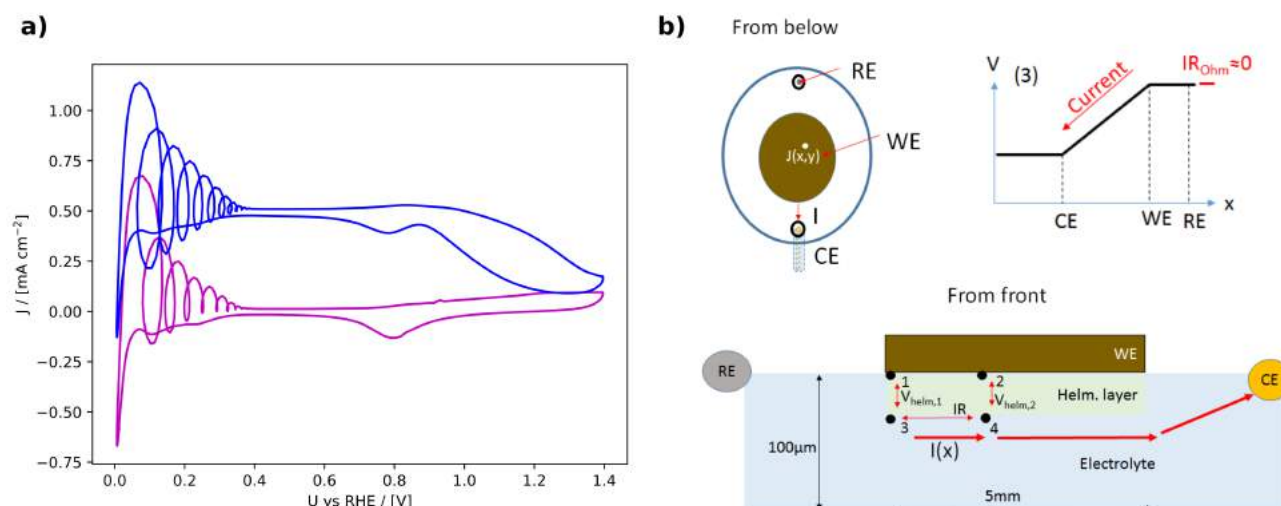


Figure 2.8: (a) CV's in He (magenta) and H₂ from Figure 2.5. The squiggles are the result of oscillations caused, in part, by electrolytic resistance across the surface of the sample. (b) Schematic diagrams of electrode connections to the working volume, indicating that while the conventional ohmic resistance is zero, the resistance within the working volume means that the electrochemical potential is not uniform; adapted from my Master's Thesis [54]

blue cycle is with H₂ as the carrier gas. The H₂ CV is shifted up with respect to the He CV due to a mass-transport-limited hydrogen oxidation current until the platinum surface starts to oxidize at 0.9 V vs RHE and becomes less active for hydrogen oxidation. This all makes sense, but the CV's are dominated by an artifact in the start of the anodic scan: rapid oscillations of current and potential.

These oscillations are worse the less conductive the electrolyte is, and occur most often when there is a sudden change in absolute current density, such as (in this case) right at the scan polarity change in the hydrogen region. The oscillations are attributed to the challenge of controlling the potential when there is a large resistance through the electrolyte from one end of the electrode to the other, first described for this setup in my Master's Thesis [54].

Briefly, the conventional ohmic drop in the EC-MS cell is zero, since the current through the electrolyte is conducted between the working electrode (WE) and the counter electrode (CE), but potential is measured to the reference electrode (RE) on the opposite side of the working electrode (top half of Figure 2.8b). Indeed, potential electrochemical impedance spectrometry (PEIS) measurements in the sniffer setup show a vertical line through zero resistance on the real axis. This is despite the fact that there are large resistances in the cell, most notably in the working volume itself. This resistance can lead to the potential drop across the Helmholtz layer on two parts of the working electrode not being identical, as indicated in the bottom of Figure 2.8. How exactly this leads to oscillations, I do not fully understand.

I realized remarkably late in my PhD project that setting the bandwidth on the Biologic SP-150 Potentiostat to 3, with everything else set up perfectly, could usually remove this artifact. Before that, I had realized that putting a 100 Ohm resistor behind the working electrode helps. This effectively introduces a conventional ohmic resistance, which seems to help the potentiostat avoid such oscillations, and is easy to correct for afterwards when plotting CV's.

The maximum size of the difference in electrochemical potential across the working electrode is important to know, as it is a possible source of error in activity measurements, such as those that will be presented in Section 3.2. For 0.1 M HClO₄ (the electrolyte used in that Section), the resistance from one end of the working volume to the other is on the order of

$$R = \frac{1}{\kappa} \frac{d}{L^{\frac{d}{2}}} = \frac{2}{\kappa L} = \frac{2}{4.2 \left[\frac{\text{S}}{\text{m}} \right] \cdot 100 [\mu\text{m}]} = 4.8 [\text{k}\Omega] \quad (2.6)$$

Where κ is the conductivity of the electrolyte, L is the working distance, d is the diameter of the disk, and to make sure the resistance is overestimated I've approximated the geometry as a resistor with a cross section of $L \cdot d/2$ but a length of d .

This is a huge resistance! The maximum current densities used in this thesis are approximately $100 \mu\text{A}$ ($0.5 \text{ mA}/\text{cm}^2$ geometric current density). At this current density, if we assume the worst case, that all of the current comes from the end of the working electrode closest to the reference electrode, then the potential at the end of the working electrode closest to the counter electrode could be off by as much as $100[\mu\text{A}] \cdot 4.8[\text{k}\Omega] = 0.48[\text{V}]$. The error is in the direction to *increase the overpotential* of the current-drawing reaction on the part of the electrode close to the CE compared to what it should be according to the potential difference between WE and RE. This is a huge potential error!

We are partially saved by two facts:

- The worst case scenario is very far from the truth. In reality, there will be more current from the side of the working electrode closest to the counter electrode. In other words, an uneven current distribution will seek to alleviate an uneven potential distribution, not exacerbate it.
- The error is reduced at small current densities, which are the interesting ones for chip EC-MS anyway. In the same electrolyte at $1 \mu\text{A}$ (corresponding to 10 pmol/s of electrons), the error is less than a worst-case scenario of 4.8 mV difference, still not great but more acceptable.

Nonetheless, solving this should be a high priority for continued development of chip EC-MS. A promising solution is to fabricate chips with liquid through-holes, so that a counter electrode can be placed behind the chip and parallel to the working electrode. A first attempt at this is described in the Master's Thesis of Jesper Pan [87], and a second attempt is being led by Thomas Pedersen of DanChip.

To improve the mood after this discussion of problems with chip EC-MS, the next Section will focus on a positive aspect: the fact that 100% of gaseous electrochemical products make it to the mass spectrometer makes chip EC-MS an excellent platform for *absolute quantification* in mass spectrometry.

2.2 Quantitative mass spectrometry: counting molecules

This Section lays out procedures for using electrochemistry as a platform for quantification in mass spectrometry. It is a bit of a side story from the main narrative to this Thesis, as well as quite technical. A reader unlikely to use the methods presented here may wish to skip to Section 2.3.

Quantification means relating the signal at a mass-to-charge ratio (m/z) or set of m/z 's to the amount of the molecule being quantified, the *analyte*. However, *amount* here can have at least two different meanings.

Mass spectrometry is routinely used to analyze the concentration of analytes in a gas or other matrix [63,64]. When the desired value is a concentration in a gas, calibrating the mass spectrometer is trivial. One need only flow a standard gas or series of standard gases with a known concentrations of the analyte past the inlet and measure the signal at a m/z value unique to the analyte. The standard gases should otherwise as much as possible resemble the gas which will be tested. In general, the signal will scale linearly with the concentration, giving a sensitivity factor. Such a sensitivity factor has the dimensions of signal per concentration.

In the context of chip EC-MS and certain other applications such as catalyst testing in microreactors, we mean something different. We use the following definition of quantification:

Definition 2.1. Quantification: Determining, from mass spectrometer signals, the rate (in molecules per second) at which an analyte is entering the vacuum chamber.

Equivalently, quantification means being able to determine the number of molecules that entered the vacuum chamber in a given time from the integrated mass spectrometer signal. In chip EC-MS as well as microreactor experiments, this is useful because all of the products of a catalytic reaction can be assumed to enter the vacuum chamber, and we typically wish to determine the number of catalytic turn-overs from the integrated signal or, at steady state, the turn-over rate from the signal.

The sensitivity factor we are looking for has the dimensions of integrated signal per molecule. If signal is measured in Amperes and molecules are counted in mol, then the sensitivity factor has units C/mol. Mathematically, the sensitivity factor for analyte i at a mass-to-charge ratio ($m/z=$) M where there are no interferences, is defined as F_M^i such that:

$$S_M = F_M^i \dot{n}_{\text{vac}}^i \quad \text{or, by extension,} \quad (2.7)$$

$$\int_{t_1}^{t_2} S_M dt = F_M^i \Delta n_{\text{vac}}^i \quad (2.8)$$

where S_M is the signal at $m/z=M$, \dot{n}_{vac}^i is the molar flux of analyte i into the vacuum chamber, and Δn_{vac}^i is the amount of analyte i to enter the vacuum chamber between times t_1 and t_2 .

This type of sensitivity factor is more difficult to determine than the signal-to-concentration sensitivity factor because, given a gas with a known analyte concentration, its determination also requires knowledge of the permeability of the vacuum inlet. Estimating the capillary flux is precisely how quantification was originally accomplished for the microreactors [70] and the electrochemical microreactor which was the predecessor to the EC-MS membrane chip [71].

Electrochemistry gives a powerful platform for accurate quantification, because there are analytes for which the electrode current can directly tell us \dot{n} . The next Subsection will describe electrochemical calibration, and the following Subsections will describe how electrochemical calibrations can be used to validate calibrations based on capillary flux and together extended to allow quantification, as understood in Definition 2.1, of any analyte.

2.2.1 Internal calibration by electrochemistry

Electrochemical calibration of mass spectrometer signals is based on establishing a steady and known value for \dot{n}^i in Equation 2.7 based on Faraday's law of electrolysis:

$$\dot{n}_{\text{el}}^i = \frac{I}{z\mathcal{F}}, \quad (2.9)$$

where I is the current, z is the stoichiometric coefficient of electrons (positive for oxidation and negative for reduction) in the electrochemical half-reaction of which i is a product, and $\mathcal{F} = 96487 \text{ C/mol}$ is Faraday's constant.

Equation 2.9 implicitly assumes that *all* of the current I goes to formation of the product i , i.e. it assumes 100% *Faradaic efficiency*. Its use is thus limited to reactions that can be run at 100% Faradaic efficiency. In practice, this is a severe limitation on the analytes that can be calibrated directly by electrochemistry. Three of the analytes that can be calibrated directly are O_2 , H_2 , and CO_2 , which can be produced at $\approx 100\%$ Faradaic efficiency by OER, HER, and CO oxidation, respectively:



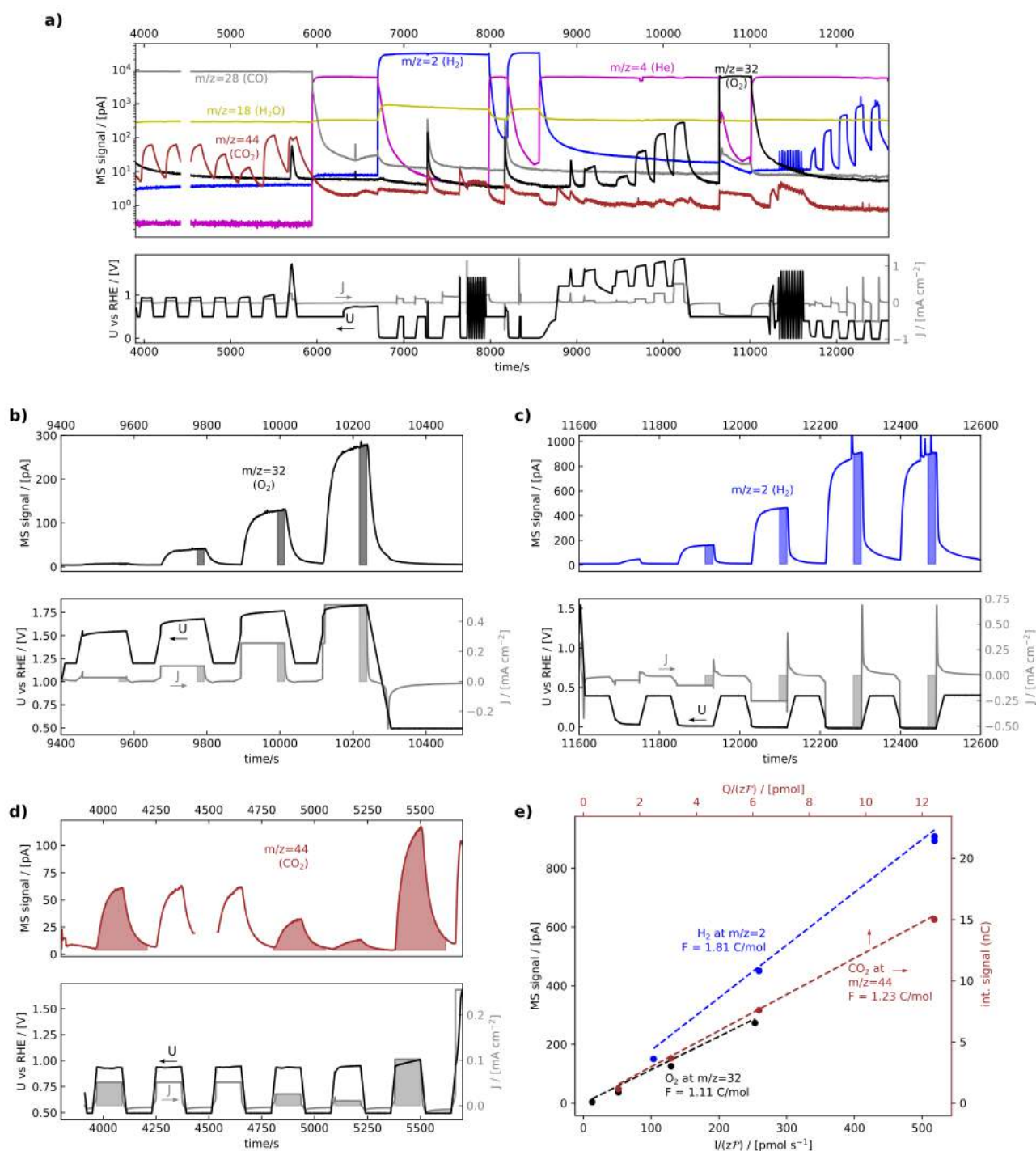


Figure 2.9: Calibration experiments for O_2 by OER, H_2 by HER, and CO_2 by CO oxidation using a platinum electrode in 1.0 M HClO_4 . **(a)** The entire experimental dataset. Zoom-ins are shown for the three calibrations: **(b)**, OER; **(c)**, HER; and **(d)** CO oxidation. **(e)**, The resulting calibration curves are plotted for H_2 and O_2 as near-steady-state signal vs production rate (bottom and left axes), and for CO_2 as integrated signal vs amount produced (top and right axes). The proportionality between the two x-axes and the two y-axes are identical such that the slopes, which are the respective sensitivity factors, are directly comparable.

Figure 2.9 shows calibrations for O₂, H₂, and CO₂ by these reactions. These calibration data are not as flawless as those in the SI to Paper I. They were chosen for this Thesis because, together with the data in Figure 2.10 below, which were taken on the same day, they include the largest number of directly comparable calibrations. I collected the data in Figures 2.9 and 2.10 together with Anna Winiwarter to obtain a full set of sensitivity factors to calibrate the results of propene stripping experiments that build on the results in Paper III.

The full dataset is shown in Figure 2.9a. From the left: the dataset starts with the electrode in CO-saturated electrolyte. The electrode is subject to several periods of 2 minutes of constant-current CO oxidation, inter-spaced by scans to a *resting potential* of 0.5 V vs RHE to separate the peaks. There is a small gap in the MS data around 4500s due to a computer glitch. After the CO₂ calibration, the carrier gas is changed from CO to He, and then to H₂ to measure the signal due to H₂ carrier gas flux through the capillary (which will be discussed in Subsection 2.2.2) and to calibrate the reference electrode. (We actually realize after the anodic scan at ≈ 7700 s that we had forgotten to strip off the adsorbed CO from before, which would have poisoned the electrode for HER/HOR, and so we repeated the RHE calibration.) Then the carrier gas was changed back to He for O₂ calibration by OER. Again, we used 2-minute constant current steps inter-spaced by time at a resting potential to get separated peaks in the m/z=32 signal. Then we switched the carrier gas briefly to O₂ to measure the signal due to O₂ carrier gas flux through the capillary, and switched back to He. Finally, after cycling the potential to clean off any contaminants that may have adsorbed or deposited on the electrode, we calibrated H₂ by HER, again with constant-current measurements inter-spaced by a resting potential.

There are two ways of extracting a sensitivity factor from calibration data made with constant-current calibration steps inter-spaced by resting periods: differential and integral. For a differential calibration, we chose a time interval over which to make the assumption of steady-state, i.e.

$$\dot{n}_{\text{vac}}^i = \dot{n}_{\text{el}}^i, \quad (2.13)$$

and the sensitivity factor F_M^i is, according to Equation 2.7, simply the ratio of the signal S_M to the production rate n_{el}^i , where the latter is calculated by Equation 2.9. For an integral approach, we do not make the assumption of steady state, but instead use the fact that, over time, every gas molecule formed at the electrode will make it to the vacuum chamber:

$$\int \dot{n}_{\text{vac}}^i dt = \int \dot{n}_{\text{el}}^i dt, \quad (2.14)$$

and then determine F_M^i by Equation 2.8.

The differential approach is usually good enough for O₂ (Figure 2.9b) and H₂ (Figure 2.9c), which have fast mass transport (Paper I) and can reach steady state within a minute. In this particular dataset, the mass transport is rather slow, perhaps due to poor alignment of the electrode, and the respective signals appear to be close to but not quite at steady state. It turns out that it's good enough (using the integral approach results in the same sensitivity factor within 2%). The highlighted areas of Figure 2.9b and c show the time interval over which the signal was averaged.

For CO₂ (Figure 2.9d), which has much slower mass transport due to its higher solubility in the electrolyte [Paper I], we have to use the integral approach. Here, the highlighted areas show the time intervals for which $\dot{n}_{\text{el}}^{\text{CO}_2}$ (bottom panel) and S_{M44} (top panel) were taken. The two calibration points affected by the gap in the MS data were excluded.

The resulting calibration curves are plotted in Figure 2.9e. The top x-axis and right y-axis are in integrated units, for CO₂. The proportionality between the two x-axes and the two y-axes are identical such that the slopes, which are the respective sensitivity factors, are directly comparable. The sensitivity factors, resulting from least-squares-fitting without forcing through zero, are written in the plots. The dotted lines shown have the sensitivity factor as their slope but *are* forced through zero, to show a non-ideality typical of these calibration curves: there is a small, approximately constant, offset. This offset implies that there is some charge passed through the electrode which cannot be accounted for by Reactions 2.10, 2.11, and 2.12. In all cases, it can possibly be attributed to

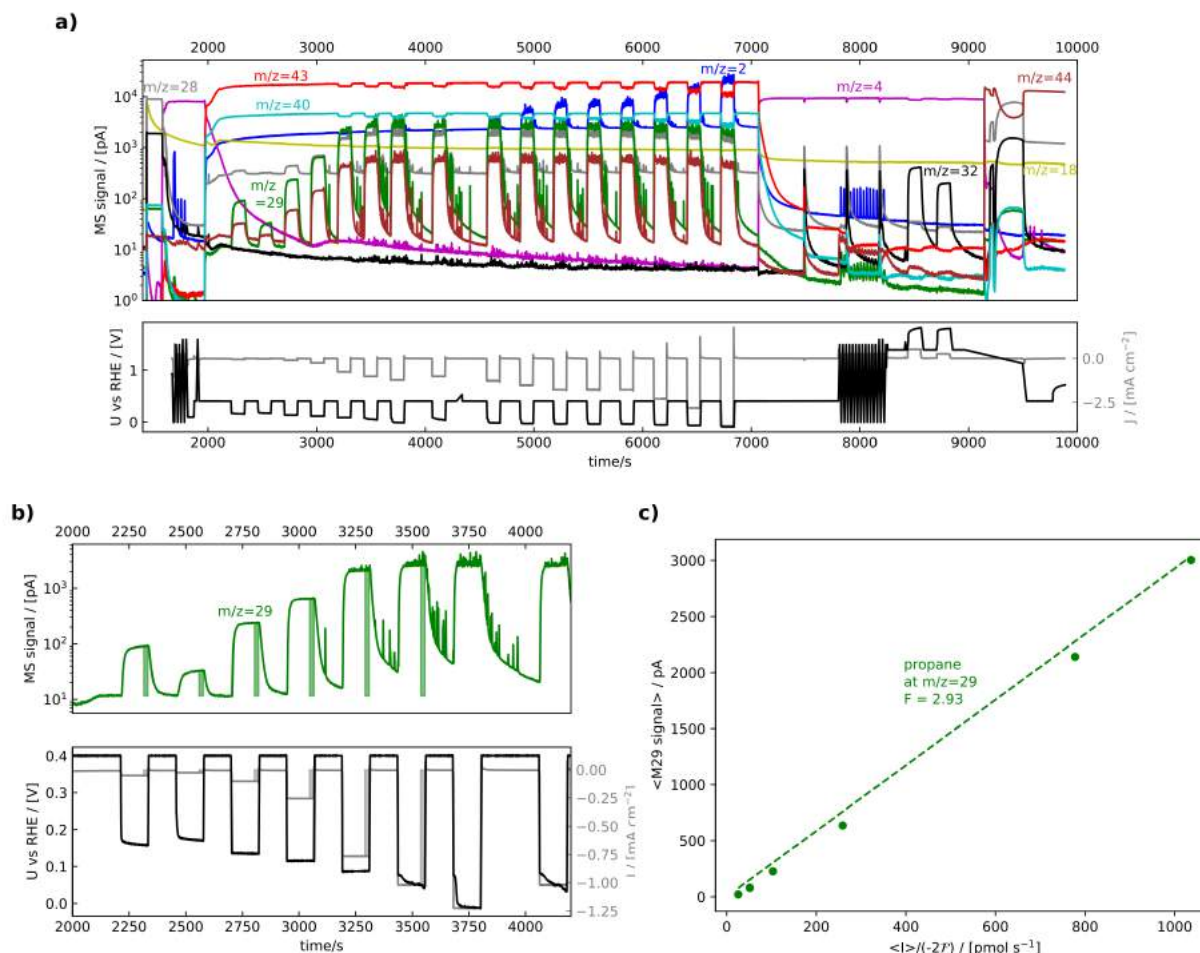


Figure 2.10: Calibration experiment for propane (C_3H_8) by reduction (hydrogenation) of propene (C_3H_6) on Pt in 1.0 M HClO_4 . (a) The entire experimental dataset, taken immediately after that in Figure 2.9a. (b), A zoom-in is shown for the propane calibration. The data points at larger current, where propene reduction is mass-transport limited and some of the current goes to HER are excluded. (c), The resulting calibration curve is plotted as near-steady-state signal vs production rate.

processes oxidizing or reducing the electrode, or adsorbing or desorbing species from its surface. This illustrates the importance of always being critical of the assumptions of 100% Faradaic efficiency, even for simple reactions, and using multiple current densities for calibration. Once a sensitivity factor F_M^i is determined, it can be used to calculate the flux of i from the signal at M according to:

$$\dot{n}_{\text{vac}}^i = \frac{1}{F_M^i} S_M = C_M^i S_M, \quad (2.15)$$

where C_M^i is a *calibration factor*, which in this simple case is just the reciprocal of the sensitivity factor.

Figure 2.10 shows a calibration for an additional reaction that can be run at 100% Faradaic efficiency on platinum: the propene reduction reaction, Reaction 2.16:



I first encountered this reaction while doing the propene stripping experiments reported in Paper III. Briefly, we found that the tendency of adsorbed propene to strip off from a palladium surface as propane or propene on a cathodic sweep correlates with the coverage on the surface, motivating a mechanism for the propene oxidation reaction (the main subject of that paper) in which surface coverage guides the reaction pathway towards certain intermediates. This is, in my opinion, a fantastic story, and was

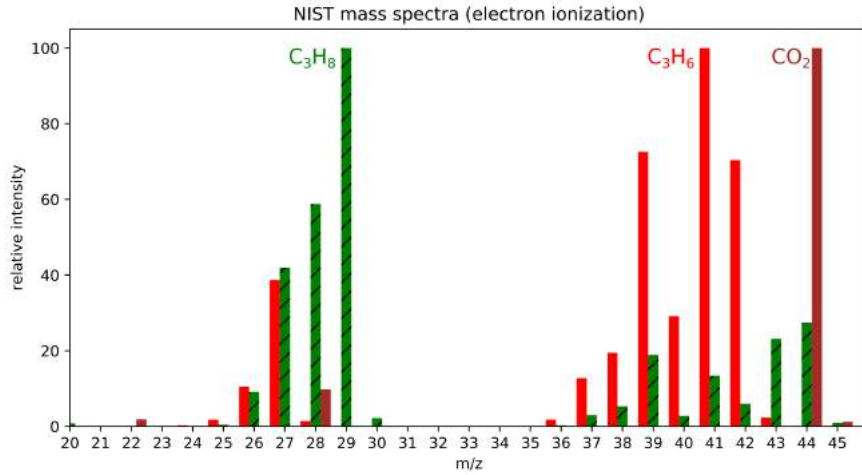


Figure 2.11: Mass spectra of propene (C₃H₆, red), propane (C₃H₈, green and hatched), and CO₂ (brown) from NIST [88]

a great project to be part of, though it is out of the scope of this Thesis. I highly recommend the paper to an interested reader of this Thesis. Anna Winiwarter has since expanded on those EC-MS experiments to probe propene reactivity. However, propene reduction is included here only because it demonstrates well some of the challenges and opportunities in quantitative EC-MS.

The first challenge in quantification of propane and propene is that there is a significant overlap in their mass spectra (Figure 2.11). Propane can itself be detected and quantified without interference at its most prominent mass fragment, $m/z=29$. The sensitivity factor of propane at $m/z=29$, $F_{M29}^{C_3H_8}$, is determined by Faradaic propene reduction in Figure 2.10b and c. However, propane interferes with two other molecules of interest at their most prominent mass fragments: propene at $m/z=41$ and CO₂ at $m/z=44$.

To deal with this, using CO₂ as an example: In situations where both propane and CO₂ are present, we should subtract the portion of the $m/z=44$ signal which is due to propane before dividing by $F_{M44}^{CO_2}$ to get the CO₂ flux. The $m/z=44$ signal which is due to propane can, in turn, be calculated from the $m/z=29$ signal, which is solely due to propane. Mathematically,

$$\dot{n}_{vac}^{CO_2} = \frac{1}{F_{M44}^{CO_2}} S_{M44}^{CO_2} \quad (2.17)$$

$$= \frac{1}{F_{M44}^{CO_2}} \left(S_{M44} - S_{M44}^{C_3H_8} \right) \quad (2.18)$$

$$= \frac{1}{F_{M44}^{CO_2}} \left(S_{M44} - \frac{I_{M44}^{C_3H_8}}{I_{M29}^{C_3H_8}} S_{M29}^{C_3H_8} \right) \quad (2.19)$$

$$= \frac{1}{F_{M44}^{CO_2}} S_{M44} - \frac{I_{M44}^{C_3H_8}}{F_{M44}^{CO_2} I_{M29}^{C_3H_8}} S_{M29}^{C_3H_8}, \quad (2.20)$$

where I_M^i is the relative intensity at $m/z=M$ for in the mass spectrum of analyte i . These are taken from NIST.

The substitution of $S_{M29}^{C_3H_8}$ for $S_{M29}^{C_3H_8}$ assumes that all of the signal at $m/z=29$ is due to propane.

Another way to write this is

$$\dot{n}_{vac}^{CO_2} = C_{M44}^{CO_2} S_{M44} + C_{M29}^{CO_2} S_{M29} \quad \text{with} \quad (2.21)$$

$$C_{M44}^{CO_2} = \frac{1}{F_{M44}^{CO_2}} \quad \text{and} \quad C_{M29}^{CO_2} = -\frac{I_{M44}^{C_3H_8}}{F_{M44}^{CO_2} I_{M29}^{C_3H_8}} \quad (2.22)$$

In general, we can write

$$\dot{n}_{\text{vac}}^i = \sum_M C_M^i S_M, \quad (2.23)$$

or, in vector form ²:

$$\dot{n}_{\text{vac}}^i = \mathbf{C}^i \cdot \mathbf{S} \quad (2.24)$$

2.2.2 External calibration based on the capillary flux

The determination of the sensitivity factors F_M^i by Faradaic production of analyte i described in the previous Subsection is referred to as *internal calibration*, since all of the molecules giving the signal in the calibration experiment are made inside the working volume of the EC-MS setup, and the amount of analyte is known. Here, we describe *external calibration*, whereby a carrier gas, originating outside the setup (in a bottle, or, in the case of air, from the room), is leaked through the capillary of the chip and into the mass spectrometer. The challenge then, in determining the sensitivity factor F_M^i to enable quantification by Definition 2.1, is to determine the flux through the capillary of analyte i given the composition of the gas in the chip. In other words, it is to determine the *capillary flux*.

The flow of molecules through the capillary goes through at least three regimes as the pressure drops from 1 bar to high vacuum [70]: (1) a viscous flow regime near ambient pressure, (2) a transition regime, and (3) a molecular flow regime governed by Kundsén diffusion near high vacuum. It is therefore not trivial to derive an analytical expression, but this has been done. It is [74]:

$$\dot{n}_{\text{cap}} = \frac{1}{RT} \frac{1}{l_{\text{cap}}} \left(\left(\frac{\pi}{8\nu} a^4 \bar{p} + \frac{2\pi}{3} a^3 \bar{v} \frac{1 + 2\frac{2\sqrt{2}}{\sqrt{\pi}} \frac{a}{\eta} \frac{\bar{p}}{\bar{v}}}{1 + 2.48\frac{2\sqrt{2}}{\sqrt{\pi}} \frac{a}{\eta} \frac{\bar{p}}{\bar{v}}} \right) (p_1 - p_{\text{tran}}) + \frac{2\pi}{3} a^3 \bar{v} (p_{\text{tran}} - p_2) \right), \quad (2.25)$$

Here, p_1 is the inlet pressure (usually 1 bar), p_2 is the outlet pressure (≈ 0), $p_{\text{tran}} = \frac{k_B T}{2\sqrt{2}\pi s^2 a}$ is the pressure at which the transition from viscous to molecular flow occurs, $\bar{p} = \frac{p_1 + p_{\text{tran}}}{2}$ is the average pressure in the viscous flow regime, η is the viscosity of the gas, s is the molecular diameter, $\bar{v} = \sqrt{\frac{8k_B T}{\pi m}}$ is the mean thermal velocity of the gas molecules, and m is the molecular mass. Furthermore, l_{cap} is the length of the capillary, and $a = h_{\text{cap}} = w_{\text{cap}}$ is its height and width, assumed to be equal (square cross-section). By design, $l_{\text{cap}} = 1$ mm, $w_{\text{cap}} = 6$ μm , and $h_{\text{cap}} = 6$ μm .

This equation has been validated experimentally for a microreactor by sealing the outlets of an interface block and measuring the rate at which the pressure dropped as air leaked through the chip's capillary into the vacuum chamber [70].

With the internal calibration described in the previous Subsection, however, there is an easier and more precise way to validate the capillary flux: compare the signal due to a molecule in the carrier gas to the signal when the same molecule is produced electrochemically. This is most easily, done for O_2 , as O_2 can be produced electrochemically with near-100% Faradaic efficiency, and is also present in air, giving a "free" carrier gas measurement.

In the dataset presented in the previous Subsection, an air measurement is provided at the very beginning (i.e. $t \approx 1500$ s) of Figure 2.10. Here, the $m/z=32$ signal is $1.88 \cdot 10^{-9}$ A. The corresponding O_2 flux, based on the sensitivity factor F calibrated internally, is

$$\dot{n}_{\text{cap}}^{\text{O}_2} = \frac{S_{M32}}{F_{M32}^{\text{O}_2}} = \frac{1.88 \cdot 10^{-9} [\text{A}]}{1.11 \left[\frac{\text{C}}{\text{mol}} \right]} = 1.70 \left[\frac{\text{nmol}}{\text{s}} \right] \quad (2.26)$$

² The `Molecule` class of the `EC_MS` python package (Appendix C.1) implements both the simple (F_M^i) and vectorized (\mathbf{C}^i) quantification techniques presented above. Fortunately, it is for only a few projects that I've had to use the vectorized approach, and this does not include any of the isotope-labeling studies presented later in this Thesis.

Molecule	η / [$\mu\text{Pa}\cdot\text{s}$]	s / [\AA]	m / [amu]	x^i	\dot{n}_{cap}^i / [nmol/s]	dataset	time / [s]	m/z=M	F_M^i / [C/mol]	F_M^i (EC) / [C/mol]
O ₂ in air	18.5	3.66	30.0	0.2095	1.70	2.10a	1525	32	1.11	1.11
N ₂ in air	18.5	3.66	30.0	0.7808	6.33	2.10a	1525	28	1.42	-
Ar in air	18.5	3.66	30.0	0.0093	0.0755	2.10a	1525	40	0.98	-
He	20.0	2.15	4.0	1	8.64	2.9a	10400	4	0.71	-
CO	17.8	3.76	28.0	1	7.14	2.9a	5000	28	1.24	-
H ₂	8.9	2.71	2.0	1	16.50	2.9a	7200	2	1.83	1.81
O ₂	20.7	3.55	32.0	1	6.24	2.9a	10900	32	1.04	1.11
CO ₂	15.0	4.53	44.0	1	9.38	2.10a	9850	44	1.32	1.23
C ₃ H ₆	8.85	4.50	42.1	1	15.11	2.10a	4400	41	1.22	-

Table 2.1: External calibrations. The flow properties of the carrier gas η , s , and m as well as the fraction x^i of component i are used to calculate the flux of i through the capillary, \dot{n}_{cap}^i . This is compared to the measured signal at a given m/z in a given dataset, where the dataset refers to Figure 2.9 or 2.10 of the previous Subsection. Dataset 2.9 was taken with a chip with $l_{\text{eff}} = 0.99$ mm and Dataset 2.10 was taken with a chip with $l_{\text{eff}} = 0.86$ mm, l_{eff} being used to calculate \dot{n}_{cap}^i . The signal at m/z=M was averaged over 50 s centered at the time indicated, chosen for a steady interference-free measurement. The sensitivity factor F_M^i is the ratio of that signal to \dot{n}_{cap}^i . This is compared, when possible, to F_M^i calculated by electrochemical (internal) calibration.

Using the value of $x_{\text{air}}^{\text{O}_2} = 20.95\%$ for the O₂ content of air and assuming that there is not significant separation effect on the gases in air by the capillary, the capillary flux of air is

$$\dot{n}_{\text{cap}}^{\text{air}} = \frac{\dot{n}_{\text{cap}}^{\text{O}_2}}{x_{\text{air}}^{\text{O}_2}} = 8.08 \left[\frac{\text{nmol}}{\text{s}} \right]. \quad (2.27)$$

In contrast, the flux of air through the capillary predicted by Equation 2.25, using the design parameters for l_{cap} , h_{cap} , and w_{cap} , is 6.86 nmol/s. How do reconcile this difference? In reality, it is h_{cap} which varies from capillary to capillary. This is a result of non-uniformity in the etching step that forms the capillary [74]. The actual capillary height, as measured by profilometry in the clean room, can vary by $\approx 20\%$ across a wafer, which leads to varying permeability, and thus varying air flux.

In fact, calibrating the O₂ signal at m/z=32, and then measuring the m/z=32 signal in air is a way to *calibrate the chip capillary*. Since the real variation in the capillary flux is due to variation in the capillary height, the most correct way to account for it would be to solve Equation 2.25 for h_{cap} with the measured $\dot{n}_{\text{cap}}^{\text{air}}$. However, in practice (so far), to make the implementation easier, we incorporate the difference in an effective capillary length:

$$l_{\text{eff}} = \frac{\dot{n}_{\text{cap, pred.}}^{\text{air}}}{\dot{n}_{\text{cap, meas.}}^{\text{air}}} l_{\text{cap}} = \frac{6.86 \left[\frac{\text{nmol}}{\text{s}} \right]}{8.08 \left[\frac{\text{nmol}}{\text{s}} \right]} 1.00 \text{ [mm]} = 0.85 \text{ [mm]} \quad (2.28)$$

If l_{eff} is used instead of l_{cap} for in Equation 2.25, the equation predicts the “correct” value for the flux of air, i.e. the measured flux as calibrated by OER.

With the chip thus calibrated, we can use Equation 2.25 with l_{eff} to calculate the capillary flux of any gas i , given its dynamic viscosity η^i , molecular diameter s^i , and molecular mass m^i . All that is then needed is a mass spectrometer signal at an m/z=M without interference using i as a carrier gas, and we can calculate its sensitivity factor F_M^i . The datasets presented in Figures 2.9a and 2.10a include the necessary data for such external calibration of several gases. The results are shown in Table 2.1. When possible, the sensitivity factor determined by electrochemistry is included for comparison. While the internal and external calibrations for O₂ in air match by the definition of l_{eff} , the agreement for H₂ and CO₂ is also quite good, validating the method.

2.2.3 Sensitivity factors from theory, and non-ideal effects

The *internal* and *external* calibration methods described above, linked via l_{eff} , enable the determination of sensitivity factors for any analyte which can either be produced electrochemically with 100% Faradaic efficiency or flowed through the chip as a carrier gas. However, these conditions often exclude analytes of interest. If sensitivity factors could be *predicted* through first principles, then any analyte could be quantified. In this Subsection, I propose such a method and check its ability to predict the variation in the sensitivity factors determined in the previous two Subsections.

It is hard to find anything in the literature about predicting mass spectrometry sensitivity from first principles, not least because applications requiring quantification as understood by Definition 2.1 are quite rare. The following steps happen between a molecule i entering the vacuum chamber and a signal at $m/z=M$ being registered (Figure 2.2) [63]:

- The molecule must reach the filament
- The molecule must be ionized by the filament
- The ionization must result in a fragment at $m/z=M$
- The fragment must be transmitted through the quadrupole while it is filtering for $m/z=M$
- The fragment starts an electron cascade on the secondary electron multiplier (SEM)

The signal S_M (in A) can thus in principle be related to the flux \dot{n}_{vac}^i by a series of probabilities P and the SEM amplification A :

$$S_M = \dot{n}_{\text{vac}}^i P_{\text{filament}} P_{\text{ionize}}(i) P_{\text{fragment}}(i, M) P_{\text{transmission}}(M) A(M), \quad (2.29)$$

Where I've tried to indicate whether each probability depends on the identity of the molecule i or the mass of the fragment M .

The probability of reaching the filament P_{filament} depends a lot on the geometry of the vacuum chamber, notably where the inlet, filament, and pump are in relation to each other. I'll assume that it doesn't depend on i or M . The ionization probability $P_{\text{ionization}}(i)$ is proportional to the ionization cross section σ^i of analyte i , which is generally available in the literature. It depends on the ionization energy, which is 70 eV for all of the work in this PhD thesis. The probability of a given fragment being formed after the molecule is ionized can be calculated from the mass spectrum:

$$P_{\text{fragment}}(i, M) = \frac{I_M^i}{\sum_{M'} I_{M'}^i} \quad (2.30)$$

where $I_{M'}^i$ is the intensity of mass fragment M' in the electron ionization mass spectrum of analyte i . These mass spectra, which also depend on the ionization energy, are often available at NIST [88]. They can also be measured directly in the EC-MS setup if i is available as a carrier gas.

The processes after fragmentation can be assumed to only depend on the fragment mass-to-charge ratio M . Both of these processes, quadrupole transmission and SEM amplification factor, will also depend on the ion acceleration. They can be grouped into a function $T(M)$ which I will refer to as the *transmission function*, implying that the transmission through the quadrupole gives most of the mass dependence, even though I'm not sure this is true.

Overall, then, the predicted sensitivity factor, which is denoted with a little f to distinguish it from the experimentally determined big F , is

$$f_M^i = \frac{S_M}{\dot{n}_{\text{vac}}^i} = k \sigma_i \frac{I_M^i}{\sum_{M'} I_{M'}^i} T(M). \quad (2.31)$$

Where k is a proportionality factor, which I choose to set $f_{\text{M28}}^{\text{N}_2} = 1$. The challenge, then, is to determine $T(M)$.

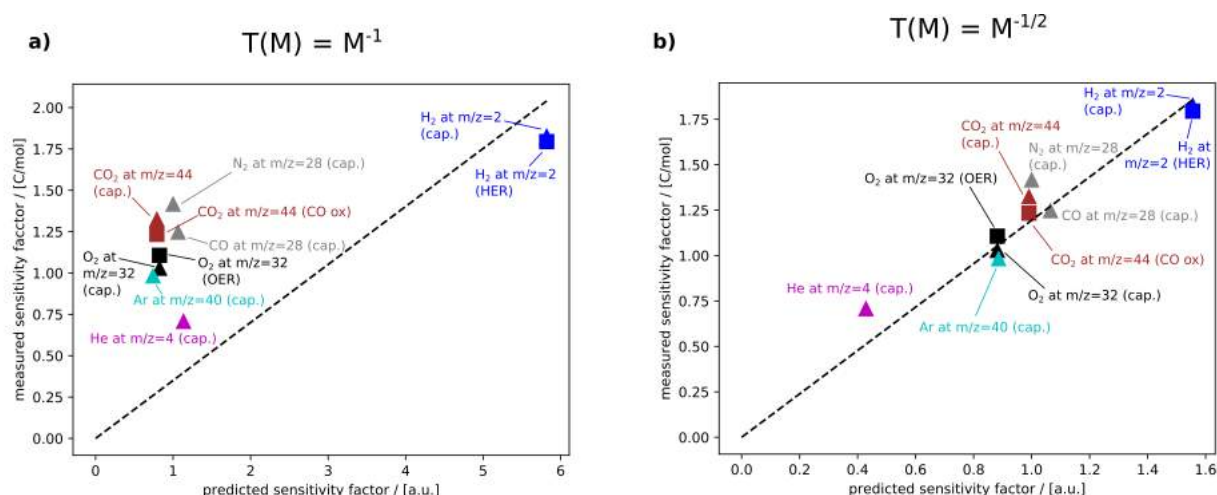


Figure 2.12: Measured sensitivity factor F_M^i vs predicted sensitivity factor f_M^i for two guesses at the transmission function: (a), inversely proportional with the m/z ratio; and (b), inversely proportional with the square root of the m/z ratio. The measured sensitivity factors, which are shown in Table 2.1, are determined via capillary flux (triangles) or an electrochemical reaction (squares).

Some hints can be found from quadrupole theory [89]: For a quadrupole mass analyzer, the transmission function should correlate inversely with the resolution $R = M/\Delta M$. A perfectly-tuned mass spectrometer should have a constant mass resolution, i.e. $\Delta M = c$. If so, the resolution varies directly with M . This implies that the transmission function should vary inversely with M , i.e., $T(M) = M^{-1}$.

Figure 2.12a shows the measured F_M^i plotted against the thus-calculated f_M^i with $T(M) = M^{-1}$. The predictive scheme does a terrible job at explaining the variation in the data.

If we keep the form of the transmission function and change the exponent, we can get a relatively good fit by putting the exponent to $-1/2$. This may indicate that the SEM amplification factor scales with $M^{+1/2}$, or may indicate that the above reasoning doesn't quite hold. In any case,

$$T(M) = M^{-\frac{1}{2}} \quad (2.32)$$

seems to give a good fit. The best-fit line of proportionality between F and f gives a root-mean-square error on the prediction of F of 12%. In other words, we can quantify an arbitrary new analyte i at mass M to within about 12% accuracy (25% within two standard deviations) without a new calibration. We have developed a generalized solution to the problem of quantification as understood by Definition 2.1!

There is, however, an important exception: if the carrier gas influences the sensitivity of the mass spectrometer, then all bets are off. This actually seems to be the case when propene is the carrier gas. Figure 2.10 shows an internal calibration for propene by propene reduction. In the higher-current steps in Figure 2.10a, propene reduction is mass-transport limited and hydrogen is also produced. Assuming that there are no Faradaic processes other than propene reduction to propene and hydrogen evolution, the amount of hydrogen produced can be determined from the electrode current and the calibrated propene signal. Figure 2.13a shows the data used to test the H₂ calibration in propene, calibrated using the H₂ sensitivity factor calculated in He. Faradaic analysis shows that the H₂ signal is consistently ≈ 3 times larger than expected based on subtracting the calibrated propene signal from the total current density, and using the calibration of H₂ at $m/z=2$ by HER in He carrier gas. This implies that the sensitivity factor of H₂ at $m/z=32$ ($F_{M2}^{\text{H}_2}$) with propene as the carrier gas is ≈ 3 times larger than it is with He as a carrier gas. The sensitivity factors for H₂ at $m/z=2$ and for propene at $m/z=29$ are included, versus the sensitivity factors predicted by Equation 2.31 with $T(M) = M^{-1/2}$, in Figure 2.13b. They are both way above the trendline set by the calibration factors measured in other carrier

gases.

These unpredictable and therefore undesirable effects of propene on the mass spectrometer sensitivities are likely due to space-charge effects. Propene has the highest capillary flux of the carrier gases used (Table 2.1) due to its low viscosity, and has a rather high ionization cross-section. This results in a high concentration of ions in the mass spectrometer, which apparently leads to generally increased sensitivity, though I do not claim to understand why. Nonetheless, the response at $m/z=29$ is linear with propane production rate (Figure 2.10c), indicating that quantification of propane using this sensitivity factor is valid when propene is the carrier gas.

The question is then:

Question 2.2. *How should we quantify propane in a carrier gas other than propene?*

This is, in fact, what we wished to do for the propene stripping experiments in Paper III, where the interesting signal is the propane that comes off in inert gas after propene has been adsorbed on the surface. I think the best strategy is to predict the sensitivity factor for propane in He based on the other calibrations and the trendline in Figure 2.12b. This prediction is indicated by the green dot in Figure 2.13b. Whereas propene reduction to propane gives a sensitivity factor of $F_{M29}^{C_3H_8} = 2.93$ C/mol, the theory presented in this Subsection indicates the calibration factor in He is $F_{M29}^{C_3H_8} = 1.3$ C/mol (to within $\approx 25\%$). We had not yet understood this effect of propene on the overall sensitivity of the mass spectrometer when publishing Paper III, and thus likely underestimated the amount of propane desorbed in the stripping experiments reported there by a factor of ≈ 2 .

2.2.4 Quantitative mass spectrometry in practice - methanol synthesis and CO reduction

The aim of this Subsection is to provide practical suggestions on how to use the calibration methods described in the previous Subsections for users of EC-MS and other techniques benefiting from quantification as understood by Definition 2.1. Let's say you want to quantify a gaseous analyte i . First you need to find a mass-to-charge ratio M at which no other molecules in your experiments will give a signal, or at least where you expect the interference to be manageable (as described in the end of Subsection 2.2.1). The goal then is to determine the sensitivity factor $F_M^i = S_M/\dot{n}_{vac}^i$. You have three options, none of which excludes the others:

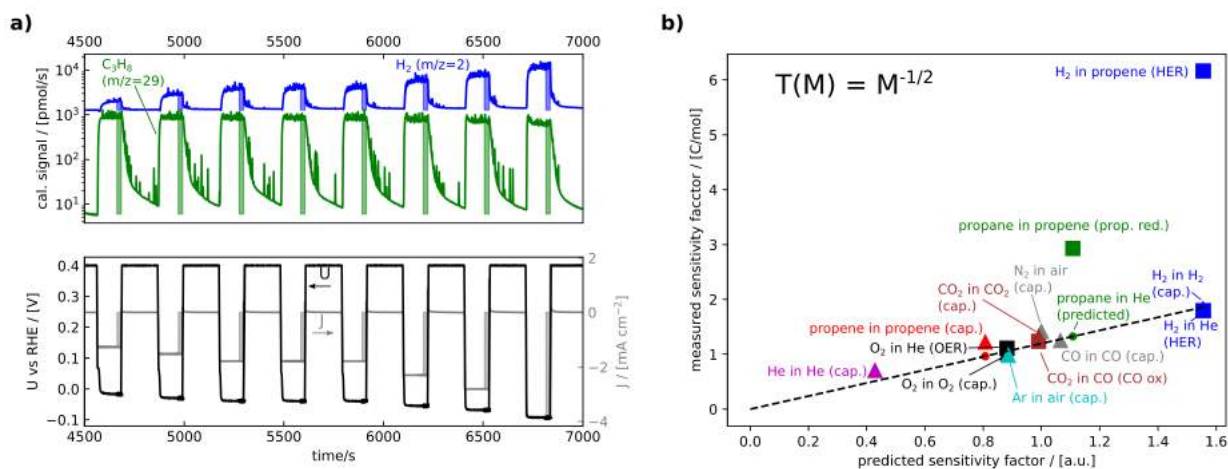


Figure 2.13: Non-ideality with propene as carrier gas: (a), Propene reduction + HER, data from Figure 2.10a. (b), Measured vs predicted calibration factors including propane at $m/z=29$ measured by propene reduction and H₂ at $m/z=2$ measured by HER in propene, which do not fit the trend of the other masses. A transmission function of $T(M) = M^{-1/2}$ was used for the predicted calibration factor. Propene was measured at $m/z=41$ and propane at $m/z=29$. The others analytes are measured at the same masses as in Figure 2.12. The green dot shows the prediction for the sensitivity factor of propane at $m/z=29$.

1. *Internal calibration*³, Subsection 2.2.1:

If you can produce a known number of molecules of your analyte by an electrochemical reaction, then do so, and measure the signal! This is the most certain way to get a sensitivity factor, as it relies on no assumptions other than Faraday’s law of electrolysis (Equation 2.9) to determine \dot{n}_{el}^i , which is equal to \dot{n}_{vac}^i at steady-state or when integrated. A drawback is if a reactant gas is needed which won’t be the carrier gas during the measurements you wish to quantify, since in some cases the carrier gas can influence the sensitivity factors. Furthermore, knowing how many molecules you produced generally requires being able to assume 100% Faradaic efficiency. In my experience, there is often a small but constant amount of residual current from some other process, so internal calibration should use several different current densities and use the slope of the line-of-best-fit between the measured S_M and expected \dot{n}_{el}^i as the sensitivity factor.

2. *External calibration*⁴, Subsection 2.2.2:

If you have i available as a gas, either pure or diluted, then you can fill the chip with this gas and measure the signal at M . However, this requires that you know the capillary flux through the chip. The capillary flux can be calculated by Equation 2.25, but only if the capillary dimensions are known, and in practice these dimensions vary a bit from chip to chip. Thus, external calibration requires a *chip calibration*.

- *Chip calibration*⁵, Subsection 2.2.2:

A chip calibration means determining the effective capillary length l_{eff} that can take the place of l_{cap} in Equation 2.25 so that it predicts the measured flux of an analyte with a sensitivity factor determined by internal calibration. Typically, this means determining $F_{M32}^{\text{O}_2}$ using OER, and then measuring the $m/z=32$ signal while the chip is open to air.

3. *Predictive calibration*⁶, Subsection 2.2.3:

If a number of other sensitivity factors, F_N^j , can be obtained by internal or external calibration, then these other sensitivity factors can be used to predict F_M^i . A predicted calibration f_N^j is calculated for each other molecule j according to Equation 2.31. This requires knowledge of the ionization cross-sections and mass spectra of all the analytes (available in the literature, usually at NIST [88]) and a *transmission function* $T(M) = M^x$ describing the dependence of the sensitivity on the mass fragment. $T(M)$ depends on the tuning of the mass spectrum, and at the setup used for this PhD project, $T(M) = M^{-1/2}$ works well. As many internal and external calibrations as possible should be used to fit and build confidence in $T(M)$. Once a line of proportionality $F_N^j = a f_N^j$ is established, F_M^i is predicted by calculating f_M^i by Equation 2.31 and multiplying by a .

Ideally, at the start of a research project, all three of the above strategies should be used for as many analytes of interest as possible. Plotting F against f will help find non-ideal effects such as that described for propene as a carrier gas in Subsection 2.2.3.

Notice that predictive calibration relies on calibrating as many molecules as possible by external calibration or internal calibration in order to determine $T(M)$ and the proportionality between F and f . Note also that external calibration depends on a chip calibration which in turn depends on an internal calibration. And internal calibration relies on using the current for an electrochemical reaction to know the flux of a molecule to the vacuum chamber. Thus: **Robust quantification as meant in Definition 2.1 is made possible by the coupling of electrochemistry and mass spectrometry.**

³Internal calibration is implemented with the function `calibration_curve` of the `EC_MS` python package (Appendix C.1). This function also produces plots of the types in Figure 2.9b-e.

⁴External calibration is implemented with the function `point_calibration` of the `EC_MS` python package.

⁵Chip calibration is implemented with the function `chip_calibration` of the `EC_MS` python package.

⁶Predictive calibration is implemented with the function `recalibrate` of the `EC_MS` python package (Appendix C.1). This function also produces plots of the type in Figure 2.12.

This quantification platform can, however, be extended to applications that do not involve electrochemistry. As an example, my colleague Alexander Krabbe is doing a project on methanol synthesis catalysts. As such, he is interested in measuring the TOF for methanol synthesis in a thermal microreactor setup. This means determining the flux of methanol to the vacuum chamber $\dot{n}_{\text{vac}}^{\text{CH}_3\text{OH}}$ from the signal at its most pronounced mass fragment $S_{\text{M}31}$. This means determining $F_{\text{M}31}^{\text{CH}_3\text{OH}}$. The problem is especially challenging since methanol, being a liquid at room temperature, is not available as a carrier gas. We developed the following procedure:

1. Determine $F_{\text{M}32}^{\text{O}_2}$ on the EC-MS setup by internal calibration using OER.
2. Use $F_{\text{M}32}^{\text{O}_2}$ on the EC-MS setup to determine the flux of air through the capillary of an EC-MS membrane chip, and thus l_{eff} (chip calibration).
3. Install the calibrated membrane chip on the microreactor setup. Since the flux of O_2 through the membrane chip's capillary $\dot{n}_{\text{vac}}^{\text{O}_2}$ is known, measuring the $m/z=32$ signal gives $F_{\text{M}32}^{\text{O}_2}$ for the *microreactor setup*!
4. Install a microreactor on the microreactor setup, and fill it with 1 bar O_2 . Since $F_{\text{M}32}^{\text{O}_2}$ for the microreactor setup is known, the $S_{\text{M}32}$ signal tells us the O_2 flux through the microreactor's capillary, and thus its l_{eff} . We now have a *chip calibration of the microreactor*.
5. Use the calibrated microreactor for external calibrations on the microreactor setup: Flow a number of carrier gases spanning a range of molecular masses, viscosities, and ionization cross-sections through the microreactor, f. eks. He, H_2 , O_2 , Ar, CH_4 , CO_2 , etc. Use the signal at the most intense mass fragment and the calculated flux with l_{eff} to determine a sensitivity factor F for each of the gases.
6. Determine the transmission function $T(M)$ that gives the best fit to a line of proportionality between the measured sensitivity factors (F) determined by external calibration and the predicted sensitivity factors (f) calculated for each of the gases. Then determine $F_{\text{M}31}^{\text{CH}_3\text{OH}}$ with predictive calculation, by calculating $f_{\text{M}31}^{\text{CH}_3\text{OH}}$ and multiplying by the proportionality constant.

The functions of EC-MS do each step of the data analysis and calculations, making the whole procedure described above quite quick and painless. Furthermore, steps 1 through 4 need only be done once, so long as the microreactor with the calibrated capillary flux is not lost or damaged. (It just so happens that EC-MS membrane chips can go on the microreactor setup but not vice versa, or this procedure could be a step shorter.)

This leads us to the question:

Question 2.3. *How often should one calibrate?*

Figure 2.14a helps answer the question.

This figure includes one data point for each “successful” experiment (meaning nothing broke before starting the measurement, results or lack thereof aside - the setup was still under development) during a project on CO reduction that took up most of the first year of my PhD and which we put on hold due to difficulties with reproducibility ⁷. Figure 2.14 was one of my many unsuccessful attempts to

⁷In that project, which is out of the scope of this Thesis and is, at present, best described in the PhD theses of Anders Bodin [90] and Daniel Trimarco [74], we used the EC-MS setup to measure transient phenomena during CO reduction on mass-selected, vacuum synthesized copper nanoparticles. Briefly: we drafted an article, included in the appendix to both of those PhD theses, describing how the copper nanoparticles show a transient high selectivity for methane production during the first few seconds of applied potential, whereas ethylene selectivity is more steady. Furthermore, we showed that this methane transient has an independent Tafel slope and depends on prior exposure to air-saturated electrolyte, indicating that oxygen activates the catalytic surface towards a reaction pathway not normally accessible. This was of high interest due to the heated debate in the literature about the effect of oxygen on copper's CO_2 and CO reduction activity [58,91–93] (see also, for example, Paper IV). We never ended up submitting the draft though,

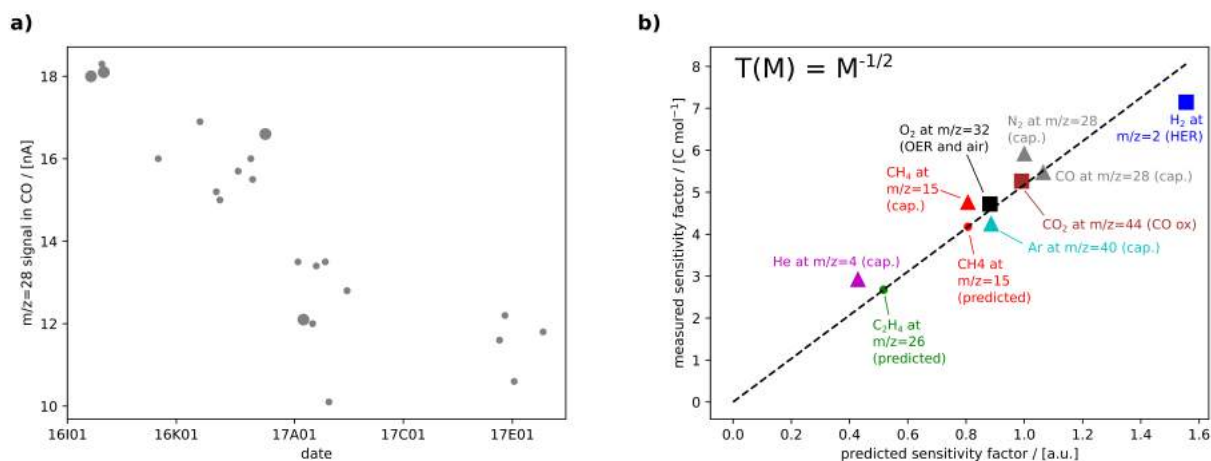


Figure 2.14: (a), Signal at $m/z=28$ with 1 bar CO in the membrane chip as carrier gas for experiments done over a period from September 2016 to May 2017. The date on the x-axis is written as yyMdd with M=A representing January, B representing February, etc. (b), Internal, external, and predicted calibrations for the dataset used in Paper I. This is a correction to Figure S6b from the SI of that paper.

find something, ideally within our control, that could separate the “good results” from the bad: it shows the $m/z=28$ signal from the CO carrier gas at the same time during each of those experiments. Unfortunately, it didn’t help at all in figuring out what kept going wrong, but it does shed light on the nature of the variability which quantitative mass spectrometry is up against.

Since all of the measurements were made with the same pressure of CO flowing through the capillary of chips from the same batch to the same mass spectrometer (which we of course did not tune in the middle of the project), all of the $m/z=28$ signals should in principle be identical. However, there is both a scatter of \pm approximately 10% and a gradual drift with a signal loss on the order of 45% over nine months. The scatter is probably mostly due to the variation in the actual chip capillary dimensions (we were breaking chips quite frequently during that project), but we can’t rule out sensitivity effects related to the recent history of the mass spectrometer. The drift is likely due to the mass spectrometer gradually falling out of tune.

The scatter indicates that it is best to have a calibration on the same day as the measurement. However, calibration of one molecule should be enough, assuming that it is the absolute sensitivity that drifts and not the relative sensitivity. This can be done by internal calibration of one molecule (for example H_2 by HER, which is the inert-gas activity test often used for comparison anyway when studying CO or CO_2 reduction), or just by measurement of the signal of air or a carrier gas if l_{eff} is known for the chip. If an external calibration is used for this purpose, each new chip has to be calibrated - meaning an air measurement through the chip and an OER measurement on the same day (though not necessarily the day of the experiment to be quantified).

The harder work is at the beginning of a project, or if the mass spectrometer is tuned: At that time, make a plot of the type in Figure 2.14b with as many internal and external calibrations as possible. This determines $T(M)$ in case any sensitivity factors need to be predicted in the absence of an internal or external calibration, and gives the relative sensitivities of all the molecules of interest. Then, scale these up or down according to one calibration taken on the day of the measurement.⁸ Of course when there is only one analyte of quantitative interest - for example in OER studies - a

because out of tens of measurements, we were only able to reproduce the result a handful of times (the big dots in Figure 2.14a), with the other experiments showing CO reduction activity not significantly higher than the blank glassy carbon substrate; and we could never see the copper on the sample after the experiment, indicating the nanoparticles were not stable. The work is ongoing, now led by Jakob Ejler, Degenhart Hochfilzer and Ezra Clark. Getting reproducible results on the mass-selected copper nanoparticles is still remarkably challenging, but they are making progress with a patient, systematic approach - in contrast to the brute-force approach that Daniel, Anders, and I had started out with.

⁸This procedure is facilitated by the `save_calibration_results` and `load_calibration_results` functions of the `EC_MS` python package.

simple calibration can be done each measurement day and the full calibration results are not strictly necessary. Either way, be aware of how much the sensitivity of the mass spectrometer has drifted - sensitivity factors should not change dramatically from day to day!

To finish up the Section, I will briefly discuss the calibration used for the CO reduction project mentioned above, which happens to be the same calibration dataset that we published in the SI of Paper I:

When studying CO reduction, we were most interested in detecting and quantifying methane (CH_4) and ethylene (C_2H_4). CH_4 is best measured at $m/z=15$ to avoid the interference of O at $m/z=16$, and C_2H_4 , at $m/z=26$ to avoid the shoulder from CO. Neither of these products can be made with 100% Faradaic efficiency by any known electrocatalyst [94,95], so internal calibration is not an option. We had CH_4 available as a carrier gas for external calibration, but not C_2H_4 . We therefore did internal calibration measurements (O_2 , H_2 , and CO_2) and external calibration measurements (O_2 , N_2 , and Ar in air; He, CO, and CH_4), set l_{eff} to equate the sensitivity factors measured by internal and external calibration of O_2 , and plotted all of the measured sensitivity factors against the calculated relative sensitivity factors. All of the calibrations fall on approximately the same line, as shown in Figure 2.14b. This enables the prediction of the C_2H_4 calibration, indicated by the green dot.

When we published Paper I, we had not yet realized that equating the sensitivity factors measured by internal and external calibration of O_2 was the best way to determine l_{eff} , and instead used a much more convoluted method. With the wrong l_{eff} , the internal and external calibrations fell on separate lines (Figure S6 of Paper I). The procedures described in this Section should therefore be considered an improved and corrected quantification framework when compared to that presented in Paper I.

2.3 Isotope labeling: tracking atoms

Isotope labeling is a powerful technique to investigate mechanisms in physics, chemistry, and biology. As the name implies, isotope labeling involves intentionally preparing a material with an isotopic enrichment, and using them to keep track of how the atoms have moved around. This is in contrast to isotope geochemistry [96] and radiometric dating (including ^{14}C dating) [97,98], whereby the pre-existing isotopic composition of a sample is used to infer its age and origin - techniques which have provided a lot of insight into the history of earth and mankind. Whereas these techniques investigate history, isotope labeling techniques investigate how potentially useful chemical reactions take place. The former is useful in understanding the climate crisis; the latter will likely be useful in developing some of the technologies to solve it.

Here are a few interesting examples of isotope labeling experiments:

- The nature of DNA replication was established by an isotope-labeling experiment, the Meselson - Stahl experiment⁹, first reported in 1958, not long after the elucidation of the structure of DNA [99].

In this experiment, *E. Coli* bacteria are grown in a Petri dish containing sugar and $^{15}\text{NH}_3$. Natural nitrogen is 99.8% ^{14}N and 0.2% ^{15}N , so after many generations, when these bacteria have incorporated ^{15}N in all of their nitrogen-containing molecules, including DNA, they are isotopically labeled with respect to normal *E. Coli* (and a bit heavier). These labeled *E. Coli* are then transferred to a dish containing sugar, natural NH_3 , and isotopically natural versions of all of the nucleic bases that are the nitrogen-containing and information-encoding part of DNA. When these *E. Coli* divide, some of the DNA of the two resulting “daughter” cells has to be synthesized afresh. When the DNA of the daughter cells was isolated and centrifuged, it weighed exactly the average of fully labeled and non-labeled DNA! Exactly half of the nitrogen of the daughter cells was ^{15}N and half was ^{14}N . This implies that exactly one whole strand of the double-helix of each daughter cell came from the parent, and thus that DNA is replicated by the two strands unraveling and each serving as the template for a new one.

- Methanol can be synthesized from syngas (CO and H_2) on a Cu/ZnO catalyst [51] by the overall reaction



but the reaction only runs at appreciable rates when CO_2 is included in the reaction feed. ^{14}C -labeling [100] and later ^{13}C -labeling studies [101] showed that the actual methanol synthesis reaction has CO_2 as the reactant:



and that the role of the CO is to consume the water released and replenish the CO_2 consumed by this reaction via the water-gas-shift reaction:



- There has been a recent explosion of literature on electrochemical N_2 reduction to NH_3 :



The amounts of NH_3 produced are typically very small because the reduction of water to H_2 (Reaction 2.11) is almost universally favored. Nonetheless, there is an extremely sensitive colimetric technique for detection of NH_3 , so many groups succeed in detecting NH_3 when they run

⁹When your experiment is good enough, apparently it gets named after you. My best chance at this kind of honor in this Thesis, though a long shot, is introduced in Subsection 3.3.4

their electrochemical reaction. However, NH_3 is common in the environment and it is very easy to get a false positive from NH_3 contamination. Quantitative reduction of $^{15}\text{N}_2$ to $^{15}\text{NH}_3$, which is easy to distinguish from $^{14}\text{NH}_3$ using nuclear magnetic resonance (NMR), is the only accepted way to prove that the measured NH_3 is formed by electrochemical N_2 reduction [102]. So far, the only electrochemical strategy proven to quantitatively produce the same amount of $^{15}\text{NH}_3$ from $^{15}\text{N}_2$ as natural NH_3 from natural N_2 is an indirect one whereby lithium is reduced and then reacts with N_2 to form lithium nitride which is then hydrolyzed [102, 103].

Most of this Thesis will deal with Oxygen isotope labeling. Natural oxygen has three stable isotopes. On earth it is 99.76% ^{16}O , 0.04% ^{17}O , and 0.20% ^{18}O [96]. There are small deviations (on the order of +/- 0.01%) in the natural isotopic composition of oxygen on earth that are useful in isotope geochemistry, but not relevant for this Thesis. Furthermore, all of the oxygen-labeling experiments in this thesis will use natural oxygen and ^{18}O -enrichment. I will therefore only look at even masses ($^{16}\text{O}_2$ at $m/z=32$, $^{16}\text{O}^{18}\text{O}$ at $m/z=34$, and $^{18}\text{O}_2$ at $m/z=36$), which are unaffected by ^{17}O except for the exceedingly rare $^{17}\text{O}_2$. So ^{17}O is ignored throughout this thesis.

While I mentioned at the start of this Chapter that isotopes of the same element are chemically identical, this is not quite true. There are small differences, most importantly due to effect of the nuclear mass on molecular vibrational energies, that can make a small thermochemical difference between isotopes. Indeed, the most employed separation methods isotopes of light elements utilize such chemical differences. [104]

The most used industrial method of separating ^{18}O from natural oxygen is by fractional distillation of NO , as the isotope effect on the vapor pressure of NO happens to be relatively strong [105]. Most of the ^{18}O produced is used in the medical industry as a precursor to ^{18}F for positron emission tomography (PET). Two commercial sources of ^{18}O are used in this Thesis: 97% H_2^{18}O from Medical Isotopes; and 98% $^{18}\text{O}_2$ from CK Gas Products.

First, though, we'll take a quick look at an electrochemistry experiment in which it is instead hydrogen which is labeled. Natural hydrogen is 99.98% ^1H and 0.02% ^2H . The isotopes of hydrogen are important enough to get their own names, and ^2H is called *deuterium* or D (such that H only refers to ^1H). D_2O is called *heavy water* and is used as a non-interfering solvent in NMR, and as a neutron mediator in nuclear reactors. It is produced mainly by the Girdler-Sulfide process, which utilizes the temperature-dependence of the equilibrium constants for the reactions [106]



The D_2O used in the coming experiment is 99% isotopic purity, from Aldrich.

2.3.1 Example experiment: RHE potential measurement in D_2O

As mentioned in the Foreword, I originally envisioned a short chapter called ‘‘Hydrogen’’, full of electrochemical H-D experiments, to proceed the chapter called ‘‘Oxygen’’, but ran out of time. This Subsection is a small consolation for the disappointed reader.

Figure 2.15a shows an experiment on a polycrystalline platinum stub in deuterated electrolyte, specifically 0.1 M HClO_4 in 99% D_2O . Starting from the left, the electrode potential is cycled while in Ar-saturated electrolyte, and an $m/z=4$ signal is seen near the cathodic potential limit, corresponding to reduction of D_2O to D_2 . It is to avoid masking the D_2 signal that I use Ar ($m/z=40$) as the carrier gas here instead of He ($m/z=4$).

The electrode potential is then set to open circuit at 1900 s, and the carrier gas is then changed from Ar to H_2 at approximately 2050 s. Thus far, this is essentially the same procedure as the RHE calibration experiment demonstrated back in Subsection 2.1.2 (Figure 2.5). However, there is an important difference. Whereas in isotopically natural electrolyte, the HOR and HER run, undetected, at equal rates in equilibrium, now the forward and back reactions, Reactions 2.38 and 2.39, are distinct:



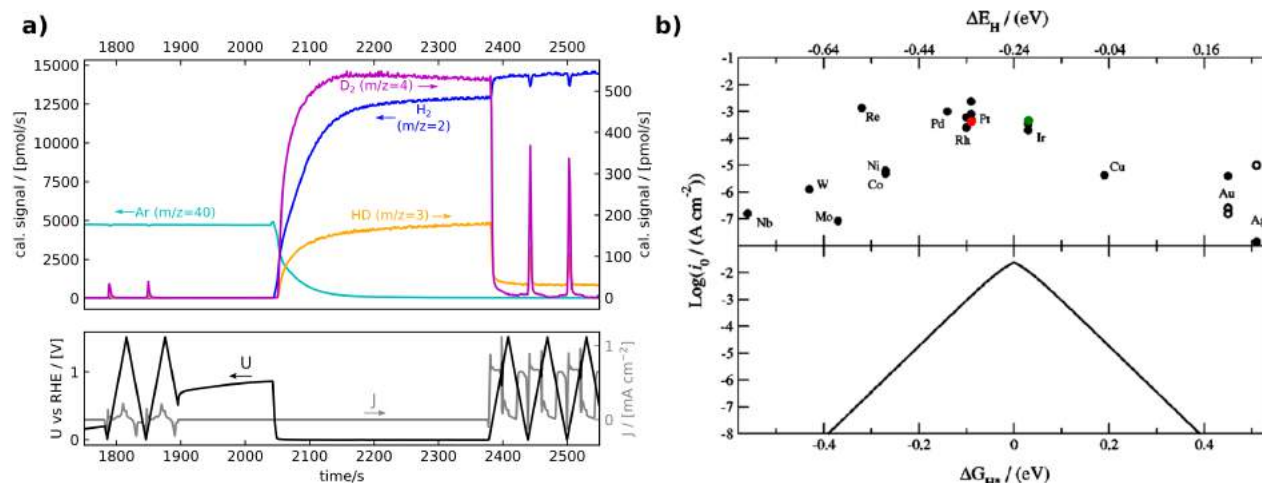


Figure 2.15: (a), Electrochemical HD exchange experiment on a polycrystalline platinum electrode. The electrolyte is 0.1 M HClO_4 in 99% D_2O . Argon carrier gas is exchanged for H_2 at 2050 s while the sample is at open-circuit potential, and HD and D_2 are observed (plotted on the right y-axis). (b), H-D exchange current density, thus measured, for Pt (red dot) and Ir (green dot) plotted on the volcano from Nørskov et al, 2005 (ref. [77]).

Thus, at the RHE condition of open-circuit voltage in 1 bar H_2 , in deuterium-labeled electrolyte, there's a lot going on. The $m/z=4$ signal rises as H_2 enters the chip, attributed to D_2 from Reaction 2.39. There is also a $m/z=3$ signal attributed to HD. This HD results in part from the H impurity of the electrolyte, but the HD/ D_2 ratio is higher under RHE conditions than it is during reduction of the electrolyte in inert atmosphere. This indicates that some of the HD is due to re-reduction of oxidized H_2 , either via H_2O or HDO formed by Reaction 2.38 that encounters the surface of the electrode again, and/or via $*\text{H}$ on the surface of the electrode (diagram in Figure 2.16). The increasing HD/ D_2 ratio over the ≈ 5 minutes of OCP in H_2 -saturated conditions indicates that at least some of it is due to H_2O or HDO , the concentration of which would build up over time. The potential, meanwhile, falls to a steady level (-0.718 V vs the reference electrode), which is used as the zero point of the RHE potential scale even though these are not strictly equilibrium conditions.

At about 2375 s, the potential is cycled again. Like in Figure 2.5a, there is an anodic current for much of the CV, where HOR is mass-transport limited. Near the cathodic potential limit of 0 V vs RHE, an $m/z=4$ signal reveals DER. (The cathodic potential limit in the first cycles in Ar was accidentally 10 mV anodic of the RHE potential, thus the smaller D_2 signal).

The fact that the forward and backwards reactions of the hydrogen equilibrium can be distinguished provides an interesting opportunity: this experiment can be used as a direct probe of the HER/HOR exchange current density, which is the equal and opposite current going to the forward and backwards reactions under equilibrium. Assuming that the electrolyte at the surface of the electrode is H_2 saturated, and ignoring isotope effects and the roughness of the electrode, the exchange current density

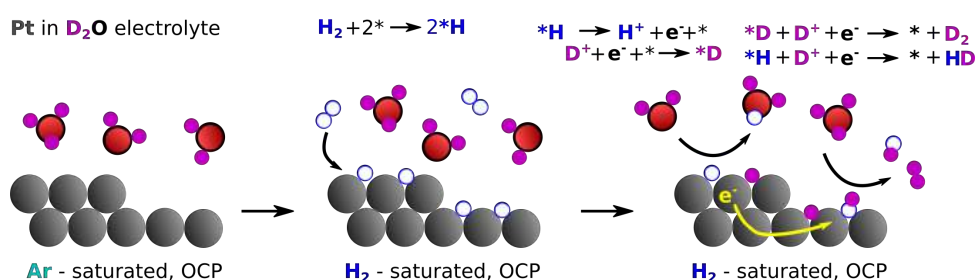


Figure 2.16: Diagram indicating some of the possible surface reactions on Pt in H_2 -saturated D_2O electrolyte at OCP.

is simply the DER current normalized to the electrode area:

$$j_0 = \frac{|I_{\text{DER}}|}{A_{\text{el}}} = \frac{2\mathcal{F}\dot{n}^{\text{D}_2}}{A_{\text{el}}} = \frac{2\mathcal{F} \cdot 540 \left[\frac{\text{pmol}}{\text{s}} \right]}{0.196[\text{cm}^2]} = 0.53 \left[\frac{\text{mA}}{\text{cm}^2} \right]. \quad (2.40)$$

This exchange current density actually agrees fairly well with early reported values for the HER/HOR exchange current density on platinum [77, 107], as shown in Figure 2.16a. That figure also includes the H-D exchange current density (0.55 mA/cm²) measured by the same experiment on a sputtered iridium electrode.

However, there are a number of newer measurements of the exchange current density which arrive at numbers much higher than this: 120 mA/cm² for platinum nanoparticles in a fuel-cell membrane-electrode assembly [108], ≈ 100 mA/cm² for mass-selected platinum nanoparticles in a photo-electrochemical system [78], and 170-960 mA/cm² with Pt nanoparticles in a floating porous membrane interfacing the liquid electrolyte and H₂ gas [109]. The authors of all these studies reporting very high values for the HER/HOR exchange current density claim that the earlier measurements, which typically employed rotating disk electrodes, were all measuring HER/HOR kinetics under mass transport limited conditions. Nonetheless, these old values for j_0 on the order of 1 mA/cm² are still often in use [79].

The use of electrochemical H-D exchange to probe the exchange current density could provide a unique opportunity to resolve the issue, as it is a direct measurement of what is happening at zero net current density, the condition for which exchange current density is defined. All other studies extrapolate from non-zero current densities. However, the question is:

Question 2.4. *Is the electrochemical H-D exchange reaction demonstrated here also mass-transport limited?*

Figure 2.15a actually tells us the mass-transport limited current for HOR. It is the current in the double-layer region during the cyclic voltammograms in H₂-saturated electrolyte, i.e., the plateau current during the cyclic voltammetry at the right in Figure 2.15. This current density is 0.7 mA/cm², which is more (but not a lot more) than the measured exchange current density. However, the main mass transport limitation is not actually getting H₂ in, it is getting D₂ out. This is because, whereas H₂ can readily fill the chip and is only limited by diffusion through the working volume, D₂ must not only diffuse through the working volume to the chip but must also escape the chip through the capillary. This is diagrammed in figure 2.17a. The respective mass transport-limited current densities are:

$$j_{\text{lim}}^{\text{HOR}} = 2\mathcal{F} \frac{p^0}{K_H^{\text{H}_2}} \frac{D^{\text{H}_2}}{L} = 0.67 \left[\frac{\text{mA}}{\text{cm}^2} \right] \quad (2.41)$$

$$j_{\text{lim}}^{\text{DER}} = 2\mathcal{F} \frac{p^0}{K_H^{\text{D}_2}} \left(\frac{L}{D^{\text{D}_2}} + \frac{1}{h^{\text{D}_2}} \right)^{-1} = 0.54 \left[\frac{\text{mA}}{\text{cm}^2} \right] \quad (2.42)$$

$$(2.43)$$

Here, $L = 100 \mu\text{m}$ is the working distance, D^i is the diffusion coefficient of species i , K_H^i is its Henry's-law constant, and h^i is its mass transfer coefficient through the chip (described in Paper I). I have ignored isotope effects, which are small in mass transport, and used the H₂ values for D₂ as well.

The calculated mass-transport limited current based on D₂ removal from the electrode surface is remarkably close to the measured H-D exchange current density. This indicates that we, too, are just probing mass transport. The electrolyte at the surface of the electrode is thus in equilibrium, i.e. H₂, HD and D₂ follow a binomial distribution:

$$\frac{1}{\sum_i c^i} \begin{pmatrix} c^{\text{H}_2} \\ c^{\text{HD}} \\ c^{\text{D}_2} \end{pmatrix} = \begin{pmatrix} x^2 \\ 2x(1-x) \\ (1-x)^2 \end{pmatrix}, \quad \text{where} \quad x \equiv \frac{c^{\text{H}^+}}{c^{\text{D}^+} + c^{\text{H}^+}}. \quad (2.44)$$

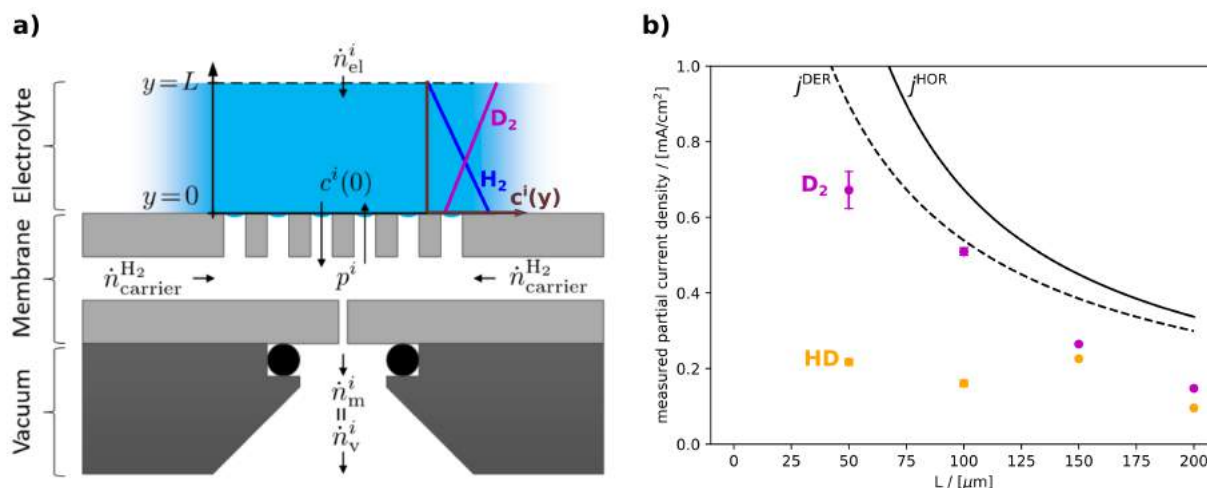


Figure 2.17: Mass transport limitation in electrochemical HD exchange (a), diagram of mass transport in EC-MS, indicating the H₂ and D₂ concentration profiles during the HD exchange experiment. (b), Measured D₂ and HD fluxes, converted to partial current densities, as a function of working distance L . The theoretical limiting currents for HOR and DER, from Equations 2.41 and 2.42 are included.

One way to confirm that a reaction is mass transport limited is to establish its dependence on the working distance L . This can be done by exchanging the 100 μm PTFE spacer (Figure 2.4) with a spacer of a different thickness. Results for electrochemical H-D exchange on Pt are shown in Figure 2.17b. While there is not a perfect match between experiment and theory, there is clearly a dependence on the apparent H-D exchange current density on distance, indicating that the answer to Question 2.4 is “yes”.

Strategies to measure the H-D exchange current density without mass transport could include (1) doing the experiment on a sample with a small coverage of mass-selected platinum nanoparticles and/or (2) depositing the sample directly on the chip membrane, essentially setting $L = 0$.

Even though this particular experiment only probed mass transport and not electrocatalytic kinetics, it indicates a promising window into the latter. Experiments avoiding mass-transport limitations by the strategies above, and testing for non-equilibrium effects on other electrocatalyst materials will follow. One particular interesting material in this regard is copper, as it shows interesting and unexpected hydrogen adsorption/desorption properties, as described in Paper VI.

2.3.2 Example experiment: CO stripping in H₂¹⁸O electrolyte

Subsection 2.1.2 showed a CO stripping experiment on platinum, and I promised that an equivalent experiment in isotope-labeled electrolyte would come in this Section. The interesting atom to label in CO stripping experiments is oxygen, as oxygen can have at least two origins: the CO and the H₂O in the electrolyte.

Figure 2.18 shows a CO stripping experiment on a sputtered rutile IrO₂ film. It is an interesting side note that crystalline IrO₂ such as the sample used for Figure 2.18 adsorbs CO at cathodic potentials, indicating that the metal atoms of the surface layer are reduced and exposed; whereas electrochemically formed hydrous IrO₂ does not adsorb CO.

From the left of Figure 2.18a, which uses a log scale so as to include all m/z signals: the plot starts with CO ($m/z=28$) as the carrier gas, and then it is switched for Ar ($m/z=40$) while the electrode is held at 0.3 V vs RHE. The $m/z=36$ signal rises as well due to ³⁶Ar. This is actually annoying because it raises the background on ¹⁸O₂, a molecule of interest in ¹⁸O-labeling experiments also at $m/z=36$. For this reason He is used as the inert carrier gas in all subsequent ¹⁸O experiments. At about 1700 s, the potential is scanned, first in the cathodic direction and then in the anodic direction. The first cycle shows some H₂ ($m/z=2$) near the cathodic potential limit and then a number of signals on the anodic scan: $m/z=46$ and 44 quickly followed by 48, and then $m/z=36$ and 34 at the anodic limit.

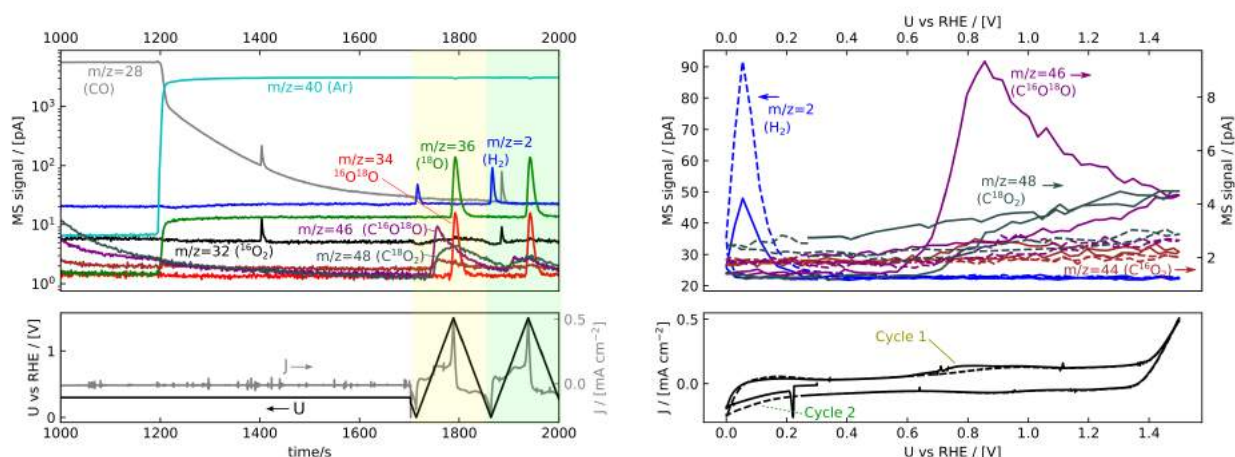
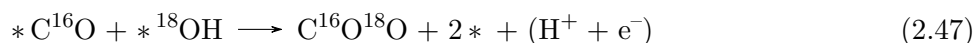
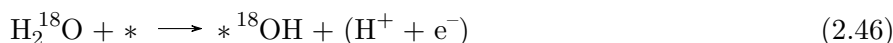


Figure 2.18: CO stripping experiment on a sputtered rutile IrO₂ electrode in 0.1 M HClO₄ in 97% H₂¹⁸O. (a), as an EC-MS plot and (b), plotted vs potential for the two indicated cycles. The mass spec data is raw (uncalibrated) signals.

These are attributed to C¹⁶O₂ (m/z=44), C¹⁶O¹⁸O (m/z=46), C¹⁸O₂ (m/z=48), ¹⁶O¹⁸O (m/z=34), and ¹⁸O₂ (m/z=36). On the next cycle, there is more H₂, the same amount of O₂, and much less of the three isotopes of CO₂, with most of the second-cycle CO₂ signal at m/z=48. The H₂ and CO₂ signals from these two cycles are plotted on linear scale against potential in Figure 2.18b, showing that the CO₂ signals, primarily m/z=46, start at ≈0.7 V vs RHE together with an anodic stripping current.

CO stripping on noble metal surfaces is believed to proceed via a Langmuir-Hinshelwood mechanism [81, 82], whereby adsorbed *CO reacts with adsorbed *OH. When the *OH comes from an ¹⁸O-labeled electrolyte, the mechanism is:



This implies that the CO₂ desorbed should be C¹⁶O¹⁸O at m/z=46. Some C¹⁶O₂ at m/z=44 can be expected due to the ¹⁶O impurity in the electrolyte, but m/z=48 came as a huge surprise! Noble metal surfaces should not be able to split CO [110]! Natural CO is 99.8% C¹⁶O, and I confirmed this for the CO from our bottle by taking a mass spectrum (it is 1% ¹³CO, but, luckily, that can be ignored for these experiments)... I had a few fantastic days of scratching my head over this result. The answer is that, while noble metal surfaces cannot split CO, water *can* split CO₂! Aqueous CO₂ is in equilibrium with carbonic acid, H₂CO₃. (That is, incidentally, why the oceans are getting more acidic.) The full process is indicated schematically in Figure 2.19. The CO₂ starts as C¹⁶O¹⁸O, but some of it interacts with H₂¹⁸O on the way out of the electrolyte and ends up switching out its ¹⁶O for an ¹⁸O (Reaction

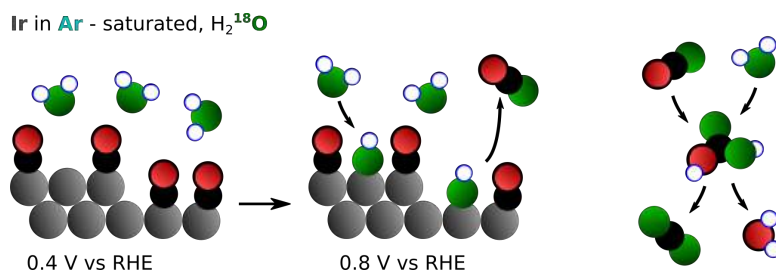


Figure 2.19: Schematic diagram for CO stripping in ¹⁸O-labeled electrolyte (left) and subsequent homogeneous isotope scrambling via carbonic acid (right). Metal atoms are gray, carbon atoms black, hydrogen atoms white with blue outline, ¹⁶O atoms red with black outline, and ¹⁸O atoms are green.

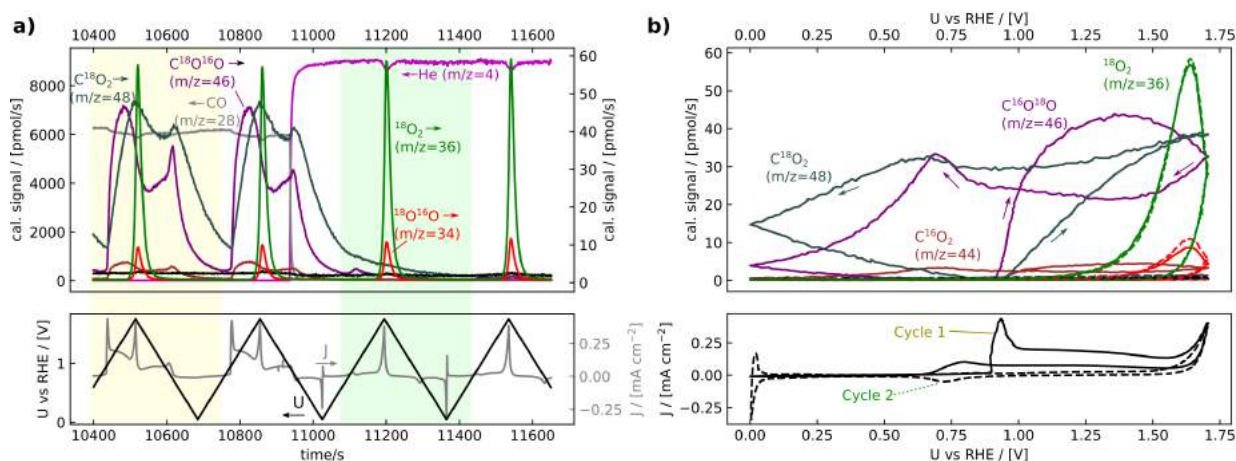
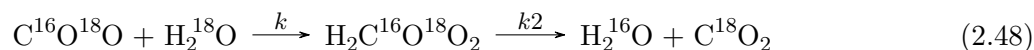


Figure 2.20: Cyclic voltammograms of a polycrystalline Pt electrode in 0.1 M HClO₄ in 97% H₂¹⁸O, saturated first with CO and thereafter with He. (a) As an EC-MS plot with carrier gases plotted on the left y-axis and product gases on the right y-axis. (b) The two cycles indicated in (a) are plotted against potential. MS signals were calibrated according to the procedures in Section 2.2.

2.48).



I actually found this very interesting, so I put some effort into exploring it. I think that the phenomenon an excellent demonstration of the world opened up by isotope studies using chip EC-MS, and so I will share with you here. CO oxidation coupled with ¹⁸O-labeling will also be used in Chapter 3 as a probe of lattice oxygen reactivity in oxygen evolution catalysts, so this Subsection also serves to familiarize the reader with the chemistry involved.

One of the first things I tried was bulk CO oxidation, akin to that in Figure 2.6a. Figure 2.20a shows two cyclic voltammograms of a polycrystalline Pt electrode in CO-saturated ¹⁸O-labeled electrolyte (0.1 M HClO₄ in 97% H₂¹⁸O), followed by two cycles in He-saturated electrolyte. CO is oxidized to CO₂ in the first two cycles, and the CO₂ isotopes have distinct profiles. The C¹⁶O¹⁸O profile has much sharper features and leads the C¹⁸O₂ profile. The origin of the features is more clear when the CO₂ signals are plotted against potential, as is done in Figure 2.20b.

At ≈ 0.9 V in the cycle in CO (cycle 1, solid lines), an anodic peak represents the oxidative stripping of the adsorbed CO monolayer and the depletion of CO in the working volume on the approach to steady state. This is accompanied by a rapid increase in the C¹⁶O¹⁸O signal. The current and the C¹⁶O¹⁸O signal start to fall at about 1.4 V vs RHE, where the platinum surface oxidizes and loses CO electro-oxidation activity. Then, starting at about 0.8 V vs RHE on the cathodic sweep, the sample regains some CO oxidation activity as the surface is reduced. The gain in CO oxidation activity outweighs the surface reduction current, but the latter is evidenced by the cathodic current at the same part of the CV in He (cycle 2). There is a corresponding peak in the C¹⁶O¹⁸O signal during the cathodic scan.

Meanwhile, the C¹⁸O₂ signal moves much more slowly. It increases gradually the entire anodic scan starting just after the oxidation feature at 0.9 V vs RHE, decreases only slowly during the cathodic scan, and barely registers a peak after the Pt surface is reduced. On the other hand, the C¹⁶O₂ signal matches the C¹⁶O¹⁸O signal, just with smaller intensity.

The question then arises:

Question 2.5. What *should* the CO₂ signal be doing?

This question is actually straight-forward to answer with the stagnant thin-layer model presented in Paper I, which takes into account diffusion through the working volume, evaporation through the chip membrane, and removal to the vacuum chamber through the chip capillary. The input to this

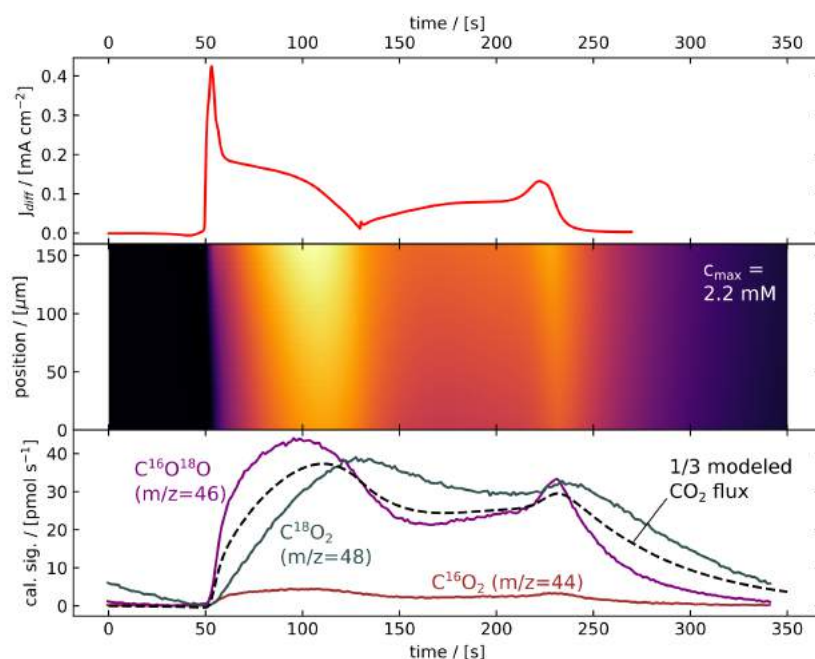


Figure 2.21: Model of CO₂ signal in Figure 2.20. Top: CO oxidation current obtained by subtracting a cyclic voltammogram in He from a cyclic voltammogram in CO. Middle: modeled concentration as a function of time (x axis) and distance from the membrane (y axis) in the working volume. The electrode is at the top. The working distance of $L = 160 \mu\text{m}$, indicating poor sample alignment, was determined by the mass-transport-limited CO oxidation current. The modeled CO₂ concentration varies from zero (black) to 2.2 mM (bright yellow). Bottom: the CO₂ flux to the mass spectrometer predicted by the model, scaled down by a factor of 3, is co-plotted with the measured calibrated CO₂ signals.

model is the production rate of an analyte at the electrode as a function of time. Such a production rate can be determined by subtracting the current in the cyclic voltammogram in He (cycle 2) from the current at the corresponding time in the cyclic voltammogram in CO. The resulting current difference is shown in the top panel of Figure 2.21. When this is converted to a CO₂ production rate assuming 2 electrons per CO₂ molecule, and fed to the model, we get the concentration profile in the middle panel of Figure 2.21. Here, the y-axis represents the position in the working volume, with the electrode on top and the chip membrane on the bottom. The predicted flux to the mass spectrometer is proportional to the calculated concentration at the chip membrane, and is shown as a dotted line in the bottom panel of Figure 2.21. It is plotted (scaled down with a factor 3) together with the actual measured CO₂ signals.

The modeled flux falls *between* the C¹⁶O¹⁸O and C¹⁸O₂ signals! In other words, while the C¹⁸O₂ signal is slower than expected, the C¹⁶O¹⁸O signal is *faster* than expected! What is going on here?

To anyone familiar with chromatography, this may seem like a separation process, whereby heavy CO₂ molecules are retained longer in the working volume. However, this is getting it a bit backwards. There is no separation process - it is just that the CO₂ molecules which happen to take longer to make it through the working volume are more likely to *become* heavy by Reaction 2.48. It is then a wonderful coincidence that the average time between reactions of CO₂ with H₂O is on the same order of magnitude as the average time that a CO₂ molecule produced at the electrode lingers in the working volume before entering the chip, and the mass spectrometer.

The actual concentration of carbonic acid (of any isotopic makeup) at any time is very small. The equilibrium constant is [111]:

$$K_{\text{eq}} = \frac{c^{\text{H}_2\text{CO}_3}}{c^{\text{CO}_2}} = \frac{k}{k_2} = 1.7 \cdot 10^{-3} \quad (2.49)$$

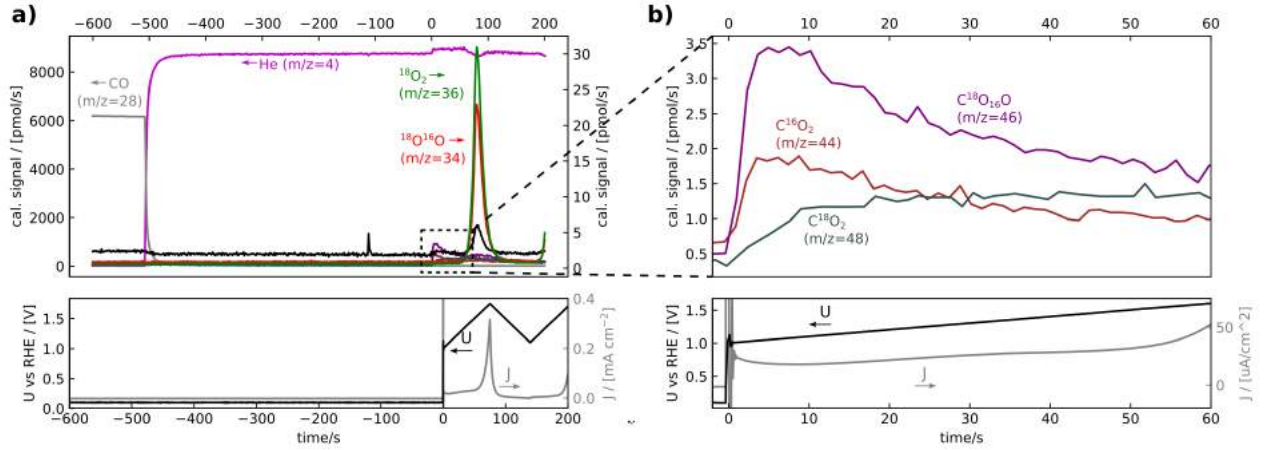


Figure 2.22: Fast CO stripping experiment. (a), The whole experiment, from when the carrier gas was switched. (b), zoom-in on the CO_2 signals during and right after the jump in electrode potential.

Thus, the first step in Reaction 2.48 is slow, with a rate constant k , and the second step is about 500 times faster. The “wonderful coincidence” can be stated

$$\tau^{\text{CO}_2} \sim \frac{1}{k} \quad (2.50)$$

The question on my mind by this point was

Question 2.6. Based on the changes in the $m/z=44$, $m/z=46$, and $m/z=48$ signals, what is the rate constant k ?

To answer this question in a manageable way requires having a well-defined isotope composition at $t = 0$, with no additional CO_2 being introduced. I established such a start condition by doing a “fast CO strip”, shown in Figure 2.22. The surface of the platinum electrode is saturated with CO, CO is replaced by He in the working volume electrolyte, and then, at $t = 0$, the electrode potential is jumped to 1.0 V vs RHE, at which point all the CO should immediately strip off as CO_2 . Initially, there is no C^{18}O_2 , as CO does not dissociate on platinum. The C^{16}O_2 -to- $\text{C}^{16}\text{O}^{18}\text{O}$ ratio is the same as the H_2^{16}O -to- H_2^{18}O ratio in the electrolyte (called x), which can be determined independently by OER, with the resulting O_2 having an isotopic composition given by the binomial distribution.

To avoid worrying about the signal CO_2 signal, which changes over the course of the experiment first as CO_2 distributes itself in the working volume by diffusion and then as it evaporates through the chip, we just work with the normalized signals, representing the isotopic composition:

$$\hat{S}_{M44} = \frac{S_{M44}}{S_{M44} + S_{M46} + S_{M48}}, \quad \text{etc.} \quad (2.51)$$

Given the start condition and k , we can write a set of differential equations relating the change in the time derivatives of \hat{S}_M to the present values of \hat{S}_M . There are a total of eight reactions passing through a molecule of carbonic acid with mixed oxygen isotopes. These eight reactions are diagrammed in Figure 2.23a. I’ve assumed that each of the three oxygen atoms of the resulting carbonic acid are equally likely to be expelled as H_2O when the new CO_2 molecule is formed, resulting in the indicated probabilities.

When the effects of these eight reactions on \hat{S}_{M44} , \hat{S}_{M46} , and \hat{S}_{M48} are added together, taking into account the activities x and $(1 - x)$ for H_2^{16}O and H_2^{18}O , respectively, we get the following set of differential equations, shown in matrix form:

$$\frac{d}{dt} \begin{pmatrix} \hat{S}_{M44} \\ \hat{S}_{M46} \\ \hat{S}_{M48} \end{pmatrix} = k \begin{pmatrix} -\frac{2}{3}(1-x) & +\frac{1}{3}x & 0 \\ \frac{2}{3}(1-x) & -\frac{1}{3} & \frac{2}{3}x \\ 0 & \frac{1}{3}(1-x) & -\frac{2}{3}x \end{pmatrix} \begin{pmatrix} \hat{S}_{M44} \\ \hat{S}_{M46} \\ \hat{S}_{M48} \end{pmatrix} \quad (2.52)$$

And the initial condition is:

$$\begin{pmatrix} \hat{S}_{M44} \\ \hat{S}_{M46} \\ \hat{S}_{M48} \end{pmatrix}_0 = \begin{pmatrix} x \\ 1-x \\ 0 \end{pmatrix} \quad (2.53)$$

Numerical solution of this set of ordinary differential equations gives \hat{S}_M as a function of time. The solution depends on the value of k . Solutions for two values of k are shown in Figure 2.23, together with the measured \hat{S}_M from the experiment in Figure 2.22. The first value of k , 0.026 s^{-1} , is taken from the literaturecitePinsent1956. Using this value of k gives a too-slow conversion of $\text{C}^{16}\text{O}^{18}\text{O}$ to C^{18}O_2 . The second value of k , 0.080 s^{-1} , is chosen to fit the data.

A likely cause for the discrepancy is temperature: $k = 0.026 \text{ s}^{-1}$ was measured at the standard temperature of 25°C , whereas it can easily get hotter at the sniffer setup in SurfCat's experimental hall. The actual temperature in the working volume electrolyte during that experiment could well have been 30°C or a bit higher, which could explain the increased rate constant.

On top of being a fun opportunity to experiment with isotopes and use some differential equations, this example illustrates yet another potential application of chip EC-MS: It can in principle be used to measure the kinetics of any homogeneous reaction that:

- Releases or consumes a gas (e.g. C^{18}O_2)
- Can be triggered by either (1) an electrochemical signal (e.g. an applied potential to strip off a monolayer of CO), or (2) introduction of a carrier gas.

2.3.3 Labeling the vacuum chamber

Towards the end of the last section, I mentioned that to determine x , which is the fraction H_2^{16}O in the labeled electrolyte, I did so indirectly by measuring the isotopic composition of O_2 produced by OER and then back-calculating x from the binomial distribution. One might wonder why I didn't measure the H_2^{16}O and H_2^{18}O signals directly at $m/z=18$ and $m/z=20$, respectively. The answer is that water is notoriously "sticky" in vacuum chambers [73]. In effect, all of the stainless steel between the EC-MS chip and the filament acts as a chromatographic column, adsorbing water. I suspect that the stainless steel walls are normally hydroxyl-terminated, and that these hydroxyls switch out with water. My experience is that after the setup is used with H_2^{18}O , it stays "labeled".

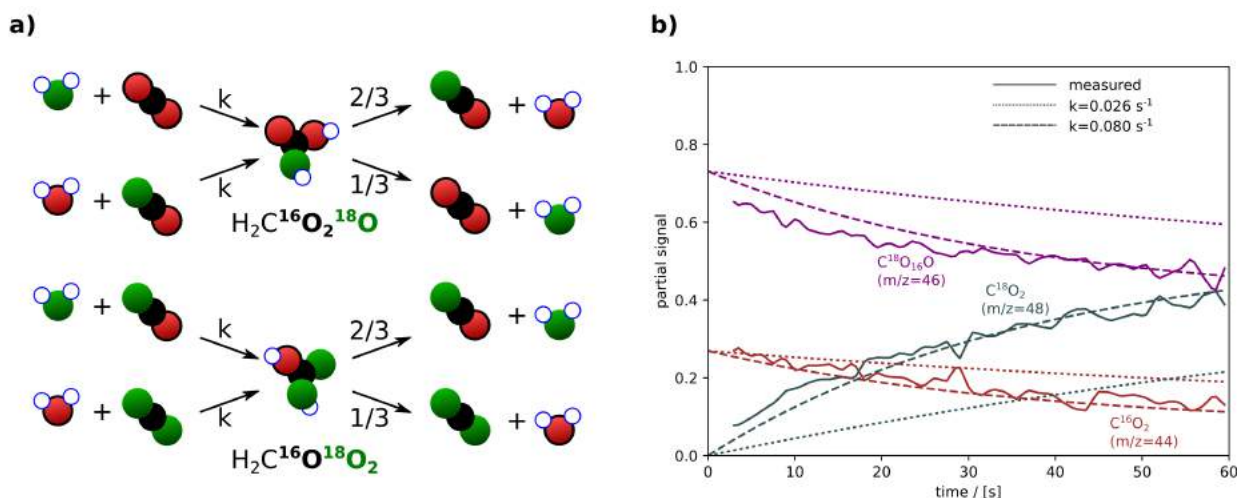


Figure 2.23: (a) Possible oxygen-exchanging reactions between H_2O and CO_2 . (b), CO_2 isotopic compositions as a function of time from the solution of a kinetic model using two different values of the rate constant k are co-plotted with the normalized measured CO_2 signals from Figure 2.22b

Figure 2.24a, from the SI of Paper II, shows cyclic voltammetry of a NiFe nanoparticle sample in 0.1 M KOH in 97% H_2^{18}O , and includes the $m/z=18$ and $m/z=20$ signals. At the start of the experiment, these two water signals are equal, which would imply $x = 0.5$. However, the distribution of oxygen isotopes (ignoring any isotope effect) would then be

$$\begin{pmatrix} \dot{n}_{16}\text{O}_2 \\ \dot{n}_{16}\text{O}^{18}\text{O} \\ \dot{n}_{18}\text{O}_2 \end{pmatrix} = \begin{pmatrix} x^2 \\ 2x(1-x) \\ (1-x)^2 \end{pmatrix} = \begin{pmatrix} 0.25 \\ 0.5 \\ 0.25 \end{pmatrix}, \quad (2.54)$$

and the $m/z=34$ to $m/z=36$ ratio would be

$$r = \frac{\dot{n}_{16}\text{O}^{18}\text{O}}{\dot{n}_{18}\text{O}_2} = \frac{2x}{1-x} = 2 \quad (2.55)$$

In reality, the $m/z=36$ to $m/z=34$ ratio (when the signals are corrected for background) is $r = 0.07$, implying (solving the above equation for x):

$$x = \frac{r}{2+r} = 0.034, \quad (2.56)$$

or that the ^{16}O impurity is only 3.4%. It would take an unrealistically powerful isotope effect to explain this discrepancy. Furthermore, the $m/z=18$ to $m/z=20$ ratio changes over the 1200 s shown, whereas the $m/z=34$ to $m/z=36$ ratio does not. Thus, the $m/z=18$ to $m/z=20$ ratio *does not* represent the H_2^{16}O to H_2^{18}O ratio in the working electrolyte! Likewise, the $m/z=18$, 19, and 20 signals do not represent the H_2O , HDO , and D_2O concentrations in the working electrolyte when doing H-D experiments.

Question 2.7. *How long does it take to fully label the vacuum chamber?*

The answer is “it depends...”, but Figure 2.24b gives an idea. This figure shows the integral of the $m/z=18$ and $m/z=20$ peaks in mass spectra taken every 0.5 hours over the course of almost 20 hours after a drop of H_2^{18}O was placed on the EC-MS chip, covering the membrane, and left overnight under an inverted petri dish to slow its evaporation. The drop was applied after the first data point, and was removed the next morning at 12.5 hours. Surprisingly, the signals never stabilized. The $m/z=20$ signal reaches a peak after about 5 hours, but then starts to fall. This may indicate that the drop loses

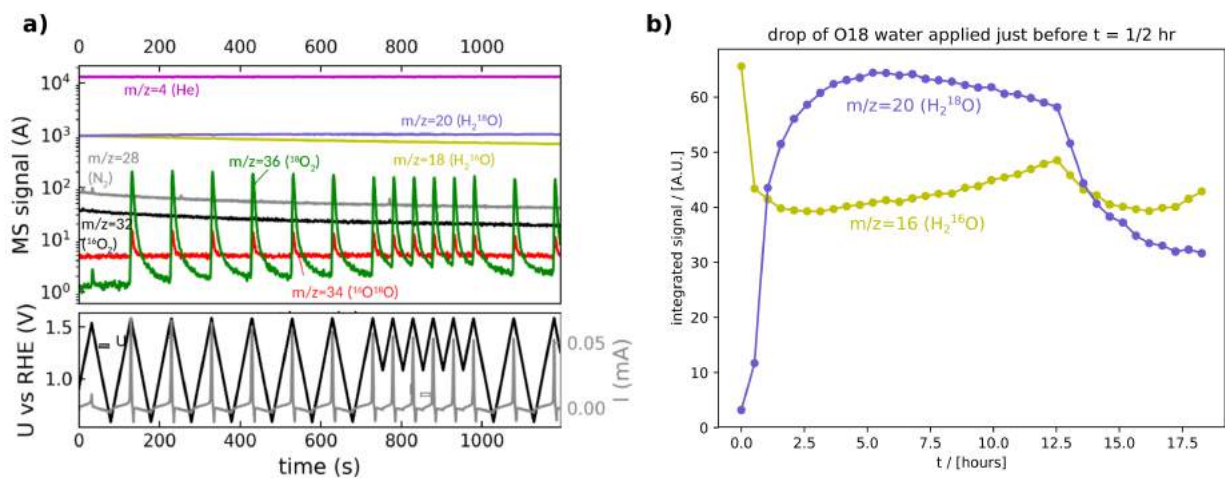


Figure 2.24: (a), OER experiment in ^{18}O -labeled electrolyte, showing that the $m/z=18$ and $m/z=20$ signals do not reflect the H_2^{16}O vs H_2^{18}O composition of the electrolyte. Adapted from the SI of Paper II. (b), Integrated $m/z=18$ and $m/z=20$ peaks in mass spectra taken over a 20 hour period. A drop of H_2^{18}O is applied at 0.5 hr and removed at 12.5 hr.

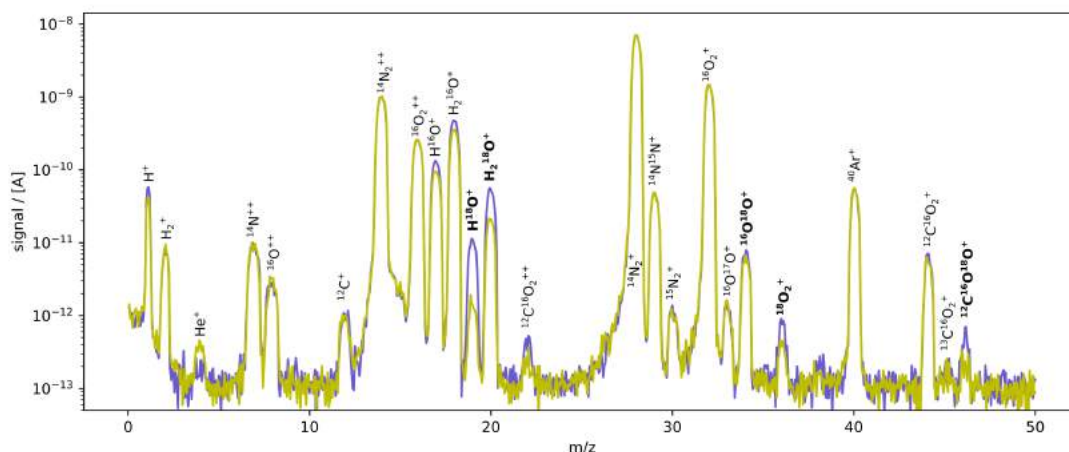


Figure 2.25: Mass spectra of air through the EC-MS chip one day after experiments with ^{18}O -labeled electrolyte (purple), and after a night at 100°C under a drop of natural H_2O (yellow). All peaks are labeled, and those in bold are related to the ^{18}O labeling of the setup.

its isotopic purity by exchange with water vapor in the air. It may also have to do with the changing temperature over the course of the night. Nor does the $m/z=18$ to $m/z=20$ ratio quickly revert to normal after the drop is removed, but keeps changing for at least the duration of these measurements.

Baking the vacuum chamber can help. I've found that this is especially effective if water vapor is leaked in, by placing a drop of water on the chip, while the chamber is heated, to speed up the removal of the ^{18}O label by switching of ^{18}OH groups for ^{16}OH groups on the stainless steel walls. Figure 2.25 shows mass spectra of air taken before and after such a baking procedure. The peaks related to ^{18}O labeling are reduced after the baking. Note that $\text{C}^{18}\text{O}^{16}\text{O}$ at $m/z=46$ is among them. However, they have not quite reached the natural ratio. Without any residual isotope labeling of the vacuum chamber, the peak at $m/z=45$ should be greater than at $m/z=46$, since ^{13}C is more than twice the natural abundance ($\approx 1\%$) of ^{18}O ($\approx 0.2\%$). This indicates that CO_2 also interacts with the OH groups on the stainless steel surfaces.

An even more effective procedure, which does succeed in removing the $\text{C}^{18}\text{O}^{16}\text{O}$ is to: **Bake the chamber to 100°C overnight under a drop of natural water with natural CO_2 as the carrier gas.**

It is very important to make sure that the vacuum chamber is not labeled before doing sensitive isotope labeling experiments such as those testing for lattice oxygen evolution described in the next Chapter. Indeed, the labeling of the vacuum chamber can even distort the apparent isotopic composition of O_2 gas, as seen in the $m/z=34$ and especially $m/z=36$ peaks in Figure 2.25.

2.3.4 Other tools: Sputter deposition, ISS, and ICP-MS

So far this chapter has exclusively described the chip EC-MS technique and its use in quantitative mass spectrometry and isotope labeling studies. Chip EC-MS has indeed been the central tool of my PhD project, but not the only one (for something completely different, see paper IV). This final Subsection will briefly describe a few other tools used in the next Chapter.

Sputter deposition

Most of the Ru, RuO_2 , Ir, and IrO_2 samples described in the next section were prepared by sputter deposition. Briefly, sputter deposition is a method of making smooth, flat thin films by physical vapor deposition, where the vapor of the desired material is formed by bombarding a target with a plasma, typically an argon plasma. This is shown schematically in Figure 2.26a.

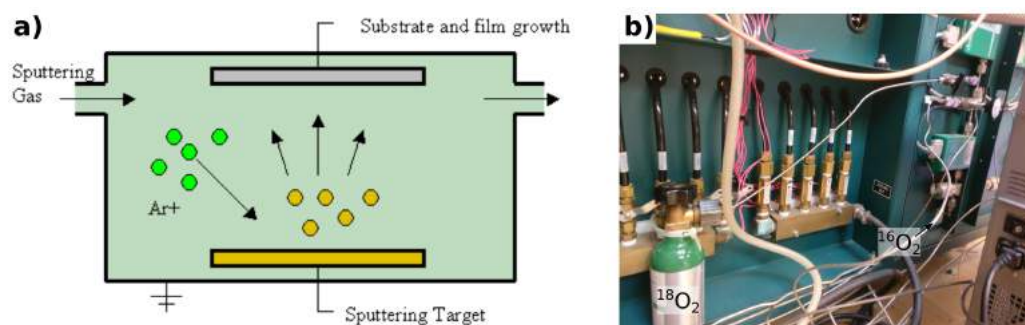


Figure 2.26: (a), sputter deposition concept, from https://en.wikipedia.org/wiki/Sputter_deposition. (b) Photograph of back of our sputter chamber with $^{18}\text{O}_2$ flask installed

The most common way to form a metal oxide by sputtering is to add O_2 to the Ar used to make the plasma. This strategy is referred to as *reactive sputtering*. Reactive sputtering is a simple way to prepare an isotope-labeled metal oxide sample, by switching out the natural O_2 with $^{18}\text{O}_2$. A few months ago, I installed a small bottle of 99% $^{18}\text{O}_2$ on our lab's sputter chamber for this purpose (Figure 2.26b). A procedure for sputtering Ru^{18}O_2 and Ir^{18}O_2 films is included in Appendix A.4.

Ion Scattering Spectroscopy (ISS), aka Low Energy Ion Scattering (LEIS)

Ion scattering spectroscopy (ISS), also known as low-energy ion scattering (LEIS), is a highly surface-sensitive analysis technique based on the inelastic collisions of an ion beam, typically He^+ , with a sample surface [51,112]. This is indicated in the left of Figure 2.27.

The mechanism behind ISS is that, in such an inelastic collision, where energy and momentum are conserved, the energy of the deflected He^+ ion, E_S , is related to the mass of the nucleus that it hits on the surface, M_P , according to the equation in Figure 2.27. The ions are then focused, separated by energy, and detected with a *hemispherical mass analyzer*. The resulting spectrum, of intensity vs deflected ion energy, then says how massive the nuclei on the sample surface that deflected the ions, are. In Figure 2.27, the He^+ ions (gray) would deflect off of the large surface atoms (blue) with a greater energy than the small surface atoms (green), as the latter would recoil more on collision. This gives rise to two the green and blue peaks, respectively.

ISS is especially useful in the context of this thesis because, since it probes the nuclei of the sample rather than its electronic structure, it is isotope sensitive. ISS is therefore the tool to answer the following question, which becomes important in the latter parts of Chapter 3:

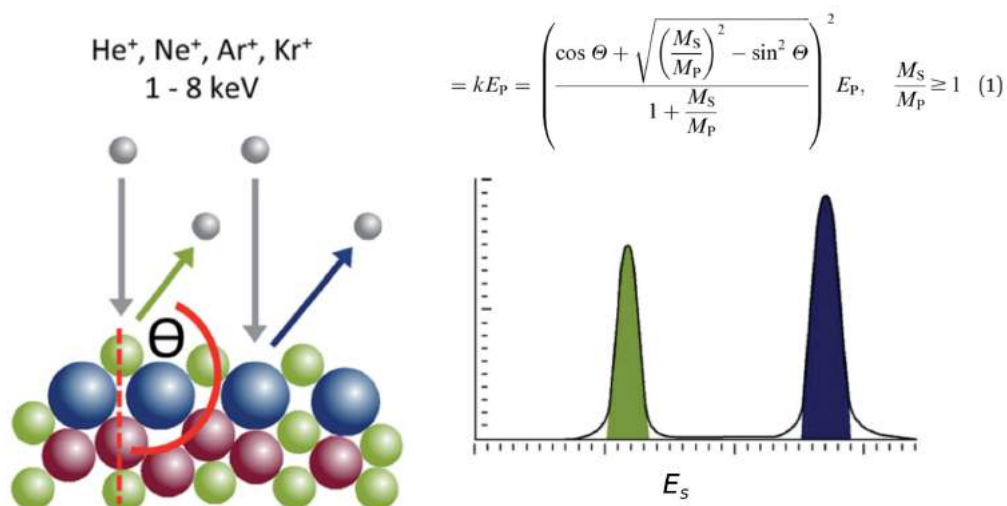


Figure 2.27: Concepts of ion scattering spectroscopy. Adapted from ref. 112

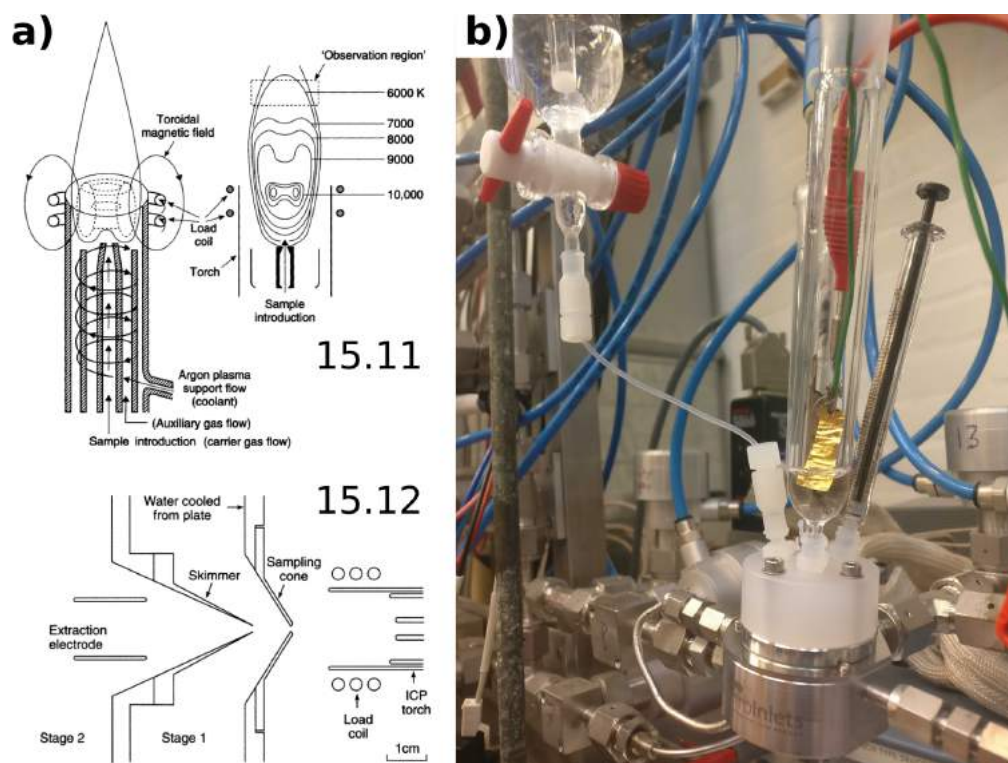


Figure 2.28: (a) Diagram of inductively-coupled plasma (ICP) torch (top) and its coupling to mass spectrometer (bottom). Adapted from ref. 63. Figure numbers in the image refer to that textbook. (b) Photo of setup for taking electrolyte samples during EC-MS experiments for dissolution analysis by ICP-MS. (The carrier gas inlet volume was going through a bit of a transition phase.)

Question 2.8. *Is the oxygen at the surface of my metal oxide sample ^{16}O or ^{18}O ?*

All of the ISS spectra presented in Section 3.3 were taken by Jakob Ejler using the Omicron setup. I took all of the ISS spectra presented in Section 3.4 using the Thetaprobe setup after Ezra Clark got it working.

Inductively Coupled Plasma - Mass Spectrometry (ICP-MS)

As described in the start of the next Chapter, stability is an important issue in electrocatalysis, especially oxygen evolution in acid, which requires rare and expensive iridium- and/or ruthenium-based electrocatalysts. Under these conditions, most materials dissolve, and even the best materials dissolve slowly.

The question, as it has been phrased by Cherevko and coworkers [113], is:

Question 2.9. *How many molecules of product, on average, does one atom of element i in the electrode make before it is lost?*

The answer to this question, called the *stability number*, is also called the *turn-over number* in conventional catalysis. The stability number depends on both the electrode material and the conditions, including the electrode potential.

Determining the stability number is best done by measuring the concentration of the metal of interest (i) in the electrolyte. The most sensitive way to measure a small concentration of metal ions is inductively-coupled plasma mass spectrometry (ICP-MS) [64,114]. In ICP-MS, the MS part is basically the same as that described in the start of Section 2.1 - a quadrupole mass analyzer is typically used for mass separation and detection. The unique part in ICP-MS is the inlet and ionization [63], with diagrams shown in Figure 2.28a. This is done by directly delivering the liquid to a plasma torch, which has an extremely hot argon plasma formed by magnetic induction from external magnetic coils. The plasma is hot enough to atomize the liquid, and the plasma delivers electric charges to any metal

atoms that were dissolved in the liquid. These metal ions are then separated from the non-ionized parts of the plasma by lenses through two pumping stages and delivered to the mass spectrometer. ICP-MS is an extremely sensitive technique, able to detect on the order of parts per trillion (nanograms per liter) of metals in solution.

Most of the work involved in ICP-MS, for the experimenter, is preparing the samples. I came up with a way to collect electrolyte from the stagnant thin-layer EC-MS cell during an experiment without losing potential control using the setup shown in Figure 2.28a. See Appendix A.5 for detailed instructions on how to take electrolyte samples using this setup. That appendix also describes the ICP-MS calibration and detection limits used in this Thesis.

Concluding remark:

This concludes the chapter on the tools used in this PhD project, the principle one of which is chip EC-MS, to which I view the data analysis package `EC_MS` as an essential extension. Together with isotope labeling, it often feels as if chip EC-MS opens a window to the world of electrocatalysis from a new and mostly unexplored angle. It is often easier to freely explore this world than to step back and ask controlled and disciplined questions. I will do my best at the latter in the next Chapter, but I hope that this Chapter has given a sense of the thrill of the exploration that I have been enjoying for most of the past three years.

Chapter 3

Isotope-Labeling Studies in Oxygen Evolution Catalysis



The oxygen evolution reaction (OER, rxn 3.1) is the source of most of the efficiency lost in water electrolysis [57, 115], whether done in an alkaline electrolyzer cell (AEC) [116, 117] or polymer electrolyte membrane electrolyzer cell (PEMEC) [46, 118]. Since hydrogen produced by water electrolysis plays a central role in the fossil-fuel-free energy system and chemical industry outlined in Section 1.2, there is a lot to win by improving oxygen evolution catalysis.

Oxygen evolution catalysts can be split into two groups, based on the pH, and thus which electrolyzer technology, they are able to operate at. AECs operate in concentrated hydroxide solution (high pH), whereas PEM electrolyzers use a solid polymer electrolyte membrane (PEM) with strongly acidic groups, and so the water splitting reactions effectively occur at low pH [42, 46]. These two technologies were described briefly in Section 1.2. Here, I give a brief outline of oxygen evolution catalysts and related challenges associated with each of these technologies to motivate the EC-MS studies presented in this Chapter.

At the high potentials ($U > 1.23$ V vs RHE) needed to drive the oxidation of water, metal oxides and hydrated metal oxides are virtually the only thermodynamically stable solids [119]. However, while many metals have a thermodynamically stable solid phase at high potential and high pH (alkaline electrolyte), almost all metals form a soluble species at high potential and low pH (acidic electrolyte). The fact that so many materials are unstable under OER conditions can make the accurate measurement of OER activity a challenge. Just measuring the electrochemical current might lead to an overestimation of the oxygen evolution activity, as Reaction 3.1 might not account for all of the electrons transferred. A few examples of this from my PhD work are shown in Section 3.1.

The fact that most materials are not stable at high potential and low pH limits OER in acid to noble metal oxides, of which IrO_2 and RuO_2 are by far the most active [120]. Even so, at least 200 mV of overpotential is required for reasonable current densities. Perhaps more importantly, both Ir and Ru are among the rarest elements on earth and among the elements produced in the least quantities - only approximately 4 [47] to 9 [121] tons of Ir and 25 tons of Ru [121] are produced annually. All of this production is a byproduct of platinum production [121] and thus extremely inelastic to changes in demand. Of the two oxides, RuO_2 is more active but considerably less stable, and so IrO_2 is used in commercial PEM electrolyzers [46]. With the iridium loadings in current state-of-the-art PEMEC's, the entire global supply of iridium could add about 2 GW of hydrogen-producing capacity per year [47], which is clearly not on a scale of relevance to adding energy storage to the world's 20 TW of energy consumption [121]. The scarcity of these materials thus makes it essential to increase their mass-normalized activity and thus reduce the required loading. In Section 3.2, we measure the O_2 from OER on RuO_2 at record low overpotentials, in the hope that accurate measurement of activity at low overpotentials can provide fundamental insight to guide the design of more active catalysts for PEMEC's.

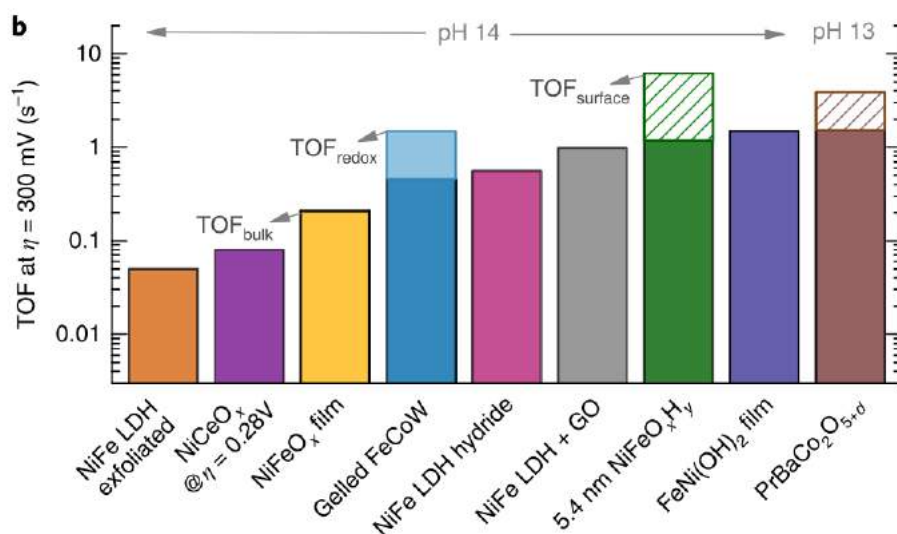


Figure 3.1: Turn-over-frequency for state-of-the-art OER catalysts in alkaline electrolyte at 300 mV overpotential. From Paper II.

In contrast, the oxygen evolution catalysts used at high pH in AEC's need not be rare and expensive metals. Indeed, the industrially used catalyst is nickel (importantly, with impurities including iron) [42, 116, 122]. Nickel-iron oxy-hydroxide is also the most active catalyst on a turn-over-frequency (TOF) basis, as seen in Figure 3.1, taken from Paper II. Turn-over-frequencies are notoriously difficult to calculate for oxygen evolution catalysts. The calculation of this turnover frequency relies on the assumption that only the surface of the catalyst is active, which we base on isotope-labeling studies showing that oxygen within the catalyst is not evolved as O_2 . These experiments are described in Section 3.3.

Such isotope-labeling studies are commonly used to establish the presence or lack of lattice oxygen involvement in the OER. This has often been described as a positive catalytic characteristic, facilitating an OER mechanism with higher rates [113, 123]. However, such conclusions need to be made carefully, as the lattice-involving mechanism can be negligible when quantitatively compared with the conventional mechanism, and can sometimes be associated with degradation of the catalyst. A thorough and quantitative set of isotope-labeling experiments coupled with dissolution measurements is shown in Section 3.4 for RuO_2 and IrO_2 . We plan to publish this work, together with that in section 3.2, in Paper VII.

The scarcity and instability of the only available OER catalysts for PEMEC's begs the question whether they are actually worth researching, when AEC's are already an industrial technology. However, PEMEC's have a few distinct advantages over AEC's that are important for utilization of variable renewable energy [46]: (1) They can run more efficiently due to the high conductivity of the solid electrolyte. (2) They have less H_2 crossover, enabling them to run safely at a wider range of current densities. (3) They have faster load response, enabling them to better utilize intermittent renewable electricity when it is cheapest, that is, when the sun is shining and the wind is blowing. For these reasons, most experts expect PEMEC's to be the dominant water electrolysis technology by 2030 [41].

In the final Chapter of this Thesis, I will estimate the impact of an incremental improvement in OER overpotential on global CO_2 emissions in order to get an idea of the impact of this PhD project.

3.1 You have to see the O₂!

Materials with high oxygen evolution activity are often reported in the literature. A common benchmark is the overpotential required to reach 10 mA/cm² [115, 124]. This value is usually normalized to the macroscopic, i.e. *geometric*, electrode area, rather than the electrochemical surface area, which is not trivial to determine for oxides. For this reason, many advances in activity are in fact just advances in synthesizing electrodes with a very high loading [115]. There is nothing wrong with this in principle - a high geometric loading of active sites enables electrochemical devices such as electrolyzer cells to be more compact, lowering capital costs - though it should be thought of as an engineering accomplishment, to be kept conceptually separate from more fundamental catalysis science, which seeks to increase the activity per active site [57]. There is, however, the problem with high-loading materials that the large amount of material means that charging or degradation phenomena can involve the passage of a lot of charge. This can lead to an overestimation of the activity if 100% Faradaic efficiency to the OER (Reaction 3.1) is assumed blindly. Especially bad is if the material contains organic building blocks, as all organic molecules are unstable with respect to oxidation to CO₂ at OER potentials. Thus, just as an example, there is reason to be skeptical of the reported activity of the high-surface-area metal-organic-framework (MOF) derived Cr_{0.6}Ru_{0.4}O_x catalyst described by Lin et al in ref. 125, which currently claims a record [115] of 178 mV overpotential at 10 mA/cm². Charging, degradation, and oxidation of residual carbon could all contribute to the current of these electrodes, even over a long experiment. Measurement of dissolved metals using ICP-MS or mass losses using quartz crystal microbalance can check for degradation processes [114]. But the best way to prove that the measured current is going to OER is to quantitatively measure the evolved O₂.

Here, I report two examples from my PhD work of OER catalysts, the first in acid and the second in alkaline, for which the measured current was not all going to O₂ production via Reaction 3.1.

3.1.1 Ru on graphene oxide

During my external stay with professor Wen Zhenhai in Fuzhou, one of the first measurements we did with their newly built EC-MS setup (Appendix A.2) was to determine the actual onset of OER from an acid electrocatalyst that they knew was unstable (the overpotential required to draw 10 mA started low but skyrocketed after a few minutes), but appeared highly active. This material, dispersed ruthenium on a high-surface-area graphene oxide, showed a strong oxidation wave starting before 1.4 V vs RHE with a large shoulder starting at 1.2 V vs RHE (Figure 3.2). It was of interest whether all of the current in the wave at 1.4 V, or even 1.2 V if the catalyst was somehow ultra-activated in the beginning, could be attributed to O₂ formation.

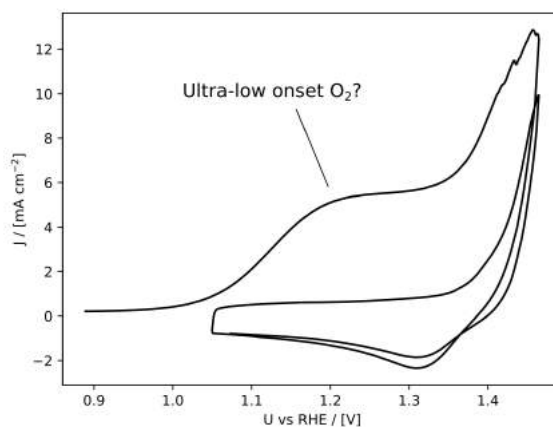


Figure 3.2: Initial cyclic voltammograms of Ru on graphene oxide material from the lab in Fuzhou, in 0.5 M H₂SO₄

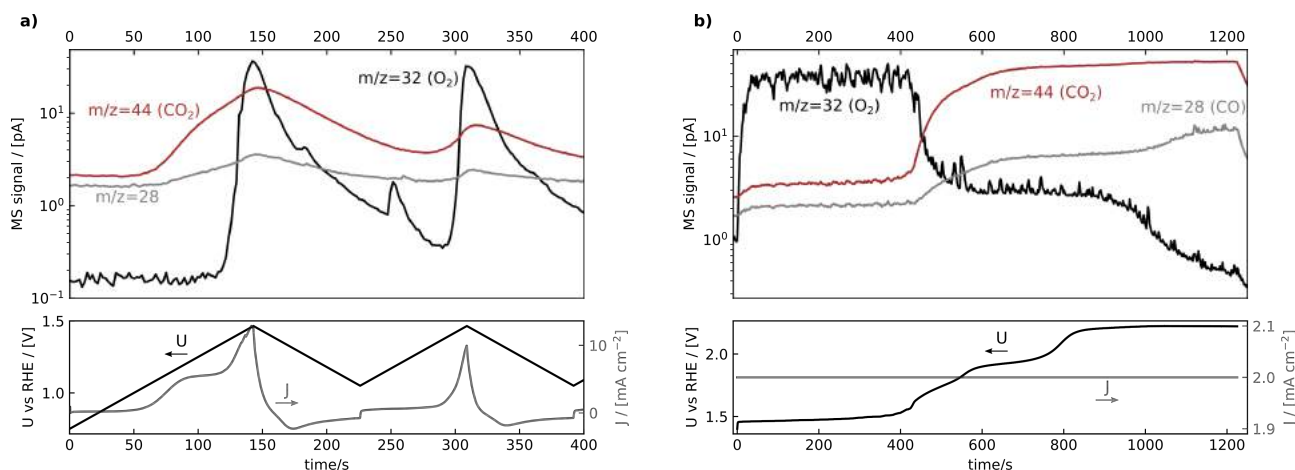


Figure 3.3: EC-MS plots of Ru on graphene oxide material from the lab in Fuzhou, in 0.5 M H_2SO_4 . (a) initial cyclic voltammograms and (b) constant-current experiment.

Figure 3.3a shows the same cyclic voltammetry data with mass spectrometry detection of the products. Clearly, the “ultra-low onset O_2 ” above is not O_2 but instead is revealed by the $m/z=44$ signal, implying CO_2 evolution, to be oxidation of the graphene oxide support. This oxidation of the support continues into the main OER wave, and can also be seen in the second cycle. The onset for O_2 , at about 1.33 V vs RHE, is remarkably low, indicating that the catalyst is highly active (though perhaps only as active as RuO_2 films, see Section 3.2). However, there is less O_2 in the second cycle, belying the catalyst’s instability.

Figure 3.3b shows a 20-minute constant-current measurement in the EC-MS setup. At 2 mA/cm^2 , it fails catastrophically at around 400 seconds into the experiment. At this point, the potential increases rapidly, and the 2 mA/cm^2 no longer goes to OER, but instead goes to oxidation of the substrate, as indicated by the switch from $m/z=32$ (O_2) to $m/z=44$ (CO_2) in the mass spectrometer. This is likely the point at which all of the ruthenium has dissolved or detached from the substrate. There is a $m/z=28$ signal which is attributed to fragmentation of CO_2 , but, interestingly, at about 1100 s, the $m/z=28$ signal starts increasing independently of the $m/z=44$ signal. This is attributed to a new mechanism for oxidation of the carbon support at these high potentials ($>2 \text{ V}$ vs RHE) resulting in evolution of CO .

This illustrates the importance of product detection when measuring activity in the highly corrosive acid OER conditions.

3.1.2 Nickel-iron: electrodeposited film vs annealed nanoparticles

As mentioned above, electrodes based on oxidized nickel and iron are used in industrial alkaline electrolyzer cells. However, the intrinsic OER activity of this electrocatalytic material is not well known, since it is typically used and studied in a highly porous foamy form [117]. An example, from ref 126, is shown in Figure 3.4a. It is very difficult to estimate the intrinsic activity, i.e., the turnover-frequency, of such materials because it is hard to determine how many active sites are accessible for the reaction. This was our primary motivation for studying a model system: vacuum-synthesized mass-selected $\text{Ni}_{0.75}\text{Fe}_{0.25}$ nanoparticles, characterized in detail in Paper II.

The mass-selected nanoparticles were formed in a cluster source as follows [127]:

1. Atoms were freed from a solid metallic target (here $\text{Ni}_{0.75}\text{Fe}_{0.25}$) by bombardment with a magnetically-bound plasma, i.e. magnetron sputtering.
2. These atoms were condensed into nanoparticles with a wide size distribution in an aggregation zone with a controlled temperature and argon pressure. Many of the nanoparticles are ionized, i.e. they carry a fundamental charge.

3. The charged nanoparticles are accelerated into a separation chamber and filtered according to m/z ratio using a modified time-of-flight mass spectrometer.
4. The beam of mass-selected nanoparticles is directed to a conductive substrate (here a 5mm Au stub) which is grounded via an ampmeter.

The deposition current, measured in part 4 above of the deposition technique, tells the number of nanoparticles deposited, since each deposited nanoparticle carries a fundamental charge. Since the size of the particles is known, this means that the mass loading is also known. Making an assumption about the shape of the nanoparticles, this means that the surface area is also known. In the case of the NiFe nanoparticles described here, SEM images (Figure 3.4b) confirm a spherical shape. This is especially useful, because it means, assuming the electrochemical reaction only occurs on the surface of the catalyst, that the number of available atomic sites can be calculated, and the turn-over frequency thus determined. These assumptions and results are discussed in more detail in Paper II and in Section 3.3.

SEM and TEM images of the mass-selected nanoparticles also confirm that they are unchanged before and after reaction (Figures 2 and 4 of Paper II). The OER activity is also stable over 1000 hours at 1.6 V vs RHE. These observations, taken together with the very small loading of the samples (approximately 150 ng of total Ni and Fe), indicate that charging or dissolution processes are negligible. We confirmed this using EC-MS by comparing the measured electrode current and the O₂ signal during cyclic voltammetry in 0.1 M KOH of a sample with 150 ng of 7 nm mass-selected Ni_{0.75}Fe_{0.25}O_x nanoparticles (the metal nanoparticles were annealed in O₂ in the vacuum chamber for this sample). The results are shown in Figure 3.5a. The O₂ signal, calibrated to mol/s as described in Chapter 2, is multiplied by four times Faraday's constant \mathcal{F} , which is the charge passed per mol of O₂ formed by water oxidation, in order to plot on the same axis as the electrode current. The integrated current and the integrated OER partial current, shown in Figure 3.5b, match. This makes it clear that all of the net current can be accounted for by OER. The oscillating contribution of the Ni²⁺/Ni³⁺ cancels itself out when integrated.

For comparison, we synthesized a porous Ni_{0.75}Fe_{0.25} oxy-hydroxide film by electrodeposition, according to the method described in ref. 122, typical for the synthesis of NiFe-based films studied in the literature [117]. In short, a current of -0.2 mA/cm^2 was passed through the substrate (a 5 mm Au stub) for 5 min in an electrolyte containing 100 mM Ni(NO₃)₂·6H₂O and 5 mM FeCl₂. We then perform the same EC-MS experiment comparing the electrode current and evolved O₂ during the first

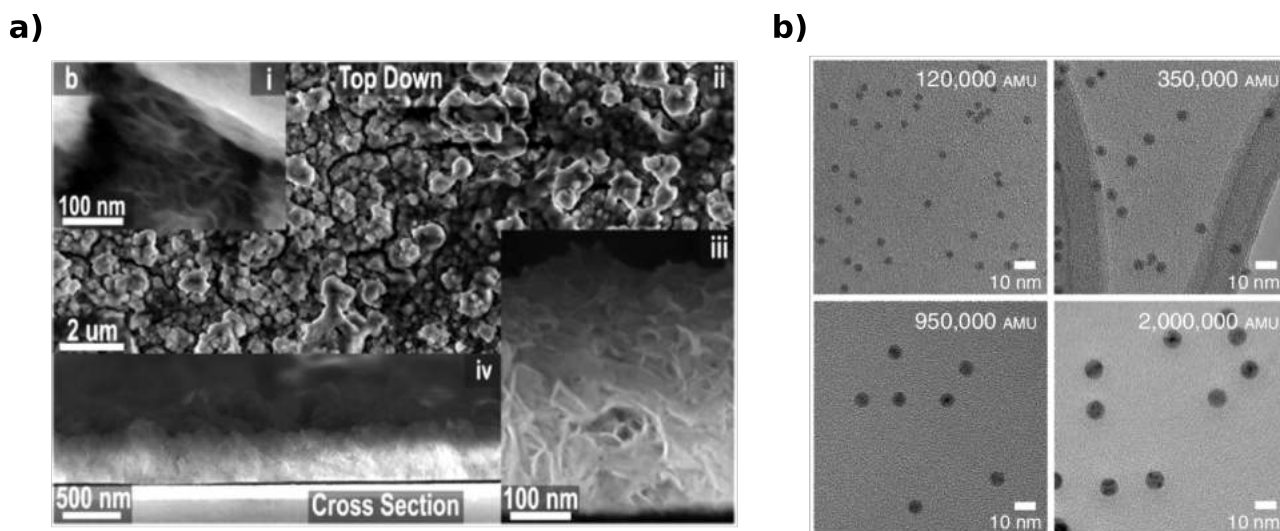


Figure 3.4: SEM images of NiFe-based OER catalysts (a), Example of a high-loading, high-surface-area NiFe oxyhydroxide catalyst studied in the literature, taken from reference 126. (b), Mass-selected vacuum-synthesized NiFe nanoparticles, from Paper II.

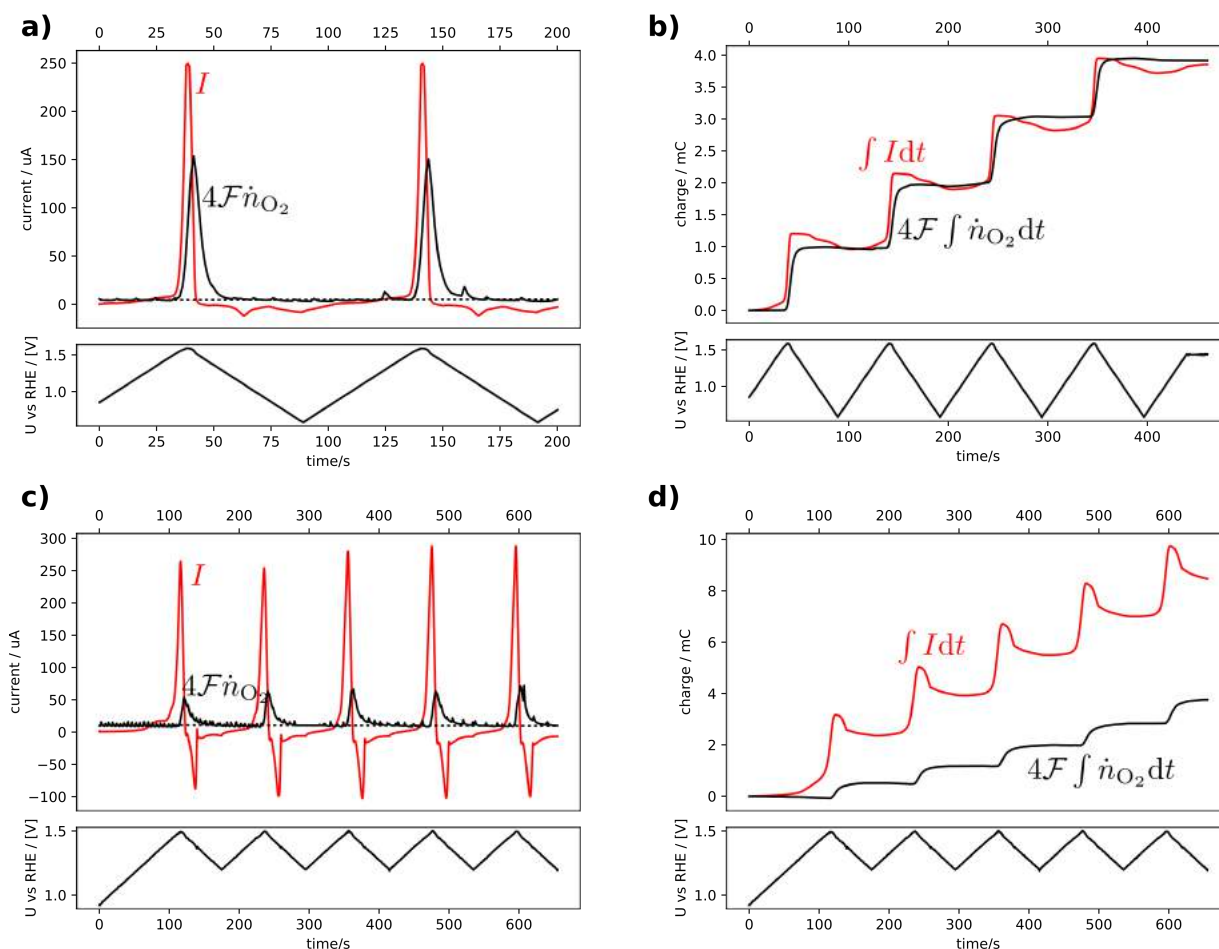


Figure 3.5: Comparison of the electrode current and the OER current equivalent of the O₂ signal in 0.1 M KOH for (a-b) 7 nm thermally annealed Ni_{0.75}Fe_{0.25}O_x nanoparticles and (c-d) an electrodeposited Ni_{0.75}Fe_{0.25}O_xH_y film. (a) and (c) show the (partial) current densities, while (b) and (d) show the integrals thereof.

cyclic voltammograms (Figure 3.5c and d). Unlike the case for the thermally oxidized nanoparticles, they do not match up over time. There is some net current transfer which cannot be accounted for by water oxidation. This may be attributed to charging of the film or dissolution of the metals, particularly Fe, which is known to leach. It could also be due to oxidation of adsorbed carbon-containing species (advantitious carbon), which would not be observed in EC-MS since the evolved CO₂ would be captured by the alkaline electrolyte as CO₃²⁻.

These results further highlight the need to measure O₂ when determining the OER activity, especially for high-loading catalysts. Electrodeposited NiFe oxy-hydroxide films are known to be stable over longer periods of time, and are closely related to the catalyst used industrially in alkaline electrolyzer cells, but Figure 3.5 makes it clear that, if O₂ is not measured, one could easily overestimate the activity by just looking at the current passed during cyclic voltammetry.

3.2 How low can we go?

Ruthenium dioxide can oxidize water at remarkably low overpotential in acidic electrolyte [118,120]. However, it is not particularly stable, with anywhere from 0.01% to 10% of the current going to Ru dissolution, depending on the preparation and experimental conditions [128]. It is also used as a super-capacitor material [129] due to a very high pseudo-capacitance. This pseudocapacitance is due to the many redox transitions on the surface sites of RuO_2 as well as the tendency of RuO_2 , especially amorphous RuO_2 , to form nano-scale interconnected domains, the surface of all of which are electrolytically accessible [130]. In the previous Section, I illustrated that it is necessary to measure the O_2 when studying OER catalysts. Together, the instability and high pseudo-capacitance (and thus large transient charging current) make this especially true for RuO_2 -based electrodes. With this in mind, as well as the ability to do very sensitive isotope-labeling experiments, described in the next Section, we started a collaboration with Reshma Rao and professor Yang Shao-Horn at MIT to use our EC-MS system to study OER on RuO_2 . One of the main goals was to see how low the onset potential for OER actually is.

3.2.1 Sputtered RuO_2 films

To check whether and how activity, stability, and lattice oxygen involvement varied with crystallinity, we sputtered RuO_2 at various temperatures. Reshma and I made the first samples together when she visited DTU in September 2018. We sputtered RuO_2 by reactive sputtering of a Ru sputter target with a magnetron sputter power of 300 W at a total pressure of 3 mTorr consisting of 80% Ar and 20% O_2 . We sputtered RuO_2 films of 25 nm nominal thickness (calibrated by quartz crystal microbalance) on a 5 nm Ti sticking layer on glassy carbon disks. The films are characterized by grazing-incidence x-ray diffraction (GIXRD) and cyclic voltammetry in Figure 3.6.

RuO_2 sputtered at room temperature (RT) appears amorphous, with no peaks visible in the diffractogram (Figure 3.6a). The films become more crystalline at higher sputtering temperature. However, while all the other peaks increase in intensity from RT to 400°C sputtering, the (110) peak passes through a maximum at a sputtering temperature of 200°C. This might indicate that a preferential orientation occurs at the right sputtering temperatures.

The relative surface areas of the samples, measured by electrochemical capacitance, however, decreases monotonically with higher sputtering temperature (Figure 3.6b). All of the films appear to be quite rough. Using a specific pseudo-capacitance (double-layer capacitance + redox charging) of

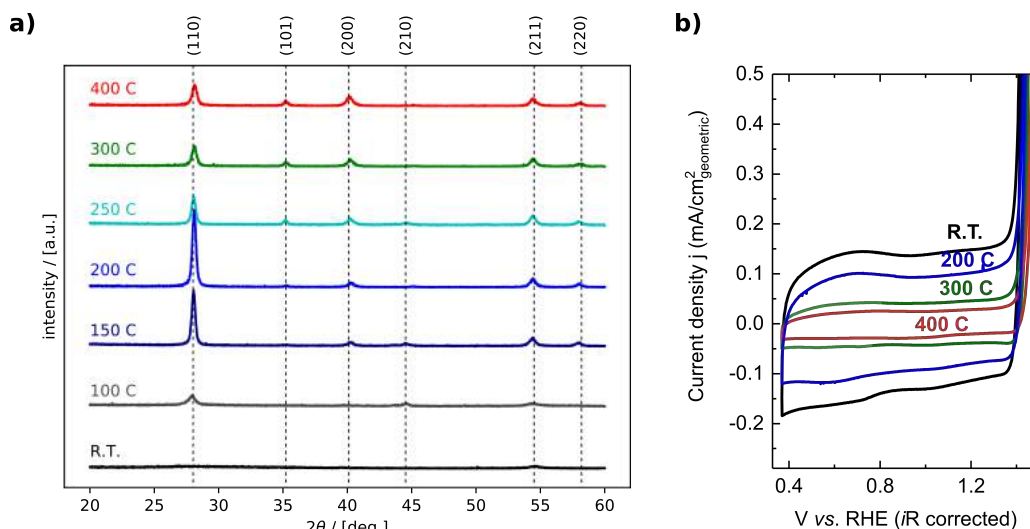


Figure 3.6: Characterization of RuO_2 films sputter-deposited at various temperatures. (a), Grazing-incidence x-ray diffraction spectra. The theoretical peak positions of rutile RuO_2 are indicated. (b) Cyclic voltammetry at a scan rate of 10 mV/s.

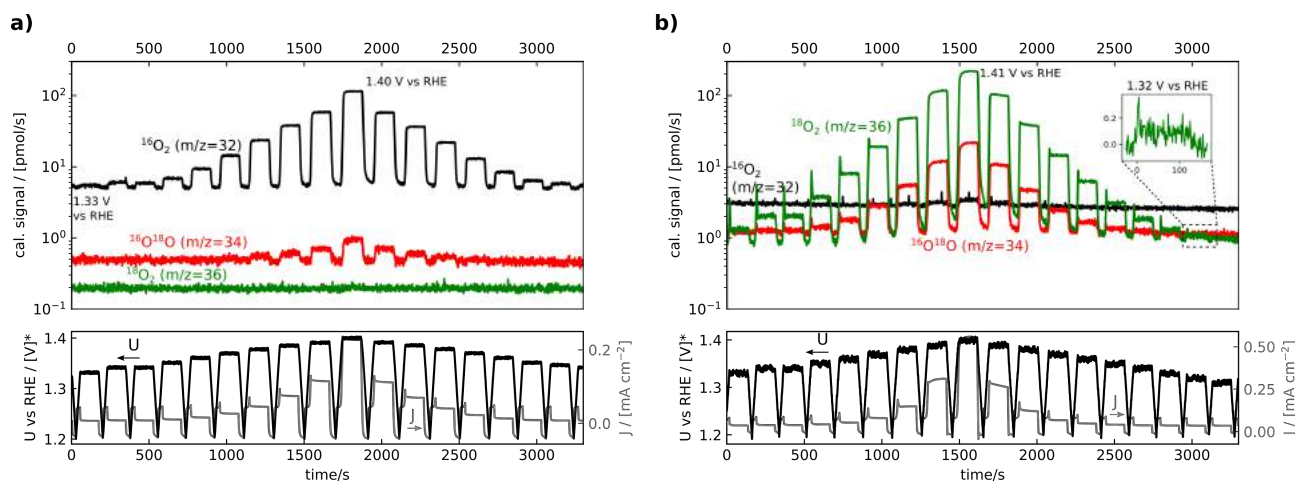


Figure 3.7: Activity measurement of a RuO_2 film sputtered at room temperature in 0.1 M HClO_4 in (a) natural (99.8% H_2^{16}O) water, and (b) 97% H_2^{18}O labeled water.

$200 \mu\text{F}/\text{cm}^2$ (this assumption is discussed in Subsection 3.2.3) [130], the roughness factors go from ≈ 9 for the 400°C -sputtered film to ≈ 60 for the RT-sputtered film.

To measure the OER activities of the sputtered films in 0.1 M HClO_4 , we scanned the potential at 5 mV/s from a “resting potential” of 1.2 V vs RHE to a working potential at which the OER measurement is made, holding each potential for 2 minutes. This was done to let the O_2 signal reach a steady state at each potential and fall to the background level between activity measurements. The RHE potential of the reference electrode was always measured in the same electrolyte and the same setup using a platinum electrode and saturating the electrolyte in H_2 , as described in Section 2.1.2. The O_2 signal was calibrated by 5-minute constant-current OER steps ($20 \mu\text{A}$, $50 \mu\text{A}$, and $100 \mu\text{A}$) from a rutile IrO_2 electrode measured in the setup on the same day, since IrO_2 is known to be much more stable than RuO_2 [118].

The activity measurement for an R.T.-sputtered film is shown in Figure 3.7a. O_2 production is stable during each 2-minute potential hold, giving a nice “square-wave” shape to the $m/z=32$ signal. The O_2 production rate follows a neat Tafel relationship with applied potential, i.e. for a constant linear increase in potential step, the O_2 signal increases by a constant factor. Specifically, the O_2 production rate increases by a factor ≈ 2 for each 10 mV step in potential. More commonly, this is stated in the reciprocal form, as the extra potential required for a factor 10 increase in activity (a “decade”), referred to as the Tafel slope. Here, the Tafel slope is ≈ 30 mV per decade

An oxygen signal is detectable down to 1.33 V vs RHE, a nominal overpotential of 100 mV. This was, to the best of our knowledge, already a record for detection of O_2 from water oxidation.

It should be emphasized that, while RuO_2 is highly active, and the room-temperature-deposited film has the highest activity of the sputtered films, in line with its high roughness factor, we have no reason to believe that our RuO_2 is more active than RuO_2 reported in the literature. The detection of O_2 at very low overpotential should, instead, be viewed as an accomplishment of the technique - specifically, the exceptionally high sensitivity of the chip-based EC-MS setup to gaseous products.

The detection limit of O_2 is limited by the background of the $m/z=32$ signal, which is probably set by outgassing of the MS filament or other components in the vacuum chamber, or extremely small leaks. Since the background is thus dominated by natural O_2 , which is 99.5% $^{16}\text{O}_2$, the background at $m/z=34$ ($^{16}\text{O}^{18}\text{O}$) and $m/z=36$ (O^{18}O_2) are considerably lower - by more than an order of magnitude comparing $m/z=36$ and $m/z=32$ as seen in 3.7a. Thus, additional sensitivity can be gained by isotopically labeling the oxygen in the electrolyte, and thus labeling the electrochemically produced O_2 .

Figure 3.7b shows an activity measurement of the same sample in 0.1 M HClO_4 in 97% H_2^{18}O . The y-axis in the top panel is on the same log-scale as that in Figure 3.7a so that the activities and backgrounds are directly comparable. Unfortunately, the $m/z=36$ background increases with the

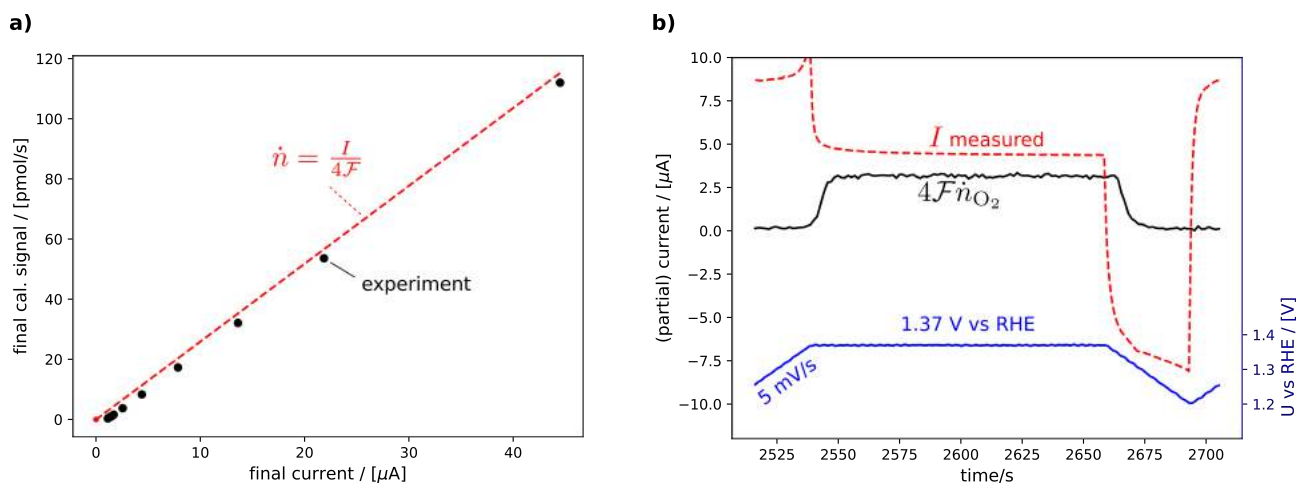


Figure 3.8: Closer look at the activity measurement of a RuO₂ film sputtered at room temperature in 0.1 M HClO₄ in natural (99.8% H₂¹⁶O) water. (a) Comparison of the averaged current and the O₂ flux as measured during the final 30 seconds of each constant-potential step. The dotted line (b) comparison of the instantaneous current (red) and O₂ partial current density (black) during the activity measurement at 1.37 V vs RHE.

change of electrolyte, indicating that the O₂ background in general comes partly from reaction of H₂O molecules, originating from the electrolyte, on the filament of the mass spectrometer. Due to this increase in background, the O₂ detection limit is only improved by less than an order of magnitude. This, however, enables clear detection of O₂ at 1.32 V vs RHE, a nominal overpotential of 90 mV.

It should be mentioned that the isotopic composition of the O₂ produced in these experiments in labeled electrolyte always reflected the isotopic composition of the electrolyte within uncertainty thereof. In other words, there was no obvious “isotope” signal consisting of a transient excess of ¹⁶O coming from the Ru¹⁶O₂ electrode. Such isotope signals are, however, observed in more sensitive experiments, and are the subject of the next two Sections.

As mentioned above, a concern with OER measurements in general, and in particular on RuO₂-based materials due to the high charging current and instability, is whether all of the electrode current is going to oxygen evolution. Figure 3.8a shows the value of the calibrated O₂ signal vs the measured electrode current, averaged over the last 30 seconds of each 2-minute potential hold in Figure 3.7a. The theoretical line assuming 100% Faradaic efficiency for O₂ production is shown in red. The experimental data has the same slope as the theoretical line, but with a slight offset, with slightly less O₂ than expected from the current. This is inconsistent with a significant dissolution current, as RuO₂ dissolution increases with the current [131].

A more likely source of this offset is the charging current. Figure 3.8b shows a zoom-in of the potential step at 1.37 V vs RHE from Figure 3.7a. The calibrated O₂ signal is multiplied by $4F$ to give a partial current density, and is plotted on the same axis (left y-axis) as the measured current. Here, we see that the measured current is dominated by capacitance while the potential is being scanned. This capacitive charging current continues during the potential hold, with the current only slowly approaching a steady state. The shape of the current during the constant-potential period is not completely exponential, but has a long tail, indicating that some parts of the electrode are harder to charge than others. In contrast, the O₂ signal is stable during the potential hold. This comparison indicates that some of the current can still be contributed to the charging of the electrode even at the end of the two-minute potential hold.

3.2.2 Hydrogen-bubble-template Ru foam

To see if we could push the limit of O₂ detection to even lower overpotentials, we synthesized a high-surface-area ruthenium foam by the hydrogen-bubble template method. Choongman Moon and I made the first ones after useful input from Anna Winiwarter, who had optimized a procedure for depositing

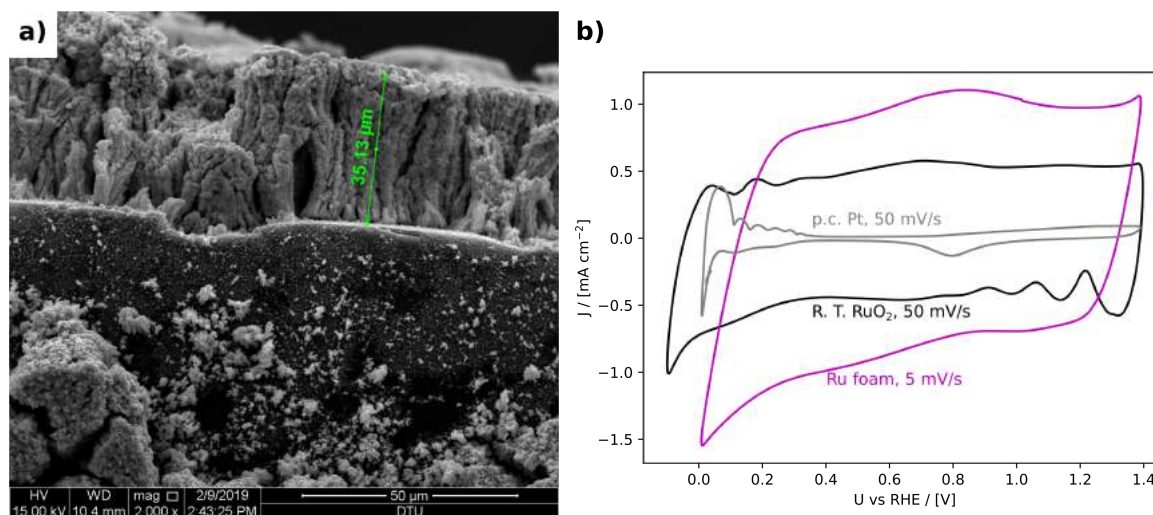


Figure 3.9: (a) SEM image of Ru foam. (b) Cyclic voltammetry in 0.1 M HClO₄ of a polycrystalline Pt electrode (gray), a room-temperature sputtered RuO₂ film (black), and Ru foam (magenta). Note the different scan rates. The features just after the cathodic and anodic turns on the R.T. RuO₂ cyclic voltammogram are artifacts of the electrode arrangement in the EC-MS setup.

palladium foam (used for Paper III). Choongman made all of the subsequent films Briefly, a glassy carbon disk suspended by a copper wire fastened with a u-cup and Teflon table was immersed in a solution of 10 mM RuCl₃ and 0.1 M HClO₄, opposite and parallel to a RuO₂/p+Si counter electrode held in place by gold wire. A bias of -6 V was applied to the working electrode with respect to the counter electrode for 10 minutes. Metallic Ru is deposited by reduction of the RuCl₃ in solution. This results in an Ru “foam” layer that is extremely porous, as the Ru deposition is mass-transport limited and occurs simultaneously with rapid bubble formation by hydrogen evolution. Figure 3.9a shows a cross-sectional SEM image of the Ru foam.

Figure 3.9b shows cyclic voltammetry of the Ru foam, with a RuO₂ film sputtered at room temperature and a polycrystalline platinum stub included for comparison. Notice the different scan rates, necessary because the charging current of the Ru foam at 50 mV/s would max out the available bias between the working and counter electrodes in the EC-MS setup. The electrochemically accessible surface area is clearly much higher than that of the room-temperature sputtered RuO₂, which al-

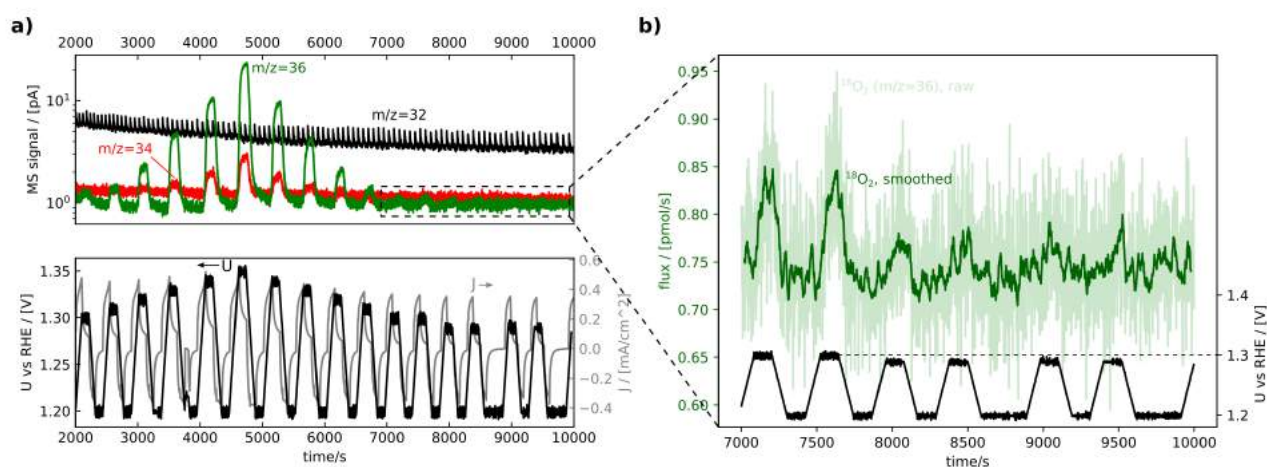


Figure 3.10: (a) EC-MS plot with raw MS data from an activity measurement at low overpotentials on the Ru foam in 0.1 M HClO₄ in 97% H₂¹⁸O. (b) Zoom-in on the lowest overpotentials, with the calibrated ¹⁸O₂ ($m/z=36$) signal (faint green). The solid green trace is a 15-point moving-average smoothing of the ¹⁸O₂ signal.

ready has a high roughness factor. Assuming the same specific capacitance of $200 \mu\text{F}/\text{cm}^2$ [130], the roughness factor of the Ru foam is on the order of 2000.

The results of an activity test on a Ru foam sample in labeled electrolyte are shown in Figure 3.10a. $^{18}\text{O}_2$ is detectable down to very low overpotentials. Note in the bottom panel that the charging current overwhelms the OER current, making the measurement of O_2 absolutely necessary to determine the activity at low overpotentials. At the lowest potential measured, 1.29 V vs RHE, the signal can barely be discerned from the noise in the $m/z=36$ signal. This data point was repeated a total of four times with varying resting times in between in order to increase confidence that there is indeed a signal. The signal is more apparent when the data is smoothed with a 15-point moving average, which is shown as the solid green trace in Figure 3.10b. Thus, we can claim to have detected O_2 produced electrochemically at 1.29 V vs RHE, just 60 mV above the standard equilibrium potential.

3.2.3 Turn-over-frequencies

Figure 3.11a shows the O_2 production rate, measured at $m/z=32$ or $m/z=36$ signal depending on the labeling of the electrolyte, averaged over the last 30 seconds of 2-minute potential holds for a number of RuO_2 sputtered films and Ru foams. All of the geometric areas were 0.196 cm^2 . There is a large variation spanning approximately three orders of magnitude, with the Ru foams producing O_2 at a much higher rate at a given potential. This can, however, be almost fully explained by surface area. In Figure 3.11, the O_2 production rate is normalized to the estimated number of active sites. This estimate was made using the following assumptions:

- Assume a density of active sites equal to the density of CUS sites on the $\text{RuO}_2(111)$ surface.
- Assume all surface contributing to the capacitance is active.
- Use the value $200 \text{ F}/\text{cm}^2$ determined by SAXS by Yoshida et al, Reference 130, applied to the portion of the CV's between 1.2 and 1.3 V vs RHE.

The first assumption seems reasonable, as (110) is the most stable surface of RuO_2 , the CUS site is believed to be the active site [118,132], and metallic Ru will have an oxidized surface at the potentials of interest. However, direct determination of the actual active sites would be highly useful. The STM method described Bandarenka and co-workers is a promising strategy [60].

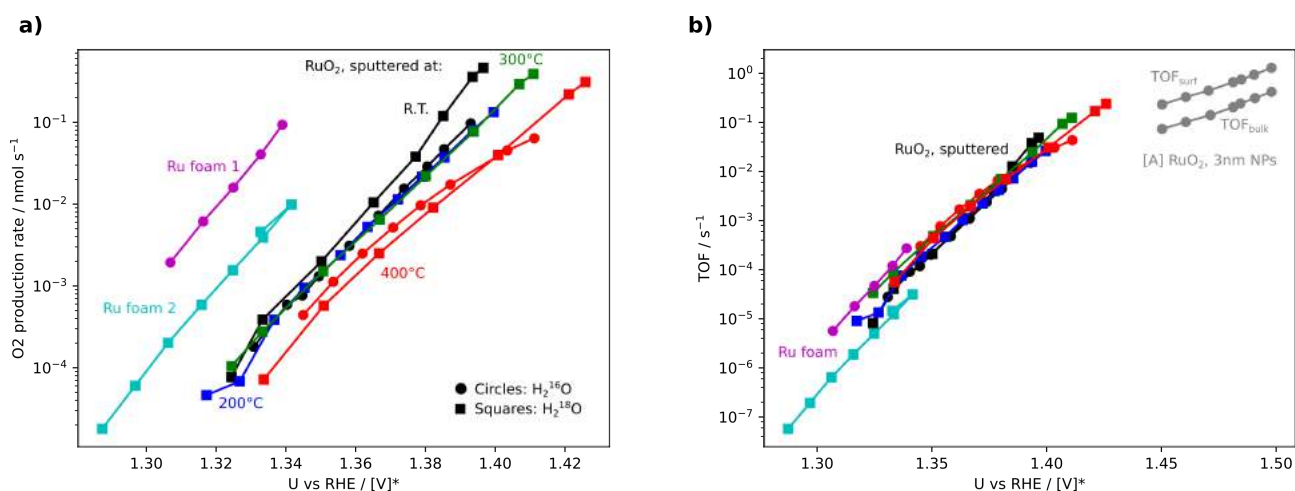


Figure 3.11: (a) O_2 production rate as a function of potential for all measured sputtered RuO_2 films and electrodeposited Ru foams. (b) TOF for films and foams, assuming a specific capacitance of $200 \mu\text{A}/\text{cm}^2$ and an active site density of 2 per nm^2 , corresponding to CUS sites on $\text{RuO}_2(110)$ [132]. [A] TOF for 3 nm RuO_2 nanoparticles are from Paoli et al, Reference 133.

The second assumption implies that there are no mass transport limitations in (H_2O) and out (H^+ and O_2) of the porous structures of the amorphous RuO_2 . This assumption is reasonable at the low current densities accessible in the EC-MS setup, but might break down at higher current densities.

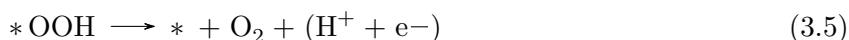
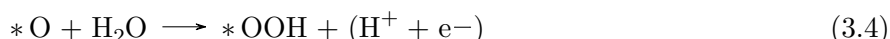
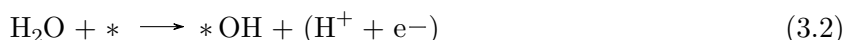
The third assumption is based on a study using small-angle x-ray scattering (SAXS) to estimate the combined surface area of the condensed RuO_2 aggregates in a series of hydrous RuO_2 electrodes [130]. The authors of that study found that comparing the electrochemical charging current to the aggregate surface area thus estimated yielded a constant specific capacitance of $200 \mu\text{F}/\text{cm}^2$, of which they estimate that $\approx 80 \mu\text{F}/\text{cm}^2$ is double-layer capacitance and $\approx 120 \mu\text{F}/\text{cm}^2$ is due to surface redox transitions. Here, I have implicitly assumed that all Ru and RuO_2 surfaces have the same double-layer and redox specific charging densities in the potential range 1.2 to 1.3 V vs RHE, chosen because all measurement datasets include potential scans spanning this range.

Figure 3.11b shows the turn-over-frequencies thus calculated. All of the RuO_2 and Ru samples converge on a common curve with ≈ 1 order of magnitude scatter. This adds validity to the assumptions made above, and suggest that the active sites are the same on the different materials. The curve has a slowly changing slope, with a Tafel slope of approximately 30 mV/decade at the upper end (1.38-1.42 V vs RHE), and a Tafel slope of approximately 20 mV/decade at the low overpotential range (1.30-1.34 V vs RHE).

It is informative to compare these TOF values to TOF values measured and calculated by other means. In Reference 133, Paoli et al report TOF values for mass-selected 3 nm RuO_2 nanoparticles deposited with the same cluster source method used in Paper II and described briefly in Subsection 3.1.2. Just like in that study, Paoli et al determine the number of active sites via the loading of the nanoparticles, which is known via the deposition current and the size of the nanoparticles. They compare two assumptions for the number of active sites: (1) that all Ru atoms are active sites (TOF_{bulk}), and (2) that only the Ru atoms at the surface of the RuO_2 nanoparticles are active sites (TOF_{surf}). These two TOF values are co-plotted with the present results in Figure 3.11a. The TOF_{surf} results for the nanoparticles broadly continue the trend observed for the electrodeposited foams and sputtered films, with a further increase in Tafel slope at higher potentials, to about 60 mV/decade at 1.46 - 1.50 V vs RHE. This further supports the assertion that the active sites are similar however Ru or RuO_2 are prepared, and that activity is limited to the surface, though this surface area can be very large.

Note that the problem of uneven potential distribution described in Subsection 2.1.3 puts some uncertainty on the activity measurements at higher current densities. Due to resistance across the electrolyte film between the electrode and the chip, the potential on the side of the working electrode closest to the counter electrode can be somewhat higher than the measured potential. Taking this into account, the activity at high current densities is likely overestimated, meaning that the curves should bend more towards higher Tafel slopes at higher current densities. If this is the case, it would actually improve the agreement with the nanoparticles. Fortunately, it is the measured behavior at low current densities, which is more reliable, which is of the most interest in this context.

The changing Tafel slope has mechanistic implications [134]. Briefly, the oxygen evolution reaction consists of four steps, most simply written as [135, 136]:



In the limit that one of these steps, step i , is slower than the rest, then the rate is

$$r = k_i^0 \theta_{i-1} \exp\left(\frac{\mathcal{F}}{RT} \alpha_i (U - U_i^\circ)\right), \quad (3.6)$$

where k_i^0 is the rate constant for the i 'th step, U_i° is its equilibrium potential. θ_{i-1} is the coverage

of the reactant to that step, i.e., $\theta_0 = \theta_*$, $\theta_1 = \theta_{*\text{OH}}$, $\theta_2 = \theta_{*\text{O}}$, and $\theta_3 = \theta_{*\text{OOH}}$. Finally, α_i is the symmetry factor to the reaction. The symmetry factor is the ratio of the change of the activation barrier of an elementary electrochemical reaction to the change in its overall ΔG resulting from a change in potential [53]. Equation 3.6 is thus an Arrhenius equation, with the activation barrier

$$E_{a,i} = -\alpha_i \mathcal{F}(U - U_i^\circ). \quad (3.7)$$

Symmetry factors for elementary electrochemical steps are typically on the order of 0.5, meaning that if you increase the potential by 1 mV, you decrease the activation barrier by 0.5 meV.

Taking the base-ten logarithm to Equation 3.6,

$$\log(r) = \log(k_i^0) + \log(\theta_{i-1}) + \alpha_i \frac{\mathcal{F}}{RT \ln(10)}(U - U_i^\circ), \quad (3.8)$$

and differentiating with respect to potential yields

$$\frac{\partial \log r}{\partial U} = \frac{\partial \log \theta_{i-1}}{\partial U} + \alpha_i \frac{\mathcal{F}}{RT \ln(10)}. \quad (3.9)$$

This is the reciprocal of the Tafel slope. If the coverage of the reactant to step i is constant ($\partial \log \theta_{i-1} / \partial U = 0$), and the symmetry factor is 0.5, this gives

$$\frac{\partial \log r}{\partial U} = 0.5 \frac{\mathcal{F}}{RT \ln(10)} = \frac{1}{120 \text{ mV}}, \quad (3.10)$$

or a Tafel slope of 120 mV per decade. In contrast, the Tafel slope of RuO₂, as mentioned above, takes on much lower values, as low as 20 mV/decade at very low TOF.

The symmetry factor for an elementary step in theory can not be more than 1 (which would give a Tafel slope of 60 mV/decade with $\partial \log \theta_{i-1} / \partial U = 0$), so the only way to have a Tafel slope of less than 60 mV per decade is to have a potential-dependent coverage of the reactant to the limiting step, i.e.,

$$\frac{\partial \log \theta_{i-1}}{\partial U} > 0. \quad (3.11)$$

This implies that the $(i - 1)$ 'th intermediate is not at saturation coverage, but is in equilibrium with empty sites (*) or other intermediates. The stronger the potential dependence (the greater $\partial \log \theta_{i-1} / \partial U$), the smaller the Tafel slope. A Tafel slope of 20 mV/decade, observed for Ru Foam at the lowest potentials, implies (still assuming $\alpha_i = 0.5$) that

$$\frac{\partial \log \theta_{i-1}}{\partial U} = \frac{\partial \log r}{\partial U} - \alpha_i \frac{\mathcal{F}}{RT \ln(10)} = \frac{1}{20 \text{ mV}} - \frac{1}{120 \text{ mV}} = \frac{1}{24 \text{ mV}}. \quad (3.12)$$

or that the coverage of the $(i - 1)$ 'th intermediate increases a factor 10 every 24 mV increase in potential.

In the assumption made above that one step is limiting, the potential-dependence of the coverage should be explained by the equilibrium between surface species, subject to the conservation law

$$\theta_* + \theta_{*\text{OH}} + \theta_{*\text{O}} + \theta_{*\text{OOH}} = 1 \quad (3.13)$$

The changing Tafel slope at low overpotential can thus provide crucial insight on which step is limiting and on the free energies of the intermediates. However, there are many free parameters, and the scatter of the data in Figure 3.11b is large, making this challenging. Furthermore, the use of polycrystalline samples which may have more than one type of active site complicates the assumptions made above. This work is ongoing.

3.2.4 The effect of O₂ in the electrolyte

Many fundamental studies of OER electrocatalysts involve electrochemical measurements in oxygen-saturated electrolyte. Indeed, the use of an overpotential referenced to 1.23 V vs RHE implies oxygen-saturated electrolyte, since the equilibrium potential is only 1.23 V vs RHE when reactants and products excluding ($\text{H}^+ + \text{e}^-$) are at unit activity, namely 1 bar O₂.

This is analogous to hydrogen evolution reaction (HER) studies, in which a hydrogen-saturated electrolyte is used. For the case of HER, which is reversible on the best catalysts such as platinum, the use of hydrogen-saturated electrolyte makes a crucial difference. Indeed, a significant hydrogen evolution current can be measured at 0 V vs RHE if the hydrogen is transported away from the electrode surface (Subsection 2.3.1). The importance of having the hydrogen-saturated electrolyte is that HER and the reverse reaction, the HOR, both occur at appreciable rates at the equilibrium potential.

However, at potentials sufficient to drive the highly irreversible OER, the equally irreversible oxygen reduction reaction (ORR) is negligible. This is abundantly clear when looking at Figure 3.12. Even if RuO₂ was a symmetrical catalyst, i.e., as good at OER as ORR, the ORR current would still be approximately four orders of magnitude lower than the OER current at the lowest potential at which we could detect O₂ evolution, 1.29 V vs RHE. Furthermore, the scaling relations in oxygen evolution catalysts imply that a near-optimal OER catalyst like RuO₂ is a rather bad ORR catalyst [136].

Nonetheless, we decided to check if O₂ saturation of the electrolyte had an effect. The use of isotope-labeled electrolyte enables the measurement by mass spectrometry of oxygen evolution under O₂-saturated conditions. Figure 3.13a shows such an experiment. The activity of a crystalline RuO₂ electrode is first measured in labeled electrolyte saturated with inert gas. At approximately 3500 s, the electrolyte is quickly saturated with natural O₂ through the membrane chip, and the activity experiment is repeated. The $m/z=36$ (¹⁸O₂) signal looks identical in the two activity measurements, whereas the background of the $m/z=34$ (¹⁶O¹⁸O) is shifted up due to the natural isotopic distribution in the O₂ carrier gas.

The results are grouped by potential in Figure 3.13b and c. There is no significant difference due to the presence of natural O₂ in the current density or ¹⁸O₂ partial current density (Figure 3.13b). The increasing relative difference of the ¹⁸O₂ partial current density and the total current

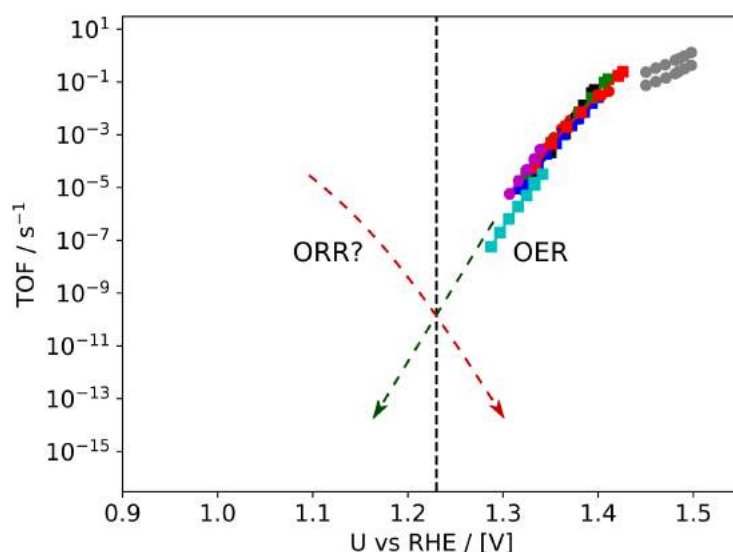


Figure 3.12: Zoomed out TOF plot showing actual OER data from Ru and RuO₂ (Figure 3.11b), centered at the OER/ORR equilibrium potential at 1 bar O₂. A hypothetical ORR curve for a catalyst with ORR activity symmetrical to RuO₂'s OER activity is shown to illustrate that ORR is negligible at OER potentials.

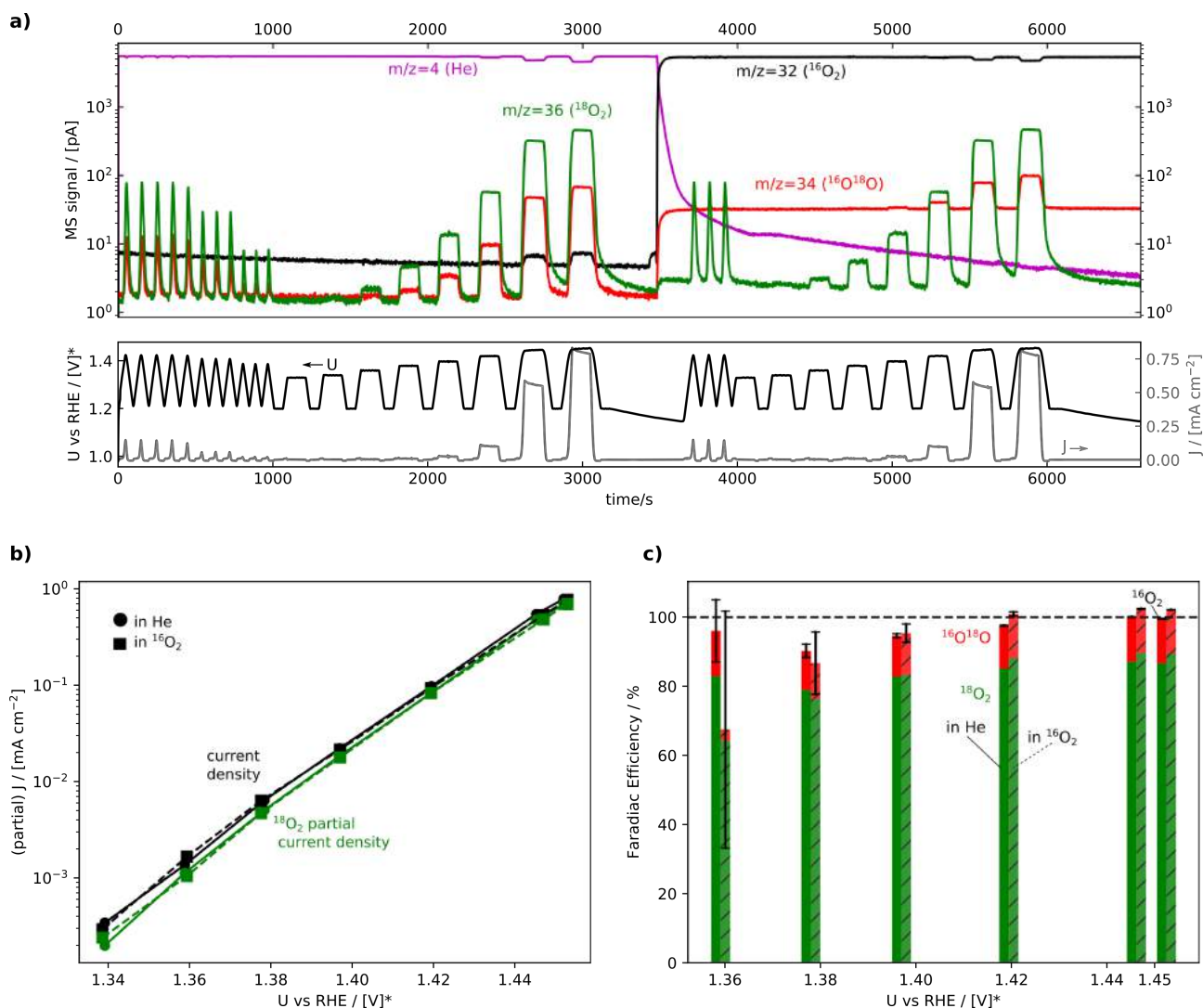


Figure 3.13: Activity of crystalline RuO₂ in He-saturated and ¹⁶O₂-saturated 0.1 M HClO₄ in H₂¹⁸O. (a) Experiment as an EC-MS plot. (b) The current density (black) and the partial current density for ¹⁸O (green) at the end of each constant-potential step. (c) The Faradaic efficiencies for ¹⁸O₂ (green) and ¹⁶O¹⁸O (red) as a function of potential. The error bar represents the uncertainty due to the standard deviation of the baseline m/z=34 MS signal.

density at smaller overpotential can be attributed to residual electrode charging current during the last 30 seconds of each constant potential step. O₂ saturation of the electrolyte makes no significant difference in the Faradaic efficiency towards ¹⁶O¹⁸O (Figure 3.13c), though the error bars in O₂-saturated electrolyte are much larger due to the m/z=34 background. Interestingly, the total labeled oxygen signal for the highest potentials, where the relative influence of background MS signal and electrode current loss to electrode charging are smallest, appears approximately 3% larger in the O₂-saturated electrolyte. This is probably due to an artifact whereby the small flux of O₂ carrier gas into the vacuum chamber influences the overall sensitivity of the mass spectrometer (see Subsection 2.2.3). That approximately 12% of the combined O₂ signal is ¹⁶O¹⁸O reflects the composition of the electrolyte which is approximately 6% ¹⁶O after addition of HClO₄.

The fact that the presence of O₂ has no influence on the overall OER current density of the catalyst should be expected, as the ORR current density is insignificant at potentials at which OER is significant. However, the same cannot be said for the individual steps of the reaction, for which the reverse elementary reaction might occur at a non-negligible rate. Thus, lack of a significant effect on the isotopic makeup of the evolved oxygen does have a mechanistic implication, if an unsurprising

one: the limiting step in OER does not come before the formation of the O-O bond. If the limiting step were prior to the formation of the O-O bond, then the O-O bond-forming step and all subsequent steps (Reactions 3.4 and 3.5) would be at equilibrium. There would then be a non-negligible rate for adsorption and dissociation of $^{16}\text{O}_2$, and recombination of the adsorbed ^{16}O with ^{18}O from the electrolyte, giving an increased $^{16}\text{O}^{18}\text{O}$ signal in the evolved oxygen. This does not appear to be the case at $U \geq 1.42$ V vs RHE, though below this potential the uncertainty due to the $m/z=34$ background is too great to draw any conclusions.

In this Section, I described the use of isotope-labeled electrolyte to take advantage of the low background signal for $^{18}\text{O}_2$ and thus lower the overpotential at which electrochemically produced oxygen can be detected and quantified. In this final Subsection, I used the lack of scrambling in $^{16}\text{O}_2$ -saturated H_2^{18}O electrolyte to probe the rate-determining step of the OER on RuO_2 . Both of these uses of isotope labeling in OER research are novel to the best of my knowledge. However, isotope labeling has been used extensively to probe another phenomenon: the involvement of lattice oxygen in the oxygen evolution reaction. This is the subject of the next Section.

3.3 To leave or to remain in the lattice

Many authors, especially in recent years, have taken interest in answering the following question for various oxygen evolution electrocatalysts, both for alkaline and acidic media:

Question 3.1. *During oxygen evolution, is lattice oxygen from the electrode material incorporated in the O_2 produced?*

The question is, in other words, whether a material shows “lattice oxygen evolution”. This is a slightly different phrase from “lattice oxygen exchange” more often used in the literature since both imply that oxygen is coming out of the material, but the former does not necessarily imply that new oxygen is going into the material.

The answer to Question 3.1, which can be probed by isotope labeling experiments as described below, is often claimed to have profound mechanistic implications. Figure 3.14 shows two examples from recent works by Grimaud et al [123] in alkaline OER and from Geiger et al [113] in acid OER. Both observe evidence of an “isotope signal” for some of the materials studied, whereby the oxygen evolved contains an isotopic label incorporated into the catalyst, implying an affirmative answer to Question 3.1. The authors take the further step (which I will claim in this Thesis requires further nuance) of concluding that lattice oxygen *exchange* is an important part of the OER mechanism for these materials. They propose the mechanisms shown.

To better test for and interpret lattice oxygen evolution, researchers should agree on a working definition of lattice oxygen (to distinguish from, e.g. surface-adsorbed oxygen and intercalated water). This is, to the best of my knowledge, broadly lacking. For this Thesis, I use the following definition:

Definition 3.1. Lattice oxygen is oxygen with oxygen-metal bonds which does not reduce to water or exchange spontaneously with oxygen in the electrolyte at any potential anodic of the open-circuit potential of the material.

This definition is one motivated by practicality: lattice oxygen is, in other words, the oxygen for which Question 3.1 can be answered by isotope-labeling studies. Any oxygen that exchanges spontaneously with the electrolyte will be lost between when the sample touches the electrolyte and

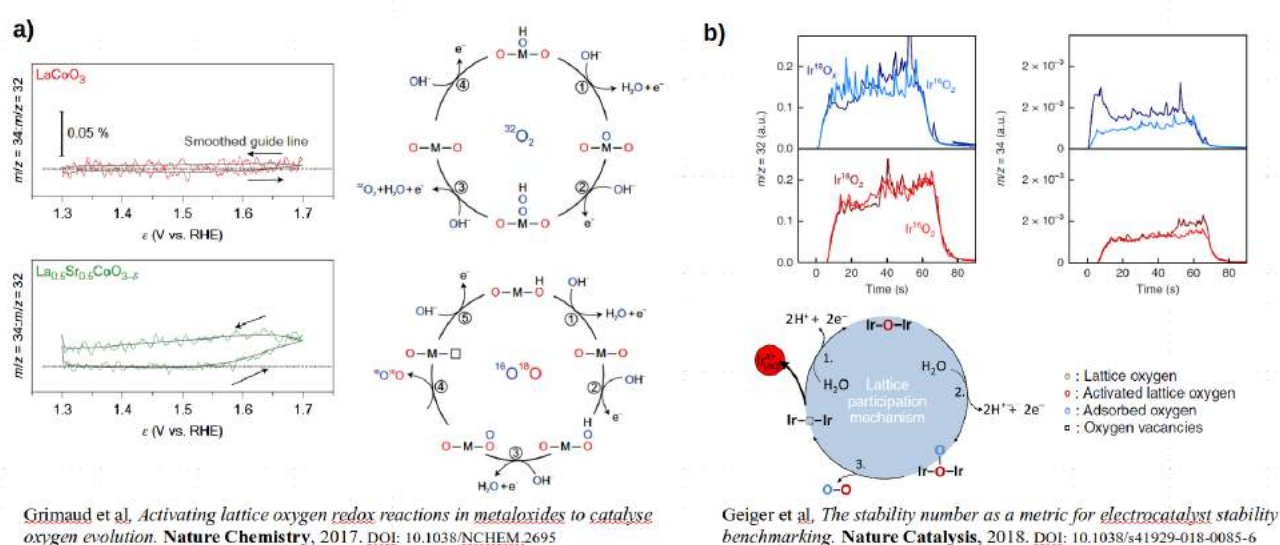


Figure 3.14: Examples of reported studies probing lattice oxygen evolution. The result of the isotope labeling experiment and the proposed mechanism is shown. (a), Some perovskite materials including $La_{0.5}Sr_{0.5}CoO_{3-\delta}$ show lattice oxygen evolution during OER in 0.1 M KOH. Taken from ref. 123. (b) Hydrrous IrO_x formed by potential cycling $Ir^{18}O_2$ in labeled electrolyte shows lattice oxygen evolution in 0.1 M $HClO_4$. Taken from ref. 113

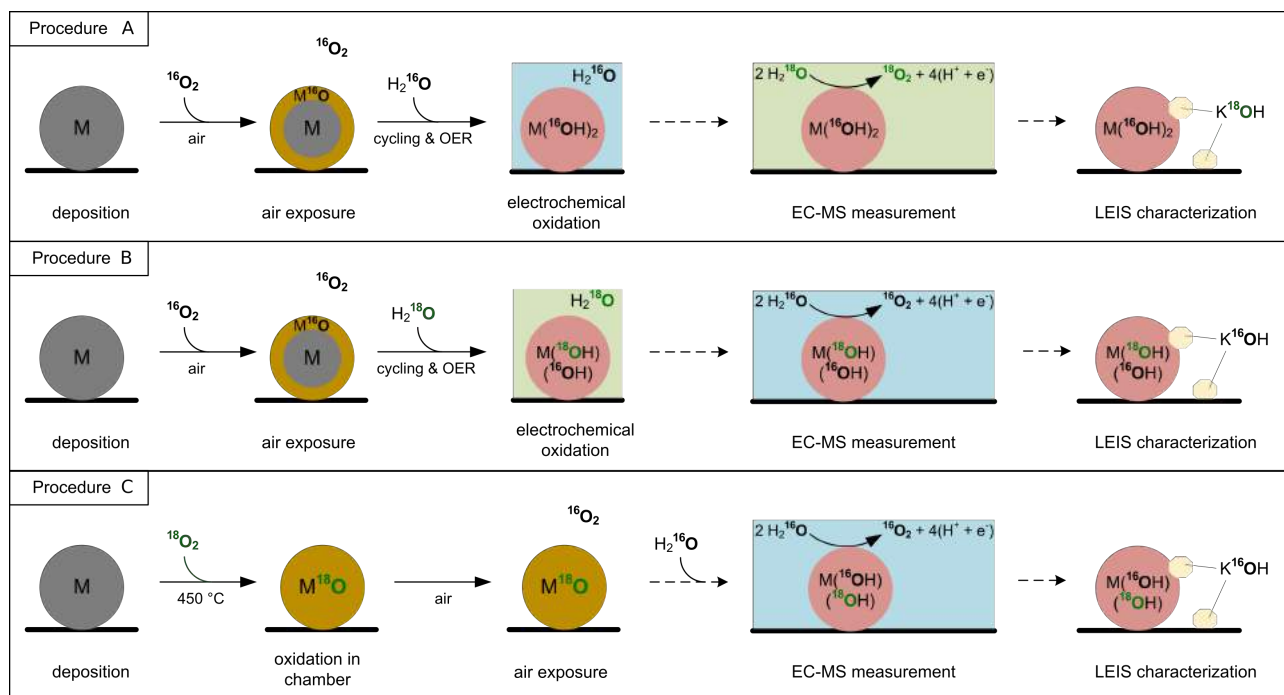


Figure 3.15: Three strategies for isotope-labeling experiments intended to detect lattice oxygen involvement in the OER, diagrammed for the case of vacuum-synthesized NiFe nanoparticles. Taken from Paper II. (a) Strategy A involves mass spectrometric detection of evolved O_2 (EC-MS step) for an unlabeled catalyst in labeled electrolyte. (b) Strategy B involves electrochemical labeling of an OER catalyst followed by EC-MS in an un-labeled electrolyte. (c) Strategy C involves direct preparation (here by annealing in $^{18}\text{O}_2$) of a labeled electrocatalyst followed by EC-MS in an un-labeled electrolyte.

when oxygen is produced. This definition of lattice oxygen excludes, for example, $\ast\text{OH}$ on a Pt surface, which has a potential-dependent coverage and is thus in equilibrium with H_2O over a range of potentials. For the rutile RuO_2 (110) surface, the oxygen bridging two ruthenium atoms is strongly bound with two metal bonds and at most one proton at and above 0.7 V vs RHE [132], and so would probably be counted as lattice oxygen (the open-circuit potential in 0.1 M HClO_4 after air exposure is approximately 0.9 V vs RHE); whereas oxygen adsorbed at the CUS site is in equilibrium with H_2O up to about 1.2 V vs RHE [132], and so would not count as lattice oxygen.

An argument could be made that surface-bound oxygen, even if it fits Definition 3.1, is not really lattice oxygen, and that lattice oxygen should only include oxygen below the surface monolayer. This definition of lattice oxygen would make the mere detection of an isotope signal insufficient to answer Question 3.1, since the isotope signal could be coming from the surface monolayer. To prove that subsurface lattice oxygen is evolved during OER, more than one monolayer-equivalent of isotope signal would have to be detected.

The examples in Figure 3.14 are but two of many studies seeking to answer Question 3.1. Table 3.1 shows a more comprehensive list. The studies go all the way back to some of the earliest DEMS studies in the 1980's but have accelerated in the past couple years. The experimental methods (catalyst preparation, isotope labeling technique, electrolyte, and isotope exchange experiment measurement technique) are included to aid comparison of the various studies. One clear characteristic of this compilation is that there is no convergence yet in the literature on the best way to conduct these lattice exchange experiments.

The studies are approximately evenly split between DEMS or OLEMS for measuring the evolved oxygen isotopes. Most studies examine the oxygen evolved during potential sweeps (linear sweep voltammetry, LSV) or cyclic voltammetry (CV), whereas only a few use constant-current measurements (CP). This is a problem because the redox changes during a potential sweep can destabilize electrode materials [131, 146], perhaps giving an isotope signal that would not be present in steady-

Electrocatalyst	Preparation	Labeling	Electrolyte	Experiment	Result	Citation
Pt	On DEMS membrane, oxidized in 98% H ₂ ¹⁸ O	≤ 98% ¹⁸ O	Natural 0.5 M H ₂ SO ₄ or 1.0 M KOH	LSV, DEMS	no excess ¹⁸ O evolved	Willsau, 1985 [137]
Ru and RuO ₂	Sputtered onto Teflon DEMS membrane	Natural	0.5 M H ₂ SO ₄ in 90% H ₂ ¹⁸ O	CVs, DEMS	some excess ¹⁶ O evolved	Wohlfahrt-Mehrens, 1987 [138]
Hydrous IrO _x	Thermal decomposition of IrCl ₆ on Ti	Natural	1 M HClO ₄ in 10% H ₂ ¹⁸ O	CVs, DEMS & chip EC-MS	> 1 ML excess ¹⁶ O evolved	Fierro, 2007 [139]; rep. in Roy, 2018
nanocrystalline RuO ₂ and Ru _{0.9} Ni _{0.1} O _{2-δ}	(co-)deposition on Ti mesh and annealing	Natural	0.1 M HClO ₄ in 98% H ₂ ¹⁸ O	CVs, DEMS	Some excess ¹⁸ O evolved at high η	Macounova, 2009 [140]
Molecular Cobaltate Clusters	Electrodeposition of 0.5 mM Co ²⁺ in labeled phosphate	≈ 87% ¹⁸ O	Natural phosphate buffer	CP, integral headspace	7-15% of ¹⁸ O loading evolved	Surendranath, 2010 [141]
AuO _x	Au oxidized at 2.0 V in 98% H ₂ ¹⁸ O	≤ 98% ¹⁸ O	Natural 1 M HClO ₄	LSV, OLEMS	≈ 1 ML ¹⁸ O ₂ evolved	Diaz-Morales, 2013 [142]
polycrystalline, (110), (100), (101), and (111) RuO ₂	oxidized in 98% H ₂ ¹⁸ O	≤ 98% ¹⁸ O	Natural 0.1 M KOH or 0.1 M H ₂ SO ₄	CVs, OLEMS	Little to no excess ¹⁸ O evolved	Stoerzinger, 2017 [143]
Spinel Co ₃ O ₄	as-received	Natural	0.5 M KOH in 10% H ₂ ¹⁸ O	CVs, DEMS	34% ML excess ¹⁶ O evolved	Amin, 2017 [144]
Spinel Co ₃ O ₄	electrochemically cycled in 10% H ₂ ¹⁸ O	≤ 10% ¹⁸ O	Natural 0.5 M KOH	CVs, DEMS	12% ML excess ¹⁸ O evolved	Amin, 2017 [144]
LaCoO ₃	solid-state synthesis, oxidized in 98% H ₂ ¹⁸ O	≤ 98% ¹⁸ O	Natural 0.1 M KOH	CVs, OLEMS	little to no excess ¹⁸ O evolved	Grimaud, 2017 [123]
La _{0.5} Sr _{0.5} CoO _{3-δ}	solid-state synthesis, oxidized in 98% H ₂ ¹⁸ O	≤ 98% ¹⁸ O	Natural 0.1 M KOH	CVs, OLEMS	Some excess ¹⁸ O evolved	Grimaud, 2017 [123]
Pr _{0.5} Ba _{0.5} CoO _{3-δ}	solid-state synthesis, oxidized in 98% H ₂ ¹⁸ O	≤ 98% ¹⁸ O	Natural 0.1 M KOH	CVs, OLEMS	Some excess ¹⁸ O evolved	Grimaud, 2017 [123]
SrCoO _{3-δ}	solid-state synthesis, oxidized in 98% H ₂ ¹⁸ O	≤ 98% ¹⁸ O	Natural 0.1 M KOH	CVs, OLEMS	Some excess ¹⁸ O evolved	Grimaud, 2017 [123]
Ni _{0.75} Fe _{0.25} O _x H _y film	electrodeposition	Natural	0.1 M KOH in 97% H ₂ ¹⁸ O	CVs, chip EC-MS	≪0.1% lattice O evolution	Roy, 2018 [145] (Paper II)
Ni _{0.75} Fe _{0.25} O _x H _y , 7 nm nanoparticles	cluster source, electrochem. oxidation	Natural	0.1 M KOH in 97% H ₂ ¹⁸ O	CVs, chip EC-MS, ISS	≪0.1% lattice O evolution	Roy, 2018 [145] (Paper II)
Ni _{0.75} Fe _{0.25} O _x H _y , 7 nm nanoparticles	cluster source, electrochem. oxidation in 97% H ₂ ¹⁸ O	Estimated 50% H ₂ ¹⁸ O	Natural 0.1 M KOH	CVs, chip EC-MS, ISS	≪0.1% lattice O evolution	Roy, 2018 [145] (Paper II)
Ni _{0.75} Fe _{0.25} O _x H _y , 7 nm nanoparticles	cluster source, thermal oxidation in ¹⁸ O ₂	Estimated 50% H ₂ ¹⁸ O	Natural 0.1 M KOH	CVs, chip EC-MS, ISS	≪0.1% lattice O evolution	Roy, 2018 [145] (Paper II)
Rutile IrO ₂	Reactive sputter deposition with 99% ¹⁸ O ₂	≈ 99% ¹⁸ O	Natural 0.1 M HClO ₄	CP, OLEMS	little to no ¹⁸ O evolved	Geiger, 2018 [113]
Hydrous IrO _x	Potential cycling of sputtered Ir ¹⁸ O ₂ film in 97% H ₂ ¹⁸ O	≈ 97% ¹⁸ O	Natural 0.1 M HClO ₄	CP, OLEMS	some ¹⁸ O evolved	Geiger, 2018 [113]

Table 3.1: Isotope-labeling experiments in the water oxidation electrocatalysis literature

state OER. Of those that measure a lattice oxygen evolution signal, some attempt to quantify the signal in terms of the total or surface oxygen loading of the catalyst [139, 141, 142, 144] whereas many observe an isotope signal but do not quantify it [113, 123, 138].

The most pronounced difference between the experiments is in how the catalyst and electrolyte are isotope labeled. Broadly, there are three strategies:

- A. The catalyst is prepared without any labeled oxygen. The lattice oxygen is thus 0.2% ^{18}O . Oxygen evolution is then measured in labeled electrolyte with an increased ^{18}O concentration [138–140, 144, 145].
- B. The catalyst is originally prepared with the natural isotopic ratio, but then it is used for oxygen evolution in a labeled electrolyte. If the OER mechanism involves an exchange between the lattice oxygen and the electrolyte, this will result in labeling of the electrocatalyst with a ^{18}O concentration in the active lattice sites up to that of the electrolyte. This electrochemically labeled catalyst is then transferred to un-labeled electrolyte, and the isotopic composition of the evolved oxygen is measured. [123, 137, 142, 144, 145, 147].
- C. The final strategy is to prepare the catalyst from the start with labeled oxygen, and then measure the isotopic composition of the the O_2 evolved in labeled oxygen. Techniques to synthesize a labeled catalyst include electrodeposition in labeled electrolyte [141], heating a metal precursor in a $^{18}\text{O}_2$ atmosphere [145], and reactive sputtering with $^{18}\text{O}_2$ in the sputtering plasma [113].

These three strategies are illustrated schematically for the case of mass-selected nanoparticles in Figure 3.15, taken from Paper II. The coming Subsection motivates and describes the isotope labeling studies in that paper.

All of the experiments described in this Section are somewhat tedious to describe, especially because I have gradually been identifying mistakes in their procedures and learning to do them better. The Subsections of this Section may help in understanding many of the techniques used in literature, especially our own Paper II, but a reader who is pressed for time may wish to skip to Section 3.4, which shows what I’ve come to think is the “correct way” to do isotope-labeling experiments.

3.3.1 Determining the TOF in NiFe nanoparticles

As described in Subsection 3.1.2, our group prepared a model system of vacuum-synthesized, mass-selected $\text{Ni}_{0.75}\text{Fe}_{0.25}$ nanoparticles in order to determine the turn-over frequency (TOF) of nickel-iron based electrodes for water oxidation in alkaline media. The primary motivation for the isotope-labeling experiments in this project was actually not to probe lattice oxygen reactivity, but instead to inform our estimate of the number of active sites for the TOF calculation, as explained below. The full story is in Paper II.

The activity of nanoparticles for a given (electro)catalytic reaction is influenced by the nanoparticle size [148]. In general, the mass-normalized activity increases with smaller nanoparticle size, as the surface area to volume ratio of a particle increases with decreasing diameter. However, this is not always the case. If, for example, the reaction is most facile on a specific type of surface site (for example, if terraces are more active than edges), then there can be an optimum in nanoparticle size. This appears to be the case, for example, in CO_2 reduction to hydrocarbons on copper nanoparticles [149] and oxygen reduction on platinum nanoparticles [150]. Alternately, if the bulk of a material is active for a reaction, as has been suggested for NiFe-based OER catalysts [126, 151], then the mass-normalized activity would not vary with nanoparticle size.

As mentioned in Subsection 3.1.2, the cluster source synthesis enables us to know the exact mass and surface loading of each sample. Figure 3.16a shows the turn-over frequency at 1.53 V as a function of nanoparticle size vs RHE calculated with three different assumptions about the number of active sites: TOF_{bulk} assumes all metal atoms are active, $\text{TOF}_{\text{surface}}$ assumes metal atoms on the outer surface of the nanoparticle are active, and $\text{TOF}_{\text{redox}}$ assumes one active site per electron transferred

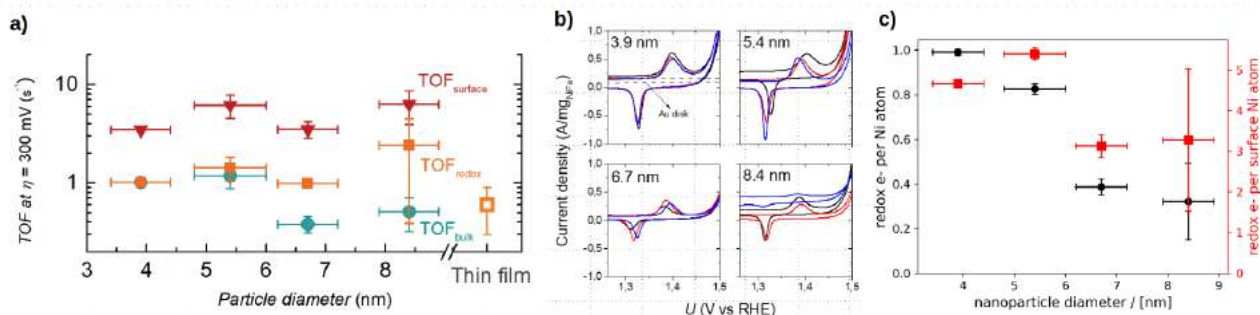


Figure 3.16: Activity and redox feature of NiFeO_xH_y nanoparticles in 1.0 M KOH. (a), Turn-over frequencies using three different assumptions about the number of active sites, as a function of particle size. (b), Cyclic voltammograms of all samples used for the TOF measurements, zoomed in on the redox feature. (c), The number of electrons transferred in this redox feature, normalized to the calculated number of surface atoms, as a function of particle size. Taken from Paper II. (a) is from the main text and (b) and (c) are from the SI.

during the $\text{Ni}^{2+}/\text{Ni}^{3+/4+}$ redox couple just before the onset of OER. This redox couple is shown for all of the samples in the CV's in Figure 3.16b.

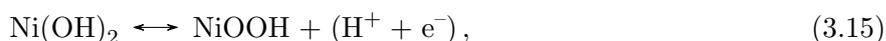
Since TOF_{bulk} (which is proportional to the mass-normalized activity) does indeed decrease with increasing nanoparticle size, we conclude that the bulk of these nanoparticles do not participate in the oxygen evolution reaction. On the other hand, the $\text{TOF}_{\text{surface}}$ and $\text{TOF}_{\text{redox}}$ do not show clear trends with nanoparticle size. This is consistent with each surface atom being an active site, or with each electron transferred during the redox wave representing an active site. For the electrodeposited NiFe LDH (also described in Subsection 3.1.2), the exact loading was unknown and so only $\text{TOF}_{\text{redox}}$ is shown. This is lower than $\text{TOF}_{\text{redox}}$ for the nanoparticles, indicating either that the number of electrons transferred in the redox feature is not the best way to measure the number of active sites, or that the activity of the active sites differ for these two differently synthesized materials.

Figure 3.16c shows the number of redox electrons per Ni atom (black, left y-axis) and per surface Ni atom (red, right y-axis). The latter is equal to the ratio between $\text{TOF}_{\text{surface}}$ and $\text{TOF}_{\text{redox}}$. For the smallest nanoparticles, the entire nanoparticle appears to be redox active, with approximately one redox electron transferred per nickel atom in the sample, whereas for the larger nanoparticles, there are fewer than 1 electron transferred per nickel atom, indicating that the particles have a redox-inactive core. There are three to five electrons transferred per surface Ni atom, indicating that the redox feature penetrates below the outer surface of the nanoparticles. The question is then whether the redox-accessible portion of the nanoparticle is also OER active. This is illustrated in Figure 3.17.

The question of whether the redox-active near-surface region contributes to OER is related to the question of which species carries the charge in and out of this region during the redox transition. If it is OH^- , then it is reasonable to believe that H_2O and O_2 can also move through the near-surface region, and that the near-surface region can contribute to the OER, which in alkaline electrolyte can be written



Unfortunately, the transport mechanism involved in the nickel redox feature is still not known [117]. It is often written by the nominal reaction



but in addition to protons, hydroxide and solvated cations have all been suggested as possible charge carriers [153].

We therefore sought to answer the question by another means. We reasoned that, if the redox-active subsurface region participated in the oxygen evolution reaction, then the H_2O and/or OH^- originally in that region would be oxidized to O_2 which we could differentiate from oxidation of the

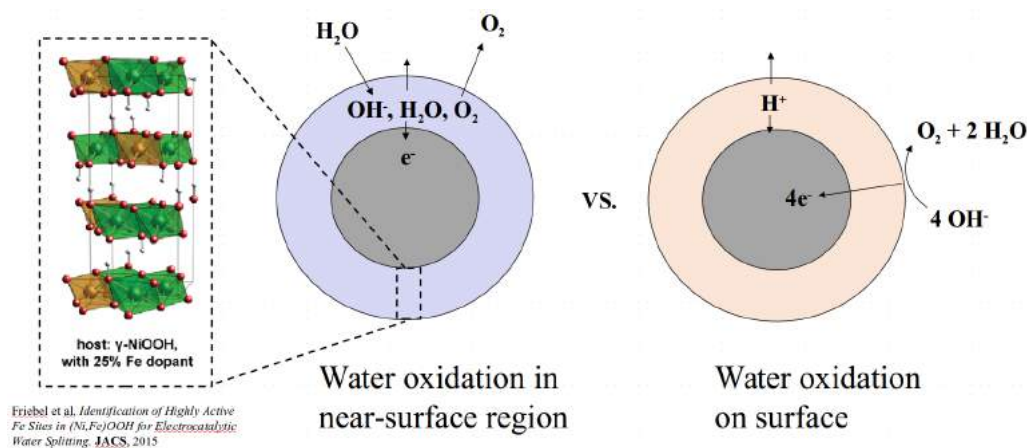


Figure 3.17: Two competing models of the nickel redox feature and oxygen evolution in NiFe nanoparticles. **Left,** The redox-active near-surface region is permeable to OH^- and O_2 , and contributes to the OER. **Right,** The redox-active near-surface region is only accessible by proton shuttling and does not contribute to OER. The diagram on the far left of a proposed layered structure for the redox-permeable NiFeOOH region is from Friebel, 2015, ref. 152.

bulk electrolyte by isotope labeling. We performed the three isotope-labeling procedures described in Figure 3.15 on mass-selected 7nm NiFe nanoparticles:

For procedure A, the as-synthesized nanoparticles were cycled between 0.5 V and 1.6 V vs RHE in un-labeled electrolyte, to form the hydrated redox-accessible near-surface region implied by Figure 3.16c. The sample was then transferred to the EC-MS setup, where the cell was filled with labeled electrolyte (0.1 M KOH in 97% H_2^{18}O), and the potential was cycled up to where oxygen was evolved (1.55 V vs RHE). The advantage to procedure A is that there is no doubt about the initial isotopic composition of the oxygen in the catalyst, as the electrode has only been exposed to natural oxygen. The disadvantage is that the ^{16}O impurity in the labeled electrolyte limits the sensitivity.

For procedure B, the as-synthesized nanoparticles were cycled between 0.5 and 1.6 V vs RHE in labeled electrolyte. A disadvantage here is that there is inevitably less than perfect control over the isotopic composition of the electrocatalyst, since it might interact with air after being taken out of the vacuum chamber and before being placed in labeled electrolyte. We actually tried to minimize this by having a pipette with labeled electrolyte ready at the load-lock, and could bring down the time in air to 15 seconds, but in 15 seconds on the order of 10^7 $^{16}\text{O}_2$ molecules will have hit each surface site and had a chance to react [51]. We expect, as a worst case, that the oxygen in the labeled catalyst consists of 50% ^{18}O , due to formation of M^{16}O , with $\text{M}=\text{Ni}_{0.75}\text{Fe}_{0.25}$, when exposed to air and subsequent formation of $\text{M}(^{16}\text{OH})(^{18}\text{OH})$ when cycled in labeled electrolyte. This is indicated in Figure 3.15.

For procedure C, the as-synthesized nanoparticles were left in the vacuum chamber, where $^{18}\text{O}_2$ was dosed and the sample was heated to 450°C . The nanoparticles were thus already oxidized when taken out into air, and presumably retained a high degree of labeled isotopic purity and the nominal M^{18}O formula. However, the sample was then put directly into the EC-MS setup with un-labeled electrolyte, where the nanoparticles likely hydrated to $\text{M}(^{18}\text{OH})(^{16}\text{OH})$ as illustrated. In hindsight, it would have been better to cycle the particles in labeled electrolyte prior to EC-MS testing to achieve a nominal $\text{M}(^{18}\text{OH})_2$ formula.

In addition to the NiFe nanoparticles, we also tested an electrodeposited NiFe oxyhydroxide film (described in subsection 3.1.2) in the same electrolyte, and an IrO_x material produced by thermal decomposition of HIrCl_6 . The latter material was produced by dropcasting a solution of 5 mM HIrCl_6 on a titanium stub and annealing in air at 500°C for two hours. This is the same material tested for lattice exchange in Fierro et al, 2007, ref. 139. In that study, the authors saw a significant amount of lattice oxygen evolution as an excess ^{16}O signal during the first cyclic voltammograms in ^{18}O -labeled electrolyte (see Table 3.1). Both the NiFe oxyhydroxide electrodeposited film and the thermal decomposition IrO_x samples were tested according to Procedure a: They were prepared with

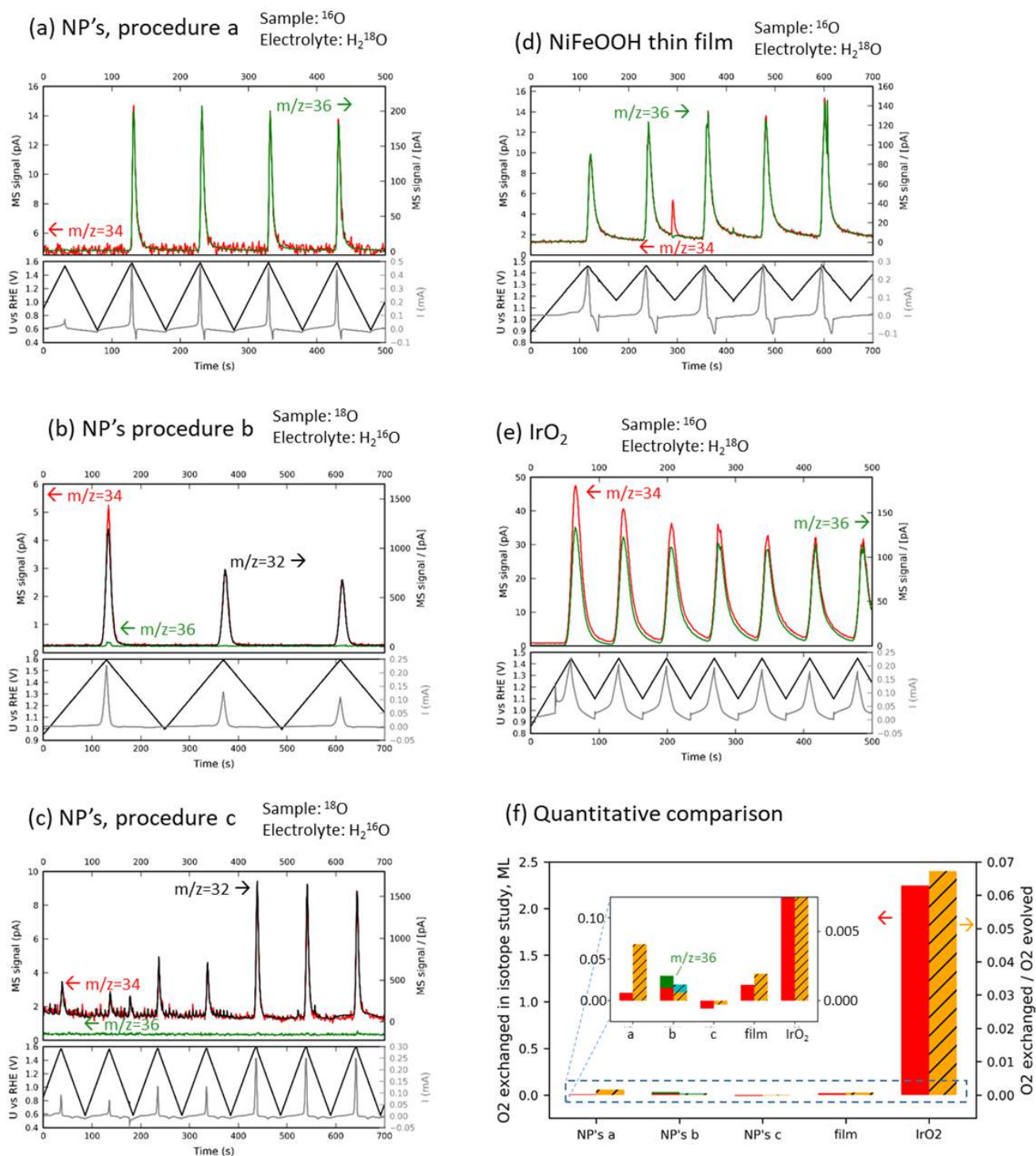


Figure 3.18: EC-MS results for isotope experiments on (a-c) NiFe NPs (a, b, and c correspond to procedures A, B, and C in Figure 3.15); and (d) an electrodeposited NiFe thin film and (e) an IrO_x thin film produced by thermal decomposition of HIrCl_6 in air, by procedure A. The signal for O_2 produced in the largest portion by oxidation of the electrolyte ($m/z=36$ for procedure A and $m/z=32$ for procedures B and C) is plotted on the right y-axis, and the other O_2 isotope(s) on the left y-axis. $m/z=32$ is omitted as a minority isotope since it is dominated by the background due to residual natural O_2 . (f) The excess minority isotope (^{16}O for procedure A and ^{18}O for procedures B and C) is quantified and normalized to (solid bars, left y-axis) the number of surface atoms in the catalyst or to (hashed bars, right y-axis) the total O_2 evolved during the part of the experiment shown here. From the SI of Paper II

the natural isotope ratio, and tested for lattice exchange in labeled electrolyte. The NiFe film was tested in 0.1 M KOH in 97% H_2^{18}O like the NiFe nanoparticles. The IrO_x was tested in 1.0 M HClO_4 in 97% H_2^{18}O . The higher concentration of HClO_4 meant that the final isotopic purity of the electrolyte was lower.

The raw EC-MS results for these five isotope-labeling experiments (NP’s procedure A-C, NiFe film and IrO_x procedure A) are shown in Figure 3.18a-e.

Here, a quick note on this plotting form: in this type of isotope labeling experiments, a “positive” result is an isotope signal originating from the electrocatalyst, namely a (transient) isotopic composition of the evolved O_2 that cannot be explained by the composition of the electrolyte. A “negative” result, on the other hand, is one in which the isotopic composition of the evolved O_2 always reflects the isotopic composition of the electrolyte. It therefore makes sense to plot the results in a way where deviations of the measured O_2 signal and the expected O_2 from oxidation of the electrolyte are clearly visible. After trying a few different plotting strategies, our group thinks that the best way to do so, without hiding any information, is to co-plot the MS signals, scaled according to the expected ratio. This can be done by multiplying one of the signals by the expected ratio, or by using two y-axes scaled according to the expected ratio. The latter technique is used in Figure 3.18a-e. In each case, the “expected ratio” was taken to be the background-corrected steady-state ratio during a constant-current OER measurement (0.5 mA/cm^2 for 10 minutes) taken right after these cycles. In this constant-current period, the total amount of O_2 evolved was much greater than the amount of oxygen in the catalyst, ensuring that the steady-state ratio reflected the isotopic concentration of the bulk electrolyte.

When plotted this way, it is immediately clear that there is a very small amount of excess ^{18}O evolved in procedure B (Figure 3.18b) in the form of $^{18}\text{O}_2$ ($m/z=36$) and $^{18}\text{O}^{16}\text{O}$ ($m/z=34$), a much larger amount of excess ^{16}O evolved from IrO_x (3.18e) in the form of $^{18}\text{O}^{16}\text{O}$, and little to no isotope signal in any of the other samples.

The astute reader may have noticed a rather important experimental mistake: each experiment starts with an anodic scan from OCP, but for the NiFe nanoparticles in both procedures A (Figure 3.18a) and C (Figure 3.18c), the first cycle does not scan anodically enough to produce a significant O_2 signal, and the sample is cycled through the Ni redox couple before a significant amount of O_2 is evolved. If oxygenated species are transferred or mobile during that redox reaction, then the labeled intercalated OH^- or O_2 might escape to the bulk electrolyte before it can be oxidized to O_2 and detected. We were aware of this mistake while preparing the manuscript, but did not get a chance to repeat these experiments, which were quite challenging for two reasons: (1) The cluster source synthesis was expensive and demanding, and (2) The membrane chips used in the EC-MS experiments at the time were not alkaline-resistant, and so chips would often breach during the measurement. So, after much frustration, we decided to use this data. We concluded, however, that it did not influence the interpretation of the results, for the following reasons: (1) We figured that at least some of the O species, such as those bound to nickel in OH groups, would stay put during the redox reaction, and (2) The results for procedures A and C were broadly consistent with the results for procedure B (Figure 3.18b) and for the electrodeposited film (Figure 3.18c), where the anodic potential of the first scan was high enough to give a significant oxygen signal.

In hindsight, this mistake is part of the simpler and more general mistake of using potential scans rather than constant-potential or (even better) constant-current experiments, since, in general, it is best to hold as much constant as possible when studying a transient phenomenon. In this case, it is best to hold the total O_2 production rate constant when studying potentially transient changes in its isotopic composition.

Figure 3.18f shows a quantitative comparison of the five isotope-exchange experiments from Figure 3.18a-e. The excess lattice oxygen (^{16}O for procedure A and ^{18}O for procedures B and C) is calibrated and normalized to either the number of surface sites (i.e., monolayers, solid bars, left y-axis) or to the total amount of O_2 evolved (right y-axis). In the case of the IrO_x catalyst, a significant portion ($\approx 6\%$) of the O_2 contained “unexpected” ^{16}O , indicating that it came from the lattice. For all of the

NiFe samples, the portion of the evolved O_2 containing O from the lattice was under 0.5%, with the apparent highest amount coming from the film and the nanoparticles tested by procedure A. Procedure A has the highest expected amount of $^{16}O^{18}O$ because the purity of the labeled electrolyte ($\leq 97\%$ $H_2^{18}O$) is less than than the purity of the un-labeled electrolyte ($\approx 99.8\%$ $H_2^{16}O$). This indicates that the the apparent portion of evolved O_2 containing lattice O when analyzed by this method is related to the noise level of the $m/z=34$ signal, i.e., that it doesn't necessarily represent real lattice O evolution, which could be zero. The amount of lattice O evolved, when normalized to the number of surface sites, is ≈ 2 monolayers for the IrO_x catalyst and $\leq 2\%$ of a monolayer for all NiFe samples.

We concluded therefore, that only the outer surface of the nanoparticles are active, implying that the turn-over frequency closest to the truth is TOF_{surface} , which for the 5.4 nm nanoparticles is $\approx 6\text{ s}^{-1}$. This is a record for OER in alkaline electrolyte, as shown in Figure 3.1 at the start of this Chapter.

Even if the experimental mistake mentioned above weakens the conclusion that the redox-active near-surface region does not participate in the OER, it does not invalidate these experiments as evidence for the other conclusion of the isotope-labeling experiments: Lattice oxygen is not exchanged during the oxygen-evolution reaction. This relies on Definition 3.1 of lattice oxygen, which excludes oxygen that would be exchanged in the Ni^{2+}/Ni^{3+} redox feature.

To illustrate the sensitivity of the experiments for lattice oxygen evolution, if it occurred, we plotted the data in another way. The majority isotope from electrolyte oxidation ($^{18}O_2$ for procedure A, $^{16}O_2$ for procedures B and C) is scaled down according to the isotopic composition of the electrolyte and plotted on the same axes as the other two O_2 isotopic signals, as the “expected” $^{16}O^{18}O$ signal. The first scan with significant oxygen evolution is shown for each sample. On the same axes, we plot the expected excess $^{16}O^{18}O$ signal if just 1% of the lattice O were to come out as O_2 . The area of this signal (in pmol) is based on the known metal loading and the nominal formula in Figure 3.15. The shape is based on the mass transport model in Paper I. This modeled signal should be compared to the *difference* between the measured and expected $^{16}O^{18}O$ signals. In all cases, it is clear from the difference of the measured and expected signals, and the noise levels, that much less than 1% of the lattice O, if any, is evolved during the first cycle.

Finally, if lattice oxygen is not exchanged during OER, that should mean that it is still present in the catalyst afterwards. To test this we did ion scattering spectroscopy (ISS, also known as low-energy ion scattering, LEIS) on the as-deposited nanoparticle samples, and again after the EC-MS experiment. The results are shown in Figure 3.19d-f. The interpretation of the ISS spectra is complicated by the fact that some residual potassium, presumably in the form of KOH, is present on the surface of the sample, even after thorough rinsing with ultrapure water (procedures B and C) or labeled water (procedure A). The oxygen in this KOH thus has the isotopic composition of the electrolyte, which is the opposite of that expected in the catalyst. This likely explains the ^{18}O signal in the ISS spectrum for procedure A (Figure 3.19d), whereas we explain the ^{16}O signal as lattice oxygen which has not exchanged during OER. This is supported by the fact that the $^{16}O/^{18}O$ ratio increases after the sample is subject to argon sputtering in the vacuum chamber. On the other hand, the potassium signal is much lower in procedues B and C, especially after sputtering, perhaps due to the greater ease of rinsing with non-labeled water. Here, the isotope ratio converges to 1:1, which matches the nominal stoichiometry motivated in Figure 3.15 and the text earlier in this subsection. Together these EC-MS and ISS results make us confident that there is little to no exchange of lattice oxygen during OER in nickel-iron based catalysts for alkaline water oxidation.

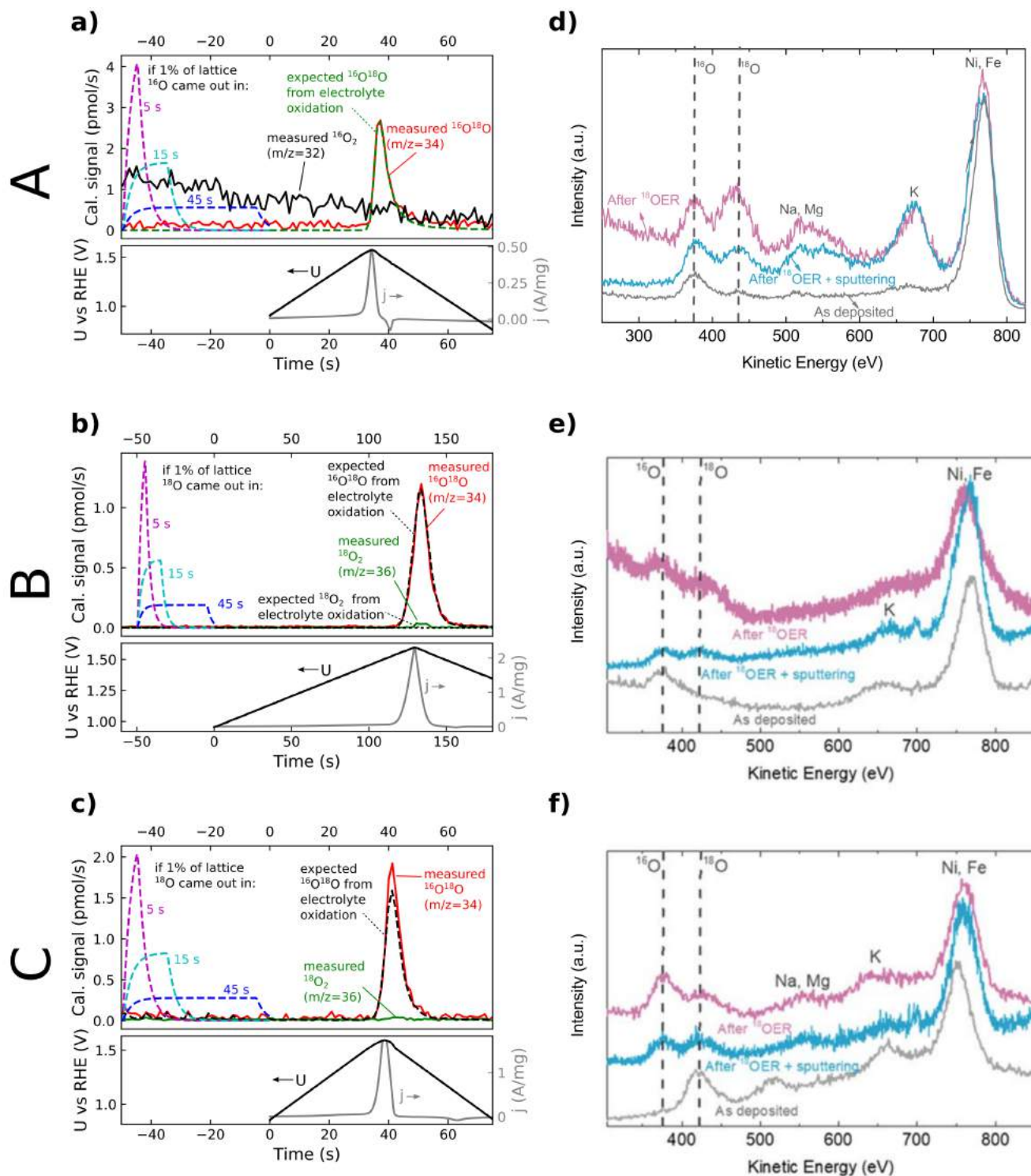


Figure 3.19: (a-c) Analysis of EC-MS results and (d-f) ISS spectra of the samples as-prepared and post-OER for procedures A (a and d), B (b and e), and C (c and f). The experimental procedures are illustrated in Figure 3.15 and the raw EC-MS data is shown in Figure 3.18. The modeled signal for 1% exchange of lattice oxygen should be compared to the *difference* between the expected and measured $^{16}\text{O}^{18}\text{O}$ signal. Procedure A is from the main text and Procedures B and C are from the SI of Paper II

3.3.2 A contradiction

The attentive reader may have noticed a contradiction:

In Section 3.2, I noted that the acid-electrolyte OER activities of all RuO₂ films and Ru foams converged when normalized to the capacitance of the films, which I pointed out is consistent with an assumption that all of the surface area accessible to the electrolyte for redox and capacitive charging is also active for the oxygen evolution reaction.

However, in Paper II, we argue that only the outer surface of the nanoparticles is active for alkaline-electrolyte OER, even though the Ni redox feature penetrates \approx 3-5 monolayers into the nanoparticles. This argument is quite central to the paper, as the conclusion that catalytic activity is confined to the outer surface of the nanoparticles is used to calculate the record TOF of 6 s⁻¹ at an overpotential of 300 mV.

We motivate the argument that OER occurs only on the outer surface, and not in the redox-active near-surface region, by isotope-labeling studies that always show O₂ with the same isotopic composition as that of the electrolyte. Our reasoning is that OER activity below the surface would either involve lattice oxygen evolution or oxidation of low-mobility intercalated water. We hypothesize that the redox activity below the surface is only due to proton shuttling.

This contradiction is especially troubling in consideration of the fact that unlabeled RuO₂ films also do not give an isotope signal during OER in isotope-labeled electrolyte. I.e., sputtered RuO₂ also gives a negative result to Strategy A in Figure 3.15). This is evident, for example, in Figure 3.13 in the previous Section, where there is no excess ¹⁶O evolution during the first cycles in ¹⁸O-labeled electrolyte (i.e., the m/z=34 to m/z=36 ratio is constant throughout the experiment). Apparently, the water in the porous structure of high-surface-area Ru and RuO₂ has no trouble diffusing out of the pores before the onset of OER, unlike our assumption for NiFe oxyhydroxide.

One motivation for these differing lines of reasoning for the two materials is that the porosity is on a different scale: whereas the nanoscale domains and cavities in hydrous RuO₂ are on the order of a few nanometers [130], the metal-metal spacing between the layers in NiFe layered double hydride is only 0.4 to 0.8 nanometers, and the layers are interconnected by hydrogen bonds, depending on the phase [117]. Thus, there is more room for water and other species to diffuse in and out of amorphous RuO₂. Another is the TEM images of the NiFe nanoparticles (Paper II, Figure 4) which indicate that they are non-porous both before and after the reaction (unfortunately, we do not have TEM images on the sputtered RuO₂ films).

Nonetheless, the uncertainty evident in this contradiction, together with the imperfections mentioned above of the isotope experiments in Paper II, mean that the conclusion of no OER activity in the redox-active near-surface region should be taken with a grain of salt. We think that these issues should motivate research into the charge transfer and mass transport processes during (near-) surface redox reactions at the oxide-electrolyte interface for oxygen evolution catalysts. A better understanding of these transport processes is essential for determining the number of sites that participate in the oxygen evolution reaction, which in turn is essential for developing catalysts with improved intrinsic activity [115].

In defense of Paper II, we do leave somewhat open our conclusion that only the outer surface is active, and we state clearly the assumptions that is based on.

3.3.3 Electrochemically labeled RuO₂ films

As mentioned at the beginning of this Chapter, oxides of iridium and ruthenium and materials based on such oxides are the only known active and somewhat stable oxygen evolution catalysts in acidic electrolyte [115, 118]. The electrocatalytic mechanism of such materials has therefore been the subject of many studies, including several using isotope-labeling [123, 138–140, 143]. Some details of these studies are compiled in Table 3.1.

In Section 3.2, I described activity measurements on well-characterized sputtered RuO₂ films in isotope-labeled electrolyte (0.1 M 97% H₂¹⁸O), effectively giving us procedure A of Figure 3.15 for

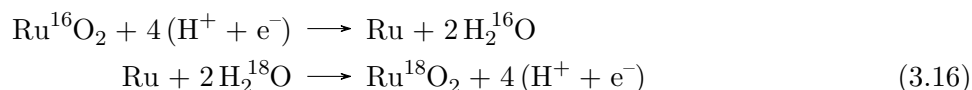
free, but did not then go into detail on the possibility of lattice oxygen evolution. In contrast, in Figure 3.18, I showed a lattice exchange study on a poorly-characterized IrO_x film formed by thermal decomposition of HIrCl_6 , reproducing the result, first reported in reference 139, of significant lattice oxygen evolution on that material. In this Subsection, I describe isotope-labeling experiments on the RuO_2 materials described in Section 3.2. Sputtered thin films (and cluster source nanoparticles) can be thought of as a model system, in contrast to the more practical but harder-to-understand real catalysts like the thermal-decomposition IrO_x (and electrodeposited NiFe). Compared to the previous literature, the work presented here adds the high sensitivity of the chip-based EC-MS system as well as surface isotopic characterization by ion scattering spectrometry (ISS).

Part of our motivation for studying OER in acid, in addition to the technological importance of PEM electrolyzers, was a practical consideration: The silicon membrane chips of the EC-MS setup are unstable in alkaline, but stable in acid. Thus, after a frustrating experience involving many experiments being compromised due to chips breaching in the work leading to Paper II, we wanted to work on something (relatively) easy.

The isotope-labeling experimental techniques that we used at first on the RuO_2 films were therefore directly taken from those described in the paper above: cyclic voltammetry of un-labeled or electrochemically labeled films, where a "positive" result is a changing isotope ratio during from cycle to cycle. Figure 3.20 shows the results of such experiments on room-temperature sputtered RuO_2 films. The sample was first tested according to Procedure A of Figure 3.15, i.e., the isotopic ratio was observed during OER from an un-labeled sample in labeled electrolyte. The result, in Figure 3.20a is that there is no excess ^{16}O in the evolved O_2 . The sample was then tested according to Procedure B, i.e. labeled electrochemically and then tested in un-labeled electrolyte. Procedure B can be more sensitive than Procedure A due to the high isotopic purity (99.8% ^{16}O) of natural oxygen.

Some authors have used steady-state OER as a labeling technique [123, 143]. This, however, only succeeds in labeling the catalyst if there is a significant amount of lattice exchange, incorporating the oxygen from the electrolyte into the catalyst. Therefore, we used ion scattering spectrometry (ISS) as a direct determination of isotope labeling. The black trace in Figure 3.20d is an ISS spectrum of an Ru^{16}O_2 film after OER in ^{18}O -labeled electrolyte (specifically, after the activity test in Figure 3.7b of the previous Section). There is a clear ^{16}O peak, centered at 375 eV, but no sign of ^{18}O , indicating that OER does not incorporate oxygen from the electrolyte into the lattice of RuO_2 . This is consistent with the lack of lattice oxygen evolution that has been reported before for crystalline RuO_2 [143], but the (absence of) labeling had not been directly probed.

Since OER itself did not incorporate the oxygen from the electrolyte into the sample, to produce a labeled sample, we instead tried reducing and oxidizing the sample in labeled electrolyte. This procedure is shown in Figure 3.20b. The sample is cycled between -0.05 V vs RHE, where hydrogen evolution takes place, and +1.4 V vs RHE, where oxygen evolution takes place. This is intended to incorporate the new isotope in the lattice according to the following nominal reactions near the surface of the electrode:



The sample was finally held at 1.4 V vs RHE for 5 minutes to ensure that the surface was oxidized when the sample was removed from electrolyte.

The blue trace in Figure 3.20d shows an ISS spectrum of a sample thus labeled. Both oxygen isotopes are clearly present. To ensure that these are not just loosely bound surface species such as adsorbed H_2O from the electrolyte and/or air, the sample was sputtered in He before taking another spectrum, shown in the green trace. The increase in the Ru signal at ≈ 850 eV indicates that some surface species are indeed removed, while both oxygen isotopes remain. The presence of ^{18}O indicates that the surface of the sample was successfully labeled. However, there is still a significant amount of ^{16}O , indicating that Reactions 3.16 are not carried out completely. In other words, the surface is not completely reduced during the labeling procedure. The approximately 1:1 ratio may indicate that 2

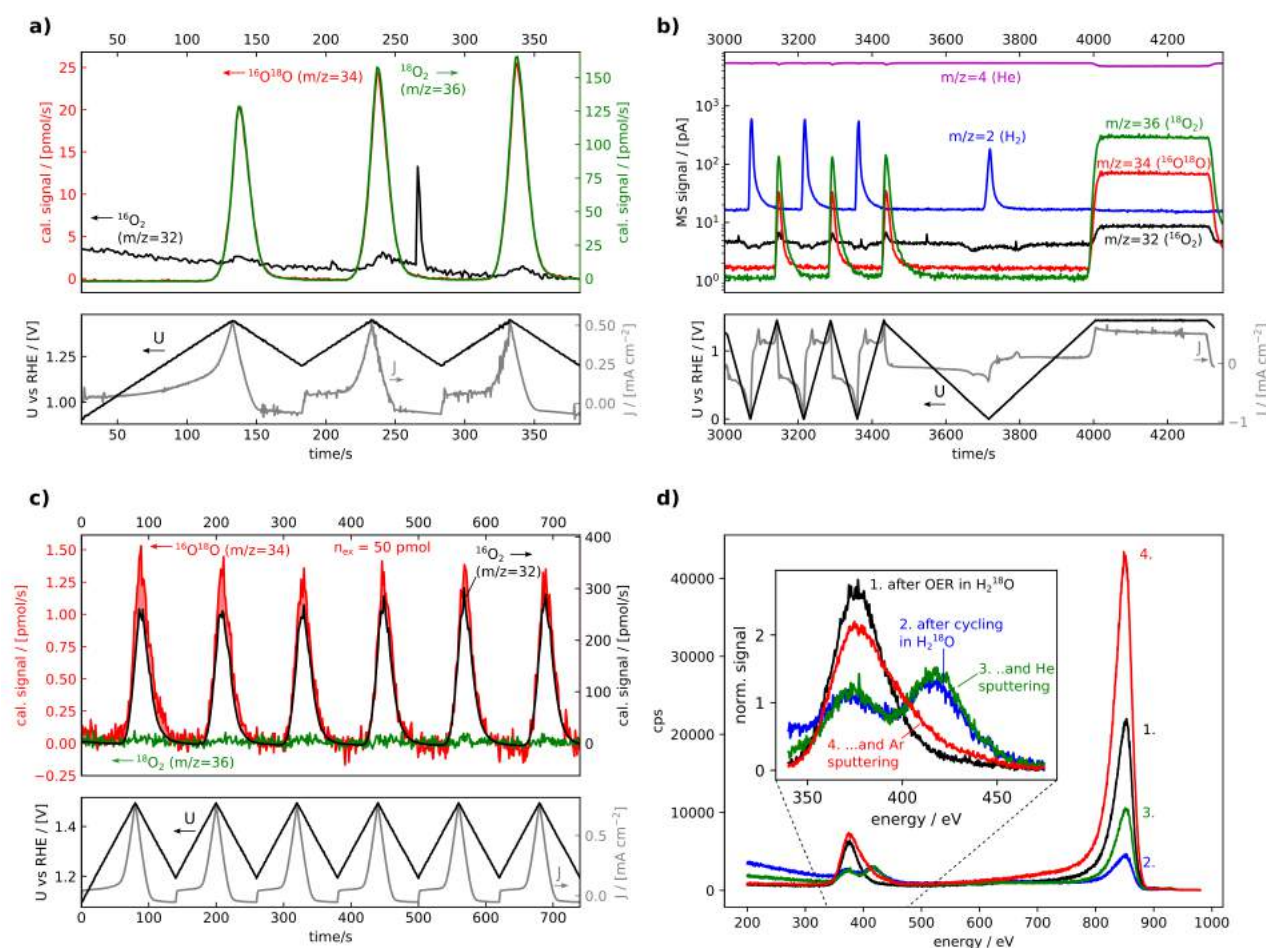


Figure 3.20: Lattice oxygen evolution experiments on RuO_2 film sputtered at room temperature with natural O_2 . (a), The first cyclic voltammograms of a fresh, un-labeled sample (Ru^{16}O_2) in labeled electrolyte (0.1 M HClO_4 in 97% H_2^{18}O). The left ($^{16}\text{O}^{18}\text{O}$ and $^{16}\text{O}_2$) and right ($^{18}\text{O}_2$) y-axes are scaled according to the $^{16}\text{O}^{18}\text{O}$ to $^{18}\text{O}_2$ measured during steady-state OER later in the experiment. (b), Electrochemical labeling procedure to incorporate ^{18}O from the labeled electrolyte into an un-labeled sample. (c), The first cyclic voltammograms of an electrochemically labeled sample in unlabeled electrolyte (0.1 M HClO_4 in 99.8% H_2^{16}O). The left ($^{16}\text{O}^{18}\text{O}$ and $^{18}\text{O}_2$) and right ($^{16}\text{O}_2$) y-axes are scaled according to the natural $^{16}\text{O}^{18}\text{O}$ to H_2^{16}O ratio of 0.40%. The area between the $^{16}\text{O}^{18}\text{O}$ and $^{16}\text{O}_2$ signals thus plotted, which is approximately 50 pmol in total on the scale of the left y-axis, is highlighted. (d), Ion scattering spectra of: (black) a sample that has evolved oxygen in labeled electrolyte (potential holds and cycling between 1.2 and 1.5 V vs RHE) but not brought to reducing potentials; and a sample that has been electrochemically labeled directly after loading in the vacuum chamber (blue), after 30 minutes of He sputtering (green), and after 30 minutes of Ar sputtering (red).

electrons are transferred rather than 4 in the (near-)surface redox processes taking place between -0.05 and 1.4 V vs RHE. Using the (110) surface to approximate the surface sites of this polycrystalline sample, the observation of 1:1 $^{18}\text{O}:^{16}\text{O}$ in ISS could perhaps indicate exchange of Bridge-bound O but not the trigonally coordinated surface O. This is consistent with the surface species as a function of potential proposed by Rao et al, 2017, ref. 132. In that study, using the "crystal truncation rods" of single-crystal x-ray diffraction, the authors show that bridge sites are fully protonated at 0.5 V vs RHE, indicating that they may exchange spontaneously with water. Any CUS-adsorbed oxygen would exchange with electrolyte, but would likely be too loosely bound for ISS observation, as it would desorb when the sample is pumped down in the vacuum chamber [154]. However, it should also be noted that we are by no means certain of this interpretation - it could be that both CUS and Bridge oxygen atoms are both sputtered away by He at the start of the scan, and that ISS is probing oxygen below the adsorbate layer.

To test whether the procedure in Figure 3.20 also labeled the bulk of the sample, we then sputtered the sample with argon for 30 minutes. A separate calibration experiment was done in which a 5 nm RuO_2 film on Ti was sputtered through until the substrate was visible in ISS, taking a total of about 2.5 hours of Ar sputtering with all other parameters held the same. This indicates that 30 minutes of Ar sputtering removes approximately 1 nm of material. The subsequent ISS spectrum, the red trace in Figure 3.20 has a much smaller ^{18}O to ^{16}O ratio, indicating that there is little to no labeling of the bulk of the material. (We don't believe the Ar sputtering to be completely uniform, so the small amount of remaining ^{18}O signal probably still comes from the surface and doesn't reflect the isotopic composition exactly 1 nm into the bulk). This sputtering, of course, was destructive to the isotope labeling of the sample, so another sample was labeled by the same procedure for an EC-MS test of lattice oxygen evolution.

Figure 3.20c shows the oxygen evolved in unlabeled electrolyte (0.1 M HClO_4 in natural H_2O) during cyclic voltammetry of a film thus labeled. The axes are scaled according to the natural ratio such that the $^{16}\text{O}^{18}\text{O}$ signal (red trace, left y-axis) and $^{16}\text{O}_2$ signal (black trace, right y-axis) would coincide exactly if all of the oxygen atoms in the evolved O_2 came from the electrolyte. Compared to this baseline, there is clearly some excess $^{16}\text{O}^{18}\text{O}$ in the first cycles, with the isotopic ratio converging to the expected natural ratio after about six cycles. Integrating the excess $^{16}\text{O}^{18}\text{O}$ signal (i.e., the highlighted area in Figure 3.20c) gives a total of 50 pmol of O that must have originated in the lattice. Since the lattice was only 50% labeled, this would imply that 100 pmol of lattice O was evolved. Considering the high surface area of the room-temperature-sputtered films (Figure 3.6), this is only approximately 0.7% of a monolayer. It is also only $\approx 0.1\%$ of the total O_2 evolved during the first six cycles.

Our ability to measure lattice oxygen evolution on RuO_2 , in contrast to ref. [143], is due to the labeling procedure and increased sensitivity of the chip-based EC-MS technique, and is not inconsistent with their results. Our ability to quantify the evolved lattice oxygen and compare it both to the number of surface sites and to the total oxygen evolved, enable us to determine that it is negligible with respect to the OER activity. Indeed, the conclusion of the quantitative isotope-labeling studies is that the catalytically relevant OER mechanism on sputter-deposited RuO_2 *does not* involve lattice oxygen evolution.

As mentioned earlier in this Section, cyclic voltammetry has the disadvantage that too many things are changing at once: a potentially transient isotopic signal gets convoluted in the changing state of the catalytic surface with potential. The appeal of using scans is that, in principle, a number of potentials are quickly sampled [140], and that the isotopic ratio can easily be compared from one scan to another [139]. However, partial reduction and re-oxidation of the (near-) surface might create unstable sites that would not be present under steady OER operation. It might also reduce out the lattice O as water.

Therefore, I also monitored the O_2 evolved during constant-current measurements on electrochemically labeled RuO_2 films. The films were prepared and labeled as described above (R.T. sputtered, cycled between -0.05 and +1.4 V vs RHE in labeled electrolyte). OER was then measured at 100 μA (a geometric current density of 0.5 mA/cm^2) for 5 minutes. The results, done in triplicate, are shown in Figure 3.21a-c) and discussed below. For comparison, a Ru foam sample (Subsection 3.2.2) and polycrystalline Pt stub were also electrochemically labeled and tested in the same way, with the results shown respectively in Figure 3.21d and e.

As mentioned in Chapter 2, isotope effects can sometimes be observed in mass spectrometry signals as a result of "memory effects" from the vacuum chamber. This problem, unfortunately, had not yet been recognized for any of the earlier experiments described above in this Chapter, but fortunately did not seem to influence the results. To "clear the memory" of the vacuum chamber, it was baked at 100°C overnight while H_2O -saturated He was leaked through the chip capillary. To make sure the vacuum chamber was un-labeled, I then started the exchange measurements with a control sample - a fresh, unlabeled RuO_2 sample, which was tested and analyzed in exactly the same way as the labeled samples. The result for the control is shown in Figure 3.21f. When the $^{16}\text{O}^{18}\text{O}$ signal is integrated and

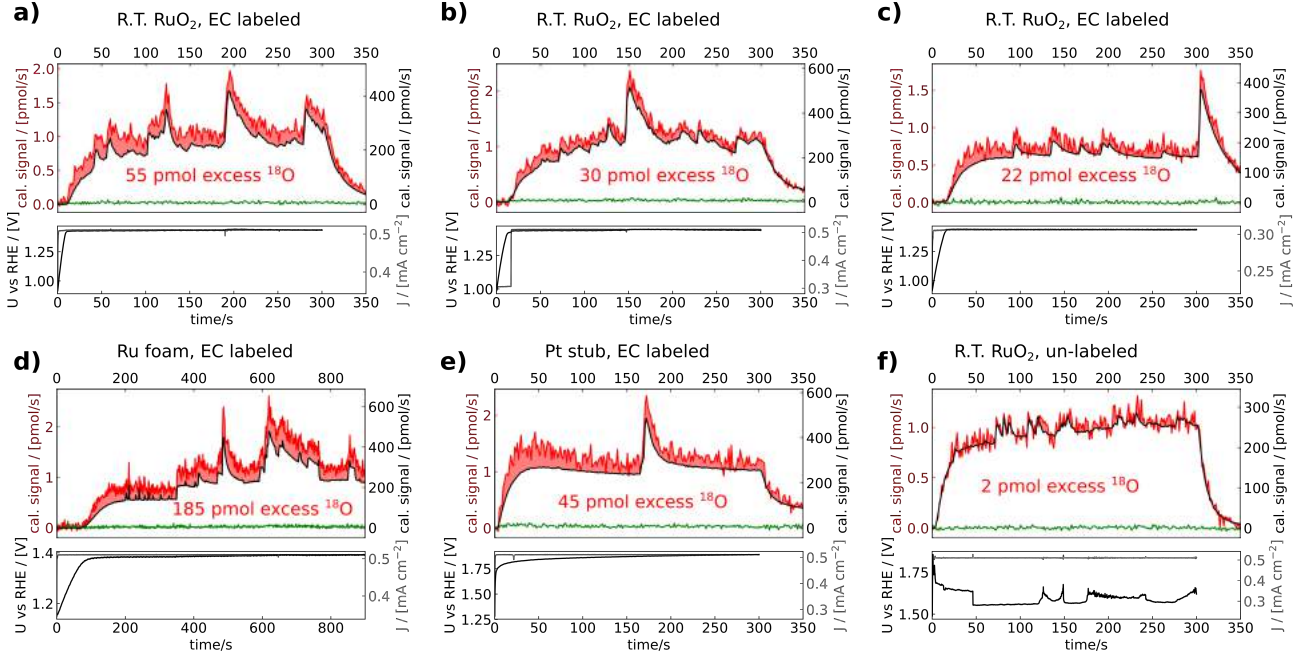


Figure 3.21: Constant-current water oxidation in unlabeled electrolyte on: (a-c) RT-sputtered RuO_2 , (d) Ru foam, and (e) polycrystalline Pt, all labeled by cycling between HER and OER potentials (-0.05 and +1.4 V vs RHE for RuO_2) followed by 10 minutes of +0.5 mA/cm^2 geometric current density in labeled electrolyte (0.1 M HClO_4 in 97% H_2^{18}O); and (f) unlabeled RT-sputtered RuO_2 . The noise in the mass spectrometric signal (a-e) is attributed to bubbles, and the noise in the potential measurement in f is attributed to poor contact to the alligator clip. In each case, the calibrated $^{16}\text{O}^{18}\text{O}$ signal (red) and $^{18}\text{O}_2$ signal (green) are co-plotted with the $^{16}\text{O}_2$ signal, with the latter being on the right y-axis which is scaled according to the natural $^{16}\text{O}^{18}\text{O}/^{16}\text{O}_2$ ratio of 0.40%. The integrated amount of excess $^{16}\text{O}^{18}\text{O}$ is indicated.

compared to that expected from the $^{16}\text{O}_2$ signal and the natural $^{16}\text{O}^{18}\text{O}/^{16}\text{O}_2$ ratio, the two coincide perfectly. The integrated difference, 2 pmol, should be considered a lower bound to the uncertainty of the measurement.

Unfortunately, the experiments in Figure 3.21 serve in part to show what a bad day looks like at the EC-MS setup. Even though the OER current is constant for all measurements, the O_2 signal varies wildly and sporadically for almost all of the measurements. This can be attributed to bubble formation during OER. The OER current required to generate a saturation concentration at the electrode is (by the model presented in Paper I)

$$j_{\text{lim}} = z\mathcal{F} \frac{p^\circ}{K_H^{\text{O}_2}} \left(\frac{L}{D^{\text{O}_2}} + \frac{1}{h} \right)^{-1} \quad (3.17)$$

$$= 4 \cdot 96486 \left[\frac{\text{C}}{\text{mol}} \right] \cdot \frac{1[\text{bar}]}{0.77 \left[\frac{\text{bar} \cdot \text{m}^3}{\text{mol}} \right]} \left(\frac{100[\mu\text{m}]}{2.1 \cdot 10^{-9} \left[\frac{\text{m}^2}{\text{s}} \right]} + \frac{1}{1.0 \cdot 10^{-4} \left[\frac{\text{m}}{\text{s}} \right]} \right)^{-1} \quad (3.18)$$

$$= 0.87 \left[\frac{\text{mA}}{\text{cm}^2} \right], \quad (3.19)$$

where p° is the ambient pressure, $K_H^{\text{O}_2}$ is the Henry's-law constant for O_2 , L is the working distance between the electrode and the chip, D^{O_2} is the diffusion constant of O_2 in water, and h is the mass-transfer coefficient of O_2 from the electrolyte where it contacts the chip into the vacuum chamber of the mass spectrometer (Paper I). The operating current of 0.5 mA/cm^2 is lower than this limiting current. However, if the electrode is not well-aligned (increasing L), or if a foamy electrode material slows the diffusion of O_2 (lower effective D), or if there are air bubbles in the edge volume just beyond the membrane of the chip that the electrochemically formed O_2 can interact with, or if there are bubble

nucleation sites (such as a chipped substrate), these factors can all contribute to bubble formation and noise of the type seen here in Figure 3.21

Nonetheless, lattice oxygen evolution is clear from all of the labeled electrodes. The lattice oxygen evolution from the labeled RuO₂ electrodes varies from 0.04% to 0.08% of the total oxygen evolved during the 10 minutes. This is slightly less than the 0.1% of total oxygen evolved in the initial result in Figure 3.20c. This may indicate that cyclic voltammetry is a better way to destabilize the lattice oxygen and get it out as O₂ than is constant-current OER. Indeed, the highest rate of lattice oxygen evolution is at the start of each experiment (this is especially clear for the third film, Figure 3.21c), which is while the potential is changing. For all three labeled RuO₂ films, the lattice oxygen evolved is a very small portion (0.4% to 0.7%) of a monolayer, implying that there is plenty of labeled oxygen left afterwards (unfortunately, we didn't get a chance to do ISS on these samples).

The Ru foam (Figure 3.21d) and polycrystalline platinum electrode (Figure 3.21e) also show some lattice oxygen evolution, especially at the beginning of the constant-current period. For the ruthenium foam, the excess ¹⁸O is vanishingly small compared to the number of surface sites:

$$\frac{n_{\text{ex}}^{18\text{O}}}{n_{\text{surf}}} \approx \frac{185 \text{ [pmol]}}{300 \text{ [nmol]}} \approx 0.5 \cdot 10^{-3} \quad (3.20)$$

I.e., approximately 0.05% of a monolayer of lattice ¹⁸O is evolved. On the other hand, for the platinum electrode (roughness factor <2) it is a significant portion of a monolayer ($\approx 15\%$). The observation of lattice oxygen evolution on platinum is interesting, since it was not observed before in DEMS, in the first isotope-labeling experiment in OER that we are aware of [137]. Again, the observation requires the quantitative detection of sub-monolayer amounts of gaseous products over multiple minutes, and so the difference may just be a difference in the sensitivity of the experimental setup.

All of the isotope-labeling experiments shown so far should be taken as a process of “learning by doing.” The use of constant-current steps, ISS to check the surface composition, and control experiments to build trust in comparisons with the natural isotope ratio, are all obvious in hindsight but took time to figure out. In Section 3.4, these techniques are put together with two other important improvements: (1) Periodic electrolyte sampling for ICP-MS to compare the number of oxygen atoms evolved to the number of metal atoms dissolved, and (2) the direct deposition of purely isotope-labeled films by reactive sputtering with ¹⁸O₂ (as had already been done in ref. 113).

First, in the next Subsection, I describe another way to “extract” the lattice oxygen and prove its presence in case it doesn't come out in OER.

3.3.4 Using CO to get out the lattice oxygen

After many “negative” initial results in lattice oxygen evolution experiments (mostly by the less-sensitive procedure A), and ISS not always being available or easy to probe the surface isotopic composition, I wanted a way to check that the desired oxygen isotope had indeed been incorporated into the electrode as lattice oxygen (i.e., did not exchange away spontaneously), ideally without taking the electrode out of the EC-MS setup.

One clever method of doing so is presented in ref. 137: They oxidize water in un-labeled electrolyte on a Pt film sputtered on a DEMS membrane and oxidized in labeled electrolyte, without observing an isotope signal. Then, to prove the ¹⁸O had indeed been incorporated in the film, they quickly reduce the film, expelling it as H₂¹⁸O, and then jump back to OER potentials. They see a transient m/z=34 signal, which they attribute to oxidation of this liberated H₂¹⁸O. However, they only show the m/z=34 signal and not the m/z=32 signal and they do not show a control experiment. I tried the same experiment without seeing an isotope signal, but this is likely due to the geometry of the setup: whereas in DEMS, constant solvent evaporation leads to a non-negligible convective flow of H₂O towards the membrane, and thus towards the catalyst when it is sputtered on the DEMS membrane, in our EC-MS setup the electrode surface is separated from the membrane by 100 μm of still electrolyte, and so the expelled H₂¹⁸O is lost to diffusion in the working volume faster than the electrode potential can be jumped back up to oxidize it. So I had to think of another way.

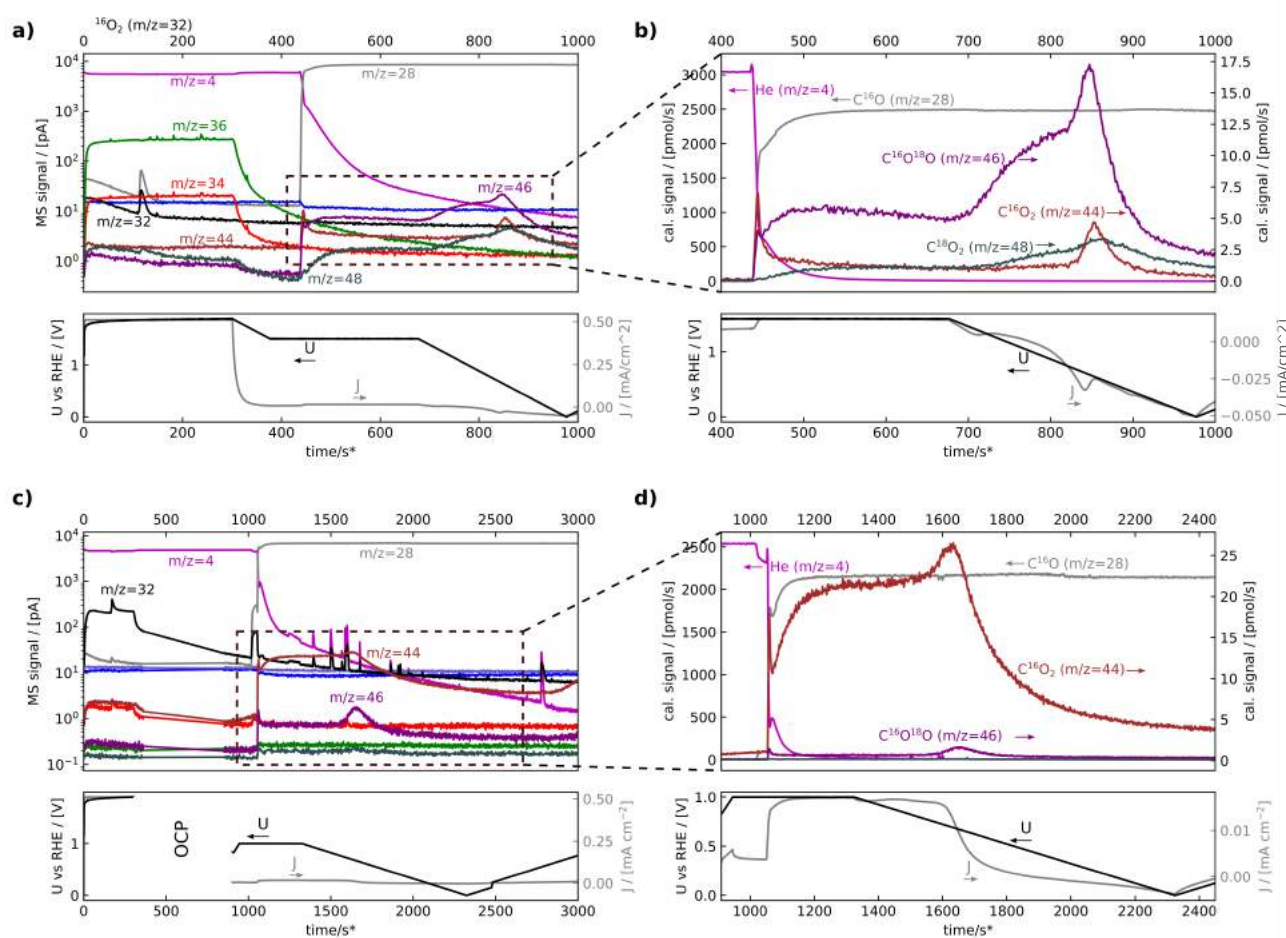


Figure 3.23: Sequential exchange (OER) and extraction (CO oxidation) experiments on Pt. (a) and (b), Procedure A of Figure 3.22: Pt with a Pt¹⁶O layer in labeled electrolyte (0.1 M HClO₄ in 97% H₂¹⁸O). (a) shows all raw mass signals on a log scale, while (b) shows the calibrated signals for CO₂ on a linear scale during the extraction experiment. The CO₂ signals are on the right y-axis and carrier gas signals are plotted on the left y-axis to show when the switch from He to CO occurs. (c) and (d), Procedure B of Figure 3.22.

Figure 3.23b shows a zoom-in on the CO₂ isotopic signals during the introduction of CO and the reduction of the surface. The CO₂ signals are plotted on the right y-axis, and the carrier gas signals (He and CO) are plotted on the left y-axis to show exactly when CO is dosed. The transient C¹⁶O₂ and C¹⁶O¹⁸O signals at the moment that CO is introduced originate within the mass spectrometer (see Subsection 2.3.3). The “isotope signal” is the C¹⁶O₂ transient that starts at ≈850 s, right as the reductive wave in the electrode current, as expected for the extraction of a buried labeled oxide layer.

The same procedure as described above can also be carried out with the isotopes reversed, as shown in Procedure B of Figure 3.22. The result of this experiment is shown in Figures 3.23c and d. There are a couple small differences in the procedure: (1) the measurement was stopped and the sample was at OCP for a while between the OER period (exchange experiment) and the CO oxidation period (extraction experiment), (2) the resting potential was 1.0 V vs RHE, leading to a higher steady-state CO oxidation current than at 1.4 V vs RHE, and (3) the potential was scanned at 1 mV/s rather than 5 mV/s. Nonetheless, the results are the same: a transient isotope signal (here for C¹⁶O¹⁸O comes together with the transient increase in overall CO oxidation activity as the oxide layer is reduced. A control experiment was also done (Pt¹⁶O in H₂¹⁶O) which showed no change in the m/z=46 to m/z=44 ratio.

Figure 3.24 shows a quantitative analysis of the experiments described above. Here, two axes are used, scaled according to the expected isotopic ratio. For the experiment with Pt¹⁶O in H₂¹⁸O

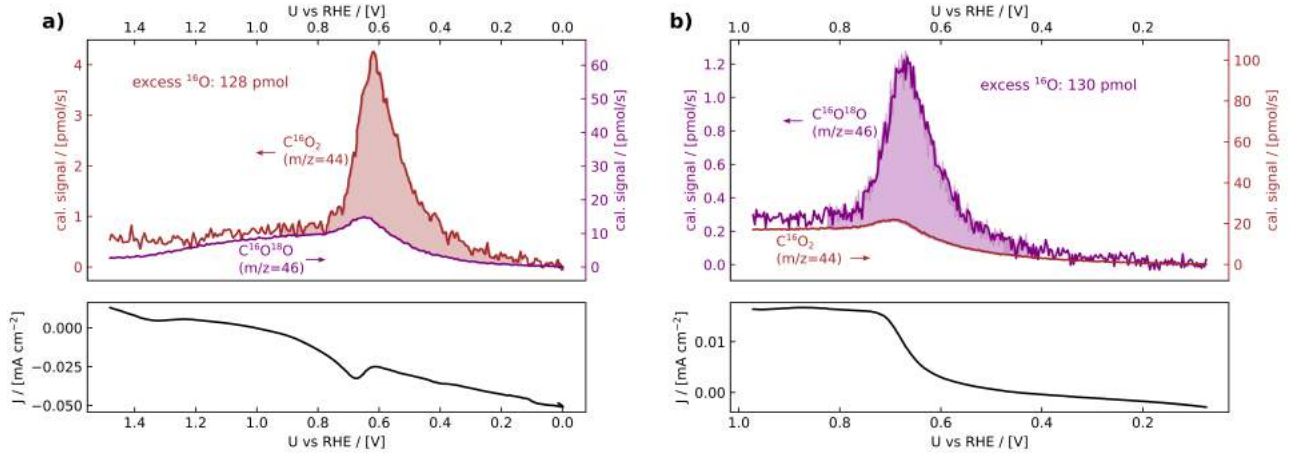


Figure 3.24: Analysis of experiments using CO oxidation to extract lattice oxygen from a labeled PtO layer. In both cases data are plotted against potential. The CO₂ with the labeled oxygen is plotted against the left y-axis and the CO₂ without the label is plotted against the right y-axis. The axes are scaled according to the expected ratio without labeled oxygen from the lattice. (a) Pt with a Pt¹⁶O layer in labeled electrolyte (0.1 M HClO₄ in 97% H₂¹⁸O). (b) Pt with a Pt¹⁸O layer in un-labeled electrolyte (0.1 M HClO₄ in 99.8% H₂¹⁶O).

(Figure 3.23a and b, Figure 3.24a) this is calculated from the ¹⁶O¹⁸O to ¹⁸O₂ ratio during the OER measurement. This ratio, by the binomial distribution, is

$$r = \frac{\dot{n}_{^{16}\text{O}^{18}\text{O}}}{\dot{n}_{^{18}\text{O}_2}} = \frac{2(x)(1-x)}{(1-x)^2} = \frac{2x}{1-x}, \quad (3.21)$$

where x is the electrolyte impurity, i.e.

$$x = \frac{c_{\text{H}_2^{16}\text{O}}}{c_{\text{H}_2^{16}\text{O}} + c_{\text{H}_2^{18}\text{O}}}. \quad (3.22)$$

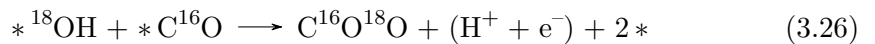
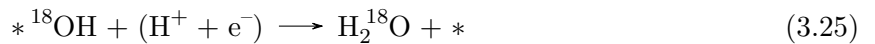
Since the CO₂ (initially) has one oxygen which is ¹⁶O 99.8% of the time, and only one oxygen from the electrolyte, the expected ratio of C¹⁶O₂ to C¹⁶O¹⁸O is x . Solving Equation 3.21 for x in terms of r , which is measured, gives

$$x = \frac{r}{2+r}. \quad (3.23)$$

For the experiment with Pt¹⁸O in H₂¹⁶O (Figure 3.23c and d, Figure 3.24a), the expected CO₂ is natural CO₂, and so the ratio is simply determined by measuring the m/z=46 to m/z=44 ratio in natural CO₂.

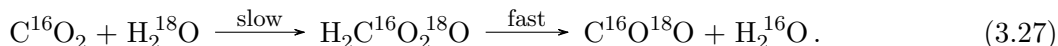
In each case the integrated difference between the two curves, thus scaled, is the evolution of labeled lattice oxygen in CO₂. In both cases, it is about 130 pmol, on the order of 25% of a monolayer's worth of oxygen (0.196 cm² of Pt(111) is 490 pmol of surface sites).

This excellent agreement may, however, be fortuitous. I would expect that the labeling procedure (10 minutes at 100 μA) would incorporate more than a monolayer's worth of labeled oxygen, and so the small amount of labeled oxygen incorporated into the CO₂ implies a branching, in which some of the reducing oxide reacts with CO and some reduces fully, releasing the oxygen as H₂O. To write it out, for lattice ¹⁸O:



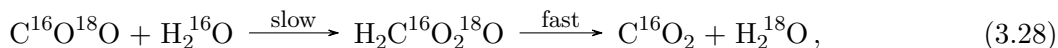
It is hard to believe that the branching ratios would be exactly the same despite the various differences in the two experimental implementations mentioned above, notably the scan rate.

Furthermore, 130 pmol is an underestimation, because some of the labeled CO_2 will exchange the labeled oxygen with the electrolyte by the homogeneous reaction going through carbonic acid before it evaporates into the chip, as described in Subsection 2.3.2. This will have a different effect in the two experiments. When the labeled CO_2 is C^{16}O_2 in H_2^{18}O -containing electrolyte, the homogeneous exchange reaction is:



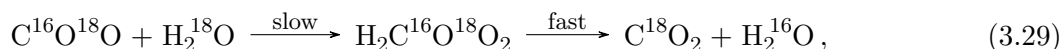
In the second step of this reaction, there is a 2/3 chance that the oxygen expelled from carbonic acid is a ^{16}O , causing the CO_2 to lose its label. (Here, we're making the simplifying omissions of the chance of a CO_2 molecule *picking up* a label from the electrolyte due to the H_2^{16}O impurity.) In other words, a labeled CO_2 molecule will have to make 1.5 *attempts*, i.e. become carbonic acid 1.5 times on average, before it loses its label.

On the other hand, when the labeled CO_2 is $^{16}\text{O}^{18}\text{O}$ in H_2^{16}O , the homogeneous exchange reaction is



and there is only a 1/3 chance that the CO_2 loses its label. A labeled CO_2 molecule takes 3 attempts on average to lose its label.

The absolute portion of CO_2 that loses its label to homogeneous scrambling can be estimated by the amount of C^{18}O_2 in Figure 3.23b. Here, about 1/5 of the CO_2 comes out as C^{18}O_2 . The majority of this CO_2 started as $\text{C}^{16}\text{O}^{18}\text{O}$ and lost the ^{16}O originally from the CO:



This takes 3 attempts on average, and so the portion of C^{16}O_2 that with a ^{16}O from the lattice which loses its label should be about double the steady-state C^{18}O_2 fraction, or about 2/5. Adjusting for this, the total lattice ^{16}O extracted in the experiment in Figure 3.23b is closer to

$$n_{\text{corrected}}^{\text{C}^{16}\text{O}_2} = n_{\text{measured}}^{\text{C}^{16}\text{O}_2} \cdot P(\text{keep label})^{-1} \approx 128[\text{pmol}] \cdot \left(\frac{3}{5}\right)^{-1} \approx 215[\text{pmol}], \quad (3.30)$$

which is about 45% of a monolayer assuming the surface atom density of Pt(111).

Similarly, since it takes 3 attempts for a CO_2 molecule to lose its label in the second experiment, about 1/5 of the labeled CO_2 loses its label to the electrolyte, and the corrected amount of extracted lattice ^{18}O is

$$n_{\text{corrected}}^{\text{C}^{18}\text{O}^{16}\text{O}} = n_{\text{measured}}^{\text{C}^{18}\text{O}^{16}\text{O}} \cdot P(\text{keep label})^{-1} \approx 130[\text{pmol}] \cdot \left(\frac{4}{5}\right)^{-1} \approx 160[\text{pmol}], \quad (3.31)$$

or about 33% of a monolayer assuming the surface atom density of Pt(111).

Despite being quite complex, I think that the results above illustrate that using CO as a probe molecule in isotope exchange experiments can be very useful, both as an in-situ proof of labeling when OER does not give an isotope signal, and to investigate the electrochemical reactivity of surface oxygen. I think it would be worth doing systematic experiments of this type, mapping out the effect of the oxide layer thickness, CO dosing potential, and other factors on the isotope signal. This will have to be future work, but I have had time to try similar experiments on a few other materials, including the Ru foam material described in Subsection 3.2.2.

Figure 3.25a shows the result of sequential lattice oxidation exchange (OER) and extraction (CO oxidation) experiments on Ru foam in un-labeled electrolyte (0.1 M HClO_4 in 99.8% H_2^{16}O). Prior to this experiment, the foam was labeled by oxidation at 100 μA for 10 minutes in labeled electrolyte (0.1 M HClO_4 in 97% H_2^{18}O). The exchange experiment was done at constant potential (1.38 V vs RHE)

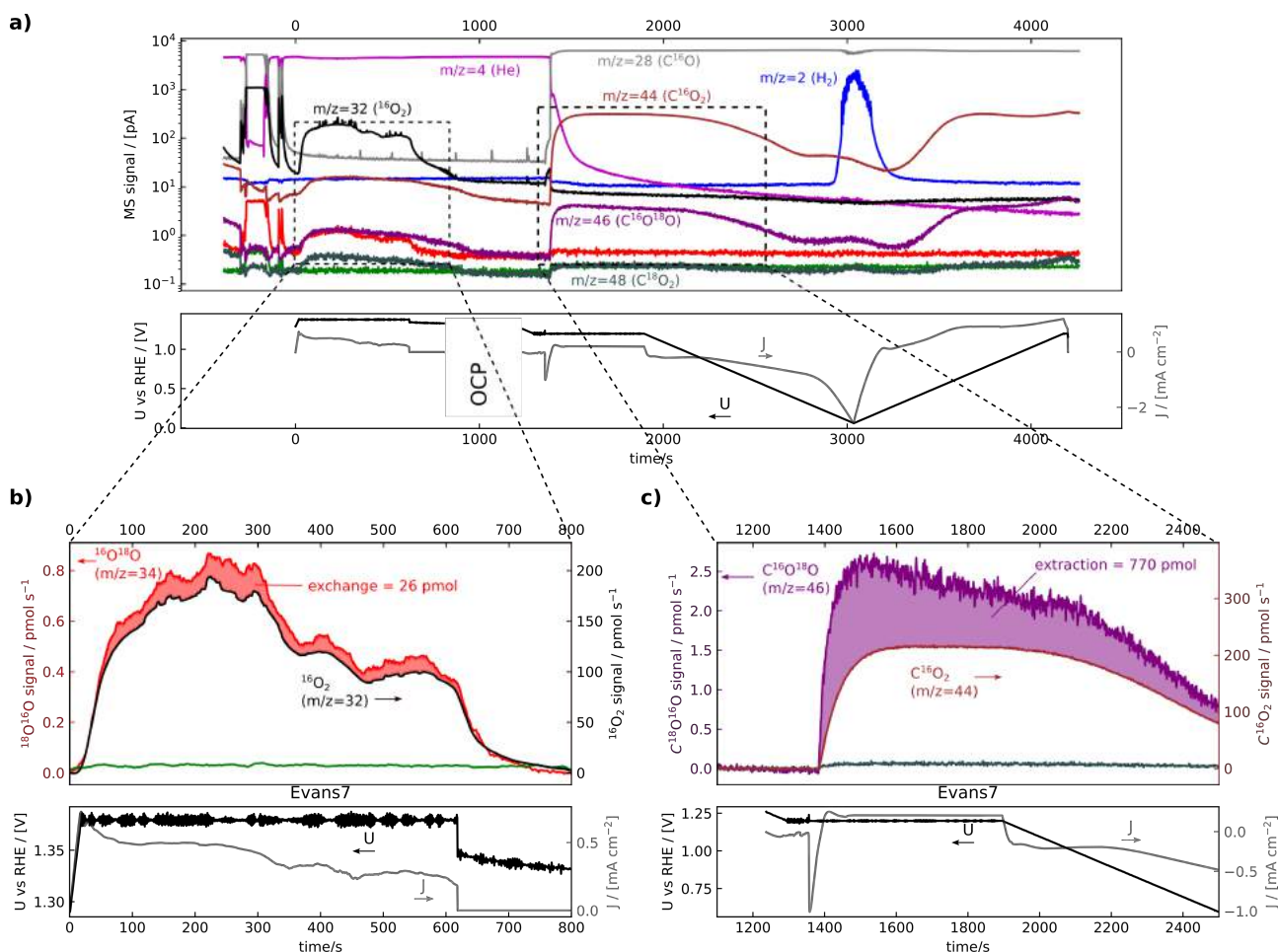


Figure 3.25: Sequential exchange (OER) and extraction (CO oxidation) experiments probing lattice oxygen reactivity in labeled Ru foam in un-labeled 0.1 M $HClO_4$. (a), overview showing raw data for both experiments. (b), Exchange experiment showing excess ^{18}O compared to natural $^{16}O^{18}O$ to $^{16}O_2$ ratio. (c), Extraction experiment showing excess ^{18}O compared to natural $C^{16}O^{18}O$ to $C^{16}O_2$ ratio.

rather than constant current. This was a mistake, as it makes it harder to compare directly to other experiments, e.g. those in 3.21. The current is quite noisy, which can likely be attributed to bubbles (see the discussion around Equation 3.17 above). However, the geometric current density (0.2-0.5 mA/cm 2), and thus the total amount of oxygen, are not far from that in Figure 3.21 (0.5 mA/cm 2). Thus, it is significant that the amount of excess $^{16}O^{18}O$ compared to that expected according to the natural isotopic ratio in Figure 3.25b, 26 pmol, is much less than that in Figure 3.21d, 185 pmol. This difference can be attributed to the labeling procedure. Whereas the potential of the Ru foam tested in 3.21d was cycled in labeled electrolyte before testing in non-labeled electrolyte, the Ru foam tested in Figure 3.25 was only oxidized at 0.5 mA/cm 2 geometric current density for 10 minutes in labeled electrolyte. Apparently, potential cycling either is more effective at incorporating oxygen in a metallic foam than simple oxidation, or the surface oxide layer that potential cycling forms is less stable and releases more of the incorporated O during OER.

After the exchange experiment and a brief period at OCP, the electrode potential is brought to 1.23 V vs RHE, and CO is dosed while the potential is held constant. An adsorption transient is seen as a brief (≈ 10 s) cathodic current, which is followed by a steady anodic current and CO_2 production. Compared to the natural isotopic ratio (measured with CO_2 as the carrier gas), there is a clear excess of $C^{16}O^{18}O$ ($m/z=34$) in the evolved CO_2 , indicating that lattice oxygen is being used to oxidize some of the CO. This is unlike the experiment on Pt (Figure 3.24), where the isotope signal did not come until the oxide layer was reduced. This might indicate that an oxidized layer on Ru can react with CO in a way that an oxidized layer on Pt can not. However, it may just be an artifact of the much

higher surface area of the Ru foam, which has a roughness factor on the order of 2000 (see Subsection 3.2.2). A control experiment with Ru foam that had not seen labeled electrolyte did not show an isotope signal during CO oxidation.

Reducing the surface of the Ru did not extract more ^{18}O - in fact, the $\text{C}^{16}\text{O}^{18}\text{O}$ to C^{16}O_2 ratio decreases when the potential is lowered below 1 V vs RHE, as does the overall CO oxidation activity. This ratio, however, increases again when the sample is brought to anodic potentials again, indicating that one cathodic sweep down to 0 V vs RHE was not enough to reduce all of the ^{18}O out of the sample, or that not all the H_2^{18}O formed escaped the porous structure of the sample. While there is great potential for using this type of experiment to explore the surface electrochemistry of Ru, for now it has served its purpose: Since much more ^{18}O could be extracted from the electrode by CO oxidation than was exchanged during OER, it proves that there is much electrochemically accessible oxygen which is not lost from the catalyst during oxygen evolution. In other words, it not only confirms that lattice oxygen exchange is not a primary OER mechanism on ruthenium, but also indicates that, at least at very low TOF, there are surface oxygen species which are spectators to OER.

That concludes this Section on lattice oxygen reactivity. However, the best experiments have been saved for the next Section, because as we got better at doing isotope-labeling studies, we also started to relate lattice oxygen evolution to metal dissolution.

3.4 Evolving vs dissolving

It is notable that all of the materials that do not show an isotope effect in Table 3.1, with the possible exception of Pt sputtered on a Teflon DEMS membrane [137], are compact and crystalline films or nanoparticles [113, 128, 143]. In contrast, most of the materials for which studies have seen evidence of lattice oxygen evolution are hydrous, porous, or high-surface-area materials [113, 123, 138, 139, 141, 144]. The authors of these studies all concluded that lattice oxygen is involved in the oxygen evolution mechanism. Equivalently, this implies that an oxygen vacancy is present at some point the electrocatalytic cycle, like in the Mars van Krevelen mechanism from thermal catalysis. However, the observation of an isotope effect does not in itself prove that lattice oxygen evolution is part of a catalytic mechanism. It could, for example, merely part of a parasitic degradation side-reaction. Likewise, many of the studies are not quantitative, and the relative importance of the Mars-van-Krevelin mechanism and other potential OER mechanisms that do not involve lattice oxygen is rarely addressed.

Lattice oxygen evolution is only compared to dissolution in one of the studies: Geiger et al, 2018, ref. [113]. In that study, the authors found that hydrous Ir^{18}O_x formed by potential cycling of a sputtered Ir^{18}O_2 film in ^{18}O -labeled electrolyte, showed lattice oxygen evolution but also increased iridium dissolution compared to the as-sputtered Ir^{18}O_2 film. The authors did not detect lattice oxygen evolution from the as-sputtered film. This comparison of lattice oxygen evolution to dissolution is highly valuable, but the authors did not absolutely quantify the lattice oxygen evolution for direct comparison to dissolution. Particularly, the question I became interested in was:

Question 3.2. *How does the number of lattice oxygen atoms evolved (n_O) compare to the number of metal atoms dissolved (n_M)? ?*

Only if $n_O \gg n_M$, can it be concluded that there is a catalytic mechanism contributing to oxygen evolution which involves lattice oxygen exchange - though this mechanism may still be such a minor portion of the overall oxygen evolution activity as to be of no practical importance. On the other hand, if $n_O \leq n_M$, then lattice oxygen evolution might just be part of an unwanted dissolution reaction.

To answer this question, I performed lattice oxygen evolution experiments of the type described in the latter half of the previous Section (Subsections 3.3.3 and 3.3.4), but also collected the electrolyte periodically during the experiment for quantification of metal dissolution with ICP-MS. The procedure for collecting electrolyte during the experiment without losing electrochemical control is described in Subsection 2.3.4.

I performed these isotope-labeling “exchange vs dissolution” experiments on sputtered Ru^{18}O_2 and Ir^{18}O_2 films, electrochemically labeled Ru and Ir films, and Ru foam. The results are described in the following Subsections.

3.4.1 Sputtered Ru^{18}O_2 and Ir^{18}O_2 films

Of the three strategies for oxygen labeling described in the beginning of Section 3.3, strategy C, whereby the as-synthesized catalyst is labeled with ^{18}O , is preferable whenever possible. It allows for a higher sensitivity than strategy A, in which an un-labeled catalyst is tested in labeled electrolyte, because the labeled electrolyte (typically $\leq 97\%$ ^{18}O) is never as isotopically pure as un-labeled electrolyte (99.8 % ^{16}O). On the other hand, it allows for a more well-defined electrocatalytic system than strategy B, in which an un-labeled as-synthesized electrocatalyst is treated electrochemically in labeled electrolyte before testing in un-labeled electrolyte, because the effectiveness of the electrochemical labeling procedure is rarely confirmed and may change the surface of the electrode.

We therefore prepared labeled Ru^{18}O_2 and Ir^{18}O_2 films by reactive sputtering of Ru or Ir with a sputtering plasma consisting of 80% Ar and 20% $^{18}\text{O}_2$ (99% isotopic purity). This produced an isotopically pure as-synthesized electrocatalyst for testing in un-labeled electrolyte.

Labeled oxide films of 25 nm nominal thickness (Ru^{18}O_2) or 10 nm thickness (Ir^{18}O_2) were prepared by sputter deposition on glassy carbon substrates with a 5 nm Ti sticking layer. The sputter deposition

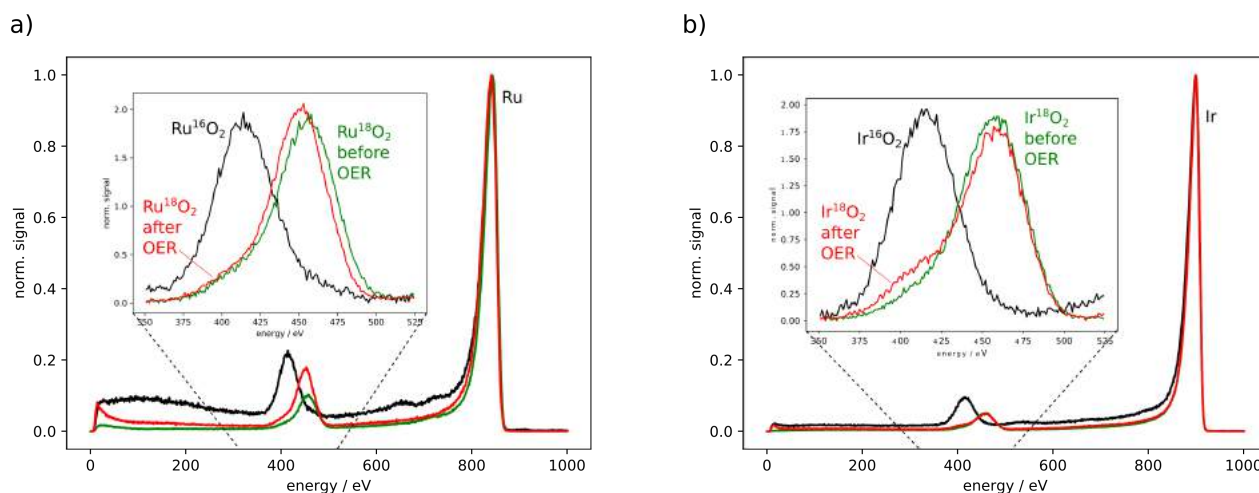


Figure 3.26: Ion-scattering spectrometry for isotope-labeled (a) RuO₂ and (b) IrO₂ sputtered films before (green) and after (red) 30 minutes of oxygen evolution at 0.5 mA cm⁻² in non-labeled electrolyte. Non-labeled films are included for reference (black). The spectra are normalized to the height of the metal peak. The insets show a zoom-in of the oxygen region and are normalized to the combined area of the oxygen peak(s).

was done at room temperature, resulting in amorphous Ru¹⁸O₂. The labeling of the as-deposited samples was confirmed by ion scattering spectroscopy as shown in Figure 3.26. It is notable that the isotopic purity of the oxygen signal in ISS remained high even after the electrode was left out for several days in air, indicating that RuO₂ and IrO₂ do not exchange bound oxygen with the O₂ or H₂O in air.

The labeled samples were placed in the chip-based EC-MS setup, oxygen evolution was run for half an hour at 0.5 mA/cm², and electrolyte samples were taken at intervals (approximately 2 min, 10 min, 20 min, and 30 min) for analysis by ICP-MS. The first ten minutes of electrolysis is shown in Figure 3.27a for the labeled Ru¹⁸O₂ film, and in Figure 3.27b for the labeled Ir¹⁸O₂ film. The results

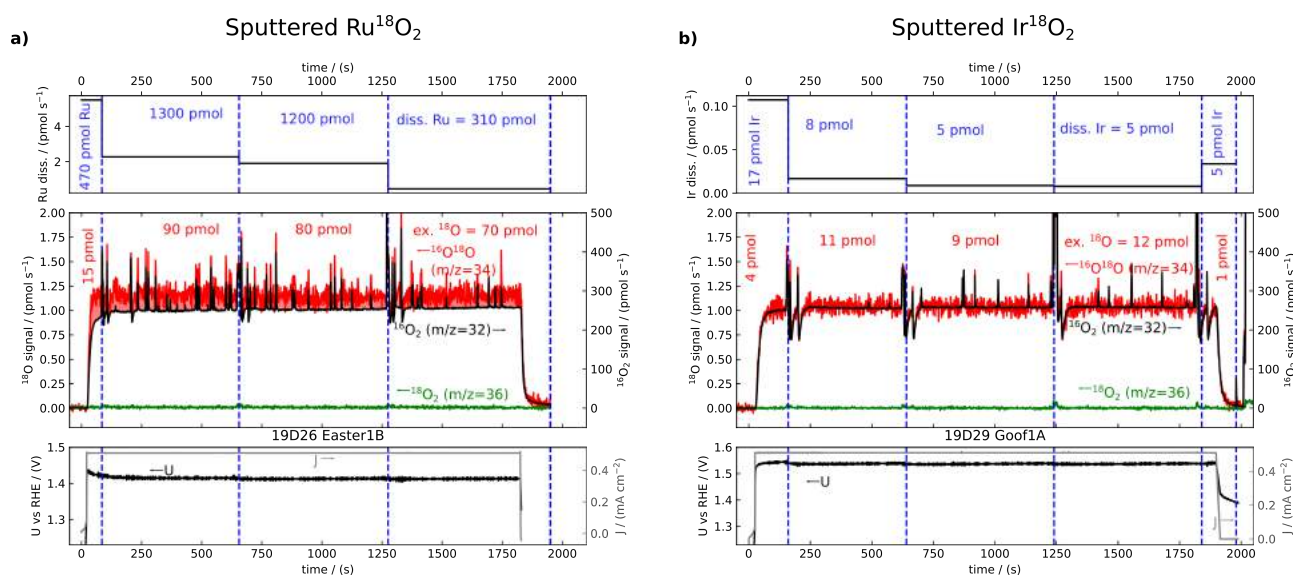


Figure 3.27: Metal dissolution (top panels) and lattice oxygen evolution (middle panels) from room-temperature sputter-deposited (a) Ru¹⁸O₂ and (b) Ir¹⁸O₂ films in un-labeled 0.1 M HClO₄. The O₂ signals are measured *in-situ* and plotted on two axes, scaled according to the natural isotopic ratio to show the excess ¹⁶O¹⁸O. The metal dissolution was measured by determining by ICP-MS the concentration of metal in electrolyte samples taken at intervals indicated by the dotted blue lines.

are plotted as EC-MS-MS plots, with the electrochemistry data in the lower panel, gas flux to the mass spectrometer in the middle panel, and averaged metal dissolution rate in the upper panel, all with a shared time axis. The gas MS data are plotted on two y-axes. The calibrated $m/z=34$ signal ($^{16}\text{O}^{18}\text{O}$) is plotted on the right y-axis and the $m/z=32$ ($^{16}\text{O}_2$) signal plotted on the left y-axes. The two axes are scaled according to the natural $^{16}\text{O}^{18}\text{O}/^{16}\text{O}_2$ ratio of 0.4%. Thus, the two traces fall perfectly on top of each other when the oxygen evolved matches the natural isotopic ratio. For the case of Ru^{18}O_2 there is a clear excess of $^{16}\text{O}^{18}\text{O}$ signal compared to the natural ratio. The excess is indicated in the plot with a light red highlight. In the first 10 minutes, there are approximately 100 pmol of lattice ^{18}O evolved. In comparison, approximately 150 nmol of oxygen was evolved in total. The mechanism by which lattice oxygen is evolved as O_2 thus only accounts for $\approx 0.07\%$ of the total OER activity during the first ten minutes. For the Ir^{18}O_2 film, the deviation of the $^{16}\text{O}^{18}\text{O}$ signal from the natural ratio is not immediately visible in Figure 3.27, but integration indicates that there is a small excess of ≈ 15 pmol of $^{16}\text{O}^{18}\text{O}$ evolved during the first ten minutes, corresponding to less than 0.01% of the total oxygen evolved. The rate of lattice oxygen evolution decreases only slightly during the remainder of the 30 minutes, such that 250 pmol of lattice oxygen is evolved during 30 minutes for Ru^{18}O_2 and 35 pmol of lattice oxygen is evolved during 30 minutes for Ir^{18}O_2 . In neither case was a significant $^{18}\text{O}_2$ signal observed.

It should be pointed out that, since the films studied here are isotope-labeled by reactive sputtering in vacuum with isotope-labeled oxygen, they have never been in contact with isotope-labeled water. Thus, incorporated H_2^{18}O can be ruled out as a source of the excess ^{18}O evolved, which is more difficult to exclude when films are electrochemically labeled.

The vertical blue dashed lines indicate when electrolyte samples were taken. There is clear noise in the gas-phase MS data while electrolyte is flowing (middle panel), but with no loss of current control and potential measurement (bottom panel). The amount of metal in the electrolyte sample, in pmol, is indicated before each dotted blue line. This amount, divided by the length of time between electrolyte samples are taken, gives an average dissolution rate in pmol/s. For both the Ir^{18}O_2 and Ru^{18}O_2 samples, the highest dissolution rate was at the start of the electrolysis experiment, as the potential increased from OCP to the operating potential giving 0.5 mA/cm^2 . In the case of Ru^{18}O_2 , the average dissolution rate remained high, approximately 2 pmol/s, corresponding to a stability number on the order of 100. The amount of ruthenium dissolving into solution was approximately 10 times the amount of lattice ^{18}O evolved as $^{16}\text{O}^{18}\text{O}$. For Ir^{18}O_2 , on the other hand, the dissolution quickly lowers to a much smaller rate of ca 90 fmol/s, corresponding to a stability number of approximately 3×10^4 . The amount of lattice oxygen evolved from Ir^{18}O_2 actually exceeds the amount of iridium dissolved between all electrolyte samples excluding the ramp-up and ramp-down periods.

As a side note of potentially high interest: The apparent Ru dissolution rate for the last electrolyte sample (0.4 pmol/s) is much lower than for the previous two electrolyte samples (2 pmol/s). The main experimental difference is that the last electrolyte sample was taken after the applied potential was turned off, while the catalyst was at OCP. Electrolyte is flowing when the electrolyte sample is taken, and stagnant otherwise, so this may be a case of influencing the thing we are trying to measure. This result indicates that it may be the combination of applied potential and electrolyte flow that leads to RuO_2 dissolution. More experiments are needed specifically probing the effect of electrolyte flow on ruthenium stability. If this is the case that ruthenium is many times more stable in still electrolyte than flowing electrolyte, it could have profound implications for PEM electrolyzers. Such a difference in stability could arise from a small concentration of dissolved ruthenium building up in the electrolyte when it is not flowing. This might imply that PEM electrolyzers with RuO_2 designed to have a small anolyte volume with some concentration of dissolved ruthenium could stabilize ruthenium anodes. This would be important, as RuO_2 requires less overpotential than the IrO_2 catalyst currently used, and is (slightly) less scarce and thus more scalable. More experiments are needed.

Based on capacitance measurements, a monolayer of the labeled films corresponds to approximately 9 nmol of oxygen for RuO_2 (roughness factor ≈ 50) and 3 nmol for IrO_2 (roughness factor ≈ 25). The amount of lattice oxygen evolved in the full 30 minutes is thus $\approx 3\%$ of a monolayer for Ru^{18}O_2 and

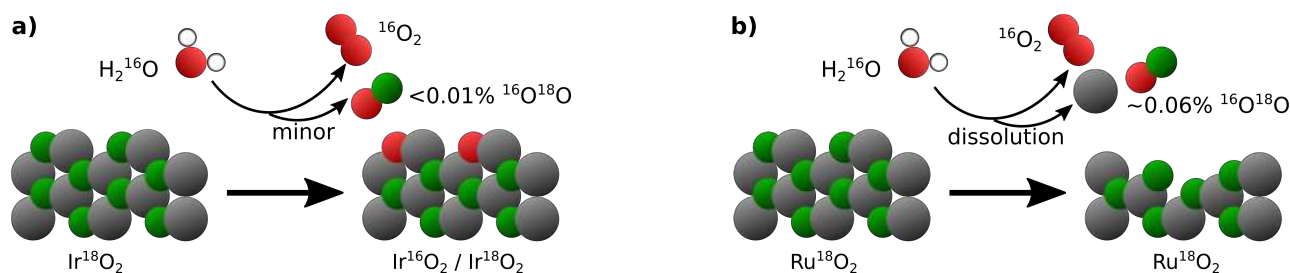


Figure 3.28: Lattice oxygen can either be due to (a) a Mars - van Krevelen type mechanism, as in the case of IrO_2 , or (b) a dissolution side-reaction, as in the case of RuO_2 .

$\approx 1\%$ of a monolayer for Ir^{18}O_2 .

If the lattice oxygen evolution is due to a Mars-van Krevelen type mechanism, then the oxygen isotope present in the electrolyte should be incorporated into the lattice, and should be present in the catalyst after the reaction. If, however, the lattice oxygen evolution is a side-product of a dissolution mechanism, then oxygen from the electrolyte would not be incorporated in the lattice. This is illustrated in Figure 3.28. Ion-scattering spectrometry after OER can thus help distinguish between the possibilities. The red traces in Figure 3.26 indicate that little to no ^{16}O has been incorporated into the surface of the Ru^{18}O_2 sample, whereas a small amount of ^{16}O has been incorporated into the surface of the Ir^{18}O_2 electrode. This indicates that the very small amount of lattice oxygen exchange observed in IrO_2 may in fact be due to a Mars - van Krevelen type mechanism, whereas the lattice oxygen evolution observed in RuO_2 may just be part of a dissolution process. As an example of such a dissolution process, the $^{16}\text{O}^{18}\text{O}$ signal observed during OER for Ru^{18}O could result from the decomposition in the chip or the vacuum chamber of RuO_4 with at least one of the oxygen atoms from the lattice, as $\text{RuO}_4(\text{g})$ has been observed by mass spectrometry during OER on RuO_2 . [113]

These results from oxygen evolution on isotope-labeled films show that lattice oxygen evolution should not be interpreted as evidence of an important oxygen evolution reaction mechanism involving oxygen vacancies without careful, quantitative studies. Specifically, the activity of the lattice-involving mechanism should be compared quantitatively to the overall OER activity, and to the rate of metal dissolution.

3.4.2 Electrochemically labeled films

We also performed the exchange vs dissolution experiments for Ru and Ir labeled electrochemically. Metallic films of 25 nm thickness (Ru) or 10 nm thickness (Ir) were prepared by sputter deposition on glassy carbon substrates with a 5 nm Ti sticking layer.

The metallic electrodes were placed in the EC-MS setup which was filled with labeled electrolyte (0.1 M HClO_4 in 97% H_2^{18}O), where they were first cycled between -0.05 V and +1.4 V (Ru) or +1.5 V (Ir) vs RHE, and then oxidized at +0.5 mA/cm^2 geometric current density for 10 minutes. They were then rinsed in natural water and put back in the setup with un-labeled electrolyte (0.1 M HClO_4 in 99.8% H_2^{16}O), and subject to a geometric current density of +0.5 mA/cm^2 for 30 minutes, with electrolyte taken at intervals for ICP-MS analysis. The results are shown in Figure 3.29.

In both cases, an isotope signal can be seen in the start of the exchange experiment, but in both cases, the integrated excess $^{16}\text{O}^{18}\text{O}$ signal is less than one monolayer equivalent. It is larger for the oxidized Ru (Figure 3.29a) than for the oxidized Ir (Figure 3.29b). However, in contrast to the sputtered oxide films, in which the isotope signal was more or less steady throughout the 30 minutes of electrolysis, for these electrochemically oxidized films the excess $^{16}\text{O}^{18}\text{O}$ evolution is transient. This could indicate that labeled layer is quite thin and dissolves completely in less than 30 minutes. Indeed, the isotope $^{16}\text{O}^{18}\text{O}$ to $^{16}\text{O}_2$ ratio has converged to the natural isotopic ratio for the oxidized Ru film after approximately 9 nmol of Ru has dissolved, corresponding roughly to one monolayer. This could indicate that only the outer monolayer had been labeled. Alternately, if the continued oxidation of the metallic film is faster than the dissolution, the labeled oxide layer could be buried beneath an

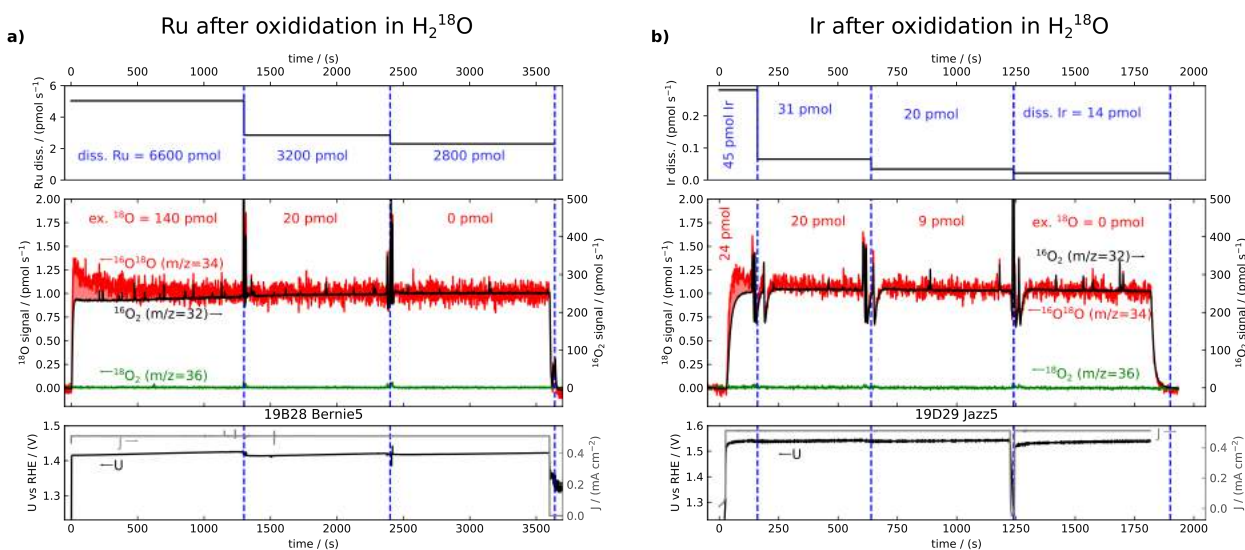


Figure 3.29: Metal dissolution and lattice oxygen evolution from metallic (a) Ru and (b) Ir films in un-labeled 0.1 M HClO_4 after formation electrochemical cycling and oxidation in ^{18}O -labeled electrolyte.

un-labeled oxide layer. This is illustrated in the first panel of Figure 3.22b. This is most likely the reason for the transience of the isotope signal for the iridium electrode, where significantly less than one monolayer of Ir has dissolved before the $^{16}\text{O}^{18}\text{O}$ to $^{16}\text{O}_2$ ratio has converged to the natural isotopic ratio.

In both cases, the amount of metal dissolution is much higher than it is for the sputtered oxide films. This is consistent with prior knowledge that RuO_2 is more stable than Ru [128, 131], and IrO_2 is more stable than Ir [131].

The same experiment was also performed for a Ru foam electrode oxidized at 0.5 mA/cm^2 for 30 minutes. The result is shown in Figure 3.30a. Again, the largest rate of excess ^{18}O evolution is at the beginning. The $^{16}\text{O}^{18}\text{O}$ to $^{16}\text{O}_2$ ratio does not converge completely to the natural isotopic ratio during the 1 hr of measurement, but comes close during the final 30 minutes. This is despite the amount of dissolved ruthenium ($\approx 15 \text{ nmol}$) being much less than a monolayer-equivalent ($\approx 300 \text{ nmol}$) on this high-surface-area film. This film, like that tested in Figure 3.25 was only oxidized at constant current, and not cycled, in labeled electrolyte. Cycling the electrode in labeled electrolyte leads to a larger amount of labeled oxygen evolution in the exchange experiment (Figure 3.21). The near-convergence with less than a monolayer of Ru dissolved may indicate that the labeled oxide layer becomes buried under an un-labeled oxide layer.

Finally, to validate that the excess ^{18}O in all of the previous experiments does indeed originate in the electrocatalyst (and not in the vacuum chamber, or an error in the data analysis), we performed a control experiment on an un-labeled IrO_2 film. This film was sputtered on a Ti sticking layer on glassy carbon at 400°C in isotopically natural O_2 . The small negative values (-7 pmol total over 10 minutes of electrolysis) obtained when integrating the $^{16}\text{O}^{18}\text{O}$ signal and subtracting that expected based on the $^{16}\text{O}_2$ signal should be taken as an indication of the uncertainty of the method.

3.4.3 Exchange and extraction

Finally, as the last result in this chapter, I show an exchange and extraction experiment (described in Subsection 3.3.4) done with electrolyte sampling for ICP-MS on a sputtered Ir^{18}O_2 film. The entire experiment is shown in Figure 3.31. Because there's a lot going on, I show the electrochemical program both with the raw *in-situ* MS data (Figure 3.31a), and again with analyzed *in-situ* MS data and ICP-MS data (Figure 3.31b).

From the left: starting just after $t=0$, an anodic geometric current density of $+0.5 \text{ mA/cm}^2$ is

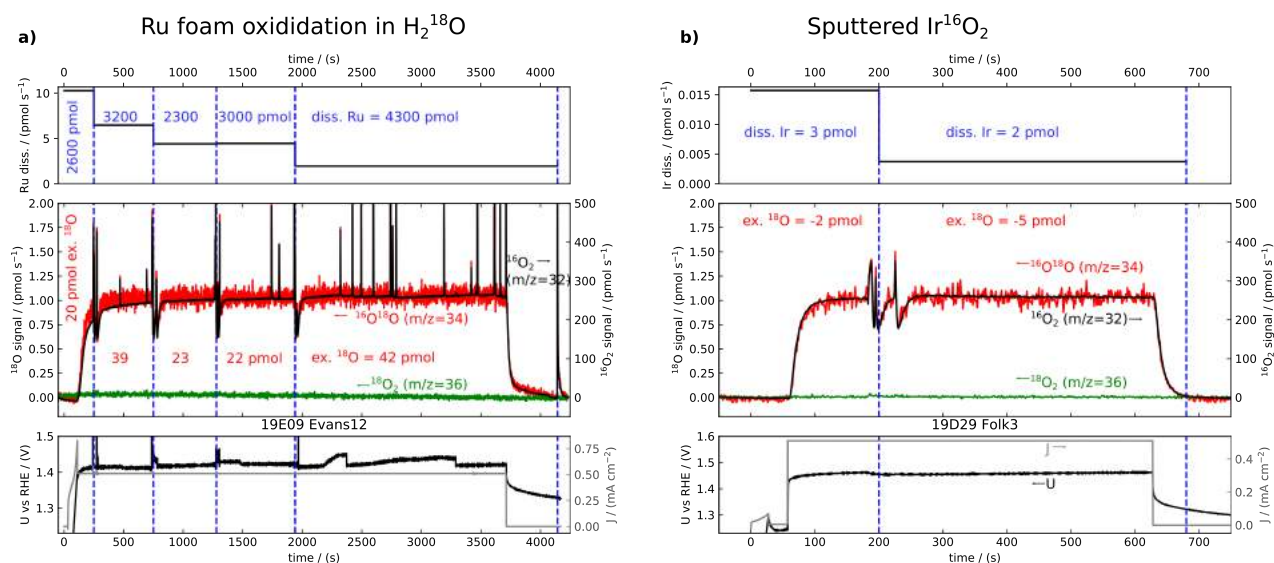


Figure 3.30: Metal dissolution and lattice oxygen evolution in un-labeled 0.1 M HClO₄ from (a) Ruthenium foam after oxidation in ¹⁸O-labeled electrolyte, and (b) an un-labeled Ir¹⁶O₂ sputtered at 400°C as a control.

applied for 23 minutes. Electrolyte samples are taken after 2 minutes, 10 minutes, and 20 minutes of electrolysis. Each time the electrolyte is exchanged to take a sample for ICP-MS, there is a spike in the $m/z=28$ signal due to N₂ in the air-saturated electrolyte that is drawn into the cell. Unfortunately, the first electrolyte exchange appears to introduce a bubble, resulting in noise in the $m/z=32$ (¹⁶O₂) and $m/z=34$ (¹⁶O¹⁸O) signals starting then and continuing to the end of the electrolysis period. There is also some sporadic noise in the working-electrode potential, which may be because I bumped the alligator clip connecting to the working electrode while exchanging the electrolyte. However, the measured electrode current remains steady at the set value of +0.5 mA/cm².

Looking at the analyzed data for the same period, the results for lattice oxygen evolution and iridium dissolution are very much as in Figure 3.27b: on the order of 30 pmol of both iridium dissolution and lattice oxygen evolution during the first 20 minutes of electrolysis, but with most of the iridium dissolution coming at the beginning while the potential is changed. Again, during steady electrolysis, the lattice oxygen evolution exceeds the iridium dissolution, indicating that there may be a minor OER mechanism involving lattice oxygen exchange. This confirms that the result is reproducible, and indicates that the method of subtracting the integrated ¹⁶O₂ signal, weighted by the natural isotopic ratio, from the integrated ¹⁸O¹⁶O signal is robust even in the face of noisy data. Again, I emphasize that the lattice oxygen evolution is an extremely small portion - only 0.01% - of the overall OER activity.

Continuing towards the right in the raw data: after the electrolysis period, the potential is ramped down to a resting potential of 1.2 V vs RHE (with a small overshoot as I decided on what potential to rest at), and another electrolyte sample is taken to see if this small potential ramp resulted in significant Ir dissolution (it didn't). Then the carrier gas is changed from He ($m/z=4$) to CO ($m/z=28$) to begin the CO oxidation (extraction) portion of the experiment. A very small steady anodic current, on the order of 3 μ A/cm², is detected right after introduction of CO, together with a C¹⁶O₂ ($m/z=44$) signal, and is attributed to steady-state CO oxidation. This steady-state CO oxidation is continued for 15 minutes, during which two electrolyte samples are taken. The electrolyte sampling again brings air-saturated electrolyte into the cell. This can no longer be seen in the $m/z=28$ signal, which is now dominated by CO, but can be seen as an ¹⁶O₂ ($m/z=32$) signal. In the analyzed data, it appears that there is a small amount of excess excess C¹⁶O¹⁸O in the CO₂ evolved during this period, but the C¹⁶O¹⁸O ($m/z=46$) background level is taken when the carrier gas is He, and so I can't exclude the possibility that this is because of the effect of CO on the background. The iridium dissolution during

this period is not significantly above the ICP-MS detection limit of ≈ 1 pmol.

The CO oxidation activity at 1.2 V vs RHE is so low because, like PtO, IrO₂ is mostly inert for CO oxidation, whereas the metallic surface is active. At about 2500, the potential was scanned slowly (1 mV/s at first, then 5 mV/s) in the cathodic direction. Unlike Pt (Figure 3.24), the cathodic scan did not result in a CO oxidation transient. Apparently, there is not a sweet spot in between the potential at which an IrO₂ surface is reduced and the potential at which *OH can no longer adsorb to oxidize CO by the Langmuir-Hinshelwood mechanism. In the absence of the desired transient, I allowed the cathodic scan to continue all the way down to 0 V vs RHE, where hydrogen evolution occurs, as evidenced by the cathodic current and the m/z=2 signal. This was a mistake, as it likely reduced

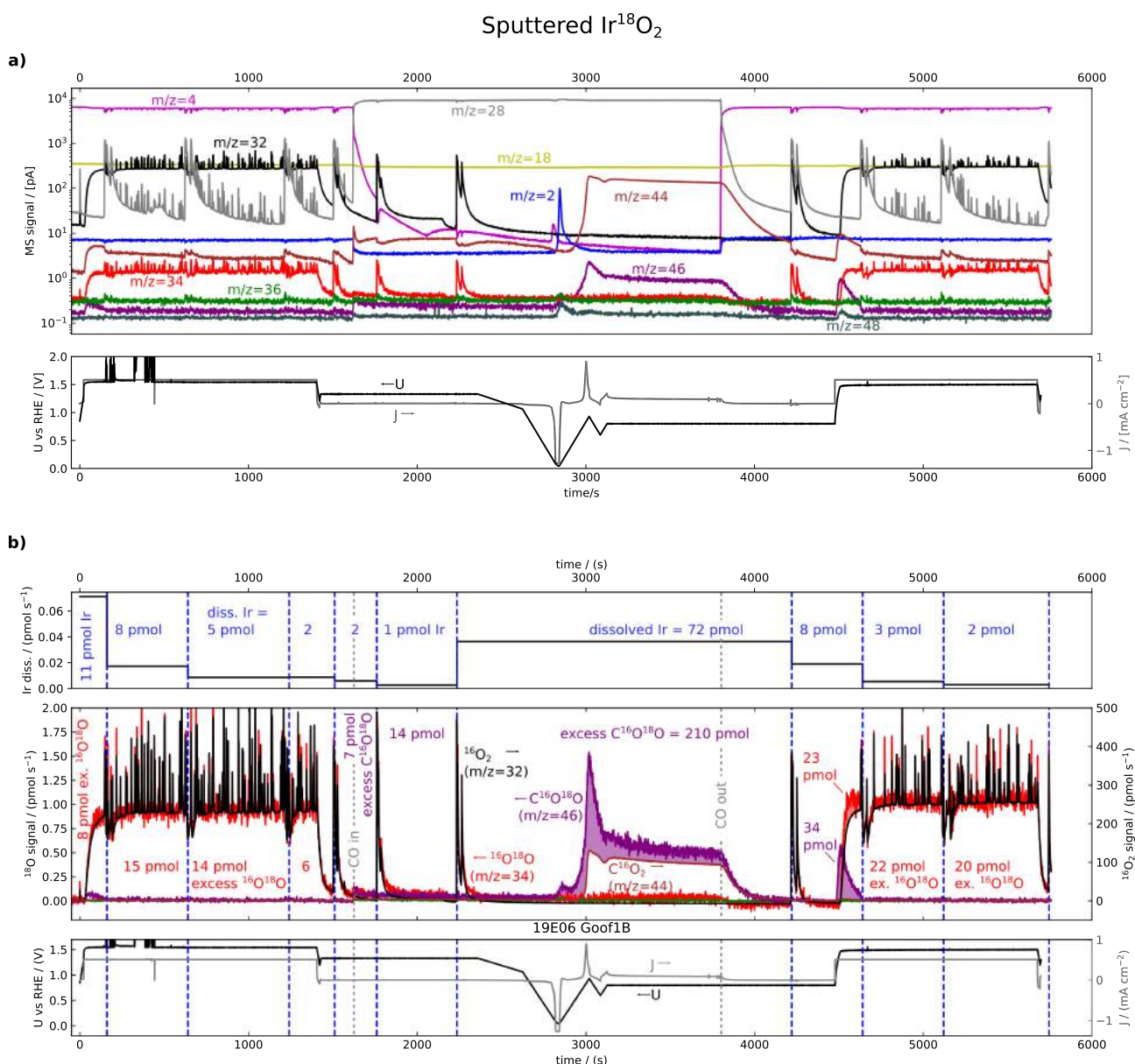


Figure 3.31: Sequential exchange (OER) and extraction (CO oxidation) experiments on a labeled Ir¹⁸O film in un-labeled 0.1 M HClO₄. **(a)**, raw EC-MS data with all masses plotted on a log scale. The highest mass signal is due to the He (m/z=4) or CO (m/z=28) carrier gas. An air signal is visible whenever electrolyte samples are taken for EC-MS as spikes in m/z=28 (N₂) and/or m/z=32 (¹⁶O₂) though electrochemically produced ¹⁶O₂ or CO (m/z=28) sometimes interfere with these signals. **(b)**, Same data, analyzed, with ICP-MS data in the top panel. The labeled signals for ¹⁶O¹⁸O and C¹⁶O¹⁸O are plotted on the left y-axis and the un-labeled ¹⁶O₂ and C¹⁶O₂ signals are plotted on the right y-axis. The axes are scaled according to the natural ¹⁶O¹⁸O to ¹⁶O₂ ratio, which is also the natural C¹⁶O¹⁸O to C¹⁶O₂ ratio.

much of the ^{18}O out of the surface layer of the electrode, and also dissolved some Ir, as dissolution is known to occur from metal oxide electrodes during the reductive potential sweep [131]. The potential was then scanned anodic again at 5 mV/s, with CO oxidation starting in earnest at about 0.8 V vs RHE. A large transient in the current indicates that an adsorbed monolayer of CO was stripped off (CO stripping). Then I went back and forth for a little bit before settling on 0.8 V vs RHE for steady-state extraction. The carrier gas is switched back to He at 3800 s, ending the CO oxidation experiment, and electrolyte is collected at about 4200s for ICP-MS.

The scans between 2500 and 3200 were not ideal. In an optimal experiment, I would have only scanned the potential to slightly lower than 0.8 V vs RHE, perhaps 0.6 V vs RHE, and then back up, to reduce the surface enough that CO could adsorb, without reducing out lattice ^{18}O , and then go back up to 0.8 V vs RHE where the CO can be oxidized. Nonetheless, looking at the analyzed data, the procedure had the desired effect. A significant excess of $\text{C}^{16}\text{O}^{18}\text{O}$ is produced by CO oxidation, indicating that lattice oxygen can be involved in CO oxidation. 210 pmol of excess $\text{C}^{16}\text{O}^{18}\text{O}$ is evolved during CO oxidation, which is significantly more than the excess $^{16}\text{O}^{18}\text{O}$ during OER (40 pmol), and also significantly more than the Ir dissolved during this period (72 pmol) despite the accidental over-reduction of the sample. Because some of the $\text{C}^{16}\text{O}^{18}\text{O}$ is expected to lose the ^{18}O label due to homogeneous exchange with H_2^{16}O in the electrolyte, the actual amount of lattice O used to oxidize CO was more than 210 pmol, though still less than a monolayer equivalent (≈ 3 nmol).

Exchange and dissolution are measured for a second OER period after the CO oxidation experiment. When 0.5 mA/cm² is applied at 4500s and the potential ramps up to meet this current demand, a CO₂ signal indicates that some CO had remained adsorbed on the surface and was oxidized off by the increasing potential. There was a significant excess of $\text{C}^{16}\text{O}^{18}\text{O}$ in this CO₂, indicating that lattice oxygen was involved in stripping off the adsorbed CO. There was also much more excess $^{16}\text{O}^{18}\text{O}$ in the O₂ evolved during this second exchange experiment than the first, which may be due to a roughening or destabilizing effect of the potential cycling during the CO oxidation portion of the experiment.

It is worth pointing out that, despite these multiple independent clear observations of lattice oxygen reactivity, all of the lattice ^{18}O evolved either in O₂ or CO₂ during the entire exchange + extraction + exchange experiment remained less than one monolayer equivalent.

3.4.4 Conclusion and perspective on oxygen evolution experiments

If, after reading this Chapter, you get an impression that all of the results remain a bit preliminary, please know that I am right there with you.

The results presented in this Section, combining isotopic labeling by reactive sputtering with $^{18}\text{O}_2$, surface isotopic characterization by ISS, fluent electrolyte sampling during the experiments for dissolution measurements by ISS, and routine and confident detection of sub-picomol per second rates of lattice oxygen evolution, all came together during the last months of my PhD. The results presented in the previous Sections and Chapters (as well as Paper II) have indicated some of the trial-and-error, mistakes, and development that was necessary to get there.

The goal is of course to use these tools and techniques to make breakthrough discoveries in OER catalysis that can lead to more efficient and cost-effective PEM electrolyzers. I expect that this could happen by the following paths:

- Insights based on the newly-detected changes in the Tafel slope of RuO₂ (Section 3.2) will help inform theorists about which elementary steps and intermediates are most important in predicting materials that can catalyze the OER at high rates at lower overpotentials.
- Quantitative comparison of lattice oxygen evolution, total oxygen evolution, and metal dissolution on an atom basis will help make it clear whether "activating lattice oxygen" is actually a desired strategy. Based on the results presented here so far on RuO₂ and IrO₂, it seems that lattice-involving mechanisms are associated with instability and, in any case, only contribute a very small portion of the overall OER activity. Hopefully this will help direct the efforts of the research community.

- The ease and sensitivity of quantitative OER activity measurements and metal dissolution measurements using the EC-MS setup and ICP-MS of the collected electrolytes will make these techniques a powerful screening tool for acid OER catalysts that are stable and active with less precious metal.

Next steps could include applying the techniques presented here to compare activity, exchange, and dissolution on calcined Ir and Ru containing catalysts more closely resembling the industrially-used “dimensionally stabilized anodes” [155], and promising recently-reported materials based on alloying of Ir and Ru with non-noble metals [156–158]. Some of this work is already being done by Mayrhofer and coworkers [113], but the sensitivity of our EC-MS setup and the combination with ISS can add a lot. An obvious starting point would be to re-visit the thermal-decomposition IrO_x result reproduced in Figure 3.18 from Reference 139, which showed significant lattice oxygen evolution but for which dissolution and ISS were not measured.

In the next Chapter, the last Chapter of this Thesis, I will attempt to gauge the possible net impact of this work on the climate crisis described in Chapter 1. To do so, I will assume that one or more of the possible impact paths above lead to a reduction of 0.1 mV in the overpotential needed to drive PEM electrolyzer cells, holding all else constant.

Chapter 4

The Net Carbon Impact of this PhD

In this short concluding Chapter, I will estimate the CO₂ emitted (Section 4.1) and, with much more uncertainty, the expectation value of the CO₂ saved during my PhD project (Section 4.2). The idea is to determine whether I have done any net good during the past three years with respect to the climate crisis described in Chapter 1.

A version of this question, rearranged to be a bit more rigorous, is:

Question 4.1. *What portion of a millivolt's improvement in efficiency of PEM electrolyzers worldwide in the year 2030 would have to be attributable to my research in order to offset the CO₂ footprint of my PhD project?*

4.1 Burning

I have had the fantastic opportunity of working with scientists all over the world during this PhD project. I owe thanks for these opportunities to our wide network of collaborators as well as the EteForsk Travel Grant that I was awarded by the Danish Ministry for Higher Education and Science in 2018. (I have been especially quick to take opportunities to travel to the United States, since I also visited friends and family on those trips.)

Figure 4.1 shows the institutes that I have visited and conferences that I have attended during the three years of my PhD on a map of the world. The routes that I have flown are shown together with their distance and the number of times that I flew that route.

While grateful for all of these opportunities, I am not proud of how much I have been traveling, and plan on much less air travel in the future. Each trip has come with an environmental cost, since air travel is the most CO₂-intensive activity an individual can choose to do.

Adding up all of the trips in Figure 4.1, I have flown 187600 km during this PhD project, equivalent to circling the earth 4.7 times at the equator. Using an average greenhouse gas emissions of 0.19 kg CO₂ equivalents per passenger per kilometer [30], this is 36 tons of CO₂, or 12 tons of CO₂ per year (3.2 tC/yr). This is actually a slight underestimation, since it uses the direct-flight distances, whereas most of the trips indicated involved at least one transfer.

Domestic CO₂ emissions per capita in Denmark in 2017 were 6.1 tons of CO₂ per year [9] (1.7

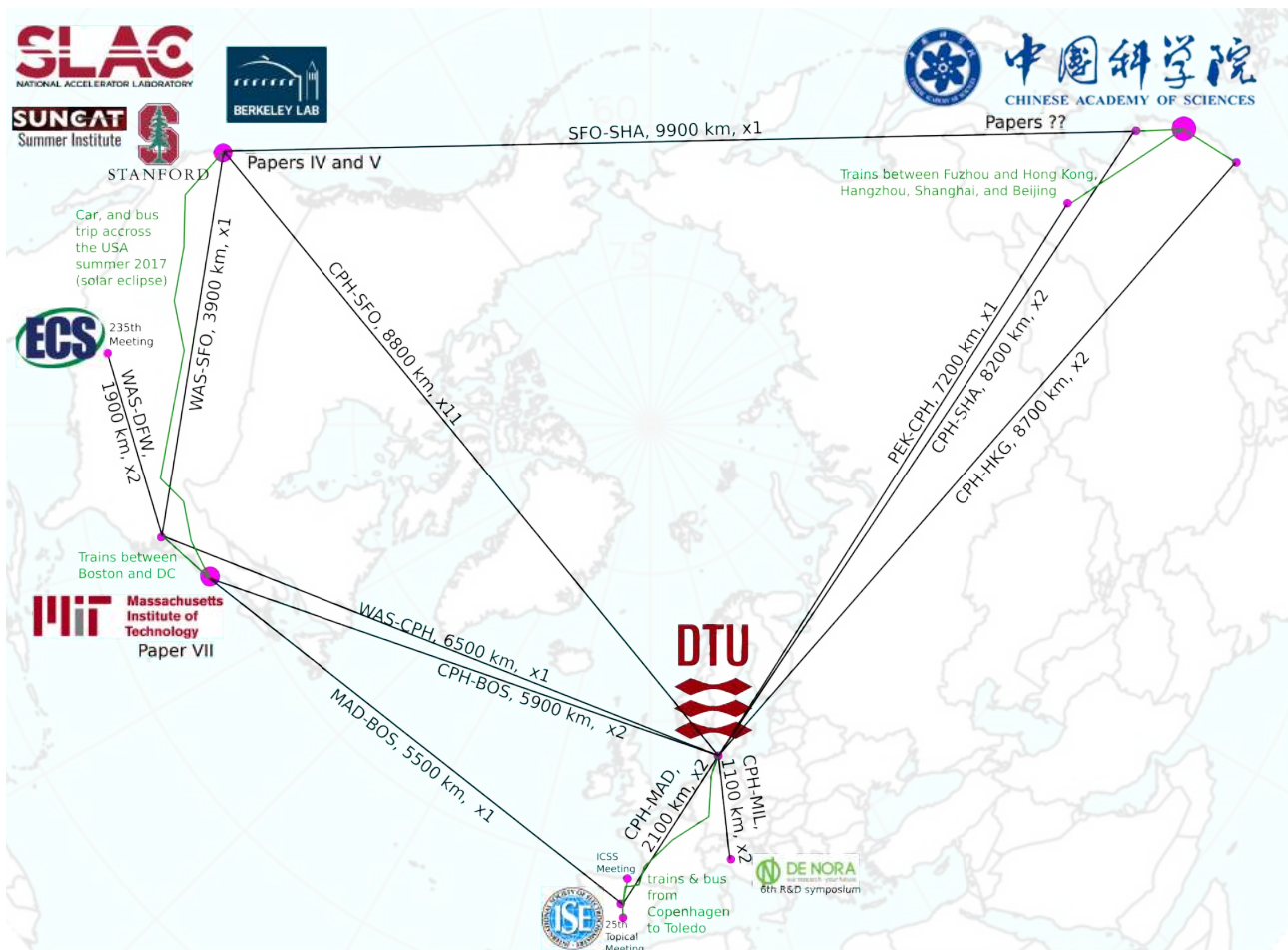


Figure 4.1: Map of research collaborations, conferences, and flights during this PhD project, superimposed on a map of the northern hemisphere. Flights are indicated as black lines, and the distance and total number of one-way flights I took over the three-year period September 2016-August 2019 are indicated. The projects requiring the most traveling have been beamline experiments at SLAC in California (Paper IV) and the collaboration with the Chinese Academy of Sciences (CAS) in Fuzhou, Fujian, China.

tC/yr), so the flying alone during my PhD project represents approximately twice the average person's CO₂ emissions in Denmark during the same period.

There are numerous sources of CO₂ emissions associated with the lab work of my PhD project. The only one considered here, which I believe to be the most significant, is that associated with electricity usage. The carbon footprint of equipment, chemicals, water, and consumables, for example, is not considered. Building 312 at DTU houses approximately 12 vacuum setups in active use including the EC-MS setup, which was the primary tool of my PhD project. The setup includes two roughing pumps, two turbo pumps, a large electronics rack, three computers and a number of control elements, and is left on 24 hours a day, 7 days a week. Others have used the EC-MS setup, and I have also used other setups, so taking responsibility for 1/12 of the hall's CO₂ emissions seems a fair average. The heating (771 MWh) + electricity (162 MWh) used by building 312 in 2017 was 933 MWh. The carbon intensity of electricity generation in Denmark in 2017 was 291 kg CO₂ per MWh of electricity [159]. Extrapolating to the 3-year PhD project, the CO₂ cost of my lab work has been:

$$3[\text{yr}] \cdot \frac{1}{12} \cdot 291 \left[\frac{\text{kgCO}_2}{\text{MWh}} \right] \cdot 933[\text{MWh}] = 68[\text{tCO}_2], \quad (4.1)$$

which is 22.6 tons of CO₂ per year (6.2tC/yr). This is a slight overestimation as I have assumed that the carbon intensity of heat is equal to that of electricity, when actually it is lower [33].

The CO₂ cost of running the EC-MS setup is thus, surprisingly, even higher than the CO₂ cost of the flying I have done during my PhD project. This would likely not be the case in the future, as progress in decarbonizing electricity is much faster than progress in decarbonizing aviation (see Chapter 1).

Adding the costs up my setup, travel, and living as an average Dane (probably an overestimation, as I have a vegetarian cyclist lifestyle when not traveling), the CO₂ cost of my 3-year PhD project is approximately:

$$c = c_{\text{el}} + c_{\text{travel}} + c_{\text{live}} = 68[\text{tCO}_2] + 36[\text{tCO}_2] + 3[\text{yr}] \cdot 6.1[\text{tCO}_2/\text{yr}] = 122[\text{tCO}_2] \quad (4.2)$$

That is the debt I have to pay, before I can even begin to claim that I'm helping to solve the climate crisis.

4.2 How much difference a millivolt makes

Answering Question 4.1 requires an estimate of how much hydrogen is produced by PEM electrolyzers in 2030, and some assumptions of how it is used.

These estimates are the job of *energy systems modeling*, which involves minimizing costs for an energy system given technoeconomic parameters of the technologies and resources available, and subject to constraints such as a cap on CO₂ emissions [160]. Results of the models vary a lot, depending on the region modeled, the assumptions made, and the techniques used. Almost all predict a role of hydrogen from water electrolysis in the energy system starting around 2030, but the amount varies a lot, with predictions of anything from 2% to 8% of total electricity generation going to hydrogen production in 2030. The usage of hydrogen also varies, from primarily energy storage [34, 160, 161] to primarily fuel cell electric vehicles [162] to primarily decarbonization of industry by steel production [35].

To estimate the impact of a marginal improvement in electrolyzer efficiency, I make the following assumptions:

- 2% of European electricity generation goes to H₂ production by water electrolysis [35] (that study assumes alkaline electrolyzers, but PEMEC's are widely believed to be the dominant technology in 2030 [41]).
- The electrolyzer cells run at a cell potential 1.7 V, representative of those compared in ref. 35.
- The amount of power going to hydrogen is constant, such that the improvement in efficiency results in more H₂.
- The extra H₂ is used to generate electricity with a round-trip efficiency of 46%, the value used in ref. 35.
- The extra H₂ displaces fuels which would have generated electricity at a carbon intensity of 340 kg/MWh, which is the average for European electricity today [163]. This also represents some uncertainty. If the H₂ replaces coke in steel production, the savings are greater. If it replaces bio-fuel from a plant fitted with carbon capture and storage, the savings might be less.
- CO₂ costs associated with implementing the hypothetical improvement in PEMEC's or storing the extra hydrogen are negligible

Finally, the big assumption - the one that has to do with my work.

- My research will result in an improvement in electrolyzer efficiency of 0.05 mV for a period of 1 year.

This should be considered an expectation value. Maybe the research in this PhD project never leads to any change, but maybe it leads to a much bigger change than expected. This could be interpreted as a 1% chance of a breakthrough that improves PEMEC's by 5 mV. Or one twentieth of the work that is needed to make a more modest breakthrough worth 1 mV. Or perhaps, though unlikely, the methods developed here are a step towards rational design of a reversible acid-stable OER catalyst saving 200 mV. There is no way to know as of yet. The use of one twentieth of a millivolt as an expectation value feels modest and reasonable, but I must admit that it is completely arbitrary. The period of one year is also arbitrary, but a finite time period over which the impact applies is necessary for the calculation. It could be taken to represent the fact that someone else, by other means, would have likely made the same progress shortly after, so my PhD project might at best be speeding things up. Because of these arbitrarinesses, in a bit, therefore, I will take out this assumption and instead look at through the window of Question 4.1, i.e. how big would the impact *have to be* for my PhD project to break even in the climate account.

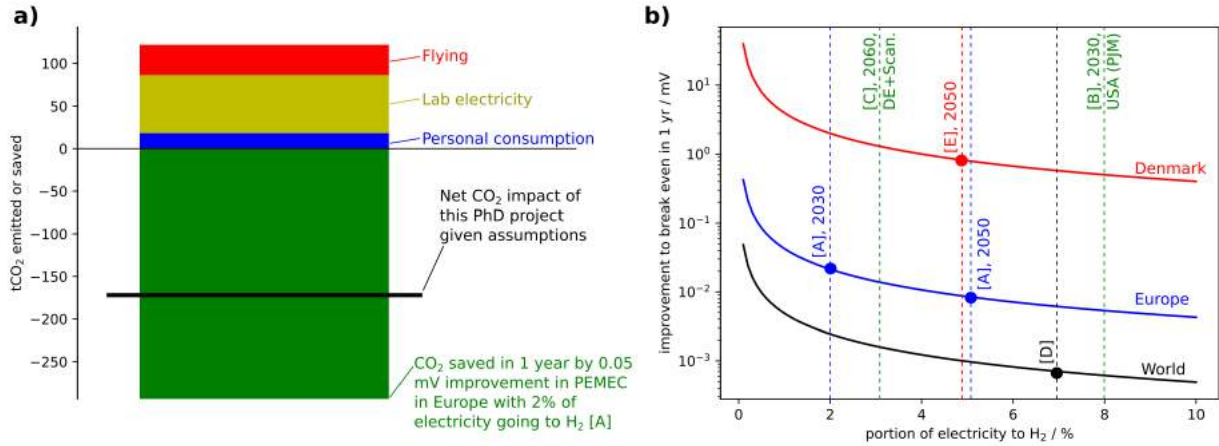


Figure 4.2: (a), CO₂ emissions (red, yellow, and red) and savings (green) associated with this PhD project with the assumptions described in the Figure and in the text. (b) Millivolts of improvement in electrolyzer operating potential needed to offset the CO₂ emissions of this PhD project in one year as a function of the percentage of the electricity generated in Denmark (red), Europe (blue), or the world (black) that goes to H₂ production. Several predicted H₂ penetrations from literature are included with their area of study indicated: [A], Sgobbi et al, 2016, ref. 35; [B], Budischak et al, 2013, ref. 34; [C], Meibom and Karlsson, 2010, ref. 162; [D], Jacobson et al, 2018, ref. 161; [E] Storgaard, 2019, ref. 160

To calculate the CO₂ saved, then, the first step is to calculate the amount of extra hydrogen generated. The amount of hydrogen generated (in mols) without the improvement is

$$n_0^{\text{H}_2} = 2\mathcal{F} \frac{xP_0}{V_{\text{EC}}}, \quad (4.3)$$

where \mathcal{F} is Faraday's constant, x is the portion of total electricity generated which goes to hydrogen production, $V_{\text{EC}} = 1.7 \text{ V}$ is the electrolyzer potential without the improvement, and P_0 is the total amount of electricity generated. For the EU in 2018, $P_0 = 3.1 \cdot 10^9 \text{ MWh}$. The quantity xP_0/V_{EC} is the total amount of charge going to hydrogen generation during the period.

With an improvement (decrease in cell potential) of ΔV , the amount of hydrogen generated is

$$n_1 = \frac{1}{2\mathcal{F}} \frac{xP_0}{V_{\text{EC}} - \Delta V}. \quad (4.4)$$

The difference is

$$\Delta n = n_1 - n_0 = \frac{xP_0}{2\mathcal{F}} \left(\frac{\Delta V}{V_{\text{EC}}(V_{\text{EC}} - \Delta V)} \right) \approx \frac{xP_0 \Delta V}{2\mathcal{F} V_{\text{EC}}^2}, \quad (4.5)$$

where the last step has used the fact that it is only a marginal improvement, i.e. $\Delta V \ll V_{\text{EC}}$.

When this hydrogen is fed back into the electricity system through a fuel cell, the amount of electricity it generates is

$$\Delta P = 2\mathcal{F} \Delta n V_{\text{FC}} = xP_0 \frac{V_{\text{FC}} \Delta V}{V_{\text{EC}}^2} = xP_0 \eta \frac{\Delta V}{V_{\text{EC}}}, \quad (4.6)$$

where V_{FC} is the voltage of the fuel cell and $\eta = V_{\text{FC}}/V_{\text{EC}}$ is the round-trip efficiency. The CO₂ saved is then

$$s = \sigma x P_0 \eta \frac{\Delta V}{V_{\text{EC}}}, \quad (4.7)$$

Where σ is the carbon intensity of the fuel that hydrogen is replacing to generate ΔP of electricity.

Plugging in the numbers from the assumptions above, the expectation value of the CO₂ emissions saved by this PhD project is

$$s = 340 \left[\frac{\text{kgCO}_2}{\text{MWh}} \right] \cdot 2[\%] \cdot 3.1 \cdot 10^9 [\text{MWh}] \cdot 46[\%] \cdot \frac{0.05[\text{mV}]}{1.7[\text{V}]} = 293 [\text{tCO}_2] \quad (4.8)$$

This is very good news, because it is greater than the 122 tons of CO₂ emissions that I estimated to result from this PhD project! This is illustrated in Figure 4.2a. For comparison, $\Delta V = 0.021$ mV saves 122 tCO₂ in a year, balancing my PhD project. A whole millivolt, $\Delta V = 1.0$ mV, is worth 5.9 MtCO₂ in Europe per year, or about one sixth the CO₂ emissions of Denmark in 2018. Every millivolt counts.

The problem is turned around in Figure 4.2b. Here, I am inquiring into the break-even point. I have set the savings s from Equation 4.7 equal to the costs c from Equation 4.2 and solved for ΔV :

$$\Delta V = \frac{cV_{\text{EC}}}{\sigma x P_0 \eta} \quad (4.9)$$

The solution is plotted as ΔV vs x for three values of P_0 corresponding to the total electricity generated in 2018 for Denmark [33], Europe [164], and the world [24].

Clearly, scale matters. If improvements resulting from this PhD project stay in Denmark and the portion of electricity used for hydrogen generation doesn't exceed 5%, then my work needs to be worth a millivolt by itself to pay for its CO₂ cost in a year. On the other hand, if the hypothetical improvement spreads to the whole world and the portion of electricity used for hydrogen generation globally does exceed 5%, then a contribution worth as little as a microvolt will do the trick.

Chapter 5

Conclusion

The Project

Chapter 1 described how greenhouse gas emissions need to be cut fast to avoid disastrous and worsening effects of climate change. To be in line with the ambitions of the Paris agreement, societies should cut emissions to half or less by 2030. In order for progress being made in wind and solar energy to drive sufficient overall emissions reductions, technological solutions are needed to keep the lights on when the wind isn't blowing and the sun isn't shining, and to spread the decarbonization to other sectors including transport and industry. Water electrolysis to make hydrogen for energy storage, fuel, and industrial reactant has the potential to help with all of these needs.

The goal of this PhD project has been to use in-situ techniques to better understand the fundamentals of a number electrocatalytic reactions. I've had the chance to work on the propene oxidation reaction (Paper III), the CO₂ and CO reduction reactions (Papers IV, V), and the hydrogen evolution reaction (Paper VI). However, this Thesis has focused on the oxygen evolution reaction (OER, Papers II and VII). The OER, as the main source of efficiency loss in water electrolysis cells, and as a required counter-reaction for any other fuel-producing electrochemical process, is arguably the most important electrochemical reaction to understand and improve.

EC-MS and isotopes

The tool I've used for most of the work in this PhD project is chip electrochemistry - mass spectrometry, described in Paper I. This technique uses a microscopic sampling volume in a silicon microchip to saturate the electrolyte with inert or reactant gas, and to deliver any evolved gases to the vacuum chamber containing the mass spectrometer. This setup is highly sensitive and features well-controlled mass transport, making it ideal for fundamental studies. (Section 2.1)

Isotope-labeling, which enables the tracking of atoms, is a powerful strategy in catalysis, including electro-catalysis. An experiment that illustrates the possibilities of using chip EC-MS together with isotope labeling is one which confirms the Langmuir-Hinshelwood mechanism for CO electro-oxidation. If a sample with an ¹⁸O-labeled surface oxide layer is reduced in C¹⁶O-saturated H₂¹⁶O electrolyte, there is a transient of C¹⁶O¹⁸O which is formed. This is when *¹⁸O on the surface of the oxide is reduced to *¹⁸OH which reacts with adsorbed *¹⁶O. This experiment can also confirm that a labeled oxide layer is still present in a sample if it is not evolved as ¹⁶O¹⁸O during OER. (Section 3.3.4)

Oxygen evolution experiments

Checking for incorporation of lattice oxygen in evolved O₂ by isotope-labeling is an experiment often used to gain insight into the OER mechanism on electrocatalyst materials (Section 3.3). Such experiments, with a lot of trial and error, have also been an important part of my PhD project. From the literature and from the experience of my own studies, I conclude that the best way to do these experiments is to prepare the OER catalyst with full ¹⁸O labeling and test in un-labeled electrolyte

using a constant-current period of oxygen generation. A control sample which has the natural ratio should be tested first, to ensure that the $m/z=32$, $m/z=34$, and $m/z=36$ signals are as expected by the natural O_2 isotopic distribution. Any excess $m/z=34$ or $m/z=36$ signal in the lattice oxygen evolution experiment should be quantified to get the absolute number of lattice oxygen atoms evolved. The electrolyte used for the isotope exchange experiment should be collected and analyzed by ICP-MS, so that the number of metal atoms dissolved can be compared quantitatively to the number of lattice oxygen atoms evolved. Only if lattice oxygen evolution exceeds metal dissolution can it be concluded that lattice oxygen exchange is part of the catalytic OER mechanism and not a degradation side-process. Finally, the isotopic composition of the electrocatalyst surface after oxygen evolution should be checked - in a truly catalytic process, ^{16}O should be incorporated into the catalyst. (Section 3.4)

Along the way to this procedure, we concluded in Paper II that nickel-iron based electrocatalysts in alkaline electrolyte do not evolve lattice oxygen. Using the recommended procedure, we showed that labeled ruthenium dioxide ($Ru^{18}O_2$) evolves some lattice oxygen but that it is most likely due to a degradation, and not a catalytic, mechanism. Labeled iridium dioxide ($Ir^{18}O_2$), on the other hand, does show a minor catalytic OER mechanism involving lattice oxygen exchange, but it amounts to only one ten-thousandth of the total evolved oxygen. This can only be detected because of the control and sensitivity enabled by the chip EC-MS method.

This sensitivity also allows us to observe oxygen evolution at low overpotential, where other process may mask it in the electrode current. On a high-surface-area ruthenium foam, we observe catalytic O_2 evolution down to 1.29 V vs RHE, a record to the best of our knowledge, though the rates are tiny, i.e., a TOF of $10^{-7} s^{-1}$. The TOF of ruthenium foam together with a series of sputtered RuO_2 films tested the same way fall on a shared TOF-vs-potential curve which we measured over seven orders of magnitude. This curve has a high and increasing potential dependence at very low overpotentials, which we hope will be useful input for rational OER catalyst design. (Section 3.2)

Net CO_2 impact

But does all this work do any good? This is the question that the previous two Sections of this final Chapter have sought to answer. The question was simplified to consider only one metric: net CO_2 ; and to only consider one effect: an improvement in water oxidation efficiency. This PhD project has been a CO_2 -intensive one due to a lot of traveling and high electricity consumption of the chip EC-MS setup. However, using results from an energy systems model of Europe for the year 2030, I found that the approximately 122 tons of CO_2 emitted during this PhD are avoided in one year (the year 2030) if they can be attributed just an 0.03 mV improvement in the OER overpotential of electrolysis cells.

Since the results presented here have a non-zero chance of contributing to a breakthrough worth much more than that, I think this is not too optimistic an expectation value. Furthermore, this is without taking into account the value of the other projects and of the education, both my own education and the teaching and supervising I have done as part of this PhD program. I think it is therefore highly likely that this PhD project has done net good. There are, of course, lots of uncertainties involved - even in the aspect of my research that I chose for this calculation because I thought it the least uncertain. However, I think it could be good practice to consider, informally, how to maximize the net CO_2 benefit of research projects.

Appendix A

Setup and technique details and instructions

The following procedures assume that the setup, hardware configuration, and Software interfaces have not changed since the publishing of this Thesis.

A.1 Sniffer setup at DTU

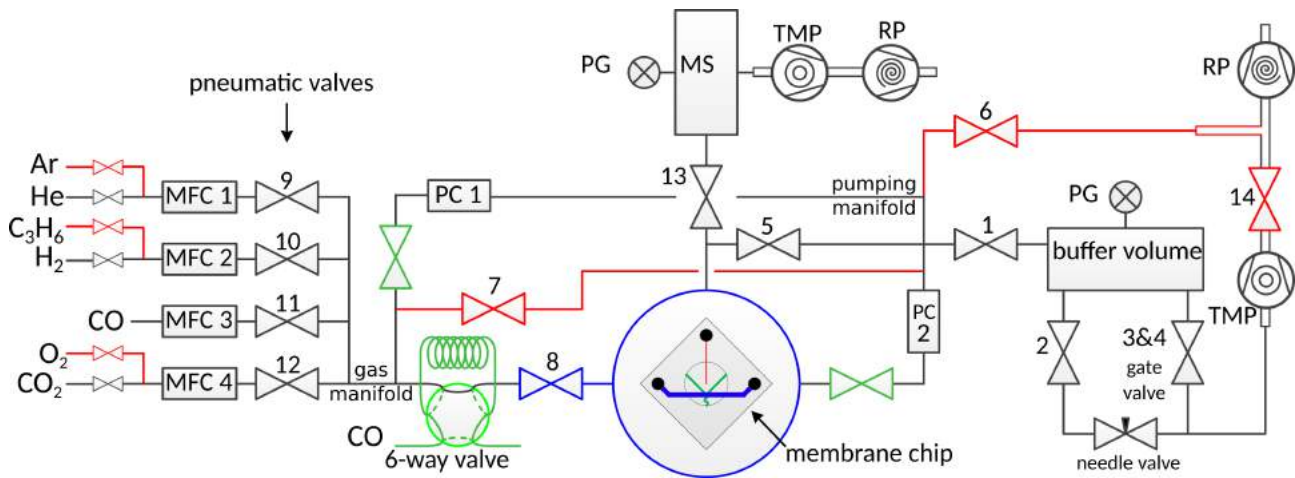


Figure A.1: Valve diagram of EC-MS setup at DTU. Adapted from Paper I. Red: components installed since that publication. Green: The 6-way valve was removed since then as well as the pneumatic valves before the pressure controllers, which were re-purposed. Blue: The interface block, as well as the valve right before it, were replaced to minimize the intervening volume, enabling faster exchange of gases.

Figure A.1 shows a valve diagram of the sniffer setup. Most of this setup was built during Daniel Trimarco’s PhD project [74], and described in Paper I. Colors indicate the parts that I have removed (green) or added (red) since Paper I’s publication.

On the left of the diagram are mass flow controllers (MFC’s) which can be used to switch between up to four gases at time. Switching between gases sharing an MFC, f.eks. Ar and He, requires pumping down behind the MFC through a line not shown. Moving right, we refer to the volume between Valves 7, 8, 9, 10, 11, and 12 and PC 1 as the *gas manifold*. The gas manifold can be evacuated through Valve 7 and filled up from one of the MFC’s while regulating the pressure with a pressure controller (PC), PC1.

Carrier gas from the gas manifold enters the interface block via Valve 8. The interface block guides it through the carrier gas reservoir channel of the chip, from which it fills the chip’s sampling volume and saturates the electrochemical environment. Fast carrier gas exchange thus requires that the volume between valve 8 and the chip, the *carrier gas inlet volume* is as small as possible. This is because the carrier gas inlet volume, unlike the gas manifold, cannot be pumped down, as the resulting vacuum in the sampling volume of the chip would suck in electrolyte. The design of the carrier gas inlet volume can also be optimized with regards to flow patterns to minimize mixing of the old and new carrier gas.

We refer to the volume between PC1, PC2, and Valves 1, 5, 6, and 7 as the *pumping manifold*. There are actually three possible ways to pump on the pumping manifold: (1) Directly to the *roughing pump* (RP) through Valve 6, or (2-3) through a buffer volume and then a *turbo molecular pump* (TMP or just turbo pump) via either a (2) valve 2 and a needle valve or (3) a gate valve.

During operation, carrier gas is flowing from the gas manifold to the pumping manifold through the chip, and its pressure is regulated by PC2, which is set to 1 bar for all of the experiments in this Thesis. Excess carrier gas flows through PC2 to the pumping manifold where it is ultimately removed through the roughing pump, typically via the buffer volume and needle valve, so that valve 14 can remain open.

When a new chip is installed, the *post-capillary volume* bound by the chip, Valve 13, and Valve 5 is vented to atmospheric pressure, and must be pumped down to high vacuum before connecting the experiment to the mass spectrometer. The mass spectrometer is always held at high vacuum by its own designated turbo and roughing pumps. The mass spectrometer of the sniffer setup is a Pfeiffer QMA125.

The procedures for chip pump-down and carrier gas exchange are described below.

An unusual feature of the sniffer setup, as mentioned in that Section, is that there are three ways to pump on the pumping manifold. Of these options, the direct roughing pump connection is the only one that can quickly remove a large amount of gas, as this would damage the turbo pump. Valve 14 should be closed while gas is fed directly to the roughing pump, as the pressure behind the turbo pump must also be kept low during operation. On the other hand, the turbo pump is required to reach high vacuum, which it can do slowly for a moderate amount of gas through the needle valve or quickly for a small amount of gas through the gate valve.

A.1.1 Changing chip

The procedure on this setup to change a chip is as follows:

1. Isolate the chip: Make sure that Valves 13, 5, and 8 are closed, that no carrier gas is flowing, and that PC2 is closed (set to 2 bar). Double-check that Valve 13 is closed!!!
2. Remove the old chip and put on the new chip.
3. Close valves 1 and 14 and open valve 6 to connect the pumping manifold to the roughing pump. (The gate valve should be closed.)
4. Open valve 5. This very quickly removes the majority of the gas from the post-capillary volume
5. Close valve 6 and open Valve 1. Open valve 14.
6. Check the pressure displayed on the pressure guage (PG) of the buffer volume. The pressure in the buffer volume should already be less than 1 mbar. If not, the chip has not been installed correctly. If so, close valves 1 and 5 and start over.
7. If the pressure in the buffer volume is greater than 0.3 mbar, start pumping through the needle by opening Valve 2.
8. When the pressure in the buffer volume is less than 0.3 mbar (as will usually be the case right away after first roughing on the pumping manifold), open the gate valve. This is done by first deactivating 4 and then activating 3.
9. When the pressure in the buffer volume is less than 0.0001 mbar, we can open to the mass spectrometer. Make sure that Valves 1 and 5 are open (so that the pressure on the buffer volume is equal to the pressure in the post-capillary volume), and open Valve 13.
10. Immediately close Valve 5. This avoids making any subsequent mistake in which carrier gas enters the mas spectrometer via the pumping manifold. Also, close the gate valve. This is done by first deactivating 3 and then activating 4.

A.1.2 Changing carrier gas

The procedure on this setup to change carrier gases is as follows. We will use the example of changing from He to H₂. This is what is done in Figure 2.5.

1. At first, He is flowing through MFC1 at 1 ml/min and continues through Valve 9, Valve 8, the chip, PC2 (set to 1 bar), Valves 1 and 2, the turbo pump, Valve 14, and the roughing pump.
2. Close valve 8. There is a reservoir of He in the interface block which will continue to fill the sampling volume of the chip for some time. Thus, the electrochemistry experiment can continue and the electrode “won’t notice” that anything is going on.
3. Stop the He flow by setting the flow on MFC 1 to zero. Valve 9 will automatically close.

4. Close Valves 1, 2, and 14. Open Valve 6.
5. Open Valve 7. This evacuates the He from the gas manifold.
6. Flush once with H₂. This can be done by setting the flow on MFC 2 to -1, which will be interpreted as “go to purge mode for 1 second”.
7. Close Valve 7.
8. Fill up the gas manifold with H₂. This is most quickly done by using the purge function. The purge time required is different for each gas. If you are unsure, enter -0.5 in the MFC, see how the pressure measured by PC1 increases, and then scale up the purge time accordingly. When the pressure is close to 1 bar, use normal flow (positive number for the MFC) to fill it up the rest of the way.
9. If you overfill the gas manifold, such that the pressure read at PC 1 is significantly greater than 1 bar, this should be corrected, as a pressure difference when Valve 8 is opened seems to cause more mixing in the carrier gas inlet volume. Use PC1 to lower the pressure to 1 bar.
10. When the pressure in the gas manifold is 1 bar: open Valve 8 and immediately set the MFC to its maximum flow value (10 ml/min for most MFC's). The change of carrier gas should be immediately apparent in the mass spectrometer signals.
11. When the He level has dropped to background level (or by three orders of magnitude), lower the H₂ flow rate to 1 ml/min. Note that the remaining He signal likely comes more from He dissolved in the electrolyte in the outer volumes of the cell, and not necessarily the carrier gas. If so, the rate at which the remaining He signal continues to drop should not depend on the carrier gas flow rate.
12. Close Valve 6, and open Valves 1, 2, and 14. The setup is now in steady operation in the new carrier gas.

A.2 ECMS-200A at CAS in Fuzhou

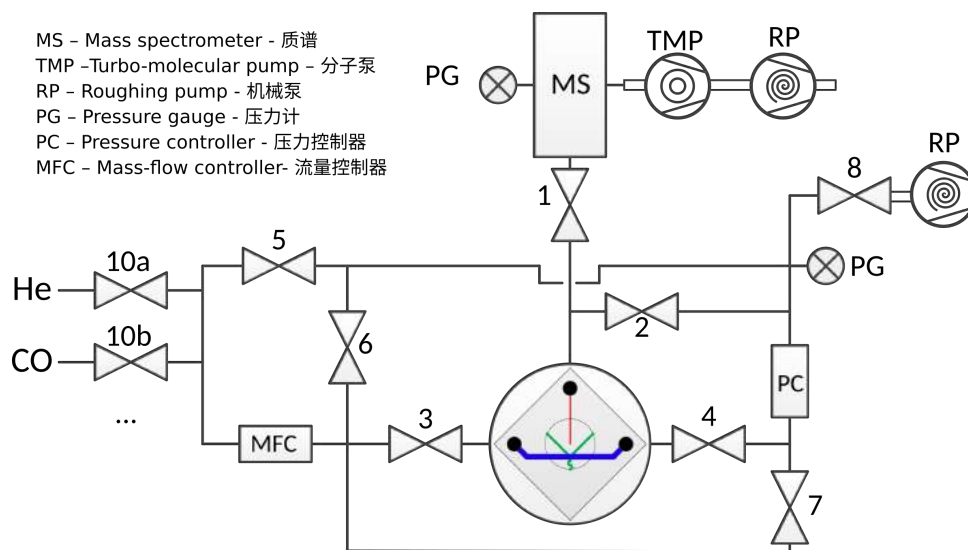


Figure A.2: Valve diagram of EC-MS setup at Fuzhou. In reality, at the time of writing this thesis, the pressure controller is actually a modified pressure regulator, which works but is not as stable.

The sniffer setup described above can be considered a “delux setup” with an excess of components to maximize functionality. The group in Fuzhou asked me to design a “budget setup” which captured the central advantages of chip EC-MS with as few components as possible. They then built my design, shown in Figure A.2 with the outside help from a Chinese mass spectrometer company, Quantang Instruments. Much to my frustration, Quantang built a box around the valve system, making it quite tedious to make changes to the system, and put their logo and the name ECMS200A on the box.

All of the concepts are the same as for the sniffer setup, but the operation is different. The procedures for chip pump-down and carrier gas exchange are described in Appendix A.2. The cost of having one less Turbo pump is the need to wait for long pumping periods and to turn off the filament of the mass spectrometer when changing chips. The carrier gas exchange procedure is actually slightly simpler than that of the sniffer setup and saves three MFC’s and a PC. The only disadvantage is that, with only one MFC, it is not easy to prepare a controlled gas mixture (a functionality I have rarely used on the sniffer setup).

A.2.1 Changing chip

The procedure to change chip is as follows:

1. Isolate the chip: Close Valves 1, 2, 3, and 4. Double-check that Valve 1 is closed!!! Also, turn off the filament of the mass spectrometer
2. Remove the old chip and install the new one.
3. Open valve 2 (Valve 8 is normally always open). This removes air from the post-capillary volume through the roughing pump.
4. Wait until the pressure is less than 0.01 mbar (1 Pa, the unit on the Chinese displays). This takes approximately half an hour.
5. Double check that the filament of the mass spectrometer is turned off, as the roughing pressure could damage it. Then open Valve 1.
6. Immediately close Valve 2.

7. When the pressure in the mass spectrometer is less than 10^{-5} mbar (10^{-3} Pa), turn on the filament again. After this, it will take a couple hours before the MS signals are stable.

A.2.2 Changing carrier gas

The procedure for changing carrier gases (with He to CO as an example) is as follows:

1. At first, He is flowing through Valve 10a, the MFC (set to 1 ml/min), Valve 3, the chip, Valve 4, the pressure controller set to 1 bar (actually a pressure regulator, adjusted to maintain 0 vs atmosphere), Valve 8 and the RP.
2. Close Valves 3 and 4. The electrochemistry experiment can then continue in He while getting the new carrier gas ready.
3. Close Valve 10a and set the MFC to zero.
4. Pump out the He. This involves opening Valves 5, 6, and 7, and setting PC to zero.
5. Close Valves 5 and 6 and set PC to 1 bar.
6. Fill up CO: Open Valve 10b. Then set the MFC to 10 ml/min. flow until the pressure read at PC is 1 bar.
7. Close Valve 7 and open Valves 3 and 4. The carrier gas change should immediately be visible
8. Set the CO flow to 1 ml/min. The setup is now in steady operation in CO carrier gas.

A.3 Spectro Inlets



Figure A.3: Photos of the setup at Spectro Inlets ApS. From their website: <https://spectroinlets.com/>

Finally, I should mention that there is now a commercially available setup which combines the best of both worlds: The functionality of the Sniffer setup and the simplicity and compactness of the ECMS200A. This is made possible in part due to some custom vacuum components. The setup, sold by Spectro Inlets ApS, is shown in the photographs in Figure A.3. I have been involved in conversations aiding the development of this setup, as a kind of test user, but can't go to detail here on its design. The Spectro Inlets setup also comes with a software automating the chip pump-down and carrier gas exchange procedures. The procedures described in Appendix A for the other two setups are thus simplified to pressing a button.

A.4 Sputtering Ru¹⁸O₂ and Ir¹⁸O₂

This appendix serves as the sample prep methods for most of Chapter 3, as well as instructions for sputter deposition using ¹⁸O₂.

A.4.1 Switching O₂ source

First, prepare the reactant gas. This requires a pump-down step to avoid mixing the natural O₂ and the 99% ¹⁸O₂.

1. Make sure the flow is off (AJA software) and the reactant gas valve on the top of the sputter chamber (manually controlled) is open!
2. Make sure both the natural oxygen (¹⁶O₂) and ¹⁸O₂ valves nearest the switch (the T intersection just before the flow controller) are closed.
3. Evacuate the switch through the sputter chamber. This is a bit tedious because the AJA software will try to close the pneumatic valve when the flow doesn't reach set point. First flow at 10 ml/min until there is so little gas that this flow rate cannot be met. Then set it to 0.5 ml/min and leave it for an hour. The AJA software seems to have a tolerance of 0.5 ml/min before automatically closing the valves, so this will leave it open.
4. Turn off the flow with the AJA software.
5. Open the valve connecting the desired O₂ source to the switch.
6. If you are using ¹⁸O₂, briefly open the valve on the bottle and close it again. The ¹⁸O₂ in the line should then be enough for depositing a film, and this will avoid making a mistake that would waste the remaining gas.

A.4.2 Deposition

The sputter deposition process for nominally 25 (10) nm of Ru¹⁸O₂ (Ir¹⁸O₂) is as follows:

1. Load the samples via the load lock, and heat the samples to the desired temperature. 400°C gives crystalline, rutile films.
2. Pre-clean the chamber with an argon plasma for 5 minutes. Use 20 ml/min Ar, 20 mTorr, and 35 Watts.
3. Put the screen in front of the samples. Sputter titanium. Use 20 ml/min Ar, 3 mTorr, and 160 W. You may need to start the plasma at 10 mTorr and then ramp down. This step is to remove any residual oxygen in the chamber to achieve isotopic purity. (This step can be skipped when not doing isotope-labeled films.)
4. After titanium has been sputtering for 15 minutes, remove the screen and allow it to keep sputtering, now onto the samples, for another three minutes. This establishes a ≈ 5 nm thick Ti sticking layer. After three minutes, close the shutter again and keep sputtering Ti for another three minutes before turning off the Ti plasma.
5. Increase the pressure to 5 mTorr and lower the Ar flow rate to 5 ml/min.
6. Start the plasma on the Ru (Ir) target. Use 60 W (30 W).
7. Start the ¹⁸O₂ flow at 1 ml/min.
8. Open the shutter to the Ru (Ir) target.

9. Time 1500 s (700 s), and then close the shutter
10. Turn off the plasma.
11. Turn off the gas flows.
12. Let the samples cool before taking them out through the load lock.

A.5 ICP-MS

Briefly, the electrolyte in the cell is sucked out with a syringe while new electrolyte flows in from an electrolyte delivery tower. The old electrolyte stored in an Eppendorf tube and the syringe is re-inserted. This results in electrolyte samples of ≈ 0.5 ml in Eppendorf tubes.

For study with ICP-MS, the raw samples are first diluted to a standard volume of 1 ml with 2% HNO_3 , 0.1 ml of this is then diluted to 10 ml with 2% HNO_3 , which is the ICP-MS sample. The concentration of this ICP-MS sample is then as if all of the metal dissolved during the experiment were diluted in 100 ml. The amount of metal n^i (typically stated in pmol) can then be determined from its mass concentration c_m^i in the ICP-MS sample (typically stated in μg per l which is numerically equivalent to ppb) by

$$n^i = 100 [\text{ml}] \frac{c_m^i}{M^i}, \quad (\text{A.1})$$

where M^i is the molar mass of i .

To determine c_m^i from the raw signal (in counts) requires calibration. A dilution series (typically 0.1, 1, 10, and 100 $\mu\text{g}/\text{l}$) is prepared from a standard stock solution. These are measured together with the samples and intervening measurements a blank solution (2% HNO_3 in water with no metals). The calibration curve is made by drawing a line of best fit through the counts vs concentrations of this dilution series on a log-log plot (the slope of this line should be 1). Typical calibration curves for Ir and Ru are shown in Figure A.4. These calibration curves are made using the function `ICPMS_calibration` of the `EC_MS` python package (see Appendix C.1).

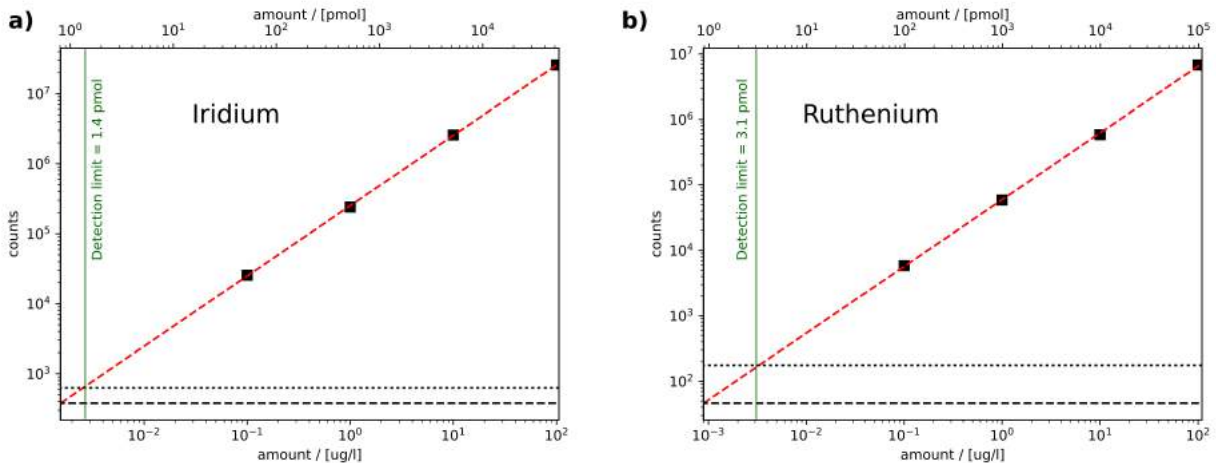


Figure A.4: Calibration curves for ICP-MS detection of (a) Ir and (b) Ru. The top x-axes represents the amount of metal originally in a sample from the EC-MS setup, and is scaled to the bottom x-axis according to Equation A.1. The dashed black line is the mean number of counts in blank measurements, and the dotted black line is that mean plus three times the standard deviation of the number of counts in the blank measurement. The detection limit, defined as where the latter intercepts the calibration curve, is indicated with a green vertical line.

The detection limit is defined as the amount corresponding to the counts of the blank measurements plus three times the standard deviation of counts the blank measurements [64]. This is 1.4 pmol for Ir and 3.1 pmol for Ru.

A.5.1 Electrolyte sampling

It is possible with the sniffer setup to take electrolyte samples out under potential control for analysis with ICP-MS. This requires an electrolyte delivery bottle on one side and a syringe on the other side, as shown in Figure 2.28 on Page 58. To set this up (items 1 through 4 are the standard procedure):

1. Align the sample in the cell

2. Mount the cell on the interface block
3. Fill the cell with electrolyte using the syringe
4. Insert the RE and CE glassware when the electrolyte forms a meniscus in the Luer fitting
5. When there is a meniscus of electrolyte coming out of the outlet (male Luer fitting), very quickly open the valve on the electrolyte delivery tower and push the tube onto the Luer fitting, connecting the tower and the cell. This should be done quickly to minimize spilling. Clean up any spill right a way with a paper wipe.
6. Close the valve.

It is important that valve is open while the electrolyte delivery tower is connected the cell to avoid developing an overpressure which could breach the chip. It is good for it to be closed during the experiment, or the pressure of the electrolyte above the valve can push electrolyte into the cell and exacerbate any leaks that might be present.

To take an electrolyte sample:

1. Open the valve to the electrolyte delivery tower
2. Pull 0.5 ml of electrolyte with the syringe. Do so as steadily as possible to avoid making an underpressure which could pull carrier gas from the chip into the working volume. Bubbles are the enemy!
3. Remove the syringe and close the valve of the electrolyte delivery tower as fast as possible to minimize spillage. Clean up any spillage.
4. Empty the syringe into an eppendorf tube or other storage. This is your sample for ICP-MS.
5. Very quickly open the valve to the electrolyte delivery tower and quickly re-insert the syringe.
6. Close the valve. You're ready to take the next sample when the time comes.

Appendix B

Papers from this PhD Project

Paper I Enabling real-time detection of electrochemical desorption phenomena with sub-monolayer sensitivity

Daniel B. Trimarco*, Soren B. Scott*, Anil H. Thilsted, Jesper Y. Pan, Thomas Pedersen, Ole Hansen, Ib Chorkendorff, and Peter C.K. Vesborg.

*These authors contributed equally to this work

Electrochimica Acta, 2018, 268, 520-530

DOI: 10.1016/j.electacta.2018.02.060

an



Enabling real-time detection of electrochemical desorption phenomena with sub-monolayer sensitivity



Daniel B. Trimarco ^{a, b, 1}, Soren B. Scott ^{a, 1}, Anil H. Thilsted ^b, Jesper Y. Pan ^c, Thomas Pedersen ^c, Ole Hansen ^c, Ib Chorkendorff ^a, Peter C.K. Vesborg ^{a, *}

^a Department of Physics, Technical University of Denmark, Fysikvej, Building 312, DK-2800 Kgs. Lyngby, Denmark

^b Spectro Inlets ApS, Fysikvej, Building 312, DK-2800 Kgs. Lyngby, Denmark

^c Department of Micro- and Nanotechnology, Technical University of Denmark, Ørstedes Plads, Building 344, DK-2800 Kgs. Lyngby, Denmark

ARTICLE INFO

Article history:

Received 22 December 2017

Received in revised form

6 February 2018

Accepted 12 February 2018

Available online 15 February 2018

Keywords:

Mass spectrometry

DEMS

OLEMS

Platinum

Electrocatalysis

ABSTRACT

Electrochemical reactions play an increasingly important role in sustainable energy conversion and chemical synthesis. Better understanding of catalytic mechanisms at electrode surfaces is thus important for the transition to a clean-energy economy, but is hindered by the difficulty of real-time detection of reaction products and intermediates during electrochemistry experiments. Herein, we present a new type of electrochemistry – mass spectrometry (EC-MS) based on a versatile gas inlet to vacuum fabricated onto a silicon microchip, and compare it to established techniques with focus on sensitivity, time response, and mass transport. The inlet system is able to capture reactant molecules directly from an electrode surface and pass them on to a mass spectrometer on a sub-second time scale with 100% collection efficiency for quantitative analysis with unprecedented sensitivity. The high sensitivity and fast time-response, coupled with well-characterized mass transport of both reactants and products in this setup enables sub-turnover resolution for analysis of electrochemical reactions. The technology and concepts presented here can serve as a platform to improve in-situ mass spectrometry in electrochemistry as well as other fields.

© 2018 Elsevier Ltd. All rights reserved.

1. Introduction

A transition from fossil fuels to sustainable energy sources like wind and solar and sustainable chemical feedstocks like water, carbon dioxide, and biomass is strictly necessary to avoid catastrophic climate change [1]. This transition is bringing a drastic change in the global energy landscape, causing electrochemical and biochemical processes to play an increasing role [2–4]. In order to improve the economics of sustainable energy conversion and chemical synthesis, it is thus important to expand fundamental understanding of electrochemical and biochemical processes.

Electrochemical and biochemical processes are generally run in wet environments at or above ambient pressure, while the most versatile tool for identifying and quantifying the reaction products, mass spectrometry, requires high vacuum [5]. A wide range of

sample introduction and ionization methods have been developed that are suitable for product identification and quantification by mass spectrometry after a batch reaction [6], but experiments investigating reaction kinetics and catalytic mechanisms in electrochemistry and biochemistry can be greatly facilitated by in-situ and real-time, i.e., second-timescale, product detection in a small reaction volume [7,8]. This underscores the need for fast, sensitive, and quantitative real-time delivery of reaction products from a liquid test environment to high vacuum [9]. As electrochemical experiments using modern instrumentation allow for finely controlled and near-instant experimental input and output in the form of electrode potential and electric current, electrochemistry – mass spectrometry (EC-MS) thus serves as a natural platform for the refining of real-time mass spectrometry methods which can then be adopted in other fields.

Membrane inlet mass spectrometry (MIMS), the earliest technique for studying dissolved analytes with mass spectrometry, which remains widely used in environmental and bio-analytical applications, was also applied to electrochemistry early on [10]. In MIMS, the liquid testing environment is separated from the

* Corresponding author.

E-mail address: peter.vesborg@fysik.dtu.dk (P.C.K. Vesborg).

¹ These authors contributed equally.

vacuum of the mass spectrometer by a semipermeable polymer membrane. To protect the vacuum, the membrane must be thick enough to prevent excessive permeation of the solvent, but as the analyte also must diffuse through the membrane, this slows the response time, generally up to several minutes [11]. A much faster response time was later achieved by the use of a porous polytetrafluoroethylene (PTFE) membrane [12], but the correspondingly higher flux of solvent and analyte across the membrane necessitated a differential pumping stage, forming the basis of differential electrochemical mass spectrometry (DEMS), where the term “differential” emphasizes that the mass spectrometer signal represents a snapshot of the analyte concentration at the membrane [13]. DEMS has since been developed extensively, particularly through the work of Helmut Baltrusch and coworkers [14–16], and has become a widely used method in electrocatalysis research [17–20]. DEMS has proven especially useful in fundamental electrochemical studies, for example comparing the product distribution of a Faradaic process on different crystal facets [21–23]. A notable variation on DEMS, termed on-line mass spectrometry (OLEMS), developed by Marc Koper and coworkers [24–26] and now used by several groups [27,28], involves a small PTFE vacuum inlet at the end of a glass tube as an EC-MS probe, scaled such that the flux to the mass spectrometer is sufficiently small that no differential pumping is needed.

Much of the development in DEMS the past three decades has focused on the cell that interfaces the electrochemical experiment and the vacuum inlet. In the original DEMS experiments, the working electrode was sputtered onto the PTFE membrane of the vacuum inlet [13], giving the fastest possible time response but complicating construction of the interface and restricting the materials that could be studied. The advent of a stagnant thin-layer cell [14] made it possible to perform DEMS on smooth electrodes, but effects of solvent evaporation made it difficult to perform experiments in a controlled environment. This was remedied by the advent of a dual thin-layer flow cell in which the working electrode and vacuum inlet are in separate compartments [29]. This dual thin-layer flow cell also served as a platform for combining DEMS with other analysis methods such as electronic quartz crystal microbalance [29] and attenuated total reflection-infrared spectroscopy [30], but always with stringent requirements on the working electrode. A subsequent modification made it possible to choose working electrodes of various sizes in DEMS, including single-crystals [31], a flexibility also offered by OLEMS, though with a less well-defined geometry for mass transport [24]. Another design of a dual-layer DEMS flow cell focused on the electrode geometry, incorporating a counter electrode parallel to and separated from the working electrode by a membrane, though requiring specialized electrode geometries [32].

Before describing the vacuum inlet system and electrochemical cell behind our new version of EC-MS, we wish to introduce a conceptual framework motivating their design. The three components of a standard quadrupole mass spectrometer (QMS): (1) electron impact ionization (EI), (2) quadrupole mass separation, and (3) detection by a secondary electron multiplier (SEM); all require high vacuum to operate. Above a pressure of approximately $p_v^0 = 10^{-6}$ mbar, mass spectra become less reproducible and signals no longer respond linearly with the amount of analyte [5]. This sets a maximum flux of molecules into the vacuum chamber of the mass spectrometer, dependent on the pumping speed. With the turbo pump used in this paper, which has a pumping speed of $S_{\text{pump}} = 50$ l/s, representative of standard turbo pumps for compact vacuum systems, the maximum desired flux into the vacuum chamber is

$$\dot{n}_v^{\text{desired}} = \frac{1}{RT} p_v^0 S_{\text{pump}} \approx 2 [\text{nmol/s}], \quad (1)$$

where R is the gas constant and $T = 298.15$ K is the absolute temperature. Considerations of the SEM and the EI filament longevity also encourage a maximum flux not much higher than this value [33].

In comparison, the production rate of gaseous analytes (hydrogen evolution on platinum, for example) under typical laboratory conditions (current density of $j^{\text{expected}} = -1$ mA/cm² and electrode area of $A_{\text{el}} = 0.2$ cm²) happens to be

$$\dot{n}_{\text{el}}^{\text{expected}} = \frac{1}{-2\mathcal{F}} j^{\text{expected}} A_{\text{el}} \approx 1 [\text{nmol/s}], \quad (2)$$

where \mathcal{F} is Faraday's constant. In other words, the expected analyte production rate during conveniently-scaled electrochemistry experiments happens to be on the same order of magnitude as the allowable influx to the mass spectrometer of a conveniently-scaled vacuum system. This implies that it should be possible to have 100% collection efficiency, i.e. $\eta = 1$, while maintaining an arbitrarily fast time response. Accepting this framework, a clear drawback of both DEMS and OLEMS becomes clear. Since the porous Teflon membranes employed allow a significant amount of solvent evaporation, the analyte will only make up a small portion of the influx to vacuum, and so the influx of analyte to the mass spectrometer must be kept below $\dot{n}_v^{\text{desired}} \sim \dot{n}_{\text{el}}^{\text{expected}}$. This is done either by differential pumping, as in DEMS, lowering the vacuum collection efficiency, η_v ; or by limiting the total influx to vacuum, as in OLEMS, lowering the membrane collection efficiency, η_m . Either way, the overall collection efficiency $\eta = \eta_m \eta_v$ is lowered. The use of a flow cell also lowers the membrane collection efficiency, as some analyte escapes in the downstream flow [15].

To give a sense of how $\dot{n}_v^{\text{desired}} \sim \dot{n}_{\text{el}}^{\text{expected}}$ compares to the expected magnitude of transient surface phenomena interesting for surface characterization and electrocatalysis, the number of surface atoms in $A_{\text{el}} = 0.2$ cm² of Pt (111) is about 3×10^{14} , or 0.5 nmol. A monolayer desorption event lasting on the order of a second thus corresponds to a flux on the same order of magnitude as $\dot{n}_v^{\text{desired}} \sim \dot{n}_{\text{el}}^{\text{expected}}$. We refer to the ability to resolve and quantify less than one monolayer of gaseous products on a scale of seconds as *sub-turnover resolution*. In this paper, we present technology enabling sub-turnover resolution for gaseous analytes with 100% collection efficiency, together with full and fast control of dissolved gases at the working electrode. We also present methods for accurate quantification with this system and demonstrate a predictive mass transport model. We anticipate that the technology and concepts presented here will serve as a platform for further improvements in EC-MS, and eventually for in-situ mass spectrometry in other fields as well.

2. Technical

2.1. Membrane chip

Our strategy for achieving a fast and lossless transfer of dissolved gases from the liquid of the test environment to the high vacuum needed for mass spectrometry takes place in two steps. First, the liquid equilibrates across a perforated membrane with a microscopic gas-phase *sampling volume*, allowing any dissolved gases near the membrane to quickly evaporate. Second, gas in this sampling volume is continuously transported through a capillary to the vacuum chamber of the mass spectrometer. The membrane,

sampling volume, and capillary are microfabricated into a silicon *membrane chip* using the standard and scalable clean-room techniques of UV lithography, deep reactive ion etching, hydrofluoric acid etching, anodic bonding, and molecular vapor deposition. The membrane is described briefly here. Other membrane chip design parameters as well as its fabrication are described in the supplementary information and in more detail elsewhere [34,35].

A photograph of the top of the membrane chip is shown in Fig. 1a, where the membrane, which has a diameter of 7 mm, shows up as a colorful region due to the diffraction of visible light caused by its microstructure. This structure is shown as a scanning electron microscope image in Fig. 1b. Densely spaced holes 2.5 μm in diameter ensure a large surface area to equilibrate with the outside environment while support pillars 50 μm in diameter provide mechanical stability to the membrane, holding it above the 3 μm high sampling volume below. The entire membrane and sampling volume are coated in a hydrophobic self-assembled monolayer (perfluorodecyltrichlorosilane, FDTs) so that an aqueous testing environment immediately above the membrane can be held out of the chip so long as the pressure difference is less than 0.3 bar across the membrane. The sampling volume connects to the mass spectrometer through an outlet in the center which leads to the capillary on the backside of the chip (see Fig. S1).

Fig. 1c is a schematic diagram of the membrane chip in operation. When the membrane is covered by a liquid testing environment, the sampling volume equilibrates with the liquid, such that the solvent vapor is present in the sampling volume at its vapor pressure, and all dissolved gases and volatile species are (in the ideal approximation) present in the sampling volume at partial pressures proportional to their concentration immediately outside the membrane according to Henry's law of volatility,

$$p_{\text{chip}}^i = K_{\text{H}}^i c^i(0), \quad (3)$$

where K_{H}^i is the Henry's law volatility constant for analyte i (in units $\text{bar} \cdot \text{l} / \text{mol} = \text{bar} / \text{M}$), $c^i(0)$ is its concentration at the membrane, and p_{chip}^i is its partial pressure in the sampling volume of the membrane chip. When the total equilibrium pressure is below ambient pressure, an auxiliary gas is needed to make up the pressure difference and avoid sucking liquid into the chip. This gas, referred to as a *carrier gas* (even though its function is to pressurize the chip, and not to assist in convective transport), is delivered to the rim of the sampling volume, and its composition and pressure are controlled externally (see Figs. S1 and S2). Helium is typically used as an inert carrier gas, as its mass spectrum does not overlap

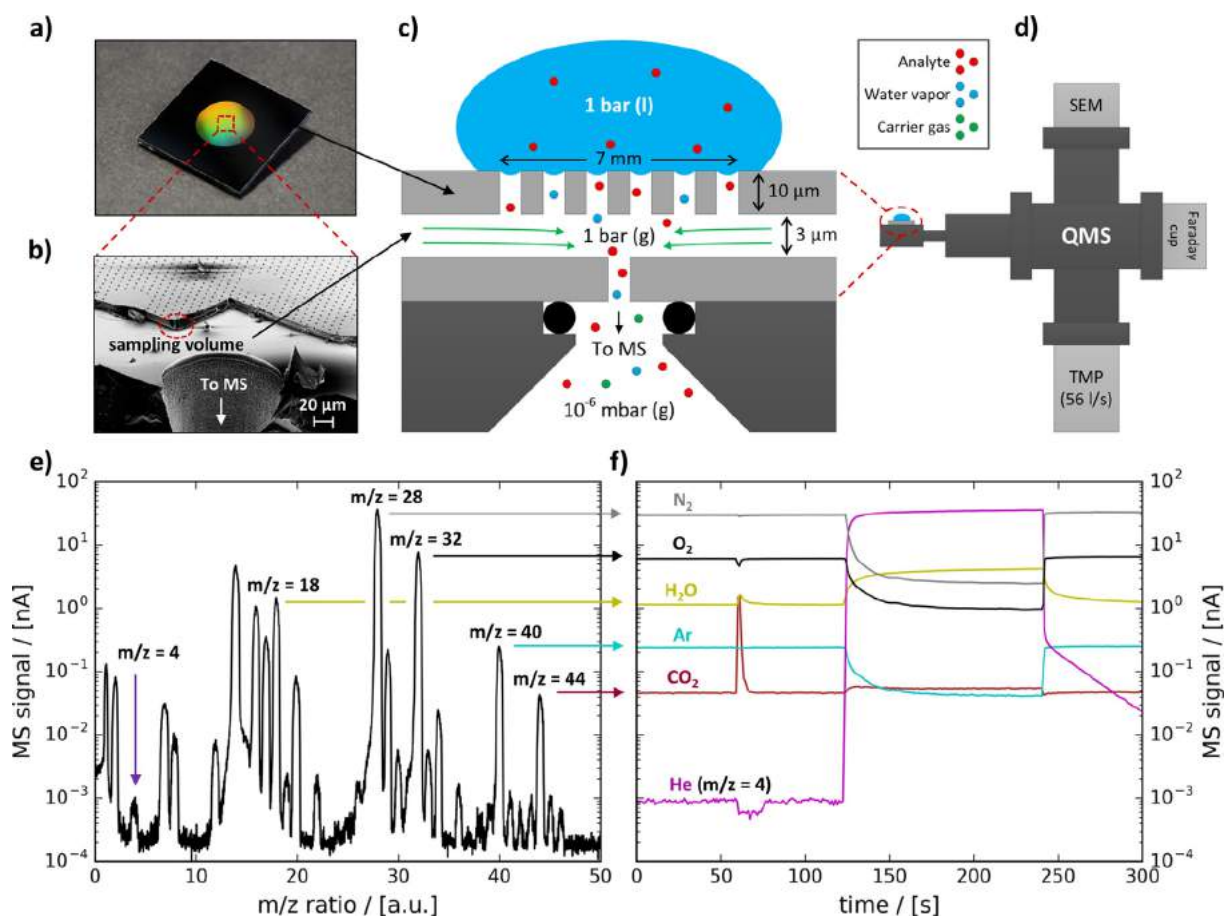


Fig. 1. Membrane chip and working principle. a, Photograph of the membrane chip. b, Scanning electron microscope image revealing internal microstructure of the membrane chip, cut across the middle. The sampling volume is made apparent by the shadow below the membrane, seen clearly in the red circle. c, Schematic diagram of the membrane chip under a drop of water (blue) containing dissolved analyte (red). Carrier gas (green) enters the sampling volume bringing the pressure up from the combined equilibrium pressure of water and analyte to atmospheric pressure. Carrier gas, water vapor, and analyte are delivered from the sampling volume through the membrane chip's capillary to the vacuum chamber. d, Schematic diagram showing the membrane chip (grey) mounted on a vacuum chamber with a quadrupole mass spectrometer (QMS). e, Mass spectrum taken while the membrane chip is uncovered and sampling air. Indicated masses are monitored as a function of time in f. The experimenter exhales on the membrane at approximately 60 s, and a drop of water is placed on the membrane at approximately 120 s. (For interpretation of the references to color in this figure legend, the reader is referred to the Web version of this article.)

with those of other molecules of interest.

The membrane chip is interfaced with the vacuum chamber of the mass spectrometer as indicated in Fig. 1d. The capillary is designed such that the total flux to the mass spectrometer, \dot{n}_v^0 , is approximately equal to the maximum operation flux described above. The actual flux through the capillary of the membrane chip was determined to be 2.1 nmol/s for air and 2.6 nmol/s for helium by benchmarking against a calibration chip [36], as described in the supplementary information. The latter value will be assumed below unless otherwise stated:

$$\dot{n}_v^0 = 2.6 \text{ [nmol/s]}. \quad (4)$$

The working principle of the chip is demonstrated in its simplest form in Fig. 1e and f. Fig. 1e shows a mass spectrum taken with the membrane chip open to air, plotted on a semi-log scale. The main signals include those due to N_2 at $m/z = 28, 14$, and 29 ; O_2 at $m/z = 32, 16$, and 34 ; H_2O at $m/z = 18, 17, 16, 2$, and 1 ; Ar at $m/z = 40$ and 20 ; and CO_2 at $m/z = 44$. The signals at select m/z values are monitored as a function of time in Fig. 1e. At $t = 60$ s, the experimenter exhales on the membrane, resulting in an increased flux of CO_2 which is seen as a spike in the signal at $m/z = 44$. At $t = 120$ s, the experimenter places a drop of water on the chip, covering the membrane. While the water signal at $m/z = 18$ increases, the signals at $m/z = 28, 32$, and 40 drop as the dissolved N_2, O_2 , and Ar near the membrane are depleted through the chip. As air can no longer enter the sampling volume, carrier gas, in this case He, makes up the pressure difference, seen as a dramatic increase in the signal at $m/z = 4$. The drop is removed at 240 s, and air once again displaces He in the chip.

2.2. Stagnant thin layer electrochemistry cell

In order to use the membrane chip as a tool for in-situ monitoring of gas-evolving reactions on an electrode surface, we developed the stagnant thin-layer cell illustrated in Fig. 2. The cell secures a sample, the *working electrode*, in a position parallel to and close to the membrane. The working electrode, any disk 5 mm in diameter, is mounted in the cell as illustrated in Fig. 2a using a PTFE U-cup and spring-loaded disk contacting core available from Pine Research Instruments as the internal hardware for the ChangeDisk RDE tip, making it easy to change working electrodes. Using an optical microscope, the surfaces of the working electrode, u-cup, and cell are brought in-plane to within a few micrometers on the bottom of the cell. The working electrode is electrically contacted from the top of the cell.

The distance between the working electrode and the membrane, referred to as the *working distance*, L , is defined by the thickness of a PTFE gasket with an inner diameter of 12 mm, placed concentric with the membrane and the working electrode, as illustrated in Fig. 2b. The docking of the cell to the membrane chip and vacuum system is shown in more detail in Fig. S3 of the supplementary information. The volume enclosed by the membrane chip on the bottom, the working electrode and cell on the top, and the gasket on the side, is referred to as the *cell internal volume*. The cell internal volume is contacted by four channels leading outwards to the top of the cell which are used to fill the cell and to make electrolytic contact to external reference and counter electrodes. Two of these channels are shown in the cross-section in Fig. 2c.

The portion of the cell internal volume which is between the working electrode and the membrane is referred to as the *working*

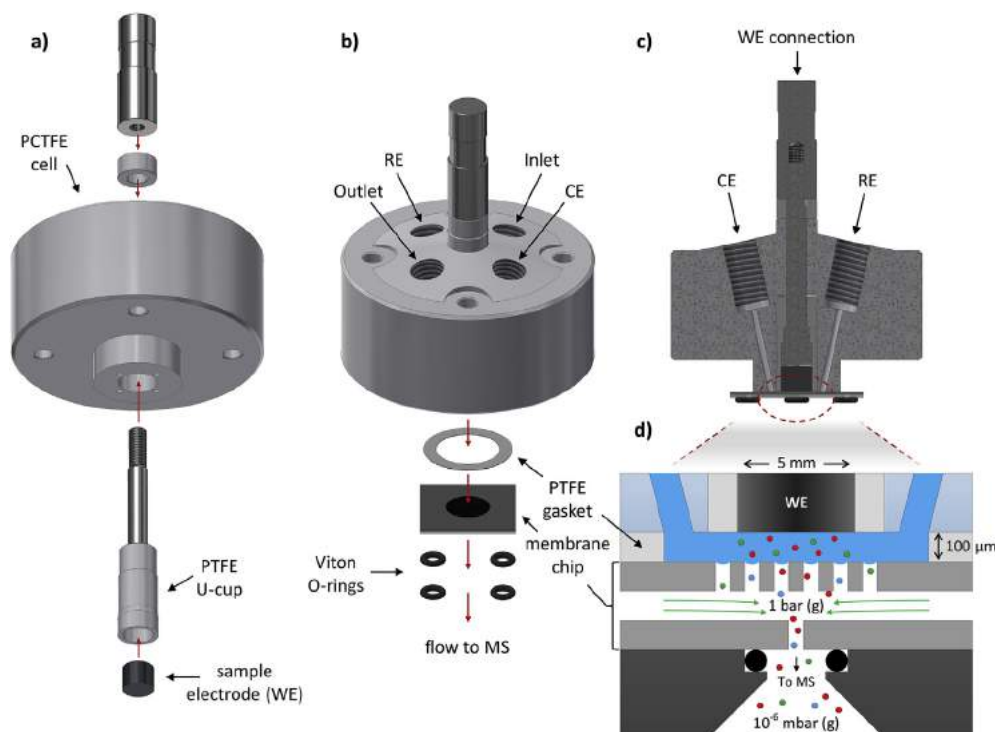


Fig. 2. Stagnant thin-layer cell. **a**, Diagram of the cell as seen from below and the cell-electrode assembly. A 5 mm disk electrode is mounted in the cell using a versatile and standardized assembly procedure. **b**, Diagram of the cell-electrode assembly as seen from above and its incorporation with the membrane chip. The working electrode is parallel to the membrane and the distance between them is defined by a PTFE gasket. **c**, Cross section of the cell-electrode assembly and membrane chip showing two of the four liquid channels of the cell. **d**, Schematic diagram of the cell-electrode assembly and membrane chip in operation.

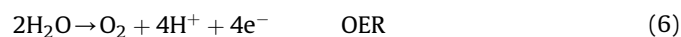
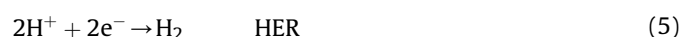
volume. With a working distance of $L = 100 \mu\text{m}$, used throughout this report, the working volume contains $2.0 \mu\text{l}$ of electrolyte. As illustrated in Fig. 2d, gaseous electrochemical reaction products diffuse across this volume from the working electrode to the membrane, where they evaporate to the sampling volume of the chip, and are delivered through the capillary to the mass spectrometer. The membrane extends beyond the working volume by 1 mm in each direction, and the 10:1 aspect ratio of this *edge volume* ensures that a negligible amount of product is lost to lateral diffusion. The working volume and edge volume are simultaneously saturated through the membrane by the carrier gas. Reactant gas can also be introduced through the chip as carrier gas, where it dissolves into the working volume through the membrane and diffuses to the working electrode. The setup thus symmetrically facilitates fast transport of both reactant and product gases to and from the sample. The full system assembly is shown in Fig. S3.

The working distance is an important design parameter for EC-MS experiments involving a stagnant thin-layer cell. The diffusion time from the working electrode to the membrane (on the order of 1–5 s at $L = 100 \mu\text{m}$ for small analyte molecules) scales with the square of the working distance. On the other hand, the electrical resistance from the working electrode to the reference electrode and counter electrode scales inversely with the working distance. We find, in general, that $L = 100 \mu\text{m}$ is a good compromise.

3. Experimental

The membrane chip and stagnant thin layer cell described above, together with a mass spectrometer, potentiostat, and gas manifold, constitute a powerful and versatile tool for studying the reactivity of electrocatalysts. Here, we demonstrate the use of the setup with experiments on a polycrystalline platinum electrode. We chose platinum because it is one of the most studied and well-understood materials in electrocatalysis [37–39]. This is due to its relatively high stability under a wide range of electrochemical conditions [40,41] and its high activity for the oxygen reduction reaction (ORR) [42,43] and hydrogen oxidation reaction (HOR) [44] of hydrogen fuel cells and for the hydrogen evolution reaction (HER) [45,46] of water electrolyzers.

We show EC-MS data for HER (Reaction 5), the oxygen evolution reaction (OER, Reaction 6), and, by introducing CO through the chip, CO oxidation (COox, Reaction 7).



3.1. Electrochemical reactions on a platinum electrode

The electrochemical experiments presented here involve two types of controlled experimental input: electrode potential and carrier gas composition. There are also two types of observed experimental response: electric current and mass spectrometer signal. All the information in an experiment can be displayed by co-plotting the inputs and outputs on a shared time axis. This type of plot is referred to as an *EC-MS plot*. For convenience, it is separated into a top frame showing calibrated mass spectrometer signals for carrier gas components (left y-axis) and electrochemical products (right y-axis) and a bottom frame showing electrode potential (left y-axis) and electric current (right y-axis).

Fig. 3a is an EC-MS plot of an extended electrochemical program on polycrystalline platinum in 1.0 M perchloric acid. Two types of electrical potential input are used: constant-potential steps (chronoamperometry), and potential scanning (cyclic voltammetry) [47]. Fast ramps (200 mV/s) are used between chronoamperometry steps for continuity. While cyclic voltammetry enables easy visualization of redox reactions and is commonly used to characterize electrochemical surfaces, chronoamperometry is essential for studying time-dependent phenomena as scanning techniques convolute the time dependence of the response with the time dependence of the input.

The mass spectrometry data in Fig. 3 is calibrated to represent the flux of molecules reaching the mass spectrometer. Because our setup provides 100% collection efficiency for gaseous products, the calibrated signal for products integrates to the amount produced at the electrode. Such absolute quantification is rare in EC-MS, with most contemporary literature reporting raw data, normalized signals, or ratios [13,15,17,18,23,25–28]. Our ability to quantify products is related to the 100% collection efficiency, which makes it straightforward to perform an internal calibration for the mass spectrometer signal corresponding to any gas that can be produced in situ at a known rate. The signals for H_2 at $m/z = 2$, O_2 at $m/z = 32$, and CO_2 at $m/z = 44$ were calibrated during the same experimental run as the measurements shown here by constant-current electrolysis steps according to reactions 5, 6, and 7, respectively, as shown in the supplementary information. When an analyte gas cannot be produced in situ at a known rate, its mass spectrometer signal can instead be calibrated through a calculation of its flux through the capillary [35,36] (used here for the carrier gases He at $m/z = 4$ and CO at $m/z = 28$) or through extrapolation from internally calibrated signals using a *relative sensitivity factor*, which can in turn be calculated according to the electron impact ionization cross-section and spectrum of the analyte molecule [48] and the transmission function of the mass spectrometer [49]. All of these calibration methods are described in detail in the supporting information.

Starting from the left of Fig. 3a, the electrode is held at 0.45 V vs RHE, in the non-reactive “double-layer region”, while the electrolyte is saturated with helium carrier gas. At $t \sim 120$ s, the potential is set to 0.035 V vs RHE for 2 min. Although this is anodic of the equilibrium potential in 1 bar H_2 , H_2 is actively removed through the membrane chip, keeping the partial pressure of H_2 lower than one bar at the electrode, and hydrogen evolution is observed both as a negative (cathodic) current and as a signal at $m/z = 2$. Following another period at 0.45 V, at $t \sim 380$ s, the potential is set to 1.750 V vs RHE for 2 min, during which oxygen evolution is observed as positive (anodic) current and signal at $m/z = 32$. Unlike HER, which quickly approaches a steady state, OER activity, measured both as current and MS signal, falls quickly during the 2 min constant potential. This has previously been attributed to formation of platinum oxide at the electrode surface [50].

From $t \sim 570$ s to $t \sim 1250$ s, the electrode potential is cycled four complete times between 0.030 V vs RHE and 1.750 V vs RHE at a scan rate of 20 mV/s. During the first two cycles, HER is observed at and around the cathodic and OER at and around the anodic turn, both as current and MS signal. At $t \sim 915$ s, just before the third cathodic turn, the carrier gas is abruptly switched from He to CO. No cathodic current or signal at $m/z = 2$ is observed at the cathodic turn at $t \sim 930$ s, indicating that the platinum surface is completely covered in CO, poisoning it for HER. During the subsequent anodic sweep, a spike in current is observed at $t \sim 975$ s, at which point the potential crosses $U \sim 0.85$ V vs RHE, igniting CO oxidation. The signal at $m/z = 44$ accordingly increases from the ignition time, reflecting the CO_2 released. OER is still seen at and around the anodic turn. Interestingly, the OER activity is not influenced by the

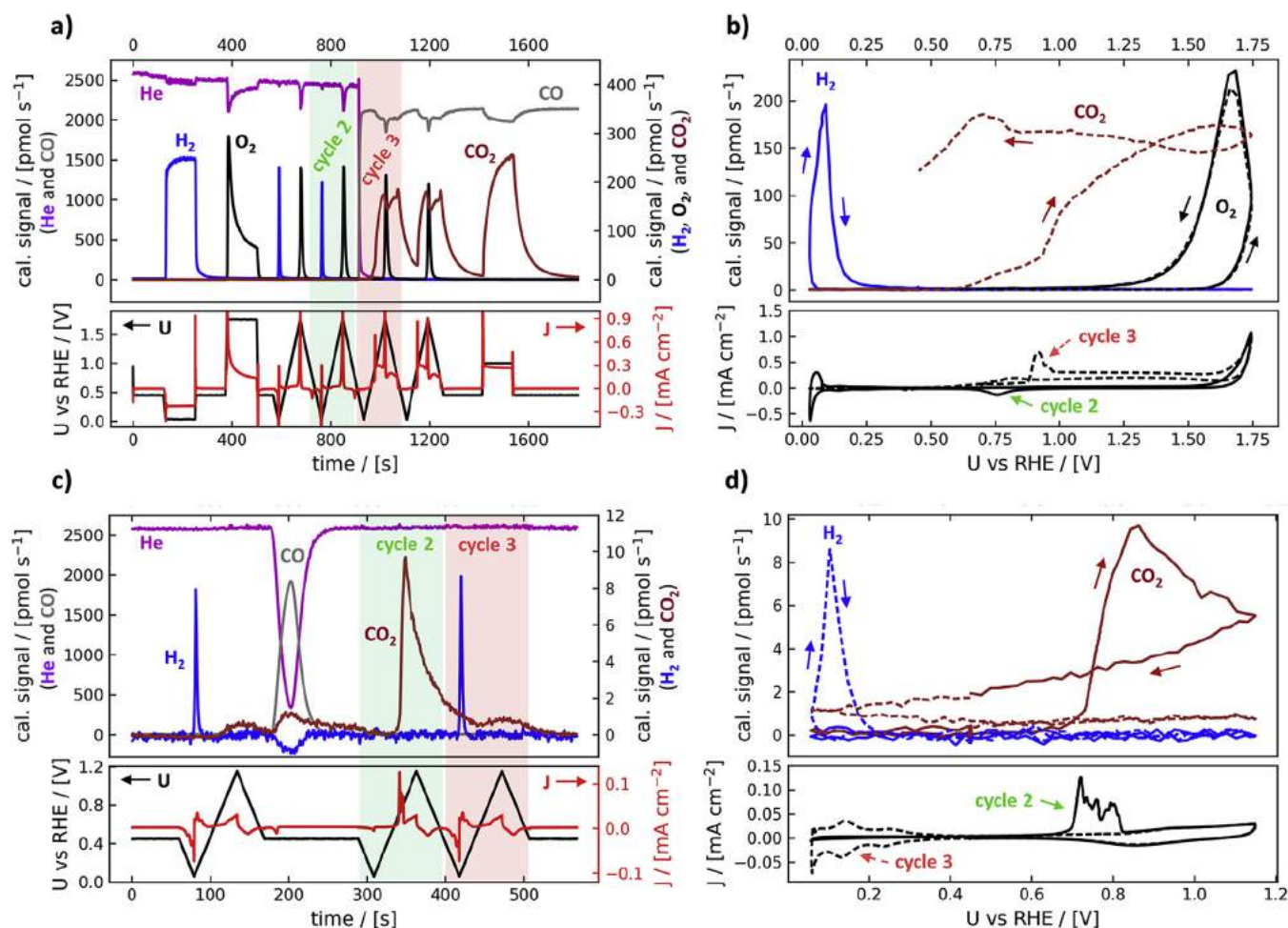


Fig. 3. Electrochemistry - mass spectrometry (EC-MS) experiments on platinum. **a**, Demonstration of constant-potential electrolysis at 120 s (hydrogen evolution), 360 s (oxygen evolution), and 1380 s (CO oxidation); cyclic voltammetry (CV) from 600 s to 1200 s; and change of carrier gas from He to CO at 900 s shown as an EC-MS plot. The lower panel shows the electrode potential (black, left axis) and electrical current (red, right axis). The upper panel shows the calibrated mass spectrometer signals for He ($m/z = 4$, magenta) and CO ($m/z = 28$, grey) on the left axis and the signals for H₂ ($m/z = 2$, blue), O₂ ($m/z = 32$, black), and CO₂ ($m/z = 44$, brown) on the right axis. The last CV cycle in He (green highlight) and the first cycle in CO (red highlight) are replotted in **b** as cycle 2 (solid traces) and cycle 3 (dashed traces), respectively. Here the two cycles are co-plotted as cyclic voltammograms, i.e. as a function of the electrode potential. The lower panel shows the electrical current and the upper panel shows the mass spectrometer signals for H₂, O₂, and CO₂. **c**, Demonstration of a gas-pulse injection and subsequent CO stripping experiment shown as an EC-MS plot, with the same coloring as above. A CO displacement current is visible at 185 s. The CV cycle immediately following the CO injection (green highlight) and the subsequent CV cycle (red highlight), are re-plotted in **d** as cyclic voltammograms. (For interpretation of the references to color in this figure legend, the reader is referred to the Web version of this article.)

presence of CO.

The potential cycles immediately before and after the switch of carrier gas, indicated by the green and red highlights in Fig. 3a, are replotted Fig. 3b with the current and $m/z = 2, 32$, and 44 signals, projected onto a potential axis, i.e. as *cyclic voltammograms*. The measurements in helium are shown with solid traces, and the measurements in CO with dashed traces. The poisoning of the hydrogen region and lack of OER poisoning described above are clear. It is also clear that there is a small delay in the $m/z = 2$ and 32 signals compared to the OER and HER currents, placing the maximum signal after the cathodic and anodic turn, respectively, and that while the $m/z = 44$ signal has a steep onset at the ignition of CO oxidation, the signal accumulates thereafter and decays very slowly after CO oxidation ceases at ~ 0.7 V in the cathodic sweep. These effects are due to mass transport of electrochemical products in the working volume, which will be discussed in detail later. The complex behavior of the CO oxidation rate, including ignition at ~ 0.85 V, plateau and gradual decline thereafter, and increase again during the cathodic scan, reflect effects of the state of the platinum surface on CO oxidation [51,52].

Following the end of cyclic voltammetry in Fig. 3a, the electrode

potential is set to 1 V vs RHE, just above the ignition of CO oxidation, for 2 min. The current remains relatively constant for the 2 min, while the $m/z = 44$ signal approaches steady state much more slowly, and then decays at the same rate after the 2-min period. The mass transport limited CO oxidation current in the setup is

$$j_{\text{mt}}^{\text{COox}} = 2\mathcal{F} \frac{D^{\text{CO}}}{L} \frac{p_{\text{chip}}^0}{K_{\text{H}}^{\text{CO}}} \approx 0.34 \left[\text{mA}/\text{cm}^2 \right], \quad (8)$$

where \mathcal{F} is Faraday's constant, $D^{\text{CO}} = 1.9 \times 10^{-9} \text{ m}^2/\text{s}$ is the diffusion constant of CO in water [53], $L = 100 \mu\text{m}$ is the working distance between the membrane and the electrode, $p_{\text{chip}}^0 = 1 \text{ bar}$ is the pressure inside the chip, and $K_{\text{H}}^{\text{CO}} = 1100 \text{ bar}/\text{M}$ is the Henry's-law volatility constant for CO [54]. The measured current during the constant-potential CO oxidation period is about $0.27 \text{ mA}/\text{cm}^2$, about 20% lower, and slowly declining. This is consistent with the observations by Mayrhofer et al. [51]: While small platinum nanoparticles show a diffusion-limited plateau for potentials just above the ignition of CO oxidation, the rate of CO oxidation on

extended polycrystalline platinum surfaces decreases immediately as the surface becomes covered by unreactive oxygen species, with significant deactivation even at 1 V vs RHE.

For many electrochemical experiments, a lasting change of reaction gas is not needed, and instead a short, controlled exposure is advantageous. To this end we use an injection loop on the carrier gas system upstream of the chip (see Fig. S2), as demonstrated as an EC-MS plot in Fig. 3c for a CO stripping experiment on the same polycrystalline platinum electrode. We refer to this technique as *pulse injection*.

Starting from the left of Fig. 3c, one complete potential cycle is undertaken between 0.060 and 1.150 V vs RHE with a scan rate of 20 mV/s starting with a cathodic sweep from 0.45 V vs RHE to characterize the state of the electrode surface. Following the cycle, the potential is held at 0.45 V vs RHE while CO is injected from the loop into the carrier gas and flows through the chip from $t \sim 180$ s to $t \sim 240$ s. A cathodic CO displacement current is observed, centered around $t \sim 185$ s. Following CO exposure, two cycles are carried out, identical to the first cycle. The first cycle shows HER poisoning followed by the oxidation of the adsorbed CO at $t \sim 340$ s, and the CO₂ released is immediately observed as a signal at $m/z = 44$, which decays slowly thereafter. The last cycle is identical to the cycle before CO exposure, confirming that the electrode surface and setup have returned to their original state free of CO. The small, broad CO₂ signals centered on the anodic turns of the first (before CO exposure) and last cycles are attributed to residual adventitious carbon species on the electrode surface, and not to CO oxidation. The cycle with the CO stripping (green highlight) and the subsequent cycle (red highlight) are plotted as cyclic voltammograms in Fig. 3d to better show the difference in current attributed to oxidation of the adsorbed CO.

The integrated CO stripping peak from the cyclic voltammograms corresponds to 370 pmol CO₂, or about 75% of a monolayer assuming a flat surface, in agreement with literature values [52]. The integrated calibrated mass spectrometer signal for CO₂, after subtracting the background from oxidation of residual adventitious carbon, is 345 pmol, or about 70% of a monolayer assuming a flat surface, in good agreement with the electrochemistry data. In comparison, the amount of hydrogen produced at ~ 420 s in Fig. 3 is 24 pmol, corresponding to 5% of a monolayer, i.e., 5% of a catalytic turnover assuming all surface atoms are active.

In addition to the remarkable signal-to-noise ratio for detection of a sub-monolayer of desorbed product, this is, to the best of our knowledge, the fastest full execution of a CO stripping experiment ever reported. By this, we mean the shortest total time required for surface area measurement by CO stripping including a confirmation, by HER poisoning, that the surface has been completely covered by CO; and a confirmation, by prior and subsequent cyclic voltammetry, that the surface has returned to its initial, completely uncovered, state.

4. Modeling

4.1. Preliminary system comparison

As mentioned in the introduction, one of the most important differences between the chip-based inlet system described here and differentially pumped inlet systems used in conventional DEMS is that there is much less solvent evaporation. The water evaporation rate is calculated in the supporting information to be 17 nL per second in DEMS, in approximate agreement with previous calculations [13], and only 1.4 pL per second in our chip-based EC-MS.

The 10000 times slower water evaporation is a specific case of the more general phenomenon that the mass transfer coefficient

for a molecule across the membrane chip is much smaller than the corresponding mass transfer coefficient across the porous Teflon membrane in DEMS. By mass transfer coefficient we mean the ratio of the flux j_m^i of analyte i across the membrane to its concentration c^i at the membrane:

$$h^i = \frac{j_m^i}{c^i(0)}. \quad (9)$$

The general equations for the mass transfer coefficient h for both systems, derived in the supplementary information, are

$$h_{\text{chip}}^i = K_{\text{H}}^i \frac{\dot{n}_{\text{v}}^0}{p_{\text{chip}}^0 A}. \quad (10)$$

for a chip-based system, where K_{H}^i is the Henry's law volatility constant of species i (from Equation (3) above), \dot{n}_{v}^0 is the total molecular flux through the membrane chip's capillary (Equation (4)), $p_{\text{chip}}^0 = 1$ bar is the total pressure inside the chip, and A is the relevant area (the electrode area for products or the membrane area for water); and

$$h_{\text{DEMS}}^i = K_{\text{H}}^i \frac{\phi d_p}{3l_p} \sqrt{\frac{8}{\pi R T M_{\text{mol}}^i}}, \quad (11)$$

for a differentially pumped system, which is governed by Knudsen diffusion [55] through the porous membrane and where ϕ is the porosity (typically 0.5 [15]), l_p is the length of the pores (typically 100 μm), d_p is the pore diameter (typically 20 nm), and M_{mol}^i is the analyte molar mass.

Mass transport of an analyte in the working volume of a stagnant thin-layer system is described by Fick's law of diffusion in the electrolyte and by this mass transfer coefficient at the membrane. A few concepts useful for describing this system can be derived analytically. One simple case is for a sustained constant production rate \dot{n}_{el} of an analyte at the electrode. When steady state is reached, the concentration c is a linear function of the distance y from the membrane:

$$c(y) = \frac{\dot{n}_{\text{el}}}{A_{\text{el}}} \left(\frac{y}{D} + \frac{1}{h} \right), \quad (12)$$

where D is the diffusion constant of the analyte in water (the superscript i has been dropped for convenience). The analyte buildup at the electrode ($y = L$) at steady state thus has two contributions, one of which is due to diffusion in the working volume and one of which is due to evaporation across the membrane. Their ratio,

$$\alpha = \frac{hL}{D}, \quad (13)$$

is a dimensionless parameter describing the relative importance of diffusion and evaporation in the system.

The partial differential equations describing the mass transport in the working volume, System S17 (supporting information), can be solved analytically using the method of Laplace transformation for the simple case of a step function in $\dot{n}_{\text{el}}(t)$. The approximate solution when the system starts at steady state and then the flux from the electrode is turned off is an exponential decay with time constant

$$\tau = \frac{L^2}{2D} + \frac{L}{h}. \quad (14)$$

Table 1
Molecular properties and response times. Diffusion coefficient [53], Henry's-law volatility constant [54], mass transfer coefficient from Equation (10) or Equation (11), system parameter α from Equation (13), and response time from Equation (14) for selected analytes in our chip-based system (chip) and a differentially pumped system (DEMS).

System	Gas	D [m ² s ⁻¹]	K_H [bar M ⁻¹]	h [m s ⁻¹]	α	τ [s]
chip	H ₂	4.5×10^{-9}	1300	1.8×10^{-4}	3.8	1.7
	O ₂	2.1×10^{-9}	770	1.0×10^{-4}	4.8	3.3
	CO ₂	1.9×10^{-9}	30	4.0×10^{-6}	0.21	27
DEMS	H ₂	4.5×10^{-9}	1300	3.1	6.8×10^4	1.1
	O ₂	2.1×10^{-9}	770	0.46	2.2×10^4	2.4
	CO ₂	1.9×10^{-9}	30	0.015	7.9×10^2	2.6

This time constant is 1.7 s for H₂, 3.3 s for O₂, and 27 s for CO₂. The fact that $\tau^{\text{H}_2} < \tau^{\text{O}_2} < \tau^{\text{CO}_2}$ explains the difference in the shapes of the signals for constant-potential H₂ and CO₂ production seen in Fig. 3, i.e., that H₂ reaches steady-state almost immediately and CO₂ has not fully reached steady-state at the end of the 2-min pulse. Mass transfer coefficients h , system parameters α , and characteristic time constants τ are tabulated for select compounds in Table 1.

4.2. Stagnant thin-layer EC-MS

A full mass-transport model for dynamic production of an analyte at the electrode based on the concepts outlined above is described in the supplementary information. To validate the model, four solutions were calculated based on the experimental data in Fig. 3. For each of the three constant-potential electrolysis experiments in Fig. 3a (HER, OER, and CO oxidation), the concentration of dissolved H₂, O₂, or CO₂, respectively, was calculated according to the model using the appropriate values for h and D . The concentration of dissolved CO₂ was also calculated for the CO stripping experiment in Fig. 3c. For the three steady-state experiments we assume 100% Faradaic efficiency for the production of analyte during the 2 min of electrolysis (and zero outside of this interval), i.e.,

$$\dot{n}_{\text{el}}(t) = \frac{I(t)}{zF}, \quad (15)$$

where $I(t)$ is the measured electrical current during the electrolysis period. For the CO stripping experiment, the input is instead based on the assumption that 100% of the difference between cycle 2 and cycle 3 in Fig. 3d goes to oxidation of adsorbed CO, i.e., using $\Delta I(t)$ instead of I in Equation (15). In each case the concentration profile can be solved numerically for $c(t, y)$ using the method of lines [56] and the flux through the membrane predicted from the concentration profile according to Equation (9). The predicted flux can be compared to the measured and calibrated mass spectrometer signal.

The modeling is represented in Fig. 4, which shows the model input \dot{n}_{el} in the top row, the solution for $c(t, y)$ in the middle row, and the predicted and measured flux co-plotted in the bottom row. The predictions are remarkably good given that no fitted parameters are used in the model.

As the setup and model are refined, we expect that it will become possible to deconvolute mass transport effects from the measured mass spectrometer signals yielding the instantaneous

rate of any reaction on the sample with a gaseous product with sub-second resolution.

4.3. Flow EC-MS

The high water evaporation rate in differentially pumped EC-MS necessitates operation in a flow system. To make a relevant comparison, we therefore develop a mass transport model to describe the transport of analyte through a membrane in the collection volume of a flow cell in steady state, as described in the supporting information.

The overall figure of merit is the collection efficiency η , defined as the ratio of the rate analyte reaches the high vacuum of the mass spectrometer at steady state \dot{n}_v to the rate at which analyte is produced upstream, \dot{n}_{el} . The collection efficiency is a product of the membrane collection efficiency η_m and the vacuum collection efficiency η_v ,

$$\eta = \frac{\dot{n}_v}{\dot{n}_{\text{el}}} = \frac{\dot{n}_m}{\dot{n}_{\text{el}}} \frac{\dot{n}_v}{\dot{n}_m} = \eta_m \eta_v. \quad (16)$$

Almost all of the variation between analytes is due the Henry's Law constant of volatility, K_H , which determines the mass transfer coefficient through Equations (10) and (11). To give an overview comparing chip-based and differentially pumped EC-MS systems, we therefore plot the collection efficiency η vs K_H in Fig. 5a. Fig. 5b, c, and d show the steady-state concentration profile in the collection volume for H₂, O₂, and CO₂, respectively.

For high-volatility analytes, where η_m approaches 1, the chip-based system is much more sensitive than the differentially pumped system, as no analyte is lost to differential pumping ($\eta_v = 1$). In this limit, the ratio of collection efficiencies is the reciprocal of $\eta_{v, \text{DEMS}}$, i.e.,

$$\frac{\eta_{\text{chip}}}{\eta_{\text{DEMS}}} \Big|_{K_H \rightarrow \infty} = \frac{\dot{n}_{m, \text{DEMS}}^{\text{H}_2\text{O}}(T)}{\dot{n}_v^0} \approx 250. \quad (17)$$

For low volatility compounds, the differentially pumped system can be more sensitive due to higher mass transfer coefficients and thus higher values of η_m . In the limit that $\eta_m \ll 1$, the ratio of analyte flux to water flux is a constant, and the inefficiency of the chip-based system can be understood as a result of diluting the water vapor and analyte to the chip pressure with carrier gas before delivery to the mass spectrometer.

$$\frac{\eta_{\text{chip}}}{\eta_{\text{DEMS}}} \Big|_{K_H \rightarrow 0} = \frac{p_{\text{vap}}^{\text{H}_2\text{O}}(T)}{p_{\text{chip}}^0} \approx 0.03. \quad (18)$$

As a rule of thumb, we propose CO₂ as a transition molecule, defining the volatility at or above which a chip-based system gives a dramatic increase in sensitivity over a differentially pumped system.

4.4. Design considerations

While the above comparison of chip-based and differentially pumped EC-MS is based on a flow model, the same comparison holds qualitatively in a stagnant system, with sensitivity replaced by time response. In a flow system, the time response is fixed according to the flow rate and internal cell volume, while membrane collection efficiency decreases with flow rate and with the solubility of the analyte. In a stagnant system, the membrane collection

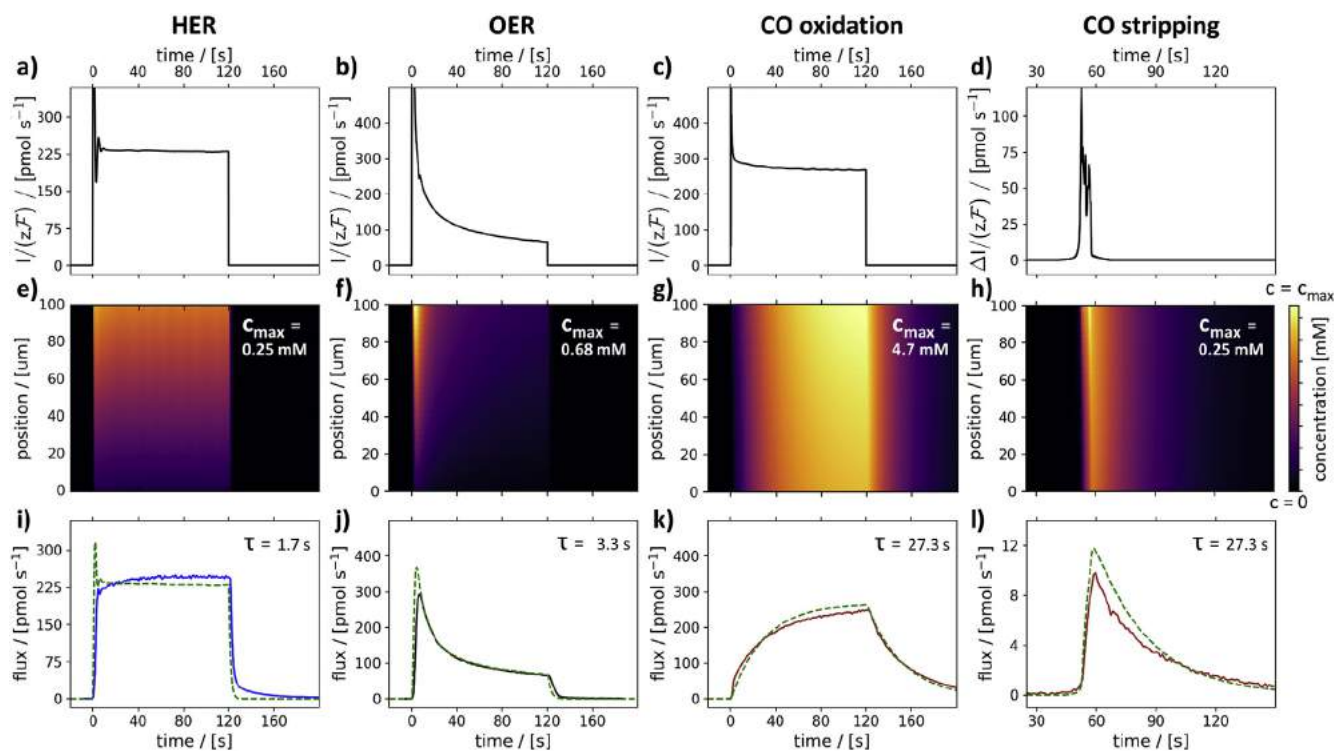


Fig. 4. Model validation. Top row, Production rate of analyte at electrode assuming 100% Faradaic efficiency for the indicated reaction. **a–c** are based on the electrical current data in Fig. 3a during the three constant-potential electrolysis periods, while **d** is based on the difference in electrical current between cycles 2 and 3 in the CO-stripping region in Fig. 3d. Middle row, Calculated concentration of analyte in the working volume as a function of time (horizontal axis) and distance from the membrane (vertical axis) given the electrode production rate from in the top row. In each panel, concentration varies from 0 (black) to the indicated c_{\max} (bright yellow). Bottom row, The flux through the membrane \dot{n}_m , calculated from the concentration profile in the middle row and equation (9), is plotted as a dashed green trace. The relevant calibrated mass spectrometer signal from Fig. 3 is co-plotted as a solid trace. The characteristic diffusion-evaporation time calculated by Equation (14) is inset, and the y-axis scale matches that of the top row except for **l**. (For interpretation of the references to color in this figure legend, the reader is referred to the Web version of this article.)

efficiency is set to unity, i.e., everything is collected if you are willing to wait long enough, but the time response depends on the solubility of the analyte, as shown in Table 1.

The relative advantage of chip-based vs differentially pumped EC-MS thus depends on a number of design parameters including

flow vs stagnant, working distance, chip pressure, differential pumping rate, electrolyte flow rate, and temperature. The equations and mass transport models introduced here can help guide the design of the optimal EC-MS setup to study a given electrochemical reaction.

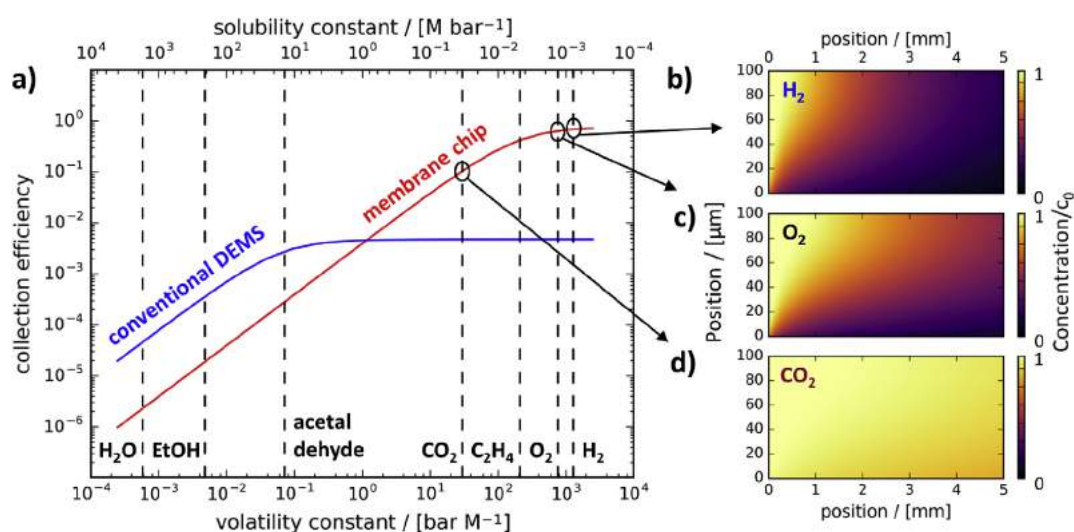


Fig. 5. Chip-based vs differentially pumped EC-MS. Model comparison of chip-based and differentially pumped electrochemistry - mass spectrometry in a flow system at steady state. **a**, Overall collection efficiency $\eta = \eta_e \eta_m$ as a function of analyte volatility for chip-based EC-MS (red) and differentially pumped EC-MS (blue) with the volatility of selected analytes indicated. **b–d**, The calculated steady state concentration profiles in the collection volume for H_2 , O_2 , and CO_2 , respectively. (For interpretation of the references to color in this figure legend, the reader is referred to the Web version of this article.)

5. Conclusion

This article has demonstrated technical and methodological considerations that are needed in order to measure and interpret minute desorption phenomena during electrochemistry experiments and thereby gain insight into the fundamental reaction mechanisms of electrochemical processes. Laboratory scale electrochemistry experiments often involve desorption phenomena yielding less than 1 nmol of analyte over a few seconds. This makes mass spectrometry an ideal detection method given its instrumental capability of analyzing small amounts of gaseous analyte species with a fast time-response. Mass spectrometry is typically operated with pumping rates which are also on the order of 1 nmol per second. However, coupling a mass spectrometer, with an operational pressure of 10^{-6} mbar directly to an electrochemical experiment is not a trivial task. Conventional methods of designing this interface rely on a membrane to separate the liquid and vacuum environments. This results in a high rate of solvent evaporation lowering sensitivity towards the analyte.

Here, we have presented a unique way of directly coupling electrochemistry and mass spectrometry by means of a micro-fabricated membrane chip and a stagnant thin-layer cell. The membrane chip acts as an equilibration zone for volatile analyte species between the electrolyte and the MS. The membrane samples the vapor pressure of any volatile analyte into a microscopic sampling volume inside the membrane chip, which is continuously delivered to the mass spectrometer without loss of analyte. By incorporating the membrane chip with a stagnant thin-layer electrochemistry cell, a direct coupling between analyte production at a working electrode and detection at a mass spectrometer was established. Furthermore, the membrane chip enables full control of the dissolved gas atmosphere at the working electrode, allowing either pulsed or steady-state dosing of reactant gases. Modeling of the well-characterized mass transport in this setup makes it possible to compare the anticipated analyte collection rate, based on the current measurement from the electrode, to the measured mass spectrometer signal. As the method is refined, it will become possible to map mass spectrometer measurements directly back to a Faradaic current on the surface of an electrode. While we have focused on electrochemistry studies, it is worth mentioning that the same design paradigm might be equally applicable to e.g. biochemical reaction studies.

It is our hope that the instrumentation presented herein, and the general framework that it represents, will lead to more in-depth studies of sub-monolayer desorption phenomena in the future. This will accelerate advances in electro-catalysis, contributing to the transition to a more sustainable future.

Methods

The membrane chip was developed and manufactured in collaboration with Spectro Inlets ApS. The mass spectrometer used in this work is a Pfeiffer QMA 125 with a 90° SEM and an open axial beam filament ionizing at 100 eV, which is continuously pumped by a 56 l/s (N₂) Pfeiffer TMP. Electrochemical measurements were made using a Biologic SP-150 potentiostat using the EC-Lab software. An Hg/Hg₂SO₄ reference electrode from Schott Instruments was used, and a gold mesh was used as the counter electrode. The reference and counter electrodes were separated from the cell internal volume by ceramic frits. A 1.0 M HClO₄ electrolyte was prepared by diluting 70% HClO₄ (Merck, Suprapur, 99.99% purity) in ultrapure water (18.2 MΩ cm, Millipore). The reference electrode was calibrated against the reversible hydrogen electrode in the same electrolyte saturated with H₂ using two platinum wires as

working and reference electrodes. The \varnothing 5.03 × 3 mm polycrystalline platinum disk, from MaTeck, was flame-annealed, cooled under argon atmosphere, and rinsed with ultrapure water before use. All glassware, as well as the stagnant thin-layer cell, were cleaned overnight in a 3:1 mixture of 98% sulfuric acid and 30% hydrogen peroxide and then thoroughly rinsed with ultrapure water before use. Helium and CO are from AGA at 6.0 purity.

For the numerical modeling, the partial differential equations were implemented in python as systems of ordinary differential equations by discretizing in *y*. A discretization of 30 was used when solving the ordinary differential equations representing the stagnant system, and of 100 when solving for the flow system. The integration was performed using `scipy.integrate.odeint`. All of the data analysis, plotting, and modeling for this article was performed using a homemade python package available at <https://github.com/ScottSoren/>.

Acknowledgments

Supported by the Villum Foundation V-SUSTAIN grant 9455 to the Villum Center for the Science 208 of Sustainable Fuels and Chemicals.

Appendix A. Supplementary data

Supplementary data related to this article can be found at <https://doi.org/10.1016/j.electacta.2018.02.060>.

References

- [1] Climate Change 2014: Synthesis Report, Intergovernmental Panel on Climate Change, 2014.
- [2] Nathan S. Lewis, Daniel G. Nocera, Powering the planet: chemical challenges in solar energy utilization, *Proc. Natl. Acad. Sci. Unit. States Am.* 104 (42) (2007).
- [3] Steven Chu, Yi Cui, Nian Liu, The path towards sustainable energy, *Nat. Mater.* 16 (1) (2016) 16–22.
- [4] Barack Obama, The irreversible momentum of clean energy, *Science* 6284 (January) (2017).
- [5] John R. Yates, *Mass Spectrometry: a Textbook*, second ed., vol. 16, Springer, Heidelberg, 2000.
- [6] Daniel C. Harris, *Quantitative Chemical Analysis*, eighth ed., W. H. Freeman and Company, New York, 2010.
- [7] Hemma Mistry, Ana Sofia Varela, Stefanie Kühn, Peter Strasser, Beatriz Roldan Cuenya, Nanostructured electrocatalysts with tunable activity and selectivity, *Nature Reviews Materials* 1 (2016) 16009.
- [8] V. Vojinović, J.M.S. Cabral, L.P. Fonseca, Real-time bioprocess monitoring: Part I: in situ sensors, *Sensor. Actuator. B Chem.* 114 (2) (2006) 1083–1091.
- [9] Yu Chie Chen, Pawel L. Urban, Time-resolved mass spectrometry, *Trac. Trends Anal. Chem.* 44 (2013) 106–120.
- [10] George Hoch, Bessel Kok, A mass spectrometer inlet system for sampling gases dissolved in liquid phases, *Arch. Biochem. Biophys.* 101 (1) (Apr 1963) 160–170.
- [11] Erik T. Krogh, Chris G. Gill, Membrane introduction mass spectrometry (MIMS): a versatile tool for direct, real-time chemical measurements, *J. Mass Spectrom.* 49 (12) (2014) 1205–1213.
- [12] S. Bruckenstein, R.R. Gadde, Use of a porous electrode for in situ mass spectrometric determination of volatile electrode reaction products, *J. Am. Chem. Soc.* 93 (3) (1971) 1966–1967.
- [13] O. Wolter, J. Heitbaum, Differential electrochemical mass spectroscopy (DEMS) - a new method for the study of electrode processes, *Berichte der Bunsengesellschaft für Phys. Chemie* 6 (1984) 2–6.
- [14] Thomas Hartung, Helmut Baltruschat, Differential electrochemical mass spectrometry using smooth electrodes: adsorption and H/D-Exchange reactions of benzene on Pt, *Langmuir* 6 (11) (1990) 953–957.
- [15] Helmut Baltruschat, Differential electrochemical mass spectrometry, *J. Am. Soc. Mass Spectrom.* 15 (12) (2004) 1693–1706.
- [16] Hatem M.A. Amin, H. Baltruschat, How many surface atoms in Co₃O₄ take part in oxygen evolution? Isotope labeling together with differential electrochemical mass spectrometry, *Phys. Chem. Chem. Phys.* 19 (2017) 25527–25536.
- [17] Martin Lanz, Petr Novák, DEMS study of gas evolution at thick graphite electrodes for lithium-ion batteries: the effect of [gamma]-butyrolactone, *J. Power Sources* 102 (1–2) (2001) 277–282.
- [18] Hongsen Wang, Zenonas Jusys, R. Jürgen Behm, Héctor D. Abruña, New

- insights into the mechanism and kinetics of adsorbed CO electrooxidation on platinum: online mass spectrometry and kinetic Monte Carlo simulation studies, *J. Phys. Chem. C* 116 (20) (2012) 11040–11053.
- [19] Herbert Oberacher, Florian Pitterl, Robert Erb, Sabine Plattner, Mass spectrometric methods for monitoring redox processes in electrochemical cells, *Mass Spectrom. Rev.* 47 (12) (2013) 987–992.
- [20] Alnald Javier, Jack H. Baricuatro, Youn-Geun Kim, Manuel P. Soriaga, Overlayer Au-on-W near-surface alloy for the selective electrochemical reduction of CO₂ to methanol: empirical (DEMS) corroboration of a computational (DFT) prediction, *Electrocatalysis* 6 (6) (Oct 2015) 493–497.
- [21] F.J. Vidal-Iglesias, J. Solla-Gullón, J.M. Feliu, H. Baltruschat, A. Aldaz, DEMS study of ammonia oxidation on platinum basal planes, *J. Electroanal. Chem.* 588 (2) (2006) 331–338.
- [22] J. Souza-García, E.A. Ticianelli, V. Climent, J.M. Feliu, Mechanistic changes observed in heavy water for nitrate reduction reaction on palladium-modified Pt(hkl) electrodes, *Chem. Sci.* 3 (10) (2012) 3063.
- [23] Youn Geun Kim, Alnald Javier, Jack H. Baricuatro, Daniel Torelli, Kyle D. Cummins, Chu F. Tsang, John C. Hemminger, Manuel P. Soriaga, Surface reconstruction of pure-Cu single-crystal electrodes under CO-reduction potentials in alkaline solutions: a study by seriatim ECSTM-DEMS, *J. Electroanal. Chem.* 780 (2016) 290–295.
- [24] A.H. Wonders, T.H.M. Housmans, V. Rosca, M.T.M. Koper, On-line mass spectrometry system for measurements at single-crystal electrodes in hanging meniscus configuration, *J. Appl. Electrochem.* 36 (11) (2006) 1215–1221.
- [25] Klaas Jan P. Schouten, Elena Pérez Gallent, Marc T.M. Koper, The influence of pH on the reduction of CO and CO₂ to hydrocarbons on copper electrodes, *J. Electroanal. Chem.* 716 (2013) 53–57.
- [26] Alexis Grimaud, Oscar Diaz-Morales, Binghong Han, Wesley T. Hong, Yueh-Lin Lee, Livia Giordano, Kelsey A. Stoerzinger, Marc T.M. Koper, Yang Shao-Horn, Activating lattice oxygen redox reactions in metal oxides to catalyze oxygen evolution, *Nature Chemistry*, (January) (2016) 1–6.
- [27] F. Sloan Roberts, Kendra P. Kuhl, Anders Nilsson, Electroreduction of carbon monoxide over a copper nanocube catalyst: surface structure and pH dependence on selectivity, *ChemCatChem* 8 (6) (2016) 1119–1124.
- [28] Cécile S. Le Duff, Matthew J. Lawrence, Paramaconi Rodriguez, Role of the Adsorbed Oxygen Species in the Selective Electrochemical Reduction of CO₂ to Alcohols and Carbonyls on Copper Electrodes, 2017. *Angewandte Chemie International Edition*, (10 mL).
- [29] Zenonas Jusys, Horst Massong, Helmut Baltruschat, A new approach for simultaneous DEMS and EQCM: electro-oxidation of adsorbed CO on Pt and Pt-Ru, *J. Electrochem. Soc.* 146 (3) (1999) 1093.
- [30] M. Heinen, Y.X. Chen, Z. Jusys, R.J. Behm, In situ ATR-FTIRS coupled with online DEMS under controlled mass transport conditions-A novel tool for electrocatalytic reaction studies, *Electrochim. Acta* 52 (18) (2007) 5634–5643.
- [31] Abd El Aziz, A. Abd-El-Latif, Jie Xu, Nicky Bogolowski, Peter Königshoven, Helmut Baltruschat, New cell for DEMS applicable to different electrode sizes, *Electrocatalysis* 3 (1) (2012) 39–47.
- [32] Ezra L. Clark, Meenesh R. Singh, Youngkook Kwon, Alexis T. Bell, Differential electrochemical mass spectrometer cell design for online quantification of products produced during electrochemical reduction of CO₂, *Anal. Chem.* 87 (15) (2015) 8013–8020.
- [33] *The Vacuum Technology Book* vol. II, Pfeiffer Vacuum GmbH, 2017.
- [34] Daniel B. Trimarco, Thomas Pedersen, Ole Hansen, Ib Chorkendorff, Peter C. K. Vesborg, Fast and sensitive method for detecting volatile species in liquids, *Rev. Sci. Instrum.* 86 (7) (2015).
- [35] Daniel B. Trimarco, Real-time Detection of Sub-monolayer Desorption Phenomena during Electrochemical Reactions: Instrument Development and Applications, Phd thesis, Technical University of Denmark, 2017.
- [36] Toke R. Henriksen, Jakob L. Olsen, Peter Vesborg, Ib Chorkendorff, Ole Hansen, Highly sensitive silicon microreactor for catalyst testing, *Rev. Sci. Instrum.* 80 (12) (2009).
- [37] Jie Zheng, Wenchao Sheng, Zhongbin Zhuang, Bingjun Xu, Yushan Yan, Universal dependence of hydrogen oxidation and evolution reaction activity of platinum-group metals on pH and hydrogen binding energy, *Science advances* 2 (3) (2016) e1501602.
- [38] Yi Fan Huang, Marc T.M. Koper, Electrochemical stripping of atomic oxygen on single-crystalline platinum: bridging gas-phase and electrochemical oxidation, *J. Phys. Chem. Lett.* 8 (6) (2017) 1152–1156.
- [39] Vojislav R. Stamenkovic, Dusan Strmcnik, Pietro P. Lopes, Nenad M. Markovic, Energy and fuels from electrochemical interfaces, *Nat. Mater.* 16 (1) (2017) 57–69.
- [40] Heine A. Hansen, Jan Rossmeisl, Jens K. Nørskov, Surface Pourbaix diagrams and oxygen reduction activity of Pt, Ag and Ni(111) surfaces studied by DFT, *Phys. Chem. Chem. Phys.* 10 (25) (Oct 2008) 3722–3730.
- [41] Jakob Kibsgaard, Yelena Gorlin, Zhebo Chen, Thomas F. Jaramillo, Meso-structured platinum thin films: active and stable electrocatalysts for the oxygen reduction reaction, *J. Am. Chem. Soc.* 134 (18) (2012) 7758–7765.
- [42] Peter Strasser, Shirlaine Koh, Toyli Annjeev, Jeff Greeley, Karren More, Chengfei Yu, Zengcai Liu, Sarp Kaya, Dennis Nordlund, Hirohito Ogasawara, Michael F. Toney, Anders Nilsson, Lattice-strain control of the activity in dealloyed core-shell fuel cell catalysts, *Nat. Chem.* 2 (6) (2010) 454–460.
- [43] M. Li, Mufan Li, Zipeng Zhao, Tao Cheng, Alessandro Fortunelli, Chih-yen Chen, Rong Yu, Lin Gu, Boris Merinov, Zhaoyang Lin, Enbo Zhu, Ted Yu, Qingying Jia, Jinghua Guo, Liang Zhang, William A. Goddard III, Yu Huang, Xiangfeng Duan, Ultrafine jagged platinum nanowires enable ultrahigh mass activity for the oxygen reduction reaction, *Science* 354 (6318) (2016) 1414–1419.
- [44] M. Wesselmarm, B. Wickman, C. Lagergren, G. Lindbergh, Hydrogen oxidation reaction on thin platinum electrodes in the polymer electrolyte fuel cell, *Electrochem. Commun.* 12 (11) (2010) 1585–1588.
- [45] E. Kemppainen, A. Bodin, B. Sebok, T. Pedersen, B. Seger, B. Mei, D. Bae, P.C.K. Vesborg, J. Halme, O. Hansen, P.D. Lund, I. Chorkendorff, Scalability and feasibility of photoelectrochemical H₂ evolution: the ultimate limit of Pt nanoparticle as an HER catalyst, *Energy Environ. Sci.* 8 (10) (2015) 2991–2999.
- [46] Jakub Tymoczko, Federico Calle-Vallejo, Wolfgang Schuhmann, Aliaksandr S. Bandarenka, Making the hydrogen evolution reaction in polymer electrolyte membrane electrolyzers even faster, *Nat. Commun.* 7 (2016) 10990.
- [47] Allen J. Bard, Larry R. Faulkner, *Electrochemical Methods: Fundamentals and Application*, second ed., Wiley, New York, 2001.
- [48] S.E. Stein, Mass spectra, in: P.J. Linstrom Mallard, WG (Eds.), NIST Chemistry WebBook, NIST Standard Reference Database Number 69, 69 edition, National Institute of Standards and Technology, Gaithersburg MD, 2017.
- [49] D.J. Douglas, Linear quadrupoles in mass spectrometry, *Mass Spectrom. Rev.* 28 (2009) 937–960.
- [50] Tobias Reier, Mehtap Oezaslan, Peter Strasser, Electrocatalytic oxygen evolution reaction (OER) on Ru, Ir, and Pt catalysts: a comparative study of nanoparticles and bulk materials, *ACS Catal.* 2 (8) (2012) 1765–1772.
- [51] K.J.J. Mayrhofer, M. Arenz, B.B. Blizanac, V. Stamenkovic, P.N. Ross, N.M. Markovic, CO surface electrochemistry on Pt-nanoparticles: a selective review, *Electrochim. Acta* 50 (25–26 SPEC. ISS.) (2005) 5144–5154.
- [52] Marc T.M. Koper, Stanley C.S. Lai, Enrique Herrero, Mechanisms of the oxidation of carbon monoxide and small organic molecules at metal electrodes, *Fuel Cell Catal.* (2009) 159–207.
- [53] E.L. Cussler, *Diffusion: Mass Transfer in Fluid Systems*, second ed., Cambridge University Press, New York, 1997.
- [54] Rolf Sander, *Compilation of Henry's law constants for inorganic and organic species of potential importance in environmental chemistry*, Database 20 (1) (1999) 107.
- [55] R.B. Bird, W.E. Stewart, E.N. Lightfoot, *Transport Phenomena*, 2 edition, John Wiley and Sons, 2007.
- [56] Mark E. Davis, *Numerical Methods and Modelling for Chemical Engineers*, 1984.

Paper II Impact of nanoparticle size and lattice oxygen on water oxidation on NiFeO_xH_y

Claudie Roy*, Bela Sebok*, Soren B. Scott*, Elisabetta M. Fiordaliso, Jakob E. Srensen, Anders Bodin, Daniel B. Trimarco, Christian D. Damsgaard, Peter C. K. Vesborg, Ole Hansen, Ifan E. L. Stephens, Jakob Kibsgaard and Ib Chorkendorff.

*These authors contributed equally to this work

Nature Catalysis, 2018, 1(11), 820-829

DOI: 10.1038/s41929-018-0162-x

Impact of nanoparticle size and lattice oxygen on water oxidation on NiFeO_xH_y

C. Roy^{1,5}, B. Sebok^{1,5}, S. B. Scott^{1,5}, E. M. Fiordaliso², J. E. Sørensen¹, A. Bodin¹, D. B. Trimarco¹, C. D. Damsgaard², P. C. K. Vesborg¹, O. Hansen³, I. E. L. Stephens^{1,4}, J. Kibsgaard¹ and I. Chorkendorff^{1*}

NiFeO_xH_y are the most active catalysts for oxygen evolution in a base. For this reason, they are used widely in alkaline electrolyzers. Several open questions remain as to the reason for their exceptionally high catalytic activity. Here we use a model system of mass-selected NiFe nanoparticles and isotope labelling experiments to show that oxygen evolution in 1 M KOH does not proceed via lattice exchange. We complement our activity measurements with electrochemistry-mass spectrometry, taken under operando conditions, and transmission electron microscopy and low-energy ion-scattering spectroscopy, taken ex situ. Together with the trends in particle size, the isotope results indicate that oxygen evolution is limited to the near-surface region. Using the surface area of the particles, we determined that the turnover frequency was $6.2 \pm 1.6 \text{ s}^{-1}$ at an overpotential of 0.3 V, which is, to the best of our knowledge, the highest reported for oxygen evolution in alkaline solution.

Renewable energy technologies, such as wind turbines and solar panels, hold the potential to satisfy both rising global energy demand and mitigate CO_2 emissions^{1,2}. The intermittent nature of wind and solar energy means that energy storage is one of the most critical challenges as it limits their widespread implementation. One possibility is to store the energy in chemical bonds³. Thus far, one of the most promising means to convert electricity into fuels is water electrolysis, in which H_2 and O_2 gases are formed⁴. Their recombination to provide electrical energy only has water as a by-product, which makes it a clean process.

The hydrogen evolution reaction, which takes place on the cathode side during water electrolysis, is possible at minimal energy losses^{5,6}. However, the slow reaction kinetics of the anodic reaction, the oxygen evolution reaction (OER), involves the transfer of four electrons and four protons and so limits the efficiency of electrolyzers⁷. No electrode material approaches the equilibrium potential of 1.23 V on the reversible hydrogen electrode scale (V_{RHE})^{8–10}, which corresponds to the minimum energy needed for the reaction. Consequently, the widespread use of electrolyzers is contingent on improvements to the OER kinetics.

Although $\text{Ni}(\text{Fe})\text{O}_x\text{H}_y$ mixed electrodes were used even in the nineteenth century in alkaline electrolyzers¹¹, the science is still under intense debate^{12,13}. Pure NiO_xH_y is an inactive catalyst, but the activity drastically increases when Fe is intercalated into the structure^{12–16}, with the optimal activity for compositions between 10% and 50% Fe (ref. 13). There are two main hypotheses as to the role of Fe: (1) Ni is the active site and Fe affects its valency, which makes it more active^{17,18} or (2) Fe itself is the active site^{19–22}, as first evidenced by X-ray adsorption spectroscopy and density functional theory calculations¹⁹, and subsequently by electrochemical scanning microscopy²². Conversely, more recently, it was suggested that both Ni and Fe sites are directly involved²³.

Some studies indicated that the bulk, and not just the outer surface, of the catalyst is active. For example, Batchellor and Boettcher

reported a linear increase of the OER current as a function of catalyst loading up to ~450 monolayer equivalents²⁴. The notion of bulk activity was supported by a recent theoretical study²⁵ that found similar thermodynamics for the OER intermediates in the bulk of the material as for the (001) surface. However, Hu and co-workers showed that the apparent turnover frequency (TOF) of NiFeO_x decreases at high loading²⁶, which suggests either that thick samples are not as active or that the OER becomes readily transport limited.

Previous studies probed $\text{Ni}^{3+/4+}/\text{Ni}^{2+}$ redox chemistry on NiFeO_xH_y electrodes at ~1.3–1.4 V_{RHE} using cyclic voltammetry (CV) and gravimetric analysis, and concluded that each nickel atom in the film contributes on average approximately one electron^{24,27}. This observation indicates that the entire film is electrochemically accessible, which motivates the hypothesis that oxygen evolution occurs between the nanosheets of the layered double hydroxide structure of the catalyst, and so blurs the distinction between surface and bulk¹⁴. Moreover, NiFeO_xH_y films, which are typically electrodeposited, are highly porous¹³. These various studies point to three possibilities: (1) the activity is confined to an outer surface, which may be large for porous materials, (2) the activity is confined to a near surface region in which there is ionic conductivity and electrolyte intercalated between the nanosheets and (3) bulk activity in which the entire material is active. This complicates the determination of the intrinsic activity, a critical step towards the design of more-efficient OER catalysts, and motivates the use of a model system with a known and well-defined surface area¹⁴.

Isotope labelling studies using ¹⁸O and operando mass spectrometry are a powerful tool to distinguish surface from bulk catalysis²⁸. Most of the catalysts probed using this method have revealed at least some degree of lattice-oxygen involvement, including Au (ref. 29), IrO_2/Ti (ref. 30), Co_3O_4 spinel³¹, molecular cobaltate nanoclusters³², Ru-based catalysts^{28,33} and perovskite materials with a high metal–oxygen bond covalency³⁴. Others, which include Pt (ref. 35), oriented thin films of rutile RuO_2 (ref. 36) and perovskites with low

¹SurfCat, Department of Physics, Technical University of Denmark, Kgs. Lyngby, Denmark. ²Center for Electron Nanoscopy, Technical University of Denmark, Kgs. Lyngby, Denmark. ³Department of Micro- and Nanotechnology, Technical University of Denmark, Kgs. Lyngby, Denmark. ⁴Department of Materials, Imperial College London, Royal School of Mines, London, UK. ⁵These authors contributed equally: C. Roy, B. Sebok, S. B. Scott. *e-mail: ibchork@fysik.dtu.dk

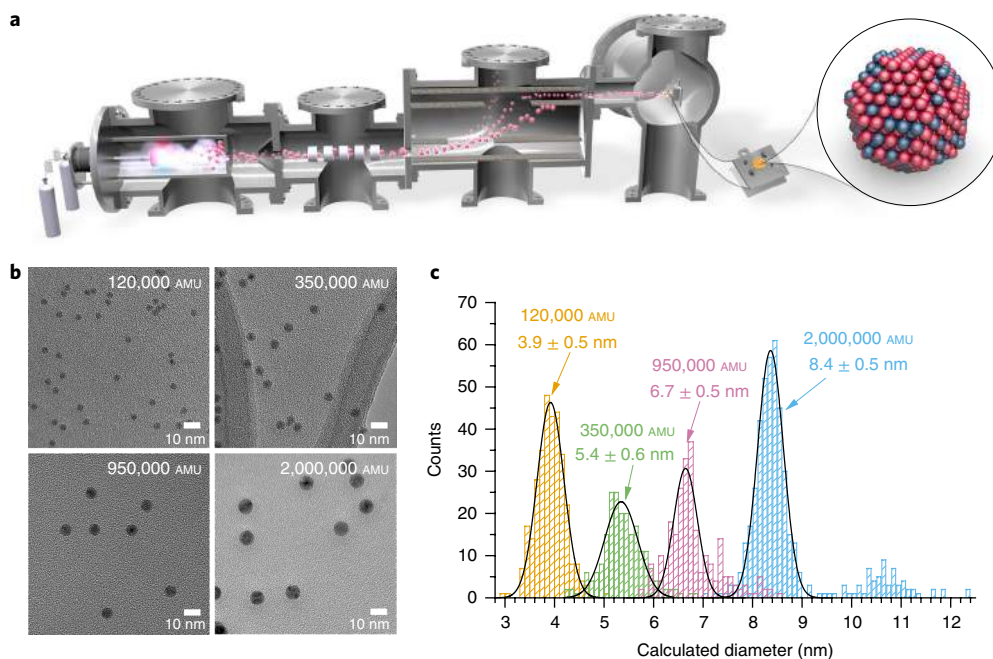


Fig. 1 | Deposition of mass-selected nanoparticles. **a**, A d.c. magnetron sputtering, gas-aggregation mass-selected nanoparticle source with lateral time-of-flight mass filter. Mass selected NiFe nanoparticles were deposited on polycrystalline gold disks for the activity measurements. **b**, TEM images of four different masses of NiFe nanoparticles. **c**, Size distributions, determined using the diameter measured on the TEM images in **b**, show the average size and 2σ for each mass deposited.

metal–oxygen bond covalency³⁴, have not. Shao-Horn and co-workers observed that lattice exchange occurs with materials that have a catalytic activity that is pH dependent, which indicates decoupled proton and electron transfers in the OER mechanism³⁴. Based on that argument, Ni(Fe)O_xH_y, which shows a higher catalytic activity in a stronger alkaline electrolyte, should also show participation of lattice oxygen³⁷. However, to the best of our knowledge, no studies have probed Ni(Fe)O_xH_y using isotopically labelled water, even though it is the catalyst of choice for industrial water electrolysis.

Such isotope studies consist of preparing the NiFeO_xH_y catalyst with one oxygen isotope (¹⁶O or ¹⁸O) or isotopic ratio, and then monitoring the O₂ products during oxygen evolution in an electrolyte that has a different isotopic ratio using a mass spectrometer (¹⁶O₂ at $m/z=32$, ¹⁶O¹⁸O at $m/z=34$ and/or ¹⁸O₂ at $m/z=36$). Should the O₂ that is evolved differ in isotopic composition from the electrolyte, then it is probably derived from the lattice oxygen or from water molecules intercalated between the layered nanosheets.

To draw a conclusion on the participation of lattice oxygen requires high sensitivity and thorough characterization: (1) to ensure that the isotopic oxygen is included in the NiFeO_xH_y catalyst, (2) to correctly identify whether it is evolved during the OER and, if so, (3) to quantify accurately the amount. To satisfy these requirements, we used a microchip-based electrochemistry–mass spectrometry (EC–MS) technology that has a high sensitivity. For example, it can detect 0.05 monolayer equivalents of H₂ desorbing from a flat Pt surface with a signal-to-noise ratio of ~20 (ref. 38). We complement the operando mass spectrometry experiments with postcharacterization by low-energy ion scattering (LEIS) spectroscopy, a surface sensitive technique that enables the differentiation of ¹⁶O and ¹⁸O.

In this study, we prepared size-selected NiFe particles using a magnetron sputtering nanoparticle source (Fig. 1a). This physical synthesis method yields homogeneous, monodisperse and chemically pure metallic particles, with a well-defined size and loading, ideal for fundamental studies^{39,40}. We compared the nanoparticles to NiFeO_xH_y electrodeposited thin films. We tested the catalytic activity

using a rotating disk electrode assembly in 1.0M KOH, in which the particles oxidize under operando conditions. We complemented these experiments with X-ray photoelectron spectroscopy (XPS), high-resolution transmission electron microscopy (HRTEM) and scanning electron microscopy (SEM), and performed isotope studies as described above. The nanoparticle samples function as a model system with a well-defined and tunable surface area.

Together, the nanoparticle model system, extensive characterization and isotope studies enabled us to answer two fundamental questions: (1) What is the intrinsic activity of the active sites on a well-defined surface of NiFeO_xH_y; (2) Does lattice oxygen participate in the reaction?

Results

NiFe model system. Figure 1b shows TEM images of the as-prepared nanoparticles. Figure 1c shows the size distribution of the as-prepared nanoparticles. The size distribution was determined from the TEM images as described in Supplementary Note 1. As presented in Fig. 1b, all the nanoparticles have a regular and spherical shape regardless of their mass. The average particle diameters were 3.9 ± 0.5 nm, 5.4 ± 0.5 nm, 6.7 ± 0.6 nm and 8.4 ± 0.5 nm, respectively, for the four selected masses (Fig. 1b,c). There was a small population of larger particles with double the intended mass, which resulted from doubly charged nanoparticles, especially in the case of the 8.4 nm particles.

Stability and effects of OER operating conditions. The 6.7 nm nanoparticles were characterized with LEIS and XPS, as shown in Fig. 2a,b, respectively. The LEIS spectra of the as-deposited nanoparticles (green curve) showed clear Ni and Fe peaks, which cannot be differentiated due to the small difference between their atomic masses. After electrochemical testing (blue curve), the LEIS spectra showed additional features identified as K, O and C, most probably from residual KOH electrolyte, nanoparticle oxidation and air exposure. XPS spectra (Fig. 2b) of the as-deposited nanoparticles revealed metallic Ni and Fe. XPS analysis after

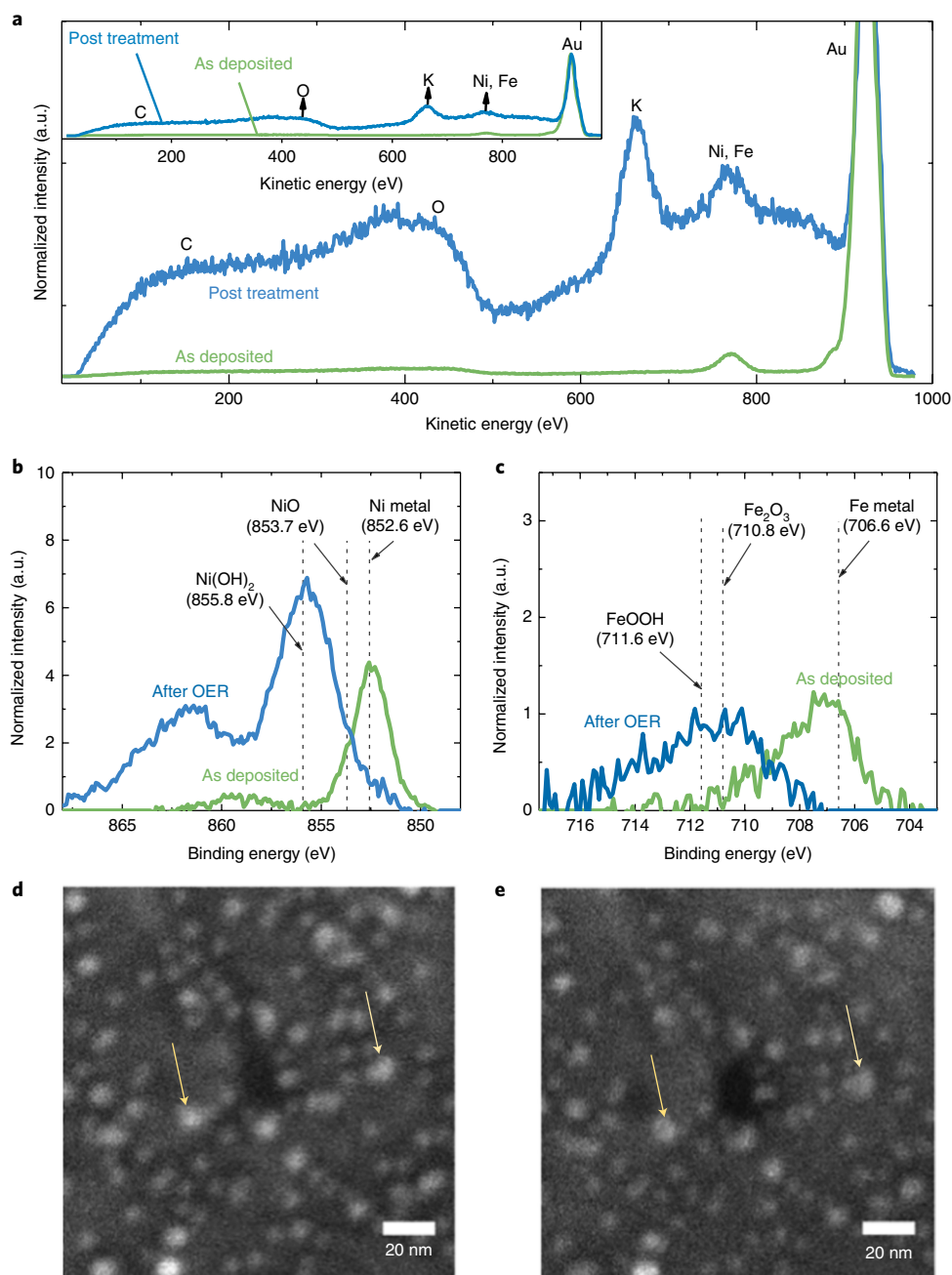


Fig. 2 | Ex situ characterization of the deposited 6.7 nm NiFe particles. **a**, LEIS spectra, **b–e**, XPS spectra (**b,c**) and SEM (**d,e**) of nanoparticles as deposited (**b,d**) and after electrochemical testing (**c,e**). The LEIS spectra are normalized to the height of the Au peak. The XPS spectra, shown for the Ni $2p_{3/2}$ (**b**) and Fe $2p_{3/2}$ (**c**) regions, are charge corrected and normalized with the Au $4f$ peak area after the subtraction of a Shirley background. The reference XPS binding energies are taken from refs ^{59–61}. The SEM images are taken at identical locations to evaluate the resistance against sintering and corrosion.

electrochemical treatment showed that oxide and hydroxide states are formed for both Ni and Fe. More precisely, NiO and Ni(OH)₂, and FeOOH and Fe₂O₃, were identified from the Ni and Fe $2p$ peaks, respectively. The composition determined based on the XPS spectra shows a similar Fe content before the electrochemical testing to the target for the deposition, namely 25%, and an Fe content of ~15% after electrochemical testing for all the nanoparticle sizes (Supplementary Note 3).

One challenge with nanoparticle catalysts is that they often coalesce under reaction conditions^{41–43}. In addition, the conditions under which the OER electrodes operate can cause metal dissolution^{44,45}. As a first step to evaluate the stability and resistance towards

corrosion and sintering, SEM images were acquired before and after the OER at identical locations to visualize directly any change in particle size or positions⁴⁶. From the example images shown in Fig. 2d,e taken before and after testing the activity, it can be seen that the 5.4 nm NiFe particles do not coalesce or dissolve during the two hour potentiostatic measurement at 1.6 V_{RHE}. Most of the nanoparticles can be found directly in both images. To probe the stability further, a chronoamperometric measurement was performed at 1.6 V_{RHE}. As presented in Fig. 3, the OER current was stable over 41 days (~1,000 hours). This result further confirms the stability of the NiFe catalyst previously reported by a stable chronoamperometric measurement at 10 mA cm⁻² over 24 hours^{47,48}.

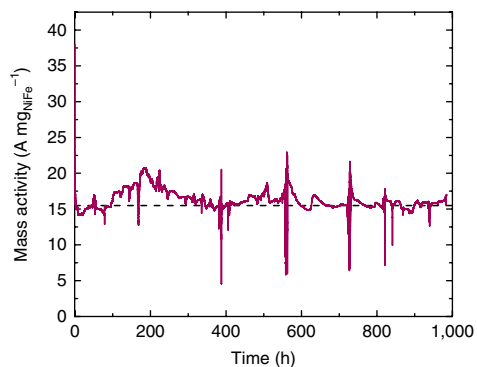


Fig. 3 | Stability of NiFe nanoparticles at 1.6 V_{RHE} in 1M KOH. The mass activity of ~100 ng of 6.7 nm NiFe nanoparticles at 1.6 V_{RHE}, with current interrupt (*iR*) correction, in 1M KOH. The dashed line is a guide to the eye.

To gain insight into the morphology and composition at the atomic level, we acquired identical-location HRTEM images of particles deposited on graphene-covered Au TEM grids both before and after two CV cycles at 10 mV s⁻¹ up to 1.5 V_{RHE}. The electrochemical treatment was mild to avoid the corrosion of the carbon grid at more anodic potentials. Before OER, the NiFe nanoparticles showed a polycrystalline structure. The typical image in Fig. 4a shows a single particle in which the Ni₃Fe phase can be identified⁴⁹. Figure 4b,c shows HRTEM images of the same nanoparticles before and after being electrochemically tested. We found that after electrochemical testing, the nanoparticles maintained their shape and their polycrystalline nature, as indicated by the non-uniform orientation of the lattice fringes, and by the contrast difference caused by diffraction. We used energy-dispersive spectroscopy (EDX) along with a focused electron beam to map the dispersion of Ni and Fe in the particles using cross-sectional line scans (Supplementary Note 4). A comparison of the Ni and Fe concentrations before and after electrochemical testing showed that some of the Fe leaches out after OER. This decrease in Fe concentration could be associated with the dissolution of FeOOH, known to be highly unstable under these experimental conditions⁵⁰.

Activity. The representative CVs of samples from each of the four nanoparticle-size groups, taken after 2 hours at 1.6 V_{RHE}, plotted in Fig. 5a show a clear difference in activity for the different particle sizes. The smallest particles, that is, 3.9 and 5.4 nm, provide the highest current normalized to the deposited metal mass. A significant OER current is observed that starts from $U \sim 1.5 V_{RHE}$ (overpotential of $\eta = 270$ mV). Using what is typically attributed to the Ni²⁺ to Ni^{3+/4+} redox couple¹³, we showed that the integral of the Ni reduction peak scales better with the calculated surface area than the total loading (Supplementary Fig. 4). Less than one electron is transferred per Ni atom in the larger nanoparticles. Figure 5b shows the average mass activity on a deposited metal basis at $\eta = 270$, 300 and 370 mV as a function of particle size. The activity was taken from the current recorded at a scan rate of 10 mV s⁻¹. No obvious difference in trend was observed when comparing the mass activities as a function of the size for different overpotentials.

To show the intrinsic activity, for Fig. 6a we converted the activity into TOF, that is, the number of O₂ molecules produced per active site per unit time, using three estimates for the number of active sites. TOF_{bulk} assumes that all the deposited Ni and Fe atoms are active, TOF_{redox} assumes one active site per electron is transferred in the Ni reduction peak of the CV and TOF_{surface} assumes that only the surface metal atoms of the nanoparticles are active sites (Methods and equations (1)–(6)). We also included the

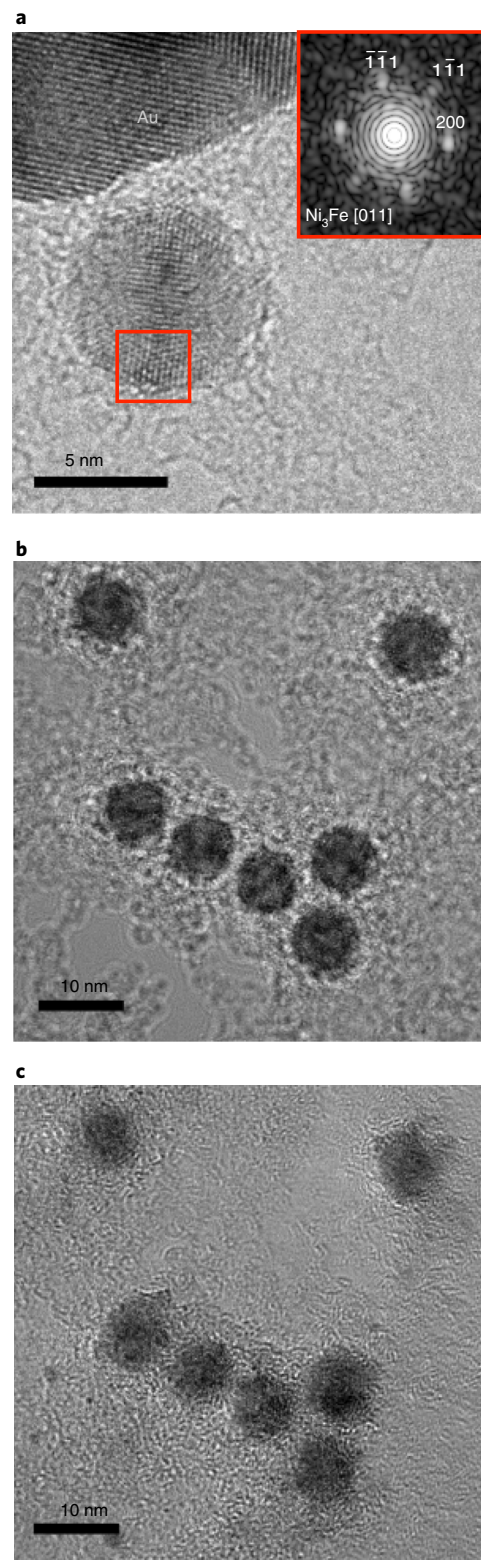


Fig. 4 | HRTEM investigation of the particles. HRTEM images of 6.7 nm (950×10^3 AMU) NiFe nanoparticles deposited on Au TEM grids. **a**, HRTEM image of a nanoparticle. Inset: The Fourier transform of the highlighted area shows the Ni₃Fe phase. **b, c**, Identical-location HRTEM images of nanoparticles before (**b**) and after (**c**) electrochemical oxidation.

TOF_{redox} calculated for NiFeO_xH_y thin films, for which the activity was measured by the same procedure as for the nanoparticles (Supplementary Fig. 5).

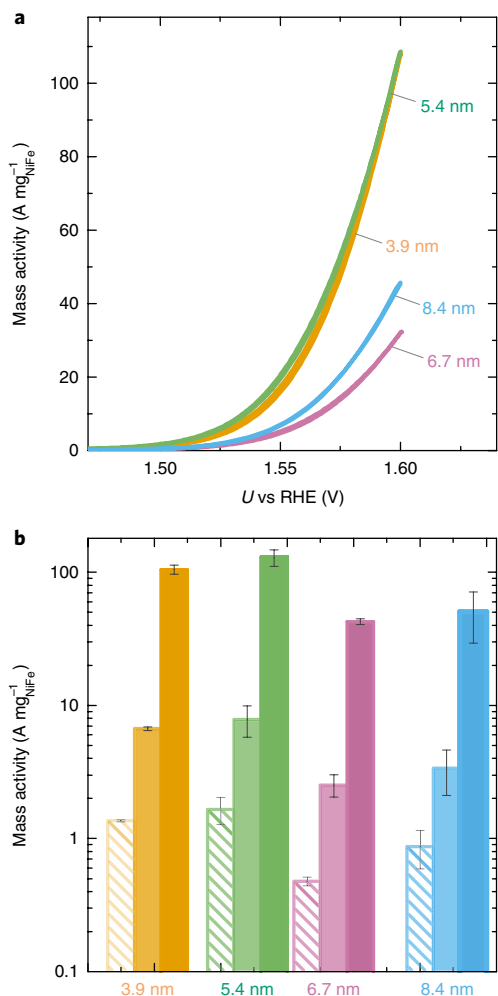


Fig. 5 | Catalytic activity of the NiFe nanoparticles. **a** CV at 10 mV s^{-1} of representative NiFeO_xH_y nanoparticle samples for each nanoparticle size. The current is normalized to the total metal mass loading. **b**, Mass-normalized activities at $\eta = 270$ (hatched), 300 (lighter shade) and 370 mV (darker shade). The average mass activity and s.d. are from three independent samples. All the activity measurements were done on Au substrates in N_2 -saturated 1 M KOH at $1,600$ revolutions per minute. The metal mass was determined from the nanoparticle deposition current.

The TOFs thus calculated show different trends with particle size. TOF_{bulk} is higher for the smaller particles, that is, 5.4 and 3.9 nm , and lower for the larger particles. $\text{TOF}_{\text{redox}}$ and $\text{TOF}_{\text{surface}}$ do not show any obvious particle-size dependence, though $\text{TOF}_{\text{redox}}$ has a larger scatter.

The $\text{TOF}_{\text{surface}}$ and TOF_{bulk} of the 5.4 nm NiFe nanoparticles were compared to state-of-the-art non-noble metal catalysts for the OER in alkaline media (Fig. 6b). The reaction rates of $6.2 \pm 1.6 \text{ s}^{-1}$ ($\text{TOF}_{\text{surface}}$) and $1.2 \pm 0.3 \text{ s}^{-1}$ (TOF_{bulk}) for 5.4 nm NiFe particles at $1.53 \text{ V}_{\text{RHE}}$ ($\eta = 300 \text{ mV}$) are among the highest reported for non-noble metal catalysts in an alkaline electrolyte^{4,16,27,47,51–54}.

Isotope labelling experiments. To provide further insight as to which TOF represents the true intrinsic activity, we used three complementary isotope labelling procedures, all on samples with 6.7 nm particles, referred to below as procedures *a*, *b* and *c*, and illustrated schematically in Fig. 7. The natural oxidation of NiFe particles when exposed to air meant we had to oxidize the catalyst in H_2^{16}O and

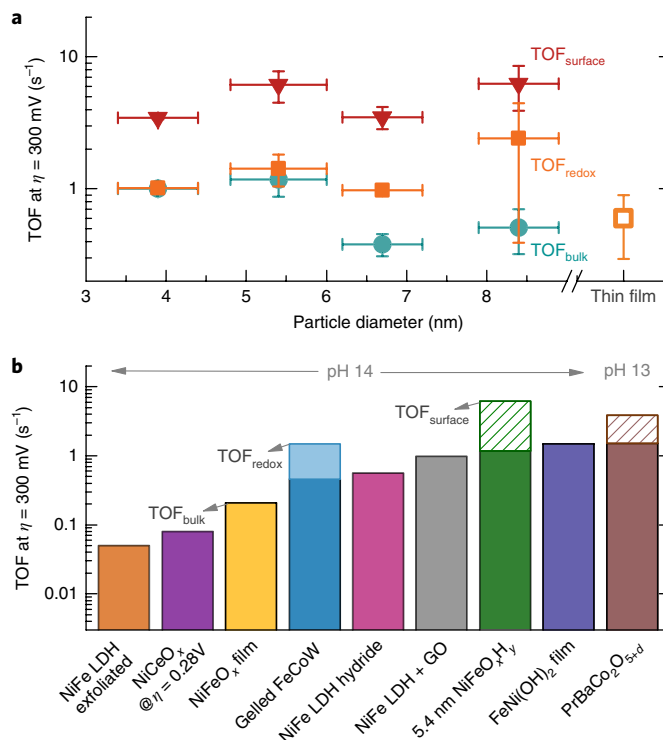


Fig. 6 | TOF as a function of size, and comparison to state-of-the-art non-noble metal catalysts. **a**, TOF calculated from the total metal mass (TOF_{bulk}), the Ni redox peak ($\text{TOF}_{\text{redox}}$) and the estimated surface atoms ($\text{TOF}_{\text{surface}}$) of the NiFe nanoparticles at $\eta = 300 \text{ mV}$ measured in N_2 -saturated 1.0 M KOH at 10 mV s^{-1} as a function of particle size. The Ni redox peak was used to measure the TOF of the NiFe thin film. The y-axis error bars come from three independent samples and were calculated using $\sqrt{\frac{\sum(x-\bar{x})^2}{(n-1)}}$, where x is the activity value and \bar{x} the average activity from the three samples (n). **b**, TOF of state-of-the-art non-noble OER catalysts in alkaline. Sources: NiFe layered double hydroxide (LDH) exfoliated⁵³, NiCeO_x @ $\eta = 0.28 \text{ V}$ (ref. 47), NiFeO_x film²⁷, gelled FeCoW (ref. 51), NiFe LDH hydride⁵², NiFe-LDH + GO (ref. 54), $5.4 \text{ nm NiFeO}_x\text{H}_y$ (this work) $\text{FeNi}(\text{OH})_2$ film¹⁶ and $\text{PrBaCo}_2\text{O}_{5+d}$ (ref. 4). When possible, both the minimum (bulk, darker solid colours) and maximum (surface, striped colour, or redox, lighter shade of the solid colour) TOFs were estimated. The $\text{TOF}_{\text{redox}}$ of gelled FeCoW was calculated using the Co redox peak, and the $\text{TOF}_{\text{surface}}$ for $\text{PrBaCo}_2\text{O}_{5+d}$ was calculated based on the surface area from N_2 physisorption (Brunauer-Emmett-Teller).

then perform OER in an ^{18}O -based electrolyte (procedure *a*). We also oxidized the NiFe particles in H_2^{18}O (procedure *b*) and $^{18}\text{O}_2$ (procedure *c*) atmosphere to study the possible differences between hydroxide and oxide compounds.

In procedure *a*, ^{16}O is incorporated into the NiFe nanoparticles through cycling in 0.1 M KOH made from ultrapure water, and the oxygen evolution process takes place in 0.1 M KOH made from ^{18}O water ($\sim 97\% \text{ }^{18}\text{O}$). Due to the natural abundance of ^{16}O , this has the advantage that the nanoparticles can easily be prepared with $99.8\% \text{ }^{16}\text{O}$. However, the lower isotopic purity of ^{18}O -labelled water limits the sensitivity towards isotope exchange of the subsequent EC-MS measurement. In procedures *b* and *c*, ^{18}O is incorporated in the NiFe structure either by cycling in an ^{18}O -labelled 0.1 M KOH electrolyte (procedure *b*) or by heating at $450 \text{ }^\circ\text{C}$ in the vacuum chamber in the presence of $^{18}\text{O}_2$ gas (procedure *c*). This allows for a greater sensitivity towards lattice exchange, but adds some uncertainty to the initial isotopic composition of the catalyst.

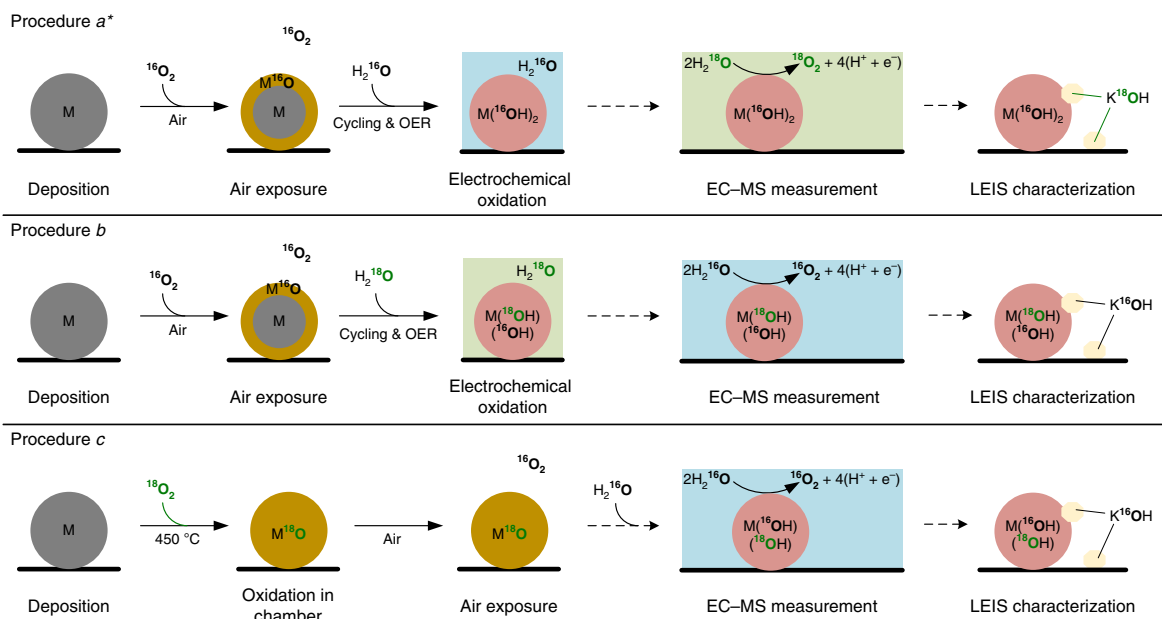


Fig. 7 | Isotope labelling experimental procedures. Schematic representation of the isotopic labelling experiments. Procedure *a* uses $H_2^{16}O$ to oxidize the nanoparticles and $H_2^{18}O$ for the oxygen evolution, and the opposite is done for Procedure *b*. Procedure *c* uses $^{18}O_2$ gas to oxidize NiFe and the oxygen evolution is performed in ^{16}O water. In the representation, M refers to Ni and Fe metal atoms. *The main text focuses on procedure *a*.

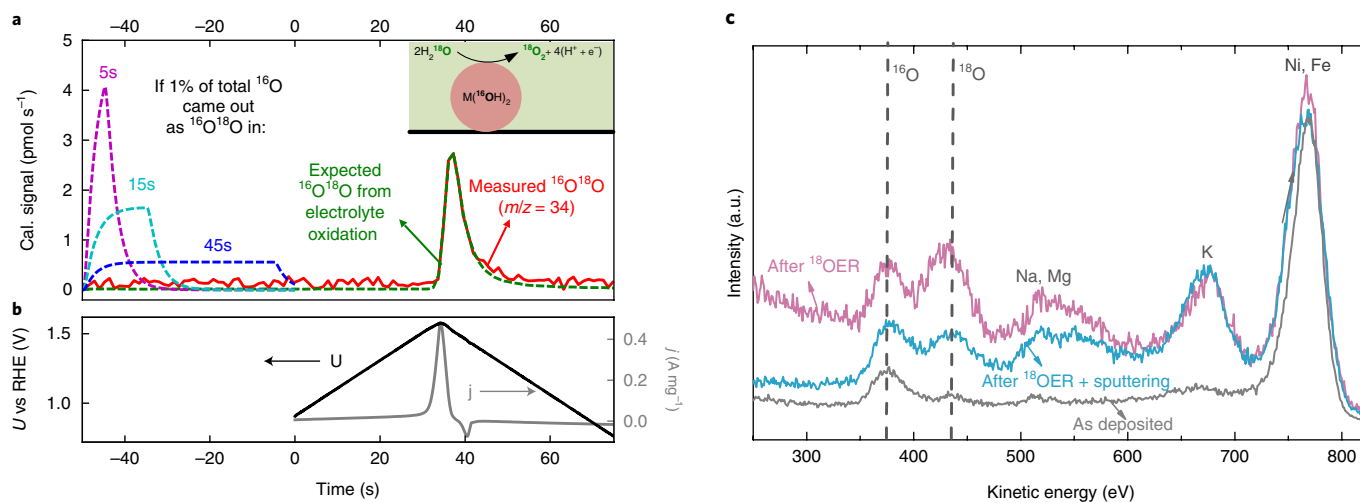


Fig. 8 | EC-MS and LEIS results from the isotope labelling experiment using procedure *a*. **a**, First linear sweep voltammometry in the $H_2^{18}O$ electrolyte after the sample preparation with ^{16}O . Calibrated mass spectrometer signal of $^{16}O^{18}O$ ($m/z=34$) (red line) detected during oxygen evolution in 0.1M KOH made with $H_2^{18}O$ during the first electrochemical potential cycle after the sample preparation with ^{16}O . The $^{16}O^{18}O$ signal expected without lattice exchange due to the composition of the electrolyte, which is a constant fraction of the $^{18}O_2$ ($m/z=36$) signal, is co-plotted (green line). Also included are simulations of the $m/z=34$ signal if 1% of the total ^{16}O contained by the oxidized catalyst came out as $^{18}O^{16}O$ in 5s (magenta), 15s (cyan) or 45s (blue). The inset is a schematic of the oxygen evolution reaction in a ^{18}O -electrolyte on a $NiFeO_xH_y$ nanoparticle. **b**, The potential (black) and current (grey) from the same experiment. **c**, The LEIS spectra of the sample as deposited (grey), after the EC-MS experiment (purple) and after sputtering (blue).

In procedure *a*, the sample of deposited particles was cycled in 0.1 M KOH made from ultrapure water until a stable CV was obtained, that is, 20 cycles 0.5–1.5 V_{RHE} . At this point we assumed that the catalyst was in the fully oxygenated form, nominally $M(^{16}OH)_2$ where $M=Ni_xFe_{1-x}$. The electrode was then transferred at an open-circuit voltage to a stagnant thin-layer cell filled with ^{18}O -labelled 0.1 M KOH for measurement by EC-MS. The first cycle up to 1.55 V_{RHE} and back to 0.5 V_{RHE} is shown in Fig. 8a,b. In Fig. 8a, the calibrated $m/z=34$ ($^{16}O^{18}O$) mass spectrometer signal is plotted

as a function of time, and in Fig. 8b the potential and current are plotted on the same time axis. Co-plotted with the measured $^{16}O^{18}O$ signal in Fig. 8a is the expected $^{16}O^{18}O$ signal due to oxidation of the electrolyte, which contains only ~97% ^{18}O . The expected $^{16}O^{18}O$ signal is the measured $^{18}O_2$ ($m/z=36$) signal multiplied by the steady-state $^{16}O^{18}O/^{18}O_2$ ratio. This ratio, as well as the calibration, were determined under operando conditions by steady-state oxygen evolution (Supplementary Note 5). The measured and expected $^{16}O^{18}O$ coincided, which indicates that all of the signal at $m/z=34$

can be explained by the oxidation of the electrolyte alone. The onset of the oxygen signal is delayed with respect to the onset of the OER current by about ~3 s, as predicted by the mass-transport model described in Trimarco et al.³⁸, which indicates that the current at low overpotential does, indeed, go to OER and not another process.

To illustrate the sensitivity, we included in Fig. 8a the expected excess $m/z = 34$ signal if 1% of the total ^{16}O contained by the catalyst, equivalent to approximately 10% of a monolayer, were released as $^{16}\text{O}^{18}\text{O}$. The release of 1% of the total ^{16}O in 45 seconds (dashed blue line in Fig. 8a), which corresponds to approximately 0.2% of a monolayer per second, is significantly above the detection limit. In comparison, the peak oxygen signal (at $m/z = 36$) in this scan corresponds to 19% of a monolayer per second, or about 100 times greater. This proves that if even 1% of the OER activity were due to lattice oxygen evolution, it would be detectable.

The results of procedures *b* and *c* (Supplementary Fig. 7a–d) are similar, but because of low natural abundance of ^{18}O (0.02%), the sensitivity towards isotope exchange at $m/z = 34$ and 36 is even higher. To determine whether the result is general, we also performed the isotope experiment (following procedure *a*) on a NiFeO_xH_y thin film, and again observed no lattice exchange (Supplementary Fig. 7e). Additionally, to prove that our set-up is, indeed, sensitive enough to detect a lattice exchange when it does take place, we performed the same experiment on IrO_2/Ti in acid, as described in Fierro et al.³⁰, and reproduced their result of an isotope exchange greater than one monolayer. In Supplementary Fig. 8, this result is directly compared with that from NiFeO_xH_y .

In procedure *a*, after the EC–MS, the sample was rinsed in H_2^{18}O before being transferred back to a vacuum for LEIS. The LEIS spectrum after OER, that is, the purple line in Fig. 8c, shows additional peaks when compared to the initial LEIS spectrum (black line), which we attribute to ^{16}O , ^{18}O , impurity Na and Mg salt deposits from the H_2^{18}O rinsing, and to residual K from the electrolyte. The sample was then Ar-sputtered for 30 minutes before another LEIS spectrum was taken. This spectrum (blue line) shows an increased $^{16}\text{O}/^{18}\text{O}$ ratio, compared to the initial one. We therefore attribute the ^{18}O peak to residual K^{18}OH and/or other hydroxide salts on the surface of the sample and the ^{16}O peak to ^{16}O that remained in the catalyst. After both procedures *b* and *c*, the $^{18}\text{O}/^{16}\text{O}$ ratio in LEIS after OER, rinsing with ultrapure water and sputtering, was approximately 1:1, with little to no K or other impurities, as shown in Supplementary Fig. 7. In both cases, there is a clear ^{18}O signal even before sputtering, which indicates that this isotope is present at the surface of the catalyst. The postsputtering 1:1 ratio presumably reflects the nominal $\text{M}^{(18}\text{OH})(^{16}\text{OH})$ formula that results from the experimental procedures, as illustrated in Fig. 7b,c. As the natural abundance of ^{18}O is so low (0.2%), the presence of ^{18}O on the LEIS spectra in procedures *b* and *c* implies that it was incorporated during the catalyst preparation before OER, and not during transfer through air from EC–MS to LEIS.

Discussion

The results obtained from the identical-location SEM (Fig. 2c), in addition to the stable current over 1,000 hours (Fig. 3), prove that the NiFeO_xH_y particles are remarkably stable against corrosion.

The activity dependence on particle size is similar at 270, 300 and 370 mV overpotential (Fig. 5b). This is consistent with a lack of subsurface activity, which would involve the diffusion of water and oxygen through the nanoparticles, and could therefore introduce greater mass transport limitations for larger particles at high overpotentials, if the diffusion is sufficiently slow. Furthermore, the activity of the particles normalized to surface area, that is, $\text{TOF}_{\text{surface}}$, does not change with particle size (Fig. 6a). In contrast, the activity of the particles normalized to the total mass, which is proportional to the TOF_{bulk} , decreases with increasing particle size. Different Fe content cannot explain the observed trends (Supplementary Fig. 2b).

$\text{TOF}_{\text{redox}}$ of the electrodeposited NiFeO_xH_y film shows a similar activity to that reported by Trotochaud et al.²⁷. This is slightly lower than the $\text{TOF}_{\text{redox}}$ for the nanoparticles, also consistent with a lack of subsurface activity and the observation that the Ni redox peak probes more than the Ni surface atoms.

Mass spectrometry and LEIS measurements for isotope experiments on NiFeO_xH_y particles using three different approaches all indicate that oxygen is retained in the catalyst during OER, both in the bulk and, to at least some degree, also on the surface of the catalyst. Isotope experiments on a NiFeO_xH_y thin film agree. The significance of this result is twofold. First, it provides additional evidence against activity below the outer surface or a near-surface region in which water is highly mobile, as this would involve lattice oxidation and/or the oxidation of low-mobility intercalated water. Second, the oxygen evolution mechanism does not proceed via lattice oxygen.

Based on the arguments above, we conclude that active sites are limited to a near-surface region, and that $\text{TOF}_{\text{redox}}$ is a lower bound to the intrinsic activity of the active sites. Previous studies that show a linear correlation between loading and activity used porous electrodes without a well-defined outer surface²⁴. Given the evidence presented here against bulk activity, we explain this observation on the basis that the surface area scales linearly with loading for these porous materials.

However, to determine if activity is limited to the outer surface atomic layer ($\text{TOF}_{\text{surface}}$) is more difficult. Although the charge passed in the Ni redox feature during cyclic voltammetry corresponds to ~3 atomic layers, this does not necessarily mean that this entire region also participates in OER. The nature of the transport involved in the Ni redox feature in alkaline is an unsolved problem¹³, and models based on the transport of protons, hydroxide or cations have been proposed⁵⁵. Whereas the Ni redox feature may only require the shuttling of a proton, OER necessarily requires the net transport of oxygen species. Our isotope result indicates that transport below the outer surface is either so slow as to inhibit OER or fast enough that any water or hydroxide in this region exchanges with the electrolyte before the onset of OER. We must admit that we cannot yet conclusively distinguish between the two possibilities.

As mentioned previously, lattice exchange is material dependent. The phenomenon is observed with Co_3O_4 (ref. 31), iridium-based catalysts³⁰ and a few perovskites³⁴. Besides being sensitive to the composition of the material, the lattice oxygen exchange also seems to be dependent on the structure. Indeed, lattice exchange was observed with amorphous and nanocrystalline RuO_2 phases with undercoordinated edge sites^{28,33}, but not with crystalline rutile RuO_2 (ref. 36). Although we did not observe lattice exchange during OER in the case of NiFeO_xH_y nanoparticles or an electrodeposited NiFeO_xH_y thin film, the results may not be generalizable to all synthesis methods. Furthermore, we cannot rule out that such phenomena could, in principle, occur at much higher potentials which, unfortunately, cannot yet be studied in our EC–MS set-up, due to bubble formation.

The absence of the participation of lattice oxygen in NiFeO_xH_y is in disagreement with the hypothesis that lattice exchange should occur with materials that have a catalytic activity that is pH dependent on the hydrogen scale³⁴, which is the case for NiFeO_xH_y (ref. 56). In contrast, it provides evidence for an associative mechanism, such as that proposed by Bell and co-workers¹⁹.

In summary, we used well-characterized mass-selected nanoparticles of Ni and Fe as a model system to investigate their fundamental properties under oxygen-evolution conditions. We provided fundamental insight into the reaction and the origin of the high performance using LEIS spectroscopy and the microchip-based EC–MS set-up. The particles showed an exceptionally high activity and stability over 1,000 hours at 1.6 V_{RHE} . Isotope-labelling experiments performed after three distinct approaches showed that there was no participation of lattice oxygen or intercalated water in the oxygen

evolution. This allows us to conclude that the active sites responsible for such exceptional activity are only located in the ~3 atomic layer redox-active near-surface region of the nanoparticles, but to determine if the activity is limited to the outer surface requires a better knowledge of the ionic transport mechanisms within this region. Normalizing the activity to the outer surface results in a TOF of $6.2 \pm 1.6 \text{ s}^{-1}$ at $\eta = 0.3 \text{ V}$, the highest reported to date. Further enhancements to the catalytic activity should focus on tailoring the atoms at the near-surface region, as opposed to the bulk.

Methods

Preparation of mass-selected NiFe nanoparticles. NiFe nanoparticles were prepared using a noble-gas aggregation magnetron sputtering nanoparticle source combined with a lateral time-of-flight mass filter (Fig. 1a) capable of mass selection of the nanoparticles before deposition³⁷ (Nano-Beam 2011, Birmingham Instruments Ltd) similar to that described by Pratontep et al.³⁸. A 75 at% Ni/25 at% Fe sputtering target (99.95%, Kurt J. Lesker Ltd) was used and the particles were deposited onto clean and smooth Au disks. The nanoparticle source was fully UHV compatible and the mass filter had a base pressure in the low 10^{-10} mbar region. The mass filter was set to be used with negatively charged particles, and to have a mass resolution of $\sim m/\Delta m = 20$ to maximize the current of the particles. The vast majority of the particles that exited the nanoparticle source carried a single charge, and thus the current measured on the sample during the deposition together with the deposition time can be translated into the number of deposited particles. If not otherwise stated, the loading of the electrodes was a 15% projected surface area coverage, which corresponds to a total metal mass loading of 50–125 ng, which means a 315–785 ng cm^{-2} loading in circular spots of 4.5 mm in diameter, depending on the particle size.

Determination of particle-size distributions. NiFe nanoparticles with masses of 120,000, 350,000, 950,000 and 2,000,000 AMU were deposited onto Cu TEM grids covered with lacey carbon (300 mesh, Agar Scientific Ltd). After deposition and transfer under atmospheric conditions, the particles were imaged in the bright-field TEM mode in an FEI Tecnai T20 G² equipped with a thermionic electron source and using a 200 keV acceleration voltage. The images were analysed with ImageJ software to extract the average area of the particle projections, and a diameter was calculated assuming a circular shape (Supplementary Note 1).

Electrochemical measurements. Electrochemical measurements were performed using a rotating disk electrode in a PTFE (Teflon) cell at 1,600 revolutions per minute in N_2 -saturated 1.0 M KOH. A carbon rod was used as the counter electrode with a Hg/HgO electrode as the reference electrode, which was calibrated to the RHE in the same electrolyte saturated with 1 bar H_2 over a clean Pt mesh before each experiment. The Ohmic drop was measured by using electrochemical impedance spectroscopy over a range of 10–200,000 Hz at an a.c. amplitude of 10 mV. The high-frequency intercept was fitted to an equivalent circuit to obtain the Ohmic losses, which typically ranged from 4 to 18 Ω . The Ohmic drop compensation was done by online Ohmic drop correction in which an 85% correction was applied. Ultrapure water (Milli-Q, 18.2 M Ω cm) with KOH (semiconductor grade, pellets, 99.9%) were used to prepare 1.0 M KOH. The initial catalytic activity was measured by recording five cyclic voltammograms at 10 mV s^{-1} up to 1.6 V_{RHE} followed by a 2 h potentiostatic measurement at 1.6 V_{RHE}. Finally, the activity was again assessed using CV. The activity of the different samples for the OER presented in this work was taken from the final CV. For each experiment, three independent samples were tested and the activity was averaged (Supplementary Figs. 9–11). The longer stability measurement was a static measurement at 1.6 V_{RHE}, for which the NiFe particles were deposited onto a gold sheet. The duration of this experiment meant only two samples were tested. The mass activity was obtained by normalizing the current with the total mass of Ni and Fe determined from the deposition current and time.

To compare the differences between lattice oxygen participation in NiFeO_xH_y nanoparticles and thin film, thin films of NiFeO_xH_y were electrodeposited. Using a three-electrode set-up, a current of -0.2 mA cm^{-2} for 5 min in an electrolyte of 0.1 M Ni(NO₃)₂·6H₂O and 5 mM FeCl₂. The composition determined by XPS indicates a mixture of approximately 32% Fe and 68% Ni at the surface.

Turnover frequency. To calculate the TOF, we used the formula:

$$\text{TOF (s}^{-1}\text{)} = \frac{r_{\text{O}_2}}{\text{of active sites}} \quad (1)$$

The rate of O₂ turnovers ($r_{\text{O}_2} \text{ s}^{-1}$) was calculated from the raw current:

$$r_{\text{O}_2} = i \times \left(\frac{N_A}{zF} \right) \quad (2)$$

Where i (A) is the current, N_A is the Avogadro number (6.022×10^{23} O₂ molecules per mol O₂), z is the number of electrons involved in the evolution of 1 O₂ molecule and F the Faraday constant (96,485 C mol⁻¹).

We determined a minimum (TOF_{bulk}) and a maximum (TOF_{surface}) TOF based on two different assumptions on the number of active sites.

For the calculation of TOF_{bulk}, we assumed that all the metal atoms deposited are active for OER. To calculate the total number of Ni and Fe metal atoms deposited on the surface ($N_{\text{metal atom}}^{\text{total}}$), the number of deposited particles ($N_{\text{particles}}$) were multiplied by the average number of atoms in each particle ($N_{\text{metal atom}}^{\text{particle}}$):

$$N_{\text{metal atom}}^{\text{total}} = N_{\text{particles}} \times N_{\text{metal atom}}^{\text{particle}} \quad (3)$$

$N_{\text{particles}}$ can be calculated from the deposition current (I_{depo} (A)), time of deposition (t_{depo} (s)) and the electric charge C (6.242×10^{-18} electrons C⁻¹) using equation (4):

$$N_{\text{particles}} = I_{\text{depo}} \times t_{\text{depo}} \times C \quad (4)$$

Finally, to calculate the number of metal atoms in a particle, we used the deposited particle mass set by the mass filter (m_{particle} (kg)), N_A (mol⁻¹) and the average molar mass ($M_{\text{Ni}_x\text{Fe}_{1-x}}$ [kgmol⁻¹]) using the composition determined from the XPS after electrochemical treatment for each sample:

$$N_{\text{metal atom}}^{\text{particle}} = \frac{N_A \times m_{\text{particle}}}{M_{\text{Ni}_x\text{Fe}_{1-x}}} \quad (5)$$

To calculate the TOF_{surface}, the number of surface Ni and Fe atoms had to be calculated. The diameter of the nanoparticles was determined by TEM images and used to calculate the surface area per particle (A_{particle}) assuming a spherical shape. This is a conservative approach as part of the nanoparticle's surface will interface with the substrate and therefore will not contribute to the OER. Finally, this area was multiplied by $N_{\text{particles}}$ and the density of surface metal atoms to get the total number of surface Ni and Fe atoms. The assumed density of the surface metal atoms (ρ_{atoms}) of 12.5 metal atoms nm⁻² is based on the metal–metal distance of 2.83 Å for NiFeO_xH_y measured in situ under OER conditions¹⁹:

$$N_{\text{surface atom}}^{\text{total}} = N_{\text{particles}} \times \rho_{\text{atoms}} \times A_{\text{particle}} \quad (6)$$

XPS and LEIS characterization. LEIS (Supplementary Figs. 12 and 13) and XPS spectra (Supplementary Figs. 14–16) were recorded for each sample after deposition (without breaking the vacuum) and after activity testing. To remove the remaining electrolyte on the surface after the activity test, the samples were thoroughly rinsed with ultrapure water (18.2 M Ω cm) before loading into the ultrahigh vacuum chamber to prevent the formation of a potassium layer hindering the detection of other elements.

For LEIS measurements, 1 keV He⁺ ions from an Omicron ISE100 ion gun were used and the energy of the scattered ions was recorded with the same 7-channel analyser used for XPS measurements operated in constant retard ratio mode (with a retard ratio of 5). The LEIS spectra presented are normalized based on the intensity of the gold peak at ~925 eV.

For the XPS measurements, unmonochromatized Mg K α radiation from a SPECS XR50 dual filament X-ray gun was used. The electron energies were measured with an Omicron NanoSAM 7-channel energy analyser operated in the constant pass energy mode. A pass energy of 50 eV was chosen to increase the signal from the low loadings of nanoparticles. For each sample, a survey scan and detailed scans of Au 4f, O 1s, Ni 2p_{3/2} and Fe 2p_{3/2} were recorded. All the spectra were charge corrected based on the Au 4f_{7/2} peak, which we assumed to correspond to metallic Au at 84 eV binding energy. A Shirley background was subtracted from the detailed spectra presented and the intensities were normalized with the Au 4f peak area.

Identical-location SEM imaging. Identical-location SEM imaging was performed on a sample that contained 5.4 nm NiFe particles on the Au electrode after deposition and transfer under atmospheric conditions and after electrochemical testing. SEM images were acquired at 5 kV using an FEI Helios EBS3 microscope equipped with a field emission gun and a through-the-lens detector for high-resolution imaging.

Identical-location TEM imaging and EDX line scans. Identical-location HRTEM images were recorded at 80 kV electron energy, using a FEI Titan E-Cell 80–300 ST TEM with a monochromated electron source and postobjective aberration correction. For the identical-location TEM studies, particles were deposited on Au-coated Cu TEM grids with suspended monolayer graphene layers (Quantifoil). After imaging, the grids were mounted to a rotating disk electrode set-up and subjected to two CVs at 10 mV s^{-1} between 1 and 1.5 V_{RHE} in 1 M KOH. After the electrochemical oxidation, the particles were transferred back to the TEM and imaged a second time. EDX line scans were recorded using a silicon drift detector from Oxford Instruments on random particles before and after electrochemical oxidation.

EC–MS experiments. To investigate oxygen exchange between the NiFe particles and the electrolyte, isotopically labelled electrolyte (with ¹⁸O) and EC–MS were used. The EC–MS set-up was based on a microfabricated membrane coated with

a fluorinated polymer and a well-defined capillary. Below the membrane, a small cavity was pressurized with He carrier gas and, together with the capillary forces, the electrolyte is kept out of the chip. The cavity was connected to a vacuum chamber equipped with a quadrupole mass spectrometer (Pfeiffer Vacuum QMA 125) through a well-defined microfabricated capillary that limited the flow of molecules to a level that can be handled by a single turbomolecular pump. For the experiments, a self-designed stagnant layer electrochemical cell was used in which the electrolyte thickness was 100 μm , which, together with the design of the vacuum chamber and microchip, gave a time response below 1 s. The area under the modelled curves in Fig. 8 (blue, magenta and cyan lines) corresponds to the nominal number labelled oxygen atom in the nanoparticle samples, and the shapes of these curves were calculated by a mass transport model that accounted for diffusion of O_2 through the 100 μm electrolyte layer. Details of the set-up, experimental method and mass-transport model are described elsewhere³⁸. All the experiments were performed using a 0.1 M KOH electrolyte made with either ultrapure water (natural isotope distribution) or ^{18}O enriched water (97.2% H_2^{18}O , 1.3% H_2^{17}O and 1.5% H_2^{16}O , Medical Isotopes). The mass spectrometer signals were calibrated internally for each experiment, as was the steady-state ratio of $m/z=34$ to $m/z=36$ for procedure *a*. The raw data for these calibrations are shown (for procedure *a*) in Supplementary Fig. 6.

Data availability

The data that support the plots within this paper and other findings of this study are available from the corresponding author upon reasonable request.

Received: 28 February 2018; Accepted: 14 September 2018;

Published online: 5 November 2018

References

- Lewis, N. S. & Nocera, D. G. Powering the planet: chemical challenges in solar energy utilization. *Proc. Natl Acad. Sci. USA* **103**, 15729–15735 (2006).
- Debe, M. K. Electrocatalyst approaches and challenges for automotive fuel cells. *Nature* **486**, 43–51 (2012).
- Montoya, J. H. et al. Materials for solar fuels and chemicals. *Nat. Mater.* **16**, 70–81 (2017).
- Hong, W. T. et al. Toward the rational design of non-precious transition metal oxides for oxygen electrocatalysis. *Energy Environ. Sci.* **8**, 1404–1427 (2015).
- Durst, J. et al. New insights into the electrochemical hydrogen oxidation and evolution reaction mechanism. *Energy Environ. Sci.* **7**, 2255–2260 (2014).
- Stamenkovic, V. R., Strmcnik, D., Lopes, P. P. & Markovic, N. M. Energy and fuels from electrochemical interfaces. *Nat. Mater.* **16**, 57–69 (2017).
- Greeley, J. & Markovic, N. M. The road from animal electricity to green energy: combining experiment and theory in electrocatalysis. *Energy Environ. Sci.* **5**, 9246 (2012).
- Cifrain, M. & Kordes, K. in *Handbook of Fuel Cells—Fundamentals, Technology and Applications* Vol. 1 (eds Vielstich, W.A., Gasteiger, H.A. & Lamm, A.) 267–280 (Wiley, Hoboken, 2010).
- Pagliaro, M., Konstandopoulos, A. G., Ciriminna, R. & Palmisano, G. Solar hydrogen: fuel of the near future. *Energy Environ. Sci.* **3**, 279 (2010).
- Seh, Z. W. et al. Combining theory and experiment in electrocatalysis: insights into materials design. *Science* **355**, eaad4998 (2017).
- The production of hydrogen and oxygen through the electrolysis of water. *Scientific American Supplement* No. 819 Vol. XXXII, article II (1891).
- Trotochaud, L., Young, S. L., Ranney, J. K. & Boettcher, S. W. Nickel–iron oxyhydroxide oxygen-evolution electrocatalysts: the role of intentional and incidental iron incorporation. *J. Am. Chem. Soc.* **136**, 6744–6753 (2014).
- Dionigi, F. & Strasser, P. NiFe-based (oxy)hydroxide catalysts for oxygen evolution reaction in non-acidic electrolytes. *Adv. Energy Mater.* **6**, 1600621 (2016).
- Burke, M. S., Enman, L. J., Batchellor, A. S., Zou, S. & Boettcher, S. W. Oxygen evolution reaction electrocatalysis on transition metal oxides and (oxy)hydroxides: activity trends and design principles. *Chem. Mater.* **27**, 7549–7558 (2015).
- Enman, L. J., Burke, M. S., Batchellor, A. S. & Boettcher, S. W. Effects of intentionally incorporated metal cations on the oxygen evolution electrocatalytic activity of nickel (oxy)hydroxide in alkaline media. *ACS Catal.* **6**, 2416–2423 (2016).
- Klaus, S., Cai, Y., Louie, M. W., Trotochaud, L. & Bell, A. T. Effects of Fe electrolyte impurities on $\text{Ni}(\text{OH})_2/\text{NiOOH}$ structure and oxygen evolution activity. *J. Phys. Chem. C* **119**, 7243–7254 (2015).
- Li, N. et al. Influence of iron doping on tetravalent nickel content in catalytic oxygen evolving films. *Proc. Natl Acad. Sci. USA* **114**, 1486–1491 (2017).
- Görlin, M. et al. Oxygen evolution reaction dynamics, Faradaic charge efficiency, and the active metal redox states of Ni–Fe oxide water splitting electrocatalysts. *J. Am. Chem. Soc.* **138**, 5603–5614 (2016).
- Friebel, D. et al. Identification of highly active Fe sites in $(\text{Ni,Fe})\text{OOH}$ for electrocatalytic water splitting. *J. Am. Chem. Soc.* **137**, 1305–1313 (2015).
- Stevens, M. B., Trang, C. D. M., Enman, L. J., Deng, J. & Boettcher, S. W. Reactive Fe-Sites in Ni/Fe (oxy)hydroxide are responsible for exceptional oxygen electrocatalysis activity. *J. Am. Chem. Soc.* **139**, 11361–11364 (2017).
- Hunter, B., Winkler, J. & Gray, H. Iron is the active site in nickel/iron water oxidation electrocatalysts. *Molecules* **23**, 903 (2018).
- Ahn, H. S. & Bard, A. J. Surface interrogation scanning electrochemical microscopy of $\text{Ni}_{1-x}\text{Fe}_x\text{OOH}$ ($0 < x < 0.27$) oxygen evolving catalyst: kinetics of the ‘fast’ iron sites. *J. Am. Chem. Soc.* **138**, 313–318 (2016).
- Xiao, H., Shin, H. & Goddard, W. A. Synergy between Fe and Ni in the optimal performance of $(\text{Ni,Fe})\text{OOH}$ catalysts for the oxygen evolution reaction. *Proc. Natl Acad. Sci. USA* **115**, 5872–5877 (2018).
- Batchellor, A. S. & Boettcher, S. W. Pulse-electrodeposited Ni–Fe (oxy) hydroxide oxygen evolution electrocatalysts with high geometric and intrinsic activities at large mass loadings. *ACS Catal.* **5**, 6680–6689 (2015).
- Doyle, A. D., Bajdich, M. & Vojvodic, A. Theoretical insights to bulk activity towards oxygen evolution in oxyhydroxides. *Catal. Lett.* **147**, 1533–1539 (2017).
- Morales-Guio, C. G., Liardet, L. & Hu, X. Oxidatively electrodeposited thin-film transition metal (oxy)hydroxides as oxygen evolution catalysts. *J. Am. Chem. Soc.* **138**, 8946–8957 (2016).
- Trotochaud, L., Ranney, J. K., Williams, K. N. & Boettcher, S. W. Solution-cast metal oxide thin film electrocatalysts for oxygen evolution. *J. Am. Chem. Soc.* **134**, 17253–17261 (2012).
- Wohlfahrt-Mehrens, M. & Heitbaum, J. Oxygen evolution on Ru and RuO_2 electrodes studied using isotope labelling and on-line mass spectrometry. *J. Electroanal. Chem. Interfacial Electrochem.* **237**, 251–260 (1987).
- Diaz-Morales, O., Calle-Vallejo, F., de Munck, C. & Koper, M. T. M. Electrochemical water splitting by gold: evidence for an oxide decomposition mechanism. *Chem. Sci.* **4**, 2334 (2013).
- Fierro, S., Nagel, T., Baltruschat, H. & Comminellis, C. Investigation of the oxygen evolution reaction on Ti/Ir O_2 electrodes using isotope labelling and on-line mass spectrometry. *Electrochem. Commun.* **9**, 1969–1974 (2007).
- Amin, H. M. A. & Baltruschat, H. How many surface atoms in Co_3O_4 take part in oxygen evolution? Isotope labeling together with differential electrochemical mass spectrometry. *Phys. Chem. Chem. Phys.* **19**, 25527–25536 (2017).
- Surendranath, Y., Kanan, M. W. & Nocera, D. G. Mechanistic studies of the oxygen evolution reaction by a cobalt–phosphate catalyst at neutral pH. *J. Am. Chem. Soc.* **132**, 16501–16509 (2010).
- Macounova, K., Makarova, M. & Krtil, P. Oxygen evolution on nanocrystalline RuO_2 and $\text{Ru}_{0.9}\text{Ni}_{0.1}\text{O}_{2-x}$ electrodes—DEMS approach to reaction mechanism determination. *Electrochem. Commun.* **11**, 1865–1868 (2009).
- Grimaud, A. et al. Activating lattice oxygen redox reactions in metal oxides to catalyse oxygen evolution. *Nat. Chem.* **9**, 457–465 (2017).
- Willsau, J., Wolter, O. & Heitbaum, J. In the oxygen evolution reaction on platinum? *J. Electroanal. Chem.* **195**, 299–306 (1985).
- Stoerzinger, K. A. et al. Orientation-dependent oxygen evolution on RuO_2 without lattice exchange. *ACS Energy Lett.* **2**, 876–881 (2017).
- Lu, X. & Zhao, C. Electrodeposition of hierarchically structured three-dimensional nickel–iron electrodes for efficient oxygen evolution at high current densities. *Nat. Commun.* **6**, 6616 (2015).
- Trimarco, D. B. et al. Enabling real-time detection of electrochemical desorption phenomena with sub-monolayer sensitivity. *Electrochim. Acta* **268**, 520–530 (2018).
- Paoli, E. A. et al. Oxygen evolution on well-characterized mass-selected Ru and RuO_2 nanoparticles. *Chem. Sci.* **6**, 190–196 (2015).
- Li, Z. Y. et al. Three-dimensional atomic-scale structure of size-selected gold nanoclusters. *Nature* **451**, 46–48 (2008).
- Ferreira, P. J. et al. Instability of Pt/C electrocatalysts in proton exchange membrane fuel cells. *J. Electrochem. Soc.* **152**, A2256 (2005).
- Meier, J. C. et al. Design criteria for stable Pt/C fuel cell catalysts. *Beilstein J. Nanotechnol.* **5**, 44–67 (2014).
- Fiordaliso, E. M., Dahl, S. & Chorkendorff, I. Strong metal support interaction of Pt and Ru nanoparticles deposited on HOPG probed by the H–D exchange reaction. *J. Phys. Chem. C* **116**, 5773–5780 (2012).
- Binninger, T. et al. Thermodynamic explanation of the universal correlation between oxygen evolution activity and corrosion of oxide catalysts. *Sci. Rep.* **5**, 12167 (2015).
- Spöri, C., Kwan, J. T. H., Bonakdarpour, A., Wilkinson, D. P. & Strasser, P. The stability challenges of oxygen evolving catalysts: towards a common fundamental understanding and mitigation of catalyst degradation. *Angew. Chem. Int. Ed.* **56**, 5994–6021 (2017).
- Hartl, K., Hanzlik, M. & Arenz, M. IL-TEM investigations on the degradation mechanism of Pt/C electrocatalysts with different carbon supports. *Energy Environ. Sci.* **4**, 234–238 (2011).
- Ng, J. W. D. et al. Gold-supported cerium-doped NiO_x catalysts for water oxidation. *Nat. Energy* **1**, 16053 (2016).
- Xu, X., Song, F. & Hu, X. A nickel iron diselenide-derived efficient oxygen-evolution catalyst. *Nat. Commun.* **7**, 12324 (2016).

49. Silva, H. et al. Synthesis and characterization of Fe-Ni/ γ -Al₂O₃ egg-shell catalyst for H₂ generation by ammonia decomposition. *Appl. Catal. A* **505**, 548–556 (2015).
50. Burke, M. S. et al. Revised oxygen evolution reaction activity trends for first-row transition-metal (oxy)hydroxides in alkaline media. *J. Phys. Chem. Lett.* **6**, 3737–3742 (2015).
51. Zhang, B. et al. Homogeneously dispersed multimetal oxygen-evolving catalysts. *Science* **352**, 333–337 (2016).
52. Gong, M. et al. An advanced Ni-Fe layered double hydroxide electrocatalyst for water oxidation. *J. Am. Chem. Soc.* **135**, 8452–8455 (2013).
53. Song, F. & Hu, X. Exfoliation of layered double hydroxides for enhanced oxygen evolution catalysis. *Nat. Commun.* **5**, 4477 (2014).
54. Long, X. et al. A strongly coupled graphene and FeNi double hydroxide hybrid as an excellent electrocatalyst for the oxygen evolution reaction. *Angew. Chem. Int. Ed.* **53**, 7584–7588 (2014).
55. Wehrens-Dijkstra, M. & Notten, P. H. L. Electrochemical quartz microbalance characterization of Ni(OH)₂-based thin film electrodes. *Electrochim. Acta* **51**, 3609–3621 (2006).
56. Lu, X. & Zhao, C. Electrodeposition of hierarchically structured densities. *Nat. Commun.* **6**, 1–7 (2015).
57. von Issendorff, B. & Palmer, R. E. A new high transmission infinite range mass selector for cluster and nanoparticle beams. *Rev. Sci. Instrum.* **70**, 4497–4501 (1999).
58. Pratontep, S., Carroll, S. J., Xirouchaki, C., Streun, M. & Palmer, R. E. Size-selected cluster beam source based on radio frequency magnetron plasma sputtering and gas condensation. *Rev. Sci. Instrum.* **76**, 045103 (2005).
59. Biesinger, M. C., Lau, L. W. M., Gerson, A. R. & Smart, R. S. C. The role of the Auger parameter in XPS studies of nickel metal, halides and oxides. *Phys. Chem. Chem. Phys.* **14**, 2434 (2012).
60. Biesinger, M. C. et al. Resolving surface chemical states in XPS analysis of first row transition metals, oxides and hydroxides: Cr, Mn, Fe, Co and Ni. *Appl. Surf. Sci.* **257**, 2717–2730 (2011).
61. Grosvenor, A. P., Biesinger, M. C., Smart, R. S. C. & McIntyre, N. S. New interpretations of XPS spectra of nickel metal and oxides. *Surf. Sci.* **600**, 1771–1779 (2006).

Acknowledgements

This work was supported by a research grant (9455) from VILLUM FONDEN. We also acknowledge UPCAT under project no. 2015-1-12315.

Author contributions

I.E.L.S., J.K. and I.C. conceived the experiments. C.R. participated in the conception of the experiments and performed the electrochemical measurements. B.S. participated in the conception of the experiments, prepared the nanoparticles and performed the UHV experiments. S.B.S. performed and helped in the design of the EC-MS experiments. D.B.T., P.C.K.V. and O.H. designed and helped with the interpretation of the EC-MS experiments. E.M.F. and C.D.D. performed the microscopy characterization. J.E.S. and A.B. contributed to the LEIS measurements. C.R., B.S. and S.B.S. co-wrote the manuscript. All the authors discussed the results and commented on the manuscript.

Competing interests

The authors declare no competing interests.

Additional information

Supplementary information is available for this paper at <https://doi.org/10.1038/s41929-018-0162-x>.

Reprints and permissions information is available at www.nature.com/reprints.

Correspondence and requests for materials should be addressed to I.C.

Publisher's note: Springer Nature remains neutral with regard to jurisdictional claims in published maps and institutional affiliations.

© The Author(s), under exclusive licence to Springer Nature Limited 2018

Paper III Towards an Atomistic Understanding of Electrocatalytic Partial Hydrocarbon Oxidation: Propene on Palladium

Anna Winiwarter*, Luca Silva*, Soren B. Scott, Kasper Enemark-Rasmussen, Manuel Saric, Daniel B. Trimarco, Peter C. K. Vesborg, Poul G. Moses, Ifan E. L. Stephens, Brian Seger, Jan Rossmeisl, and Ib Chorkendorff.

*These authors contributed equally to this work

Energy and Environmental Science, 12, 1055-1067, 2019.

DOI: 10.1039/C8EE03426E



Cite this: *Energy Environ. Sci.*,
2019, 12, 1055

Towards an atomistic understanding of electrocatalytic partial hydrocarbon oxidation: propene on palladium†

Anna Winiwarter,^a Luca Silvioli,^b Soren B. Scott,^a Kasper Enemark-Rasmussen,^c Manuel Sariç,^b Daniel B. Trimarco,^d Peter C. K. Vesborg,^a Poul G. Moses,^e Ifan E. L. Stephens,^f Brian Seger,^a Jan Rossmeisl^b and Ib Chorkendorff^{*a}

The efficient partial oxidation of hydrocarbons to valuable chemicals without formation of CO₂ is one of the great challenges in heterogeneous catalysis. The ever-decreasing cost of renewable electricity and the superior control over reactivity qualify electrochemistry as a particularly attractive means of addressing this challenge. Yet, to date, little is known about the factors regulating hydrocarbon oxidation at the atomic level. A relevant showcase reaction is propene electro-oxidation to key industrial commodity chemicals, such as acrolein, acrylic acid and propylene oxide. In this study, we investigate the partial electrochemical oxidation of propene on high-surface area Pd electrodes using a combination of electrochemical measurements, advanced product characterization and theoretical modeling. We report a new reaction product, propylene glycol, and high selectivity towards acrolein. We further identify key reaction intermediates and propose a mechanism dictated by the surface coverage of organic species formed *in situ*, where stable reactant adsorption at low coverage determines the selectivity towards allylic oxidation at high coverage. Our fundamental findings enable advances in partial hydrocarbon oxidation reactions by highlighting atomic surface structuring as the key to selective and versatile electrochemical catalyst design.

Received 22nd November 2018,
Accepted 19th February 2019

DOI: 10.1039/c8ee03426e

rsc.li/ees

Broader context

The transition from fossil to renewable energy sources must accelerate to mitigate the devastating effects of climate change. Within this context, society electrification is a highly regarded strategy, in which the industrial sectors are also expected to migrate to electrified manufacturing processes. Many thermocatalytic industrial chemical processes – some established for more than a century – are expensive and energetically inefficient and therefore require modernization. In many cases, electrochemistry has great potential for replacing outdated processes. Electrochemical reactions are inherently safer and allow fine selectivity control in optimized systems. They are also more versatile and scalable, and thus suited for decentralization and embedding in national energy grids, which will help compensate renewable energy fluctuations. In particular, a great opportunity lies in optimizing electrochemical partial oxidation reactions, which offer shortcuts to valuable products not accessible in the traditional chemical industry due to the tendency of carbon compounds to fully oxidize in thermally driven processes. Understanding the factors that control electrocatalytic reactions at the atomic level is the first step to creating efficient large scale electrochemical processes. Our work provides fundamental insights into the mechanism of hydrocarbon electro-oxidation through the study of a model, yet industrially relevant reaction: partial propene oxidation.

^a SurfCat, Department of Physics, Technical University of Denmark, Fysikvej, Byg. 311, 2800 Kgs. Lyngby, Denmark. E-mail: ibchork@fysik.dtu.dk

^b Nano-Science Center, Department of Chemistry, University of Copenhagen, Universitetsparken 5, 2100 Copenhagen, Denmark. E-mail: jan.rossmeisl@chem.ku.dk

^c Department of Chemistry, Technical University of Denmark, Kemitorvet, Byg. 207, 2800 Kgs. Lyngby, Denmark

^d Spectro Inlets, COBIS, Ole Maaløes Vej 3, 2200 Copenhagen, Denmark

^e Haldor Topsoe A/S, Haldor Topsøes Allé 1, 2800 Kgs. Lyngby, Denmark

^f Department of Materials, Imperial College London, Royal School of Mines, London, SW7 2AZ, UK

† Electronic supplementary information (ESI) available. See DOI: 10.1039/c8ee03426e

* These authors contributed equally.

1. Introduction

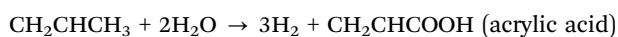
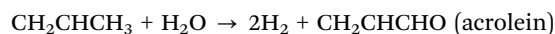
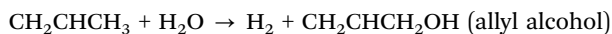
Wind and solar energy are increasingly outcompeting fossil fuels for electricity generation.¹ Increasing renewable electricity output calls for the electrochemical production of commodity chemicals, such as alcohols, aldehydes and acids.^{2–4} Selective direct oxidation of hydrocarbons to partially oxidized products while avoiding full oxidation to CO₂, the most thermodynamically favored product, remains elusive in gas phase heterogeneous catalysis.^{5–11} Compared to thermal heterogeneous catalysis, an electrochemical approach to selective partial oxidation can

be advantageous. Mild oxidizing conditions and fine control over reaction parameters could direct the reaction to one specific product while preventing the formation of CO_2 .^{12–14} At the same time, electrochemical reactors based on fuel cell technology would allow for decentralized production with flexible feedstocks.¹⁵

Propene is an interesting model molecule for studying mechanisms concerning hydrocarbon selective oxidation. It provides two different reaction sites: the C–C double bond (vinyl group) and the allyl carbon. Oxidation of the double bond leads to the formation of 1,2-propylene oxide, which is hydrolyzed to propylene glycol in an aqueous environment.¹⁶



The allylic carbon, on the other hand, can be oxidized to produce allyl alcohol, acrolein, and acrylic acid.¹⁷



The structures of propene and relevant oxidation products are reported in Fig. 1.

High annual production capacities for several partial oxidation products of propene highlight the importance of this reaction; examples are propylene oxide (9.81 Mt, 2016),¹⁸ propylene glycol (2.56 Mt, 2017 prognosis),¹⁹ and acrylic acid (7.66 Mt, 2016).¹⁸ Acetone, despite annual production volumes on the same order of magnitude as those mentioned,²⁰ is not considered hereafter a desired product, as it does not form electrocatalytically in our reaction system.

A few prior studies have examined the direct electrochemical oxidation of propene.^{21–27} The most promising results have been reported on palladium electrodes in an acidic environment. Stafford²⁸ reported acrolein, acrylic acid, acetone and CO_2 as the main products on palladium in an acidic aqueous electrolyte. Otsuka *et al.*²⁹ used a fuel cell set-up and found mainly acrolein and acrylic acid at lower cell voltage, but increasing amounts of acetone and CO_2 at higher cell voltage. However, neither of these studies provide a full picture of faradaic efficiency *versus* potential, nor do they propose a mechanistic explanation for the observed selectivity towards allylic oxidation.

Herein, we present a systematic study of propene oxidation on high surface area palladium electrodes. We use dilute HClO_4 as the electrolyte, known to be non-interacting with the electrode, to decouple electrolyte effects from surface dynamics.³⁰ We differentiate the electrocatalytic pathway from non-electrochemical side reactions, confirming that acetone is produced by a homogeneous reaction with Pd^{2+} .^{28,29} We report the identification of a key electrochemical reaction intermediate, allyl alcohol, as well as an additional product, propylene glycol, which to the best of our knowledge has not been reported on this catalyst before. Using a combination of density functional theory

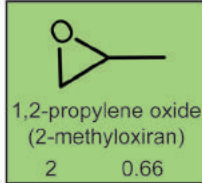
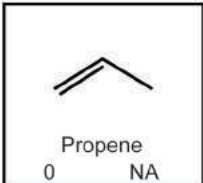
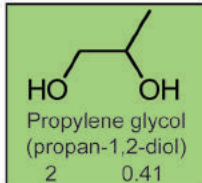
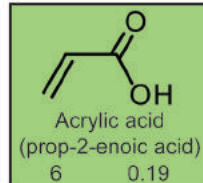
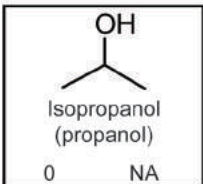
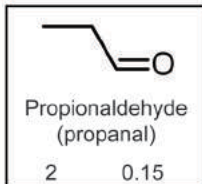
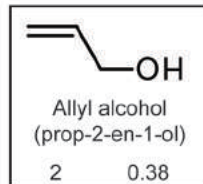
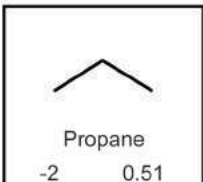
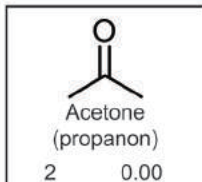
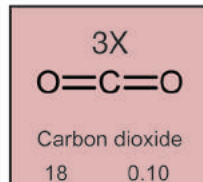
 Name Rev. Pot. (V/RHE) n°e	 1,2-propylene oxide (2-methyloxiran) 2 0.66	 Acrolein (prop-2-en-1-al) 4 0.25
 Propene 0 NA	 Propylene glycol (propan-1,2-diol) 2 0.41	 Acrylic acid (prop-2-enoic acid) 6 0.19
 Isopropanol (propanol) 0 NA	 Propionaldehyde (propanal) 2 0.15	 Allyl alcohol (prop-2-en-1-ol) 2 0.38
 Propane -2 0.51	 Acetone (propanon) 2 0.00	 3X $\text{O}=\text{C}=\text{O}$ Carbon dioxide 18 0.10

Fig. 1 Overview of propene and its main derivatives. A green background highlights industrially relevant products, while red denotes undesired compounds. The thermodynamic reversible potential for formation by propene oxidation was calculated from the reaction free energy, including solvation for all liquid products. Calculations details are reported in the ESI.†

(DFT) modeling and electrochemical mass spectrometry (EC-MS), we provide fundamental insights into the mechanism governing the changes in product distribution with potential in bulk experiments. The surface coverage plays a crucial role in steering the oxidation activity and selectivity: surface chemistry under reaction conditions forces reactants to weaker adsorption configurations, enabling selective oxidation of the allyl carbon.

2. Experimental methods

Deposition of porous Pd

High surface area Pd electrodes were prepared by electrodeposition on glassy carbon sheets (1×1.5 cm, HTW-Germany) or on glassy carbon disks (5 mm diameter, Pine Instruments) for the EC-MS measurements. The sheets/disks were initially thoroughly polished with $1/4 \mu\text{m}$ diamond on a polishing cloth (Struers). Before each experiment the glassy carbon electrodes were cleaned of metal contamination by immersion in aqua regia, followed by repeated rinsing and sonication in ultrapure water. For the electrical contact, a Pt wire was attached to the glassy carbon and wrapped in Teflon tape to prevent contact with the electrolyte. The Pd deposition was carried out using a 2 mM PdCl_2 solution (99.999%, Sigma Aldrich) in 2 M H_2SO_4 (suprapur, Merck) in a 2-electrode setup with a Pt mesh (99.9%, GoodFellow) as a counter electrode. For optimal adhesion, a thin Pd layer was deposited at -1 V *vs.* the counter

electrode for 1 min, followed by deposition at -4 V *vs.* counter for 3 min with simultaneous H_2 evolution (hydrogen bubble template method).^{31,32} The electrode was thoroughly rinsed with ultrapure water before further use.

Electrochemical experiments

Electrochemical experiments with product analysis were carried out in a 3-electrode setup in a 3-compartment glass cell (H-cell, see Fig. 2), as described previously.³³ The electrolyte was prepared by dilution of concentrated $HClO_4$ (suprapur, Merck) in ultrapure water (18.2 M Ω resistivity, Millipore, Synergy UV system). A Pt mesh counter and a $Hg/HgSO_4$ reference electrode were employed. The reference electrode was calibrated regularly *versus* the RHE scale by measuring the open circuit voltage (OCV) at a Pt electrode in H_2 saturated electrolyte until stable for at least 10 minutes. Gases (Ar 5.0, AGA or propene 4.0, BOC) were supplied through a glass frit, connected to a gas loop allowing for circulation of the gas during the reaction. Additional experiments were carried out in a conventional RDE setup.

For each measurement, a freshly prepared sample was placed in electrolyte and held at 0.4 V *vs.* RHE while the electrolyte was purged with propene. No electrochemical reaction is observed at this potential. The potential was then stepped up to the potential of interest and held for one hour.

The electrochemical surface area (ECSA) was determined after each experiment, using the PdO reduction peak in cyclic voltammograms. These CVs were measured in fresh electrolyte. Rather than assuming oxidation of a full monolayer of Pd, we calibrated the charge from PdO reduction with CO stripping experiments on the same electrode (for details see the ESI[†]).

All glassware was cleaned with aqua regia before use.

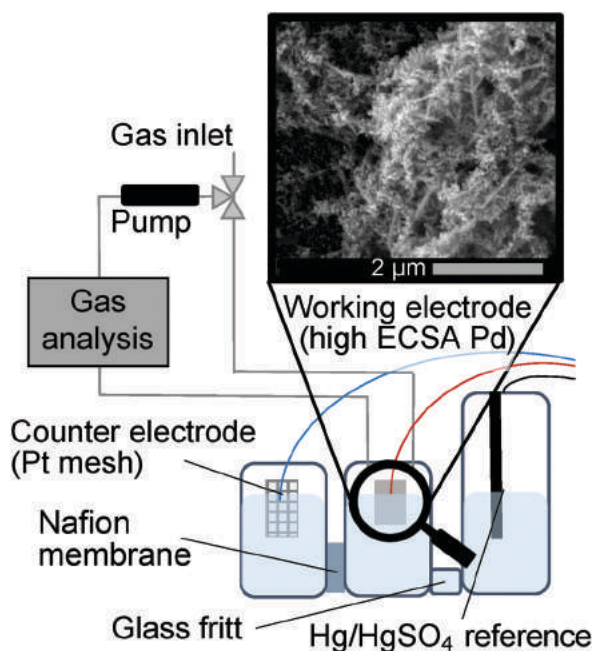


Fig. 2 Schematic of the 3-compartment cell used for bulk oxidation experiments. The inset shows a SEM image of a high surface area palladium electrode.

Product analysis

Gaseous products were determined by gas chromatography (GC). Different methods were used for liquid product characterization: static headspace gas chromatography (HS-GC) for acetone and propanal, high pressure liquid chromatography (HPLC) for acrolein and acrylic acid, and quantitative nuclear magnetic resonance spectroscopy (qNMR) for allyl alcohol, isopropanol and propylene glycol. The Pd concentration in the electrolyte was determined with inductively coupled plasma-mass spectrometry (ICP-MS). For experimental details, see the ESI[†].

EC-MS

For electrochemistry-mass spectrometry (EC-MS) measurements, we used the setup and methodology described previously.³⁴ This setup uses a membrane microchip to interface the electrochemical environment and the vacuum system containing the mass spectrometer. CO and propene stripping experiments involved (1) dosing the reactant gas (CO or propene) through the membrane chip while holding the electrode at a constant potential, (2) flowing He through the chip until the mass spectrometer signal for the reactant gas returned to the baseline, and (3) cycling the electrode potential. All EC-MS measurements were performed in 1.0 M $HClO_4$ in order to have sufficient electrolytic conductivity through the thin layer of electrolyte. Mass spectrometer signals were converted to amounts of propene, propane, and CO_2 using internal calibration measurements (see the ESI[†] for details).

DFT calculations

All ground state DFT and climbing image nudged elastic band (NEB) calculations were performed with the Grid-based Projector Augmented Wave (GPAW) program and the Atomic Simulation Environment (ASE) package.^{35–37} The Kohn–Sham wavefunctions are represented on real-space uniform grids (finite difference mode); we used the BEEF-vdW exchange and correlation functional, a grid spacing of 0.18 Å and k -point sampling of $(2 \times 2 \times 1)$. For NEB calculations, the RPBE exchange and correlation functional was used instead to quantify the energy gap between initial and transition states in chemical reaction steps. More computational details and information on structures and reference compounds are reported in the ESI[†].

3. Results and discussion

Electrocatalytic activity

Cyclic voltammograms (CVs) of high surface area Pd in Ar and propene saturated 0.1 M $HClO_4$ are shown in Fig. 3a (black and red line, respectively). The onset of Pd oxidation is at *ca.* 0.65 V *vs.* RHE; two oxidation waves can be distinguished with peaks around 0.8 and 1.1 V *vs.* RHE, suggesting a range of different facets are present on the Pd electrode.^{38–41} In the cathodic scan a sharp reduction peak is present at *ca.* 0.7 V *vs.* RHE, where PdO is reduced. In propene saturated $HClO_4$ the onset of oxidative current is shifted significantly to almost 0.9 V *vs.* RHE, followed by an oxidative peak with a significantly higher peak current than in Ar at a potential of *ca.* 1.1 V *vs.* RHE. We attribute this peak to the

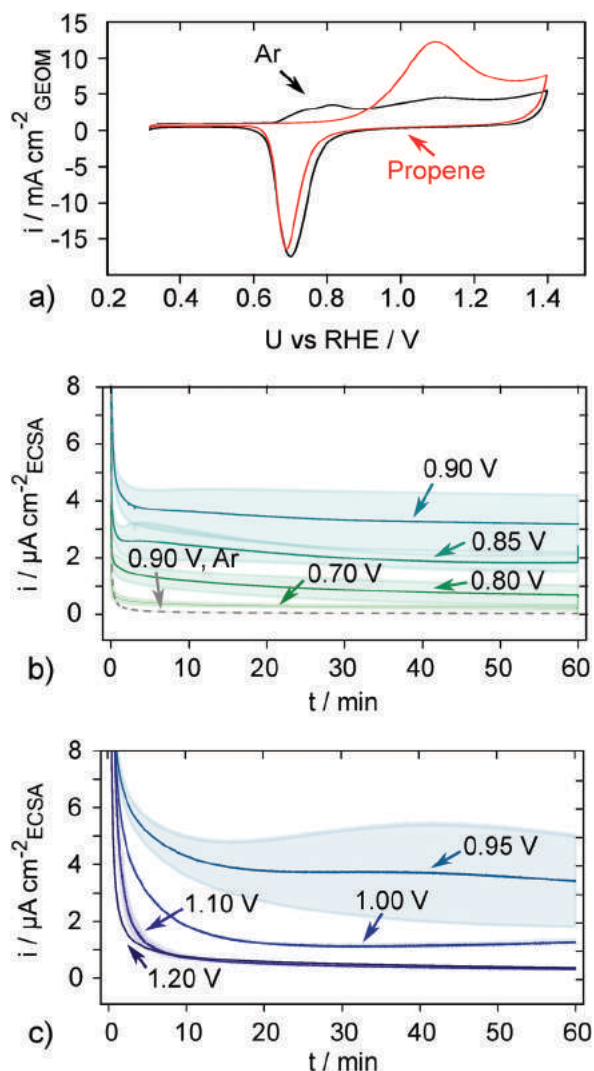


Fig. 3 (a) Cyclic voltammograms (stable) of high surface area Pd in 0.1 M HClO₄ saturated with Ar (black) and propene (red), respectively, recorded at a scan rate of 50 mV s⁻¹ in a rotating disc electrode setup (no rotation) while purging with gas. (b and c) Current–time traces of propene oxidation at constant potentials in 0.1 M HClO₄: average and standard deviations of three ($E \leq 0.95$ V) or two ($E = 1.0$ V, 1.1 V) electrodes and a single, representative experiment for 1.2 V. The current–time trace in Ar saturated electrolyte at 0.9 V vs. RHE is shown for comparison. (b) Mildly oxidizing potentials, (c) strongly oxidizing potentials.

oxidation of propene in addition to PdO formation. The PdO reduction peak area is similar in the presence of propene, supporting the interpretation that the increased current in the anodic scan is in fact irreversible oxidation of propene rather than increased surface oxidation, as the latter would also manifest in a more pronounced reduction peak.

In order to investigate the selectivity for different products, we carried out chronoamperometry experiments in 0.1 M HClO₄. Products were accumulated for 1 h at a constant potential in order to reach high enough product concentrations for reliable product detection (see the Methods section for details). ECSA normalized current–time traces recorded during product accumulation are shown in Fig. 3b and c. In all cases, a significant

initial current drop is observed. For a more detailed analysis of the current–time traces, see Fig. S4 (ESI[†]). The highest current densities are observed at 0.90 and 0.95 V vs. RHE. At the same potentials, the variation between the individual experiments is also the largest. With the equilibrium potential for the oxidation of Pd at pH 1 being 0.91 V vs. RHE,⁴² the high variability at these potentials is presumably related to the instability of the catalyst due to the surface redox and/or dissolution processes, which may modify the surface area to an unknown degree. The drop in current density at potentials larger than 0.95 V vs. RHE can be explained by the formation of passivating PdO on the surface.

Product distribution and potential

Primary oxidation products. Fig. 4 shows the propene oxidation activity and product distribution as a function of potential. The faradaic efficiencies and partial current densities are shown for various products in Fig. 4a–c and Fig. 4d–f, respectively. The current was calculated based on the concentration at the end of the 1 h period. For better readability, the products are divided into three groups: the main target product acrolein, other propene oxidation products of interest (allyl alcohol, acrylic acid and propylene glycol), and undesired side products (acetone, CO₂ and dissolved Pd).

The partial current density and faradaic efficiency for acrolein production are highest in the middle of the potential range studied, with maxima of 2.1 $\mu\text{A cm}^{-2}$ and 62%, respectively, at 0.9 V vs. RHE. At potentials above 1.1 V vs. RHE the concentration was too low for quantification. The trends for acrylic acid follow those for acrolein, reaching a maximum faradaic efficiency of 11% at 0.9 V vs. RHE. Allyl alcohol shows a similar dependency, except that the peak maximum is shifted to 0.85 V vs. RHE. Propylene glycol, on the other hand, is only produced at 1.0 V vs. RHE and more anodic, and both the specific current density and faradaic efficiency increase with increasing anodic potential. In addition to the mentioned products, small amounts of propanal were observed, but were too small to measure quantitatively (see Fig. S14 and S25, ESI[†]). The non-electrochemical product isopropanol was also observed in small quantities (1% of liquid products by mol at 0.9 V vs. RHE).

We attribute the high standard deviation in product faradaic efficiency below 0.9 V vs. RHE to the lack of significant quantities of products (see the ESI[†]); however, at 0.9 and 0.95 V vs. RHE we hypothesize the error is caused by the instability of the catalyst due to oxidation and dissolution processes as discussed above.

The overall faradaic efficiency considering only propene oxidation products is significantly less than 100% at strongly oxidizing potentials (Fig. 4), which may partially relate to oxidation of the surface and corrosion of the catalyst. Based on the charge required for the formation of one monolayer PdO (Fig. S4, ESI[†]), we estimated that at potentials more anodic than 0.95 V vs. RHE, Pd oxidation can account for up to 10–15% faradaic efficiency, increasing the total faradaic efficiency to at least 90%.

Homogeneous reactions. We noted undesired side reactions are taking place in the electrolyte. The acid catalyzed hydration of propene to isopropanol in the presence of water is well known⁴³ and was also observed in the electrolyte after purging with propene without an electrode (see the ESI[†]). Separate experiments with isopropanol added directly to the electrolyte showed no activity for

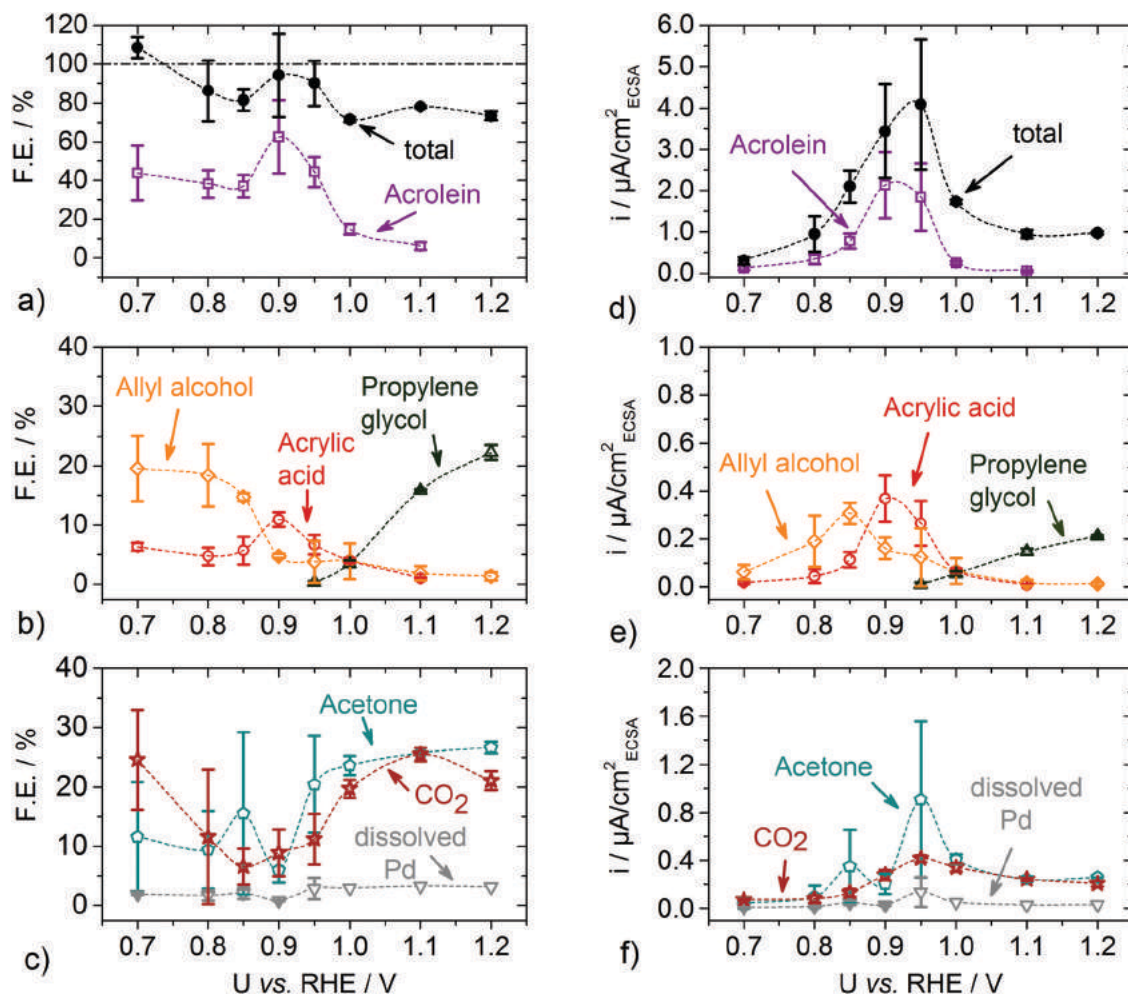


Fig. 4 Product distribution from chronoamperometry experiments presented in Fig. 3b and c as a function of potential: (a–c) faradaic efficiencies; (d–f) partial current densities. Additional undetected products were propanal (concentration unreliable as close to the quantification limit, see the ESI†) and isopropanol (chemical product, see the text).

electrochemical oxidation of the alcohol, excluding this compound from the primary reaction mechanism.

Previous studies on this system have reported homogeneous side reactions with Pd^{2+} in solution.^{28,29} The concomitant increase of the acetone concentration with the Pd-ion concentration throughout the experiments suggests a direct relationship. In order to verify the role of Pd^{2+} as a catalyst/reactant for the oxidation to acetone, we analyzed the products formed when purging propene through a 0.1 M HClO_4 solution containing different concentrations of Pd^{2+} ions (Fig. 5).

The concentration of the main product acetone linearly increases with Pd concentration with a slope close to one, indicating the role of Pd^{2+} in acetone production and suggesting that the Pd^{2+} ions are fully consumed within the reaction time. For Pd^{2+} concentrations of 100 μM and above, the formation of metal nanoparticles was evident from discoloration of the solution and formation of a precipitate. The reaction is expected to proceed through a Wacker-type mechanism as follows ($\Delta G = -167 \text{ kJ mol}^{-1}$):²⁹

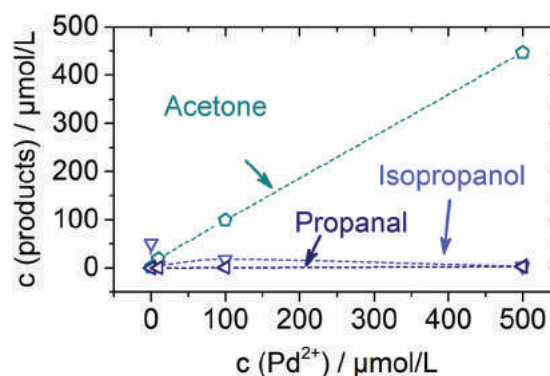
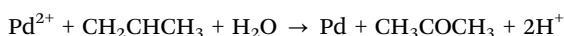


Fig. 5 Homogeneous reaction of propene in 0.1 M HClO_4 with different concentrations of PdCl_2 . All products formed under these conditions are shown in the figure.

While closing the catalytic cycle by re-oxidation of Pd at the electrode has been proposed,²⁹ we did not see evidence for this in our system (see Fig. S26, ESI†). Therefore we do not consider acetone as a desirable product.

Product stability. Degradation of products before quantification resulting in an underestimation of the amounts produced could explain the low total faradaic efficiencies in Fig. 4a. We therefore followed changes in product concentrations with time after the end of the experiment. We observed a significant decrease in acrolein concentration over time, which we could assign to the formation of hydration products 3-hydroxypropanal and propane-1,3,3-triol (see the ESI†). Despite our efforts to quantify acrolein and acrylic acid as fast as possible using HPLC, this might lead to a slight underestimation in their quantification.

Surface chemistry and mechanistic analyses

In the following, we rationalize the observations in bulk oxidation tests with mechanistic analyses by means of DFT modeling and propene stripping experiments, proposing a reaction mechanism for the potential window in which the catalyst surface is metallic. We further provide insights into the relationship between surface population and catalytic activity, highlighting the correlation of surface coverage with the reaction outcome.

Surface species, intermediates and reaction pathway – DFT.

Fig. 6 shows the energies of propene oxidation products, intermediates and transition states relative to water, propene, and the palladium fcc(111) surface, calculated by DFT and adjusted to +0.9 V *vs.* RHE using the computational hydrogen electrode reference system.⁴⁴ For the energy levels at 0.0 V *vs.* RHE, see Fig. S29 (ESI†). Fig. 6a reports the reaction energetics as calculated on a clean Pd slab (termed clean), while Fig. 6b shows the energy for the same intermediates adsorbed on a Pd slab with high surface coverage, mimicked by six CO spectator molecules adsorbed per unit cell (termed CO poisoned), contouring the intermediates' adsorption site(s). In Fig. 6, in addition to the energies of the intermediates, we report the initial states for chemical oxidation steps as half light/half teal blue lines, with energy values corresponding to the sum of the respective adsorbates' energy, and the calculated gas phase product reversible potentials. The kinetic reaction barriers are represented by dashed curves linking initial, transition and final states. The other dashed lines between intermediates indicate an elementary step of a (H^+/e^-) couple loss with negligible kinetic barrier.

The first catalytic step in propene electro-oxidation is adsorption of propene. Comparing the possible adsorption geometries, we find that adsorption *via* deprotonation of the allyl carbon is the most favorable for the potential range of interest (Fig. S27, blue bars, ESI†); additionally, propene activation in the allylic position is consistent with the observed product distribution. We therefore focus the mechanistic analysis on propene oxidative adsorption and reactivity *via* allylic carbon activation, followed by reaction with adsorbed *OH or *O. In Scheme 1, we report the elementary steps considered in the mechanistic study.

The consideration of elementary steps whereby adsorbed propene reacts with *OH and *O (Langmuir–Hinshelwood mechanism) is motivated by different factors. First, the onset of significant propene oxidation activity at about 0.7 V *vs.* RHE (Fig. 4) corresponds well with the DFT-calculated OH adsorption energy and OH adsorption features in the cyclic voltammogram in argon (Fig. 3a). Second, the

calculated adsorption energy of propene through the allyl carbon is significantly more exergonic than *OH adsorption, suggesting the reason for the observed low activity is palladium's stronger affinity toward carbon as compared to oxygen. Third, the *OH adsorption features of the cyclic voltammograms in Fig. 3a are suppressed in propene until the onset of propene oxidation, implying that water activation is limiting the working potential window and that *OH adsorption is required for the oxidation of propene. This kind of competitive adsorption of two Langmuir–Hinshelwood reactants is familiar from CO electro-oxidation on platinum.^{34,45,46}

The suppression of surface oxidation in the presence of propene also justifies our modeling of the reaction on metallic palladium fcc(111). Moreover, this facet has the lowest surface energy of all Pd surfaces, so we expect it to be the most abundant facet on polycrystalline Pd.⁴⁷ As explained in greater detail later, reactivity is limited by strong binding of propene, so we omit modeling facets more reactive than (111) as they would perform poorer in the reaction mechanism presented. Instead, we model the reaction by poisoning the catalyst with CO (Fig. 6b), to limit surface site accessibility and investigate the mechanism with destabilized intermediates.

Allylic propene adsorption on Pd begins with *CH₂CHCH₂ (1), which further deprotonates to *CHCHCH₂ (2) or *CCHCH₂ (3), if sites are available. The intermediates adsorb in atop, bridge and 3-fold hollow geometries, respectively; (1) and (2) are significantly stabilized on the clean surface through coordination of the vinyl group (Fig. S27, ESI†). At high surface coverage (Fig. 6b), vinylic coordination is hindered as it requires greater site availability than bare allylic adsorption. Adsorbed propene degradation is favorable on clean Pd (Fig. 6a), yielding adsorbed C1 and C2 species as reported with grey lines in Fig. 6 (the most thermodynamically favored degradations) and Fig. S28 (all degradation products, ESI†). Similarly to vinylic coordination, we observe that on the poisoned surface the degradation is inhibited, *i.e.* the energy levels for C1 and C2 species shift upwards relative to adsorbed propene. At the theoretical potential for water activation (0.7 V *vs.* RHE), *O and *OH calculated adsorption energies are roughly equivalent and the two coexist on the surface. At increasingly anodic potentials, *O coverage progressively replaces *OH on clean Pd, while on the CO poisoned surface *OH remains the most stable source of oxygen over a wide potential range. For potentials higher than 1.1 V *vs.* RHE, experimentally we observe a significant activity drop, presumably because of catalyst surface oxidation with a different reaction mechanism involved, whose modeling is beyond the scope of this report.

At potentials above water activation (>0.7 V *vs.* RHE), we cannot exclude a contribution from *OH and *O to propene proton abstraction; nonetheless we do not anticipate this phenomenon to make a significant contribution to the reaction mechanism: both theoretical simulations and electrochemical mass spectrometry (see below) suggest the oxidative adsorption of propene to occur at much more cathodic potentials.

We then investigate the kinetic barriers to products, calculating the relevant transition state energies on clean and CO poisoned Pd. We find significant activation barriers for all coupling steps

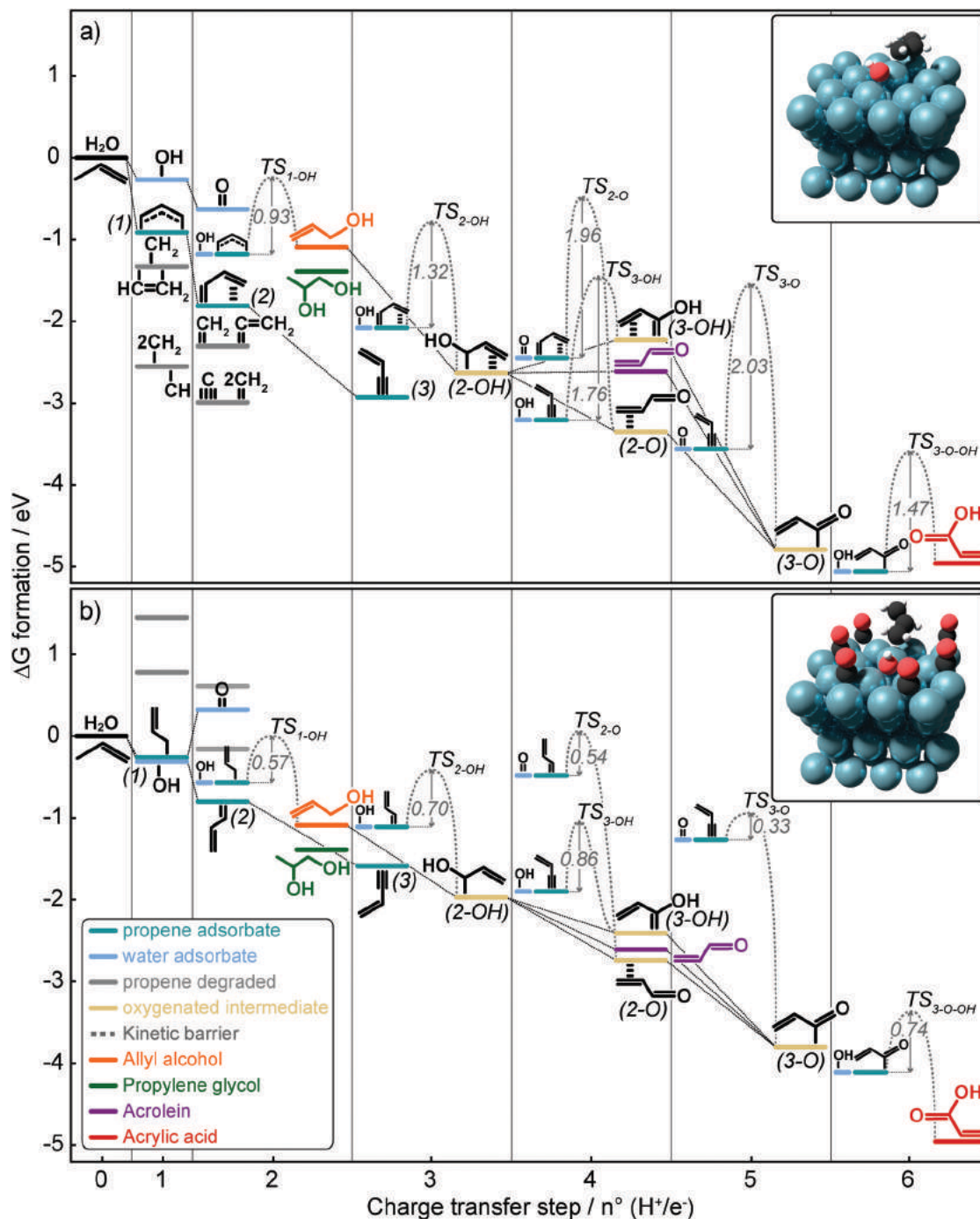


Fig. 6 Proposed reaction scheme for propene oxidation in water on (a) the clean Pd fcc(111) surface and (b) 6*CO poisoned Pd fcc(111). The DFT Gibbs energy of formation for adsorbed intermediates and transition states at $U = 0.9$ V vs. RHE are given as a function of the number of H^+/e^- couples exchanged with the system. We assign labels in brackets to all intermediates for easier referencing in the text. The graphical insets provide visual examples of the model catalyst surface with adsorbates.

between adsorbed propene and *O or *OH, which we consider the reaction rate determining steps. Their transition states can be safely modelled since they all are potential independent, chemical reaction steps. In general, we predict high energy barriers if the intermediates react on a clean Pd surface, as reported in Fig. 6a. For (1) + OH coupling, required to form allyl alcohol, we calculate an activation energy close to 1 eV, which we consider virtually

unsurmountable at the experimental conditions tested. For all other steps, the kinetic barriers are even higher: For oxidation of (2) *CHCHCH₂ and (3) *CCHCH₂, we find an unfavorable activation energy for oxygen incorporation of around 2 eV, both with *O and *OH. Besides, (3) is an intermediate that cannot convert to the primary product acrolein, as all allylic protons are lost. While (3) in theory can react to acrylic acid, its strong

Elementary step	$\Delta G[eV]@0.9V_{RHE}$	
	Clean	CO poisoned
$CH_2CHCH_2 + * \rightarrow *CH_2CHCH_2 + (H^+/e^-)$ (propene) (1)	-0.91	-0.26
$*CH_2CHCH_2 \rightarrow *CHCHCH_2 + (H^+/e^-)$ (1) (2)	-0.90	-0.54
$*CHCHCH_2 \rightarrow *CCHCH_2 + (H^+/e^-)$ (2) (3)	-1.13	-0.79
$H_2O + * \rightarrow *OH + (H^+/e^-)$	-0.27	-0.31
$*OH \rightarrow *O + (H^+/e^-)$	-0.36	0.64
$*CH_2CHCH_2 + *OH \rightarrow CH_2(OH)CHCH_2 + 2*$ (1) (allyl alcohol)	0.09 [†]	-0.52 [†]
$*CHCHCH_2 + *OH \rightarrow *CH(OH)CHCH_2 + *$ (2) (2-OH)	-0.55 [†]	-0.86 [†]
$CH_2(OH)CHCH_2 + * \rightarrow *CH(OH)CHCH_2 + (H^+/e^-)$ (allyl alcohol) (2-OH)	-1.54	-0.88
$*CH(OH)CHCH_2 \rightarrow *C(OH)CHCH_2 + (H^+/e^-)$ (2-OH) (3-OH)	0.40	-0.44
$*CH(OH)CHCH_2 \rightarrow CHOCHCH_2 + *$ (2-OH) (acrolein)	0.02	-0.64
$*CH(OH)CHCH_2 \rightarrow CHOCH*CH_2 + (H^+/e^-)$ (2-OH) (2-O)	-0.72	-0.77
$*CHCHCH_2 + *O \rightarrow CHOCH*CH_2 + *$ (2) (2-O)	-0.92 [†]	-2.26 [†]
$*CCHCH_2 + *OH \rightarrow *C(OH)CHCH_2 + *$ (3) (3-OH)	0.97 [†]	-0.51 [†]
$CHOCH*CH_2 \rightarrow CHOCHCH_2 + *$ (2-O) (acrolein)	0.74 [†]	0.13 [†]
$*CCHCH_2 + *O \rightarrow *COCHCH_2 + *$ (3) (3-O)	-1.23 [†]	-2.53 [†]
$*C(OH)CHCH_2 \rightarrow *COCHCH_2 + (H^+/e^-)$ (3-OH) (3-O)	-2.56	-1.39
$CHOCH*CH_2 \rightarrow *COCHCH_2 + (H^+/e^-)$ (2-O) (3-O)	-1.44	-1.06
$*COCHCH_2 + *OH \rightarrow COOHCHCH_2 + 2*$ (3-O) (acrylic acid)	0.10 [†]	-0.85 [†]

[†] energy of chemical step, potential independent

Scheme 1 Elementary reaction steps with relative free energy variation at 0.9 V vs. RHE for clean (Fig. 6a) and CO poisoned (Fig. 6b) catalytic substrates. The labels and colors correspond to those in Fig. 6.

interaction with the surface should block its participation in the reaction mechanism.

However, the reaction energetics significantly change if the adsorption geometry of adsorbates is restricted due to the high surface coverage modeled with *CO. The intermediates' binding energies on the model CO poisoned surface are significantly weakened (Fig. 6b), while the transition states' energetics are only marginally affected. Such selective destabilization results

in the critical attenuation of the kinetic barriers, allowing for the reaction to proceed at room temperature. Similarly, adsorbed intermediates are destabilized relative to desorbed products, enabling an exergonic pathway to final products.

In propene electro-oxidation, a mechanistic model that neglects the effects of surface coverage has evident limitations, as it cannot explain the observed product distribution. By comparison between clean surface and *CO hindered reactivity, we propose that propene electro-oxidation to allyl alcohol, acrolein and acrylic acid is enabled only in high surface coverage regimes. Notably, strong energetic drivers to propene degradation on clean Pd suggest not all the adsorbates are oxidized to a desorbing product, increasing the surface population. To test experimentally whether there is a high surface coverage under reaction conditions, we performed propene stripping experiments.

Probing surface population – propene stripping. We carried out propene stripping experiments in an electrochemistry-mass spectrometry (EC-MS) setup to test for the presence of surface adsorbates under reaction conditions. Fig. 7a shows the result of a propene stripping experiment as an EC-MS plot,³⁴ with calibrated mass spectrometer signals (propene = C₃H₆ at *m/z* = 41, propane = C₃H₈ at *m/z* = 29, and CO₂ at *m/z* = 44) in the upper panel, and electrochemistry data in the lower panel. The propene is dosed before *t* = 0 while the electrode is held at a constant dose potential (here +0.65 V vs. RHE) and then purged from the solution. The potential was then cycled, first cathodic to +0.1 V vs. RHE and then anodic to +1.4 V vs. RHE, while gaseous products were monitored with a mass spectrometer. The majority of desorption products come off during this first cycle (Fig. 7a). Thereafter, the electrode is cycled several times (see Fig. S10, ESI[†]), and the electrolyte is replaced to ensure a clean system for the next propene dose. This procedure was then repeated changing the dose potential.

Propene and propane desorb on the initial cathodic sweep, and CO₂ desorbs on the subsequent cathodic and anodic sweeps. Propene desorption likely represents propene in weak adsorption geometries which can be displaced by surface hydrogen adsorption. Propane is presumed to derive from the hydrogenation of propene adsorbed through vinylic coordination. The dip in the propene signal at the cathodic potential limit may indicate that weakly-adsorbed propene can also be reduced with sufficient over-potential. CO₂ desorption after the initial cathodic sweep indicates the presence of strongly bound adsorbates, which cannot be displaced by *H or reduced to propane. Interestingly, a secondary CO₂ peak is observed in the subsequent cathodic scan, as has been observed previously in allyl alcohol stripping experiments.^{48,49} A small amount of CO may have also been observed as a desorption product for some of the stripping experiments, but is challenging to quantify due to interference from both propane and CO₂ in its primary mass fragment, *m/z* = 28. In cyclic voltammetry without propene dosing, a much smaller amount (<5% ML) of CO₂ is observed in each anodic sweep and attributed to oxidation of residual carbon contamination from the air.

It should be noted that the EC-MS setup used here is not sensitive towards non-volatile, liquid products. Based on Fig. 4, we expect that significant liquid products are produced while

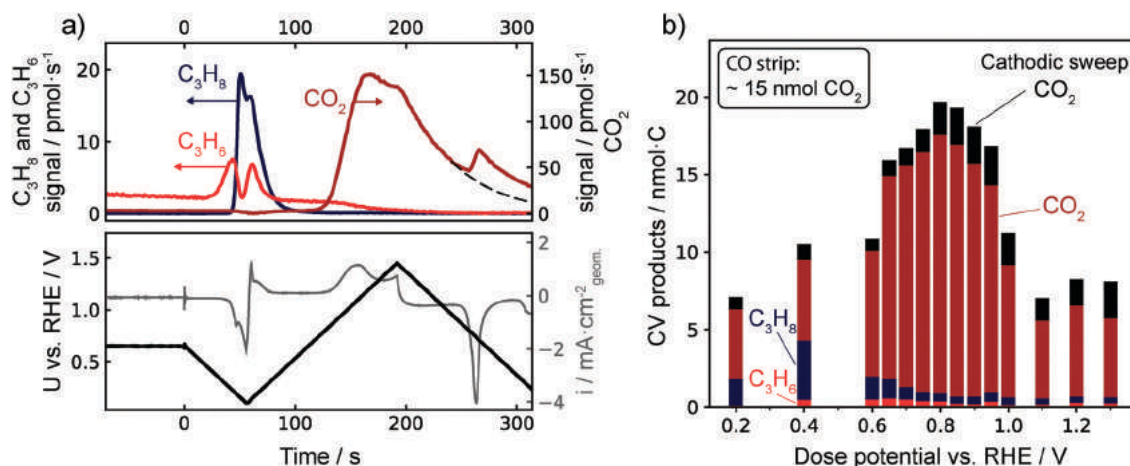


Fig. 7 Propene stripping experiments: (a) EC-MS plot of propene stripping. Propene has been dosed and purged at a dose potential of 0.65 V vs. RHE. Starting at $t = 0$, the potential is scanned cathodically to 0.1 V vs. RHE and then cycled between 0.1 V vs. RHE and 1.4 V vs. RHE while the desorption products propene (C_3H_6), propane (C_3H_8), and CO_2 are monitored. (b) The amount of carbon desorbed in the form of the three observed desorption products during the first full cycle of the stripping experiments is plotted as a function of the potential at which propene was dosed. CO_2 evolving during the first anodic and the subsequent cathodic scan is quantified separately as indicated.

propene is dosed for dosing potentials in the range 0.8–1.0 V vs. RHE. However, since the adsorbates remaining on the surface after propene is purged already had the chance to form liquid products during the stripping experiment itself is minor. Fig. 7b shows the integrated amount of each desorption product from successive propene stripping experiments as a function of the potential at which the propene was dosed. The products are added together based on the number of carbon atoms so that their proportions represent the portion of the adsorbed propene resulting in each stripping product. A broad maximum is observed in the range 0.7–0.9 V vs. RHE, where the primary desorption product is CO_2 . The coverage (on a carbon-atom basis) in this potential range exceeds the saturation coverage of CO based on a CO stripping experiment on the same electrode (Fig. S9, ESI†). This confirms that under steady-state electrolysis, the electrode surface is largely poisoned by strongly-bound adsorbates, as predicted by the DFT model.

Vinyl- vs. allyl-carbon adsorption mechanism. DFT calculations for propene adsorption through allylic carbon deprotonation predict a contribution deriving from double bond coordination to the surface. Indeed, the adsorption geometry changes and the binding energy significantly weakens if the vinylic contribution is impeded (see Fig. S27, ESI†). The propene stripping experiment in Fig. 7 also suggests an active role of the unsaturated carbons in the molecule's coordination with the surface, as indicated by the significant amount of propane desorbing in a cathodic sweep. The propene desorption during the stripping experiment, on the other hand, may represent propene adsorbed through purely allylic coordination. Vinylic adsorption forces the molecule into a flat adsorption geometry, requiring the availability of more surface sites than solely allylic coordination. With the high carbon coverage regimes suggested by DFT under reaction conditions, this cumbersome adsorption mechanism might be hindered, while purely allylic

adsorption requiring less surface availability could become relatively more favorable.

To gain insights into the competition between vinyl coordination and other adsorption geometries, we designed and performed a modification of the propene stripping experiment. In these experiments, shown schematically in Fig. 8a, and exemplified in Fig. 8b, propane desorption is used as a probe for the amount of propene that can adsorb through the vinyl group. The potential at which we dose propene is the same each time, +0.4 V vs. RHE, at which no liquid products are formed, and at which the vinyl adsorbate that can be stripped off to propane is at its maximum coverage (Fig. 7b). After dosing and purging out the propene, the electrode is scanned cathodically to 0.1 V vs. RHE and then anodically up to a cleaning potential which is varied each time. The portion of strongly-adsorbed species that are oxidized off of the surface as CO_2 increases with increasing cleaning potential (Fig. 8c, left y-axis). The cleaning potential thus controls the coverage of the surface prior to the next propene dose.

When propene is dosed now, it must compete with the remaining adsorbates for sites. According to our hypothesis, the coverage of vinyl-bound propene resulting from a propene dose that can desorb as propane in the cathodic scan after the dose should increase with the availability of sites for vinylic coordination, and thus with the cleaning potential. The integrated post-dose propane (C_3H_8) and propene (C_3H_6) is plotted as a function of the cleaning potential in Fig. 8c (right y-axis). To ensure that the changing amount of propane is a result of the surface coverage prior to the propene dose, we stepped up the cleaning potential and then repeated a few cleaning potentials stepping down. The post-dose propane follows the pre-dose CO_2 desorption and the cleaning potential. This indicates that adsorption through the vinyl group is inhibited on a highly covered surface, confirming that the coverage directs the adsorption geometry. The propene (C_3H_6) desorption on the other hand does not depend on the cleaning potential, indicating that the amount of propene

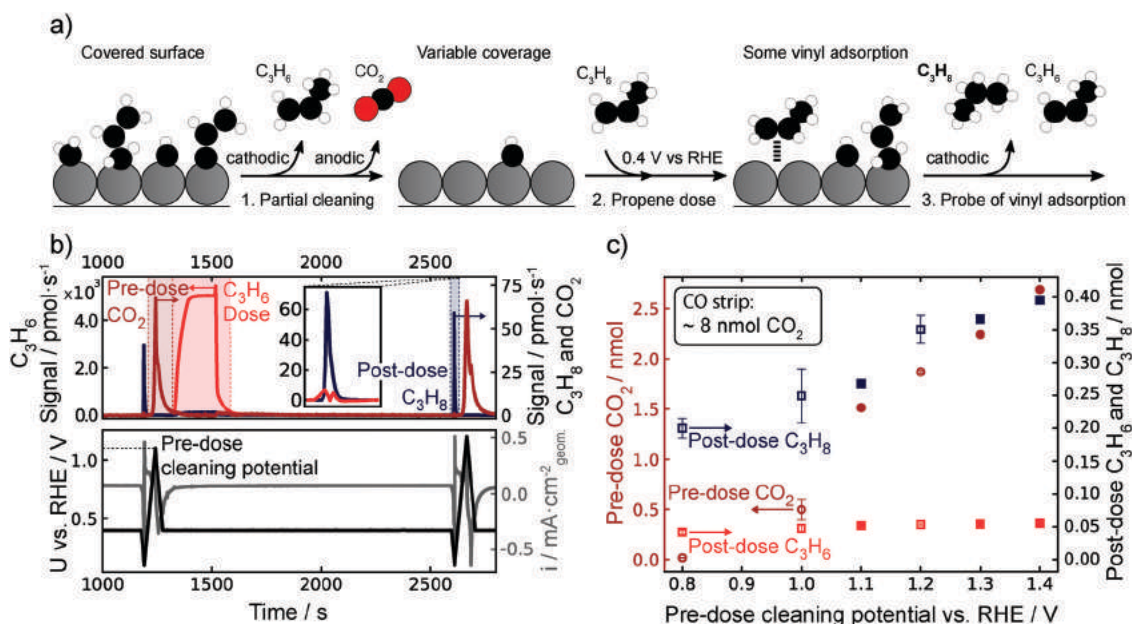


Fig. 8 EC-MS plot of propene stripping “site evacuation” experiments. A surface which has previously been covered by adsorbates by propene dosing (at $t = 0$) is cleaned by scanning to an anodic potential (cleaning potential), stripping a portion of the strongly-adsorbed species off as CO_2 . Propene is then dosed again and purged, and the sample is scanned cathodically to 0.1 V vs. RHE and back before starting the next experimental sequence. (a) Schematic. (b) Experimental data. The inset shows a zoom-in on the signals for propene and propane during the post-dose scan. (c) The integrated flux of CO_2 (circles) from the scans prior to and C_3H_8 and C_3H_6 (squares) from the scans after each propene dose are plotted against the cleaning potential, which is stepped up and down. For values repeated while stepping down the cleaning potential (0.8, 1.0, and 1.2 V vs. RHE), the marker and error bars represent the mean and standard deviation of the measurements, respectively.

adsorbed exclusively through the allylic carbon is not influenced by the pre-dose coverage.

In our analysis, we do not explicitly consider steps and under-coordinated sites. These sites are more reactive than terraces and therefore we assume under reaction conditions these sites are readily passivated by carbon species and remain poisoned during catalytic activity, without participating in the proposed mechanism. Nevertheless, our results do not allow for definite exclusion of their role in the mechanism.

Allyl alcohol conversion tests. In the reaction scheme proposed above, the 2-electron partial oxidation product allyl alcohol is considered an intermediate in the production of the 4- and 6-electron partial oxidation products acrolein and acrylic acid. This is motivated by the fact that allyl alcohol has its peak production rate just cathodic of the latter products (Fig. 4). To test this hypothesis, we performed direct allyl alcohol oxidation experiments.

Fig. 9 shows the average total current density and the faradaic efficiency for direct oxidation of allyl alcohol on Pd at the intermediate potential 0.8 V vs. RHE for 60 min. Two different alcohol concentrations were tested; a 0.1 mM solution to represent the approximate concentration of allyl alcohol that was produced during 1 h of propene oxidation, and a 10 mM solution corresponding to the concentration of propene in the propene oxidation experiments. At the low concentration, the average current density was equivalent to the experiments in propene. At high concentration, it was increased more than 50-fold. Interestingly, the lower concentration experiment produced more of

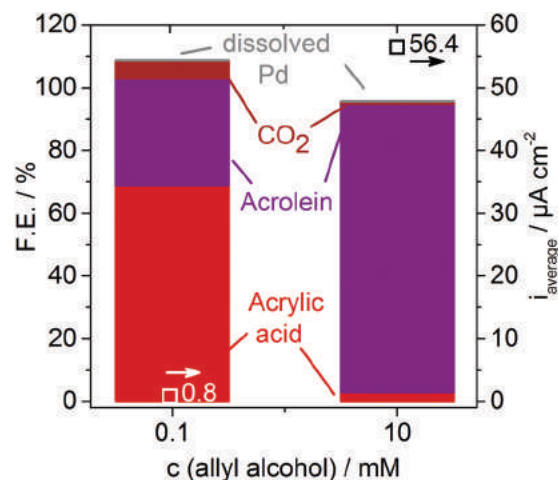


Fig. 9 Product distribution (faradaic efficiency, bar chart) for steady-state oxidation of different concentrations of allyl alcohol in 0.1 M HClO_4 at 0.8 V vs. RHE for one hour. The average of the current density over the measurement time period is shown on the right axis (squares).

the further oxidized acrylic acid ($4e^-$ process) whereas the higher concentration produces more of the less oxidized acrolein ($2e^-$ process). Additional minor products are acrolein or acrylic acid, respectively, CO_2 and traces of propanal. Dissolution of Pd was observed, but no acetone, as is expected in the absence of propene. The observed high current densities for allyl alcohol oxidation are in agreement with the theoretical hypothesis that oxygen incorporation is the rate determining step.

Discussion

In steady-state propene oxidation experiments, we observed a complex potential dependence of the product distribution and high selectivity towards partial oxidation product acrolein, though with low ECSA-normalized current densities and signs of catalyst degradation. Reaction modeling predicts that on a clean surface the carbon intermediates bind too strongly and degrade rather than incorporate oxygen and convert to products. However, computed energies and propene stripping experiments indicate that the surface coverage of propene-derived species is high under reaction conditions and plays a key role in the adsorption mechanism. Hence, we propose a reaction scheme, summarized in Fig. 10. At low coverage, lack of spatial constraints promotes flat propene adsorption through combined allyl-vinyl binding. Depending on the potential, this adsorbate can degrade to smaller C_xH_y fractions and/or be oxidized further, deprotonating the allyl carbon and sinking into a 3-fold hollow site. DFT predicts these species to be highly stable and not to react further under steady-state conditions, increasing the surface coverage. They can however be stripped off as CO_2 in an anodic sweep. The allyl-vinyl adsorbed propene can be reduced to propane in a cathodic sweep. At high carbon coverages, low site availability restricts

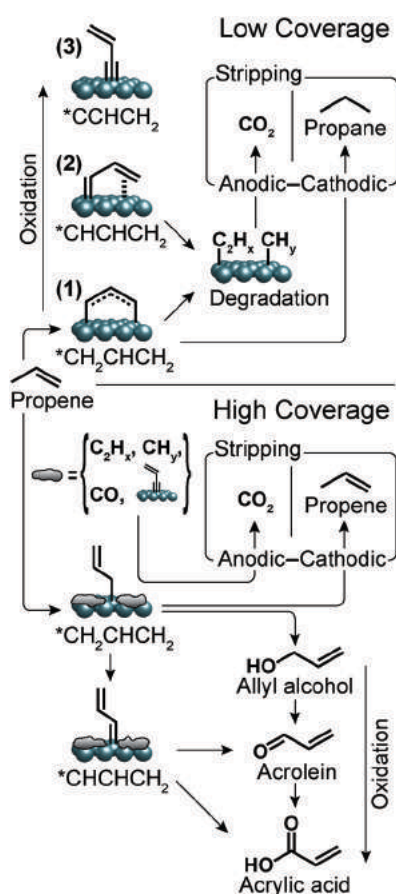


Fig. 10 Graphical representation of the proposed pathways for propene adsorption and conversion. The scheme is divided into two sectors, according to the coverage regime. In each sector, an inset addresses the desorbed species detected in propene stripping experiments.

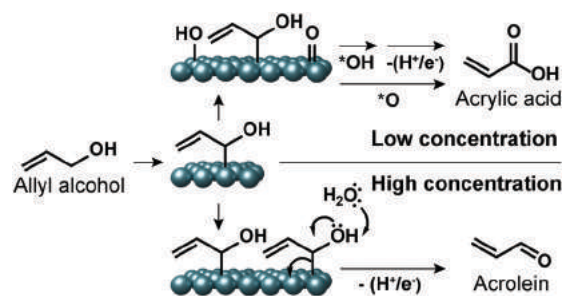


Fig. 11 Proposed mechanism for the oxidation of allyl alcohol at low (0.1 M, top) and high (10 M, bottom) concentrations, yielding two different product distributions.

the adsorption geometry to be primarily allylic and in the atop position. This induces the formation of weakly bound, reactive adsorbates, enabling steady-state conversion to the observed reaction products, though at the price of reduced activity due to partial poisoning. The forced displacement of reactants from a stabilized adsorption configuration to a more unstable, reactive position by surface adsorbates also causes a reduction in kinetic barriers, as shown with DFT. This resembles an effect known from Lindlar-type catalysts for selective hydrogenation of multiply unsaturated alkenes,^{50,51} where partial poisoning of the surface, e.g. by methanol, destabilizes the adsorption of intermediates, preventing full hydrogenation.⁵²

Interestingly, the propene oxidation product propylene glycol, which requires oxidation of the double bond, is only produced significantly at potentials anodic of 1.0 V vs. RHE. This could also be explained as a coverage effect. The lower coverage at high potentials, evidenced by the stripping experiments (Fig. 7b), enables coordination of the vinyl group. However, we do not exclude a different adsorption mechanism on an oxidized surface, though an extensive study on such oxidized surfaces is beyond the scope of this work. That said, the direct partial oxidation of propene to propylene glycol is of high industrial interest, since the existing pathways to propylene glycol (*via* propene oxide) have numerous disadvantages.⁵³

The direct oxidation of allyl alcohol yielded different product concentrations depending on the concentration of allyl alcohol employed. This can be rationalized with a similar mechanistic approach to the oxidation of propene, as illustrated in Fig. 11: the adsorption of allyl alcohol is energetically favored, resulting in a high coverage at high concentrations, but lower coverage at the lower concentration we employed. While surface-bound oxygen species are required for the oxidation to acrylic acid, oxidation to acrolein can also occur by hydroxyl group deprotonation of allyl alcohol. Therefore, at high alcohol coverages, the dominating process will be formation of acrolein, due to the lack of surface oxygen species. At low coverage, surface oxygen species will be available, making way for the direct oxidation to acrylic acid.

4. Conclusions

In this study, using a combination of theoretical modeling and experimental techniques, we presented an in-depth analysis of

propene oxidation on high surface area polycrystalline Pd in 0.1 M HClO₄.

The mechanistic findings in the report are the groundwork to efficient electrochemical conversion of propene. First, in propene oxidation steric effects at the surface regulate the reaction outcome by steering the adsorbate geometry. Thus, it is crucial to tune the catalyst surface population and coverage regimes. Second, with Langmuir–Hinshelwood kinetics on a carbophilic catalyst, the formation of oxygen species at the surface is rate limiting. Balancing oxygen and carbon adsorption while limiting vinylic coordination should ensure higher catalytic turnover, concurrently enabling selectivity towards allylic oxidation products. On the other hand, selective activation of the vinyl group on weaker adsorption sites would promote formation of other industrially relevant products, propylene oxide and propylene glycol, while minimizing degradation. Third, it is important to improve the catalyst stability under oxidative reaction conditions, either by engineering catalysts active at lower potentials, or by synthesis of catalytic materials resistant to anodic corrosion.

Through this work, we outline possible catalyst design strategies for propene partial electro-oxidation reactions and beyond. In practice, one could achieve greater surface coverage control *e.g.* by deposition of poisoning additives to form different atomic surface ensembles.⁵⁴ Alternatively, we are currently developing intermetallic catalysts with embedded carbophilic metals (Pd, Pt, Ru, Rh, and Ir) in inert or oxophilic matrices (Ag, Sn, Au, and graphite); this should activate specific reactant functionalities without prior poisoning, retaining all the mass activity of the precious metal used. Ultimately, the application of a multi-angle approach such as the one presented and a prudent generalization of our conclusions can support the study of other hydrocarbon partial oxidation reactions.

Author contributions

A. W. and L. S. contributed equally. A.W., B. J. S., I. C. and I. E. L. S. designed the bulk electrolysis experiments. A. W. carried out the catalyst preparation, electrochemical experiments and product analysis. K. E.-R. designed and performed NMR characterization of products. S. B. S., D. B. T., P. C. K. V. and I. C. designed the stripping experiments, S. B. S. carried them out. J. R., L. S., M. S. and P. G. M. designed the DFT study, L. S. carried it out. A. W., L. S. and S. B. S. wrote the manuscript; all authors were involved in discussing and interpreting the results and editing the manuscript.

Conflicts of interest

There are no conflicts to declare.

Acknowledgements

We gratefully acknowledge the funding by Danmarks Innovationsfonden, part of the ProActive project (5160-00003B) and by Villum Fonden, part of the Villum Center for the Science of Sustainable Fuels and Chemicals (V-SUSTAIN grant 9455). 800 MHz NMR

spectra were recorded at the NMR Center at DTU supported by the Villum Foundation.

References

- 1 N. S. Lewis and D. G. Nocera, *Proc. Natl. Acad. Sci. U. S. A.*, 2006, **103**, 15729–15735.
- 2 B. Lee, H. Naito, M. Nagao and T. Hibino, *Angew. Chem., Int. Ed.*, 2012, **51**, 6961–6965.
- 3 M. T. M. Koper, *Catalysis in Chemistry and Biology*, World Scientific, 2018, pp. 229–232.
- 4 C. Reller, R. Krause, E. Volkova, B. Schmid, S. Neubauer, A. Rucki, M. Schuster and G. Schmid, *Adv. Energy Mater.*, 2017, **7**, 1602114.
- 5 N. Agarwal, S. J. Freakley, R. U. McVicker, S. M. Althahban, N. Dimitratos, Q. He, D. J. Morgan, R. L. Jenkins, D. J. Willock, S. H. Taylor, C. J. Kiely and G. J. Hutchings, *Science*, 2017, **358**, 223–227.
- 6 Z. Liang, T. Li, M. Kim, A. Asthagiri and J. F. Weaver, *Science*, 2017, **356**, 299–303.
- 7 K. T. Dinh, M. M. Sullivan, P. Serna, R. J. Meyer, M. Dincă and Y. Román-Leshkov, *ACS Catal.*, 2018, 8306–8313.
- 8 A. Marimuthu, J. Zhang and S. Linic, *Science*, 2013, **339**, 1590–1593.
- 9 M. D. Hughes, Y.-J. Xu, P. Jenkins, P. McMorn, P. Landon, D. I. Enache, A. F. Carley, G. A. Attard, G. J. Hutchings, F. King, E. H. Stitt, P. Johnston, K. Griffin and C. J. Kiely, *Nature*, 2005, **437**, 1132–1135.
- 10 B. K. Min and C. M. Friend, *Chem. Rev.*, 2007, **107**, 2709–2724.
- 11 Y. Choi, I. Sinev, H. Mistry, I. Zegkinoglou and B. Roldan Cuenya, *ACS Catal.*, 2016, **6**, 3396–3403.
- 12 Z. W. Seh, J. Kibsgaard, C. F. Dickens, I. Chorkendorff, J. K. Nørskov and T. F. Jaramillo, *Science*, 2017, **355**, eaad4998.
- 13 B. Lee and T. Hibino, *J. Catal.*, 2011, **279**, 233–240.
- 14 M. E. O'Reilly, R. S. Kim, S. Oh and Y. Surendranath, *ACS Cent. Sci.*, 2017, 2–7.
- 15 N. Danilovic, K. E. Ayers, C. Capuano, J. N. Renner, L. Wiles and M. Pertoso, *ECS Trans.*, 2016, **75**, 395–402.
- 16 S. J. Khatib and S. T. Oyama, *Catal. Rev.*, 2015, **57**, 306–344.
- 17 P. Sprenger, W. Kleist and J.-D. Grunwaldt, *ACS Catal.*, 2017, **7**, 5628–5642.
- 18 Nexant, Nexant Petroleum and Petrochemical Economics (PPE) Program, 2017.
- 19 C. J. Sullivan, A. Kuenz and K.-D. Vorlop, *Ullmann's Encyclopedia of Industrial Chemistry*, Wiley-VCH Verlag GmbH & Co. KGaA, Weinheim, Germany, 2018, pp. 1–15.
- 20 M. Weber, W. Pompeckzi, R. Bonmann and M. Weber, *Ullmann's Encyclopedia of Industrial Chemistry*, Wiley-VCH Verlag GmbH & Co. KGaA, Weinheim, Germany, 2014, pp. 1–19.
- 21 J. O. Bockris, H. Wroblowa, E. Gileadi and B. J. Piersma, *Trans. Faraday Soc.*, 1965, **61**, 2531–2545.
- 22 M. Bełtowska-Brzezinska, T. Luczak, H. Baltruschat and U. Müller, *J. Phys. Chem. B*, 2003, **107**, 4793–4800.

- 23 T.-C. Chou and J.-C. Chang, *Chem. Eng. Sci.*, 1980, **35**, 1581–1590.
- 24 K. Scott, C. Odouza and W. Hui, *Chem. Eng. Sci.*, 1992, **47**, 2957–2962.
- 25 G. Göransson, J. S. Jirkovský, P. Krtil and E. Ahlberg, *Electrochim. Acta*, 2014, **139**, 345–355.
- 26 L. L. Holbrook and H. Wise, *J. Catal.*, 1975, **38**, 294–298.
- 27 V. M. Schmidt and E. Pastor, *J. Electroanal. Chem.*, 1996, **401**, 155–161.
- 28 G. R. Stafford, *Electrochim. Acta*, 1987, **32**, 1137–1143.
- 29 K. Otsuka, Y. Shimizu, I. Yamanaka and T. Komatsu, *Catal. Lett.*, 1989, **3**, 365–370.
- 30 N. Markovic, *J. Electrochem. Soc.*, 1997, **144**, 1591.
- 31 R. Ojani, E. Hasheminejad and J. B. Raoof, *Int. J. Hydrogen Energy*, 2014, **39**, 8194–8203.
- 32 J. Liu, L. Cao, W. Huang and Z. Li, *J. Electroanal. Chem.*, 2012, **686**, 38–45.
- 33 E. Bertheussen, T. V. Hogg, Y. Abghoui, A. K. Engstfeld, I. Chorkendorff and I. E. L. Stephens, *ACS Energy Lett.*, 2018, **3**, 634–640.
- 34 D. B. Trimarco, S. B. Scott, A. H. Thilsted, J. Y. Pan, T. Pedersen, O. Hansen, I. Chorkendorff and P. C. K. Vesborg, *Electrochim. Acta*, 2018, **268**, 520–530.
- 35 J. Enkovaara, C. Rostgaard, J. J. Mortensen, J. Chen, M. Dułak, L. Ferrighi, J. Gavnholt, C. Glinsvad, V. Haikola, H. A. Hansen, H. H. Kristoffersen, M. Kuisma, A. H. Larsen, L. Lehtovaara, M. Ljungberg, O. Lopez-Acevedo, P. G. Moses, J. Ojanen, T. Olsen, V. Petzold, N. A. Romero, J. Stausholm-Møller, M. Strange, G. A. Tritsarlis, M. Vanin, M. Walter, B. Hammer, H. Häkkinen, G. K. H. Madsen, R. M. Nieminen, J. K. Nørskov, M. Puska, T. T. Rantala, J. Schiøtz, K. S. Thygesen and K. W. Jacobsen, *J. Phys.: Condens. Matter*, 2010, **22**, 253202.
- 36 A. Hjorth Larsen, J. Jørgen Mortensen, J. Blomqvist, I. E. Castelli, R. Christensen, M. Dułak, J. Friis, M. N. Groves, B. Hammer, C. Hargus, E. D. Hermes, P. C. Jennings, P. Bjerre Jensen, J. Kermode, J. R. Kitchin, E. Leonhard Kolsbjerg, J. Kubal, K. Kaasbjerg, S. Lysgaard, J. Bergmann Maronsson, T. Maxson, T. Olsen, L. Pastewka, A. Peterson, C. Rostgaard, J. Schiøtz, O. Schütt, M. Strange, K. S. Thygesen, T. Vegge, L. Vilhelmsen, M. Walter, Z. Zeng and K. W. Jacobsen, *J. Phys.: Condens. Matter*, 2017, **29**, 273002.
- 37 S. R. Bahn and K. W. Jacobsen, *Comput. Sci. Eng.*, 2002, **4**, 56–66.
- 38 M. Hara, U. Linke and T. Wandlowski, *Electrochim. Acta*, 2007, **52**, 5733–5748.
- 39 F. Hernandez and H. Baltruschat, *Langmuir*, 2006, **22**, 4877–4884.
- 40 N. Hoshi, K. Kagaya and Y. Hori, *J. Electroanal. Chem.*, 2000, **485**, 55–60.
- 41 N. Hoshi, M. Kuroda and Y. Hori, *J. Electroanal. Chem.*, 2002, **521**, 155–160.
- 42 M. Pourbaix, *Atlas of electrochemical equilibria in aqueous solutions*, Pergamon Press, 1974.
- 43 P. Y. Bruice, *Organic Chemistry*, Pearson Education, 2007.
- 44 J. K. Nørskov, J. Rossmeisl, A. Logadottir, L. Lindqvist, J. R. Kitchin, T. Bligaard and H. Jónsson, *J. Phys. Chem. B*, 2004, **108**, 17886–17892.
- 45 K. J. J. Mayrhofer, M. Arenz, B. B. Blizanac, V. Stamenkovic, P. N. Ross and N. M. Markovic, *Electrochim. Acta*, 2005, **50**, 5144–5154.
- 46 M. T. M. Koper, S. C. S. Lai and E. Herrero, *Fuel Cell Catalysis*, John Wiley & Sons, Inc., Hoboken, NJ, USA, 2009, pp. 159–207.
- 47 L. Vitos, A. V. Ruban, H. L. Skriver and J. Kollár, *Surf. Sci.*, 1998, **411**, 186–202.
- 48 E. Pastor, S. Wasmus, T. Iwasita, M. C. Arévalo, S. Gonzalez and A. J. Arvia, *J. Electroanal. Chem.*, 1993, **353**, 81–100.
- 49 M. C. Arévalo, J. L. Rodríguez and E. Pastor, *J. Electroanal. Chem.*, 2001, **505**, 62–71.
- 50 H. Lindlar, *Helv. Chim. Acta*, 1952, **35**, 446–450.
- 51 D. Albani, M. Shahrokhi, Z. Chen, S. Mitchell, R. Hauert, N. López and J. Pérez-Ramírez, *Nat. Commun.*, 2018, **9**, 2634.
- 52 G. Horányi and K. Torkos, *J. Electroanal. Chem. Interfacial Electrochem.*, 1980, **111**, 279–286.
- 53 T. A. Nijhuis, M. Makkee, J. A. Moulijn and B. M. Weckhuysen, *Ind. Eng. Chem. Res.*, 2006, **45**, 3447–3459.
- 54 D. Strmcnik, M. Escudero-Escribano, K. Kodama, V. R. Stamenkovic, A. Cuesta and N. M. Marković, *Nat. Chem.*, 2010, **2**, 880–885.

Paper IV Absence of Oxidized Phases in Cu under CO Reduction Conditions

Soren B. Scott, Thomas V. Hogg, Alan T. Landers, Thomas Maagaard, Erlend Bertheussen, John C. Lin, Ryan C. Davis, Jefferey W. Beeman, Drew Higgins, Walter S. Drisdell, Apurva Mehta, Brian J. Seger, Thomas F. Jaramillo, and Ib Chorkendorff.

ACS Energy Letters. 4, 803804, 2019

DOI: 10.1021/acsenergylett.9b00172

Absence of Oxidized Phases in Cu under CO Reduction Conditions

Soren B. Scott,[†] Thomas V. Hogg,[†] Alan T. Landers,^{‡,¶} Thomas Maagaard,[†] Erlend Bertheussen,[†] John C. Lin,^{‡,§} Ryan C. Davis,^{||} Jeffrey W. Beeman,^{⊥,#} Drew Higgins,^{‡,§} Walter S. Drisdell,^{⊥,#} Christopher Hahn,^{‡,§} Apurva Mehta,^{||} Brian Seger,[†] Thomas F. Jaramillo,^{*,‡,§} and Ib Chorkendorff^{*,†}

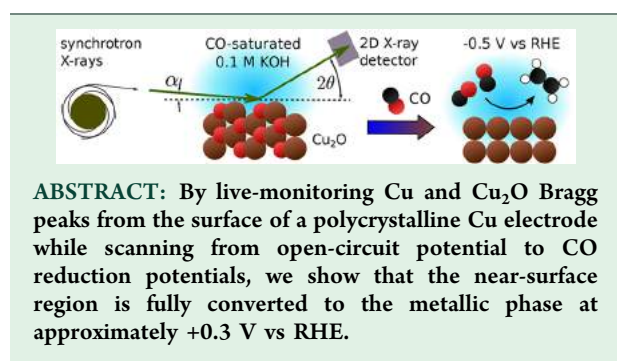
[†]Section for Surface Physics and Catalysis, Department of Physics, Technical University of Denmark, 2800 Kgs Lyngby, Denmark

[‡]Center for Interface Science and Catalysis & ^{||}Stanford Synchrotron Radiation Lightsource, SLAC National Accelerator Laboratory, Menlo Park, California 94025, United States

[¶]Department of Chemistry & [§]Department of Chemical Engineering, Stanford University, Stanford, California 94305, United States

[⊥]Joint Center for Artificial Photosynthesis & [#]Chemical Sciences Division, Lawrence Berkeley National Laboratory, Berkeley, California 94720, United States

Supporting Information



ABSTRACT: By live-monitoring Cu and Cu₂O Bragg peaks from the surface of a polycrystalline Cu electrode while scanning from open-circuit potential to CO reduction potentials, we show that the near-surface region is fully converted to the metallic phase at approximately +0.3 V vs RHE.

Copper can catalyze the electrochemical reduction of CO₂ and CO to multicarbon fuels with significant activity and Faradaic efficiency,^{1,2} and copper-based gas-diffusion electrodes for reduction of CO₂ and CO to ethylene in alkaline electrolyte are approaching technological viability.^{3,4} However, uncertainty about the atomic structure of the electrode surface and near-surface region under reaction conditions remains a challenge to the development of more active and selective electrodes materials.

Importantly, the presence of oxygen is a matter of debate. Despite the high equilibrium potentials for reduction of bulk oxidized phases of copper ($U_{\text{RHE}}^{\circ} > 0.4$ V; see Table S1), several studies have reported signs that oxygen is present near the surface of copper electrodes under reaction conditions ($U_{\text{RHE}}^{\circ} < 0$ V),^{5,6} and DFT calculations have indicated that subsurface oxygen may promote CO₂ and CO reduction activity.^{6,7} Other experiments and calculations have indicated that subsurface oxygen is not stable under the cathodic reaction conditions,^{8–10} and recent comparisons have shown that the intrinsic CO and CO₂ reduction activity on copper-based electrodes does not depend on the initial oxidation state.^{2,11}

We used in situ grazing incidence X-ray diffraction (GIXRD) with synchrotron radiation to probe the structure of a polycrystalline copper thin film under CO reduction conditions

in 0.1 M KOH (pH \approx 13) using a three-electrode setup with a flow cell and techniques described in the SI and in detail elsewhere.¹⁴ By varying the incident angle (α), GIXRD diffractograms were taken at probe depths of \sim 2.5 nm ($\alpha = 0.15^{\circ}$) and \sim 20 nm ($\alpha = 0.20^{\circ}$). Product quantification has been described elsewhere for polycrystalline copper under the same CO reduction conditions.²

Figure 1a shows typical GIXRD diffractograms in CO-saturated electrolyte, taken at the surface-sensitive incident angle of $\alpha = 0.15^{\circ}$, before (+0.65 V vs RHE) and after (−0.4 V vs RHE) reduction. The first potential is near the measured open-circuit potential (OCP, typically \sim 0.7 V vs RHE; see Figure S1), and CO reduction is significant at the latter potential.² The broad Cu₂O(111) peak centered at $2\theta = 16.9^{\circ}$ in the prerelation diffractogram, attributed to the native oxide formed while the sample is exposed to air and/or at OCP, disappears in the postreduction diffractogram. That peak's large width indicates that the oxide phase is less crystalline than the metallic phase (\sim 5 nm crystallites compared to \sim 15 nm; see Figure S2). No peaks for other oxidized Cu phases such as CuO or Cu(OH)₂ were observed. Results are similar in Ar-saturated electrolyte (Figure S3). The high pH likely plays a role in the formation of long-range order in the Cu₂O phase at OCP, as Cu₂O diffraction peaks were not observed at OCP at lower pH.¹⁴

Figure 1b shows the live reduction of a fresh sample in Ar-saturated electrolyte (see Figure S4 for CO). The Cu₂O(111) peak disappears and the Cu(111) peak becomes more intense at approximately $t = 40$ s, when the potential is between 0.4 and 0.3 V vs RHE. The reduction of electrodes in Ar and CO are compared in Figure 1c. For both samples, the Cu₂O(111) peak disappears and the Cu(111) peak grows to maximum intensity between 0.4 and 0.3 V vs RHE, just cathodic of the standard reduction potential of Cu₂O (Table S1). The abrupt increase of

Received: January 23, 2019

Accepted: February 20, 2019

Published: February 20, 2019

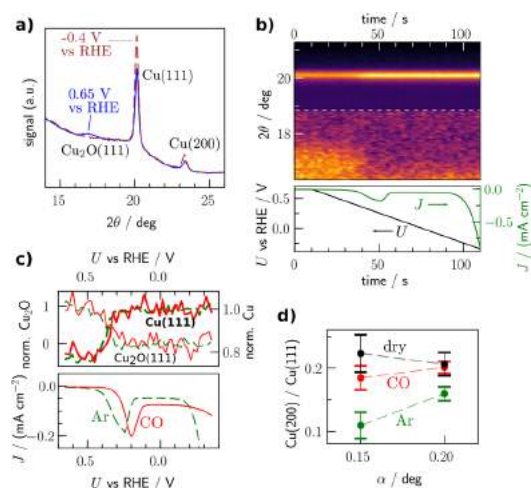


Figure 1. In situ GIXRD of polycrystalline Cu electrodes. (a) Diffractograms at incident angle $\alpha = 0.15^\circ$ of a Cu sample in CO-saturated 0.1 M KOH. (b) Live monitoring of diffraction signal during reduction of a sample in Ar-saturated electrolyte. (c) Normalized integrated Cu(111) and Cu₂O(111) Bragg peaks during reduction of samples in Ar-saturated or CO-saturated electrolyte. (d) Ratio of the integrated Cu(200) and Cu(111) peaks for dry samples and reduced samples (-0.4 or -0.5 V vs RHE) in Ar- or CO-saturated electrolyte as a function of incident angle. Points and error bars represent means and standard deviations, respectively.

the Cu(111) peak to its maximum intensity by $+0.3$ V vs RHE rules out a significant content of any oxidized phase at more cathodic potentials within the attenuation depth of 2.5 nm (~ 12 monolayers), as the presence of such a phase, crystalline or amorphous, would reduce the intensity of the Cu(111) peak. The delay in the cathodic current wave with respect to the change in XRD peak intensity for the sample reduced in CO-saturated electrolyte might indicate an electrochemical reduction mechanism in which CO acts as a chemical reductant, as CO is known to reduce copper oxides in thermal catalysis.¹⁵

Figure 1d shows the Cu(200)/Cu(111) intensity ratio, which can be influenced by surface faceting (Figure S5). While this ratio is similar in Ar and CO prior to reduction (Figure S6), at $\alpha = 0.15^\circ$ the ratio increases after reduction for samples in CO-saturated electrolyte. The ratios converge at $\alpha = 0.20^\circ$, confirming that the difference is due to a surface phenomenon. The results are consistent with the STM observation of polycrystalline Cu electrodes that reconstruct first to (111) and then to (100)¹² and provides evidence for the CO-promoted reconstruction to (100)-like surfaces. This reconstruction helps explain why polycrystalline Cu electrodes show high selectivity for CO reduction to ethylene, similar to stepped (100) surfaces.¹ Small shifts of peak centers ($\Delta 2\theta \approx -0.02^\circ$) were also observed during the reduction (Figure S6), possibly reflecting hydrogen-induced expansion.¹³

In this study, we used in situ GIXRD to examine changes in the surface composition and morphology of polycrystalline copper under CO reduction conditions. The Cu₂O(111) diffraction peak disappears during the cathodic scan at about 0.3 V vs RHE while the Cu(111) peak simultaneously increases to its maximum intensity, with no further increase at more cathodic potentials, demonstrating that the oxide is fully reduced to the metallic phase at potentials relevant to CO reduction. Compared to other studies that also show the reduction of oxidized copper phases prior to the onset of CO or CO₂

reduction by means of in situ X-ray absorption spectroscopy¹⁶ and Raman spectroscopy,¹⁰ our results stand out for the high time resolution and the surface sensitivity enabled by the grazing incidence configuration. We also provide preliminary GIXRD evidence of preferential surface faceting guided by electrochemical environment, in agreement with STM studies.¹² Taken together, these results help explain why the intrinsic CO reduction activity of polycrystalline copper-based electrodes is largely invariant with the structure or oxidation state of the precursor.² Surface roughening caused by these faceting changes and undercoordinated sites present during the reconstruction may also contribute to copper's CO reduction activity.

■ ASSOCIATED CONTENT

Supporting Information

The Supporting Information is available free of charge on the ACS Publications website at DOI: 10.1021/acseenergylett.9b00172.

Experimental details and additional data (PDF)

■ AUTHOR INFORMATION

Corresponding Authors

*E-mail: jaramillo@stanford.edu.

*E-mail: ibchork@fysik.dtu.dk.

Notes

The authors declare no competing financial interest.

■ ACKNOWLEDGMENTS

The Center for Surface Physics and Catalysis is funded by the Villum Foundation V-SUSTAIN Grant 9455. Part of this work was performed by the Joint Center for Artificial Photosynthesis, a DOE Energy Innovation Hub, supported through the Office of Science of the U.S. Department of Energy (DOE), under Award No. DE-SC0004993. Part of this work was performed at the Stanford Nano Shared Facilities and the Stanford Nano-fabrication Facility, supported by the National Science Foundation under Award ECCS-1542152. X-ray data were collected at Stanford Synchrotron Radiation Lightsource, SLAC, which is supported by the DOE Office of Basic Energy Sciences under Contract No. DE-AC02-76SF00515. S.B.S. acknowledges the Danish Ministry for Higher Education and Science for an EliteForsk travel grant.

■ REFERENCES

- (1) Hori, Y. In *Modern Aspects of Electrochemistry*; 2008; Vol. 42, pp 89–189.
- (2) Bertheussen, E.; et al. *ACS Energy Lett.* **2018**, 3 (3), 634.
- (3) Han, L.; et al. *ACS Energy Lett.* **2018**, 3 (4), 855–860.
- (4) Dinh, C.-T.; et al. *Science* **2018**, 360 (6390), 783.
- (5) Mistry, H.; et al. *Nat. Commun.* **2016**, 7, 12123.
- (6) Eilert, A.; et al. *J. Phys. Chem. Lett.* **2017**, 8 (1), 285.
- (7) Favaro, M.; et al. *Proc. Natl. Acad. Sci. U. S. A.* **2017**, 114 (26), 6706.
- (8) Lum, Y.; et al. *Angew. Chem., Int. Ed.* **2018**, 57 (2), 551.
- (9) Garza, A. J. *J. Phys. Chem. Lett.* **2018**, 9 (3), 601.
- (10) Mandal, L.; et al. *ACS Appl. Mater. Interfaces* **2018**, 10 (10), 8574.
- (11) Clark, E. L.; et al. *ACS Catal.* **2018**, 8 (7), 6560.
- (12) Kim, Y.-G.; et al. *J. Electroanal. Chem.* **2016**, 780 (1), 290.
- (13) Huynh, T. M. T.; et al. *ChemElectroChem* **2014**, 1 (8), 1271.
- (14) Farmand, M. *Phys. Chem. Chem. Phys.* 2019, in press; DOI: 10.1039/C8CP07423B.
- (15) Goldstein, E. A.; et al. *Proc. Combust. Inst.* **2011**, 33 (2), 2803.
- (16) Eilert, A.; et al. *J. Phys. Chem. Lett.* **2016**, 7 (8), 1466.

Paper V Progress and Perspectives of Electrochemical CO₂ Reduction on Copper in Aqueous Electrolyte

Stephanie A. Nitopi*, Erlend Bertheussen*, Soren Bertelsen Scott, Xinyan Liu, Albert K. Engstfeld, Sebastian Horch, Brian Seger, Ifan Stephens, Karen Chan, Christopher Hahn, Jens K. Nørskov, Thomas Jaramillo, and Ib Chorkendorff.

*These authors contributed equally to this work

Chemical Reviews. 12, 7610-7672, 2019

DOI: 10.1021/acs.chemrev.8b00705

Note:

I became involved in this Paper, a review and perspective article, because I wrote a motivation for the CO₂ reduction reaction as part of my master's thesis, which I expanded and adapted for this Paper. My primary contributions to the Paper were writing the introduction and producing a map of proposed mechanistic pathways of CO₂ reduction. The Paper is 63 pages long, and so only the introduction is reproduced in this thesis.



Progress and Perspectives of Electrochemical CO₂ Reduction on Copper in Aqueous Electrolyte

Stephanie Nitopi,^{†,‡} Erlend Bertheussen,^{‡,‡} Soren B. Scott,[‡] Xinyan Liu,[†] Albert K. Engstfeld,^{‡,§} Sebastian Horch,[‡] Brian Seger,[‡] Ifan E. L. Stephens,^{‡,‡} Karen Chan,^{†,||} Christopher Hahn,^{†,||} Jens K. Nørskov,^{*,†,‡,||} Thomas F. Jaramillo,^{*,†,||} and Ib Chorkendorff^{*,†,||}

[†]SUNCAT Center for Interface Science and Catalysis, Department of Chemical Engineering, Stanford University, Stanford, California 94305, United States

[‡]Section for Surface Physics and Catalysis, Department of Physics, Technical University of Denmark, 2800 Kgs. Lyngby, Denmark

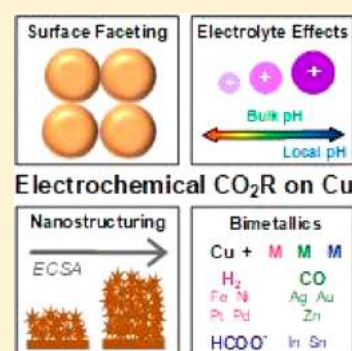
[§]Institute of Surface Chemistry and Catalysis, Ulm University, D-89069 Ulm, Germany

^{||}SUNCAT Center for Interface Science and Catalysis, SLAC National Accelerator Laboratory, Menlo Park, California 94025, United States

[‡]Department of Materials, Imperial College London, Royal School of Mines, London SW7 2AZ, United Kingdom

Supporting Information

ABSTRACT: To date, copper is the only heterogeneous catalyst that has shown a propensity to produce valuable hydrocarbons and alcohols, such as ethylene and ethanol, from electrochemical CO₂ reduction (CO₂R). There are variety of factors that impact CO₂R activity and selectivity, including the catalyst surface structure, morphology, composition, the choice of electrolyte ions and pH, and the electrochemical cell design. Many of these factors are often intertwined, which can complicate catalyst discovery and design efforts. Here we take a broad and historical view of these different aspects and their complex interplay in CO₂R catalysis on Cu, with the purpose of providing new insights, critical evaluations, and guidance to the field with regard to research directions and best practices. First, we describe the various experimental probes and complementary theoretical methods that have been used to discern the mechanisms by which products are formed, and next we present our current understanding of the complex reaction networks for CO₂R on Cu. We then analyze two key methods that have been used in attempts to alter the activity and selectivity of Cu: nanostructuring and the formation of bimetallic electrodes. Finally, we offer some perspectives on the future outlook for electrochemical CO₂R.



CONTENTS

1. Introduction	7611	3.1.1. Influence of Various Cu(hkl) Surfaces on Product Distribution	7619
1.1. Motivation for CO ₂ Recycling	7611	3.1.2. Influence of Various Cu(hkl) Surfaces on Activity	7621
1.1.1. Closing the Carbon Cycle	7611	3.1.3. Restructuring and Other Challenges Regarding Single Crystal Measurements	7621
1.1.2. Strategies for CO ₂ Recycling	7613	3.2. Reduction of Possible Intermediates	7623
1.2. Electrochemical CO ₂ Reduction	7614	3.2.1. CO as a Crucial Intermediate	7623
1.2.1. Desired Products: Thermodynamics and Economics	7614	3.2.2. Reduction of Oxygenated C ₁ and C ₂ Species	7624
1.2.2. Copper as a Unique Electrocatalyst	7615	3.3. Electrolyte Effects	7625
2. Considerations for Conducting and Comparing Electrochemical CO ₂ Reduction Experiments	7617	3.3.1. pH Effects	7625
2.1. Reporting Data	7617	3.3.2. Cation Effects	7627
2.2. Intrinsic Kinetics vs Mass Transport Effects	7617	3.3.3. Anion Effects	7628
2.3. Deactivation of Cu Electrodes	7618	3.4. Electrochemical Conditions	7629
2.4. Deconvolution of Various Effects in Complex Catalysts	7618	3.4.1. Temperature and Pressure	7629
3. Experimental Probes of CO ₂ Reduction Mechanisms	7619	3.5. Summary	7629
3.1. Influence of Surface Facet on CO ₂ and CO Reduction	7619	4. Theoretical Studies on Copper	7630

Received: November 26, 2018

Published: May 22, 2019

4.1. Introduction to Theoretical Approaches	7630
4.1.1. Implicit Models	7631
4.1.2. Explicit Models	7631
4.1.3. H-Shuttling Model	7631
4.2. Theoretical Insights	7632
4.2.1. Trends in Electrochemical Barriers	7632
4.2.2. CO as a Crucial Intermediate	7632
4.2.3. Pathway toward Methane	7632
4.2.4. CO Dimerization	7633
4.2.5. C ₂ Pathways	7633
4.2.6. Kinetics	7634
4.2.7. Rate-Limiting Electron Transfers	7634
4.3. Summary	7635
5. Electrochemical CO ₂ Reduction Pathways on Cu	7635
6. Nanostructured Copper	7638
6.1. Nanoparticles	7638
6.1.1. Nanoparticle Size Effects	7638
6.1.2. Loading/Interparticle Distance	7639
6.1.3. Shape Effects	7640
6.1.4. Effect of Support and Catalyst–Ionomer Interaction	7641
6.2. Three-Dimensionally Interconnected Catalyst Materials	7641
6.2.1. Oxide-Derived Copper	7642
6.2.2. Non-Oxide-Derived Copper	7644
6.2.3. Role of Oxygen in CO ₂ R Electrocatalysis	7644
6.2.4. Activity Comparisons	7646
6.3. Vapor-Fed Systems	7647
6.4. Summary	7648
7. Copper Bimetallics	7649
7.1. Copper and H ₂ Producing Guest Metals (Fe, Ni, Pt, Pd)	7649
7.2. Copper and CO Producing Guest Metals (Ag, Au, Zn)	7651
7.2.1. Synergistic Effects for CO Production	7651
7.2.2. Synergistic Effects for >2e ⁻ Products	7651
7.3. Copper and HCOO ⁻ Producing Guest Metals (In, Sn)	7654
7.4. Activity Comparisons	7656
7.5. Summary	7658
8. Conclusions and Future Outlook	7658
Associated Content	7660
Supporting Information	7660
Author Information	7660
Corresponding Authors	7660
ORCID	7660
Author Contributions	7660
Notes	7660
Biographies	7660
Acknowledgments	7661
References	7661

1. INTRODUCTION

There is a pressing need to advance the development of CO₂ utilization technologies such as electrochemical CO₂ reduction (CO₂R); as a result, this has been a rapidly expanding field of research in recent years. In particular, there is a large body of work on copper (Cu) materials for this reaction, since Cu is, as of yet, unique in its ability to catalyze the electrochemical conversion of CO₂ to valuable fuels and chemicals. While many a great review and perspective articles have been published in this area, they have typically had a more narrow

focus in terms of either timespan or topics covered.^{1–21} Here we aim to provide an organized and comprehensive review of CO₂R on copper and the multitude of approaches that have been used to tune its catalytic activity and selectivity. The scope strives to include all studies of electrochemical CO₂R in aqueous electrolytes on Cu-based catalysts, beginning with many of the early works in the 1980s–1990s through those published in 2018, and it takes into consideration both experimental and theoretical methods, planar and nanostructured Cu, and Cu modified with other elements. This work is also a perspective in which we critically analyze the literature in attempts to normalize/compare the various results and show general trends throughout the field. Additionally, we suggest several techniques and protocols that can allow for more reliable comparisons, enable a more fundamental understanding of the catalysis, and help drive this technology toward commercialization. This section first provides a broad context by summarizing anthropogenic carbon streams, comparing different strategies to recycle CO₂, and touching upon the economics of electrochemical CO₂ conversion. Then, planar polycrystalline copper is introduced as a unique electrocatalyst for this reaction, which will serve as the basis for all the discussions that follow.

1.1. Motivation for CO₂ Recycling

At the core of biological metabolism is the ability to convert carbon between different oxidation states in order to store and release energy, as well as to synthesize functional molecules. Likewise, the oxidation of carbon is at the center of human civilization's collective "industrial metabolism" consisting of our energy infrastructure and chemical industry. Whereas in biological metabolism, reduction of CO₂ in photosynthesis balances the oxidation of carbon in cellular respiration, carbon reduction is as of yet a missing piece of humanity's industrial metabolism. This imbalance has become a significant perturbation to Earth's natural carbon cycle, as indicated in the top two sections of Table 1. The resulting accumulation of the greenhouse gas CO₂ in the atmosphere is the primary driver of today's climate change.²² While the Paris Climate Accord commits signatories to the goal of achieving "a balance between anthropogenic emissions by sources and removals by sinks of greenhouse gases in the second half of this century",²³ it leaves it to individual nations to volunteer the specifics of how to achieve this goal. The problem is urgent: net CO₂ emissions need to decrease rapidly and cross zero around the year 2050 if global warming is to be limited to the relatively safe level of 1.5 °C above preindustrial levels.²⁴ Strategies to reduce net CO₂ emissions fall under three categories: decarbonization, carbon sequestration, and carbon recycling, all three of which will most likely need to play a role. This Review will focus in-depth on the scientific progress and challenges of carbon recycling based on electrochemical CO₂ reduction on Cu catalysts. For context, we will first briefly comment on decarbonization and carbon sequestration, as well as the other major CO₂ recycling strategies.

1.1.1. Closing the Carbon Cycle. Significant progress is presently being made in decarbonization. Economic growth is increasingly decoupled from energy consumption and from CO₂ emissions (Figure 1),^{25–27} electricity from renewable sources such as wind turbines and photovoltaics is increasing in volume and decreasing in price,²⁸ private investment in renewable energy is outpacing investment in fossil fuels,²⁹ and global annual CO₂ emissions are plateauing.²⁵ However,

Table 1. Global Carbon Fluxes^c

Carbon flux ^a	Amount/[GtC/yr]	Year ^{citation}
Carbon Cycle Overview		
Air–land natural exchange	120	2007 ³⁸
Air–ocean natural exchange	90	2007 ³⁸
Anthropogenic carbon emissions	11	2014 ³⁹
Total anthropogenic GHG emissions by CO ₂ equivalent	13	2010 ²²
Fate of Anthropogenic Emissions		
Net ocean uptake	4	2014 ³⁹
Net land uptake	3	2014 ³⁹
Accumulated in atmosphere	4	2014 ³⁹
Anthropogenic Emissions by Sector (100% = 13 GtC/yr)		
Electricity generation	3.3 (25%)	2010 ²²
Agriculture and land-use change (deforestation)	3.2 (24%)	2010 ²²
Industry (excluding electricity)	2.8 (21%)	2010 ²²
Transportation	1.9 (14%)	2010 ²²
Buildings	0.9 (6%)	2010 ²²
Other	1.4 (10%)	2010 ²²
Carbon in Industrial Reactions, CO ₂ as Ultimate Byproduct ^b		
Cement (calcination): $\text{CaCO}_3 \rightarrow \text{CaO} + \text{CO}_2$	0.59	2017 ³³
Steel (via CO): $2\text{Fe}_2\text{O}_3 + 6\text{C} + 3\text{O}_2 \rightarrow 4\text{Fe} + 6\text{CO}_2$	0.38	2017 ³⁴
Plastic (disposal): $(\text{CH}_2)_n + 3n\text{O}_2 \rightarrow 2n\text{H}_2\text{O} + 2n\text{CO}_2$	0.26	2015 ³⁵
Ammonia (via H ₂): $3\text{CH}_4 + 6\text{H}_2\text{O} + 4\text{N}_2 \rightarrow 8\text{NH}_3 + 3\text{CO}_2$	0.045	2016 ³⁶
Aluminum (carbon anode): $2\text{Al}_2\text{O}_3 + 3\text{C} \rightarrow 4\text{Al} + 3\text{CO}_2$	0.019	2016 ³⁷
Total nonfuel carbon as industrial reactant	1.28	

^aSome of the carbon fluxes have been converted from carbon dioxide flux emissions to molecular mass (1 GtC/yr is equivalent to 3.66 GtCO₂/yr). The data from ref 22 are reported, not in terms of carbon or carbon dioxide flux, but by total greenhouse gas emissions converted to the equivalent mass of CO₂ emissions based on the green house gas's global warming potential. These data were converted to carbon flux as if they were CO₂ emissions. ^bThe bottom section of the table shows the minimum nonenergy carbon usage of the most important carbon-using industrial processes, calculated based on global production and the stoichiometry of the simplified reaction shown. Figures for steel and plastic exclude recycling. For plastic, we write the combustion reaction to represent the stoichiometric amount of CO₂, even though most plastic today is not incinerated but ends up in landfills or the environment after use. ³⁵ ^cFor more details, see section 2 of the Supporting Information (SI).

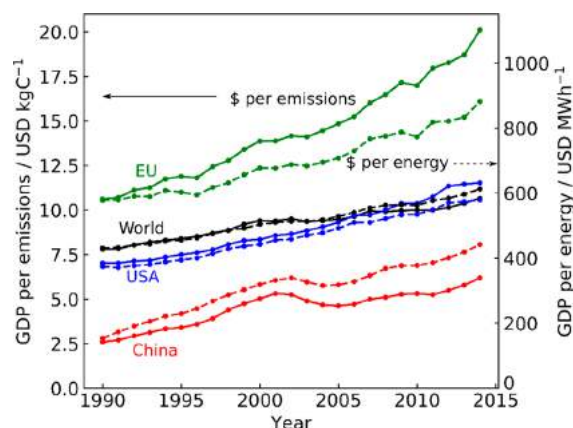


Figure 1. World GDP (purchasing power parity, 2011 dollars) is growing relative to energy consumption and CO₂ emissions. Data obtained from The World Bank.²⁷

significant challenges remain for full decarbonization.³⁰ First, renewable energy sources such as wind and solar are variable and produce electrical power, which has to be utilized immediately or stored. While a number of energy storage technologies exist, including pumped hydro, compressed air, batteries, redox flow batteries, and flywheels, they all have limitations in terms of scalability, versatility, and/or maximum storage time.^{31,32} As of yet there is no technology in use that could feasibly store enough renewable electricity to power society through a cloudy and windless day. Second, not all

energy is easily electrifiable. In transport, especially, which accounts for 14% of global CO₂ emissions²² (middle portion of Table 1), there are clear advantages to energy in the form of liquid fuel. Finally, not all CO₂ emissions are due to energy use. The bottom section of Table 1 shows a lower-bound estimation to the direct nonenergy carbon use in industry, calculated as the stoichiometric amount of carbon used or released globally in the production of several key products: cement,³³ steel,³⁴ plastic,³⁵ ammonia,³⁶ and aluminum.³⁷ Together, these products involve as much carbon as 12% of global carbon emissions. Increased recycling can help to lower this number, and decarbonization may be possible, if difficult, in some of these industries.³⁰ However, it is clear that industry would continue to have an appetite for carbon even if energy were to be fully decarbonized.

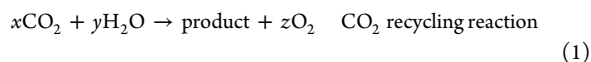
In contrast to decarbonization, carbon sequestration is a strategy that accepts some continued net production of CO₂ but aims to prevent its release to the atmosphere.^{24,40} There are at present 18 large-scale carbon capture and storage (CCS) projects in operation worldwide, separating about 40 megatonnes of CO₂ per year (9.6 MtC/yr), from industrial point sources and storing it underground.⁴¹ This is just under 0.1% of global carbon emissions, but this could in principle be scaled up indefinitely as there are suitable geological formations for the storage of hundreds of years of CO₂ at the present emissions rate.⁴² In particular, if the carbon stored underground originates from the atmosphere rather than from fossil fuels, as in the case when CO₂ resulting from the combustion of biomass is stored, the result is net-negative emissions. This strategy, bioenergy with carbon capture and

storage (BECCS), can provide electricity at the same time as net-negative emissions, and will be necessary for stabilizing the climate in all but the most optimistic projections, but is as of yet largely unused.²⁴ Unfortunately for net CO₂ emissions, most existing and planned projects for CCS fall under the category of enhanced oil recovery (EOR), whereby CO₂ is pumped underground to aid in the extraction of additional fossil fuels.⁴¹ This highlights one of the main challenges with carbon sequestration: the lack of a viable business case. CO₂ separation from a power plant, for example, costs on the order of \$60 to \$100 USD per ton CO₂ (approximately \$200 to \$350 USD/tC),⁴⁰ and together with transportation and storage costs, this results in a total increase of more than 25% in the cost of the electricity generated by a power plant utilizing CCS.⁴³ Under existing policies and economics, carbon sequestration is thus rarely economically viable without EOR, which in effect adds value to the CO₂ by using it to facilitate the extraction of additional fossil fuels. The immense potential of CCS, and in particular BECCS, for reducing net carbon emissions will only be realized once regulations make the cost of emitting CO₂ higher than the costs of separation and storage.⁴⁰

The limitations to full implementation of decarbonization and carbon sequestration outlined above all point to a common missing piece of human civilization's collective "industrial metabolism", namely, carbon recycling based on the conversion of CO₂ to more reduced products. CO₂ recycling can enable the storage of renewable electricity from intermittent sources in a dense and versatile form, provide a renewable carbon feedstock to chemical industries, and add value to CO₂ captured at industrial point sources or directly from the air.

1.1.2. Strategies for CO₂ Recycling. CO₂ is the most oxidized form of carbon, together with carbonate minerals, with a formal oxidation state of +4. As a result, conversion of CO₂ into a more energetic product involves transfer of electrons to carbon, reducing its oxidation state. The family of reactions by which CO₂ is converted to a more reduced product is most often called CO₂ reduction. These reactions are also often referred to as CO₂ hydrogenation for thermally driven processes involving reaction with hydrogen (H₂) or CO₂ fixation in natural photosynthesis and bioinspired catalysis.⁴⁴

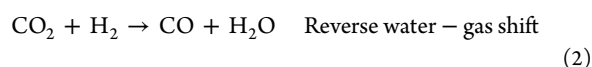
In order for the production and ultimate combustion of CO₂ reduction/hydrogenation products to represent a closed cycle, the ultimate source of electrons and protons for the reduction of CO₂ must be water (H₂O), as combustion of a hydrogenated carbon product releases H₂O. CO₂ reduction/hydrogenation/fixation thus follows the overall formula:



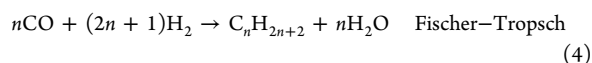
Natural photosynthesis by plants and other phototrophs fixates a much larger amount of carbon globally than human activity releases (Table 1),^{38,39} so using biomass as a carbon source is an obvious carbon recycling strategy. However, the utility of biobased carbon is limited by the amount of land required. Well-intended markets for transportation biofuels such as ethanol and biodiesel need energy-intensive care (e.g., fertilizers, pesticides, etc.) and have led to deforestation in some cases, thus greatly mitigating or even eliminating any potential CO₂ emissions savings.^{45,46} As mentioned earlier, biomass energy with carbon capture and storage (BECCS) has the potential of achieving net negative emissions; however, the

land requirement is immense. Near-term availability of biomass for BECCS in the US, for example, corresponds at most to about 370 MtCO₂/yr (0.1 GtC/yr), less than 10% of US emissions.⁴⁷ The picture is similar on a global scale.⁴⁸ High-yield biomass such as short-rotation forestry can yield up to about 800 tC/km²/yr,⁴⁹ meaning that it would require about 14 million square kilometers to offset the present global carbon emissions of 11 GtC/yr. Repurposing this amount of land, about the same area as is used globally for food crop production,²² is clearly not feasible. Thus, while important, harnessing the power of natural photosynthesis can only play a limited role in reaching net-zero emissions, leaving room for other CO₂ recycling strategies.

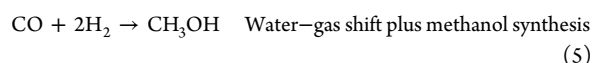
There are pathways in the traditional chemical industry, all thermally activated, that could be used for CO₂ hydrogenation, using H₂ as the reductant.^{50,51} CO₂ can be reduced to carbon monoxide (CO) by the reverse water gas shift reaction:



If an excess of H₂ is used and the water is condensed out, the product gas is a mixture of H₂ and CO, which is called synthesis gas or syngas. Syngas can be used as the precursor to methane on a Ni catalyst,⁵² to multicarbon hydrocarbons on an Fe or Co catalyst,⁵³ or to methanol on a Cu/ZnO catalyst.^{54,55} These reactions are called methanation, the Fischer–Tropsch reaction, and methanol synthesis, respectively.

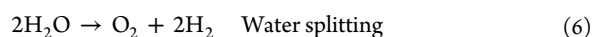


In methanol synthesis, some CO₂ is required in the syngas stream because CO₂ is actually the immediate reactant.⁵⁶ The role of CO is to react with the water released by CO₂ hydrogenation and generate more CO₂ via the water–gas shift (reverse of Reaction 2). The net reaction is

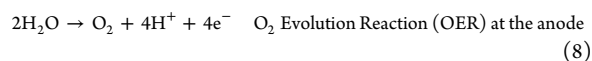
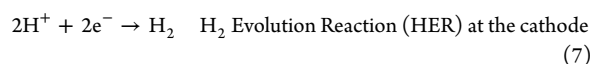


All of these processes run at high pressures and temperatures; for example, ~100 bar and 250 °C are typical conditions for methanol synthesis, the mildest of the three reactions.⁵¹

In order for CO₂ hydrogenation by the above reactions to be a renewable process, the hydrogen must come from water splitting using renewable energy:



such that the combined reaction is in the form of Reaction 1 above. The water splitting would be driven electrochemically using electrical energy from renewable sources such as wind and solar,^{30,57,58} according to the half-reactions

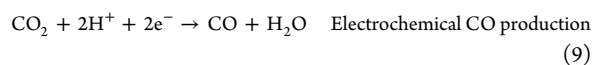


Compared to hydrogen, carbon-based fuels have the advantages of higher volumetric energy density and greater ease of integration in the present infrastructure (drop-in fuels). Furthermore, carbon-based chemicals will still be needed regardless of energy decarbonization.⁵⁹

Table 2. Electrochemical Reactions with Equilibrium Potentials

Reaction	E^0 /[V vs RHE]	(Product) Name, abbreviation
$2\text{H}_2\text{O} \rightarrow \text{O}_2 + 4\text{H}^+ + 4\text{e}^-$	1.23	Oxygen Evolution Reaction, OER
$2\text{H}^+ + 2\text{e}^- \rightarrow \text{H}_2$	0	Hydrogen Evolution Reaction, HER
$x\text{CO}_2 + n\text{H}^+ + ne^- \rightarrow \text{product} + y\text{H}_2\text{O}$		CO_2 Reduction, CO_2R
$\text{CO}_2 + 2\text{H}^+ + 2\text{e}^- \rightarrow \text{HCOOH}_{(\text{aq})}$	-0.12	Formic acid
$\text{CO}_2 + 2\text{H}^+ + 2\text{e}^- \rightarrow \text{CO}_{(\text{g})} + \text{H}_2\text{O}$	-0.10	Carbon monoxide
$\text{CO}_2 + 6\text{H}^+ + 6\text{e}^- \rightarrow \text{CH}_3\text{OH}_{(\text{aq})} + \text{H}_2\text{O}$	0.03	Methanol, MeOH
$\text{CO}_2 + 4\text{H}^+ + 4\text{e}^- \rightarrow \text{C}_{(\text{s})} + 2\text{H}_2\text{O}$	0.21	Graphite
$\text{CO}_2 + 8\text{H}^+ + 8\text{e}^- \rightarrow \text{CH}_4_{(\text{g})} + 2\text{H}_2\text{O}$	0.17	Methane
$2\text{CO}_2 + 2\text{H}^+ + 2\text{e}^- \rightarrow (\text{COOH})_{2(\text{s})}$	-0.47	Oxalic acid
$2\text{CO}_2 + 8\text{H}^+ + 8\text{e}^- \rightarrow \text{CH}_3\text{COOH}_{(\text{aq})} + 2\text{H}_2\text{O}$	0.11	Acetic acid
$2\text{CO}_2 + 10\text{H}^+ + 10\text{e}^- \rightarrow \text{CH}_3\text{CHO}_{(\text{aq})} + 3\text{H}_2\text{O}$	0.06	Acetaldehyde
$2\text{CO}_2 + 12\text{H}^+ + 12\text{e}^- \rightarrow \text{C}_2\text{H}_5\text{OH}_{(\text{aq})} + 3\text{H}_2\text{O}$	0.09	Ethanol, EtOH
$2\text{CO}_2 + 12\text{H}^+ + 12\text{e}^- \rightarrow \text{C}_2\text{H}_4_{(\text{g})} + 4\text{H}_2\text{O}$	0.08	Ethylene
$2\text{CO}_2 + 14\text{H}^+ + 14\text{e}^- \rightarrow \text{C}_2\text{H}_6_{(\text{g})} + 4\text{H}_2\text{O}$	0.14	Ethane
$3\text{CO}_2 + 16\text{H}^+ + 16\text{e}^- \rightarrow \text{C}_2\text{H}_5\text{CHO}_{(\text{aq})} + 5\text{H}_2\text{O}$	0.09	Propionaldehyde
$3\text{CO}_2 + 18\text{H}^+ + 18\text{e}^- \rightarrow \text{C}_3\text{H}_7\text{OH}_{(\text{aq})} + 5\text{H}_2\text{O}$	0.10	Propanol, PrOH
$x\text{CO} + n\text{H}^+ + ne^- \rightarrow \text{product} + y\text{H}_2\text{O}$		CO Reduction, COR
$\text{CO} + 6\text{H}^+ + 6\text{e}^- \rightarrow \text{CH}_4_{(\text{g})} + \text{H}_2\text{O}$	0.26	Methane
$2\text{CO} + 8\text{H}^+ + 8\text{e}^- \rightarrow \text{CH}_3\text{CH}_2\text{OH}_{(\text{aq})} + \text{H}_2\text{O}$	0.19	Ethanol, EtOH
$2\text{CO} + 8\text{H}^+ + 8\text{e}^- \rightarrow \text{C}_2\text{H}_4_{(\text{g})} + 2\text{H}_2\text{O}$	0.17	Ethylene

An alternative to CO production by the reverse water–gas shift (Reaction 2) is electrochemical reduction of CO_2 to CO:

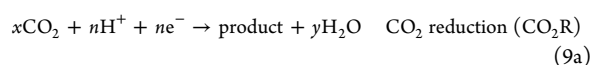


balanced by the OER (Reaction 8). The electrochemically produced CO can then be reacted further as described above to form hydrocarbons or alcohols from CO_2 . This combined approach using electroreduction of CO_2 in a high-temperature solid-oxide electrolysis cell and subsequent thermal hydrogenation proved especially promising in an analysis of CO_2 recycling strategies.⁶⁰

However, direct electrochemical reduction of CO_2 can have a number of advantages compared to hydrogenation of CO_2 or CO by electrochemically produced H_2 :^{2,61} it (1) combines the electrochemical water splitting and subsequent thermal hydrogenation into a single electrochemical process, (2) enables products that cannot easily be prepared by thermally driven processes, and (3) can often run at or near room temperature and ambient pressure. These features imply that processes based on electrochemical CO_2 reduction are more suitable to decentralization than the thermal counterparts, and that electrochemical CO_2 reduction processes can be designed to enable relatively quick adjustment of production in order to match the overproduction of electricity from intermittent renewable sources.⁶²

1.2. Electrochemical CO_2 Reduction

In electrochemical CO_2 reduction, the cathodic reaction is of the general form



Like in water splitting, the anodic reaction in electrochemical CO_2R must be the oxygen evolution reaction (OER, Reaction 8) in order to sum to the overall reaction given by

Reaction 1 above. In other words, water is the only renewable and scalable source of electrons and protons.⁶³ In this section, we first discuss the carbon dioxide reduction reaction in general, with a focus on the thermodynamics and economics of reducing CO_2 to various products. We then summarize the actual CO_2R activity and selectivity of metal electrodes, highlighting the unique ability of copper to reduce CO_2 to hydrocarbons and alcohols.

1.2.1. Desired Products: Thermodynamics and Economics. Table 2 lists the equilibrium potentials for CO_2R to commonly reported electrochemical products. All of the CO_2R standard potentials here are calculated via the Gibbs free energy of reaction using gas-phase thermochemistry data and, for aqueous products, Henry's Law data, from NIST.⁶⁴ CO_2 is always considered a gas, water a liquid, and the state of the product is gas or aqueous as indicated. Regardless of which CO_2R product is formed at the cathode, the fact that the CO_2R reaction together with OER (Reaction 8) must add to an overall reaction of the form of Reaction 1 means that the stoichiometric coefficients for electrons and protons in a sustained CO_2 reduction reaction must be equal. Acidic products are therefore considered in the fully protonated form. Similar tables and lists provided in previous CO_2R reviews,^{1,2,15,16,44} studies of CO_2R electrocatalysis,⁶⁵ and process/economic analyses for electrochemical CO_2 conversion^{66–69} all show some variation due to the use of different potential scales, deprotonated products, and/or different standard states (for instance liquid instead of aqueous).

As described in detail in subsequent sections of this Review, CO is an important intermediate in CO_2R to hydrocarbons, aldehydes, and alcohols on Cu, and a promising approach to CO_2R is a stepwise one via CO, in which CO reduction (COR) is an important reaction in its own right.⁷⁰ The equilibrium potentials for CO reduction to a few products are therefore also included in this table, and an equation relating

CO reduction equilibrium potential to CO₂ reduction equilibrium potential is given in section 1 of the [Supporting Information \(SI\)](#).

We recommend reporting and using potentials on the thermodynamically relevant and pH-independent RHE scale for all calculations of overpotential and energetic efficiency. For more discussion of thermodynamics and equilibrium potentials, please see section 1 of the [SI](#).

While the equilibrium potentials of CO₂ reduction to hydrocarbons, aldehydes, and alcohols are slightly positive of RHE, their direct electrochemical production still requires significant energy input, as the minimum possible potential to drive the overall reaction (i.e., the difference between the CO₂R equilibrium potential and the equilibrium potential of OER) is larger than 1 V. Furthermore, both the OER and CO₂R currently require large overpotentials, meaning that a CO₂R device will run at a larger cell potential than this thermodynamic potential. Nonetheless, the thermodynamic cell potential indicates the minimum energy requirement for a given product, and thus, given a cost of energy, provides a means to estimate the economic viability of a product. More thorough techno-economic analyses have also been performed, which include capital and operational costs as well as assumptions about the overpotential and Faradaic efficiency of the desired CO₂ reduction reaction.^{66,68,69,71}

[Figure 2](#) shows a simple mapping of the economics and energetics of possible CO₂ reduction products. The approx-

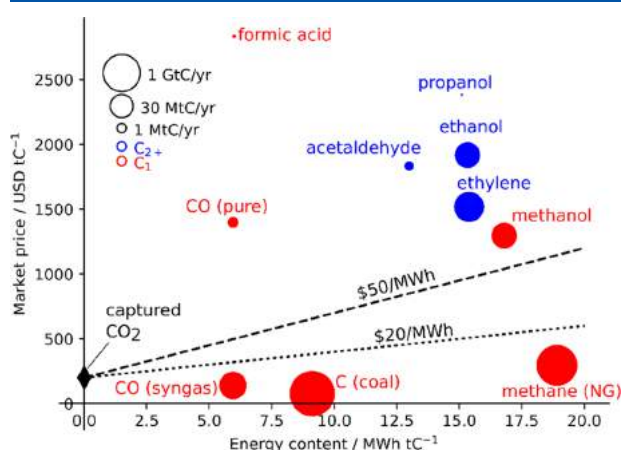


Figure 2. Market price of select CO₂ recycling products as a function of energy content. Lines represent minimum energy and CO₂ costs. Capital costs are not considered.

imate market price of selected possible CO₂ reduction products are plotted against the minimum energy needed for their production by CO₂R balanced with OER. The marker size indicates the (logarithmic) size of the global market, which spans more than 4 orders of magnitude. All economic quantities are normalized to the mass of carbon. The dashed and dotted lines indicate the minimum cost of production given a captured CO₂ price of \$200/tC and an electricity price of \$50/MWh or \$20/MWh, respectively. \$200/tC is a representative price for carbon captured from a power plant.⁴⁰ \$50/MWh is representative of recent solar installations.²⁹ Current record lows for solar installation are around \$20/MWh, which will likely become more common in the future. Products above the line for a given CO₂ capture cost and electricity cost may be economically feasible depending on

capital and other costs, which are not considered here, but are in other analyses. Products below the line are not economically feasible. Direct air capture is estimated to cost \$2000/tC with current technologies,⁴⁰ which would push the lines up above nearly all products, though this will likely come down in the future. Taxes on carbon emissions push the effective price of captured CO₂ down, since capturing CO₂ avoids the tax. The raw data, sources, and calculations are given in section 2 of the [SI](#). For a more full picture, we refer the reader to techno-economic analyses of CO₂ reduction in the literature.^{66,68,69,71}

Despite its simplicity, [Figure 2](#) captures a widely shared conclusion:^{28,40,68,69,72,73} CO₂ reduction to specialty chemicals such as formic acid (0.2 MtC/yr⁷⁴) and propanol (0.1 MtC/yr⁶⁹) give a better chance of near-term economic feasibility, whereas making an impact on the GtC/year scale relevant for global climate change will likely require renewable production of fuels competitive with the likes of coal (4 GtC/yr²²) and natural gas (1.4 GtC/yr⁷⁵). This is not feasible in the near term, as coal and natural gas are cheaper than the minimum energy required to synthesize them from CO₂ even at \$20/MWh.

Ethylene (120 MtC/yr⁷⁶) and ethanol (40 MtC/yr⁶⁹) represent promising compromises between profitable niche market and impactful mass market for CO₂ reduction. Ethylene is produced on a large scale as a precursor for plastics and ethylene glycol in a highly energy-demanding and unselective process involving repeated cycles of steam cracking at 750–950 °C followed by quenching, distillation, and recompression.^{77,78} At an electricity price of \$50 USD/MWh, it is worth about twice as much as the minimum energy input, with a global market about 100 times larger than the specialty chemicals. Ethanol is a fuel with high volumetric energy density that can be substituted for fossil fuels in the transport industry with minimal modifications, and thus represents a market with high growth potential.⁷⁹ Ethanol is produced primarily as a biofuel today, and is sold for a price much higher than the minimum energy required for its production by CO₂R at \$50/MWh. Ethylene and ethanol are both major products in CO₂ and CO electroreduction on copper, as described below.

1.2.2. Copper as a Unique Electrocatalyst. Studies of electrochemical CO₂ reduction date back to at least the 1950s.⁸⁰ The first study to quantify both gaseous and liquid products, and thus account for 100% of Faradaic efficiency, was reported by Yoshio Hori and co-workers in 1985.⁸¹ In this study, constant-current electrolysis of CO₂-saturated 0.5 M KHCO₃ at 5 mA cm⁻² (geometric) was performed for up to an hour as a batch experiment on a number of polycrystalline metal electrodes. This and subsequent studies utilizing basically the same methods^{82–85} led to a classification of metal electrodes into four groups:¹ Pb, Hg, Tl, In, Sn, Cd, and Bi produce primarily formate (HCOO⁻); Au, Ag, Zn, Pd, and Ga produce primarily carbon monoxide (CO); Ni, Fe, Pt, and Ti reduce very little CO₂ and instead almost exclusively reduce water to H₂; and Cu stands out in uniquely producing a number of hydrocarbons, aldehydes, and alcohols. Cu is thus the only pure metal that reduces CO₂ to products requiring more than two electrons transfers (collectively referred to as “further reduced products” or “>2e⁻ products”) with substantial Faradaic efficiencies. These results are summarized in [Table 3](#), adapted from Hori’s 2008 review of CO₂ reduction on metal electrodes.¹

Table 3. Faradaic Efficiencies of CO₂ Reduction Products on Metal Electrodes in CO₂-Saturated 0.1 M KHCO₃ (pH = 6.8)^a

Metal	<i>E</i> [V vs RHE]	<i>J</i> _{total} [mA/cm ² geo]	CH ₄ [%]	C ₂ H ₄ [%]	EtOH [%]	PrOH [%]	CO [%]	HCOO ⁻ [%]	H ₂ [%]	Total [%]
Pb	-1.24	-5.0	0	0	0	0	0	97.4	5.0	102.4
Hg	-1.12	-0.5	0	0	0	0	0	99.5	0	99.5
Tl	-1.21	-5.0	0	0	0	0	0	95.1	6.2	101.3
In	-1.16	-5.0	0	0	0	0	2.1	94.9	3.3	100.3
Sn	-1.09	-5.0	0	0	0	0	7.1	88.4	4.6	100.1
Cd	-1.24	-5.0	1.3	0	0	0	13.9	78.4	9.4	103.0
Au	-0.65	-5.0	0	0	0	0	87.1	0.7	10.2	98.0
Ag	-0.98	-5.0	0	0	0	0	81.5	0.6	12.4	94.6
Zn	-1.15	-5.0	0	0	0	0	79.4	6.1	9.9	95.4
Pd	-0.81	-5.0	2.9	0	0	0	28.3	2.8	26.2	60.2
Ga	-0.85	-5.0	0	0	0	0	23.2	0	79.0	102.0
Cu	-1.05	-5.0	33.3	25.5	5.7	3.0	1.3	9.4	20.5	103.5
Ni	-1.09	-5.0	1.8	0.1	0	0	0	1.4	88.9	92.4
Fe	-0.52	-5.0	0	0	0	0	0	0	94.8	94.8
Pt	-0.68	-5.0	0	0	0	0	0	0.1	95.7	95.8
Ti	-1.21	-5.0	0	0	0	0	tr.	0	99.7	99.7

^aThe potential has been converted from the reported SHE potential to the RHE scale [*T*=18.5 °C, pH=6.8] by adding $(RT/F)\ln(10)\text{pH} = 0.39$ V. Adapted with permission from Hori.¹ Copyright 2008, Springer Science Business Media, LLC.

Note that in all cases, a significant overpotential is required to reach the specified current density, usually -5 mA/cm². The largest overpotentials are required by the formate-producing metals, which also typically show very high CO₂R Faradaic efficiencies (for example, 97% of -5 mA/cm² for Pb at -1.23 V vs RHE, an overpotential of 1.1 V) due to very low HER activity. The smallest overpotential for CO₂R is achieved by Au, which produces CO with high Faradaic efficiency, 87% of -5 mA/cm² at -0.7 V vs RHE, an overpotential of 0.6 V. Copper uniquely produces a variety of hydrocarbon and oxygenated products at an intermediate potential -1.04 V vs RHE (e.g., an overpotential of 0.9 V for CO₂R to CO and an overpotential of 1.2 V for CO₂R to methane). Note also that these results, by measuring CO₂ reduction selectivity for each electrode at only one current density, effectively provide only a snapshot, as CO₂ reduction selectivity can change with conditions and electrode potential.

The splitting of the metals into these four groups based on their selectivity has been explained as the result of their binding energy to key CO₂R and HER intermediates, including *H, *OCHO (bound to the surface through O), *COOH (bound to the surface through C), and *CO.⁸⁶ The unique ability of Cu to reduce CO₂ to >2e⁻ products may be due to the fact that it is the only metal that has a negative adsorption energy for *CO but a positive adsorption energy for *H, as shown in Figure 3.

After the previously mentioned constant-current electrolysis experiments to compare different metal electrodes, Hori and co-workers also performed constant-potential electrolysis experiments on Cu in CO₂-saturated 0.1 M KHCO₃ (pH = 6.8), the most common electrolyte for CO₂ reduction studies, to characterize the CO₂R product distribution as a function of potential.⁸⁵ The results, shown in Figure 4 (hollow markers) span a potential range of -0.8 to -1.45 V vs NHE, or approximately -0.4 to -1.05 V vs RHE. In order of least cathodic to most cathodic onset potential (which loosely refers to the potential closest to the equilibrium potential at which a product is produced in detectable quantities), the major CO₂ reduction products are CO, HCOO⁻, C₂H₄, and CH₄. CO and HCOO⁻ pass through potentials of maximum Faradaic efficiency, and the Faradaic efficiency toward C₂H₄ reaches a

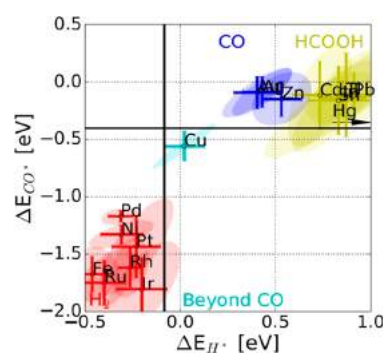


Figure 3. CO₂ reduction metal classification. Reproduced with permission from Bagger et al.⁸⁶ Copyright 2017, John Wiley and Sons.

plateau by about -1.0 V vs RHE. Similar conclusions were reached years later by Kuhl et al.;⁶⁵ electrolysis experiments were performed at potentials between -0.6 and -1.2 V vs RHE and, using more sensitive product detection techniques for liquid products, a total of 16 products were observed. These results are coplotted with Hori's in Figure 4 (filled markers).

The ability to reduce CO₂ to valuable hydrocarbons, aldehydes, and alcohols is of great interest; as a result, there has been much work done in the field to better understand the reactivity of Cu and how it can be tuned to achieve greater selectivity, stability, and efficiency. Thus, the remainder of this work will focus exclusively on Cu and Cu-based electrocatalysts. In the sections that follow, we will discuss experimental probes used to identify CO₂R reaction mechanisms on Cu and the complementary theoretical methods and descriptions of CO₂R. We will then discuss two materials classes that have been studied in attempts to alter the reactivity of planar polycrystalline Cu (nanostructured Cu and bimetallics with Cu). Finally, we will provide some overall perspectives and an outlook for the future of CO₂R.

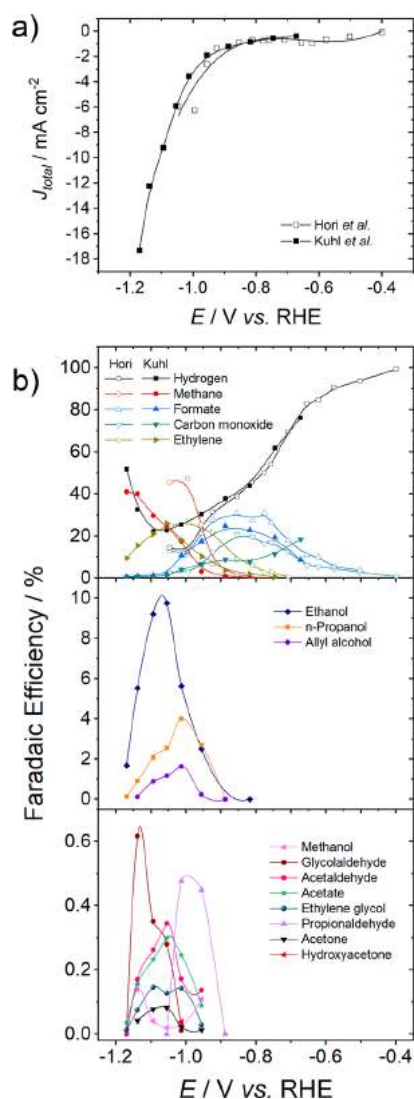


Figure 4. CO₂R activity and selectivity on polycrystalline copper in CO₂-saturated 0.1 M KHCO₃ (pH = 6.8): (a) total current density and (b) product Faradaic efficiencies; data obtained from Hori et al.⁸⁵ (hollow) and Kuhl et al.⁶⁵ (filled).

2. CONSIDERATIONS FOR CONDUCTING AND COMPARING ELECTROCHEMICAL CO₂ REDUCTION EXPERIMENTS

Before diving into the results in subsequent sections, we would like to set the stage by discussing some of the difficulties encountered when trying to reliably compare the electrocatalytic behavior of Cu between different electrochemical cells and conditions. For more detailed discussions of these challenges in an objective evaluation of CO₂R performance, we direct the reader to recent perspective articles, which also provide recommendations to help standardize methods for measuring and reporting CO₂R data.^{87,88}

2.1. Reporting Data

First, we would briefly like to discuss the metrics by which electrocatalytic activity and selectivity are reported. The selectivity is most often described in terms of *Faradaic efficiency*, which is the portion of the electrical current going to a specific product in steady-state electrolysis. The activity for

CO₂R to a specific product is described in terms of the *overpotential*, which is the absolute difference between the actual potential needed to make a product and the thermodynamic potential, or in terms of the *partial current density* at a given potential, which is the total current times the Faradaic efficiency. A more active catalyst is one that achieves a given partial current density at a lower overpotential, and/or provides a larger partial current density at a given overpotential. A major goal of applied electrocatalysis research is the development of electrode materials and conditions that are selective and active (as well as cheap and stable) for production of desired products. However, understanding the fundamentals of electrocatalysis on simple materials and model systems facilitates the design of better electrodes,⁵⁷ and the trade-off between practical application and fundamental insight is important to keep in mind when comparing different works in the field.

An essential consideration is how the measured activity is normalized. The geometric area of the electrode is most commonly used to report the current density. While useful for assessing the overall electrode performance, this metric is inherently dependent on the catalyst loading or surface area. Thus, it is also important to consider the current normalized by the electrochemically active surface area (ECSA) of the electrode. This facilitates activity comparisons between catalysts with different roughness factors (RF, defined here as the ratio of ECSA/geometric electrode area), allowing one to determine if higher catalytic activity results from a higher average turnover frequency or simply from an increased number of active sites. There exist a variety of methods in electrocatalysis for determining the ECSA based on capacitance, underpotential deposition (UPD), CO stripping, and redox features that can be employed depending on the surface chemistry and morphology, and the best method varies based on the material studied. So far, only capacitance has found wide use for estimating the ECSA of nanostructured polycrystalline copper electrodes.^{89–95} We emphasize that on any nonplanar surface, the measurement of the ECSA is at best an approximation; consequently, we recommend that researchers take the limitations of each method of determining the ECSA into account when analyzing their data. Furthermore, we would also like to highlight the need for all future work, particularly on nanostructured electrodes, to report the ECSA whenever possible. It is only possible to evaluate whether a novel catalyst represents an improvement in intrinsic activity compared to state-of-the-art materials if the ECSA-normalized activity can be compared with the literature. As will be shown in subsection 6.2.4 and section 7.4, much of the suggested activity improvements in the field can be attributed to increased surface area.

2.2. Intrinsic Kinetics vs Mass Transport Effects

As a consequence of the HER and CO₂R, which deplete protons or (equivalently) produce hydroxide ions, a pH gradient can develop at the electrode surface. This high local pH has several competing effects on these reactions due to a complicated interplay between mass transport, buffer equilibria, and pH, which will be discussed in more detail in subsection 3.3.1. Notably, in the CO₂/bicarbonate system, CO₂ is both a reactant and a buffer, which means that changes in pH near the cathode surface can cause the concentration of dissolved CO₂ to deviate from the concentration in the bulk electrolyte. For planar polycrystalline Cu, it was found that the

Stephanie A. Nitopi, Erlend Bertheussen, Soren Bertelsen Scott, Xinyan Liu, Albert K. Engstfeld, Sebastian Horch, Brian Seger, Ifan Stephens, Karen Chan, Christopher Hahn, Jens K. Nrskov, Thomas Jaramillo, and Ib Chorkendorff. Progress and Perspectives of Electrochemical CO₂ Reduction on Copper in Aqueous Electrolyte. *Chemical Reviews*. XXXX, XXX, XXX-XXX, 2019

Pages I-AX and BC - BK of this publication are not included in this thesis

covalent organic frameworks (COFs), materials with three-dimensional active sites that can induce confinement effects, and functionalized surfaces (tethering promoters/ligands to the electrode surface).^{57,202,373,429} Materials discovery efforts should continue in these directions to identify novel catalyst materials with enhanced properties. Finally, CO reduction has been increasingly studied in recent years, both as a proxy to better understand CO₂ reduction mechanisms, as well as for fundamental understanding of this important reaction in its own right. If viable COR catalysts are developed, this could enable tandem or cascaded reaction systems in which CO₂R is split into two separate steps: (1) CO₂ reduction to CO, then (2) CO reduction to the desired product(s). Unique synergies could also be achieved by coupling CO₂ electroreduction with alternate types of catalytic processes (biological, thermal, etc.).

In summary, while many challenges and opportunities remain in developing catalysts and reactor systems with high activity, selectivity, stability, and scalability, much progress has also been attained in recent years, priming this technology for commercial application. With continued research and development, electrochemical CO₂ reduction could have a substantial impact on the sustainability of our global energy economy.

ASSOCIATED CONTENT

Supporting Information

The Supporting Information is available free of charge on the ACS Publications website at DOI: 10.1021/acs.chemrev.8b00705.

Thermochemistry: Raw Data and Calculations; Economics: Raw Data and Calculations; Computational Studies: Energetics and Kinetics of Elementary Steps; Tabulated Data for Activity Comparison Plots.(PDF)

AUTHOR INFORMATION

Corresponding Authors

*E-mail: ibchork@fysik.dtu.dk.

*E-mail: jaramillo@stanford.edu.

*E-mail: jkno@dtu.dk.

ORCID

Erlend Bertheussen: 0000-0002-6482-8937

Ifan E. L. Stephens: 0000-0003-2157-492X

Karen Chan: 0000-0002-6897-1108

Christopher Hahn: 0000-0002-2772-6341

Thomas F. Jaramillo: 0000-0001-9900-0622

Ib Chorkendorff: 0000-0003-2738-0325

Author Contributions

[#]Stephanie Nitopi and Erlend Bertheussen contributed equally to this work.

Notes

The authors declare no competing financial interest.

Biographies

Stephanie Nitopi is currently a Ph.D. candidate in the Chemical Engineering department at Stanford University, and a member of Professor Tom Jaramillo's group and the SUNCAT Center for Interface Science and Catalysis. She was a recipient of a Stanford Graduate Fellowship in Science & Engineering, and her research has focused on the electrochemical conversion of carbon dioxide to fuels and chemicals on copper catalysts. Prior to Stanford, Stephanie was in

the Schreyer Honors College at The Pennsylvania State University where she received her B.S. in Chemical Engineering in 2014.

Erlend Bertheussen received his Bachelor's degree in Nanotechnology from the University of Bergen in 2012. He then moved to Denmark to do a Master's in Physics and Nanotechnology at the Technical University of Denmark (DTU), where his interest for electrochemical energy conversion started. He subsequently started a Ph.D. degree in Physics at DTU, where he performed work within the field of CO reduction on copper electrodes. After graduating in the spring of 2018, he took a position as an R&D Engineer in the start-up company RenCat ApS.

Soren B. Scott received a Bachelor's in Chemistry from the University of Copenhagen in 2013 before being introduced to the idea of CO₂ electroreduction while working as a research assistant at the Joint Center for Artificial Photosynthesis at Lawrence Berkeley National Lab. He returned to Denmark for a Master's in Chemical Engineering at the Technical University of Denmark (DTU, 2016) and has since then been a Ph.D. student at DTU's Department of Physics. In 2018, Soren was awarded an EliteForsk travel grant from the Danish Ministry of Higher Education and Science. His current research uses in situ mass spectrometry to probe electrocatalytic interfaces.

Xinyan Liu received her B.S. in chemical engineering from Tsinghua University (Beijing, China) in 2013. She then obtained her Ph.D. in chemical engineering from Stanford University in 2018 under the supervision of Prof. Jens K. Nørskov, during which she has worked on density functional theory based microkinetic modeling of Fischer–Tropsch synthesis, electrochemical hydrogen evolution reaction, and electrochemical carbon monoxide/dioxide reduction reactions. Her expertise is in microkinetic modeling and data mining.

Albert K. Engstfeld (1983, Germany) graduated from the Ulm University in 2009 in chemistry with specialization in physical chemistry and surface science. He received his Ph.D. in 2015 from Ulm University on "Design and electrochemical/–catalytic properties of well-defined bimetallic model catalyst electrodes," research conducted under the supervision of Prof. R.J. Behm. After a postdoc position at the Institute for Surface Physics & Catalysis (Technical University of Denmark), he returned in 2017 to Ulm University. He is currently working as a group leader (Nanostructured Metal Surfaces) at the Institute of Surface Chemistry and Catalysis. By combining an ultrahigh vacuum system with electrochemical methods, he is focused on a fundamental understanding of restructuring/corrosion processes and electrocatalytic properties of nanostructured (bi)metallic single crystal model electrodes on an atomic scale level.

Sebastian Horch received his Ph.D. degree in Physics (1994) from Bonn University, Germany. He was Feodor Lynen Research Fellow at Arizona State University in 1995. Until 1999, he was Assistant Research Professor in the Center for Atomic-scale Materials Physics (CAMP) at Aarhus University, Denmark. Since 1999, he is Associate Professor at the Department of Physics, Denmark's Technical University (DTU). His main area of research is Surface Science using high resolution scanning probe microscopy.

Brian Seger completed his Ph.D. in chemical engineering from Notre Dame under Prof. Prashant Kamat in 2009. After completing postdocs at the University of Queensland under Lian Zhou Wang and at DTU under Prof. Ib Chorkendorff, he became an assistant professor in the Surface Science and Catalysis section of DTU Physics in 2014 and then promoted to associated professor in 2017. He has published 45 peer reviewed papers that have been cited over 5,000 times. His research focuses on electrochemical CO₂ reduction, photoelectrochemistry, semiconductor-electrolyte interfaces, and electro-synthesis reactions.

Ifan E. L. Stephens was appointed as Senior Lecturer at the Department of Materials at Imperial College London in July 2017. Prior to Imperial, he was at the Department of Physics at the Technical University of Denmark (DTU); he was first employed as a postdoctoral researcher, then as assistant professor and finally as associate professor and leader of the Electrocatalysis Group there. In 2015, the Department of Mechanical Engineering at Massachusetts Institute of Technology (MIT) awarded Ifan the Peabody Visiting Associate Professorship. His team conducts model electrocatalysis experiments to enable the large-scale conversion of renewable energy to fuels and chemicals and vice versa. Ifan has authored or coauthored more than 60 papers in peer reviewed journals. He is coinventor on one patent and five patent applications. He is cofounder of the spinoff company, HPNow.

Karen Chan is an Associate Professor at the Department of Physics, Technical University of Denmark. Prior to this she was Associate Staff Scientist at SLAC National Accelerator Laboratory as part of the Joint Center for Artificial Photosynthesis. Her expertise is in the atomistic and continuum level modeling of electrochemical interfaces with applications in sustainable energy conversion. She obtained her Ph.D. in 2013, advised by Michael Eikerling and held a postdoc fellowship from 2013–2016 at Stanford University, advised by Jens K. Nørskov.

Christopher Hahn completed his doctorate at the University of California Berkeley in 2012, where he studied bandgap engineering of 1-dimensional nitride and oxynitride materials for solar water splitting. After receiving his Ph.D., he conducted his postdoctoral research on catalyst discovery for electrochemical CO₂ reduction at Stanford University within the SUNCAT Center for Interface Science and Catalysis. He began his current position at SLAC National Accelerator Laboratory in 2015, where he is conducting research with the Joint Center for Artificial Photosynthesis on catalyst discovery and understanding reaction mechanisms for electrochemical CO₂ reduction.

Jens K. Nørskov is the Villum Kann Rasmussen professor at the Technical University of Denmark. His research aims at developing theoretical methods and concepts to understand and predict properties of materials. He is particularly interested in surface chemical properties, heterogeneous catalysis, electro-catalysis, and applications in energy conversion.

Thomas Francisco Jaramillo is an Associate Professor of Chemical Engineering at Stanford University and of Photon Sciences at SLAC National Accelerator Laboratory, where he is the Director of the SUNCAT Center for Interface Science and Catalysis. A native of Puerto Rico, Prof. Jaramillo earned his B.S. in Chemical Engineering at Stanford University, followed by M.S. and Ph.D. in Chemical Engineering at the University of California at Santa Barbara (UCSB). Prof. Jaramillo conducted postdoctoral research in the Department of Physics at the Technical University of Denmark (DTU) as a Hans Christian Ørsted Postdoctoral Fellow. Prof. Jaramillo's research efforts are aimed at developing catalysts and processes that can accelerate important chemical transformations related to energy conversion with improved sustainability, efficiency, and durability. Prof. Jaramillo has earned a number of honors and awards for his efforts, including the Resonate Award from the Resnick Institute (2014), the Presidential Early Career Award for Scientists & Engineers (PECASE, 2011), the U.S. Dept. of Energy Hydrogen and Fuel Cell Program Research & Development Award (2011), the National Science Foundation (NSF) CAREER Award (2011), and the Mohr-Davidow Ventures (MDV) Innovator Award (2009).

Ib Chorkendorff is Professor in Heterogeneous Catalysis at DTU Physics. He earned his Ph.D. in 1985 at Odense University Denmark,

and after a postdoc at University of Pittsburgh, USA, he was employed in 1987 at DTU as Associate Professor for starting up the field of experimental surface science and catalysis. From 2005 to 2016 he was director of the Danish National Research Foundation Center for Individual Nanoparticle Functionality (CINF) and from 2016 he has been director of The Villum Center for the Science of Sustainable Fuels and Chemicals (V-SUSTAIN). Ib Chorkendorff's research activities focus on finding new catalysts for improving energy production/conversion and for environmental protection. He has authored or coauthored more than 330 scientific papers, 18 patents, and one textbook "Concepts of Modern Catalysis and Kinetics". He is cofounder of three start-up companies RENCAT APS, HPNOW APS and Spectroinlets APS. Ib Chorkendorff has received numerous prizes and honors among others the Ulrik and Marie Brinch award and the Ingeborg and Leo Dannin's Prize for Natural Science Research. He is elected Fellow of The Academy for Technical Sciences (ATV) and Elected member of the Royal Danish Academy of Sciences and Letters.

ACKNOWLEDGMENTS

The material from Stanford/SLAC researchers is based upon work performed by the Joint Center for Artificial Photosynthesis, a DOE Energy Innovation Hub, supported through the Office of Science of the U.S. Department of Energy under Award No. DE-SC0004993. The work by researchers at the Technical University of Denmark was supported by a research grant (9455) from VILLUM FONDEN. B.S. also acknowledges a grant from Innovation Fund Denmark (8057-00018B ECOEthylene). This project has received funding from the European Research Council (ERC) under the European Union's Horizon 2020 research and innovation programme (Grant Agreement No. 741860).

REFERENCES

- (1) Hori, Y. Electrochemical CO₂ Reduction on Metal Electrodes. In *Modern Aspects of Electrochemistry*, Vayenas, C. G.; White, R. E.; Gamboa-Aldeco, M. E., Eds.; Springer, 2008; Vol. 42, pp 89–189.
- (2) Gattrell, M.; Gupta, N.; Co, A. A Review of the Aqueous Electrochemical Reduction of CO₂ to Hydrocarbons at Copper. *J. Electroanal. Chem.* **2006**, *594*, 1–19.
- (3) Vasileff, A.; Xu, C.; Jiao, Y.; Zheng, Y.; Qiao, S.-Z. Surface and Interface Engineering in Copper-Based Bimetallic Materials for Selective CO₂ Electroreduction. *Chem.* **2018**, *4*, 1809–1831.
- (4) Gamler, J. T. L.; Ashberry, H. M.; Skrabalak, S. E.; Koczkur, K. M. Random Alloyed versus Intermetallic Nanoparticles: A Comparison of Electrocatalytic Performance. *Adv. Mater.* **2018**, *30*, 1801563.
- (5) Birhanu, M. K.; Tsai, M.-C.; Kahsay, A. W.; Chen, C.-T.; Zeleke, T. S.; Ibrahim, K. B.; Huang, C.-J.; Su, W.-N.; Hwang, B.-J. Copper and Copper-Based Bimetallic Catalysts for Carbon Dioxide Electroreduction. *Adv. Mater. Interfaces* **2018**, *5*, 1800919.
- (6) Xie, H.; Wang, T.; Liang, J.; Li, Q.; Sun, S. Cu-Based Nanocatalysts for Electrochemical Reduction of CO₂. *Nano Today* **2018**, *21*, 41–54.
- (7) Gu, Z.; Shen, H.; Shang, L.; Lv, X.; Qian, L.; Zheng, G. Nanostructured Copper-Based Electrocatalysts for CO₂ Reduction. *Small Methods* **2018**, *2*, 1800121.
- (8) Rendón-Calle, A.; Buijes, S.; Calle-Vallejo, F. A Brief Review of the Computational Modeling of CO₂ Electroreduction on Cu Electrodes. *Curr. Opin. Electrochem.* **2018**, *9*, 158–165.
- (9) Raciti, D.; Wang, C. Recent Advances in CO₂ Reduction Electrocatalysis on Copper. *ACS Energy Lett.* **2018**, *3*, 1545–1556.
- (10) Handoko, A. D.; Wei, F.; Jenndy, Yeo, B. S.; Seh, Z. W. Understanding Heterogeneous Electrocatalytic Carbon Dioxide Reduction through Operando Techniques. *Nat. Catal.* **2018**, *1*, 922–934.

- (11) Lee, C. W.; Yang, K. D.; Nam, D.-H.; Jang, J. H.; Cho, N. H.; Im, S. W.; Nam, K. T. Defining a Materials Database for the Design of Copper Binary Alloy Catalysts for Electrochemical CO₂ Conversion. *Adv. Mater.* **2018**, *30*, 1704717.
- (12) Arán-Ais, R. M.; Gao, D.; Roldan Cuenya, B. Structure- and Electrolyte-Sensitivity in CO₂ Electroreduction. *Acc. Chem. Res.* **2018**, *51*, 2906–2917.
- (13) Jhong, H. R. M.; Ma, S.; Kenis, P. J. A. Electrochemical Conversion of CO₂ to Useful Chemicals: Current Status, Remaining Challenges, and Future Opportunities. *Curr. Opin. Chem. Eng.* **2013**, *2*, 191–199.
- (14) Xu, S.; Carter, E. A. Theoretical Insights into Heterogeneous (Photo)Electrochemical CO₂ Reduction. *Chem. Rev.* **2018**, DOI: 10.1021/acs.chemrev.8b00481.
- (15) Qiao, J.; Liu, Y.; Hong, F.; Zhang, J. A Review of Catalysts for the Electroreduction of Carbon Dioxide to Produce Low-Carbon Fuels. *Chem. Soc. Rev.* **2014**, *43*, 631–675.
- (16) Kortlever, R.; Shen, J.; Schouten, K. J. P.; Calle-Vallejo, F.; Koper, M. T. M. Catalysts and Reaction Pathways for the Electrochemical Reduction of Carbon Dioxide. *J. Phys. Chem. Lett.* **2015**, *6*, 4073–4082.
- (17) Zhu, D. D.; Liu, J. L.; Qiao, S. Z. Recent Advances in Inorganic Heterogeneous Electrocatalysts for Reduction of Carbon Dioxide. *Adv. Mater.* **2016**, *28*, 3423–3452.
- (18) Zhang, B.; Zhang, J. Rational Design of Cu-Based Electrocatalysts for Electrochemical Reduction of Carbon Dioxide. *J. Energy Chem.* **2017**, *26*, 1050–1066.
- (19) Vickers, J. W.; Alfonso, D.; Kauffman, D. R. Electrochemical Carbon Dioxide Reduction at Nanostructured Gold, Copper, and Alloy Materials. *Energy Technol.* **2017**, *5*, 775–795.
- (20) Pander, J. E.; Ren, D.; Huang, Y.; Loo, N. W. X.; Hong, S. H. L.; Yeo, B. S. Understanding the Heterogeneous Electrocatalytic Reduction of Carbon Dioxide on Oxide-Derived Catalysts. *Chem-ElectroChem* **2018**, *5*, 219–237.
- (21) He, J.; Johnson, N. J. J.; Huang, A.; Berlinguette, C. P. Electrocatalytic Alloys for CO₂ Reduction. *ChemSusChem* **2018**, *11*, 48–57.
- (22) Intergovernmental Panel on Climate Change. *Climate Change 2014: Synthesis Report*; 2014.
- (23) Conference of the Parties to the United Nations Framework Convention on Climate Change. *Adoption of the Paris Agreement*; 2015; pp 1–32.
- (24) Intergovernmental Panel on Climate Change. *IPCC Special Report on the Impacts of Global Warming of 1.5 °C - Summary for Policy Makers*; Incheon, 2018.
- (25) International Energy Agency. *IEA2017.Pdf*; IEA Newsroom; 2017.
- (26) Obama, B. The Irreversible Momentum of Clean Energy. *Science* **2017**, *355*, 126–129.
- (27) World Bank Group: IEA Statistics. GDP per unit of energy use <https://data.worldbank.org/indicator/EG.GDP.PUSE.KO.PP?contextual=default&locations=US-CN-EU-IW>.
- (28) Chu, S.; Cui, Y.; Liu, N. The Path towards Sustainable Energy. *Nat. Mater.* **2017**, *16*, 16–22.
- (29) Randall, T. *Wind and Solar Are Crushing Fossil Fuels*; Bloomberg, 2016.
- (30) Davis, S. J.; Lewis, N. S.; Shaner, M.; Aggarwal, S.; Arent, D.; Azevedo, I. L.; Benson, S. M.; Bradley, T.; Brouwer, J.; Chiang, Y.-M.; et al. Net-Zero Emissions Energy Systems. *Science* **2018**, *360*, No. eaas9793.
- (31) Yang, Z.; Zhang, J.; Kintner-Meyer, M. C. W.; Lu, X.; Choi, D.; Lemmon, J. P.; Liu, J. Electrochemical Energy Storage for Green Grid. *Chem. Rev.* **2011**, *111*, 3577–3613.
- (32) Gyuk, I.; Johnson, M.; Vetrano, J.; Lynn, K.; Parks, W.; Handa, R.; Kannberg, L. D.; Hearne, S.; Waldrip, K.; Braccio, R. *Grid Energy Storage*; 2013.
- (33) van Oss, H. G. *Cement in January 2018*.
- (34) World Steel Association. *World Steel Figures 2018*; Brussels and Beijing, 2018.
- (35) Geyer, R.; Jambeck, J. R.; Law, K. L. Production, Use, and Fate of All Plastics Ever Made. *Sci. Adv.* **2017**, *3*, 19–24.
- (36) Apodaca, L. E. *Mineral Commodity Summaries - Ammonia*; 2016; Vol. 32.
- (37) Bray, E. L. *Mineral Commodity Summaries - Aluminum*; 2017; Vol. 1.
- (38) Houghton, R. A. Balancing the Global Carbon Budget. *Annu. Rev. Earth Planet. Sci.* **2007**, *35*, 313–347.
- (39) Le Quére, C.; Moriarty, R.; Andrew, R. M.; Canadell, J. G.; Sitch, S.; Korsbakken, J. I.; Friedlingstein, P.; Peters, G. P.; Andres, R. J.; Boden, T. A.; et al. Global Carbon Budget 2015. *Earth Syst. Sci. Data* **2015**, *7*, 349–396.
- (40) Majumdar, A.; Deutch, J.; Bras, R.; Benson, S.; Carter, E.; Ort, D.; Ramage, M.; Socolow, R.; Toone, E.; Whitesides, G.; et al. *Task Force on the RD&D Strategy for CO₂ Utilization and/or Negative Emissions at the Gigatonne Scale*; 2016.
- (41) Global CCS Institute. *The Global Status of CCS*; 2013.
- (42) North American Carbon Atlas Partnership. *The North American Carbon Storage Atlas*; 2012.
- (43) Rubin, E. S.; Davison, J. E.; Herzog, H. J. The Cost of CO₂ Capture and Storage. *Int. J. Greenhouse Gas Control* **2015**, *40*, 378–400.
- (44) Appel, A. M.; Bercaw, J. E.; Bocarsly, A. B.; Dobbek, H.; DuBois, D. L.; Dupuis, M.; Ferry, J. G.; Fujita, E.; Hille, R.; Kenis, P. J. A.; et al. Frontiers, Opportunities, and Challenges in Biochemical and Chemical Catalysis of CO₂ Fixation. *Chem. Rev.* **2013**, *113*, 6621–6658.
- (45) Searchinger, T.; Heimlich, R.; Houghton, R. A.; Dong, F.; Elobeid, A.; Fabiosa, J.; Tokgoz, S.; Hayes, D.; Yu, T.-H. Use of U.S. Croplands for Biofuels Increases Greenhouse Gases Through Emissions from Land-Use Change. *Science* **2008**, *319*, 1238–1240.
- (46) Al-Riffai, P.; Dimaranan, B.; Laborde, D. *Global Trade and Environmental Impact Study of the EU Biofuels Mandate*; 2010.
- (47) Baik, E.; Sanchez, D. L.; Turner, P. A.; Mach, K. J.; Field, C. B.; Benson, S. M. Geospatial Analysis of Near-Term Potential for Carbon-Negative Bioenergy in the United States. *Proc. Natl. Acad. Sci. U. S. A.* **2018**, *115*, 3290–3295.
- (48) Turner, P. A.; Mach, K. J.; Lobell, D. B.; Benson, S. M.; Baik, E.; Sanchez, D. L.; Field, C. B. The Global Overlap of Bioenergy and Carbon Sequestration Potential. *Clim. Change* **2018**, *148*, 1–10.
- (49) Kaul, M.; Mohren, G. M. J.; Dadhwal, V. K. Carbon Storage and Sequestration Potential of Selected Tree Species in India. *Mitig. Adapt. Strateg. Glob. Chang.* **2010**, *15*, 489–510.
- (50) Eckert, M.; Fleischmann, G.; Jira, R.; Bolt, H. M.; Golka, K. *Ullmann's Encyclopedia of Industrial Chemistry*; Wiley-VCH Verlag GmbH & Co. KGaA: Weinheim, Germany, 2000.
- (51) Chorkendorff, I.; Niemantsverdriet, J. W. *Concepts of Modern Catalysis and Kinetics*; Wiley-VCH Verlag GmbH & Co. KGaA: Weinheim, FRG, 2003.
- (52) Rönsch, S.; Schneider, J.; Matthischke, S.; Schlüter, M.; Götz, M.; Lefebvre, J.; Prabhakaran, P.; Bajohr, S. Review on Methanation - From Fundamentals to Current Projects. *Fuel* **2016**, *166*, 276–296.
- (53) Yang, J.; Ma, W.; Chen, D.; Holmen, A.; Davis, B. H. Fischer-Tropsch Synthesis: A Review of the Effect of CO Conversion on Methane Selectivity. *Appl. Catal., A* **2014**, *470*, 250–260.
- (54) Jadhav, S. G.; Vaidya, P. D.; Bhanage, B. M.; Joshi, J. B. Catalytic Carbon Dioxide Hydrogenation to Methanol: A Review of Recent Studies. *Chem. Eng. Res. Des.* **2014**, *92*, 2557–2567.
- (55) Olah, G. A.; Goepfert, A.; Prakash, G. K. S. *Beyond Oil and Gas: The Methanol Economy*, 2nd ed.; 2009.
- (56) Studt, F.; Behrens, M.; Kunkes, E. L.; Thomas, N.; Zander, S.; Tarasov, A.; Schumann, J.; Frei, E.; Varley, J. B.; Abild-Pedersen, F.; et al. The Mechanism of CO and CO₂ Hydrogenation to Methanol over Cu-Based Catalysts. *ChemCatChem* **2015**, *7*, 1105–1111.
- (57) Seh, Z. W.; Kibsgaard, J.; Dickens, C. F.; Chorkendorff, I.; Nørskov, J. K.; Jaramillo, T. F. Combining Theory and Experiment in Electrocatalysis: Insights into Materials Design. *Science* **2017**, *355*, No. eaad4998.

- (58) Carmo, M.; Fritz, D. L.; Mergel, J.; Stolten, D. A Comprehensive Review on PEM Water Electrolysis. *Int. J. Hydrogen Energy* **2013**, *38*, 4901–4934.
- (59) Whipple, D. T.; Kenis, P. J. A. Prospects of CO₂ Utilization via Direct Heterogeneous Electrochemical Reduction. *J. Phys. Chem. Lett.* **2010**, *1*, 3451–3458.
- (60) Graves, C.; Ebbesen, S. D.; Mogensen, M.; Lackner, K. S. Sustainable Hydrocarbon Fuels by Recycling CO₂ and H₂O with Renewable or Nuclear Energy. *Renewable Sustainable Energy Rev.* **2011**, *15*, 1–23.
- (61) Kondratenko, E. V.; Mul, G.; Baltrusaitis, J.; Larrazábal, G. O.; Pérez-Ramírez, J. Status and Perspectives of CO₂ Conversion into Fuels and Chemicals by Catalytic, Photocatalytic and Electrocatalytic Processes. *Energy Environ. Sci.* **2013**, *6*, 3112–3135.
- (62) Götz, M.; Lefebvre, J.; Mörs, F.; McDaniel Koch, A.; Graf, F.; Bajohr, S.; Reimert, R.; Kolb, T. Renewable Power-to-Gas: A Technological and Economic Review. *Renewable Energy* **2016**, *85*, 1371–1390.
- (63) Dau, H.; Limberg, C.; Reier, T.; Risch, M.; Roggan, S.; Strasser, P. The Mechanism of Water Oxidation: From Electrolysis via Homogeneous to Biological Catalysis. *ChemCatChem* **2010**, *2*, 724–761.
- (64) NIST Chemistry WebBook, NIST Standard Reference Database Number 69, Mallard, P. J.; Linstrom, W. G., Eds.; National Institute of Standards and Technology: Gaithersburg MD, 20899.
- (65) Kuhl, K. P.; Cave, E. R.; Abram, D. N.; Jaramillo, T. F. New Insights into the Electrochemical Reduction of Carbon Dioxide on Metallic Copper Surfaces. *Energy Environ. Sci.* **2012**, *5*, 7050–7059.
- (66) Verma, S.; Kim, B.; Jhong, H. R. M.; Ma, S.; Kenis, P. J. A. A Gross-Margin Model for Defining Technoeconomic Benchmarks in the Electroreduction of CO₂. *ChemSusChem* **2016**, *9*, 1972–1979.
- (67) Oloman, C.; Li, H. Electrochemical Processing of Carbon Dioxide. *ChemSusChem* **2008**, *1*, 385–391.
- (68) Spurgeon, J. M.; Kumar, B. A Comparative Technoeconomic Analysis of Pathways for Commercial Electrochemical CO₂ Reduction to Liquid Products. *Energy Environ. Sci.* **2018**, *11*, 1536–1551.
- (69) Jouny, M.; Luc, W.; Jiao, F. General Techno-Economic Analysis of CO₂ Electrolysis Systems. *Ind. Eng. Chem. Res.* **2018**, *57*, 2165–2177.
- (70) Li, C. W.; Ciston, J.; Kanan, M. W. Electroreduction of Carbon Monoxide to Liquid Fuel on Oxide-Derived Nanocrystalline Copper. *Nature* **2014**, *508*, 504–507.
- (71) Bushuyev, O. S.; De Luna, P.; Dinh, C. T.; Tao, L.; Saur, G.; van de Lagemaat, J.; Kelley, S. O.; Sargent, E. H. What Should We Make with CO₂ and How Can We Make It? *Joule* **2018**, *2*, 825–832.
- (72) Clark, E. L.; Hahn, C.; Jaramillo, T. F.; Bell, A. T. Electrochemical CO₂ Reduction over Compressively Strained CuAg Surface Alloys with Enhanced Multi-Carbon Oxygenate Selectivity. *J. Am. Chem. Soc.* **2017**, *139*, 15848–15857.
- (73) Lewis, N. S.; Nocera, D. G. Powering the Planet: Chemical Challenges in Solar Energy Utilization. *Proc. Natl. Acad. Sci. U. S. A.* **2006**, *103*, 15729–15735.
- (74) Afshar, A. A. N. *Chemical Profile: Formic Acid*; 2014.
- (75) British Petroleum (BP). *Natural Gas*, 67th ed.; 2018.
- (76) True, W. R. Global Ethylene Capacity Poised for Major Expansion. *Oil Gas J.* **2008**, *110*, 90–95.
- (77) Eckert, M.; Fleischmann, G.; Jira, R.; Bolt, H. M.; Golka, K. *Ullmann's Encyclopedia of Industrial Chemistry*; WILEY-VCH Verlag, 2007.
- (78) Kniel, L.; Stork, K.; Winter, O. *Ethylene - A Keystone to the Petrochemical Industry*; M. Dekker, New York, 1980.
- (79) Mussatto, S. I.; Dragone, G.; Guimaraes, P. M. R.; Silva, J. P. A.; Carneiro, L. M.; Roberto, I. C.; Vicente, A.; Domingues, L.; Teixeira, J. A. Technological Trends, Global Market, and Challenges of Bio-Ethanol Production. *Biotechnol. Adv.* **2010**, *28*, 817–830.
- (80) Teeter, T. E.; Van Rysselberghe, P. Reduction of Carbon Dioxide on Mercury Cathodes. *J. Chem. Phys.* **1954**, *22*, 759–760.
- (81) Hori, Y.; Kikuchi, K.; Suzuki, S. Production of CO and CH₄ in Electrochemical Reduction of CO₂ at Metal Electrodes in Aqueous Hydrogencarbonate Solutions. *Chem. Lett.* **1985**, *14*, 1695–1698.
- (82) Hori, Y.; Kikuchi, K.; Murata, A.; Suzuki, S. Production of Methane and Ethylene in Electrochemical Reduction of Carbon Dioxide At Copper Electrode in Aqueous Hydrogencarbonate Solution. *Chem. Lett.* **1986**, *15*, 897–898.
- (83) Hori, Y.; Murata, A.; Takahashi, R.; Suzuki, S. Enhanced Formation of Ethylene and Alcohols at Ambient Temperature and Pressure in Electrochemical Reduction of Carbon Dioxide at a Copper Electrode. *J. Chem. Soc., Chem. Commun.* **1988**, *0*, 17.
- (84) Hori, Y.; Wakebe, H.; Tsukamoto, T.; Koga, O. Electrocatalytic Process of CO Selectivity in Electrochemical Reduction of CO₂ at Metal Electrodes in Aqueous Media. *Electrochim. Acta* **1994**, *39*, 1833–1839.
- (85) Hori, Y.; Murata, A.; Takahashi, R. Formation of Hydrocarbons in the Electrochemical Reduction of Carbon Dioxide at a Copper Electrode in Aqueous Solution. *J. Chem. Soc., Faraday Trans. 1* **1989**, *85*, 2309–2326.
- (86) Bagger, A.; Ju, W.; Varela, A. S.; Strasser, P.; Rossmeisl, J. Electrochemical CO₂ Reduction: A Classification Problem. *Chem-PhysChem* **2017**, *18*, 3266–3273.
- (87) Clark, E. L.; Resasco, J.; Landers, A.; Lin, J.; Chung, L.-T.; Walton, A.; Hahn, C.; Jaramillo, T. F.; Bell, A. T. Standards and Protocols for Data Acquisition and Reporting for Studies of the Electrochemical Reduction of Carbon Dioxide. *ACS Catal.* **2018**, *8*, 6560–6570.
- (88) Pander, J. E.; Ren, D.; Yeo, B. S. Practices for the Collection and Reporting of Electrocatalytic Performance and Mechanistic Information for the CO₂ Reduction Reaction. *Catal. Sci. Technol.* **2017**, *7*, S820–S832.
- (89) Li, C. W.; Kanan, M. W. CO₂ Reduction at Low Overpotential on Cu Electrodes Resulting from the Reduction of Thick Cu₂O Films. *J. Am. Chem. Soc.* **2012**, *134*, 7231–7234.
- (90) Bertheussen, E.; Verdager-Casadevall, A.; Ravasio, D.; Montoya, J. H.; Trimarco, D. B.; Roy, C.; Meier, S.; Wendland, J.; Nørskov, J. K.; Stephens, I. E. L.; et al. Acetaldehyde as an Intermediate in the Electroreduction of Carbon Monoxide to Ethanol on Oxide-Derived Copper. *Angew. Chem., Int. Ed.* **2016**, *55*, 1450–1454.
- (91) Raciti, D.; Livi, K. J.; Wang, C. Highly Dense Cu Nanowires for Low-Overpotential CO₂ Reduction. *Nano Lett.* **2015**, *15*, 6829–6835.
- (92) Ma, M.; Djanashvili, K.; Smith, W. A. Selective Electrochemical Reduction of CO₂ to CO on CuO-Derived Cu Nanowires. *Phys. Chem. Chem. Phys.* **2015**, *17*, 20861–20867.
- (93) Min, S.; Yang, X.; Lu, A. Y.; Tseng, C. C.; Hedhili, M. N.; Li, L. J.; Huang, K. W. Low Overpotential and High Current CO₂ Reduction with Surface Reconstructed Cu Foam Electrodes. *Nano Energy* **2016**, *27*, 121–129.
- (94) Roberts, F. S.; Kuhl, K. P.; Nilsson, A. High Selectivity for Ethylene from Carbon Dioxide Reduction over Copper Nanocube Electrocatalysts. *Angew. Chem., Int. Ed.* **2015**, *54*, 5179–5182.
- (95) Kwon, Y.; Lum, Y.; Clark, E. L.; Ager, J. W.; Bell, A. T. CO₂ Electroreduction with Enhanced Ethylene and Ethanol Selectivity by Nanostructuring Polycrystalline Copper. *ChemElectroChem* **2016**, *3*, 1012–1019.
- (96) Singh, M. R.; Clark, E. L.; Bell, A. T. Effects of Electrolyte, Catalyst, and Membrane Composition and Operating Conditions on the Performance of Solar-Driven Electrochemical Reduction of Carbon Dioxide. *Phys. Chem. Phys.* **2015**, *17*, 18924–18936.
- (97) Lum, Y.; Yue, B.; Lobaccaro, P.; Bell, A. T.; Ager, J. W. Optimizing C-C Coupling on Oxide-Derived Copper Catalysts for Electrochemical CO₂ Reduction. *J. Phys. Chem. C* **2017**, *121*, 14191–14203.
- (98) Raciti, D.; Mao, M.; Wang, C. Mass Transport Modelling for the Electroreduction of CO₂ on Cu Nanowires. *Nanotechnology* **2018**, *29*, 044001.

Paper VI Desorbing uphill: Anodic Hydrogen Evolution on Cu and Ru Electrodes

Sren B. Scott*, Albert K. Engstfeld*, Zenonas Jusys, Degenhart Hochfilzer, Nikolaj Knsgaard, Daniel B. Trimarco, Peter C.K. Vesborg, R. Jrgen Behm, and Ib Chorkendorff

In preparation

DRAFT

Desorbing uphill: Anodic Hydrogen Evolution on Cu and Ru Electrodes

Søren B. Scott^{1,‡}, Albert K. Engstfeld^{2,‡}, Zenonas Jusys², Degenhart Hochfilzer¹, Nikolaj Knøsgaard¹, Daniel B. Trimarco³, Peter C.K. Vesborg¹, R. Jürgen Behm², Ib Chorkendorff¹

¹ Section for Surface Physics and Catalysis, Department of Physics, Technical University of Denmark, 2800 Kgs. Lyngby, Denmark

² Institute of Surface Chemistry and Catalysis, Ulm University, D-89069 Ulm, Germany

³ Spectro Inlets ApS, Ole Maaløes Vej 3, 2200 København

[‡] These authors contributed equally to this work

Abstract

Electrochemical hydrogen adsorption and desorption, and the state of adsorbed hydrogen (*H) on metal surfaces, are both of fundamental interest and of practical importance for the hydrogen evolution reaction (HER) and for electrochemical hydrogenation reactions including CO₂ and CO electroreduction. Here, we report a previously unknown phenomenon whereby *H desorbs as H₂ during an anodic potential sweep and at potentials anodic of 0 V vs RHE. Using electrochemistry - mass spectrometry, we observe, quantify, and characterize the phenomenon on two different materials in two different environments - polycrystalline Cu in alkaline and Ru(0001) in acid. For both Cu and Ru, the anodic H₂ evolution seems to coincide with *OH adsorption, suggesting a displacement mechanism. We propose that an unexpectedly high barrier to the Volmer step relative to the Tafel step causes the displaced *H to desorb as H₂ rather than the thermodynamically favorable H⁺.

reaction	Delta G	name	label
$2 (H^+ + e^-) \leftrightarrow H_2$	$2 eU$	HER/HOR	rxn_H2
$* + (H^+ + e^-) \leftrightarrow *H$	$G(*H) + eU$	Volmer	rxn_Volmer
$*H + *H \leftrightarrow H_2 + 2*$	$- 2G(*H)$	Tafel	rxn_Tafel
$*H + (H^+ + e^-) \leftrightarrow H_2 + *$	$-G(*H) + eU$	Heyrowsky	rxn_Heyrowsky
$H_2O \leftrightarrow *OH + (H^+ + e^-)$	$G(*OH) - eU$	OH adsorption	rxn_OH
$*H + H_2O \leftrightarrow *OH + 2(H^+ + e^-)$	$G(*OH) - G(*H) - 2 eU$	OH + Volmer	rxn_OH_H_mixed
$2 *H + H_2O \rightarrow H_2 + *OH + * + (H^+ + e^-)$	$G(*OH) - 2 G(*H) - eU$	Anodic H2 A	rxn_an_H2_A
$*H + H_2O \rightarrow H_2 + *OH$	$G(*OH) - G(*H)$	Anodic H2 B	rxn_an_H2_B

Table 1 Reactions. Here, * represents a free surface site.

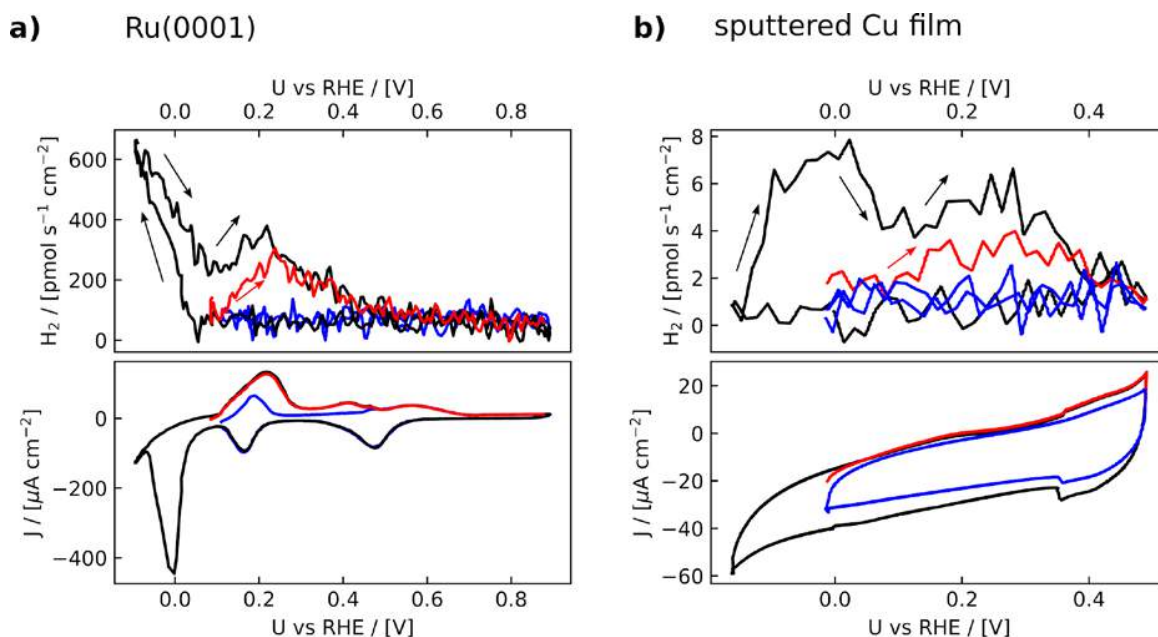
A better understanding of hydrogen adsorption and desorption on metal surfaces under aqueous electrochemical conditions, would aid the rational design of electrocatalysts for a number of processes where the atomic coordination of adsorbed hydrogen (*H) plays a crucial role, such as the hydrogen evolution and oxidation reaction (HER/HOR), but also electrochemical hydrogenation reactions including the carbon dioxide reduction (CO₂R) and CO reduction reaction (COR)^{1,2}, the reduction of organic molecules such as aliphatic ketones³ or nitrate reduction^{4,5}.

Focusing on the HER of water electrolyzer cathodes⁶⁻⁸, and the HOR of fuel cell anodes^{9,10}, the overall HER/HOR is given by Reaction rxn_H2 in Table 1 (written with HER in the forward direction). Reaction rxn_H2 can be split up into a hydrogen adsorption step forming *H (Volmer step, rxn_Volmer) and a step where H₂ desorbs either through a recombination of *H (Tafel step, rxn_Tafel) or a coupled proton-electron transfer (Heyrovsky step, rxn_Heyrowsky). Trends between materials in the rate of the HER between various materials are well-described by the free energy of hydrogen adsorption, G(*H), where the optimal G(*H) is 0 V vs. RHE (all potentials

are given vs. the RHE scale)^{9,11,12}. In other words, an optimal HER catalyst is characterized by an equilibrium potential for the Volmer step with $U = 0$ V. Because the H^* adsorption energy is such a powerful descriptor of the HER activity, and because activation barriers are not trivial to calculate for electrochemical reactions^{6,10,13}, the kinetics of these elementary steps have often received less attention, but can likely explain phenomena such as slower HER kinetics in alkaline electrolyte than in acid on near-optimal catalysts such as Pt¹⁴. Further nuancing the simple $G(*H)$ -descriptor-based model of the HER, Strmcnik and coworkers have suggested that other adsorbates such as $*OH$ can influence the HER activity if $*OH$ is not fully desorbed (rxn_OH) under HER conditions^{15,16}. In a related observation, Koper and coworkers have shown that on more reactive atomic sites such as the step sites on Pt, hydrogen adsorption/desorption can be coupled to $*OH$ desorption/adsorption ($rxn_OH_H_mixed$)^{17,18}. For example, on Ru(0001) it is accepted that the H^*/OH^* regions overlap¹⁹⁻²¹, while for other metals such as Rh(111)²², Ir(111)²³ and other more open surfaces the phenomenon is still under debate²⁰.

In these reactions, the Volmer reaction is part of a Langmuir-Hinshelwood type reaction mechanism, in which adsorbed hydrogen reacts with the other adsorbed species. In particular, such a mechanism is predicted to have a lower barrier for hydrogenation of adsorbed CO ($*CO$) to $*CHO$ ²⁴, which is widely believed to be the rate-limiting step in CO and CO₂ hydrogenation on copper electrodes. Because copper is unique in its ability to reduce CO₂ and CO to hydrocarbons², it is therefore of great interest to learn more about adsorbed hydrogen on copper.

In order to elucidate the influence of OH^* on the hydrogen desorption/adsorption we performed a cyclic voltammetry study in combination with online mass spectrometry on Ru(0001), which shows a strong interaction of OH and H; and Cu(poly), which shows a weak interaction with H^* and a stronger interaction with OH^* . On both electrodes we observe the formation of H₂ at potentials anodic of 0.0 V, which is demonstrated in Figure_CVmass for Ru(0001) in 0.1 M HClO₄ in (a), and a sputter-deposited copper film in 0.1 M KOH in (b). The results were obtained in two different electrochemistry-mass spectrometry setups: dual thin layer flow cell DEMS^{25,26}, and chip-based EC-MS²⁷, for Ru(0001) and Cu(poly), respectively. The geometric electrode current density (See experimental part) is plotted against electrode potential and the concurrent calibrated H₂ signal from the mass spectrometer, also normalized to the electrode area, are plotted in the lower and upper panel, respectively. For both electrodes, the following three experiments were performed:



Figure_CVmass: Mass spectrometry $m/z = 2$ signal (top panel) and CVs (bottom panel) of **a)** Ru(0001), recorded in 0.1 M HClO_4 at 50 mV s^{-1} and of **b)** sputtered Cu film, recorded in 0.1 M KOH at 20 mV s^{-1} . Black and blue curves were recorded with and without excursion into the H adsorption regime, respectively. The red trace starts at 0.0 V or 0.1 V preceded by a potential cycle to -0.15 V or -0.1 V for Cu(sputter) and Ru(0001) and holding the potential for 30 s, and 10 s, respectively,.

1. A full cyclic voltammogram (CV), shown in black, with a cathodic limit of -0.15 V for Cu (onset of HER), -0.10 for Ru (HER region). H_2 is observed at and/or immediately after the cathodic turn, as expected (accounting for a delay/broadening effect due to mass transport, especially pronounced in Figure_massCV (b)).
2. A CV, shown in blue, with a cathodic potential limit before the onset of the HER (0 V for Cu, $+0.1$ for Ru), which shows no H_2 signal.
3. An anodic sweep, shown in red, from the same cathodic potential limit as the blue curve, which, however, follows a scan into the HER region and a subsequent pause at the “resting potential”.

For clarity, the data for the full experiments are plotted on time axes in **FigureSI_vs_t**.

An unexpected key observation from the three experiments is the appearance of a H_2 signal at potentials anodic of 0.0 V (referred to as *anodic H_2*). While in the black trace, this could be caused by a delay/broadening effect due to mass transport, especially pronounced in Figure_massCV (b), the anodic H_2 signal is clearly separated from the HER signal in the red trace. In order to discuss the underlying cause of the phenomenon, we focus first on the CVs recorded on Ru(0001) (Figure 1 a). In this case, the features of the CV are very well described in

the literature^{19,28} and the overall shape, peak shapes and peaks locations of the presented CVs match those reported in these previous studies. A detailed description can be found in the SI.

On Ru(0001) the anodic hydrogen signal starts at approximately +0.1 V (black and red curves), following an anodic feature at 0.20 V in the corresponding CV's. This feature is related to the cathodic peak at 0.0 V (black trace). The underlying processes of this peak couple were attributed to the cathodic displacement of *OH by *H (rxn_OH_H_mixed) and the anodic displacement of *H by *OH, respectively²⁰. Holding the potential at 0.1 V vs RHE after hydrogen adsorption in the cathodic scan does not seem to change the state of the surface, as the subsequent anodic scan is unchanged by the potential hold (compare black and red trace in Figure 1a). The observation of H₂ indicates that *H is removed, in part, by Reaction rxn_an_H2_A and/or rxn_an_H2_B and not by the proposed rxn_OH_H_mixed in ref.²⁰. To further distinguish between reactions rxn_OH_H_mixed, rxn_an_H2_A and/or rxn_an_H2_B we did a quantitative charge evaluation of the redox features in CV, taking into account both the H₂ from the HER and anodic H₂. The full results are shown in Table S1 and the details on the quantification are given in the SI. The most important findings are summarized as follows.

First, the integrated anodic H₂ signal from the Ru(0001) electrode is approximately 720 pmol/cm², or about 0.25 H₂ molecules (0.5 ML H*) per surface atom. This value is in good agreement with CO displacement measurements performed at ca. 0.1 V, just before the onset of anodic H₂ formation¹⁹. Secondly, in the full CV (black trace of Figure 1b), the charge passed in the cathodic scan minus that corresponding to the cathodic HER exceeds the charge passed in the anodic scan by about 150 uC/cm², or about 0.5 electrons per surface atom. Together, these observations are consistent with the proposed Reaction rxn_an_H2_A, whereby the 0.5 ML of *H present on the surface is desorbed without charge transfer in a Tafel step coupled to OH adsorption.

In the case of the sputtered Cu electrode (Figure 1b) the CV does not show any pronounced features, except for a sharp increase in current at around 0.35 V. Note that the CV of Cu(poly) recorded in alkaline shows very different shapes depending on the pre-treatment²⁹. Several previous studies attempt to elucidate the nature of the observed peaks, but a complete picture is still missing³⁰⁻³³. In general these features are associated with an oxidation of the Cu electrode surface (OH*/O*), which is reasonable, considering that the equilibrium potential for, e.g., reaction $\text{Cu}_2\text{O} + \text{H}_2\text{O} + 2\text{e}^- \leftrightarrow 2\text{Cu} + 2\text{OH}^-$ is $E_0 = -0.222\text{ V}$. Nevertheless, the anodic H₂ signal also appears at potentials larger 0 V, i.e., approximately +0.1 V, in the anodic scan (black and red traces). This follows a small anodic current feature in the corresponding CVs at +0.1 V which is not present in the CV when the electrode potential has not been exposed to the

HER region (blue trace). The integrated H₂ signal in the red curve corresponds to approximately 32 pmol/cm². Assuming the surface site density of Cu(111), 2.9 nmol/cm², this corresponds to approximately 1.1% of a monolayer. Note that observing such a small signal requires an extremely sensitive electrochemistry-mass spectrometry system, described in detail in ref. ²⁷. While the appearance of a H₂ signal at potentials larger 0.0 V is as unexpected as on Ru(0001) it is in addition very astonishing to observe H adsorption on Cu electrodes, which has so far not been reported for this material. In order to explore the latter phenomenon in more detail, we did an additional set of experiments, described below, to localize the potentials at which *H adsorbs and desorbs.

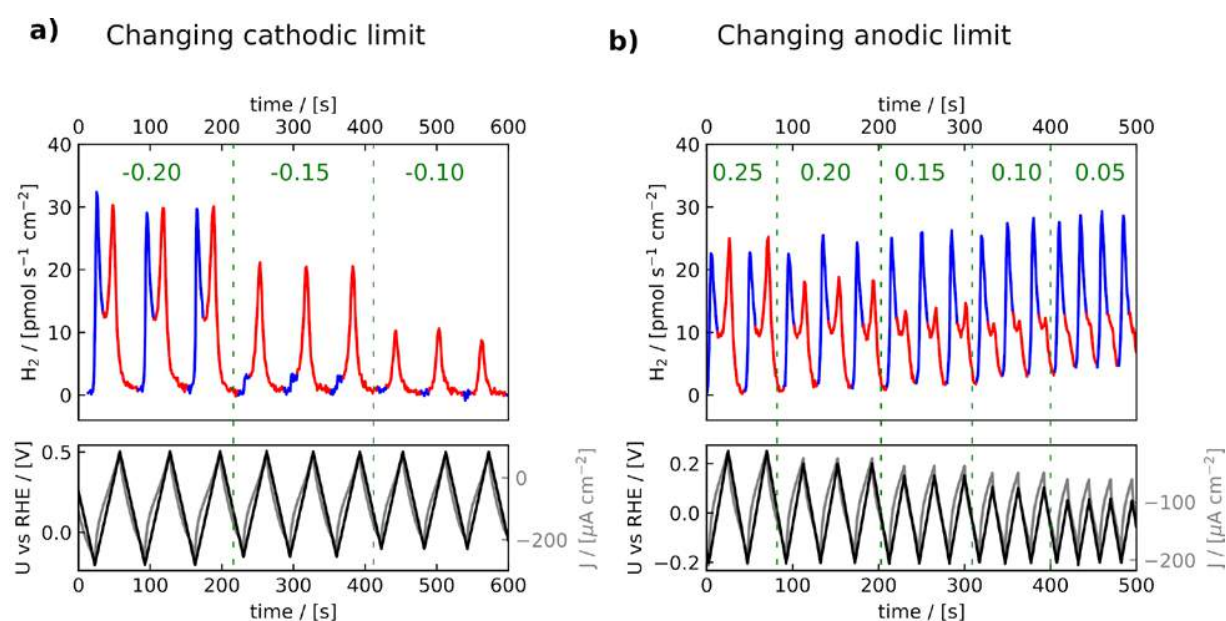


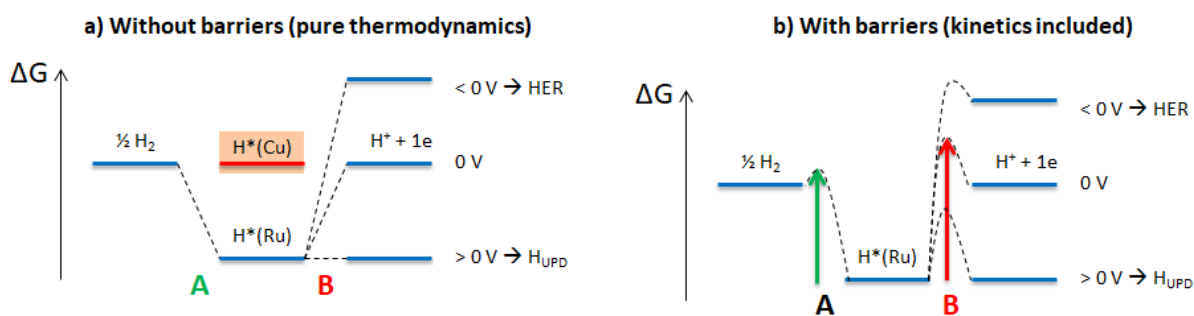
Figure **potential_limits**. Cyclic voltammetry on mechanically polished polycrystalline copper at 20 mV/s in pH=10.5 potassium carbonate/bicarbonate buffer. (a) The *H adsorption potential is probed by varying the cathodic potential limit. The anodic potential limit is held at 0.5 V vs RHE while the cathodic potential limit is indicated. (b) The anodic H₂ desorption potential is probed by varying the anodic potential limit. The cathodic potential is held at -0.2 V vs RHE while the anodic potential limit is indicated. In each case, the H₂ signal (upper panel) is colored blue from the cathodic crossing of 0 V vs RHE to the anodic crossing of 0.05 V vs RHE to indicate cathodic hydrogen evolution, and red during the rest of the CV to indicate anodic hydrogen desorption.

For this set of measurements, we used a mechanically polished Cu disk, investigated in 0.1 M KOH and in potassium carbonate/bicarbonate buffers at a range of pH values spanning 7 to 13, with Figure **potential_limits** showing the results for pH=10.5. The electrode shows a much larger

anodic hydrogen desorption signal of approximately 300 pmol/cm², which is attributed to its greater roughness. This also indicates that the anodic hydrogen desorption might be related to surface sites more common on the mechanically polished surface than the sputter-deposited surface. The *H adsorption and desorption potentials were pH-independent on the RHE scale (Figure SX). The magnitude of the anodic hydrogen peak was also independent of the scan rate or the amount of H₂ evolved by HER prior to the anodic scan (Figure SXX).

In the initial potential cycles of Figure **potential_limitsa**, from -0.2 V to +0.5 V, cathodic hydrogen evolution (colored blue for clarity) and anodic hydrogen desorption (red) are both prominent, with about the same amount of H₂ each. When the cathodic potential limit is increased 50 mV to -0.15 V, the cathodic HER almost vanishes, whereas the anodic hydrogen desorption is largely unaffected. This indicates that the *H species on the surface which desorbs as H₂ at anodic potentials reaches a saturation coverage before the onset of conventional hydrogen evolution. In Figure **potential_limitsb**, the anodic potential limit is changed instead. The anodic hydrogen desorption signal decreases gradually as the anodic potential limit of each cycle is lowered from 0.25 V to 0.05 V. This indicates that the anodic H₂ desorption phenomenon occurs slowly, over a range of potentials, consistent with the hypothesis that it is the result of a displacement reaction by *OH, which is predicted to have a potential-dependent coverage in the same potential range. \cite{Propotoff}

Overall, we suggest that the underlying processes on Cu are very similar than on Ru(0001) and that reaction rxn_an_H2_A is the driving force for the observed process.



Figure_energy_diagram: (a) If the free energy of *H is increased due to *OH adsorption at $U > 0 \text{ V}$ vs RHE, simple thermodynamics indicates it should desorb by the Volmer step as ($\text{H}^+ + \text{e}^-$). (b) However, kinetic barriers can make the desorption of *H by the Tafel step more kinetically favorable.

*OH displacement of *H resulting in H₂ by the Tafel step is surprising, since the formation of (H⁺ + e⁻) by the Volmer step is thermodynamically more favorable anodic of 0 V vs RHE. This is illustrated schematically in **Figure_energy_diagram a**, where A is the Tafel step and B is the Volmer step. In order to rationalize the formation of H₂ at potentials $U > 0$ V, possible reaction barriers are included **Figure_energy_diagram b**. For the sake of simplicity we draw the diagram with H*(Ru), since the free energy level is clearly defined to be lower than G(H₂) or G(H⁺). Adsorption of *OH takes up surface sites and increases the free energy of *H until *H is unfavorable compared to both H₂ and (H⁺ + e⁻). While the Volmer pathway to (H⁺ + e⁻) is more downhill overall at $U > 0$ V vs RHE, the Tafel pathway may be the more facile path for *H removal due if there is a larger kinetic barrier for the Volmer step. The presence of such kinetic barriers can be elucidated by performing CV experiments at different scan rates. At least in the case of Ru(0001) electrodes it has indeed been shown that the locations of the peaks associated with H* formation (centered at 0 V vs RHE in Figure 1b) and *H removal (centered at +0.2 V vs RHE in Figure 1b) depend strongly on the scan rate (See ref. ²⁸ and Figure_RuScanRate in the SI).

In acidic media, the Volmer step is believed to have a low barrier or no barrier on many materials including, for example, Pt(111)¹³, Ru@Pt core@shell nanoparticles³⁴, and Ni₂P³⁵, so the presence of a high Volmer barrier on Ru in acidic media is unexpected. Furthermore, in the limited DFT study thus far of barriers in electrochemical elementary steps, the Tafel and Heyrovsky steps, in which an H-H bond is formed (HER) or broken (HOR), are generally predicted to have larger barriers than the Volmer step¹³.

The anodic H₂ desorption on polycrystalline copper in alkaline electrolyte represents a much smaller portion of a monolayer than on Ru(0001). The direct evidence of an adsorbed *H species on Cu is nonetheless highly significant, as Cu is generally believed to adsorb hydrogen weakly ($G(*H) > 0$)^{12,36}.

The small coverage together with the fact that it depends strongly on the surface preparation - one anodic H₂ molecule per 100 surface sites for sputter-deposited Cu, and one anodic H₂ molecule per 20 surface sites for mechanically polished Cu - may indicate that the *H precursor to the anodic H₂ is limited to particular surface sites, such as undercoordinated sites which bind *H stronger than close packed surfaces. The ability of copper electrodes to reduce CO₂ and CO to hydrocarbons is also closely coordinated with the presence of such undercoordinated sites², indicating that the *H precursor to anodic H₂ could also be an important reactant in one or more of the steps on the electrocatalytic pathway for CO₂ reduction to hydrocarbons. More studies, including DFT studies and EC-MS measurements on copper single crystals, should be done to confirm this.

The production of H₂ from an electrode surface during an anodic scan at potentials anodic of 0 V vs RHE is a new and surprising phenomenon. On both Ru and Cu electrodes, the anodic hydrogen requires prior adsorption of *H and coincides with *OH adsorption, motivating a mechanism in which *OH displaces *H, and *H desorbs as H₂ rather than (H⁺ + e⁻) due to an unexpectedly high barrier for the Volmer reaction. In the case of Ru(0001) in acidic electrolyte, the desorbed H₂ corresponds to 0.25 ML equivalents and can account for the difference in charge passed on the anodic and cathodic scans of 0.5 e⁻ per surface atom, given the recombination of 0.5 ML *H by the Tafel step. In the case of polycrystalline Cu electrodes, the desorbed H₂ is a much smaller portion of a monolayer (<=0.05 ML, requiring a very sensitive EC-MS system to detect), a portion which correlates with the roughness of the surface. The observation of the anodic H₂ phenomenon provides a new window through which to study electrochemical hydrogen adsorption and desorption, which is of high importance for critical electrochemical reactions such as HER and CO₂ reduction. This preliminary report should motivate future work including (1) DFT studies to explain the high Volmer barrier that causes the anodic H₂ evolution, (2) anodic H₂ quantification on single-crystal Cu electrodes, and (3) isotope-labeling studies to differentiate between a Tafel-type (rxn_an_H2_A) or Heyrovsky-type (rxn_an_H2_B) anodic hydrogen evolution mechanism.

- (1) Hori, Y. Electrochemical CO₂ Reduction on Metal Electrodes. In *Modern Aspects of Electrochemistry*; Vayenas, C. G., White, R. E., Gamboa-Aldeco, M. E., Eds.; Springer, 2008; Vol. 42, pp 89–189.
- (2) Nitopi, S. A.; Bertheussen, E.; Scott, S. B.; Liu, X.; Albert, K.; Horch, S.; Seger, B.; Stephens, I. E. L.; Chan, K.; Nørskov, J. K.; et al. Progress and Perspectives of Electrochemical CO₂ Reduction on Copper in Aqueous Electrolyte. *Chem. Rev.* **2019**, 10.1021/ACS.CHEMREV.8B00705, DOI: 10.1021/acs.chemrev.8b00705.
- (3) Bondue, C. J.; Koper, M. T. M. A Mechanistic Investigation on the Electrocatalytic Reduction of Aliphatic Ketones at Platinum. *J. Catal.* **2019**, 369, 302–311.
- (4) Rosca, V.; Duca, M.; de Groot, M. T.; Koper, M. T. M. Nitrogen Cycle Electrocatalysis. *Chem. Rev.* **2009**, 109 (6), 2209–2244.
- (5) Duca, M.; Koper, M. T. M. Powering Denitrification: The Perspectives of Electrocatalytic Nitrate Reduction. *Energy Environ. Sci.* **2012**, 5 (12), 9726–9742.
- (6) Koper, M. T. M. Thermodynamic Theory of Multi-Electron Transfer Reactions: Implications for Electrocatalysis. *J. Electroanal. Chem.* **2011**, 660 (2), 254.
- (7) Tymoczko, J.; Calle-Vallejo, F.; Schuhmann, W.; Bandarenka, A. S. Making the Hydrogen Evolution Reaction in Polymer Electrolyte Membrane Electrolysers Even Faster. *Nat. Commun.* **2016**, 7, 10990.
- (8) Kibsgaard, J.; Chorkendorff, I. Considerations for the Scaling-up of Water Splitting Catalysts. *Nat. Energy* **2019**, 10.1038/s41560-019-0407-1.
- (9) Zheng, Y.; Jiao, Y.; Zhu, Y.; Li, L. H.; Han, Y.; Chen, Y.; Jaroniec, M.; Qiao, S.-Z. High Electrocatalytic Hydrogen Evolution Activity of an Anomalous Ruthenium Catalyst. *J. Am. Chem. Soc.* **2016**, 138 (49), 16174–16181.
- (10) Skúlason, E.; Tripkovic, V.; Björketun, M. E.; Gudmundsdóttir, S.; Karlberg, G.; Rossmeisl, J.; Bligaard, T.; Jónsson, H.; Nørskov, J. K. Modeling the Electrochemical

- Hydrogen Oxidation and Evolution Reactions on the Basis of Density Functional Theory Calculations. *J. Phys. Chem. C* **2010**, *114* (42), 18182–18197.
- (11) Galizzioli, D.; Trasatti, S. Work Function, Electronegativity, and Electrochemical Behaviour of Metals. *J. Electroanal. Chem. Interfacial Electrochem.* **1973**, *44* (3), 367–388.
 - (12) Nørskov, J. K.; Bligaard, T.; Logadottir, A.; Kitchin, J. R.; Chen, J. G.; Pandelov, S.; Stimming, U. Trends in the Exchange Current for Hydrogen Evolution. *J. Electrochem. Soc.* **2005**, *152* (3), J23.
 - (13) Chan, K.; Nørskov, J. K. Electrochemical Barriers Made Simple. *J. Phys. Chem. Lett.* **2015**, 10.1021/acs.jpcclett.5b01043, 2663–2668.
 - (14) Rossmeisl, J.; Chan, K.; Skúlason, E.; Björketun, M. E.; Tripkovic, V. On the PH Dependence of Electrochemical Proton Transfer Barriers. *Catal. Today* **2016**, *262*, 36–40.
 - (15) Strmcnik, D.; Uchimura, M.; Wang, C.; Subbaraman, R.; Danilovic, N.; van der Vliet, D.; Paulikas, A. P.; Stamenkovic, V. R.; Markovic, N. M. Improving the Hydrogen Oxidation Reaction Rate by Promotion of Hydroxyl Adsorption. *Nat. Chem.* **2013**, *5* (4), 300–306.
 - (16) Strmcnik, D.; Lopes, P. P.; Genorio, B.; Stamenkovic, V. R.; Markovic, N. M. Design Principles for Hydrogen Evolution Reaction Catalyst Materials. *Nano Energy* **2016**, *29*, 29–36.
 - (17) Van Der Niet, M. J. T. C.; Garcia-Araez, N.; Hernández, J.; Feliu, J. M.; Koper, M. T. M. Water Dissociation on Well-Defined Platinum Surfaces: The Electrochemical Perspective. *Catal. Today* **2013**, *202* (1), 105–113.
 - (18) Diaz-Morales, O.; Hersbach, T. J. P.; Badan, C.; Garcia, A. C.; Koper, M. T. M. Hydrogen Adsorption on Nano-Structured Platinum Electrodes. *Faraday Discuss.* **2018**, *210*, 301–315.
 - (19) El-Aziz, A. .; Kibler, L. . New Information about the Electrochemical Behaviour of Ru(0001) in Perchloric Acid Solutions. *Electrochem. commun.* **2002**, *4* (11), 866–870.
 - (20) Koper, M. T. M. Blank Voltammetry of Hexagonal Surfaces of Pt-Group Metal Electrodes: Comparison to Density Functional Theory Calculations and Ultra-High Vacuum Experiments on Water Dissociation. *Electrochim. Acta* **2011**, *56* (28), 10645–10651.
 - (21) Mercer, M. P.; Hoster, H. E. Electrochemical Kinetics: A Surface Science-Supported Picture of Hydrogen Electrochemistry on Ru(0001) and Pt/Ru(0001). *Electrocatalysis* **2017**, *8* (6), 518–529.
 - (22) Housmans, T. H. M.; Koper, M. T. M. CO Oxidation on Stepped Rh[n(111)×(111)] Single Crystal Electrodes: Anion Effects on CO Surface Mobility. *Electrochem. commun.* **2005**, *7* (6), 581–588.
 - (23) Wan, L.-J.; Hara, M.; Inukai, J.; Itaya, K. In Situ Scanning Tunneling Microscopy of Well-Defined Ir(111) Surface: High-Resolution Imaging of Adsorbed Sulfate. *J. Phys. Chem. B* **1999**, *103* (33), 6978–6983.
 - (24) Nie, X.; Esopi, M. R.; Janik, M. J.; Asthagiri, A. Selectivity of CO(2) Reduction on Copper Electrodes: The Role of the Kinetics of Elementary Steps. *Angew. Chemie Int. Ed.* **2013**, *52* (9), 2459–2462.
 - (25) Baltruschat, H. Differential Electrochemical Mass Spectrometry. *J. Am. Soc. Mass Spectrom.* **2004**, *15* (12), 1693–1706.
 - (26) Schnaidt, J.; Beckord, S.; Engstfeld, A. K.; Klein, J.; Brimaud, S.; Behm, R. J. A Combined UHV-STM-Flow Cell Set-up for Electrochemical/Electrocatalytic Studies of Structurally Well-Defined UHV Prepared Model Electrodes. *Phys. Chem. Chem. Phys.* **2017**, *19* (6), 4166–4178.
 - (27) Trimarco, D. B.; Scott, S. B.; Thilsted, A. H.; Pan, J. Y.; Pedersen, T.; Hansen, O.; Chorkendorff, I.; Vesborg, P. C. K. Enabling Real-Time Detection of Electrochemical Desorption Phenomena with Sub-Monolayer Sensitivity. *Electrochim. Acta* **2018**.

- (28) Alves, O. B.; Hoster, H. E.; Behm, R. J. Electrochemistry at Ru(0001) in a Flowing CO-Saturated Electrolyte—Reactive and Inert Adlayer Phases. *Phys. Chem. Chem. Phys.* **2011**, *13* (13), 6010.
- (29) Engstfeld, A. K.; Maagaard, T.; Horch, S.; Chorkendorff, I.; Stephens, I. E. L. Polycrystalline and Single-Crystal Cu Electrodes: Influence of Experimental Conditions on the Electrochemical Properties in Alkaline Media. *Chem. - A Eur. J.* **2018**, *24* (67), 17743–17755.
- (30) Droog, J. M. M.; Alderliesten, C. A.; Alderliesten, P. T.; Bootsma, G. A. Initial Stages of Anodic Oxidation of Polycrystalline Copper Electrodes in Alkaline Solution. *J. Electroanal. Chem. Interfacial Electrochem.* **1980**, *111* (1), 61–70.
- (31) Droog, J. M. M.; Schlenter, B. Oxygen Electrosorption on Copper Single Crystal Electrodes in Sodium Hydroxide Solution. *J. Electroanal. Chem. Interfacial Electrochem.* **1980**, *112* (2), 387–390.
- (32) Raciti, D.; Cao, L.; Livi, K. J. T.; Rottmann, P. F.; Tang, X.; Li, C.; Hicks, Z.; Bowen, K. H.; Hemker, K. J.; Mueller, T.; et al. Low-Overpotential Electroreduction of Carbon Monoxide Using Copper Nanowires. *ACS Catal.* **2017**, *7* (7), 4467–4472.
- (33) Bertheussen, E.; Hogg, T. V.; Abghoui, Y.; Engstfeld, A. K.; Chorkendorff, I.; Stephens, I. E. L. Electroreduction of CO on Polycrystalline Copper at Low Overpotentials. *ACS Energy Lett.* **2018**, *3* (3), 634–640.
- (34) Elbert, K.; Hu, J.; Ma, Z.; Zhang, Y.; Chen, G.; An, W.; Liu, P.; Isaacs, H. S.; Adzic, R. R.; Wang, J. X. Elucidating Hydrogen Oxidation/Evolution Kinetics in Base and Acid by Enhanced Activities at the Optimized Pt Shell Thickness on the Ru Core. *ACS Catal.* **2015**, *5* (11), 6764–6772.
- (35) Hansen, M. H.; Stern, L. A.; Feng, L.; Rossmeisl, J.; Hu, X. Widely Available Active Sites on Ni₂P for Electrochemical Hydrogen Evolution - Insights from First Principles Calculations. *Phys. Chem. Chem. Phys.* **2015**, *17* (16), 10823–10829.
- (36) Bagger, A.; Ju, W.; Varela, A. S.; Strasser, P.; Rossmeisl, J. Electrochemical CO₂ Reduction: A Classification Problem. *ChemPhysChem* **2017**, *18* (22), 3266–3273.

Paper VII Mechanistic study of oxygen evolution on RuO_2 down to 60 mV overpotential

Soren B. Scott*, Reshma R. Rao*, Choongman M. Moon, Jakob E. Sørensen, Jakob Kibsgaard, Yang Shao-Horn, and Ib Chorkendorff

*These authors contributed equally to this work

In Preparation

Abstract

Ruthenium and ruthenium dioxide are the most active catalysts for water oxidation in acidic electrolyte, but are not sufficiently stable at high current density for commercial applications. Herein, we apply an electrochemistry-mass spectrometry (EC-MS) system with unprecedented sensitivity to extend the activity trends of ruthenium-based electrodes to extremely low current densities, down to a turn-over frequency, (TOF) of $5 \times 10^{-4} \text{ s}^{-1}$ at 60 mV overpotential. We show that the potential-dependence of the TOF, i.e the Tafel slope, goes through three regimes, which we explain by modeling the coverage of the reaction intermediates, confirming a mechanism in which $^*\text{OOH}$ on the cus site of $\text{RuO}_2(110)$ is stabilized with respect to $^*\text{OH}$ by the oxygen at the bridge site. Both Ru and RuO_2 electrodes show improved stability in the small electrolyte volume of EC-MS setup compared to a conventional rotating disk electrode (RDE) setup, indicating that transport of dissolved species is important to the dissolution mechanism. Finally, by quantitative isotope labeling studies, we show that a small amount of lattice oxygen is evolved as O_2 , but that the number of oxygen atoms evolved is small compared to the number of ruthenium atoms dissolved, indicating that lattice oxygen evolution is part of a dissolution mechanism, rather than the water oxidation mechanism.

Note

This paper will include most of the results from Sections 3.2 and 3.4.

It will include Figures 3.6, 3.7, 3.10, 3.11, 3.27, and 3.26.

Appendix C

Python Packages Developed During this PhD Project

Package C.1 EC_MS

The EC_MS python package is available at https://github.com/ScottSoren/EC_MS

Documentation is on its way, as are ipython tutorials. Tutorials will be available at <https://github.com/ScottSoren/Tutorials>.

Package C.2 EC_Xray

The EC_MS python package is available at https://github.com/ScottSoren/EC_Xray

Documentation is on its way.

Tutorials are already available at <https://github.com/ScottSoren/Tutorials>

Bibliography

- [1] Fukuyama, F. *The End of History and the Last Man* (Free Press, 1992).
- [2] US Department of Energy Office of Science. Carbon Cycling and Biosequestration: Integrating Biology and Climate Through Systems Science (2008). URL genomicscience.energy.gov/carboncycle/.
- [3] Le Quéré, C. *et al.* Global Carbon Budget 2015. *Earth System Science Data* **7**, 349–396 (2015).
- [4] Rockström, J. *et al.* Planetary Boundaries: Exploring the Safe Operating Space for Humanity. *Ecology and Society* **14**, 472–475 (2009).
- [5] Intergovernmental Panel on Climate Change. Climate Change 2014: Synthesis Report. Tech. Rep., United Nations (2014). URL <https://www.ipcc.ch/report/ar5/syr/>.
- [6] Le Quéré, C. *et al.* Global Carbon Budget 2018. *Earth System Science Data* **8**, 605–649 (2018).
- [7] Dlugokencky, E. & Tans, P. Trends in Atmospheric Carbon Dioxide (2019). URL <http://www.esrl.noaa.gov/gmd/ccgg/trends/global.html>.
- [8] Morice, C. P., Kennedy, J. J., Rayner, N. A. & Jones, P. D. Quantifying uncertainties in global and regional temperature change using an ensemble of observational estimates: The HadCRUT4 data set. *Journal of Geophysical Research: Atmospheres* **117** (2012).
- [9] Ritchie, H. & Roser, M. CO2 and other Greenhouse Gas Emissions. URL <https://ourworldindata.org/co2-and-other-greenhouse-gas-emissions>.
- [10] Pidcock, R., Pearce, R. & McSweeney, R. Mapped: How climate change affects extreme weather around the world (2019). URL <https://www.carbonbrief.org/mapped-how-climate-change-affects-extreme-weather-around-the-world>.
- [11] Schiermeier, Q. Climate as culprit. *Nature* **560**, 20–22 (2018).
- [12] United Nations High Commissioner for Refugees. Climate change and disaster displacement (2019). URL <https://www.unhcr.org/climate-change-and-disasters.html>.
- [13] Intergovernmental Panel on Climate Change. IPCC special report on the impacts of global warming of 1.5 C - Summary for policy makers. Tech. Rep. October 2018, United Nations (2018). URL <http://www.ipcc.ch/report/sr15/>.
- [14] UNFCCC. Conference of the Parties (COP). Adoption of the Paris Agreement (2015). URL <http://unfccc.int/resource/docs/2015/cop21/eng/109r01.pdf>. arXiv:1011.1669v3.
- [15] Meinshausen, M., Meinshausen, N., Hare, W., Raper, S. C., Frieler, K., Knutti, R., Frame, D. J. & Allen, M. R. Greenhouse-gas emission targets for limiting global warming to 2 C. *Nature* **458**, 1158–1162 (2009).
- [16] Allen, M. Planetary boundaries: Tangible targets are critical. *Nature Climate Change* **1**, 114–115 (2009).

- [17] Peters, G. P. Beyond carbon budgets. *Nature Geoscience* **11**, 378–380 (2018).
- [18] Intergovernmental Panel on Climate Change. Mitigation Pathways Compatible with 1.5 C in the Context of Sustainable Development. Tech. Rep., United Nations (2018). URL <https://www.ipcc.ch/sr15/chapter/2-0/>.
- [19] European Commission. 2030 climate & energy framework (2014). URL <https://ec.europa.eu/clima/policies/strategies/2030{ }en>.
- [20] Farand, C. Denmark's new government raises climate change to highest priority (2019). URL <https://www.climatechangenews.com/2019/06/26/denmarks-new-government-raises-climate-change-highest-priority/>.
- [21] Bloomberg NEF. World Reaches 1,000GW of Wind and Solar, Keeps Going. URL <https://about.bnef.com/blog/world-reaches-1000gw-wind-solar-keeps-going/>.
- [22] Creutzig, F., Agoston, P., Goldschmidt, J. C., Luderer, G., Nemet, G. & Pietzcker, R. C. The underestimated potential of solar energy to mitigate climate change. *Nature Energy* **2** (2017).
- [23] International Renewable Energy Agency. Renewable Energy Now Accounts for a Third of Global Power Capacity (2019). URL <https://www.irena.org/newsroom/pressreleases/2019/Apr/Renewable-Energy-Now-Accounts-for-a-Third-of-Global-Power-Capacity>.
- [24] Enerdata. Share of wind and solar in electricity production. URL <https://yearbook.enerdata.net/renewables/wind-solar-share-electricity-production.html>.
- [25] Randall, T. Wind and Solar Are Crushing Fossil Fuels (2016). URL <https://www.bloomberg.com/news/articles/2016-04-06/wind-and-solar-are-crushing-fossil-fuels>.
- [26] Searchinger, T. D., Beringer, T., Holtsmark, B., Kammen, D. M., Lambin, E. F., Lucht, W., Raven, P. & van Ypersele, J. P. Europe's renewable energy directive poised to harm global forests. *Nature Communications* **9**, 10–13 (2018).
- [27] Bentsen, N. S. Carbon debt and payback time Lost in the forest? *Renewable and Sustainable Energy Reviews* **73**, 1211–1217 (2017).
- [28] Caro, D., Davis, S. J., Bastianoni, S. & Caldeira, K. *Greenhouse Gas Emissions Due to Meat Production in the Last Fifty Years*, 27–37 (Springer International Publishing, Cham, 2017). URL <https://doi.org/10.1007/978-3-319-32059-5{ }2>.
- [29] Pidcock, R. & Yeo, S. Analysis: Aviation could consume a quarter of 1.5C carbon budget by 2050 (2019). URL <https://www.carbonbrief.org/aviation-consume-quarter-carbon-budget>.
- [30] Larsson, J., Kamb, A., Nässén, J. & Åkerman, J. Measuring greenhouse gas emissions from international air travel of a country's residents: methodological development and application for Sweden. *Environmental Impact Assessment Review* **72**, 137–144 (2018).
- [31] Free Exchange. How to design carbon taxes (2018). URL <https://www.economist.com/finance-and-economics/2018/08/18/how-to-design-carbon-taxes>.
- [32] Bodin, A. H. *Klimakrisens Rødder* (Multivers, Copenhagen, Denmark, 2019).
- [33] Energinet. Electricity Balance (2017). URL <https://www.energidataservice.dk/dataset/electricitybalance>.
- [34] Budischak, C., Sewell, D., Thomson, H., Mach, L., Veron, D. E. & Kempton, W. Cost-minimized combinations of wind power, solar power and electrochemical storage, powering the grid up to 99.9% of the time. *Journal of Power Sources* **225**, 60–74 (2013).

- [35] Sgobbi, A., Nijs, W., De Miglio, R., Chiodi, A., Gargiulo, M. & Thiel, C. How far away is hydrogen? Its role in the medium and long-term decarbonisation of the European energy system. *International Journal of Hydrogen Energy* **41**, 19–35 (2016).
- [36] European Commission. A Clean Planet for all: A European long-term strategic vision for a prosperous, modern, competitive and climate neutral economy. *IN-DEPTH ANALYSIS IN SUPPORT OF THE COMMISSION COMMUNICATION COM (2018) 773* (2018).
- [37] David, A., Mathiesen, B. V., Averfalk, H., Werner, S. & Lund, H. Heat Roadmap Europe: Large-Scale Electric Heat Pumps in District Heating Systems. *Energies* **10**, 578 (2017).
- [38] Cano, Z. P., Banham, D., Ye, S., Hintennach, A., Lu, J., Fowler, M. & Chen, Z. Batteries and fuel cells for emerging electric vehicle markets. *Nature Energy* **3**, 279–289 (2018).
- [39] Thiel, C., Nijs, W., Simoes, S., Schmidt, J., van Zyl, A. & Schmid, E. The impact of the EU car CO₂ regulation on the energy system and the role of electro-mobility to achieve transport decarbonisation. *Energy Policy* **96**, 153–166 (2016).
- [40] Lechtenböhmer, S., Nilsson, L. J., Åhman, M. & Schneider, C. Decarbonising the energy intensive basic materials industry through electrification Implications for future EU electricity demand. *Energy* **115**, 1623–1631 (2016).
- [41] Schmidt, O., Gambhir, A., Staffell, I., Hawkes, A., Nelson, J. & Few, S. Future cost and performance of water electrolysis: An expert elicitation study. *International Journal of Hydrogen Energy* **42**, 30470–30492 (2017).
- [42] Xiang, C., Papadantonakis, K. M. & Lewis, N. S. Principles and implementations of electrolysis systems for water splitting. *Materials Horizons* **3**, 169–173 (2016).
- [43] Bhandari, R., Trudewind, C. A. & Zapp, P. Life cycle assessment of hydrogen production via electrolysis - A review. *Journal of Cleaner Production* **85**, 151–163 (2014).
- [44] Buttler, A. & Spliethoff, H. Current status of water electrolysis for energy storage, grid balancing and sector coupling via power-to-gas and power-to-liquids: A review. *Renewable and Sustainable Energy Reviews* **82**, 2440–2454 (2018).
- [45] Zeng, K. & Zhang, D. Recent progress in alkaline water electrolysis for hydrogen production and applications. *Progress in Energy and Combustion Science* **36**, 307–326 (2010).
- [46] Carmo, M., Fritz, D. L., Mergel, J. & Stolten, D. A comprehensive review on PEM water electrolysis. *International Journal of Hydrogen Energy* **38**, 4901–4934 (2013).
- [47] Babic, U., Suermann, M., Büchi, F. N., Gubler, L. & Schmidt, T. J. Critical Review Identifying Critical Gaps for Polymer Electrolyte Water Electrolysis Development. *Journal of The Electrochemical Society* **164**, F387–F399 (2017).
- [48] Chen, K. & Jiang, S. P. Review - Materials Degradation of Solid Oxide Electrolysis Cells. *Journal of The Electrochemical Society* **163**, F3070–F3083 (2016).
- [49] Debe, M. K. Electrocatalyst approaches and challenges for automotive fuel cells. *Nature* **486**, 43–51 (2012).
- [50] Fishedick, M., Marzinkowski, J., Winzer, P. & Weigel, M. Techno-economic evaluation of innovative steel production technologies. *Journal of Cleaner Production* **84**, 563–580 (2014).
- [51] Corkendorf, I. & Niemantsverdriet, J. W. *Concepts of Modern Catalysis and Kinetics* (2003).

- [52] Majumdar, A., Deutch, J., Bras, R., Benson, S., Carter, E., Ort, D., Ramage, M., Socolow, R., Toone, E., Whitesides, G. & Wrighton, M. Task Force on the RD&D strategy for CO₂ Utilization and/or Negative Emissions at the gigatonne scale. Tech. Rep., Department of Energy (2016). URL <https://www.energy.gov/sites/prod/files/2016/10/f33/9-22-16{ }SEABNuclearPowerTFReportandtransmittal.pdf>.
- [53] Bard, A. J. & Faulkner, L. R. *Electrochemical methods: fundamentals and application* (Wiley, New York, 2001), 2nd edn.
- [54] Scott, S. B. *Investigating the Electrochemical Reduction of Carbon Dioxide using In Situ Mass Spectrometry*. Master's thesis, Technical University of Denmark (2016).
- [55] Lewis, N. S. & Nocera, D. G. Powering the planet: Chemical challenges in solar energy utilization. *PNAS* **104** (2007).
- [56] Chu, S., Cui, Y. & Liu, N. The path towards sustainable energy. *Nature Materials* **16**, 16–22 (2016).
- [57] Seh, Z. W., Kibsgaard, J., Dickens, C. F., Chorkendorff, I., Nørskov, J. K. & Jaramillo, T. F. Combining theory and experiment in electrocatalysis: Insights into materials design. *Science* **355**, 1–12 (2017).
- [58] Nitopi, S. A., Bertheussen, E., Scott, S. B., Liu, X., Albert, K., Horch, S., Seger, B., Stephens, I. E. L., Chan, K., Nørskov, J. K., Jaramillo, T. F. & Chorkendorff, I. Progress and Perspectives of Electrochemical CO₂ Reduction on Copper in Aqueous Electrolyte. *Chemical Reviews* DOI: 10.1021/acs.chemrev.8b00705 (2019).
- [59] Nørskov, J. K., Studt, F., Abild-Pedersen, F. & Bligaard, T. *Fundamental Concepts in Heterogeneous Catalysis* (2014).
- [60] Pfisterer, J. H., Liang, Y., Schneider, O. & Bandarenka, A. S. Direct instrumental identification of catalytically active surface sites. *Nature* **549**, 74–77 (2017).
- [61] Katsounaros, I., Cherevko, S., Zeradjanin, A. R. & Mayrhofer, K. J. Oxygen electrochemistry as a cornerstone for sustainable energy conversion. *Angewandte Chemie - International Edition* **53**, 102–121 (2014).
- [62] Wuttig, A., Liu, C., Peng, Q., Yaguchi, M., Hendon, C. H., Motobayashi, K., Ye, S., Osawa, M. & Surendranath, Y. Tracking a Common Surface-Bound Intermediate during CO₂-to-Fuels Catalysis. *ACS Central Science* **2**, 522–528 (2016).
- [63] Gross, J. H. *Mass spectrometry*, vol. 16 (Springer, Heidelberg, 2000), second edn.
- [64] Harris, D. C. *Quantitative Chemical Analysis* (W. H. Freeman and Company, New York, 2010), eighth edn.
- [65] Griffiths, J. A Brief History of Mass Spectrometry. *Analytical Chemistry* **80**, 5678–5683 (2008).
- [66] Hoch, G. & Kok, B. A mass spectrometer inlet system for sampling gases dissolved in liquid phases. *Arch. Biochem. Biophys.* **101**, 160–170 (1963).
- [67] Bruckenstein, S. & Gadde, R. R. Use of a porous electrode for in situ mass spectrometric determination of volatile electrode reaction products. *Journal of the American Chemical Society* **93**, 1966–1967 (1971).
- [68] Wolter, O. & Heitbaum, J. Differential Electrochemical Mass Spectroscopy (DEMS) - A New Method for the Study of Electrode Processes. *Berichte der Bunsengesellschaft für Phys. Chemie* **6**, 2–6 (1984).

- [69] Wonders, A. H., Housmans, T. H. M., Rosca, V. & Koper, M. T. M. On-line mass spectrometry system for measurements at single-crystal electrodes in hanging meniscus configuration. *Journal of Applied Electrochemistry* **36**, 1215–1221 (2006).
- [70] Henriksen, T. R., Olsen, J. L., Vesborg, P., Chorkendorff, I. & Hansen, O. Highly sensitive silicon microreactor for catalyst testing. *Review of Scientific Instruments* **80** (2009).
- [71] Trimarco, D. B., Pedersen, T., Hansen, O., Chorkendorff, I. & Vesborg, P. C. K. Fast and sensitive method for detecting volatile species in liquids. *Review of Scientific Instruments* **86** (2015).
- [72] Hewlett, R. G. & Anderson, O. E. *The New World: A History of the United States Atomic Energy Commission, Volume I 1939-1946*, (University of California Press, 1962), reissue in edn.
- [73] *The Vacuum Technology Book*, vol. II (Pfeiffer Vacuum GmbH, 2017). [arXiv:1011.1669v3](https://arxiv.org/abs/1011.1669v3).
- [74] Trimarco, D. B. *Real-time detection of sub-monolayer desorption phenomena during electrochemical reactions: Instrument development and applications*. Phd thesis, Technical University of Denmark (2017).
- [75] Baltruschat, H. Differential electrochemical mass spectrometry. *Journal of the American Society for Mass Spectrometry* **15**, 1693–1706 (2004).
- [76] Trimarco, D. B., Vesborg, P. C. K., Pedersen, T., Hansen, O. & Chorkendorff, I. A device for extracting volatile species from a liquid (2016).
- [77] Nørskov, J. K., Bligaard, T., Logadottir, A., Kitchin, J. R., Chen, J. G., Pandelov, S. & Stimming, U. Trends in the Exchange Current for Hydrogen Evolution. *Journal of The Electrochemical Society* **152**, J23 (2005).
- [78] Kemppainen, E., Bodin, A., Sebok, B., Pedersen, T., Seger, B., Mei, B., Bae, D., Vesborg, P. C. K., Halme, J., Hansen, O., Lund, P. D. & Chorkendorff, I. Scalability and feasibility of photoelectrochemical H₂ evolution: the ultimate limit of Pt nanoparticle as an HER catalyst. *Energy Environ. Sci.* **8**, 2991–2999 (2015).
- [79] Tymoczko, J., Calle-Vallejo, F., Schuhmann, W. & Bandarenka, A. S. Making the hydrogen evolution reaction in polymer electrolyte membrane electrolyzers even faster. *Nature Communications* **7**, 10990 (2016).
- [80] Chan, K. & Nørskov, J. K. Electrochemical Barriers Made Simple. *The Journal of Physical Chemistry Letters* 2663–2668 (2015).
- [81] Mayrhofer, K., Arenz, M., Blizanac, B., Stamenkovic, V., Ross, P. & Markovic, N. CO surface electrochemistry on Pt-nanoparticles: A selective review. *Electrochimica Acta* **50**, 5144–5154 (2005).
- [82] Koper, M. T. M., Lai, S. C. S. & Herrero, E. Mechanisms of the Oxidation of Carbon Monoxide and Small Organic Molecules at Metal Electrodes. *Fuel Cell Catalysis* 159–207 (2009).
- [83] Ganassin, A., Sebastian, P., Climent, V., Schuhmann, W., Bandarenka, A. S. & Feliu, J. On the pH Dependence of the Potential of Maximum Entropy of Ir(111) Electrodes. *Scientific Reports* **7**, 1–14 (2017).
- [84] Jensen, K. D. *Electrochemical Insights into Platinum Catalysts for Fuel Cells*. Phd thesis, Technical University of Denmark (2017).

- [85] Jusys, Z., Massong, H. & Baltruschat, H. A New Approach for Simultaneous DEMS and EQCM: Electro-oxidation of Adsorbed CO on Pt and Pt-Ru. *Journal of The Electrochemical Society* **146**, 1093 (1999).
- [86] Clark, E. L., Singh, M. R., Kwon, Y. & Bell, A. T. Differential Electrochemical Mass Spectrometer Cell Design for Online Quantification of Products Produced during Electrochemical Reduction of CO₂. *Analytical Chemistry* **87**, 8013–8020 (2015).
- [87] Pan, J. Y., Hansen, O., Pedersen, T., Vesborg, P., Thilsted, A. & Trimarco, D. *Microchip for Detection of Volatile Gasses in Liquids Supervisors*. Master's thesis, Technical University of Denmark (2018).
- [88] Mallard, P. & Linstrom, W. (eds.) *NIST Chemistry WebBook, NIST Standard Reference Database Number 69* (National Institute of Standards and Technology, Gaithersburg MD, 20899).
- [89] Douglas, D. J. Linear Quadrupoles in Mass Spectrometry. *Mass spectrometry reviews* 937–960 (2009).
- [90] Bodin, A. *Synthesis of Nanoparticle Model Systems for Sustainable Catalysis by Gas Aggregation*. Ph.D. thesis, Technical University of Denmark (2017).
- [91] Mistry, H., Varela, A. S., Bonifacio, C. S., Zegkinoglou, I., Sinev, I., Choi, Y.-W., Kisslinger, K., Stach, E. A., Yang, J. C., Strasser, P. & Cuenya, B. R. Highly selective plasma-activated copper catalysts for carbon dioxide reduction to ethylene. *Nature Communications* **7**, 12123 (2016).
- [92] Gao, D., Zegkinoglou, I., Divins, N. J., Scholten, F., Sinev, I., Grosse, P. & Roldan Cuenya, B. Plasma-Activated Copper Nanocube Catalysts for Efficient Carbon Dioxide Electroreduction to Hydrocarbons and Alcohols. *ACS Nano* **11**, 4825–4831 (2017).
- [93] Eilert, A., Cavalca, F., Roberts, F. S., Osterwalder, J., Liu, C., Favaro, M., Crumlin, E. J., Ogasawara, H., Friebel, D., Pettersson, L. G. M. & Nilsson, A. Subsurface Oxygen in Oxide-Derived Copper Electrocatalysts for Carbon Dioxide Reduction. *The Journal of Physical Chemistry Letters* **8**, 285–290 (2017).
- [94] Hori, Y. Electrochemical CO₂ Reduction on Metal Electrodes. In Vayenas, C., White, R. & Gamboa-Aldeco, M. (eds.) *Modern Aspects of Electrochemistry*, vol. 42, chap. 3, 89–189 (Springer, 2008). URL http://dx.doi.org/10.1007/978-0-387-49489-0_{_}3. arXiv: 1011.1669v3.
- [95] Qiao, J., Liu, Y., Hong, F. & Zhang, J. A review of catalysts for the electroreduction of carbon dioxide to produce low-carbon fuels. *Chemical Society Reviews* **43**, 631–675 (2014).
- [96] Harnung, S. E. & Johnson, M. S. *Chemistry and the Environment* (Cambridge University Press, 2012).
- [97] Taylor, R. E. & Bar-Yosef, O. *Radiocarbon Dating: An Archaeological Perspective* (Routledge, 2014).
- [98] Allegre, C. J. & Sutcliffe, C. *Isotope Geology* (Cambridge University Press, Cambridge, 2008).
- [99] Meselson, M. & Stahl, F. W. The replication of DNA in *Escherichia coli*. *Proceedings of the National Academy of Sciences* **44**, 671–682 (1958).
- [100] Chinchen, G., Denny, P., Parker, D., Spencer, M. & Whan, D. Mechanism of methanol synthesis from CO₂/CO/H₂ mixtures over copper/zinc oxide/alumina catalysts: use of ¹⁴C-labelled reactants. *Applied Catalysis* **30**, 333–338 (1987).

- [101] Studt, F., Behrens, M., Kunkes, E. L., Thomas, N., Zander, S., Tarasov, A., Schumann, J., Frei, E., Varley, J. B., Abild-Pedersen, F., Nørskov, J. K. & Schlögl, R. The Mechanism of CO and CO₂ Hydrogenation to Methanol over Cu-Based Catalysts. *ChemCatChem* **7**, 1105–1111 (2015).
- [102] Andersen, S. Z. *et al.* A rigorous electrochemical ammonia synthesis protocol with quantitative isotope measurements. *Nature* **570**, 504–508 (2019).
- [103] Tsuneto, A., Kudo, A. & Sakata, T. Lithium-mediated electrochemical reduction of high pressure N₂ to NH₃. *Journal of Electroanalytical Chemistry* **367**, 183–188 (1994).
- [104] Chapter 20 - Isotope Separation Methods. In de Groot, P. A. (ed.) *Handbook of Stable Isotope Analytical Techniques*, 1025–1032 (Elsevier, Amsterdam, 2009). URL <http://www.sciencedirect.com/science/article/pii/B9780444511157000206>.
- [105] Dibudak, H., Aksu, E., Eken, M., Gürbüz Güner, S. N. & Karacan, F. Enrichment of Oxygen-18 Isotope By Fractional Distillation. *Turkish Journal of Nuclear Sciences* **30**, 13–23 (2018).
- [106] Agarwal, A. K. Improved Recovery in H₂SH₂O Exchange Process for Increasing Heavy Water Production. *Current Science* **110**, 1910 (2016).
- [107] Trasatti, S. Work function, electronegativity, and electrochemical behaviour of metals III: Electrocatalytic Hydrogen Evolution in Acid Solutions. *Journal of Electroanalytical Chemistry and Interfacial Electrochemistry* **39**, 163–184 (1972).
- [108] Durst, J., Simon, C., Hasché, F. & Gasteiger, H. A. Hydrogen Oxidation and Evolution Reaction Kinetics on Carbon Supported Pt, Ir, Rh, and Pd Electrocatalysts in Acidic Media. *Journal of The Electrochemical Society* **162**, F190–F203 (2015).
- [109] Zalitis, C. M., Kucernak, A. R., Sharman, J. & Wright, E. Design principles for platinum nanoparticles catalysing electrochemical hydrogen evolution and oxidation reactions: edges are much more active than facets. *Journal of Materials Chemistry A* **5**, 23328–23338 (2017).
- [110] Bernasek, S. L. & Somorjai, G. A. Small molecule reactions on stepped single crystal platinum surfaces. *Surface Science* **48**, 204–213 (1975).
- [111] Haynes, W. M., Bruno, T. J. & Lide, D. R. (eds.) *Handbook of Chemistry and Physics, 96th Edition* (CRC Press, 2015), 96 edn.
- [112] Cushman, C. V., Major, G. H., Linford, M. R., Brüner, P., Zakel, J., Grehl, T., Lunt, B. M. & Smith, N. J. Low energy ion scattering (LEIS). A practical introduction to its theory, instrumentation, and applications. *Analytical Methods* **8**, 3419–3439 (2016).
- [113] Geiger, S., Kasian, O., Ledendecker, M., Pizzutilo, E., Mingers, A. M., Fu, W. T., Diaz-Morales, O., Li, Z., Oellers, T., Fruchter, L., Ludwig, A., Mayrhofer, K. J., Koper, M. T. & Cherevko, S. The stability number as a metric for electrocatalyst stability benchmarking. *Nature Catalysis* **1**, 508–515 (2018).
- [114] Frydendal, R., Paoli, E. A., Knudsen, B. P., Wickman, B., Malacrida, P., Stephens, I. E. & Chorkendorff, I. Benchmarking the Stability of Oxygen Evolution Reaction Catalysts: The Importance of Monitoring Mass Losses. *ChemElectroChem* **1**, 2075–2081 (2014).
- [115] Kibsgaard, J. & Chorkendorff, I. Considerations for the scaling-up of water splitting catalysts. *Nature Energy* (2019).
- [116] LeRoy, R. L. Analysis of Time-Variation Effects in Water Electrolyzers. *Journal of The Electrochemical Society* **126**, 1674 (1979).

- [117] Dionigi, F. & Strasser, P. NiFe-Based (Oxy)hydroxide Catalysts for Oxygen Evolution Reaction in Non-Acidic Electrolytes. *Advanced Energy Materials* **6** (2016).
- [118] Reier, T., Nong, H. N., Teschner, D., Schlögl, R. & Strasser, P. Electrocatalytic Oxygen Evolution Reaction in Acidic Environments - Reaction Mechanisms and Catalysts. *Advanced Energy Materials* **7** (2017).
- [119] Pourbaix, M. *Atlas of Electrochemical Equilibria in Aqueous Solutions* (Pergamon Press, Oxford, New York, 1966).
- [120] Miles, M. H. Periodic Variations of Overvoltages for Water Electrolysis in Acid Solutions from Cyclic Voltammetric Studies. *Journal of The Electrochemical Society* **123**, 1459 (2006).
- [121] Vesborg, P. C. & Jaramillo, T. F. Addressing the terawatt challenge: Scalability in the supply of chemical elements for renewable energy. *RSC Advances* **2**, 7933–7947 (2012).
- [122] Trotochaud, L., Young, S. L., Ranney, J. K. & Boettcher, S. W. Nickel-Iron oxyhydroxide oxygen-evolution electrocatalysts: The role of intentional and incidental iron incorporation. *Journal of the American Chemical Society* **136**, 6744–6753 (2014).
- [123] Grimaud, A., Diaz-Morales, O., Han, B., Hong, W. T., Lee, Y.-L., Giordano, L., Stoerzinger, K. A., Koper, M. T. & Shao-Horn, Y. Activating lattice oxygen redox reactions in metal oxides to catalyze oxygen evolution. *Nature Chemistry* 1–6 (2016).
- [124] McCrory, C. C. L., Jung, S., Peters, J. C. & Jaramillo, T. F. Benchmarking Heterogeneous Electrocatalysts for the Oxygen Evolution Reaction. *Journal of the American Chemical Society* **135**, 16977–16987 (2013).
- [125] Lin, Y., Tian, Z., Zhang, L., Ma, J., Jiang, Z., Deibert, B. J., Ge, R. & Chen, L. Chromium-ruthenium oxide solid solution electrocatalyst for highly efficient oxygen evolution reaction in acidic media. *Nature Communications* **10** (2019).
- [126] Batchellor, A. S. & Boettcher, S. W. Pulse-Electrodeposited NiFe (Oxy)hydroxide Oxygen Evolution Electrocatalysts with High Geometric and Intrinsic Activities at Large Mass Loadings. *ACS Catalysis* **5**, 6680–6689 (2015).
- [127] Von Issendorff, B. & Palmer, R. E. A new high transmission infinite range mass selector for cluster and nanoparticle beams. *Review of Scientific Instruments* **70**, 4497–4501 (1999).
- [128] Roy, C., Rao, R. R., Stoerzinger, K. A., Hwang, J., Rossmeisl, J., Chorkendorff, I., Shao-Horn, Y. & Stephens, I. E. Trends in Activity and Dissolution on RuO₂ under Oxygen Evolution Conditions: Particles versus Well-Defined Extended Surfaces. *ACS Energy Letters* **3**, 2045–2051 (2018).
- [129] González, A., Goikolea, E., Barrena, J. A. & Mysyk, R. Review on supercapacitors: Technologies and materials. *Renewable and Sustainable Energy Reviews* **58**, 1189–1206 (2016).
- [130] Yoshida, N., Yamada, Y., Nishimura, S. I., Oba, Y., Ohnuma, M. & Yamada, A. Unveiling the origin of unusual pseudocapacitance of RuO₂ · n H₂O from its hierarchical nanostructure by small-angle x-ray scattering. *Journal of Physical Chemistry C* **117**, 12003–12009 (2013).
- [131] Cherevko, S., Geiger, S., Kasian, O., Kulyk, N., Grote, J.-P., Savan, A., Shrestha, B. R., Merzlikin, S., Breitbach, B., Ludwig, A. & Mayrhofer, K. J. Oxygen and hydrogen evolution reactions on Ru, RuO₂, Ir, and IrO₂ thin film electrodes in acidic and alkaline electrolytes: A comparative study on activity and stability. *Catalysis Today* **262**, 170–180 (2016).

- [132] Rao, R. R. *et al.* Towards identifying the active sites on RuO₂ (110) in catalyzing oxygen evolution. *Energy and Environmental Science* **10**, 2626–2637 (2017).
- [133] Paoli, E. A., Masini, F., Frydendal, R., Deiana, D., Schlaup, C., Malizia, M., Hansen, T. W., Horch, S., Stephens, I. E. L. & Chorkendorff, I. Oxygen evolution on well-characterized mass-selected Ru and RuO₂ nanoparticles. *Chem. Sci.* **6**, 190–196 (2015).
- [134] Shinagawa, T., Garcia-Esparza, A. T. & Takanabe, K. Insight on Tafel slopes from a microkinetic analysis of aqueous electrocatalysis for energy conversion. *Scientific Reports* **5**, 1–21 (2015).
- [135] Man, I. C., Su, H.-Y., Calle-Vallejo, F., Hansen, H. A., Martínez, J. I., Inoglu, N. G., Kitchin, J., Jaramillo, T. F., Nørskov, J. K. & Rossmeisl, J. Universality in Oxygen Evolution Electrocatalysis on Oxide Surfaces. *ChemCatChem* **3**, 1159–1165 (2011).
- [136] Busch, M., Halck, N. B., Kramm, U. I., Siahrostami, S., Krtil, P. & Rossmeisl, J. Beyond the top of the volcano? A unified approach to electrocatalytic oxygen reduction and oxygen evolution. *Nano Energy* **29**, 126–135 (2016).
- [137] Willsau, J., Wolter, O. & Heitbaum, J. In the oxygen evolution reaction on platinum? *Journal of Electroanalytical Chemistry* **195**, 299–306 (1985).
- [138] Wohlfahrt-Mehrens, M. & Heitbaum, J. Oxygen evolution on Ru and RuO₂ electrodes studied using isotope labelling and on-line mass spectrometry. *Journal of Electroanalytical Chemistry* **237**, 251–260 (1987).
- [139] Fierro, S., Nagel, T., Baltruschat, H. & Comninellis, C. Investigation of the oxygen evolution reaction on Ti/IrO₂ electrodes using isotope labelling and on-line mass spectrometry. *Electrochemistry Communications* **9**, 1969–1974 (2007).
- [140] Macounova, K., Makarova, M. & Krtil, P. Oxygen evolution on nanocrystalline RuO₂ and Ru_{0.9}Ni_{0.1}O_{2-δ} electrodes - DEMS approach to reaction mechanism determination. *Electrochemistry Communications* **11**, 1865–1868 (2009).
- [141] Surendranath, Y., Kanan, M. W. & Nocera, D. G. Mechanistic Studies of the Oxygen Evolution Reaction by a Cobalt-Phosphate Catalyst at Neutral pH. *J. Am. Chem. Soc.* **132**, 16501–16509 (2010).
- [142] Diaz-Morales, O., Calle-Vallejo, F., de Munck, C. & Koper, M. T. M. Electrochemical water splitting by gold: evidence for an oxide decomposition mechanism. *Chemical Science* **4**, 2334 (2013).
- [143] Stoerzinger, K. A., Diaz-Morales, O., Kolb, M., Rao, R. R., Frydendal, R., Qiao, L., Wang, X. R., Halck, N. B., Rossmeisl, J., Hansen, H. A., Vegge, T., Stephens, I. E. L., Koper, M. T. M. & Shao-Horn, Y. Orientation-Dependent Oxygen Evolution on RuO₂ without Lattice Exchange. *ACS Energy Letters* **2**, 876–881 (2017).
- [144] Amin, H. M. & Baltruschat, H. How many surface atoms in Co₃O₄ take part in oxygen evolution? Isotope labeling together with differential electrochemical mass spectrometry. *Phys. Chem. Chem. Phys.* **19**, 25527–25536 (2017).
- [145] Roy, C., Sebok, B., Scott, S. B., Fiordaliso, E. M., Sørensen, J. E., Bodin, A., Trimarco, D. B., Damsgaard, C. D., Vesborg, P. C., Hansen, O., Stephens, I. E., Kibsgaard, J. & Chorkendorff, I. Impact of nanoparticle size and lattice oxygen on water oxidation on NiFeOxHy. *Nature Catalysis* **1**, 820–829 (2018).

- [146] Kasian, O., Geiger, S., Stock, P., Polymeros, G., Breitbach, B., Savan, A., Ludwig, A., Cherevko, S. & Mayrhofer, K. J. J. On the Origin of the Improved Ruthenium Stability in RuO₂/IrO₂ Mixed Oxides. *Journal of The Electrochemical Society* **163**, F3099–F3104 (2016).
- [147] Stoerzinger, K. A., Diaz-Morales, O., Kolb, M., Rao, R. R., Frydendal, R., Qiao, L., Wang, X. R., Halck, N. B., Rossmeisl, J., Hansen, H. A., Vegge, T., Stephens, I. E. L., Koper, M. T. M. & Shao-Horn, Y. Orientation-Dependent Oxygen Evolution on RuO₂ without Lattice Exchange. *ACS Energy Letters* **2**, 876–881 (2017).
- [148] Mistry, H., Varela, A. S., Köhl, S., Strasser, P. & Cuenya, B. R. Nanostructured electrocatalysts with tunable activity and selectivity. *Nature Reviews Materials* **1**, 16009 (2016).
- [149] Reske, R., Mistry, H., Behafarid, F., Roldan Cuenya, B. & Strasser, P. Particle size effects in the catalytic electroreduction of CO₂ on Cu nanoparticles. *Journal of the American Chemical Society* **136**, 6978–6986 (2014).
- [150] Hernandez-Fernandez, P., Masini, F., McCarthy, D. N., Strebler, C. E., Friebel, D., Deiana, D., Malacrida, P., Nierhoff, A., Bodin, A., Wise, A. M., Nielsen, J. H., Hansen, T. W., Nilsson, A., Stephens, I. E. L. & Chorkendorff, I. Mass-selected nanoparticles of Pt_xY as model catalysts for oxygen electroreduction. *Nature Chemistry* **6**, 732–738 (2014).
- [151] Doyle, A. D., Bajdich, M. & Vojvodic, A. Theoretical Insights to Bulk Activity Towards Oxygen Evolution in Oxyhydroxides. *Catalysis Letters* **147**, 1533–1539 (2017).
- [152] Friebel, D., Louie, M. W., Bajdich, M., Sanwald, K. E., Cai, Y., Wise, A. M., Cheng, M.-J. J., Sokaras, D., Weng, T.-C. C., Alonso-Mori, R., Davis, R. C., Bargar, J. R., Nørskov, J. K., Nilsson, A. & Bell, A. T. Identification of highly active Fe sites in (Ni,Fe)OOH for electrocatalytic water splitting. *Journal of the American Chemical Society* **137**, 1305–1313 (2015).
- [153] Wehrens-dijksma, M. & Notten, P. H. L. Electrochemical Quartz Microbalance characterization of Ni(OH)₂-based thin film electrodes **51**, 3609–3621 (2006).
- [154] Over, Y. D., Kim, A. P., Seitsonen, S., Wendt, E., Lundgren, M., Schmid, P., Varga, A., Morgante & Ertl, G. Atomic-Scale Structure and Catalytic Reactivity of the RuO₂(110) Surface. *Science* **287**, 1474 (2000).
- [155] Escudero-Escribano, M., Pedersen, A. F., Paoli, E. A., Frydendal, R., Friebel, D., Malacrida, P., Rossmeisl, J., Stephens, I. E. & Chorkendorff, I. Importance of Surface IrO_x in Stabilizing RuO₂ for Oxygen Evolution. *Journal of Physical Chemistry B* **122**, 947–955 (2018).
- [156] Reier, T., Pawolek, Z., Cherevko, S., Bruns, M., Jones, T., Teschner, D., Selve, S., Bergmann, A., Nong, H. N., Schlögl, R., Mayrhofer, K. J. & Strasser, P. Molecular insight in structure and activity of highly efficient, low-Ir Ir-Ni oxide catalysts for electrochemical water splitting (OER). *Journal of the American Chemical Society* **137**, 13031–13040 (2015).
- [157] Seitz, L. C., Dickens, C. F., Nishio, K., Hikita, Y., Montoya, J., Doyle, A., Kirk, C., Vojvodic, A., Hwang, H. Y., Nørskov, J. K. & Jaramillo, T. F. A highly active and stable IrO_x/SrIrO₃ catalyst for the oxygen evolution reaction. *Science* **353**, 1011–1014 (2016).
- [158] Diaz-Morales, O., Raaijman, S., Kortlever, R., Kooyman, P. J., Wezendonk, T., Gascon, J., Fu, W. T. & Koper, M. T. M. Iridium-based double perovskites for efficient water oxidation in acid media. *Nature communications* **7**, 12363 (2016).
- [159] Danish Energy Agency. Key figures - Denmark - 2017. URL <https://ens.dk/en/our-services/statistics-data-key-figures-and-energy-maps/key-figures>.

- [160] Sørensen, S. S. *Analysis of energy storage and flexibility in the Danish future energy system with the Balmorel Energy System Model*. Master's thesis, Technical University of Denmark (2019).
- [161] Jacobson, M. Z., Delucchi, M. A., Cameron, M. A. & Mathiesen, B. V. Matching demand with supply at low cost in 139 countries among 20 world regions with 100% intermittent wind, water, and sunlight (WWS) for all purposes. *Renewable Energy* **123**, 236–248 (2018).
- [162] Meibom, P. & Karlsson, K. Role of hydrogen in future North European power system in 2060. *International Journal of Hydrogen Energy* **35**, 1853–1863 (2010).
- [163] Moro, A. & Lonza, L. Electricity carbon intensity in European Member States: Impacts on GHG emissions of electric vehicles. *Transportation Research Part D: Transport and Environment* **64**, 5–14 (2018).
- [164] European Environment Agency. Overview of electricity production and use in Europe (2018). URL <https://www.eea.europa.eu/data-and-maps/indicators/overview-of-the-electricity-production-2/assessment-4>.